UNIVERSIDAD CARLOS III DE MADRID

TESIS DOCTORAL

Multimode Fibre Broadband Access and Self-Referencing Sensor Networks

Autor:
David Sánchez Montero

Director/es:
Carmen Vázquez García

DEPARTAMENTO DE TECNOLOGÍA ELECTRÓNICA

Leganés, Enero de 2011

TESIS DOCTORAL

MULTIMODE FIBRE BROADBAND ACCESS AND SELF-REFERENCING SENSOR NETWORKS

Autor: David Sánchez Montero

Director/es: Carmen Vázquez García

Firma del Tribunal Calificador:

Firma

Presidente: (Nombre y apellidos)

Vocal: (Nombre y apellidos)

Vocal: (Nombre y apellidos)

Vocal: (Nombre y apellidos)

Secretario: (Nombre y apellidos)

Calificación:

Leganés/Getafe, de de

Agradecimientos

Este trabajo es el fruto de seis años de trabajo y esfuerzo que empezó allá por el mes de Noviembre de 2004. Mediante estas breves notas quisiera agradecer a todas las personas que, directa o indirectamente, han colaborado o me han ayudado a la consecución del mismo.

En primer lugar querría agradecer a mis padres y también dedicarles este trabajo puesto que ellos han sido los que sentaron las primeras bases al proporcionarme la posibilidad de realizar y desarrollar los estudios universitarios previos que deseé. Ellos, además, han sabido inculcarme el espíritu del estudio y del esfuerzo, siempre necesarios para acometer este tipo de proyectos. Por supuesto, también me animaron a salir por primera vez de casa, a vivir en una ciudad distinta y a valerme por mí mismo. Por todo ello, muchísimas gracias¡¡.

A mi novia, Susana, por colmar mis objetivos personales y animarme también a realizar este proyecto, además de infundirme alegría y optimismo en los momentos difíciles habidos durante este trabajo. Su apoyo incondicional también ha sido de muchísima ayuda. También ella se merece que le dedique este trabajo de una manera especial y personal. Muchas gracias a ti también, guapa¡¡.

A mis abuelos Eutimio, Emilia, Luisa y Víctor que, aunque por desgracia ya no están presentes, seguro se alegran y enorgullecen de mí desde donde estén.

Por supuesto, mención especial cabe realizar de la directora de este trabajo, Carmen, por brindarme la posibilidad embarcarme en esta aventura y por apostar y confiar en mí desde el primer momento. También agradecerle todo su trabajo, esfuerzo, orientación y dedicación aportados para este trabajo así como haberme inculcado los conceptos del rigor, la precisión y la responsabilidad científica.

A mis compañeros de piso Gorka y Julius por compartir desde casi seis años tanto mis virtudes como mis defectos. En particular a Julius por su constante ayuda desde la experiencia de realizar el doctorado así como por sus sabios consejos.

Agradezco también la consecución de este trabajo a Juan Carlos (por “minar mi moral” y por su contagioso optimismo), a Pedro (por su permanente disposición a echar una mano en lo que haga falta), a Pablo (por saber escuchar siempre a los demás y sus buenos consejos), a Barrios (por su sentido del humor y sus ganar de ‘liarla’), a Carlos (por estar siempre atento a los problemas que nos afectan y compartir sus valiosas opiniones), a Guillermo (por su exquisito trato y por sus acertadas opiniones), a Julio (por ser una excelente persona), a Dani (por sus ayudas en el terreno “científico, técnico y experimental”) y a Jesús (por su predisposición organizativa para cualquier evento), personas que llegaron prácticamente a la misma vez que yo, a las que considero mucho más que compañeros de trabajo, y que hemos compartido multitud de alegrías y problemas desde nuestra llegada a la Universidad.

Quiero hacer también partícipes de mi agradecimiento a mis amigos de Sevilla, tanto aquéllos del Colegio Calasancio Hispalense como de la Escuela Politécnica Superior de Sevilla, y de Aldeanueva del Camino (Cáceres) por su apoyo y por permitirme compartir tiempo con todos ellos. Sé que se alegran por mí aunque les haya dedicado últimamente menos tiempo del que debiera.

En especial, agradecer a mis compañeros pertenecientes al Grupo de Displays y Aplicaciones Fotónicas (GDAF) que con su sabiduría y experiencia han supuesto un constante apoyo y ayuda para conseguir mis objetivos. Cabe destacar José Manuel Sánchez Pena, corresponsable del grupo de investigación GDAF, el cual ha permitido la compra de equipos o la realización de viajes muy importantes desde el plano científico para mi investigación.

Querría agradecer al resto de compañeros del Departamento de Tecnología Electrónica que con su calidad humana, profesionalidad y buen trato me han ayudado a lo largo de estos años y han servido de ejemplo para mí. Especial mención a Óscar y Marimar en la Secretaría del Departamento por sus gestiones, atención y simpatía.

También querría agradecer a los doctores José Luis Santos y José Manuel Baptista, pertenecientes a INESC-Porto, y por extensión a todos los integrantes del mismo, por su cálida acogida, por la ayuda recibida y por la supervisión de mi trabajo, relativo a la auto-referencia en sensores de fibra óptica, durante mis estancias en 2008 y 2009 en la Unidade de Optoelectrónica e Sistemas Electrónicos en Porto, Portugal.

Quería hacer extensible estos agradecimientos al doctor Joseba Zubia, y a todo su equipo, de la Universidad del País Vasco bajo cuya tutela realicé una estancia en el campus de Bilbao. Agradecerles a todos ellos su predisposición y su amabilidad y sentir, porqué no decirlo, cierta envidia por la maravillosa ciudad en la que desarrollan su magnífica labor científica en el campo de las fibras ópticas de plástico.

Igualmente agradecer a los doctores Kevin Heggarty y Bruno Fracasso por su ayuda y recomendaciones con el inglés científico y con las clases de VPI impartidas y a las que asistí con mucho entusiasmo. También agradecerles el cálido recibimiento otorgado durante mi breve estancia en la École Nationale Supérieure des Télécommunications de Bretagne, Brest, Francia.

Por último, agradecer al doctor Dieter Jäger y al doctorando Ingo Möllers del Zentrum Für Halbleitertechnick und Optoelectronik (ZHO) en Duisburgo, Alemania, por su amabilidad al haberme permitido la posibilidad de realizar medidas en su laboratorio así como su supervisión durante los experimentos.

A todos ellos mi mayor reconocimiento y gratitud.

CONTENTS

List of Figures

List of Tables

Acronyms list / Lista de Acrónimos

Acronym (Acrónimo)	English Term (Término en Inglés)	Spanish Term (Término en Castellano)
ADSL	Asymmetric Digital Subscriber Line	Línea de Suscripción Digital Asimétrica
AM	Amplitude Modulation	Modulación en Amplitud
ANT	Access Network Termination	Terminación de Red de Acceso
AOM	Acousto-Optic Modulator	Modulador Acustoóptico
AP	Access Point	Punto de Acceso
ATM	Asynchronous Transfer Mode	Modo de Transferencia Asíncrona
AWG	Arrayed Waveguide Grating	Red de Difracción de Guía Ondas Distribuida
BEN	Benzyl Benzoate	Benzoato de Benzol/Benceno
BER	Bit Error Rate	Tasa de Error de Bit
B-ISDN	Broadband Integrated Services Digital Network	Red Digital de Servicios Integrados (RDSI) de Banda Ancha
BLS	Broadband Light Source	Fuente de Luz de Amplio Espectro
BPM	Beam Propagation Method	Método por Propagaciónde Rayos
BPSK	Binary Phase-shift Keying	Modulación Binaria por Desplazamiento de fase
CATV	Community Antenna TeleVision	Televisión por Antena Común
CDM	Code Division Multiplexing	Multiplexación por División de Código
CDN	Content Distribution Network	Red de Distribución de Contenidos
CM	Coherence Multiplexing	Multiplexación por Coherencia
CNR	Carrier-to-Noise Ratio	Relación Señal Portadora-Ruido
CO	Central Office	Oficina Central
CPE	Customer Premises Equipment	Equipo Local del Cliente
CS	Control Station	Estación de Control
CSE	Carrier Suppression Effect	Efecto de Supresión de Portadora
CW	Continouos Wave	Onda Continua
CWDM	Coarse Wavelength Division Multiplexing	Multiplexación Vasta en Longitud de Onda
DFB	Distributed FeedBack	Realimentación Distribuida
DMA	Differential Mode Attenuation	Atenuación Modal Diferencial
DMD	Differential Mode Delay	Retardo Modal Diferencial
DP	Diphenyl	Difenil
DPSO	Diphenyl Sufoxide	Difenil Sulfóxido
DSB	Double SideBand	Banda Lateral Doble
DSP	Digital Signal Processing	Procesado Digital de Señales
DTFT	Discrete-Time Fourier Transform	Transformada de Fourier Discreta en el Tiempo
DVB	Digital Video Broadcasting	Difusión de Video Digital Terrestre

DWDM	Dense Wavelength Division Multiplexing	Multiplexación en Longitud de Onda Densa
EDFA	Erbium Doped Fibre Amplifier	Amplificador de Fibra Dopada con Erbio
EMD	Equilibrium Mode Distribution	Distribución Modal Equilibrada
EMI	Electro-Magnetic Interference	Interferencia Electro-Magnética
E/O	Electro-Optic	Electro-Óptico
EPON	Ethernet Passive Optical Network	Red Óptica Pasiva con protocolo Ethernet
FBG	Fiber Bragg Grating	Red de Bragg en fibra
FC	Fibre Connector	Conector de Fibra
FDDI	Fibre Distributed Data Interface	Interfaz de Datos Distribuida por Fibra
FDM	Frequency Division Multiplexing	Multiplexación por División en Frecuencia
FDTD	Finite Difference Time Domain Method	Método de las Diferencias Finitas en el Domnio del Tiempo
FEM	Finite Element Method	Método de Elementos Finitos
FIR	Finite Impulse Response	Respuesta al Impulso Finita
FM	Frequency Modulation	Modulación en Frecuencia / Frecuencia Modulada
FOS	Fibre-Optic Sensor	Sensor de Fibra Óptica
F-P	Fabry-Perot	Fabry-Perot
FSR	Free Spectral Range	Rango Espectral Libre
FTTB	Fiber To The Building	Fibra hasta el Edificio
FTTC	Fiber To The Curb	Fibra hasta la Acera
FTTH	Fiber To The Home	Fibra hasta el Hogar
GbE	Gigabit- Ethernet	Gigabit- Ethernet
Gbps	Gigabits per second	Gigabits por segundo
GDAF	Displays and Photonics Applications Group	Grupo de Displays y Aplicaciones Fotónicas
GHz	GigaHertz	GigaHercio
GI	Graded-Index	Índice Gradual
GIPOF	Graded-Index Polymer Optical Fibre	Fibra Óptica de Plástico de Índice Gradual
GOF	Glass Optical Fibre	Fibra Óptica de Vidrio/Sílice
GPON	Gigabit-capable Passive Optical Network	Red Óptica Pasiva con capacidad de Gigabit
GPRS	Global Packet Radio Service	Servicio General de Paquetes Vía Radio
GSM	Global System for Mobile Communications	Sistema Global para las Comunicaciones Móviles
HDTV	High-Definiton TeleVision	Televisión de Alta Definición
HG	Home Gateway	Puerta de Acceso al Hogar
IEC	International Electrotechnical Comission	Comisión Internacional Electrotécnica
IEEE	Institute of Electrical and Electronics Engineers	Instituto de Ingenieros Eléctricos y Electrónicos
IIR	Infinite Impulse Response	Respuesta al Impulso Infinita

IM	Intensity Modulator	Modulador en Intensidad
IMT2000	International Mobile Telecommunications-2000	Telecomunicaciones Móviles Internacionales-2000
INESC-Porto	National Institute of Engineering and Computer Systems of Porto	Instituto Nacional de Ingeniería y Sistemas Informáticos deOporto
IPTV	Internet Protocol TeleVision	Televisión por Internet
IR	InfraRed	Infrarojo
ISI	Inter-Symbol Interference	Interferencia entre Símbolos
ISO	International Organization for Standardization	Organización Internacional de Estandarización
ITU	International Telecommunication Union	Unión Internacional de Telecomunicaciones (UIT)
ITU-T	ITU Telecommunication Standardization Sector	Sector de Estandarización de las Telecomunicaciones de la UIT
LAN	Local Area Network	Red de Área Local
LASER	Light Amplification by Stimulated Emission of Radiation	Láser
LCA	Lightwave Component Analyzer	Analizador de Redes Óptico
LD	Laser Diode	Diodo Láser
LED	Light Emitting Diode	Diodo Emisor de Luz
LTE	Long Term Evolution	Evolución de la norma 3G de Comunicaciones Móviles
MC	Mode coupling	Acoplamiento Modal
MEMS	Microelectromechanical Systems	Sistemas Microelectromecánicos
MGDM	Mode Group Diversity Multiplexing	Multiplexación por Diversidad de Grupos Modales
MHz	MegaHertz	MegaHercio
MIMO	Multiple Input Multiple Output	Múltiple Entrada Múltiple Salida
MMF	MultiMode Fibre	Fibra Multimodo
MZ	Mach-Zehnder	Mach-Zehnder
MZI	Mach-Zehnder Interferometer	Interferómetro Mach-Zehnder
MZM	Mach-Zehnder Modulator	Modulador Mach-Zehnder
NA	Numerical Aperture	Apertura Numérica
NGA	Next-Generation Access	Acceso de Nueva Generación
OADM	Optical Add-Drop Mutitplexer	Multiplexor Óptico de Inserción-Extracción
OFL	OverFilled Launch	Excitación Completa de Modos
OFDM	Orthogonal Frequency Division Multiplexing	Multiplexación por División de Frecuencias Ortogonales
OFM	Optical Frequency Multiplication	Multiplicación Óptica en Frecuencia
ODN	Optical Distribution Network	Red Óptica de Distribución
OLT	Optical Line Termination	Terminación de Línea Óptica
ONT	Optical Network Terminal	Terminal de Red Óptica
OSA[1]	Optical Society of America	Sociedad de Óptica de América
OSA[2]	Optical Spectrum Analyzer	Analizador de Espectros Ópticos

[1] from Chapter 2
[2] from Chapter 5

OTDR	Optical Time Domain Reflectometer	Reflectómetro Óptico en el Dominio del Tiempo
P2P	Peer to Peer	Igual a igual / Punto a punto
PAN	Personal Area Network	Red de Área Personal
PC[3]	Personal Computer	Ordenador Personal
PC[4]	Physical Contact	Contacto Físico
PD	PhotoDetector	Fotodetector
PDM	Polarization Division Multiplexing	Multiplexación por División de la Polarización
PF-GIPOF	Perfluorinated GIPOF	Fibra GIPOF Perfluorinada
PLC	Power Line Communications	Comunicaciones mediate Cable Eléctrico
PMMA	Polymethylmethacrylate	Polimetilmetacrilato
POF	Polymer Optical Fibre	Fibra Óptica de Plástico
PON	Passive Optical Network	Red Óptica Pasiva
PVDF	Polyvinylidene Fluoride	Polivinilidenofluoruro
QoS	Quality of Service	Calidad del Servicio
RAP	Remote Access Point	Punto de Acceso Remoto
RF	Radio-Frequency	Radiofrecuencia
RFID	Radio Frequency IDentification	Indentificación por Radiofrecuencia
RH	Relative Humidity	Humedad Relativa
ROC	Region Of Convergence	Región de Convergencia
RoF	Radio-over-Fibre	Radio sobre Fibra
RoMMF	Radio-over-Multimode-Fibre	Radio sobre Fibra Multimodo
RML	Restricted Mode Launch	Excitación Restrictiva en Modos
RR	Ring Resonator	Resonador en Anillo / Anillo Resonante
SCM	Sub-Carrier Multiplexing	Multiplexación por Subportadora
SDH	Synchronous Digital Hierarchy	Jerarquía Digital Síncrona
SDM	Space Division Multiplexing	Multiplexación por División Espacial
SI	Step Index	Salto de Índice
SLED Fiber Source	Super-Luminiscent Erbium-Doped Fiber Source	Fuente Luminosa Superluminiscente de Fibra dopada con Erbio
SMF	SingleMode Fibre	Fibra Monomodo
SNR	Signal to Noise Ratio	Relación Señal-Ruido
SSB	Single SideBand	Banda Lateral Única
TDM	Time Division Multiplexing	Multiplexación por División en Tiempo
TIA	Telecommunications Industry Association	Asociación de la Industria de Telecomunicaciones
UFL	UnderFilled Launch	Excitación Incompleta de Modos
UMD	Uniform Mode Distribution	Distribución Uniforme de Modos
UMTS	Universal Mobile	Sistema Universal de

[3] from Chapter 2
[4] from Chapter 3

	Telecommunications System	Telecomunicaciones Móviles
UTP	Unshielded Twisted Pair	Par Trenzado no Apantallado
UWB	Ultra Wide Band	Banda Ultraancha
VCSEL	Vertical Cavity Surface Emitting Laser	Diodo Láser de Emisión Superficial con Cavidad Vertical
VDSL	Very high bit-rate Digital Subscriber Line	Línea de Suscripción Digital de muy alta tasa de transferencia
VOA	Variable Optical Attenuator	Atenuador Óptico Variable
VoD	Video on Demand	Video bajo Demanda
VoIP	Voice over Internet Protocol	Voz sobre IP
WAN	Wide Area Network	Red de Área Amplia
WDM	Wavelength Division Multiplexing	Multiplexación en Longitud de Onda
WiMAX	Worldwide Interoperability for Microwave Access	Interoperabilidad Mundial para Acceso por Microondas
WKB	Wentzel-Kramers-Brillouin	Wentzel-Kramers-Brillouin
x-DSL	Digital Subscriber Line	Línea de Suscripción Digital

Chapter 1

INTRODUCTION

1.1 Motivation of this Work

Growing research interests are focused on the high-speed telecommunications and data communications networks with increasing demand for accessing to the Internet even from home. This increasing demand for high-speed information transmission has been driven by the huge successes during the last decade of new multimedia services such as Internet Protocol Television (IPTV) or Video on Demand (VoD), as well as an increased data traffic driven by High-Definition TV (HDTV) and Peer-to-Peer (P2P) applications which have changed people's habits and their demands for service delivery. Consequently, consumer adoption of broadband access to facilitate use of the Internet for knowledge, commerce and, obviously, entertainment is contingent with the increment of the optical broadband access network capacity. Recent interests are focused on gigabit-order data transmission such as the Gigabit Ethernet system and, therefore, it is desirable to introduce optical fibre networks even to the customer's premises for covering more than 10Gbps.

Related to this latter premise, a growing number of service providers are turning to solutions capable of exploiting the full potential of optical fibre for service delivery, being the copper based x-Digital Subscriber Line (xDSL) infrastructure progressively replaced by a fibre-based outside plant with thousands of optical ports and optical fibre branches towards residential and business users, constituting the core of the FTTx (Fibre to the Home/Node/Curb/Business) deployments. These include passive optical networks (PONs), whose standardization has accelerated product availability and deployment. The ongoing evolution to deliver Gigabit per second Ethernet and the growing trend to migrate to Wavelength Division Multiplexing (WDM) schemes have benefited significantly from the Coarse WDM (CWDM) and Dense WDM (DWDM) optoelectronics technologies, as they provide a more efficient way to deliver traffic to Customer Premises Equipment (CPE) devices. These systems, commonly referred to as WDM-PON, are still under standardization process and field trials and are the basis of the so-called next-generation broadband optical access networks to prepare for the future upgrade of the FTTx systems currently being deployed. There is a widely-spread consensus concerning service providers that FTTx is the most powerful and future-proof access network architecture for providing broadband services to residential users.

In the FTTx system concepts deployed up to now, singlemode optical fibre is used, which has a tremendous bandwidth and thus a huge transport capacity for many services such as

the ITU G.983.x ATM[1]-PON system. Research is ongoing to further extend the capabilities of shared singlemode fibre access networks. The installation of singlemode fibre has now conquered the core and metropolitan area networks and is subsequently penetrating into the access networks. However, it requires great care, delicate high-precision equipment, and highly-skilled personnel, being mainly deployed for long-haul fibre optic communications, constituting the so-called Optical Distribution Network (ODN) and the core telecommunication network of the next generation of optical broadband access networks. Nevertheless, as it comes closer to the end user and his residential area, the costs of installing and maintaining the fibre network become a driving factor, which seriously hampers the large-scale introduction of FTTx.

In contrast, multimode optical fibre (MMF) provides a cost-reducing alternative for the commonly used singlemode fibre. Multimode fibre is easier to install than singlemode fibre. Due to larger core diameter of multimode fibre, the coupling of light from a light source into the fibre and the (fixed or demountable) splicing of fibres together is easier, allowing less delicate splicing equipment and less requirements on the skills of the installation personnel. In particular, in the access network, this may yield a considerable reduction of installation costs although the bandwidth-times length product of singlemode fibre is significantly higher than that of multimode fibre. As in the access network, the fibre link lengths are less than 10km, however, the bandwidth of presently commercially available silica multimode fibres is quite sufficient.

Also inside the customer's premises, there is a growing need for convergence of the multitude of communication networks. Presently, unshielded twisted copper pair (UTP) cables are used for voice telephony, cat-5 UTP cables for high-speed data, coaxial cables for CATV[2] and FM[3] radio signals distribution, wireless Local Area Network (LAN) for high-speed data, FireWire for high-speed short-range signals, and also power lines for control signals and lower-speed data. These different networks are each dedicated and optimised for a particular set of services. Also no cooperation between the networks exists. It is therefore not easy to upgrade services, to introduce new ones, nor to create links between services (e.g., between video and data). By establishing a common broadband in-house network infrastructure, in which a variety of services can be integrated, however, these difficulties can be surmounted. These transmission media used at present are not suited for provisioning high-bandwidth services at low cost. For instance, today's wiring in local area networks (LANs) is based mainly on copper cables (twisted pair or coaxial) and silica (glass) fibre of two kinds: singlemode and multimode. Copper based technologies suffer strong susceptibility to electromagnetic interferences and have limited capacity for digital transmission as well as the presence of crosstalk. Compared to these copper based technologies, optical fibre has smaller volume, it is less bulky and has a smaller weight. In comparison with data transmission capability, optical fibre offers higher bandwidth at longer transmission distances. However, conventional singlemode silica based fibres are a costly solution because they require precise connecting and delicate installation and handling. An alternative technology is then the use of conventional multimode fibre (both

[1] ATM: Asynchronous Transfer Mode
[2] CATV: Community Antenna TeleVision
[3] FM: Frequency Modulation

silica and polymer) with larger core diameters. This fact allows for large tolerance on axial misalignments, which results in cheaper connectors as well as associated equipment, but with a bandwidth penalty with regards to their singlemode counterparts, mainly due to the introduction of modal dispersion. Multimode silica fibre is commonly applied to short-reach and medium-reach applications due to its low intrinsic attenuation. On the other hand, compared to multimode silica optical fibre, polymer optical fibre (POF) offers several advantages over conventional multimode optical fibre over short distances (ranging from 100m to 1000m) such as the even potential lower cost associated with its easiness of installation, splicing and connecting. This is due to the fact that POF is more flexible and ductile, making it easier to handle. Consequently, POF termination can be realized faster and cheaper than in the case of multimode silica fibre. This POF technology could be used for data transmission in many applications areas ranging like in-home and access networks, fibre to the apartment, wireless LAN backbone or office LAN among others.

Improvement in the bandwidth of POF fibre can be obtained by grading the refractive index, thus introducing the so-called Graded-Index POFs (GIPOFs). Although by grading the index profile significantly enhanced characteristics have been obtained, the bandwidth and attenuation still limit the transmission distances and capacity. Reduction of loss has been achieved by using amorphous perfluorinated polymers for the core material. This new type of POF has been named perfluorinated GIPOF (PF GIPOF). This new fibre with low attenuation and large bandwidth has opened the way for high capacity transmission over POF based systems. In addition to, as perfluorinated polymer fibre has a relative low loss wavelength region ranging from 650nm to 1300nm (even theoretically in the third transmission window), it allows for WDM transmission of several data channels. However, attenuation and bandwidth characteristics of the current state-of-the-art PF GIPOF are not at par with those of standard singlemode silica fibres, but they still are superior to those of copper based technologies. Nevertheless, although these losses are coming down steadily due to ongoing improvements in the production processes of this still young technology, link lengths for in-building/home scenarios are short (less than 1 km), and thus the loss per unit length is of less importance. It should be noted that available light sources for silica fibre based systems can be used with PF GIPOF systems. The same is true of connectors as in the case of Gigabit Ethernet equipment.

Therefore, it can be stated that polymer optical fibre technology has reached a level of development where it can successfully replace copper based technology and multimode glass fibre for data transmission in short distance link applications such as in the office, in-home and LAN scenarios. Transmission of 10Gbps data over 100m and transmission of 1.25Gbps Ethernet over 1 km have been experimentally demonstrated. Perfluorinated graded index polymer fibre is forecasted to be able to support bit-rate distance products in the order of 10Gbps·km. Short distance communications system like in-home network and office LANs represent a unique opportunity for deployment of PF GIPOF based systems for broadband applications. We can conclude that PF GIPOF technology is experiencing rapid development towards a mature solution for data transmission at short haul communications. The challenge remains in bringing this POF technology (transceiver, connectors,…) to a competitive price and performance level at the customer’s premises. The belief is that a better understanding of the factors that affect the fibre bandwidth will prove very useful in increasing the bandwidth of POF links in real situations.

On the other hand, although multimode fibre (both silica and polymer counterparts) is easier to install, its bandwidth is still significantly lower than that of singlemode fibre, as abovementioned. This limited bandwidth hampers the desired integration of multiple broadband services into a common multimode fibre access or in-building/home network. Overcoming the bandwidth limitation of such fibres requires the development of techniques oriented to extend the capabilities of multimode fibre networks, including those based both on silica and polymer optical fibres, to attend the consumer's demand for multimedia services. It would be also quite advantageous to introduce multiplexing methods for combining more service groups on the multimode fibre infrastructure. Techniques such as mode group diversity multiplexing, optical frequency multiplication, orthogonal frequency division multiplexing, subcarrier multiplexing or wavelength division multiplexing have been reported so far in literature. In addition to, as cost is a key issue in local and residential networks, cheap coarse wavelength multiplexing techniques are an interesting option and can also benefit from the lower PF GIPOF fibre attenuation in the 800-1300nm range. In addition, it should be noted that some of these techniques provide the possibility of short-reach transmission in Radio-over-Fibre (RoF) applications, such as in-building/home transmission of microwave signals, and wireless access systems. It is worth mentioning that there is not the desire of making a competition between optical and wireless solutions, since wireless is and will always be present inside the building or home. In contrast, research and development are focusing on the coexistence of both technologies.

The potentials of these multimode fibres to support broadband radio-frequency, microwave and even millimetre wave transmission over short, intermediate and long distances are yet to be fully known. It has been widely reported that the frequency characteristics of the fibre should show significant high-frequency components, i.e. higher-frequency transmission lobes are expected in the fibre frequency response. These higher-frequency transmission lobes allow to transport information signals by modulating them on specific carrier frequencies. These modulated carriers can be positioned in such a way that they will optimally fit into the higher-frequency transmission lobes of the multimode fibre link and each of the multiple subcarriers may constitute an independent transmission channel on the multimode fibre, which allows to integrate various groups of services independently in a single FTTx infrastructure. Furthermore, it has been stated that the contrast ratio between these resonances and the secondary-side lobes reveals a dramatically reduction as the frequency increases thus providing potential for broadband transmission at even higher frequencies than those determined by the transmission lobes.

The position of these higher-frequency lobes depends on the fibre link length, and on the exact fibre characteristics, which may vary due to external circumstances such as induced stress by bending or environmental temperature variations. Any system that would take advantage of such high-frequency transmission lobes would have to adapt to those variations, e.g. monitoring the fibre link frequency response by injecting some weak pilot tones, and allocating the subcarriers accordingly would be a feasible solution. Anyway, this in turn is contingent on the availability of accurate models to describe the microwave radio signals propagation over multimode fibres both silica- and polymer-based. With such a predictive tool, notwithstanding its restricted bandwidth, a single multimode fibre network that may carry a multitude of broadband services using the higher-order transmission lobes would become more feasible. Thus, easy-to-install multimode fibre networks for access and

in-building/home can be realised in which wirebound and wireless services were efficiently integrated.

In this framework, the first part of this work, which comprises chapter 3 and chapter 4 respectively, focuses on the description and experimental validation of both types of multimode fibres, the silica-based fibre and graded-index polymer optical (GIPOFs) counterparts with an extensive set of measurementts. Like any communication channel, a multimode optical fibre channel also suffers from various signal distortions limiting its usefulness. The primary mechanisms contributing to the channel impairment in MMFs are discussed. Silica-based MMF and PF GIPOF both are essentially large-core optical waveguide supporting multiple transverse electromagnetic modes and they suffer from similar channel impairments. In this first part of the work, the primary challenges related to both types of MMF channels are examined. Although some of these issues are interrelated, they are separately identified for clarity. In each chapter, first the origin of the problem is briefly described and then its specific impact on PF GIPOF and silica-based MMF is elaborated.

The models described within these two chapters, and developed elsewhere, try to solve the factors that can have a large impact on the data rate transmission performance thus providing a full description of the dispersion in such fibres, as well as incorporating all possible parameters involved in the determination of the frequency response and the total bandwidth. Theoretical simulations and measurements have been carried out for a standard silica-based multimode optical fibre as well as for a perfluorinated (PF) GIPOF. Being the latter the most promising candidate for in-building/home and local area networks or the so-called ‘last mile’, referred to as the final leg of delivering connectivity of the FTTx broadband access network, it is also worth mentioning that the majority of the installed in-building fibre (approximately between an 85% and a 90%) consists of silica-based 62.5/125μm multimode fibre, as recommended by the ISO/IEC 802.11 standard. So, there is recently an important drive to utilize this existing infrastructure to support the ever increasing capacity demand on high-speed services. Consequently, some of the key factors affecting the frequency characteristics of this fibre type have been also addressed and studied.

On the other hand and concurrent with the above discussion, the principal stimulus for the optical fibre-sensing technology is communications. And the number of fibre-optic sensors (FOS) products can be expected to grow tremendously in the years to come as rapid progress continues to be made in the related optoelectronics and communication fields thanks to the development of the next generation of optical broadband access networks. Consequently, fibre sensors rely on communication technology to provide a basic component set and also to facilitate specialist technologies through which slightly different versions of optical fibres can be fabricated purely for the sensing community. Furthermore, the increasing access networking feasibility as well as the growing demand in buildings, homes and residential areas of services such as fully automation, control and sensing can enhance the integration of fibre-optic sensor applications and systems for a final convergence within a fully ‘optical domain’ of the access network. While these applications do not depend on high data rates, the reliability of the network will be of utmost importance and optical fibre sensors can meet the requirements of such a converged infrastructure.

There are numerous realizations of fibre-optic sensors but one extensively investigated transducing mechanism in optical sensing applications is the intensity modulation of the propagating light. Approaching simple configurations, intensity sensors modulate the optical power loss as the physical magnitude changes, thus providing the measurement as an optical intensity modulation signal. These intrinsically safe intensity-based FOS can measure a wide variety of physical magnitudes such as temperature, pressure, humidity or displacement and optical fibre applications such as remote optical sensing, biosensors, civil engineering, military applications and satellite communications can be developed. Despite their attractiveness since they are reliable, small-sized and cost-effective sensing approach, intensity-based fibre-optic sensors have a series of limitations imposed by variable losses in the system that are not related to the environmental effect to be measured. Potential error sources include variable losses due to connectors and splices, microbending loss, macrobending loss and mechanical creep and misalignment of light sources and detectors.

Consequently, intensity sensors, especially in remote configurations, need a self-referencing method to minimize the influences of long-term aging of source and receptor characteristics, as well as undesirable random short-term fluctuations of optical power loss in the fibre link connecting the central office (CO), where the measurements are taken, to the remote sensing points, where the optical sensors are located. Different self-referencing approaches, such as fibre bypassing and time/frequency/wavelength normalization have been reported in the last two decades, providing mechanisms whereby the intensity variation of the light at the sensing head may be distinguished and measured independently of all undesirable perturbations. In the case of frequency-based self-referencing methods, radio-frequency (RF) modulated Fabry-Perot (FP), Mach-Zehnder (MZ), Michelson and Ring Resonators (RR) incoherent configurations have been reported as well as new optical configurations based on fibre delay lines and Fibre Bragg Gratings (FBGs).

On the other hand, the capability to passively multiplex a number of sensors on a limited number of fibre leads is a desirable feature of sensor systems from the standpoint of reducing system costs. Passively multiplexing fibre optic sensors maintains the passive nature of the fibre optic sensor and permits totally passive networks of fibre optic sensors to be built. Generic multiplexing approaches based on time, frequency and wavelength-based techniques have been developed and implemented. In many cases, these approaches are analogues to the multiplexing schemes developed for optical fibre communications systems, and consequently can take advantage of many of the fibre-based modulators, frequency shifters and wavelength combiners and splitters developed for communications in order to implement the sensor network. Moreover, fibre optic intensity sensors can be easily integrated in wavelength-division-multiplexed (WDM) networks. Fibre Bragg Gratings (FBGs) are used in WDM sensor networks for remotely addressing multiple points providing an effective and compact strategy for exploiting fibre links for both propagating directions of the light with a single fibre lead.

The second part of this work, comprising chapter 5 and chapter 6, focuses on the development of multiplexing and measurement techniques for optical-fibre intensity-based sensors. These optical fibre sensors can be easily integrated into the optical FTTx networks constituting the final leg of delivering connectivity from the service providers to the

consumers or namely the 'last-mile'. A CWDM network operating in reflective configuration for multiplexing remote radio-frequency (RF) self-referencing fibre-optic intensity sensors is analyzed and experimentally investigated. In the described approach, the use of Fibre Bragg Gratings as spectral selective mirrors allows to implement delay lines in the electrical domain, achieving more compact sensor-heads and easy-reconfigurable sensing points. Two measurement parameters for the sensing heads are defined and comparatively studied in terms of design parameters, linearity, sensitivity and resolution. The proposed sensor configuration is modeled following the Z-transform formalism, which permits an easy analysis of the system frequency response. Experimental results are presented, showing the characterization of the network performance for a correct desired point of operation.

Finally, considering the next-generation broadband optical access network scenario, a low-cost monitoring system for measuring the optical power losses of drop fibres in Wavelength Division Multiplexing (WDM) Passive Optical Networks (PON) is proposed. It is based on radio-frequency (RF) intensity modulation and Fibre Bragg Grating (FBG) self-referencing measurement techniques using amplitude normalization. Actually, WDM-PON schemes are very recently being adopted by some operators for provisioning telephone, high-definition television and high-speed internet access (triple-pay service) as aforementioned and constitute the basis of the future upgrade of the FTTx systems currently being deployed.

The work comprised in this document has been developed in the framework of the activities carried out in the Displays and Photonics Applications group (GDAF) at University Carlos III de Madrid.

1.2 Outline of the Thesis

Future Internet Access technologies are supposed to bring us a very performing connection to the main door of our homes. At the same tine, new services and devices and their increase use will require data transfers at speeds exceeding 1Gbps inside the building or home at the horizon 2012. Both drivers lead to the deployment of a high-quality, future-proof network inside buildings and homes. This environment may end up taking advantage of optical cabling solutions as an alternative to more traditional copper or pure wireless approaches. Related to this latter fact, the objectives of this work are:

- The achievement of a full convergence scenario between optical networks from the telecommunication services providers to the end users underscores the necessity of accurate and realistic fibre models in assessing the performance of broadband access networks with the premises of high-capacity and total compatibility. Silica-based MMFs and PF GIPOFs are the most promising candidates for such a convergence within the in-building/home scenario. Contributions to a better understanding of the possibilities of signal transmission outside the baseband of such fibres are investigated, in order to extend their capabilities, together with the evaluation of current fibre frequency response theoretical models by means of an extensive set of measurements.

- The achievement of a full convergence scenario between optical networks from the telecommunication services providers to the end users is also contingent on research and development in the field of optical fibre sensors, mainly driven by the growing demand of fully building/home and industry automation, leading to a reliable integration of the optical networks. Related to this, development of multiplexing and measurement techniques for fibre-optic intensity-based sensors are analyzed and experimentally investigated. In the sensor network topology proposed, by replacing the fibre delay line with an electronic delay in the reception stage, it is possible to avoid long fibre delay coils in the remote sensing points and achieving a compact, flexible and re-configurable self-referencing technique. Applications in both scenarios can be considered, on the one hand the in-building/home network and on the other hand the WDM-PON access network topology through which operators provision the different services.

The remaining part of this work is divided into seven chapters and organized as follows:

- In Chapter 2 of this document, the perspective of a convergence to a full optical next-generation access networks is analyzed. Present and future data-rate users' demand are presented, yielding to an optical domain for the access networks currently being deployed. In which, silica-based multimode fibres and graded-index polymer optical fibres appear to be the solution for short- and medium-reach optical networks, for the future bandwidth requirements with the most cost savings. In addition to, FTTx deployments with WDM-PON topologies are considered in the long-term the target architecture for the next-generation access networks. Such a convergence would also include the sensing and control applications which are gained more and more interest in the home scenario and optical fibre sensors can also benefit to get a total compatible access network system. Because of that a representative example of a fibre-optic intensity sensor, intrisically with self-referencing property, for in-building/home applications is presented demonstrating the capabilities of optical fibres for a full convergence access network scenario. In addition, a brief state-of-the-art of the different self-referencing techniques for optical intensity sensors is reported including basic guidelines for their deployment.

- A detailed description of the theoretical model concerning graded-index polymer optical fibres (PF GIPOFs) reported elsewhere is presented in Chapter 3 of this document. The influence of most paremeters that modify the frequency response in such fibres is addressed by means of a huge set of theoretical simulations. In adittion to, the frequency response and the 3-dB bandwidth value of different transmission lengths of commercially available PF GIPOFs with different core diameters is measured at two different launching conditions. The long-term stability and the temperature dependence of such optical fibre link has also been addressed.

- On the other hand, considering the deployment of silica-based multimode optical fibres within broadband optical access networks, the theoretical model reported elsewhere has also been evaluated and the conditions upon which broadband

transmission is possible in RF regions far from baseband have been studied. Both issues have been addressed in Chapter 4 of this document. In addition to, thermal effects on the silica-based MMF frequency response have been studied demonstrating their influence on the high-order resonances.

- In Chapter 5, a brief state-of-the-art of the radio frequency-based approach for self-referencing is further described, achieving remote, all-optical and colorless self-referencing approaches both in transmission and reflective configurations. Moreover, RF-based reflective configurations for remote interrogation of fibre-optic sensors based on Fibre Bragg Gratings (FBG) are described in both traditional all-optical and novel electro-optical approaches, respectively. Finally, a novel reflective electro-optical FBG-based configuration with self-referencing technique using electronically reconfigurable delays at the reception stage is reported and analyzed using the theory of digital filters. Two measurement parameters for this configuration are proposed and verified.

- A state-of-the-art of multiplexing architectures and addressing techniques for passive fibre-optic sensor networks are reported in Chapter 6 of this document. Features like noise, bandwidth, cost, flexibility and optical power per sensor are compared for the configurations reported. Furthermore, the wavelength-division multiplexing (WDM) approach is deeper described as FBG-based self-referencing sensor networks can take advantage of the intrinsic wavelength splitting feature provided by the Fibre Bragg Grating device. Finally, a reflective star self-referenced electro-optical FBG-based fibre-optic intensity sensor network with electronic delays at the reception stage is demonstrated in a CWDM topology. It is shown the performance of both measurement parameters in terms of their self-reference property, crosstalk, sensitivity, linear response and resolution. The scalability of such technique is also analyzed. Additionally to this, a RF self-referencing system for monitoring drop fibres in WDM-PON networks is also proposed and evaluated, thus achieving a cost-effective approach with medium impact of the power budget and being an in-service scalable to monitoring Dense WDM (DWDM) PON systems.

- The main conclusions of this work and future research tasks are reported in Chapter 7.

- A summary of the work is written in Spanish in Chapter 8.

- Finally, related publications of the author concerning the work developed within this document are attached.

- Appendix to this work has been included comprising four sections for a better understanding of the document. Their contents are the following:

    i. The basics of the VPI simulation software and other details of the simulation reported in Chapter 4 are given in Appendix A.

ii. An introduction to the discrete-time optical signal processing theory is briefly introduced in Appendix B. The notation given in this section serves as analytical framework for the study of the performance in the self-referencing technique for optical intensity sensors, described in Chapter 5 and Chapter 6 of this document.
iii. A further description of the analytical expressions for the self-referencing parameters and their sensitivities, described in Chapter 5 and Chapter 6 of this document, is reported in Appendix C.
iv. Specifications and characterization of the equipment used within this research work (i.e. optical sources, optical detectors, optical fibres, etc.) are described in Appendix D.

1.3 Acknowledgements

The research work of this dissertation has been supported by the following Spanish projects: TEC2006-13273-C03-03-MIC (FOTOCOMIN) and TEC2009-14718-C03-03 (DEDOS) of the Spanish Interministerial Comission of Science and Technology (CICyT) and FACTOTEM-CM:S-0505/ESP/000417 and FACTOTEM-2/2010/00068/001 of Comunidad Autónoma de Madrid.

Additional financial support was obtained from the Integrated Action Hispano-Portuguesa 'Self-referenced fibre optic intensity configurations for single and multi-sensors' (HP2007-0093) and from the European Networks of Excellence: ePhoton/One+ (FP6-IST-027497)[4] and BONE: Building the Future Optical Network in Europe (FP7-ICT-216863)[5].

Research stays at Bilbao (Spain) and Porto (Portugal), within the framework of this work, were partially supported by the Mobility Programme from the Vicerrectorado de Investigación of the Universidad Carlos III de Madrid.

[4] ePhoton/One+ is supported by the Sixth Framework Programme (FP6) of the European Union.
[5] BONE is supported by the Seventh Framework Programme (FP7) of the European Union.

Chapter 2

TOWARDS NEXT GENERATION BROADBAND ACCESS NETWORKS AND FULL CONVERGENCE WITHIN THE OPTICAL DOMAIN.

This chapter is intended to be a progress report on the use of optical fibre as a successor to traditional copper-based transmission media, such as twister copper pair or coaxial cable, for 'access' or 'last mile' broadband connectivity to homes, apartment buildings and even business. Pressures for more per-user bandwidth are growing with, even more, effective architectures designed, standardized and placed in service. In this context, a full integration of demanding services from users within a common network infrastructure becomes an actual and emerging premise.

2.1 Perspective in Next-Generation Access Networks

2.1.1 Introduction

Today, high-speed internet connection at home is becoming a commodity in most countries. In May 2008 Strategy Analytics forecasted that there would be more than 621 million broadband line subscriptions worldwide in 2012, based on a figure of 335 million at the end of 2007 showing a cumulative annual growth rate of around 12 percent [1]. This steady increase in the total internet traffic over the last two decades has not only increased the bandwidth requirement of the backbone network; but also the demand for bandwidth in the premises is rapidly increasing, fueled by video- and graphic-rich applications. And these new interactive services require a broadband communication network, which should extent into the customer's premises up to the terminals. Thus, steady increases in bandwidth requirements of access networks and local area networks (LANs) have created a need for short-reach and medium-reach links supporting data rates of Gbps (such as Gigabit Ethernet, GbE), 10Gbps (such as 10-Gigabit Ethernet, 10GbE) and even higher (such as 40- and 100- Gigabit Ethernet standards, namely 40GbE and 100GbE respectively, which started in November 2007 and have been very recently ratified in June 2010). Detailed studies carried out in the framework of the Architectures for Flexible Photonic Home and Access Networks (ALPHA) [2] and Home Gigabit Access (OMEGA) [3], Information and Communications Technology Framework Programme 7 (ICT-FP7) projects, have defined the required bit-rates to be transmitted to the customer's premises for different profiles for the traffic flows, reaching a total future-proof very-high-bit-rate link in the order of 2Gbps per user.

At present, unshielded twisted pair (UTP) and coaxial cables, both copper based, are used as the physical medium to deliver telecom services within the customer's premises. But these two media suffer from serious shortcomings when they are considered to serve the increasing demand for broadband services. Moreover, a cost-effective and future-proof means for bringing high bandwidth services to the individual users on a mass basis has not yet emerged and several competing technologies are under consideration: UTP copper wire, coaxial cable, wireless links, single and multimode silica optical fibres (namely GOFs, i.e. Glass Optical Fibers), and plastic optical fibres (POFs). It is currently clear that twisted pair has a limited bandwidth and it is susceptible to electromagnetic interference (EMI). Coaxial cable offers a larger bandwidth (however copper attenuation at high frequencies stands at 1.5dB/m@500MHz to 4.3dB/m@3GHz), but it poses practical problems due to its thickness and the effort required to make a reliable connection. Moreover, the coaxial cable is also not immune to EMI. Both transmission media, UTP and coaxial cable, also suffer from crosstalk.

On the other hand, optical fibre is extensively used for long-distance data transmission and it represents an alternative for transmission at the customer's premises as well. Optical fibre connections offer complete immunity to EMI and present increase security, since it is very difficult to intercept signals transmitted through the fibre. Moreover, optical communication systems based on silica optical fibres allow communication signals to be transmitted not only over long distances with low attenuation but also at extremely high data rates, or bandwidth capacity. In singlemode optical fibre systems, this capability arises from the propagation of a single optical signal mode in the low-loss windows of silica located at the near-infrared wavelengths of 0.85μm, 1.3μm, and 1.55μm. Furthermore, since the introduction of erbium-doped fibre amplifiers (EDFAs), the last decade has witnessed the emergence of singlemode GOF as the standard data transmission medium for wide area networks (WANs), especially in terrestrial and transoceanic communication backbones. The success of the singlemode GOF in long-haul communication backbones has given rise to the concept of optical networking, which is a central theme with currently driving research and development activities in the field of photonics. The main objective is to integrate voice, video, and data streams over all-optical systems as communication signals make their way from WANs down to smaller local area networks (LANs), and eventually to the end user by Fibre To The x (FTTx).

Although singlemode silica fibre solutions have the potential of achieving very large bandwidths, they suffer from high connectorization costs compared to copper or wireless solutions. For this reason, singlemode silica fibre has not been widely adopted by the end user (premises) where most of the interconnections are needed and less cost-sharing between users is obtainable. The underlying factor is the fact that the singlemode GOF core is typically only a few micrometers in diameter with the requirement of precise handling. Yet as the optical network gets closer to the end user, starting at the LAN (Local Area Network) stage, the system is characterized by numerous connections, splices, and couplings that make the use of thin singlemode GOF impractical. Current solutions depend on multimode GOF with a larger core diameter (typically 50μm or 62.5μm) to ease these fibre connection and systems installation issues. However, the increased fibre diameter is accompanied by an increase in the number of optical signal modes to many tens of thousands and consequent optical pulse broadening. The unwanted pulse broadening is due

to modal dispersion, in which different modes (light paths) within the fibre carry components of the signals at different velocities, which ultimately results in pulse overlap and a garbled communications signal. Additional pulse broadening contribution from wavelength-dependent dispersion (i.e. material dispersion) due to the wavelength dependence of the modal group velocity also occurs, but to a lesser extent than modal dispersion. To overcome and compensate for modal dispersion, the refractive index of the fibre core is graded parabola-like from a high index at the fibre core center to a low index in the outer core region (i.e. by forming a graded-index (GI) fibre core profile), so that the high-order and low-order modes inside the fibre ideally travel at the same group velocity.
Anyway, as multimode GOF is still brittle and fragile at large core diameters, hence polymer optical fibre (POF) is being seriously considered as a high-bandwidth fibre link for certain short-distance applications because of its ductility and mechanical flexibility. Similar to its GOF counterpart, the bandwidth performance of (intrinsically) multimode POF is limited by modal dispersion of the signal pulses. This problem can be alleviated by also forming graded-index (GI) POF that has a parabola-like index profile. Although firstly developed polymethylmethacrylate (PMMA)-based GI POF fibres have been demonstrated to obtain very high transmission bandwidth, but they suffer from high losses (150dB/km) and operate at 650nm outside of the communication wavelengths where high-speed transceivers are more mature and achieve higher performances. Recently, a new type of POF, the perfluorinated-based (PF) graded-index polymer optical fiber (GIPOF), has been introduced that has low losses and low material dispersion, even with regards to its silica-based counterpart.

For all the above reasons, singlemode silica-based fibre (SMF) is mainly used as the backbone of the network because of its extremely low loss and large bandwidth, which are desirable for high-data-rate long-haul systems. On the other hand, multimode fibre (both silica-based GI-MMF and GIPOF) provides the necessary bandwidth for short reach links at a much lower installation and component cost compared to SMF and copper wire. Therefore, it is widely used for the “last mile” reach in the access network to interconnect buildings or to build a scalable unified campus network, for example. However, in the case of GIPOF, the higher than silica attenuation also inhibits their use in relative long link applications, being mainly driven for covering in-building optical networks, thus full covering the growing need of a full convergence of the multitude of communication networks within an ‘optical domain’. Also the growing demand of fully building automation and services has leaded to a huge development and research on the field of optical fibre sensors for the final convergence within this ‘optical domain’. It was estimated in [4] that this last mile would correspond to 95% of all optical networks and it is now clear that the expected market is huge and researches and companies all over the world are competing to find a solution to the convergence issue.

To resume, MMFs (both silica- and polymer-based) are still far from SMF bandwidth and attenuation, but they are called to the next step on access network links due to its low cost systems requirements (light sources, optical detectors, larger fibre core,…) against the high cost of the singlemode components. It is worth mentioning that in-building networks may comprise quite a diversity of networks: not only networks within residential homes, but also networks inside office buildings, hospitals, and even more extensive ones such as

networks in airport departure buildings and shopping malls. Thus the reach of in-building networks may range from less than 100 metres up to a few kilometers.

2.1.2 Access network services and bandwidth demand

Research into next-generation access (NGA) network technology is being driven by Nielsen's Law with internet-access bandwidths doubling approximately every 21 months [5]. End-user access bandwidths could reach 1 Gbps by 2015, and 10 Gbps by 2020. Emerging themes in next-generation access (NGA) research include: convergence technologies, green telecoms, and soft photonics, whilst seamless wireline-wireless convergence is addressed by Radio-over-Fibre (RoF) technologies. Photonics will transport gigabit data across the access network, but the final link to the end-user (measured in distances of metres, rather than km's) could well be wireless, with portable/mobile devices converging with photonics. RoF technologies can address the predicted multi-Gbps data wave, whilst conforming to reduced carbon footprints (i.e. green telecoms). Soft photonics is also an increasingly important aspect to telecoms, describing the use of ever more powerful digital signal processing (DSP) electronics, particularly within receiver equipment, to achieve higher performance (e.g. high data rates) via the use of intelligent and adaptive systems. NGA networks will provide a common resource, with passive optical networks (PONs) supplying bandwidth to buildings, and offering optical backhaul for such systems.

Fibre type	1000BaseSX 850nm Modal Bandwidth/Operating Range (MHz·km)/(Meters)	1000BaseLX 1300nm Modal Bandwidth/Operating Range (MHz·km)/(Meters)
62.5µm[1]	160/220	500/550
62.5µm OM-1[2]	200/220	500/550
50µm	400/500	400/550
50µm OM-2	500/550	500/550
50µm OM-3	2000/n.a.[3]	500/n.a.
SMF	n.a.	n.a./5000

Table 2.1.- Gigabit Ethernet transmission over fibre standards (IEEE 802.3z). Approved in 1998.

On the one hand, Ethernet is the most widespread wired LAN technology, including in-home networks, and the development of Ethernet standards goes hand in hand with the adoption and development of improved MMF channels. Ethernet standards for 1Gbps and 10Gbps designed for multimode and singlemode fibres are now in use [6]. Table 2.1 (above) and Table 2.2 (below) show the minimum performance specified by IEEE 802.3 standard for the various interfaces. For example, Gigabit Ethernet (GbE) standard operating at 1.25Gbps@1300nm supports a range of transmission lengths of 100m over copper wire, 550m over multimode silica fibre and 5km over singlemode silica fibre as seen in Table

[1] TIA (Telecommunications Industry Association), Document 492AAAA compliance. Commonly referred to as 'FDDI-grade' fibre.
[2] ISO (International Standards Organization), Document 11801 compliance.
[3] n.a.: not available.

2.1. Actually OM4 fibre type is under consideration although is not yet within a published standard. OM4 fibre type defines a 50µm core diameter MMF with a minimum modal bandwidth (under OverFilled Launching condition, OFL) of 3500MHz·km@850nm and 500MHz·km@1300nm, respectively.

Fibre type	10GBaseSR 850nm Modal Bandwidth/Operating Range (MHz·km)/(Meters)	10GBaseLR(/ER) 850nm Modal Bandwidth /Operating Range (MHz·km)/(Km)	10GBaseLRM 1300nm Modal Bandwidth /Operating Range (MHz·km)/ (Meters)
62.5µm	160/26	n.a.	n.a.
62.5µm (OM-1)	200/33	n.a.	500/300
50µm	400/66	n.a.	400/240
50µm (OM-2)	500/82	n.a.	500/300
50µm (OM-3)	2000/300.	n.a.	500/300
SMF	n.a.	10 (/40)	n.a/10000.

Table 2.2.- 10-Gigabit Ethernet transmission over fibre standards (IEEE 802.3aq). Approved in 2006.

Figure 2.1 provides a brief description of the current 10GbE and the possible future Ethernet standards over copper and fibre links. The trend of extending the reach and data rate of the links is obvious in the previous standards and the 10GbE standards shown in the figure. Although the twisted pair of copper wires is a relatively low-cost and low-power solution compared to the MMF solutions, the motivation for the transition from the copper-based links to the MMF links is their much higher available bandwidth. However, the need for even higher performance MMF solutions is apparent, and much more is to be expected, for example, with new ultra-HDTV format such as 4K (4000 horizontal pixels, with an expected increase in the required bandwidth of a factor of approximately 16).

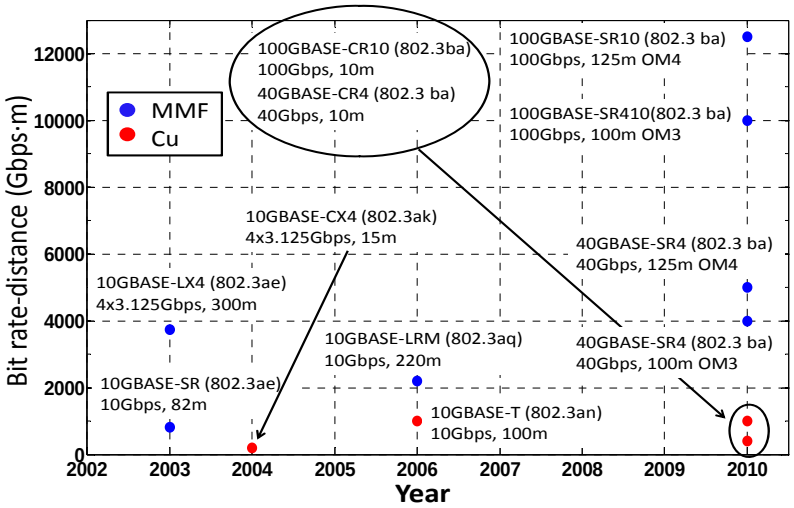

Fig. 2.1.- 10-Gigabit Ethernet standards over MMF and copper links [7].

Another important point in access networks communications is within the field of the wireless signal transmission (for both mobile and data communication), namely Wireless Local Area Networks (WLANs). Wireless technologies are developing fast but there is a need to link base stations/servers to the antenna by using fixed links together with the future exploitation of capacities well beyond present day standards (IEEE802.11a/b/g), which offer up to 54Mbps and operate at 2.4GHz and 5GHz, as well as 3G mobile networks such as IMT2000/UMTS[4], which offer up to 2Mbps and operate around 2GHz. Moreover, IEEE802.16, otherwise known as WiMAX, is another recent standard aiming to bridge the last mile through mobile and fixed wireless access to the end user at frequencies between 2-11GHz. In addition, WiMAX also aims to provide Fixed Wireless Access at bit-rate in the excess of 100Mbps and at higher frequencies between 10-66GHz. All these services use signals at the radio-frequency (RF) level that are analogue in nature, at least in the sense that they cannot be carried directly by digital baseband modulation. Optical cabling solutions can also offer the possibility for semi-transparent transport of these signals by using Radio-over-Fibre (RoF) technology. This Radio-over-Fibre technology has been proposed as a solution for reducing overall system complexity by transferring complicated RF modem and signal processing functions from radio access points (RAPs) to a centralised control station (CS), thereby reducing system-wide installation and maintenance costs. Furthermore, Radio-over-Fibre (RoF) in combination with multimode fibres can be deployed within homes and office buildings for baseband digital data transmission supporting 3.5GHz wireless signals, within the Ultra Wide Band (UWB). The UWB transmission is an emerging technology for wireless high-speed due to the high data-rate capabilities, low power consumption and immunity to multipath fading. Several studies have reported on Ultra Wide Band (UWB) transmission for in-building applications, including wall and multipath effects [8]. MMF is also widely used in within-building fibre installations for baseband data transmission systems at far more than 10Gbps.

However, in general, low carrier frequencies offer low bandwidth and the 6GHz UWB unlicensed low band is not available worldwide due to coexistence concerns [9]. These include radio and TV broadcasts, and systems for (vital) communication services such as airports, police and fire, amateur radio users and many others. In contrast, the 60 GHz-band, within millimetre wave, offers much greater opportunities as the resulting high radio propagation losses lead to numerous pico-cell sites and thus to numerous radio access points due to the limited cell coverage. These pico-cells are a natural way to increase capacity (i.e. to accommodate more users) and to enable better frequency spectrum utilisation. Therefore, for broadband wireless communication systems to offer the needed high capacity, it appears inevitable to increase the carrier frequencies to the range of millimetre-wave and to reduce cell sizes [10-12]. Considering in-house wireless access networks, coaxial cable is very lossy at such frequencies and, as the bulk of the installed base of in-building fibre is silica-based MMF while PF GIPOF is also emerging as an attractive alternative (due to the aforementioned low cost potential and easier handling required in in-building networks); it is also mandatory to overcome the modal bandwidth

[4] IMT2000: International Mobile Telecommunications-2000 ; UMTS: Universal Mobile Telecommunications System

limitation in multimode fibres to deliver modulated high frequency carriers to remote access points.

As it can be seen, MMF links have big possibilities and there is still a lot to research, even more with the inclusion of wireless signals over MMF in order to get a total compatible access network system. Consequently, for all the reasons above mentioned, the deployment of such emerging next generation access (NGA) network technology is contingent with the research and evaluation of predictive models for the frequency response in both the aforementioned fibre types, silica-based GI-MMF and PF GIPOF, respectively. Some contributions on the development and validation of those models will be shown on Chapter 3and Chapter 4 of this Thesis work.

2.1.3 Multimode optical fibre expanded capabilities

Actual trends of increasing speed and coverage in the NGA services marketplace indicate further deployment of higher-capacity communications technologies well into the foreseeable future. Although multimode fibres, both silica-based and polymer-based counterparts, are the best candidate for the convergence and achievement of a full service access network context, it has been previously addressed their main disadvantage concerning the limited bandwidth performance, limited by modal dispersion. Different analogue and digital techniques or topology schemes have been reported in literature to carry microwave and millimetre-wave over optical networks, surmounting the bandwidth bottleneck. The most employed techniques are following deeper described in the below subsections.

It is worth noting that some other methods try to electrically improve this bandwidth performance using, for example, equalization techniques [13]. In addition to, it is well known than an m-ary digital modulation scheme with m>2 (multi-level coding) can enhance transmission capacity by overcoming the bandwidth limitations of a transmitter or a transmission medium and, therefore, multilevel modulation schemes that are used in radio-frequency communications have also been demonstrated in fibre-optic links [14, 15]. Other attempts to overcome the bandwidth limit includes selective excitation of a limited number of modes in different ways: offset launch [16], conventional center launch [17] or even by means of a twin-spot technique [18]. On the other hand, from the multimode fibre frequency response, the effect of having a wideband frequency-selective channel for data transmission can be overcome by using orthogonal frequency-division multiplexing (OFDM). In OFDM, the high-data-rate signal is error-correction encoded and then divided into many low-data-rate signals. By doing this, the wideband frequency-selective channel is separated into a series of many narrowband frequency-nonselective channels. OFDM technique has been applied to fibre-optic transmission [19, 20] and shown to offer some protection against the frequency selectivity of a dispersive multimode fibre. Finally, alternative modulation schemes have also been applied [21, 22] as well as spatial light filtering, either at the fibre input [23] or its output [24].

2.1.3.1 Subcarrier Multiplexing (SCM)

Subcarrier Multiplexing (SCM) is a maturing, simple, and cost effective approach for exploiting optical fibre bandwidth in analogue optical communication systems in general and in RoF systems in particular, which was firstly addressed at the end of the 1990's in [25], taking advantage of the relative flat passband channels existing in the multimode fibre frequency response. In SCM, the RF signal (the subcarrier) is used to modulate an optical carrier at the transmitter's side. As a result, there is an optical spectrum consisting of the original optical carrier f_O, plus two side-tones located at $f_O \pm f_{SC}$, where f_{SC} is the subcarrier frequency. If the subcarrier itself is modulated with data (analogue or digital), then sidebands centred on $f_O \pm f_{SC}$ are produced as illustrated in Figure 2.2. However, the frequency ranges suitable for passband transmission vary from fibre to fibre as well as with the fibre length. They can also vary for a given fibre, depending on the launching conditions or if it is subjected to mechanical stress. To overcome this issue, an adaptative channel/s allocation system would be necessary. This could have the form of a link training sequence during startup, where the baseband, which is always available, can serve as control channel or by means of diversity coding technique [26].

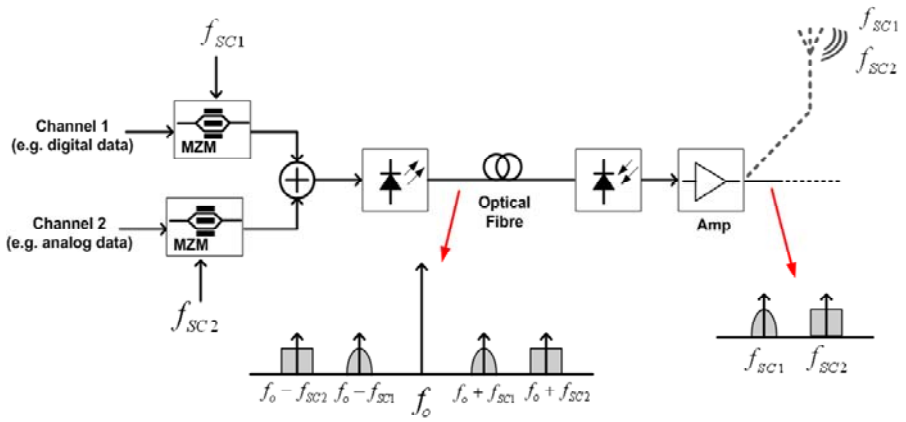

Figure 2.2.- Sub-Carrier Multiplexing of Mixed Digital and Analogue Signals. Dashed line: optional.

To multiplex multiple channels on to one optical carrier, multiple subcarriers are first combined and then used to modulate the optical carrier as shown in Figure 2.2 and demonstrated in [27, 28]. At the receiver's side the subcarriers are recovered through direct detection. These can be optionally radiated in wireless systems (dashed lines in Fig. 2.2). Different modulation schemes may be used on separate subcarriers. One subcarrier may carry digital data, while another may be modulated with an analogue signal such as video or telephone traffic. In this way, SCM supports the multiplexing of various kinds of mixed mode broadband data. Modulation of the optical carrier may be achieved by either directly modulating the laser, or by using external modulators such as Mach-Zehnder modulators (MZM).

Experiments achieving 1.6Gbps over 1km of 62.5µm MMF by subcarrier modulation of Vertical Cavity Surface Emitting Lasers (VCSELs) [22] demonstrated the feasibility of such technique, overcoming the traditional distance limitation of 275m or less, specified for

Gigabit Ethernet, at 850nm. Another relevant work that takes advantage of the bandpass characteristics of the MMF response is reported in [25], where two subcarriers are used at 1GHz and 3GHz, respectively, each one carrying 625Mbps in BPSK (Binary Phase-Shift Keying) format over a link of 500 metres of silica-based MMF.

One of the main advantages of SCM is that it supports mixed mode data traffic. Each subcarrier may transport a signal having an independent modulation format. Therefore, it can be used for a wide range of applications such as CATV [29], wireless LANs and millimitre-wave applications to name but a few. This is a consequence of the fact that the modulation technique used and data carried on each subcarrier are independent of the subcarriers used. Furthermore, because the subcarriers are at low frequencies, components required for SCM-based systems are readily available. Modulators, mixers and amplifiers employed in cable and other satellite systems can still be used in SCM systems leading to low system costs. In contrast, the disadvantage of SCM is that being an analogue communication technique, it is more sensitive to noise effects and distortions due to non-linearities. This places stringent linearity requirements on the performance of components, especially for applications such video where a Carrier-to-Noise-Ratio (CNR) > 55 dB may be required, for example.

2.1.3.2 Wavelength Division Multiplexing (WDM)

Focusing on wireless systems, the use of Wavelength Division Multiplexing (WDM) for the distribution of, for instance, RoF signals has gained importance recently. WDM enables the efficient exploitation of the fibre network's bandwidth. However, the transmission of RoF signals is seen as inefficient in terms of spectrum utilisation, since the modulation bandwidth is always a small fraction of the carrier signal frequency. RoF on WDM systems have been reported [30-33], where optical millimetre-wave signals from multiple sources are multiplexed and the composite signal is transported through an optical fibre and, finally, demultiplexed to address each Remote Access Point, for wireless applications. Furthermore, there have been several reports on Coarse WDM (CWDM) and Dense WDM (DWDM) applied to RoF networks.

A challenging issue concerns the application of millimetre-waves in wireless systems as the optical spectral width of a single optical millimetre-wave source may approach or exceed WDM channel spacing. For example, Fig. 2.3 shows an optical spectrum of DWDM millimetre-wave RoF signals with optical DSB (Double Sideband) modulation (a) and SSB (Single Sideband) modulation (b), where it has been assumed that the carrier frequency of the millimetre-wave signal is 60 GHz. Fig. 2.3(a) indicates that to transmit a single data channel at 60GHz band, more than 120GHz bandwidth is necessary for DSB modulation. In addition, from a viewpoint of cost reduction, it is preferable to use the channel allocation in accordance with ITU (International Telecommunication Union) grid because of the availability of optical components. Then, the minimum channel spacing in this case is 200 GHz [34]. In the case of SSB modulation, this is 100GHz as shown in Fig. 2.3(b).

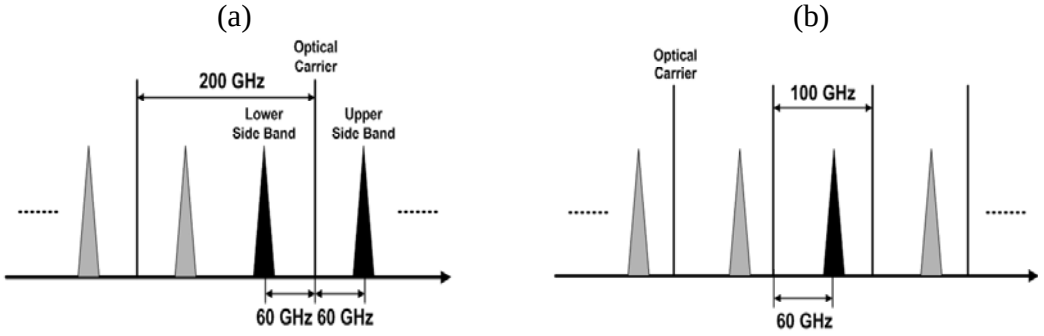

Figure 2.3.- Optical spectrum of DWDM mm-wave RoF signals of conventional optical (a) DSB and (b) SSB.

An hybrid approach combining SCM and WDM techniques for MMF bandwidth enhancement is reported in [35] demonstrating a 40x5.1Gbps WDM/SCM system over both 500m and 3km of 62.5μm and 50 μm core diameter MMF, respectively.

2.1.3.3 Optical Frequency Multipliying (OFM)

In addition to offering mobility to users, wireless communications are increasingly offering higher bandwidths and, consequently, the radio carrier frequencies need to increase. Therefore, techniques for carrying microwave signals over multimode fibre while overcoming its limited bandwidth are being investigated. The optical frequency multiplying (OFM) is a method by which a low-frequency RF signal is up-converted to a much higher microwave frequency through optical signal processing. At the headend station, a wavelength-tunable laser diode is used, of which the wavelength is periodically swept over a range $\Delta\lambda_o$ with a sweep frequency f_{SW} while keeping the output power constant. The data is impressed on this wavelength-swept optical signal by means of chirp-free intensity modulation, by means of a differentially driven Mach-Zehnder phase modulators, as shown in Fig. 2.4(a). After having passed through the optical fibre link, the signal impinges on a periodic optical multi-passband filter (e.g. optical comb or Fabry-Perot filter). In sweeping across *N* transmission peaks of this filter (back and forth during one wavelength sweep cycle), light intensity bursts arrive on the photodiode with a frequency $2N \cdot f_{SW}$. Thus, the output signal of the photodiode contains a microwave frequency component at $2N \cdot f_{SW}$, and higher harmonics of which the strength depends on the bandpass characteristics of the periodic filter. After bandpass filtering in order to select the desired harmonic, and some amplification, the microwave carrier can be radiated, e.g. by an antenna. Note that only the optical sweep frequency is limited by the bandwidth of the optical fibre link, and that microwave carrier frequency can exceed this bandwidth by far due to the optical frequency multiplication mechanism.

Simulations and experiments have shown that extremely pure microwave signals can be generated, notwithstanding a moderate laser spectral linewidth, due to the inherent phase noise cancellation in the OFM technique [36, 37].

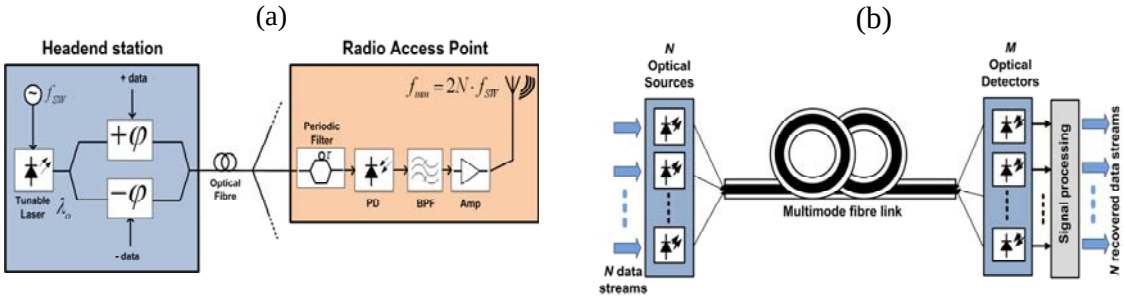

Figure 2.4.- (a) Feeding microwave data signals over a multimode network by OFM technique. (b) Principle of mode group diversity multiplexing (MGDM).

2.1.3.4 Mode Group Diversity Multiplexing

Multimode fibre, both silica and polymer versions, has the potential of a larger information transport capacity as it guides a large number of modes that can be considered as communication channels [38]. However, this transport capacity is limited by modal dispersion as a result of the many modes that are usually excited simultaneously but one way to increase the bandwidth is by using selective mode group launching and transmitting different signals over each of them and on the same operating wavelength. By this technique, an up to fourfold increase of the bandwidth has been reported by injecting a small light spot radially offset from the fibre core center, exciting less than 50% of the fibre modes. Thus, the fibre transport capacity may be increased by mode group diversity multiplexing (MGDM) if a limited amount of mode coupling occurs, as it is the case in high-quality multimode fibres. In that case, N mode groups can be selective excited in parallel with separate data from N optical sources (laser diodes), see Fig. 2.4(b). At the receiving side, M≥N detectors produce M signals which each contain a mix of the N input data streams due to the mode mixing incurred in the fibre. A signal processing circuit subsequently recovers the N original data streams by properly processing the M received streams. Since the first time MGDM transmission on a 100m- long 93.5μm core diameter GI-MMF was demonstrated [39] many experiments have been carried out reporting the operation of this technique. For instance, a speed of 10Mbps per channel (3 channels obtained by exciting with angle beams of 0º, 8º and 16º degrees) over 100m silica-based SI-MMF and 500m 62.5μm core diameter silica-based GI-MMF is reported in [40]. Other experiments reported 2x10.7Gbps over 300m of a standard 62.5μm silica-based GI-MMF.

2.1.4 Access network architectures

The general structure of a modern telecommunication network consists of three main portions: backbone (or core) network, metro/regional network, and access network. On a very high level, core backbone/core networks are used for long-distance transport and metro/regional networks are responsible for traffic grooming and multiplexing functions. Structures of backbone and metro networks are usually more uniform than access networks and their costs are shared among large number of users. These networks are usually built

with state-of-the-art fibre optics and wavelength division multiplexing (WDM) technologies to provide high-capacity connections.

On the other hand, access networks provide the end-user connectivity. They are placed in close proximity to end user, between the local exchange and in-house networks of the customers' premises, and deployed in large volumes. Although access networks exists in many different forms for various practical reasons, up to now, local loops within this domain are mostly made up of copper based SDM[5] connections. However, this network configuration suffers from attendant limitations that make it inappropriate to offer broadband services to all customers. Hence, there is a trend to replace copper cables by optical fibre infrastructures as the underlying medium for the implementation of FTTx (and all its variants) systems, see Fig. 2.5(a), in order to achieve a performance compatible with access network requirements. FTTH/B (Fibre To The Home/Building) deployments are considered the target architecture in the long-term due to their virtually unlimited scalability.

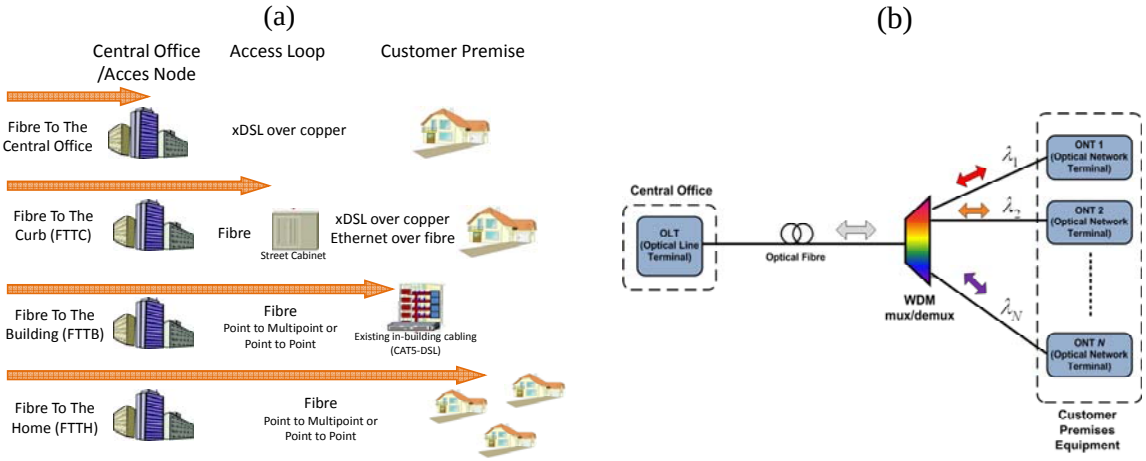

Figure 2.5.- (a) Different FTTx networks. (b) Architecture of WDM-PON.

It has been indicated by several roadmaps that the peak link data rate should be at least 100Mbps (symmetrical) for private customers and 1 to 10Gbps for business applications. Inherent access network requirements are highlighted in Table 2.3. These hundreds of megabits per second per user are reasonably reachable in the coming future and the Fibre To The Home (FTTH, or some intermediate version such as FTT-curb) network constitutes a fibre access network, connecting a large number of end users to a central point, commonly known as an access node. Each access node will contain the required active transmission equipment used to provide the applications and services over optical fibre to the subscriber. These access networks may connect some of the following:

- Fixed wireless network antenna (WLAN, WiMAX,...),
- Mobile network base stations,
- Subscribers in residential houses, terraces or blocks of flats,
- Large building such as schools, hospitals and business,

[5] Space Division Multiplexing

- Key security and monitoring structures like surveillance cameras, building automation, security alarms and control devices,
- Fibre-optic sensors from the subscribers' homes or intelligent buildings.

Parameter	Remarks
Transmission distances	Typ. <10km, max. 20km, e.g. for alternative topologies
Peak data rate	100Mbps (private customers) Nx1 Gbps up to 10Gbps (business)
Temperature range	Controlled: +10ºC to +50ºC Uncontrolled operation in buildings: -5ºC to +85ºC Uncontrolled operation in the field: -33ºC to +85ºC
Long lifetime	
Humidity and vibrations (shock) have to be considered at non-weather protected locations	
No optical amplifiers in the field	
No optical dispersion compensation	

Table 2.3.- Access network requirements.

Going on from this, FTTx networks are seen as an enabler of increasingly higher-speed services and worldwide projects are in progress in which optical fibres are pushed towards the subscribers' premises to implement broadband FTTx systems. These systems are backed up by emerging standards such as Gigabit Passive Optical Network (GPON, International Telecommunication Union - Telecommunication Standarization Sector [ITU-T] Recommendation G.984.2) or 10-Gigabit Passive Optical Network (10G-PON, International Telecommunication Union - Telecommunication Standarization Sector [ITU-T] Recommendation G.987.1) or 10G-EPON (Institute of Electrical and Electronics Engineers [IEEE] Standard IEEE 802.3av).

In order to specify the interworking of passive and active infrastructure, it is important to make a clear distinction between the topologies used for the deployment of the fibres (passive infrastructure) and the technologies used to transport data over fibres (active equipment). Hereafter we will focus on the first topic.

The most widely used topologies are point-to-multipoint, which is often combined with passive optical network (PON) architecture, and point-to-point, typically using Ethernet transmission technologies. Point-to-multipoint topologies are deployed by one of the standardized PON technologies, either GPON (Gigabit-capable PON, which is today's frontrunner in Europe) or EPON (Ethernet over PON, which has been massively deployed in Asia using time-sharing protocols to control the access of multiple subscribers to the shared feeder fibre). In contrast, point-to-point technologies provide dedicated fibres between the access node and the subscriber. Consequently, each subscriber is directly connected by a dedicated fibre. It is worth mentioning that the access node acts as the starting point of the optical fibre path to the subscribing home and holds functionalities such as the house of all active transmission equipment, the management of all fibre terminations and the facilitation of the interconnection between the optical fibres and the active equipment. On the other hand, Wavelength Division Multiplexing PON (WDM-PON) promises to combine the best of both worlds, i.e. sharing feeder fibres while still providing dedicated point-to-point connectivity. A basic scheme of the WDM-PON

architecture is depicted in Fig. 2.5(b). This architecture provides dedicated and transparent connectivity on a wavelength per subscriber basis, and thus allow very-high uncontended bit rates for each connected subscriber. It also provides the same inherent security as with dedicated fibre. This architecture uses wavelength filters (namely, WDM multiplexers and demultiplexers) instead of splitters in the field to map each wavelength from the feeder fibre onto a dedicated drop fibre. As a result, there is a logical upgrade path from current TDM-PON (Time Division Multiplexing-based PON) deployments to WDM-PON at the level of physical infrastructure. However, the key challenge for WDM-PON is to provide diverse upstream wavelengths while having a single Optical Network Terminal (ONT) type, where the fibre is terminated. The technologies required for WDM-PON are available today, but they have to undergo some cost reduction in order to be considered suitable for mass deployment. However, multiplexers and demultiplexers are available partially for silica-based MMFs and not yet for POFs.

2.1.5 Access network to home network convergence

Trends to increasing speed and coverage of next generation access (NGA) services and their applications for the in-building/home networks (herafter, in-building network without lost of generality) lead to the realization and implementation of reliable low-cost network interface nodes between these short- and medium-reach high-bandwidth networks and the fixed core communications infrastructure. From a general description, the boundary between the access network and the in-building/home network lies between the access network termination (ANT) and the building/home gateway (HG). Furthermore, the in-building network should connect the HG to several access points (APs) scattered around the building/home, as seen in Fig. 2.6. Other important point is that, in order to form a ubiquitous (i.e. use sparsely distributed everywhere devices such as TVs, home cinema or PCs everywhere at home) broadband access network, there is also the need to interconnect long-haul core networks, based on SMF, and in-building networks to conform an ultra-high-bandwidth convergence scenario where devices and services will have to interwork at home and in continuity to the operator's network. Regarding its performance, the in-building network should have at least the same quality as the access network to which is connected to avoid a some-how ironic, but indeed possible situation in which the in-building network becomes the actual bottleneck of the full system. And multimode optical fibre, as explained before, is one of the keys for these short- and medium-reach networks covering in-building (and in-home) scenarios. Another point for the requirement of convergence stands for the fact that in the near future peak access speed per user on the order of several hundreds of Mbps can be envisaged for next-generation GPON FTTx access, offering over this access network ultra-small latency time (less than 1ms round-trip time) thanks to simple framing and coding of short packets. This performance needs also to be equaled by the in-building networks for low-latency services.

These hybrid (SMF and MMF) transmission systems are being investigated and previous researches have successfully demonstrated, for example, a single directional 2.6Gbps transmission over an hybrid link composed of 25km-long SMF and a 2.2km-long 50μm MMF [41], as well as advanced modulated data over 20km-long SMF and 300m-long MMF for millimeter-wave RoF application [42, 43].

Multimode fibres, both silica- and polymer-based, offer the physical infrastructure to create a fusion and convergence of the access network via FFTx for next generation access (NGA) services. Both fibres types may be used not only to transport fixed data services such as GbE (or 10GbE) but also to transparently distribute in-building (and also for short- and medium-reach links) signals of present and future broadband services leading to a significant system-wide cost reduction. Even though it is quite obvious that the last connectivity to the terminal will tend to be wireless, optical technology is a very promising backbone alternative candidate to the *no new wires* approach such as pure power line communications (PLC), HomePNA (alliance in home networking technologies) or simply WLANs. Furthermore, Radio-over-Fiber (RoF) technology in combination with multimode fibres offers the convergence of nearly all wired and wireless communications within office and home buildings, see Fig. 2.6.

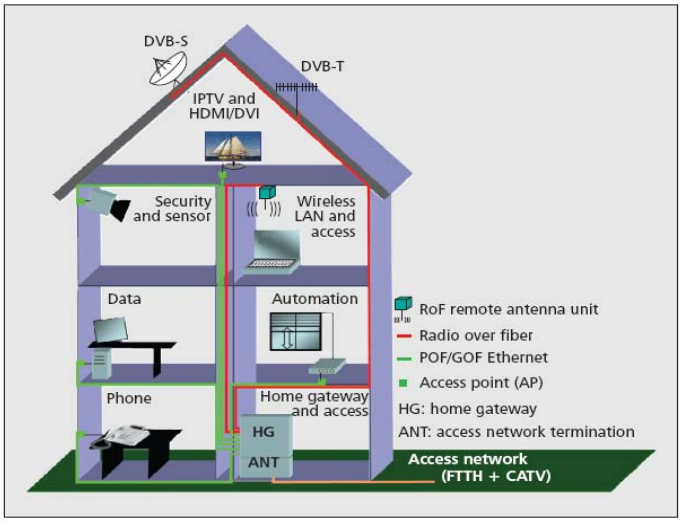

Fig. 2.6.- General in-home access network architecture and services [44].

On the other hand, due to the ability to transmit different wired and wireless standards transparently over MMF, we can conclude that such MMF-based systems can particularly address the following applications:

- Audio & Video information, entertainment (HDTV, P2P, DVB[6], CATV, ...).
- Telecommunication including internet and telephone (VoIP[7], IPTV, ...).
- Electronic control, automation and sensing (i.e. Digital Homes).
- Housekeeping applications which become network-enabled,.
- Access (GSM900/1800, UMTS/LTE[8], WiMAX) (wireless).
- LAN (WLAN, GPRS) (wireless).
- PAN[9] (Bluetooth) (wireless).

[6] DVB: Digital Video Broadcasting.
[7] VoIP: Voice over Internet Protocol.
[8] LTE: Long Term Evolution.
[9] PAN: Personal Area Network.

- Sensor, Telemetry, etc. (ZigBee, RFID[10], DVB-H/T) (wireless).

In addition to the applications described so far, sensing and control applications are gaining more and more interest in the home scenario. While these applications do not depend on high data rates and low latency times, the reliability of the network will be of utmost importance and optical fibres can also meet the requirements of these networks. Interoperability and convergence of all services and devices is obviously essential, thus requiring universally convergent protocols for the in-building networks [45]. It is worth pointing out that, as FTTx is heading toward Ethernet-based GPON (future 10G-PON upgrading), Ethernet seems to be the most promising standard in the upcoming in-building network architectures [46].

Regarding in-building network topologies, multipoint architectures are gaining the deployment of a future convergence network, opposite from the case of point-to-point solutions. The latter refer to the actual case in which most of the networks are based on a HG typically placed at the building/apartment entrance, where the external access network is terminated, and terminal premises are connected to this gateway, through either wired point-to-point star-like topology links or wireless links, which acts as a central switch. In this case if replacing copper cables by optical fibres, the latter would be used simply as a cable replacement for copper. This solution is straightforward if only baseband digital traffic is requested but if RF-like applications, as aforementioned, are also required such as analog or digital cable, terrestrial TV, satellite TV or transportation of radio signals towards remote antennas for example, the implementation of such multiformat HG including RoF solutions becomes clearly more complex and inflexible, so longer-term solutions are required. In such framework, to increase flexibility, multiplexing and transparency to different transmission and modulation formats would be beneficial and optical technologies give solutions for such architectures, with multipoint transparent architectures that can eventually use the wavelength domain to achieve multiplexing (i.e. WDM approaches and its variants, CWDM and DWDM).

Further details can be obtained in [44] or in the testbeds implemented by France Télécom in [47, 48]. These solutions basically transfer to the in-building networking architectures that are used today in the access and metro networks, such as the 1xN PON-like architecture, see Fig. 2.7 [44] where all PON mechanisms can be reused, including WDM, CWDM and DWDM multiplexing approaches. However, the main drawback relies on the fact that the optical components available to implement these advanced optical architectures in the in-building network scenario (i.e. short- and middle-reach distances) are mainly available only for silica SMF and, partially, for MMF, while WDM multiplexers and demultiplexers support only SMF. For the POF (and all its variants) these components are not (yet) available. Thus nowadays, the point-to-point architecture can support any fibre type, while the more advanced multipoint architectures support only SMF. So, further development of such devices needs to be done in order to achieve a full-convergence scenario.

[10] RFID: Radio-Frequency IDentification.

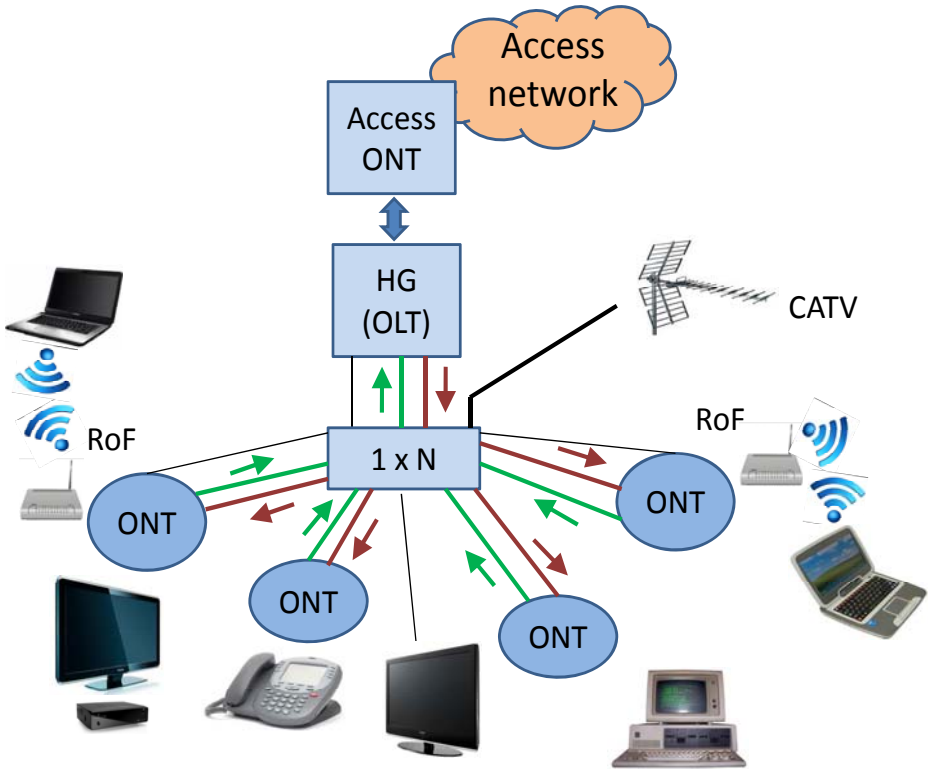

Fig. 2.7.- 1xN PON-like architecture for in-home access network. ONT: Optical Network Terminal, OLT: Optical Line Termination, HG: Home Gateway.

2.2 Fibre Optical Intensity Sensors with Self-Referencing

2.2.1 Introduction

In a deeper step and focusing on the sensing and control applications within the in-building scenario, optical-fibre development to date has concentrated mostly on their use in systems for telecommunications and data transfer thus being the principal stimulus for the optical fibre sensors technology. As a result, the realisation that optical fibres could also be used for sensors and sensing systems has increased rapidly since the 1980s with a wide range of applications, and lastly enhanced by modern signal processing techniques. Fibre optic sensors (FOS) exhibit a set of very attractive characteristics, including immunity to electromagnetic interference (opposite from electronic circuits and sensors), increased sensitivity over existing techniques, passiveness, resistance to hostile environments that may comprise hazardous chemicals or of any other kind [49-51], flexibility, geometric versatility, ruggedness, biological compatible, sensor multiplexing and distributed sensing over a single lead fibre. Furthermore, the increasing in-building networking feasibility can enhance the automation and integration of sensor applications and systems and vice versa. Recently, it is shown that one seventh of all fabricated sensors are used for home appliances [52]. This rate will increase with a higher demand on home automation and security applications by supporting higher integration and networking of devices in the building or

home. For both sensing scenarios, there are three different categories of fibre-optic sensors that could be required:

- Environment sensors: air pressure, temperature, wind, humidity,
- Monitoring sensors: health care, movement, lighting/illumination,
- Building sensors: statics, burglary/hold-up alarm, fire, gas and liquid detection, etc.

On the other hand, their main disadvantages are the high cost (compared to other technologies) as well as the unfamiliarity of the end user. Table 2.4 summarizes the different markets in which fibre-optic-based sensors have penetrated over these last three decades. There is also a summary of some of the optical technology options and applications that can be taken for fibre-optic sensors.

Area	Methods (examples)
Medical	Analytical; surface absorption; total internal reflection; laser Doppler;...
Defence	Surveillance; acoustic; magnetic; navigation; fire; flush; radiation; temperature; fail-safe switches;...
Aerospace	Encoders; switches; oil-in-water; particulates in fuels, oils; pressure displacement; machinery condition monitoring;...
Offshore	Gas detection; fire, smoke; well head controls; pollution controls; temperature;...
Industrial	Flow; pressure, temperature; combustion energy control;...

Table 2.4.- Optical fibre sensors market areas [53].

Over the past years, intensive research and development efforts have produced a large body of fibre-optic sensor technology [54], based both on multimode and singlemode fibres. Considering multimode optical fibres, an optical sensor for monitoring the corrosion of aluminium alloys is reported in [55] with applications in modern military aircraft maintenance. Another example of MMF fibre-optic sensor is the optical hydrophone reported in [56] for high-frequency measurements of ultrasound fields up to 100MHz. On the other hand, singlemode fibre optical sensors have also been widely employed as reported in [57] in which a self-referencing fibre-optic pressure sensor is developed based on a white light Michelson interferometer obtaining dynamic ranges from 0 to 38.08MPa with a resolution of 0.03MPa. Another example of SMF optical sensor is reported in [58] in which temperature is measured through a SMF taper.

As aforementioned, fibre-optic sensors, being electrically passive and intrinsically safe, can remotely operate in the presence of strong electromagnetic interference, hostile environment and explosiveness. As a result of this research in fibre-optic sensors (FOS) during the past years a huge volume of physical magnitudes such as temperature, strain, rotation, pressure, force, displacement, acceleration, corrosion, flow, humidity and gas concentration among other measurands [59-62] can be measured and still raising.

A generic classification of fibre-optic sensors is presented in Fig. 2.8 based on this author's criteria. It is worth pointing out that this is an attempt to unify criteria while accepting that the final result can be influenced by the author's viewpoint. A deep state-of-the-art regarding each fibre-optic sensor type can be found in [63] and [64].

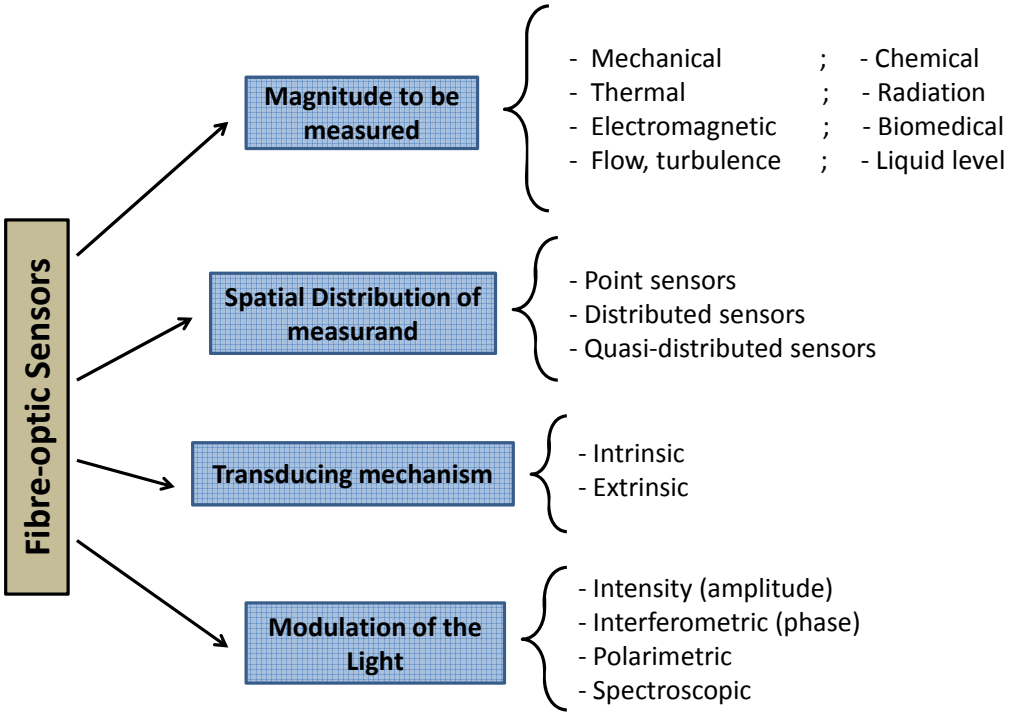

Figure 2.8.- General classification of fibre-optic intensity sensors (FOS).

Related to this latter classification, in recent optical sensing applications, one extensively investigated transducing mechanism is the intensity modulation, in which the intensity of the transmitted signal varies in accordance with the variable being measured (i.e. measurand). In general, intensity sensors usually are very attractive since they are simple in concept, reliable, small-sized and offer a wide range of applications at lower costs [65-68].

Light intensity modulation techniques reported in literature approach displacement (or microdisplacement) between two fibres [69], reflective mechanisms through a mirror or liquid between and emitter and receiver fibre [70-72], optical fibre microbending [73-75], optical fibre tapering [76-79] or based on evanescent field effects [80-83]. Other modulation techniques take advantage of spectrally based fibre optic sensors, which depend on a light beam being modulated in wavelength by an environmental effect. Examples of these types of sensors include those based on blackbody, fluorescence, absorption, etc. This latter technique is commonly used to determine temperature as the absorption profile of the probe, which is doped with rare-earth elements in most of the cases, is temperature-dependent [84-86]. All these kind of sensors can be applied to in-building/home scenario and can be easily integrated within an in-building/home network.

Although such sensors use a simple but effective measuring process for detection, their main drawback is interference from variation in losses non-correlated to the sensor modulation, so some strategy must be integrated. To overcome this limitation, in order to ensure accurate measurements by these optical fibre intensity modulated sensors, the implementation of a reference channel (physical or virtual) is vital. Such a channel will provide insensitivity to source intensity fluctuations and to variable transmission losses of the fibre link including connectors, which are often indistinguishable from transducer-caused effects. Different self-referencing methods to minimize the influences on the accuracy of measurements of long-term aging of optical source characteristics as well as short-term fluctuations of optical power loss in the leads to and from the transducer have been reported in literature [87, 88]. These undesirable variations in the power loss are inevitable in practical engineering applications, especially those that involve remote operation.

2.2.2 Self-referencing strategies

A general schematic for supporting remote intensity sensors is shown in Fig. 2.9. In this system, the transmission and reception stages are located in a single point, namely Central Office (CO), where the light is launched into a lead fibre towards the remote sensing point, where it passes through the optical sensor and returns to the CO through a return fibre. This Central Office can be identified, for instance, with the OLT, ANT or HG previously described in the former section 2.1.5. Coming back to Fig. 2.9, it shows the intensity-modulated measurement error sources which can be identified as the optical source (transmitter), the photodetector (receiver) and the optical fibre link (including its associated connectors).

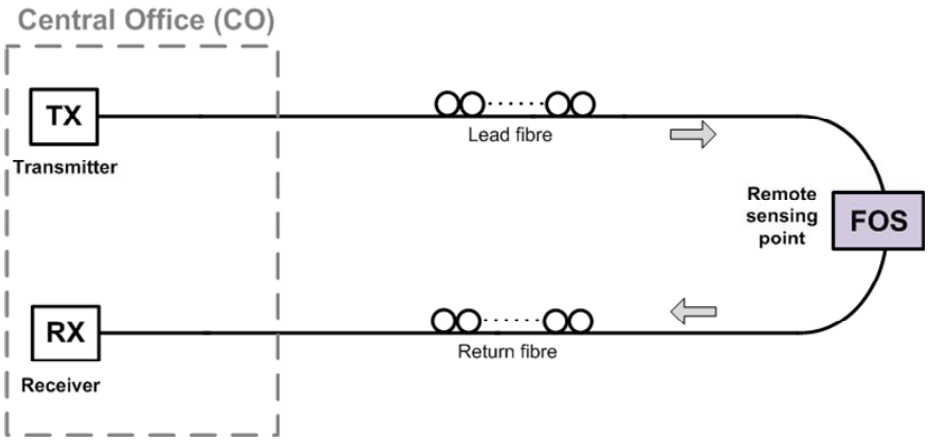

Figure 2.9.- General schematic of a fibre link for remotely addressing fibre-optic intensity sensors (FOS), with a transmission configuration in the sensing point.

Different self-referencing approaches have been reported in literature, providing mechanisms whereby the intensity variation of the light at the sensing head may be distinguished and measured independently of all the undesired perturbations. This limitation is not easy to overcome due to several factors. Firstly, the intensity of the light

due to the fibre attenuation or due to passive optical devices such as couplers or connectors is not constant. Secondly, source intensity fluctuations as well as sensitivity changes in the photodetector responses also contribute to have less accuracy of measurements. Finally, long-term aging of optical and opto-electronical device characteristics, namely thermal instability, in addition to environmental-dependent performances of such devices can lead to non-error free measurements in the final result.

Despite being not possible to avoid these measurement error sources, it is possible to minimize these undesirable influences on the measurements accuracy. To overcome this limitation, the implementation of a reference channel has been widely deployed in literature. Effective referencing of the variations associated with optical signal transmission effects needs that the reference signal should propagate either in parallel with the sensing signal (measurand) or should follow it very closely throughout the system. Furthermore, both signals must have the same susceptibility to all optical loss mechanisms to ensure similarity of such variations. Such a channel (i.e. signal) is used to calibrate the transducer-physical magnitude response undergoing all other losses in the system (and containing the information relative to the variation in losses non-correlated to the sensor modulation). Both channels, sensing channel and reference channel, must be separated and identified, as shown in Fig. 2.10, either physically or virtually by means in time, frequency or wavelength separation techniques. These channels or signals can be distinguished following different techniques or even combining them [88]:

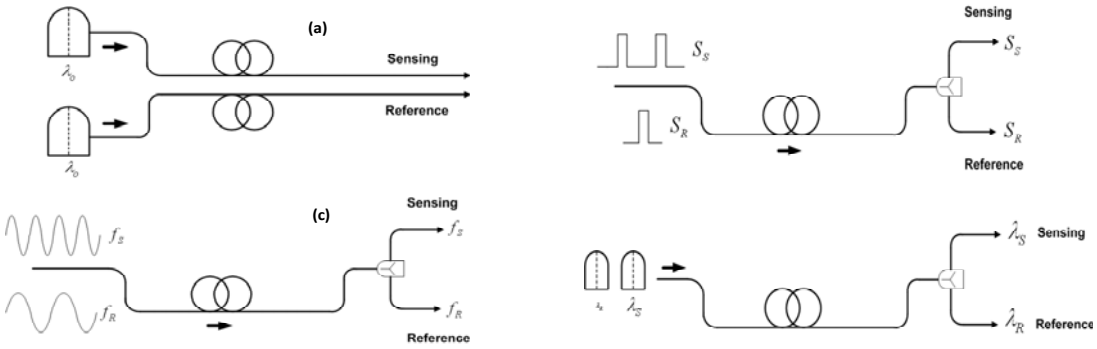

Figure 2.10.- Common signal separation techniques employed in referenced systems: (a) spatial separation; (b) temporal separation; (c) frequency separation; (d) wavelength separation.

- **Spatial (or physical) separation:** i.e. both separate optical fibres running parallel for the reference and sensing channels, respectively, see Fig. 2.10(a). At the sensor, the measurand signal will be intensity-modulated by the parameter being measured whereas the reference signal may be bypassed [89]. Although this strategy might be expected to provide an output free from the optical transmission effects, the use of separate optical fibre links for the two channels defeats this objective. Immunity to the optical source fluctuations is generally provided by using a single optical source in conjunction with a beamsplitter, a coupler or an optical circulator. This process produces two optical signals with the same relationship to any optical source fluctuations. The major benefit of this scheme is that can be used in almost all optical sensor types whether they are intrinsic or extrinsic, and in transmission-

mode or reflection-mode. The two optical fibres may be sleeved together along the entire optical path to ensure a similarity in their response to environmental effects. Nevertheless, there is a cost penalty associated with the use of two separate optical fibres for the transmission of both signals.

At the same time, different methods, with slight improvements, to implement this technique have appeared in literature such as balanced bridge configurations [90] based on a four-port sensing head with two input ports and two output ports (similar to the electrical Wheatstone bridge), see Fig. 2.11, in which undesirable fluctuations of the optical intensity are eliminated by rating the four optical signals propagating throughout the optical paths of the topology being the global output variable proportional to the transducer's transfer function M.

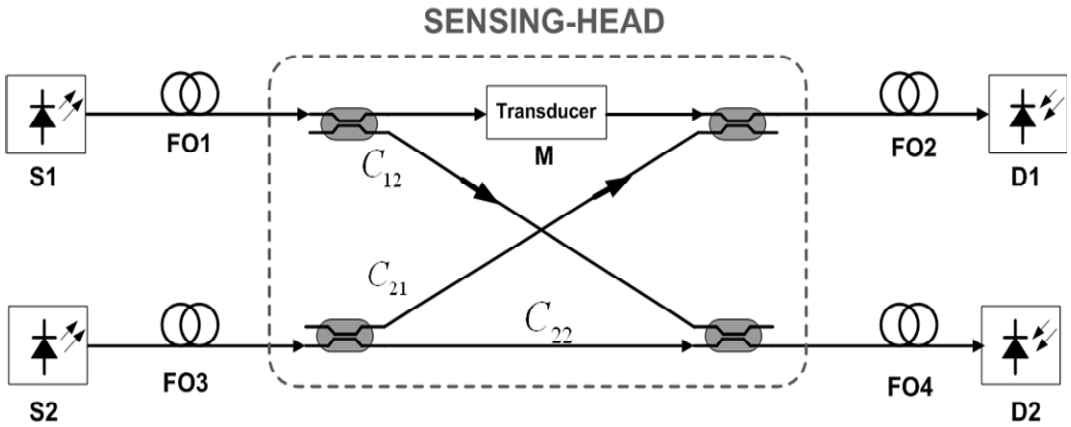

Figure 2.11.- Characteristic four-port coupler-based arrangement for a balanced bridge referencing scheme. Both optical sources (S1 and S2) need to be modulated either applying TDM (Time Division Multiplexing) or FDM (Frequency Division Multiplexing) to recover the four signals at the detectors (D1 and D2).

- **Temporal separation (different time slots):** temporally referenced sensor systems utilize a short optical pulse which is allowed to circulate in an optical loop [91] or in a Fabry-Perot cavity [92], for example. This referencing technique produces a series of temporally-spread pulses having a similar relationship with the original pulse. However, in practice, the obtained value represents the value of the measurand plus the insertion loss of the optical loop; although useful signal processing techniques have been developed to minimize this limitation [93]. The temporal separation technique generally uses a beamsplitter to provide two optical signals (i.e. channels) from a single input beam. In this case, the sensors are specifically configured to introduce a time delay between these two optical signals. Subsequent temporal separation between signals allows them to propagate on a single optical fibre lead through Time Division Multiplexing (TDM) techniques [94]. Furthermore, both signals then exhibit similar variations with optical source fluctuations. Nevertheless, the efficiency would be reduced by any differences between the optical signal paths, see Fig. 2.10(b).

- **Frequency separation:** it follows the same principle as the temporal separation aforementioned but using different carrier frequencies. This separation technique

requires an electrical frequency modulation of the optical source (or sources), see Fig. 2.10(c). Subsequent frequency separation between channels allows them to propagate on a single optical fibre lead through Frequency Division Multiplexing (FDM) techniques. Reference and measurand channels need to be electronically filtered at the reception stage. As in temporal separation, this technique allows the use of a single photodetector in reception for their demodulation. Unlike the TDM technique, however, the FDM approach enables simultaneous parallel transmission of signals through a unique optical fibre lead. It can be noticed that FDM and TDM signal separation techniques are interchangeable and are often only used to simplify the design of optical receiver electronics.

- **Wavelength separation (different wavelength bands):** most wavelength reference systems are based on two separate channels comprising the reference and measurand transmission wavelength bands, see Fig. 2.10(d). Wavelength referencing schemes differ in the way the two wavelength band signals are generated: this can involve two separate optical sources [95] or, alternatively, both signals may be extracted from the same optical source [96, 97]. Furthermore, the reference and measurand optical signals can also be allowed to share a common optical fibre link when they are placed within different wavelength bands. An output free from variations associated with optical transmission effects could then be achieved by selecting two signal wavelength bands close together to ensure their similar behaviour throughout the system. This wavelength separation can be achieved by using Wavelength Division Multiplexing (WDM) devices. However, without the use of any further referencing mechanism, this scheme is prone to errors arising from thermal drifts of the optical source although the wavelength bands can be matched by an approximation to a similar thermal-behaviour of the source at such bands [98]. It is worth noticing that, in such strategy, there is a trade-off between the effective wavelength separation for both channels and the optical crosstalk induced. The nearer the channels are in wavelength, the more similar thermal behaviour but power crosstalk can be obtained, unless high-precision demultiplexers are used.

None of the aforementioned referencing methods can be said to be fully effective against all the variations seen before. Even those incorporating advanced referencing strategies are liable to suffer from some uncertainty of measurement. For example, the balanced bridge referencing topology may be susceptible to errors arising from the environmental sensitivity of the coupler used in the sensing head. Furthermore, the number of components can be generally higher than other strategies and, consequently, less cost-effective plus the need of more complex sensing heads at the transducing point in comparison with the fibre bypass strategy, which is intrinsically very simple but non-effective if we consider the short-term fluctuations suffered by both fibres despite very similar optical paths. However, this technique constitutes a robust spatial referencing configuration.

On the other hand, temporal separation strategies for referencing are susceptible to be not effective for the undesirable fluctuations in the intensity of the light at the common optical paths for both channels. In order to minimize such effect a solution would be to shorten the fibre loop used to generate the reference and the measurand pulses, but this improvement

would led to the use of a more complex electronics control as the temporal separation becomes shorter. However, this strategy has the advantage of the reduced number of components needed to be implemented.

Finally, relative to the wavelength separation strategy, although such a technique provides a similar effective referencing performance with regards to balanced bridge-based ones, the long-term aging of the optical sources plus environmental temperature changes can produce variable wavelength emissions in such optical sources which could not be compensated. In addition to this, the real performance of optical devices such as couplers, multiplexers/ demultiplexers and photodetectors implies a wavelength-dependence on their characteristics which could influence the system performance.

To resume, among all the strategies that offer the potential for near full referencing, there are some that may find widespread utilization. These include the spatial referencing methods based on parallel optical fibres mainly the balancing bridge scheme, the temporal referencing schemes and the wavelength referencing schemes utilizing optical source monitoring. Furthermore, most of these referencing strategies offer scope for further improvements.

As said before, the two most important error sources in fibre-optic intensity-based sensor systems are due to the optical source and due to the optical devices employed in the optical fibre link (including the optical fibre itself). A first error source can be associated to the thermal instability of the optical source that produces source intensity fluctuations as well as wavelength emission variations. Such a thermal instability can be produced by environmental temperature changes or heat dissipation mechanisms in the semiconductor optical source. A second source of error can be appreciated due to the changes in the optical paths meaning fluctuations in the intensity of the light received. Both the aforementioned optical intensity variations due to error sources combined with the transducer intensity modulation of the light may be undistinguishable one regards to the other. In order to allow the distinction between the intensity variation of the light at the sensing head independently of all the undesired perturbations, it is desirable to provide the same optical paths for the reference and for the sensing channels excepting in the measuring point (i.e. sensor head). Nevertheless, considering the latter premise, the utilization of different optical sources or different photodetectors would be not overcome. Despite this fact the following considerations can be made in order to improve referencing techniques for fibre-optic intensity-based sensors:

- Preferable referencing schemes are contingent with the use of a unique optical source and a unique photodetector in order to avoid different environmental dependences (or different heating dependences) depending on the different devices characteristics. Alternatively, differential methods can be devised for simultaneous sources and receivers usually being less cost-effective.

- Both reference and sensing channels must follow the same optical path in the system except the measurement point. Consequently, referencing topologies providing the same optical fibre lead for both channels are preferable.

- The sensing head must be designed in order to properly separate the reference signal and the measurand signal as closer as possible from the point in which the transducer modulates the intensity of the light. Then, both signals must be recombined just outside the transducer. By this premise, the environmental effects in both signals can be equalized.

- No matter the referencing strategy employed, both the reference and the measuring signal must show the same dependence with regards to fluctuations due to connectors, couplers, etc in order to avoid indistinguishable measurements from transducer-caused effects.

- Desirable performances of a referencing scheme are also compatibility and scalability within telecommunication optical fibre networks, thus allowing the integration of multiplexed self-referencing fibre-optic sensors within a single optical fibre topology. Some contributions in this field are reported in Chapter 5 and Chapter 6.

2.2.3 Representative example of a self-referencing approach applied to liquid detection

A representative example that demonstrates the capabilities of fibre-optic sensors in home networks plus assuring self-referencing, for measuring liquid levels in harsh environments such as oil/petrol tanks or bio-mass boilers to be used in condominiums and buildings, is described within this section. Moreover, the fibre-optic sensor itself is a polymer optical fibre (POF)-based coupler that changes its coupling ratio (K) depending on the different refraction indexes around it (provided by different alternative liquids surrounding the sensor) [99]. In addition to, it intrinsically assures self-reference property as the sensitive parameter K has no dependence of transmission power fluctuations or undesirable power losses at the link or in the sensor network. The sensing area has been obtained by a 3 step process: introducing bending losses, eliminating the fibre cladding and polishing a defined fraction of the fibre core. This technique increases the external media refractive index sensitivity of the sensor [100].

A scheme of the fibre-optic sensor is shown in Figure 2.12(a), where P_1 is the input port and P_2 and P_4 are, the direct and coupled output ports of the sensor, respectively. The coupling ratio of the device is defined as $K = P_2 / (P_2 + P_4)$. From Fig. 2.12(a) T, R and g define, respectively, the Fresnel transmission coefficient, the curvature radius applied at the sensing area and the gap between the cores of the two fibres at the coupling area. Parameter ε indicates the fibre polishing depth (see inset III of Fig. 2.12(a)). A photograph of the manufactured sensor device is shown in Fig. 2.12(b).

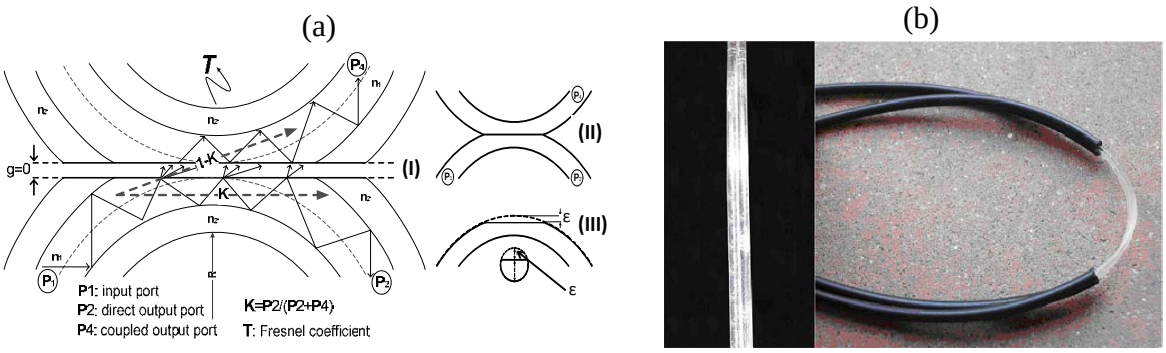

Figure 2.12.- (a) Longitudinal section of the coupling (and sensing) area of the liquid sensor. Inset: liquid sensor scheme (I and II) and one arm sensor fibre after polishing (III). (b) Photograph of the sensor device.

The principle of operation is the following. By introducing a bend on a multimode fibre, the higher-order propagating modes in the fibre are refracted because the angle of incidence increases in the interface core-cladding. This refracted light produces an increase of the power losses in the receiver, given by the Fresnel transmission coefficient *T*, which is a function of the angle of incidence for a certain beam with the normal to the core surface and the critical angle of the optical fibre. The greater the angle of incidence, the greater value of *T* can be obtained. Thus, the optical power is transferred and guided in the fibre cladding due not only to the curvature, but also to the polished core, see Figure 2.12(a). When the sensor is immersed into different liquids, these losses change because of the different refractive indexes surrounding the coupler which means a variation of the coupling ratio *K* of the sensor and, therefore, a variation of optical power at port P_4 at the reception stage. If the surrounding liquid is oil, its refractive index (n_{oil} = 1.46) becomes very similar to the refractive index of the fibre cladding (n_{cl} = 1.417) and all the modes guide through the cladding are refracted outside the fibre. In that case, the value of *T* increases whereas the optical power at port P_4 decreases. Consequently, the coupling ratio *K* increases and the coupler becomes more directive. As the liquid refractive index decreases (n_{water} = 1.33 or $n_{air} \approx 1$) the ratio of the optical power guides again into the fibre core increases as well as the optical power received in port P_4, so *K* decreases. This change of *K* can be measured and, consequently, it is possible not only to distinguish the air-liquid change but also to detect the kind of liquid in which the sensor is immersed, depending on the measured value of this parameter.

The characteristics of the manufactured fibre-optic sensor are the following: n_{co} = 1.492 and n_{cl} = 1.417 with a polishing depth of ε = 0.23 ± 0.01mm. Both coupler arms have been joined by gluing over the length of the sensing area (3 cm of polished fiber) with no-gap interface (*g* = 0). The set-up scheme for the measurements comprises a laser diode operating at a wavelength λ = 630 nm, two optical power meters at reception and a tank in which the sensor is immersed into different liquids. Regarding to the measurements, coupling ratio values for Carthamus tinctorius oil (n = 1.466) and water besides air surrounding the sensor have been experimentally measured. It has been taken five measurements for each sensor configuration (each configuration is determined by the bending radius applied to the sensor and the type of liquid as external media). If we define repeatability as the percentage of the output parameter variation for a determined number of

measurement cycles (under the same conditions), the worst case was found to be 1.02% (with R = 25 mm and air as external medium), which is a very good result. All these measurements have been taken for an environmental temperature of T = +28.6ºC (average value) with a maximum deviation of ΔT = ±3ºC. Additionally, different bending radii (*R* = 60 mm, 25 mm, 12 mm and 7 mm) at the fiber sensing area have been applied and investigated.

Moreover, a self-referencing test has also been done to prove the inherent self-referencing property of the proposed liquid level sensor. Figure 2.13(a) shows the average value and the measurement errors at each measurement point of the coupling ratio *K* versus different bending radius and different external media. Depending on the media surrounding the sensing area, the value of *K* changes for each fixed bending radius. With proper control electronics and detection schemes the liquid can be distinguished; highest sensitivity is obtained for a bending radius *R* = 25 mm. For this sensor configuration the following coupling ratios are obtained: K_a = 0.545 ± 0.001 (air); K_w = 0.563 ± 0.001 (water) and K_o = 0.605 ± 0.002 (oil) with coupling ratio increments of ΔK = 0.018 (from air to water); ΔK = 0.060 (from air to oil) and ΔK = 0.042 (from water to oil). Measurement errors are given as standard deviation and are, in all cases, at least one order of magnitude below the average value of *K* when it changes, depending on the surrounding liquid.

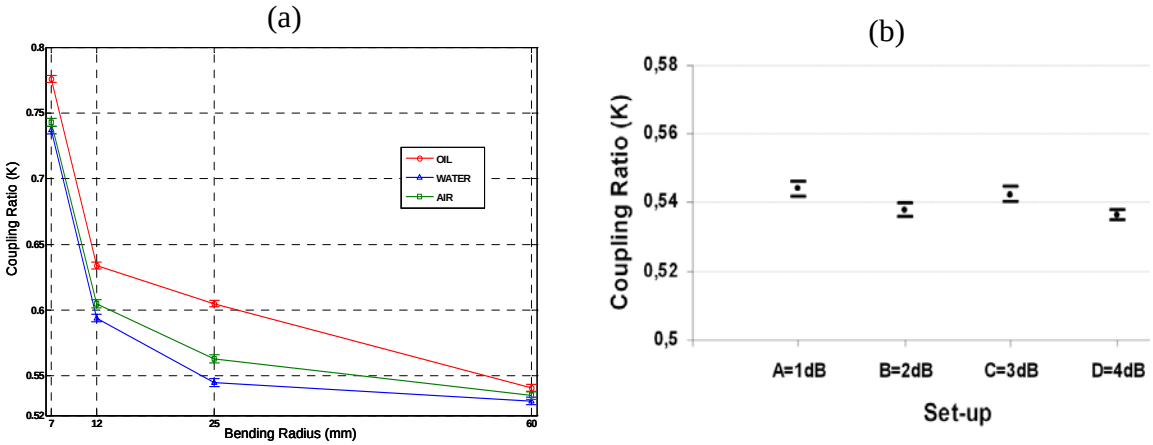

Figure 2.13.- (a) Measurements of the sensor coupling ratio versus bending radius, for different liquids. Standard deviation in measurements is also represented for each measurement point. (b) Measurement of the coupling ratio of the sensor for different link losses (up to 4dB from set-up A to set-up D).

On the other hand, the independence of the sensor against hypothetical link losses due to its self-referencing characteristic has also been tested as can be seen in Figure 2.13(b). From a nominal coupling ratio of *K*=0.54 a maximum deviation of ΔK = ±0.002 (six measurements with a temporal space of half an hour between each other were taken per set-up) is obtained. The maximum link losses tested are 4dB and are made by bending the fiber into turns using Mode Scramblers.

Both the simulated and the experimentally measured *K* results are congruent and show a good agreement between theory and measurements. For instance, Fig. 2.14 shows a simulation of K versus polishing depth for different bending radii (*R*=6mm. 7mm and

8mm) with water as external liquid surrounding the sensor. In order to make a comparison between measured and simulated results an arbitrary point, marked as point A, has been selected; obtaining a simulated value of K=0.75, for ε=0.23mm, R=7mm and water as external medium whereas the measured value of the coupling ratio for a manufactured sensor with these parameters was found to be K=0.744 as seen in Fig. 2.13(a). It is worth mentioning that the point A corresponds with the fabricated prototype requiring less computational time requirements. The simulation technique used is based on the ray tracing method in which light is treated as rays [101] and can help to optimize the design of physic parameters in this type of sensors.

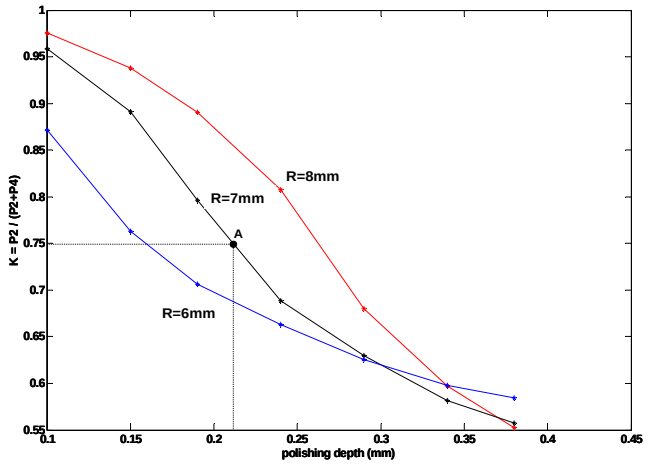

Figure 2.14.- K versus polishing depth simulation for different bending radii (6, 7 and 8 mm) considering water as the external medium.

Finally, the temperature dependence of the sensor device has been tested inside a climatic chamber over a 25ºC temperature range, from T = +25ºC to T = +50ºC. Figure 2.15(a) shows the deviation of K at that temperature range. The sensor coupling ratio deviation is found to be around 1% ($\Delta K \leq 0.006$) from its nominal value. This deviation is mainly produced by the glue used for the sensor manufacturing showing the low temperature dependence of the device as is derived from results shown in Figure 2.15(b). This figure shows the influence of temperature in a plastic optical fibre (POF) for different fibre status. Five tests have been made: "jacketed POF" (fibre with no action taken on it), "bare POF" (stripped fibre), "polished POF" (fibre whose core is partially polished with a polishing depth of ε = 0.23 mm), "bare POF+glue" (stripped fibre with a glue layer over the cladding) and "polished POF+glue" (fibre partially polished with a glue layer on it). Although polishing the fibre core have significant effects when increasing the temperature (with regards to the stripped POF), it can be seen from Figure 2.14(b) that output optical power variations are mainly produced by the effect of gluing when considering the same fibre status, obtaining deviations of 0.15 dB between glued/not-glued bare fibre and 0.12 dB between glued/not-glued polished fibre.

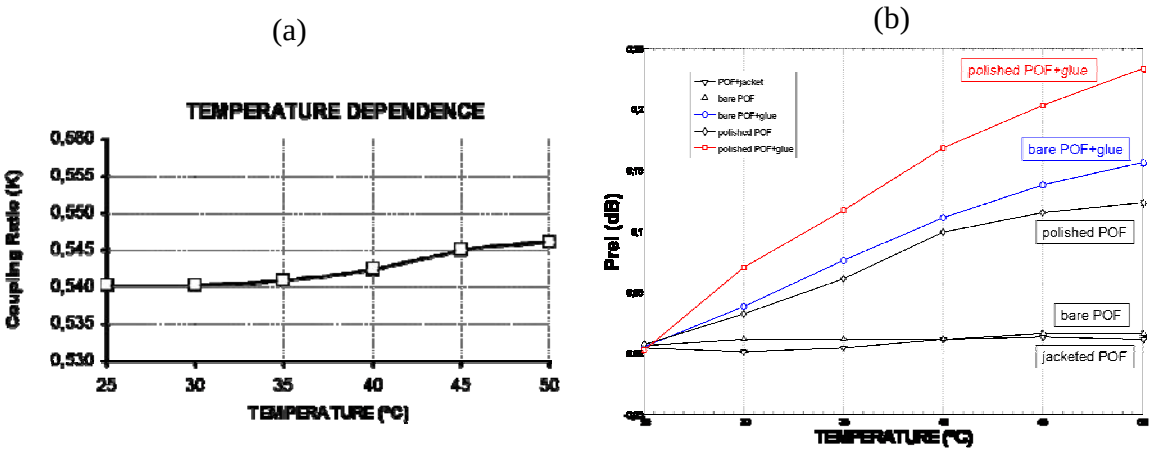

Figure 2.15.- (a) Temperature dependence of the coupling ratio of the sensor from T=25ºC to T=50ºC. (b) Temperature dependence for different fibre status T=25ºC to T=50ºC.

2.3 Summary and Conclusions

Today's electronic home equipment consists of a growing variety of interconnected devices, such as:

- Audio&Video information, entertainment.
- Telecommunication including internet and telephone.
- Electronic home control, automation and sensing, e.g. heating and air conditioning. access and light control and security services.
- Housekeeping applications which become network-enabled.

In the whole fibre network society to be realized in near future, it is said that silica based optical fibres for long-haul backbone systems will be only several percents of the total use, and that the remaining more than 90 percents will be for local area networks (LANs) of several hundred meters or even units of kilometres.

In the final link to the end users, telecommunication networks have to deliver a large variety of services with widely ranging signal characteristics. Coaxial cable bus networks have been optimised to provide television and radio broadcast signals, increasingly along with fast data by means of cable modems. Twisted copper pair point-point links were laid out to deliver voice telephony services, nowadays together with fast data via ADSL (Asymmetric Digital Subscriber Line) and VDSL (Very high bit-rate Digital Subscriber Line) modems. And wireless links are today bringing an increasing share of the voice telephony traffic, plus some data, by means of GSM (Groupe Special Mobile), GPRS (General Packet Radio Service) and UMTS (Universal Mobile Telecommunications System) and even fast data by wireless LANs. Basically these services may be grouped in four families: voice/audio, video, data and (low-speed) home control. Traffic demands range from a symmetrical 64kbps for basic voice, to a few Mbps asymmetrical for digital video, up to 10Mbps symmetrical for fast data file transfer (e.g. for teleworking). The services also put different Quality-of-Service (QoS) demands, ranging from best-effort

internet data to real-time video. The various physical network infrastructures are mostly optimised for their main service. This in general impedes the introduction of new services, the upgrading services, and the creation of links between the services (e.g. between the services on the coaxial network and the twisted pair network).

A common infrastructure that is able to carry all the service types would alleviate these problems. Furthermore, functional requirements for a future convergence network should include:

- provision of high bandwidth services and content to each customer,
- a flexible network architecture design that can accommodate future innovations,
- connection by the proposed media of each end subscriber directly to the active equipment, to ensure maximum available capacity for future service demands,
- support for future network upgrade and extension,
- minimize disruption during network deployment, to help future networks gain acceptance from network owners

Such a converged infrastructure needs to be broadband to meet the signal requirement of all services. And, of key importance in the user environment, it needs to be easy to install and to maintain, thus yielding both low capital expenditure and low operational expenditure costs. Optical fibre by virtue of its wide bandwidth is an ideal candidate or the infrastructure medium and FTTx deployments with WDM-PON topologies are considered in the long-term the target architecture for the next-generation access networks due to their unlimited scalability among other factors.

However, installing silica singlemode fibres (predominantly used in today's telecommunication networks) requires careful handling by skilled personnel and delicate equipment for fibre fusing and connectorising at the terminal equipment. Multimode fibres have a much larger core diameter and thus alignment in fibre splicing and connectorising is more relaxed. Its bandwidth per unit length is considerably less and its losses are higher than those of singlemode fibre are, but may not be decisive as link lengths are relatively short in the user environment. These link lengths may range from well below 1 km in residential houses, to only a few kilometres in larger building such as offices, hospitals, airport halls, etc. Also the injection of light from optical sources is easier, without requiring sophisticated lens coupling systems. Furthermore, return losses of light reflected into the sources are higher, thus improving the system's robustness against reflections from bad connectors or splices. Moreover, polymer (intrinsically multimode) optical fibre may be even easier to install than silica multimode fibre, as it is ductile, easy to splice and to connectorise even maintaining high bandwidth performances as in the case of PF GIPOFs. It is obvious that the deployment of such emerging next generation access (NGA) network technology and its convergence would be not possible without the research and evaluation of predictive and accurate models for the frequency response in both the aforementioned fibre types, silica-based GI-MMF and PF GIPOF, respectively, to overcome the inherent limitations of such a transport information media. Those models must be validated with some experiments. Some contributions on this topic are reported on Chapter 3 and Chapter 4.

On the other hand, optical-fibre development to date has concentrated mostly on their use in systems for telecommunications and data transfer thus being the principal stimulus for the optical fibre sensors technology. Research and multiple solutions on optical fibre sensors have been addressed also fuelled by the increasing in-home networking feasibility. The development of such a network can enhance the automation and integration of sensor applications and systems and vice versa. It can be estimated that one seventh of all fabricated sensors are used for home appliances. This rate will increase with a higher demand on home automation and security applications by supporting higher integration and networking of devices in the home.

Fibre optic sensors also exhibit a set of very attractive characteristics, including immunity to electromagnetic interference, resistance to hostile environments that may comprise hazardous chemicals or of any other kind, geometric versatility, ruggedness, sensor multiplexing and distributed sensing over a single fibre. A brief introduction on the state-of-the-art of optical fibre sensors in general focussing afterwards on the intensity-based ones has been addressed. They have been demonstrated in literature to be very simple and easily made selective to specific measurand leading to a cost-effective solution compared to, for example, interferometric solutions. Moreover, they can be asily integrated in optical networks by means of different multiplexing techniques.

However, the main drawback of this type of fibre-optic sensors is that they are susceptible to two dominant types of errors: the first caused by the variable optical losses suffered by the signals propagating through the series of optical components comprising the system, and the second caused by thermal inestabilities (caused by ambient temperature changes and/or electrical heat disipation) of the optical source(s) and detectors. These optical variations will be additionally added to the intensity changes introduced by the measurand. The resulting error signal may therefore include contributions from the optical source, variable losses in the connecting fibres and couplers, sensitivity changes at the detector and the sensitivity of the system to environmental perturbations. In constrast, key issues to minimize these effects must be addressed in addition to the special attention that must be paid to the integration of these sensor networks with current data networks. These issues constitute a further contributions of this Thesis, and will be described in Chapter 5 and Chater 6.

A representative example that demonstrates the capabilities of fibre-optic intensity-based sensors with self-referencing property for measuring liquid levels in harsh environments such as oil/petrol tanks or bio-mass boilers to be used in condominiums and buildings has been presented in this chapter. It consists on a self-made POF-based self-referencing coupler sensor device for liquid detection. The use of a coupler as a sensor device intrinsically means a self-referencing sensor. The advantage of this technique is based on the fact that undesirable variations of the optical power at any point of the link between the emitter and the receiver do not change the value of K, because it equally affects both sensor outputs (P_2 and P_4) and consequently the ratio between them is unaltered. Furthermore, such fibre-optic sensors can enhance the automation and security applications by supporting higher integration and networking of devices in the home within a fully ‘optical domain’.

2.4 References

[1] B. N. S. Strategy Analytics, "Global Broadband Forecast: 1H2008," May 2008.

[2] B. Charbonnier, "End-user Future Services in Access, Mobile and In-Building Networks," *FP7 ICT-ALPHA project, public deliv. 1.1p*, pp. http://www.ict-alpha.eu, July 2008.

[3] S. Meyer, "Final usage Scenarios Report," FP7 ICT-OMEGA Project, public deliv. 1.1 Aug. 2008.

[4] J. K. W. Daum, P.E. Zamzow, O. Ziemann, *Polymer Optical Fibers for Data Communication*. USA: Springer, 2001.

[5] http://www.ftthcouncil.eu.

[6] http://www.ieee802.org.

[7] A. Polley, "High Performance Multimode Fiber Systems: A Comprehensive Approach," in *School of Electrical and Computer Engineering*. vol. Thesis: Georgia Institute of Technology, Dec. 2008.

[8] M.Z.. Win, R.A. Scholtz, "On the robustness of ultra-wide bandwidth signals in dense multipath environments," *IEEE Communications Letters*, vol. 2, pp. 51-53, 1998.

[9] W. Alliance, "Worlwide regulatory status [Online]. Available: http://www.wimedia.org."

[10] O. Andrisano, V. Tralli, and R. Verdone, "Millimeter Waves for Short-Range Multimedia Communication Systems," *Proc. IEEE*, vol. 86, pp. 1383-1401, 1998.

[11] A. M. J. Koonen, M.G. Larrodé, "Radio-Over-MMF Techniques, Part II: Microwave to Millimeter-Wave Systems," *J. Lightwave Technol.*, vol. 26, pp. 2396-2408, 2008.

[12] P. Smulders, "Exploiting the 60 GHz Band for Local Wireless Multimedia Access: Prospects and Future Directions," *IEEE Communications Magazine*, pp. 140-147, 2002.

[13] X. Zhao and F. S. Choa, "Demonstration of 10-Gb/s transmissions over a 1.5-km-long multimode fiber using equalization techniques," *IEEE Photonics Technology Letters*, vol. 14, pp. 1187-1189, 2002.

[14] L. Raddatz, I. H. White, D. G. Cunningham, M. C. Nowell, M. R. T. Tan, and S. Y. Wang, "Fiber-optic m-ary modulation scheme using multiple light sources," in *Optical Fiber Communication. OFC 97., Conference on*, 1997, pp. 198-199.

[15] M. J. O'Mahony, "Duobinary transmission with p-i-n f.e.t. optical receivers," *Electronics Letters*, vol. 16, pp. 752-753, 1980.

[16] L. Raddatz, I.H. White, D.G. Cunningham, M.C. Nowell, "An experimental and theoretical study of the offset launch technique for the enhancement of the bandwidth of multimode fiber links," *J. Lightwave Technol.*, vol. 16, pp. 324-331, 1998.

[17] M. Webster, L. Raddatz, I. H. White, and D. G. Cunningham, "A statistical analysis of conditioned launch for gigabit ethernet links using multimode fiber," *J. Lightwave Technology*, vol. 17, pp. 1532-1541, 1999.

[18] Q. Sun, J. D. Ingham, R. V. Penty, I. H. White, and D. G. Cunningham, "Twin-Spot Launch for Enhancement of Multimode-Fiber Communication Links," in *Lasers and Electro-Optics, 2007. CLEO 2007. Conference on*, 2007, pp. 1-2.

[19] S. Qun, "Error performance of OFDM-QAM in subcarrier multiplexed fiber-optic transmission," *IEEE Photonics Technology Letters*, vol. 9, pp. 845-847, 1997.

[20] B. J. Dixon, R. D. Pollard, and S. Iezekiel, "Orthogonal frequency-division multiplexing in wireless communication systems with multimode fiber feeds," *IEEE Transactions on Microwave Theory and Techniques*, vol. 49, pp. 1404-1409, 2001.

[21] E. J. Tyler, M. Webster, A. Wonfor, R. V. Penty, and I. H. White, "Transmission of a single 2.5 Gb/s subcarrier modulated channel over 300 m of 62.5 μm multimode fibre," in *IEEE 13th Annual Meeting Lasers and Electro-Optics Society 2000 Annual Meeting. LEOS 2000*, 2000, pp. 354-355, vol.1.

[22] T. K. Woodward, S. Hunsche, A. J. Ritgerz, and J. B. Stark, "1.6 Gb/s transmission over 1 km of 62.5 micron-core multimode fiber by subcarrier modulation of 850 nm VCSELs," in *Optical Fiber Communication Conference, 1999, and the International Conference on Integrated Optics and Optical Fiber Communication. OFC/IOOC '99. Technical Digest*, 1999, pp. 80-82 vol.4.

[23] X. Shen, J. M. Kahn, and M. A. Horowitz, "Compensation for multimode fiber dispersion by adaptive optics," *Opt. Lett.*, vol. 30, pp. 2985-2987, 2005.

[24] K. M. Patel, A. Polley, K. Balemarthy, and S. E. Ralph, "Spatially resolved detection and equalization of modal dispersion limited multimode fiber links," *J. Lightwave Technol.*, vol. 24, pp. 2629-2636, 2006.

[25] L. Raddatz and I. H. White, "Overcoming the modal bandwidth limitation of multimode fiber by using passband modulation," *IEEE Photonics Technology Letters,* vol. 11, pp. 266-268, 1999.

[26] S. Kanprachar and I. Jacobs, "Diversity of coding for subcarrier multiplexing on multimode fibers," *IEEE Trans. Commun.,* vol. 51, pp. 1546-1553, 2003.

[27] E. J. Tyler, M. Webster, R. V. Penty, and I. H. White, "Penalty free subcarrier modulated multimode fiber links for datacomm applications beyond the bandwidth limit," *IEEE Photonics Technology Letters,* vol. 14, pp. 110-112, 2002.

[28] J. Zeng, S.C.J. Lee, F. Breyer, S. Randel, Y. Yang, H.P.A van den Boom, A.M.J. Koonen, "Transmission of 1.25 Gb/s per Channel over 4.4. km Silica Multimode Fibre Using QAM Subcarrier Multiplexing," in *European Conf. Opt. Commu., ECOC2007,* Berlin, Germany, 2007, p. Paper 7.4.3.

[29] I. Gasulla and J. Capmany, "Simultaneous baseband and radio over fiber signal transmission over a 5 km MMF link," in *International Topics Meeting on Microwave Photonics, 2008. Jointly held with the 2008 Asia-Pacific Microwave Photonics Conference. MWP/APMP 2008.* 2008, pp. 209-212.

[30] R. A. Griffin, P.M. Lane, J.J. O'Reilly, "Radio-Over-Fiber Distribution Using an Optical Millimeter-Wave/DWDM Overlay," *Proc. OFC/IOOC 99,* vol. 2, pp. 70-72, 1999.

[31] R. A. Griffin, "DWDM Aspects of Radio-over-Fiber," *Proc. LEOS 2000 Annual Meeting,* vol. 1, pp. 76-77, 2000.

[32] C. Lim, A. Nirmalathas, M. Attygalle, D. Novak and R. Waterhouse, "On the Merging of Millimeter-Wave Fiber-Radio Backbone With 25-GHz WDM Ring Networks," *J. Lightwave Technol.,* vol. 21, pp. 2203-2210, 2003.

[33] G. H. Smith, D. Novak and C. Lim,, "A millimeter-wave full-duplex fiber-radio star-tree architecture incorporating WDM and SCM," *IEEE Photon. Tech. Lett.,* vol. 10, pp. 1650-1652, 1998.

[34] H. Toda, T. Yamashita, T. Kuri and K. Kitayama, "Demultiplexing Using an Arrayed-Waveguide Grating for Frequency-Interleaved DWDM Millimeter-Wave Radio-on-Fiber Systems," *J. Lightwave Technol.,* vol. 21, pp. 1735-1741, 2003.

[35] E. J. Tyler, P. Kourtessis, M. Webster, E. Rochart, T. Quinlan, S. E. M. Dudley, S. D. Walker, R. V. Penty, and I. H. White, "Toward terabit-per-second capacities over multimode fiber links using SCM/WDM techniques," *J. Lightwave Technol.,* vol. 21, pp. 3237-3243, 2003.

[36] A. M. J. Koonen, "Novel signal multiplexing methods for integration of services in in-building broadband multimode fibre networks," in *Proceedings of ISSLS,* Edinburgh, Scotland, 2004.

[37] T. Koonen, A. Ng'Oma, P. Smulders, H. v. Boom, I. Tafur Monroy and G. Khoe, "In-house networks using multimode polymer optical fiber for broadband wireless services," *Photonic Network Communications,* vol. 5, pp. 177-187, 2003.

[38] H. R. Stuart, "Dispersive multiplexing in multimode fiber," in *Optical Fiber Communication Conference, 2000,* 2000, pp. 305-307 vol.3.

[39] C. P. Tsekrekos, M. de Boer, A. Martinez, F. M. J. Willems, and A. M. J. Koonen, "Demonstration of a Transparent 2-Input 2-Output Mode Group Diversity Multiplexing Link," in *European Conference on Optical Communications, 2006. ECOC 2006,* 2006, pp. 1-2.

[40] J. Siuzdak, L. Maksymiuk, and G. Stepniak, "A 2 and 3 channel mode group diversity multiplexing transmission over graded and step index multimode fibers," in *34th European Conference on Optical Communication, 2008. ECOC 2008,* 2008, pp. 1-2.

[41] K. Jin Joo, K. Kyong Hon, L. Min-Hee, L. Hyun Sik, L. El-Hang, O. K. Kwon, R. Jay, and Y. Byueng-Su, "2.5-Gb/s Hybrid Single-Mode and Multimode Fiber Transmission of 1.5-μm Wavelength VCSEL," *IEEE Photonics Technology Letters,* vol. 19, pp. 297-299, 2007.

[42] A. Nkansah, A. Das, N. J. Gomes, and S. Pengbo, "Multilevel Modulated Signal Transmission Over Serial Single-Mode and Multimode Fiber Links Using Vertical-Cavity Surface-Emitting Lasers for Millimeter-Wave Wireless Communications," *EEE Transactions on Microwave Theory and Techniques,* vol. 55, pp. 1219-1228, 2007.

[43] P. Shen, A. Nkansah, J. James, and N. J. Gomes, "Multilevel modulated signal transmission for millimeter-wave radio over fiber system," in *International Topicsl Meeting on Microwave Photonics, 2008. Jointly held with the 2008 Asia-Pacific Microwave Photonics Conference. MWP/APMP 2008,* 2008, pp. 27-30.

[44] R. Gaudino, D. Cardenas, M. Bellec, B. Charbonnier, N. Evanno, P. Guignard, S. Meyer, A. Pizzinat, I. Möllers, D. Jäger, "Perspective in next-generation home networks: Toward optical solutions?," *IEEE Communications Magazine,* vol. 48, pp. 39-47, 2010.

[45] B. A. Miller, T. Nixon, C. Tai, and M. D. Wood, "Home networking with Universal Plug and Play," *IEEE Communications Magazine,* vol. 39, pp. 104-109, 2001.

[46] P. E. Green, "Fiber to the home: the next big broadband thing," *IEEE Communications Magazine*, vol. 42, pp. 100-106, 2004.

[47] H. Ramanitra, P. Guignard, A. Pizzinat, B. Charbonnier, and L. Guillo, "Scalable Optical Multi-service Home Network," in *Conference on Optical Fiber communication/National Fiber Optic Engineers Conference, 2008. OFC/NFOEC* 2008, pp. 1-3.

[48] H. Ramanitra, P. Chanclou, Z. Belfqih, M. Moignard, H. Le Bras, and D. Schumacher, "Scalable and multi-service passive optical access infrastructure using variable optical splitters," in *Optical Fiber Communication Conference, 2006 and the 2006 National Fiber Optic Engineers Conference. OFC 2006*, 2006, p. 3 pp.

[49] F. A. Muhammad, H. S. Al-Raweshidy, and J. M. Senior, "Analysis of curved D-fiber for methane gas sensing," *IEEE Photonics Technology Letters,* vol. 7, pp. 538-539, 1995.

[50] D.P. Saini, S.L. Coulter, "Fiber sensors sniff out environmental pollutants," *Photonics Spectra,* p. 91, 1996.

[51] J. Clowes, J. Edwards, I. Grudinin, E. L. E. Kluth, M. P. Varnham, M. N. Zervas, C. M. Crawley, and R. L. Kutlik, "Low drift fibre optic pressure sensor for oil field downhole monitoring," *Electronics Letters,* vol. 35, pp. 926-927, 1999.

[52] R. C. Luo, Y. Chih-Chen, and S. Kuo Lan, "Multisensor fusion and integration: approaches, applications, and future research directions," *IEEE Sensors Journal,* vol. 2, pp. 107-119, 2002.

[53] G. D. Pitt. *et al.*, "Optical-fibre sensors," *IEE Proceedings Optoelectronics,* vol. 132, pp. 214-248, 1985.

[54] E. Udd, "Fiber Optic Sensor Overview," in *Fiber Optic Smart Structures*, E. Udd, Ed. New York: John Wiley&Sons, 1995.

[55] S. Dong, Y. Liao, Q. Tian, "Intensity-based optical fiber sensor for monitoring corrosion of aluminium alloys," *Appl. Opt.,* vol. 45, pp. 5773-5777, 2005.

[56] P.A. Lewin, C. Mu, S. Umchid, A. Daryoush, and M. El-Sherif, "Acousto-optic point receiver hydrophone probe for operation up to 100 MHz," *Ultrasonics,* vol. 43, pp. 815-821, 2005.

[57] Y. Zhao and F. Ansari, "Intrinsic Single-Mode Fiber-Optic Pressure Sensor," *IEEE Photon. Tech. Lett.,* vol. 13, pp. 1212-1214, 2001.

[58] N. Díaz-Herrera, M.C. Navarrete, O. Esteban, and A. González-Cano., "A fibreoptic temperature sensor based on the deposition of a thermochromic material on an adiabatic taper," *Meas. Sci. Technol.,* vol. 15, pp. 353-358, 2004.

[59] O. Frazao, L.M. Marques, S. Santos, J. M. Baptista, and J. L. Santos, "Simultaneous measurement for strain and temperature based on a long-period grating combined with a high-birefrigence fiber loop mirror," *IEEE Photon. Tech. Lett.,* vol. 18, pp. 2407-2409, 2006.

[60] J. M. Corres, F. J. Arregui, and I. R. Matias, "Design of Humidity Sensors Based on Tapered Optical Fibers," *J. Lightwave Technol.,* vol. 24, pp. 4329-4336, 2006.

[61] F.J. Arregui, R.O. Claus, K.L. Cooper, C. Fernández-Valdivielso, I. R. Matías, "Optical Fiber Gas Sensor Based on Self-Assembled Gratings," *J. Lightwave Technol.,* vol. 19, pp. 1932-1937, 2001.

[62] A. Dandridge, A.B. Tveten, G. H. Sigel, Jr., E. J. West, and T. G.Giallorenzi, "Optical fiber magnetic field sensor," *Electron. Lett.,* vol. 16, pp. 408-409, 1980.

[63] D.S.Montero, "Coarse WDM Passive Optical Networking of Self-Referenced Fibre-Optic Intensity Sensors with Reconfigurable Characteristics," in *Electronics Technology Dpt.* vol. Master Thesis Madrid: Universidad Carlos III de Madrid, 2010.

[64] J. M. López-Higuera, *Handbook of Optical Fibre Sensing Technology*. New York: John Wiley&Sons Inc., 2002.

[65] J. M. Baptista, P. M. Cavaleiro and J. L. Santos, "Self-referencing resonant fiber optic intensity sensor based on a Mach-Zehnder topology," *Review of Scientific Instruments,* vol. 67, pp. 3788-3794, 1996.

[66] J. M. Baptista, J. L. Santos, and A. S. Lage, "Measurement of refractive index in oils using a self-referenced fiber optic intensity sensor," in *The 14th Annual Meeting of the IEEE Lasers and Electro-Optics Society, 2001.* LEOS 2001, pp. 875-876 vol.2.

[67] S. Dutta, S. Basak, R. Kumar, and P. K. Samanta, "Fabrication of intensity based fiber optic pH sensor," in *Nanoelectronics Conference (INEC), 2010 3rd International*, pp. 370-371.

[68] N. Lagakos, T. Litovitz, P. Macedo, R. Mohr, and R. Meister, "Multimode optical fiber displacement sensor," *Appl. Opt.*, vol. 20, pp. 167-168, 1981.

[69] P. M. B. S. Girao, O. A. Postolache, J. A. B. Faria, and J. M. C. D. Pereira, "An overview and a contribution to the optical measurement of linear displacement," *IEEE Sensors Journal*, vol. 1, pp. 322-331, 2001.

[70] C. Vazquez, J. Garcinuño, J. M. S. Pena, and A. B. Gonzalo, "Multi-sensor system for level measurements with optical fibres," in *IECON 02 [28th Annual Conference of the Industrial Electronics Society, IEEE 2002* 2002, pp. 2657-2662 vol.4.

[71] L. Yuan, "Automatic-Compensated Two-Dimensional Fiber-Optic Sensor," *Optical Fiber Technology*, vol. 4, pp. 490-498, 1998.

[72] M. Noshad, H. Hedayati, and A. Rostami, "A proposal for high-precision fiber optic displacement sensor," in *Microwave Conference, 2006. APMC 2006. Asia-Pacific*, 2006, pp. 568-571.

[73] M. Linec and D. Donlagic, "A Plastic Optical Fiber Microbend Sensor Used as a Low-Cost Anti-Squeeze Detector," *IEEE Sensors Journal*, vol. 7, pp. 1262-1267, 2007.

[74] J. D. Weiss, "Fiber-optic strain gauge," *J. Lightwave Technol.*, vol. 7, pp. 1308-1318, 1989.

[75] A. MacLean, C. Moran, W. Johnstone, B. Culshaw, "A distributed fiber optic sensor for hydrocarbon detection," in *14th International Conference on Optical Fiber Sensors* Venice, 2000, p. 382.

[76] J. Arrue, F. Jiménez, G. Aldabaldetreku, G. Durana, J. Zubia, M. Lomer, and J. Mateo, "Analysis of the use of tapered graded-index polymer optical fibers for refractive-index Sensors," *Opt. Express*, vol. 16, pp. 16616-16631, 2008.

[77] D. Viegas, S. Abad, J. Santos, L. Ferreira, and F. Araujo, "Miniature High Temperature Fiber Bragg Grating Sensor Design Based on U-Shape Lossless Taper for Thermal Mapping Applications," *IEEE Photonics Technology Letters*, vol. 22(11), pp. 8111-813, 2010.

[78] D. Monzón-Hernández, J. Mora, P. Pérez-Millán, A. Díez, J. L. Cruz, and M. V. Andrés, "Temperature Sensor Based on the Power Reflected by a Bragg Grating in a Tapered Fiber," *Appl. Opt.*, vol. 43, pp. 2393-2396, 2004.

[79] C. Bariáin, I.R. Matias, F.J. Arregui, M. López-Amo, "Experimental results towards development of humidity sensors by using a hygroscopic material on biconically tapered optical fibre," in *Photonics China*, Beijing, 1998, p. 95.

[80] I. K. Ilev and R. W. Waynant, "All-fiber-optic sensor for liquid level measurement," *Review of Scientific Instruments*, vol. 70, pp. 2551-2554, 1999.

[81] R. T. Ramos and E. J. Fordham, "Oblique-tip fiber-optic sensors for multiphase fluid discrimination," *J. Lightwave Technol.*, vol. 17, pp. 1392-1400, 1999.

[82] Y. Zaatar, D. Zaouk, J. Bechara, A. Khoury, C. Llinaress, and J. P. Charles, "Fabrication and characterization of an evanescent wave fiber optic sensor for air pollution control," *Materials Science and Engineering B*, vol. 74, pp. 296-298, 2000.

[83] D. V. Rani, W. Chun-Wei, S. Kailiang, and K. Rakesh, "Enhancement of Dynamic Range of Evanescent Wave Fiber-Optic Oxygen Sensor," in *Frontiers in Optics*, 2007, p. JSuA46.

[84] S. A. Wade, J. C. Muscat, S. F. Collins, and G. W. Baxter, "Nd_{3+}-doped optical fiber temperature sensor using the fluorescence intensity ratio technique," *Review of Scientific Instruments*, vol. 70, pp. 4279-4282, 1999.

[85] Z. Y. Zhang, K. T. V. Grattan, A. W. Palmer, B. T. Meggitt, and T. Sun, "Characterization of erbium-doped intrinsic optical fiber sensor probes at high temperatures," *Review of Scientific Instruments*, vol. 69, pp. 2924-2929, 1998.

[86] C. Fernández-Valdivieso, I.R. Matias, A. Madrid, F.J. Arregui, "An optical fiber temperature sensor based on thermochromic effect under-water applications," in *14th International Conference on Optical Fiber Sensors OFS'2000*, Venice, 2000, p. 146.

[87] G. Murtaza, J.M. Senior, "Referencing strategies for intensity modulated optical fibre sensors," *Optics and Laser Technology*, vol. 25, pp. 235-245, 1993.

[88] G. Murtaza, J.M. Senior, "Referenced intensity-based optical fibre sensors," *International Journal of Optoelectronics*, vol. 9, pp. 339-348, 1994.

[89] J. Berthold, W. Ghering, and D. Varshneya, "Design and characterization of a high temperature fiber-optic pressure transducer," *J. Lightwave Technology*, vol. 5, pp. 870-876, 1987.

[90] E. Bois, S. J. Huard, and G. Boisde, "Loss compensated fiber-optic displacement sensor including a lens," *Appl. Opt.*, vol. 28, pp. 419-420, 1989.

[91] G. Adamovsky, "Time domain referencing in intensity modulation fiber optic sensing systems," in *Proc. of SPIE on Optical Testing and Metrology* 1986, pp. 145-151.

[92] T.S.J. Lammerink, J.H.J. Fluitman, "Measuring method for optical fibre sensors," *J. Phys. E: Sci. Intrum.*, vol. 17, pp. 1127-1129, 1984.

[93] G. Adamovsky, "Fiber-optic displacement sensor with temporally separated signal and reference channels," *Appl. Opt.*, vol. 27, pp. 1313-1315, 1988.

[94] R. Penty, "Optical TDM makes faster networks possible," *Laser Focus World*, p. 191, 2000.

[95] M. Bacci, M. Brenci, G. Conforti, R. Falcial, A. G. Mignani, and A. M. Scheggi, "Thermochromic transducer optical fiber thermometer," *Appl. Opt.*, vol. 25, pp. 1079-1082, 1986.

[96] J.M. Senior, G. Murtaza, A.I. Stirling, G.H. Wainwright, "Dual wavelength intensity modulated optical fibre sensor systems," in *Proc. of SPIE on Fibre Optics*, 1989, p. 332.

[97] G. Murtaza and J. M. Senior, "Methods for providing stable optical signals in dual wavelength referenced LED based sensors," *IEEE Photonics Technology Letters*, vol. 6, pp. 1020-1022, 1994.

[98] J.M. Senior, G. Murtaza, "Optical fibre sensor system," in *European Patent*. vol. EP0470168BI 1993.

[99] D.S. Montero, C. Vazquez, I. Möllers, J. Arrue, D. Jäger, "A Self-Referencing Intensity BAsed Polymer Optical Fiber Sensor for Liquid Detection," *Sensors*, vol. 9, pp. 6446-6455, 2009.

[100] M. Lomer, J. Arregui, C. Jáuregui, P. Aiestaran, J. Zubia, and J.M. López Higuera, "Lateral polishing of bends in plastic optical fibres applied to a multipoint liquid-level measurement sensor," *Sens. Actuators A*, vol. 137, pp. 68-73, 2007.

[101] J. Arrue, J. Zubia, G. Fuster, D. Kalymnios, "Light power behaviour when bending plastic optical fibres," *IEE Proc. Optoelect.*, vol. 145, pp. 313-318, 1998.

Chapter 3

GRADED-INDEX POLYMER OPTICAL FIBRE TRANSFER FUNCTION.

3.1 Introduction

Polymer Optical Fibres (POFs) are being developed as an important high-speed communication media for short and medium-reach applications. Polymer fibres have a large core-diameter (50–1000μm) and a large numerical aperture (0.2–0.9). This allows for easy connectorization of systems and efficient launching from semiconductor lasers or Light Emitting Diodes (LEDs) compared to singlemode silica optical fibre, which dramatically decreases the total cost of the system. In addition to having the advantages of being intrinsically an optical medium, they show a great resistance to mechanical damage as a consequence of the intrinsic flexibility of the polymer material [1, 2]. This is the reason why recently POFs are used in the short range communication area within 200m, namely in a building, home, and termination area of Fibre To The Home (FTTx), although the transmission attenuation is relatively large (20-300dB/km) due to the inorganic molecular structure. However, in all commercially available step-index POFs (SIPOFs) the bandwidth of transmission is limited to about 5MHz·km [3] due to modal dispersion. Therefore, even in the short range communication area, the SIPOF will not be able to cover the data rate of more than 100Mbps that would be necessary in fibre distributed data interface (FDDI), synchronous digital hierarchy (SDH), and broadband integrated services digital network (B-ISDN), etc. standards of the telecommunication area. Therefore, the SIPOF is basically aimed at low data-rate transmission, image guiding and illumination. To resume, Table 3.1 shows the applications and requirements for POF data transmission.

On the other hand, the graded-index type of polymer optical fibre (GIPOF) can combine these properties with a large capacity for digital transmission, as provides a bandwidth of about 500 times larger than that of any conventional SIPOF. Accordingly, the GIPOF, as a physical transmission medium, is foreseen to be one of the candidates for the replacement of the metallic (copper) cables traditionally used in customer premises networks, interconnect and access links. The utilization of conventional silica-based optical fibres (GOFs) could also be envisaged in these applications, but the corresponding connectors are expensive. In addition, the fabrication and termination of GOFs are more difficult than those of POFs and also the silica material is more expensive than polymer, so the cost of the overall GOF-based system would be inevitably high.

Application	Typical parameters	Specific Requirements
Mobile networks • Cars • Trains/ships • Airplanes	• Lengths between 10m (car) and 200m (ships, airplanes) • Data rates up to >>1Gbps	• Complete systems • Critical environmental conditions • Extreme high reliability and long live time
LAN • Office • Home • Condominium	• Lengths 25 – 100m • Data rates 100Mbps to 1Gbps	• Simple installation • Different data formats • Mix of different components
Interconnection • On board • Intra board	• Many parallel channels • Data rates to 10Gbps • Centimetres to meters	• Very small • Low power operation • Automatic requirement

Table 3.1.- Applications and requirements for data transmission with POF [4].

Until recently, the only commercially available types of POF were step-index fibres based on non-fluorinated polymers such as polymethylmethacrylate (PMMA) in addition with the utilization of several kinds of dopants. Because these traditional types of polymer optical fibre had high attenuation and large modal dispersion, they were restricted to very low performance applications: usually distances less than 50 meters and bit rates less than 100 Mbps. Also, traditional polymer optical fibre materials like PMMA had strong absorption in the near infrared. As a result, they could only be used at a few wavelengths in the visible portion of the spectrum, typically 530nm and 650nm. Today, unfortunately, almost all gigabit optical sources operate in the near-infrared (typically 850nm or 1300 nm), where PMMA and similar polymers are essentially opaque. Nevertheless, in this scenario, a number of researchers previously demonstrated that undistorted bit streams of 2.5Gbps could be transmitted through a polymethylmethacrylate (PMMA) GIPOF over a distance of 100m [5, 6]. In more recent experiments the record transmission length of 200m was successfully reached [6, 7]. The greatest remaining problem is that of limited bending radius which can, however, be reduced through an improved primary coating [8].

On the other hand, the next generation in POF technology began with the application of an amorphous perfluorinated (PF) polymer, polyperfluoro-butenylvinylether, to GIPOF, obtaining PF-based GIPOFs. Because this polymer has very low attenuation (around 10dB/km) in the near infrared, it is immediately compatible with gigabit transmission sources, and can be used over distances of hundreds of meters. Furthermore, this perfluorinated fibre can also be made with a graded refractive index supporting larger bandwidths than conventional POFs. With this new POF technology, Gigabit Ethernet (GbE) links using commercially available transceivers have been demonstrated at distances up to 300 meters. Also, around 10Gbps links up to 100 meters have also been demonstrated [9, 10] being far away with the successful experimental transmission of 1Gbps over 1km which was reported in [11], which ensures coverage of the required bit rate not only in IEEE 1394 home networks but also in IEEE802.3 Gigabit Ethernet-based local area networks (LANs) as well as analog CATV signals with high frequencies, for example. Furthermore, in [12] 10.7Gbps NRZ-signals were transmitted for the first time over 220m of 120μm core diameter PF GIPOF. This distance complies with the novel IEEE

10GBASE-LRM standard [13], which is developed for the support of 10GbE installed fibres. Based on all these experiments it is clearly demonstrated that PF GIPOF could cover broadband fields, from the areas of very short-reach networks to the access networks. On the contrary, while they have excellent low-loss characteristics, this polymer is expensive and hence the fibres are overpriced for general consumers when the core diameter is as large as several hundreds micrometers.

However, all these transmission data rate achievements have been accomplished so far without real reference to prediction tools. Anyway, the existing simulation models have been developed for GOF systems some decades ago [14-16] and involve some approximations that appear invalid in consideration of polymer optical fibres, including those with graded-index core profiles.

The model described in this chapter tries to take into account the factors that can have a large impact on the data rate transmission performance providing a full description of the dispersion in such fibres as well as incorporating all possible parameters involved in the determination of the total bandwidth. It is based on analytically evaluating the frequency response of the fibre instead of the direct calculation of the pulse broadening from the moments of the impulse response [17-20]. A similar approach to the latter but applied to step-index polymer optical fibres has been recently reported in [21] by solving the power flow equation by a fast implementation of the finite-difference method in matrix form.

3.2 Transmission properties of Graded-Index Polymer Optical Fibres

For the transmission of communication signals, attenuation and bandwidth are important parameters. Both parameters will be briefly described in the following subsections. In any case, the optical signal is distorted and attenuated when it propagates over the fibre. These effects have to be modeled when describing the signal transmission. They behave quite differently in different types of fibres. Whereas signal distortions in singlemode fibres are primarily caused by chromatic dispersion, i.e. the different speeds of individual spectral parts, the description of dispersion in multimode fibres is considerably more complex. Not only does chromatic dispersion occur in them, but also has the generally much greater modal (or intermodal) dispersion. This latter parameter is directly related to the GIPOF fibre dispersion characteristics which will be defined in subsection 3.3.

3.2.1 Attenuation

Polymethylmethacrylate (PMMA) (better known as Plexiglass®) has been widely used as core material for graded-index fibre [22]. However, the use of PMMA is not attractive due to its high attenuation of about 100dB/km at 570nm. This fact drives a serious problem in the PMMA-based POFs at the near-IR (near-infrared) to IR regions because of the large attenuation due to the high harmonic absorption loss by carbon-hydrogen (C-H) vibration (C-H overtone). On the other hand, it has been reported that one can eliminate this

absorption loss by substituting the hydrogen atoms in the polymer molecule for heavier atoms [23]. In this case, if the absorption loss decreases with the substitution of hydrogen for deuterium or halogen atoms (such as fluorine), the possible distance for signal transmission would be limited by dispersion, and not by attenuation.

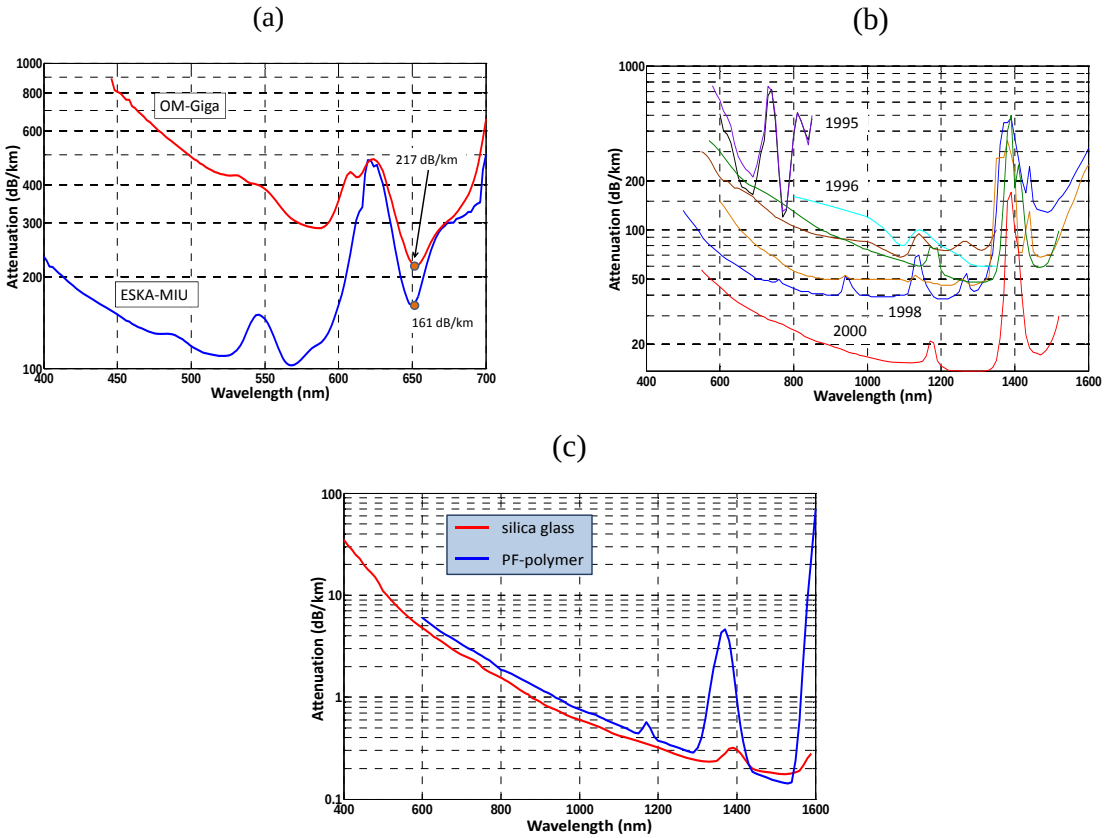

Figure 3.1.- (a) Spectral attenuation of ESKA-MIU and OM-Giga. (b) Development of the attenuation for PF GIPOF. (c) Theoretical comparison of the attenuation in PF polymer and silica fibres [4].

Many polymers have been researched and reported in literature in order to improve the bandwidth performance given by the first PMMA-based graded-index polymer optical fibres [24]. Nevertheless, today, perfluorinated (PF) GIPOF is widely used because of its high bandwidth and low attenuation from the visible to the near IR wavelengths compared to PMMA GIPOF [25]. This fact is achieved mainly by reducing the number of carbon-hydrogen bonds that exist in the monomer unit by using partially fluorinated polymers. In 1998, the PF-based GIPOF had an attenuation of around 30dB/km at 1310nm. Attenuation of 15dB/km was achieved only three years after and lower and lower values of attenuation are being achieved. The theoretical limit of PF-based GIPOFs is ~0.5 dB/km at 1250-1390nm [26]. A comparative of the attenuation of different optical fibres versus the wavelength can be seen in Fig. 3.1(a). This figure deploys the spectral attenuation for two commercial PMMA GI-POFs, such as OM-Giga and ESKA-MIU. Notice that for wavelengths higher than 700nm the attenuation reaches a thousand-order value. On the contrary, different attenuation spectra of PF GIPOFs are compared in Fig. 3.1(b). The years indicate the history of development of this fibre technology. Finally, Fig. 3.1(c) compares

the attenuation values theoretically possible for fluorinated polymers with those achieved for singlemode silica fibres, becoming quite similar. From these two latter figures, the lower attenuation of the PF GIPOF at IR wavelengths is revealed, compared to its PMMA-based counterpart.

In the estimation, the attenuation factors are divided in two: material-inherent scattering loss and material-inherent absorption loss. The first factor is mainly given by the Rayleigh scattering, following the relation $\alpha_R \sim (\lambda)^{-4}$. The second factor is given by the absorption caused by molecular vibrations. A detailed explanation on the estimation processes is described in [27] as well as in [28].

3.2.2 Bandwidth

Apart from attenuation, an important characteristic of an optical fibre as a transmission medium is its bandwidth. Bandwidth is a measure of the transmission capacity of a fibre data link. Several factors determine the bandwidth of polymer optical fibres, specifically of graded-index polymer optical fibres. As GIPOFs are intrinsically multimode fibres and because such fibres can guide many modes, modal dispersion is the limiting bandwidth factor [29]. So bandwidth and dispersion are two parameters closely related. In a generic description, modal dispersion is caused by the fact that the lower order modes propagate mainly along the waveguide axis, while the higher-order modes follow a more zigzag path, which is longer. If a short light pulse is excited at the input of the fibre, the lowest order modes arrive first at the end of the fibre and the higher order modes arrive later. The output pulse will thus be built up of all modes, with different arrival times, so the pulse is broadened.

The refractive index profile formed in the core region of multimode optical fibres plays a great role determining its bandwidth, because modal dispersion is generally dominant in the multimode fibre although an optimum refractive index profile can produce the minimum modal dispersion (by means of a parabola-like index profile). In this latter case, multimode fibres exhibit its larger bandwidth being almost independent of the launching conditions [30]. In such fibres, light travelling in a low refractive-index structure has a higher speed than light travelling in a high index structure (through the general expression $v = c/n$) and the higher order modes bend gradually towards the fibre axis in a shorter period of time because the refractive index is lower at regions away from the fibre core. The time difference between the lower order modes and the higher order modes is smaller, and so the broadening of the pulse leaving the fibre is reduced and, consequently, the transmission bandwidth can be increased over the same transmission length. Furthermore, if a light is launched with a very low numerical aperture in the center of the core, few fibre modes will be excited, thus achieving the so-called Restricted Mode Launching (RML) condition. Accordingly, the arrival time differences between fibre modes will be even smaller, which result in a smaller broadening of a pulse travelling over the fibre. Thus bandwidth can be also increased by launching light into the POF with a low numerical aperture [22]. In this latter case, a bit rate (which is directly related to the fibre bandwidth) for PF GIPOF of

about 10 Gbps·km in the 1300nm window can theoretically be achieved [31]. From the experiments shown in Figure 3.2, it is demonstrated that PF GIPOFs could cover broadband fields, from the areas of very short reach networks to access networks, as aforementioned.

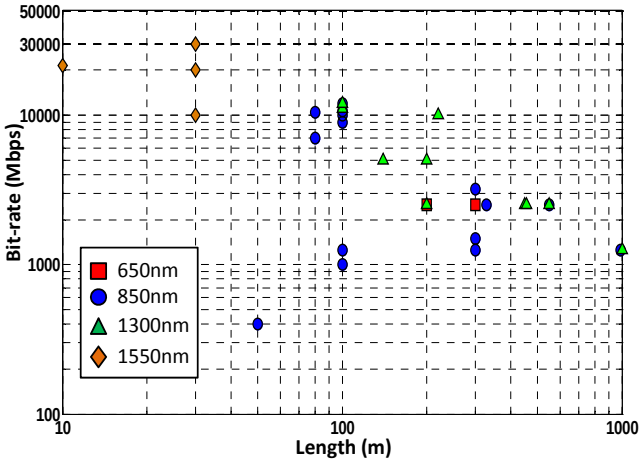

Figure 3.2.- Development of data rate achieved by PF GIPOF links. ■ PF GIPOF@650nm ; ● PF GIPOF@850nm ; ▲ PF GIPOF@1300nm ; ♦ PF GIPOF@1550nm. [4]

On the other hand, dispersion (thus bandwidth decrease) could also be introduced by the effect that the speed of propagation of light of different wavelengths differs. This is called chromatic dispersion. In PF-based POFs the chromatic dispersion is much smaller than in silica MMF for wavelengths up to 1100nm. For wavelengths above 1100nm, the dispersion of the PF-based GIPOF retains and the dispersion of silica MMF increases. The expression of such dispersion is given by Eq. 3.1.

$$\Delta t_{\text{chrom}} = D(\lambda) \cdot \Delta\lambda \cdot L \qquad (3.1)$$

where $D(\lambda)$ is the dispersion parameter (usually given in ps/nm·km) defined as $D(\lambda) = -\frac{\lambda}{c} \cdot \frac{d^2 n(\lambda)}{d\lambda^2}$, $\Delta\lambda$ is the spectral width of the light source, and L is the length of the fibre.

From above, it is clearly seen the close relation between bandwidth and dispersion in an optical fibre. Although dispersion in GIPOF will be discussed in the following section, at this point it is worth briefly mentioning that in such optical fibre type, due to the fact that having very low chromatic dispersion as well as low attenuation, bandwidth is mainly limited by the modal dispersion suffered in this transmission media.

An overview of the published transmission experiments with graded-index polymer optical fibres is presented Table 3.2, to the author's knowledge. Only it has been taken into account those experiments which have been published at important POF conferences and in the most important scientific journals (IEEE, OSA). In addition to, the most important parameters concerning the fibre and the experiment are also indicated. The greatest bit rates

for POF systems cover tens of Gbps data rates, which far exceed the Gigabit Ethernet and 10-Gigabit Ethernet requirements.

Year	Material	ϕ core (um)	Atten. (dB/km)	λ (nm)	Remarks	Ref.
1982	MMA-co-VPAc	--	1070	670	first GI-POF	[32]
1991	PMMA	200-1500	113	650	1GHz·km	[33]
1994	PMMA	420	200	647	2.5Gbps over 100m	[34]
1997	PF	125-300	56	1300	600MHz·km	[35]
1997	PF (CYTOP®)	120	56	1300	2.5Gbps over 200m	[36]
1998	PMMA	500	145	650	2GHz·km	[37]
1999	PF	170	31	1310	2.5Gbps over 550m	[38]
1999	PF	130	33	1300	11Gbps over 100m	[39]
2000	PF	120	15	1300	509 MHz·km@1300nm 522MHz·km@850nm	[40]
2001	PF	--	27	840	1.25Gbps over 990m	[41]
2002	PMMA	1000	120	650	3.45GHz·km	[42]
2003	PMMA	500	--	650	1.25Gbps over 100m	[43]
2003	PF	120	40	850	1500MHz·100m	[44]
2004	PF	120	25	850	400MHz·km	[45]
2004	PF	--	--	850	10Gbps over 100m, W-shaped index profile	[46]
2007	PVDF[1]-clad PMMA	700	--	650	2.32GHz·km	[2]
2007	PF	120	40	800-1300	800MHz·km	[47]
2007	PF	120	40	1300	10Gbps over 220m	[12]
2007	PF	50	115	1550	40Gbps over 30m	[48]
2008	PF	120	--	1300	10Gbps over 100m	[49]
2008	PF	50	--	1300	40Gbps over 100m	[49]
2010	MMA-co-PFPMA	600	172	670	1.34GHz·km	[50]
2010	PMMA	1000	--	667	5.3Gbps over 50m	[51]
2010	PF	50	--	1302	47.4Gbps over 100m	[52]

Table 3.2.- A review of published data of GIPOF.

From the literature two different approaches have been used to evaluate the pulse dispersion, which is directly related to the fibre bandwidth, in polymer optical fibres and reported in Refs. [18] and [19], respectively. In [18] the approach assumes a uniform excitation and neglects both differential mode attenuation (namely DMA although other authors use the expression distributed loss) and mode coupling effects, which may have a significant impact on the baseband, as it will be described later (and as it will be also described in Chapter 4 for silica-based multimode fibres, affecting both the baseband and broadband transmission regions). On the other hand, the approach taken in [19] incorporates the mode coupling effect in the dispersion model using the bandwidth formula, given by Eq. 3.2 [16], and assumes a uniform launching condition but ignores the differential mode attenuation (DMA). Furthermore, it no longer associates the contribution

[1] PVDF: Polyvinylidene fluoride

of the material dispersion which is known to have a strong effect in POFs and estimates a coupling length of 2m which seems to be too small for ordinary GIPOFs [53, 54].

$$BW = BW_o \left(\frac{z}{z_c} \right)^{1/2} \tag{3.2}$$

where z is the transmission distance (link length) and z_c is the so-called coupling length, being BW_o the corresponding bandwidth. Once again, both terms BW_o and z_c are dependent on the launching conditions and, therefore, are difficult to obtain with accurate numerical values. Any attempt to measure BW_o and z_c should be altered by a large error because the effect of DMA and that of chromatic dispersion which cannot be prevented from affecting the results.

In principle the same processes affecting the bandwidth in SIPOFs take place in GIPOFs; however there are basic differences:

- With GIPOF, there is no core/cladding transition to serve as an essential cause for mode coupling, mode conversion and differential mode attenuation.
- Fluorinated GI-POFs are used in wavelength ranges in which Rayleigh scattering is less significant.
- To form the index profile, various zones of the fibre, as seen from the axis, are provided with varying concentrations of a dopant or a copolymer so that the attenuation usually gets a gradient. This is probably the most significant cause of differential mode attenuation in GIPOFs.

Nonetheless, knowledge of the bandwidth alone is not adequate for estimating what the actual capacity of the complete link will be. In order to determine this parameter, it is further necessary to know the actual transmission procedure as well as the complete transmission function. For example, it would be possible to transmit signals of significantly broader bandwidth if an electrical compensation of the frequency response takes place. This can be done, for example, by applying a high-pass filter for compensation. In addition, the type of signal involved (digital or analogue) is also of significance and finally the required system reserves must be considered. However, the following general relationship can be used as a rule of thumb of digital systems [4]:

Maximum bit rate [Mbps] =2 x Bandwidth [MHz]

The theoretical transmission capacity of a fibre is often indicated as bandwidth, *BW*, which states up to what frequency the individual frequency parts are attenuated by 50% at most, being assumed that it is possible to transmit signals the spectrum of which lies within this bandwidth. The bandwidth characteristic is usually specified as the 3-dB bandwidth. The 3-dB bandwidth is determined by obtaining the frequency response (i.e. by analyzing the fibre transfer function), which relates the output signal to the input one in an optical fibre considering it as a transmission line. The bandwidth is then the frequency $f_{\text{-3dB}}$ with which the amplitude of the frequency response has dropped to 50% (3 dB). However, when

measuring bandwidth, a two to four ranging factor of deviation from the theoretical value of an ideal fibre can be generally expected. The reason for this is the combination of differential mode attenuation (DMA) and mode coupling. Both effects will be described in a following section. As a result of the continuous energy exchange that takes place between the faster and slower modes, the delay does not rise in proportion to the length. The increased attenuation (i.e., DMA effect) of those beams (modes) having a particularly large propagation angle –many reflections occur at the cladding– has the additional effect of reducing the pulse width and increasing the bandwidth.

Computer simulations of the 3-dB bandwidth versus the index exponent, α, of a graded-index type POF as well as versus the operating wavelength, considering in both a PF polymer based one, have been carried out. The refractive index profile of a graded-index optical fibre is expressed in the power-law form given by Eq. 3.6. The figures are shown in Fig. 3.3(a) and Fig. 3.3(b), respectively, and are based on the analysis reported elsewhere [55] which assumes a uniform excitation and neglects both the differential mode attenuation (DMA) and mode coupling. The bandwidth of the GIPOF was obtained by using the simple relation between the width of the impulse response of the fibre, assuming a Gaussian pulse distribution, and the bandwidth shown in Eq. 3.3:

$$BW = f_{-3\mathrm{dB}} = \sqrt{\frac{\ln 2}{2\pi^2}} \cdot \frac{1}{\sigma_{\mathrm{total}}} = \frac{0.1874}{\sigma_{\mathrm{total}}} \quad ; \text{with} \quad \sigma_{\mathrm{total}} = \left(\sigma^2_{\mathrm{chromatic}} + \sigma^2_{\mathrm{modal}}\right)^{1/2} \tag{3.3}$$

where σ_i is the rms width of the impulse response, depending on the contribution considered.

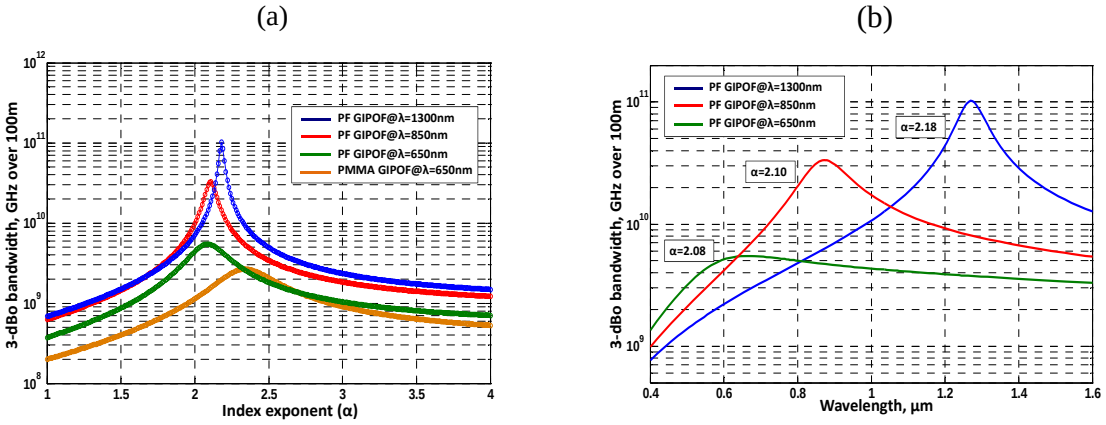

Figure 3.3.- (a) Relation between the index exponent α and the bandwidth of 100m PF-based GIPOF. PMMA-based GIPOF at 650nm is plotted for comparison. (b) Wavelength dependence of the bandwidth of the 100m-long PF polymer-based GIPOF link.

Fig. 3.3(a) shows the calculated bandwidth of a PF-based GIPOF operating at different wavelengths, in which it is assumed that the source spectral width is 1nm, with regards to the index exponent. The data of the bandwidth of a PMMA-based GIPOF at 650nm is also shown for comparison showing a maximum limited to approximately 1.8GHz for 100m by the large material dispersion. On the other hand, the smaller material dispersion of the PF polymer-based GIPOF permits a maximum bandwidth of 4GHz even at 650nm.

Furthermore, when the signal wavelength is 1300nm, theoretical maximum bandwidth achieves 92GHz for 100m. The difference of the optimum index exponent value between 650nm and 1300nm wavelengths is caused by the inherent polarization properties of material itself. The wavelength dependence of the bandwidth characteristic of a PF GIPOF is shown in Fig. 3.3(b), when the index profile is controlled to have the index exponents of 2.08, 2.10 and 2.18. These latter selected index exponents are the optimum ones for the PF GIPOF when the source wavelengths are 0.65, 0.85 and 1.3 μm, respectively. It is indicated in this figure that several hundreds of MHz·km can be achieved in a wide wavelength range from 0.6μm to 1.3μm when properly controlling the index exponent parameter. This fact is also supported due to the low material dispersion in PF GIPOFs, as aforementioned. In addition to, it can be emphasized that this PF-polymer low material dispersion allows a higher tolerance in the index profile of the PF GIPOF with regards to silica fibres, even for high-speed transmission. It is also noteworthy that, since the PF polymer has low material and profile dispersions and the wavelength dependence of the optimum profile is decreased, a high bandwidth performance can be maintained over a wide wavelength range, compared to multimode silica or PMMA-based GIPOF fibres.

3.3 Dispersion in Graded-Index Polymer Optical Fibres

It has been previously stated that pulse broadening is generally caused by modal dispersion and chromatic dispersion. For multimode fibres it is necessary to consider the factors of material, modes and profile dispersion: The latter considers the wavelength dependence on the relative refractive index difference in graded index fibres. Waveguide dispersion additionally occurs in singlemode fibres, whereas profile dispersion and modal dispersion do not. All the kinds of dispersion appearing in optical fibres are summarized in Fig. 3.4. The mechanisms dependent on the propagation paths are marked in blue, whereas the wavelength-dependent processes are marked in red. Those mechanisms only affecting singlemode fibres are outside from the scope of this work so they will be avoided.

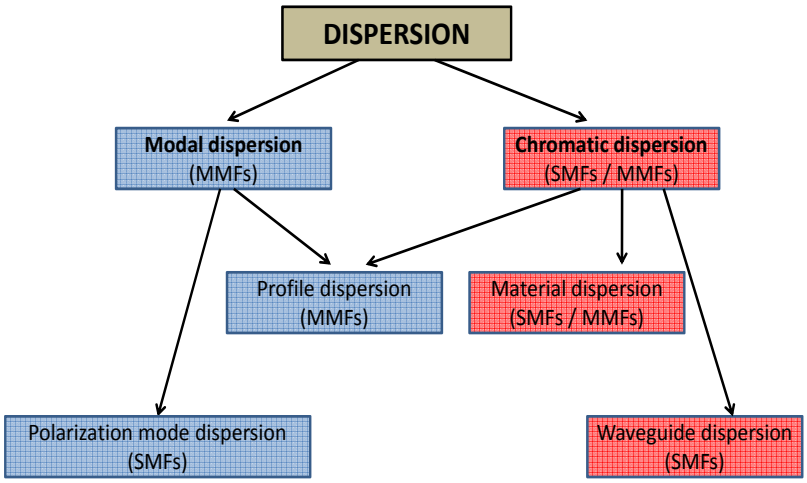

Figure 3.4.- Dispersion mechanisms in optical fibres.

The polymer fibres used today are generally multimode (with the recent exception of their single-mode counterparts [56]) so that waveguide dispersion and polarization-mode dispersion can be neglected. This leaves modal dispersion and chromatic dispersion as the relevant processes to be considered.

As aforementioned, the optical signal propagating through an optical fibre is split up into the different modes which propagate at different speeds and then arrive at the receiver at different points in time, thus transmitting a distorted signal. In contrast to chromatic dispersion, modal dispersion is influenced by different effects which do not exclusively depend on the fibre. The delay between the modes is determined by the refractive index profile of the fibre and depends exclusively on the fibre. How the signal power is split up into the individual modes, however, is determined by the coupling of the light into the fibre. For example, when the light is coupled very narrowly around the fibre axis and almost parallel into the fibre, then only one individual mode would be excited, i.e. the entire signal power would be coupled into this mode and would not even notice the time delay since only one mode is providing power. The other extreme would be a very wide coupling of the transmission angle and the surface. In this case the power would be divided evenly to all modes whereby the skews of all modes would play a role. This example clearly shows that when modeling multimode fibres you not only have to take the fibre itself into account but also the coupling in and out of the light. Furthermore, modes in polymer fibres do not spread independently of each other but are coupled to each other. A part of the power can be coupled over to other preferred neighboring modes because of impurities and non-ideal interfaces between the core and the cladding. This mode coupling effect arises particularly strongly in polymer fibres which is why current models for the propagation of light in optical fibres have to be expanded [57, 58]. Mode coupling effects on GIPOFs will be discussed in section 3.4.

To analyze the different types of dispersion that appear in a multimode fibre, specifically in a graded-index polymer optical fibre, set of figures comprising Fig. 3.5 report the chromatic and modal dispersion and the total bandwidth of a 100m-long PF GIPOF as a function of the refractive index exponent, α, for the 1300nm and 650nm wavelengths. Fig. 3.5(c) and Fig. 3.5(d) depict the corresponding 3-dB baseband bandwidths, related to Fig. 3.5(a) and Fig. 3.5(b), respectively. These plots are based on the same analysis of the previous section, which assumed a uniform excitation and neglected both the DMA and mode coupling effects. From these figures, the chromatic bandwidth is seen to show little dependence on α, which means that the material dispersion is the dominant contribution (with regards to the profile dispersion) in the transmission window considered. On the other hand, in case of Fig. 3.5(a) as well as in case of Fig. 3.5(b), the modal bandwidth shows a highly peaked resonance with α. This is the well known characteristic feature of the grading. With the present choice of parameters values, that maximum bandwidth (i.e. minimum dispersion) approximately occurs at 2.18 at 1300nm and 2.08 at 650nm, as shown in Fig. 3.5(a) and Fig. 3.5(b), respectively. Furthermore, the presence of crossover points (namely α_1 and α_2, for example) in both figures shows that the total bandwidth may be limited either by the modal dispersion or the chromatic dispersion depending on the value of the index exponent. Taking Fig. 3.5(a) as example, the chromatic dispersion will essentially limit the total bandwidth for $\alpha_1 < \alpha < \alpha_2$, whilst for $\alpha < \alpha_1$ or $\alpha > \alpha_2$ the modal dispersion will cause the

main limitation. In other words, when the index exponent is around the optimum value (α -resonance), the modal dispersion effect on the possible 3-dB bandwidth (i.e. on the possible bit rate) is minimized and the chromatic dispersion dominates this performance. On the other hand, when the index exponent is deviated from the optimum, the modal dispersion increases becoming the main source of bandwidth limitation. It is worth noting that, with increasing the fibre numerical aperture (NA), the number of transmitted modes in the GIPOF also increases. Using the definition of the modal dispersion (i.e. time delay between the fastest and slowest modes reached at the fibre end), it is clear that this parameter also increases with the total number of transmitted modes. Consequently, the possible 3-dB bandwidth is affected by the fibre NA when the index exponent is apart from the optimum value. On the contrary, the possible 3-dB bandwidth achieved when the GIPOF has an optimum index profile is almost independent on the relative refractive index difference of the core and the cladding of the GIPOF even if the number of transmitted modes increases with increasing the fibre NA, because the modal dispersion is minimized and because the dopant concentration dependence of the chromatic dispersion is small.

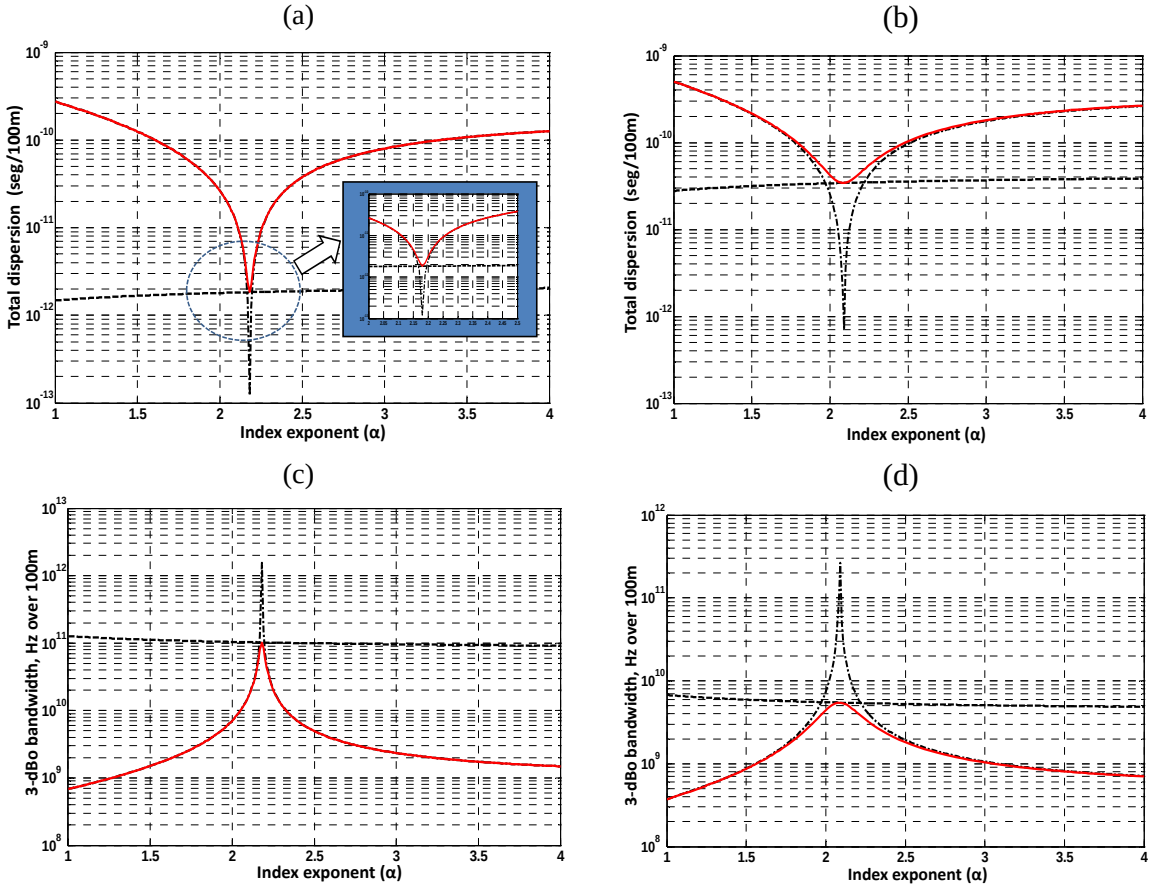

Figure 3.5.- (a) Pulse width versus index exponent of 100m-long PF-based GIPOF, assuming equal power in all modes and a 1300nm light source having a rms spectral width of 1nm. Inset: zoom near the optimum profile region. (b) Pulse width versus index exponent of 100m-long PF-based GIPOF, assuming equal power in all modes and a 650nm light source having a rms spectral width of 1nm. (c) 3-dBo baseband bandwidth corresponding to Fig. 3.5(a). (d) 3-dBo baseband bandwidth corresponding to Fig. 3.5(b).
In all figures (—) Total dispersion ; (-·-) Modal dispersion ; (---) Chromatic dispersion.

3.3.1 Dispersion Modeling Approaches

Light guiding in polymer fibres is based, as in all conventional optical fibres, on the principle of total internal reflection in which the fibre core has a greater refractive index than that of the surrounding cladding. Basically, the same approaches and methods can be used for describing wave guidance as with silica fibres. However, polymer fibres have characteristics which make some approaches difficult or even impossible. The greatest limitation when describing the propagation characteristics is surely the extremely large number of modes which are capable of propagating. In principle, all modes of a polymer fibre can be calculated. This, however, requires a lot of memory, computation time and very good resolution, too. For these reasons many simplified descriptions have been established in which either the concept of mode groups is introduced, and such mode groups are calculated, or the light propagation is dealt with the ray theory and additional wave phenomena outside the ray theory are described. Such hybrid approaches in particular are often used. The most current procedures for describing light propagation in polymer fibres will subsequently be briefly described.

3.3.1.1 Approaches with Wave Theory

The propagation characteristics of optical fibres are generally described by the wave equation which results directly from Maxwell's equations and characterizes the wave propagation in a fibre as a dielectric wave guide in the form of a differential equation. In order to solve the equation, the field distributions of all modes and the attendant propagation constants, $\beta(w)$, which results from the use of the boundary conditions have to be determined, being w the angular frequency.

The wave equation is basically a vector differential equation which can, however, under the condition of weak wave guidance be transformed into a scalar wave equation in which the polarization of the wave plays no role whatsoever [59]. The prerequisite for the weak wave guiding is that the refractive indices between the core and cladding hardly differ, being fulfilled quite well in silica fibres when the difference in refractive index between the core and cladding region is below 1%. However, polymer fibres have quite large numerical apertures and thus greater differences in the refractive indices which is why this approximation is only partially valid. Nevertheless, calculations based on the scalar wave equation only show very small inaccuracies with regards to the group delay. Then, the equations which describe the electric and magnetic fields are decoupled so that you can write a scalar wave equation.

The models based on the solution of the wave equation in the form of a model solver differ fundamentally only in regard to the solution method and whether or not you are proceeding from a more computer-intensive vector wave equation or the more usual scalar wave equation. In the technical literature solutions for the vector wave equation with the aid of finite element method (FEM) [60, 61], with finite differences (Finite Difference Time Domain Method - FDTD, [62]) and the beam propagation method (BPM) [63] are well-known. These are generally used for very small, mostly singlemode waveguides in which polarization characteristics play a role. Multimode fibres including polymer fibres are quite

large and receive the polarization of light for only a few centimeters. That is why analytical estimations of the scalar wave equation, the so-called WKB (Wentzel-Kramers-Brillouin) Method and Ray Tracing, are primarily used for the modeling of POF.

Analytical solutions for the wave equation exist for different refractive index profiles such as step index and graded index profile. Then you only have to determine the propagation constants and propagation times of the modes in order to describe the fibre. In most cases the so-called WKB Method is used with which the propagation times of many modes can be calculated efficiently [9, 64]. This analytical method is an approach for the solution of the scalar wave equation developed by Wenzels, Kramers and Brillouin from whom the name derives. The solutions with the WKB Method contain simplifications which correspond to the description of the fibre with the ray theory thus building a bridge between the ray and mode description of the fibre. The WKB Method primarily makes available expressions for describing the propagation constants and the group delay. It permits quick estimations of bandwidth or the transmission capacity of a fibre. In principle, all types of fibres with any number of monotonously decreases in the refractive index profiles can be calculated whereby discontinuous places such as steps in a profile (including MSI[2] fibres, too) can be handled without any problems because the description takes place in integral form [65]. The group propagation times of the modes can be established by differentiating the latter integral form to the angular frequency w. In this way, it is possible to get the term $\partial\beta(w)/\partial w$ (being $\beta(w)$ the modal propagation constant) which describes the group delay. After reordering the previous equation it is possible to obtain the expression for the propagation time.

In this method, whereas the field distributions in step index profile fibres can be determined analytically and are described by Bessel functions, in which the conditional equation for the propagation constant results from the boundary conditions in which the transversal components of the electric and magnetic fields are always supposed to merge into each other at the core-cladding interface, the refractive index distribution over the radius of a graded index fibre can generally be described with a power-law, as Eq. 3.6 states. Fibres with power-law profiles possess the characteristic that the modes can be put in mode groups which have the same propagation constant and also similar mode delay (at least for exponents close to $\alpha = 2$). The propagation times of the modes are only then dependent on the propagation constant and then the group delay can be determined with the aid of the WKB Method by differentiating the propagation constant from the angular frequency [66, 67], given by Eq. 3.12. All the theoretical framework will be further developed in Section 3.6.

3.3.1.2 Ray Tracing Procedure

The Ray Tracing procedure proceeds from the point of view that light propagation can be described within the fibre as in free space. This approximation is that much more exact the greater the dimensions of the fibre are and the greater the number of guided modes to be considered. When calculating the propagation characteristics, a very large number of rays

[2] MSI: Multi-Step Index.

are generated at the transmitter and each ray follows its own path along the fibre. In doing so, its attenuation as well as the elapsed propagation time is logged. At the end of the fibre a histogram about the rays received is drawn up which includes propagation time, attenuation, location or propagation direction [68, 69]. This procedure is based on tracing a huge amount of rays to obtain a statistic but implying the main disadvantage of this procedure: it requires great computing power. Further details of this analytical procedure can also be found in [70].

3.4 Mode coupling in Polymer Optical Fibres

Mode coupling is rather a statistical process in which modes exchange power with each other. Due to the mode coupling, the optical energy of the low-order modes would be coupled to higher order modes, even if only the low-order modes are launched selectively by the Restricted Launch condition (RML). This effect generally occurs through irregularities in the fibre, whether they are roughness of the core-cladding interface or impurities in the core material. These irregularities are microscopic and also lead to light scattering. This effect can therefore only be described with statistical means. In addition to, mode coupling is a process which is rather strong in polymer fibres and decisively influences the propagation characteristics of these fibres [57, 71, 72]. Since these high-order modes can degrade the bandwidth performance of the GIPOFs, the group delay difference among all the modes (from the lowest to highest order) should be minimized by the refractive index profile. However, from the literature, in step-index (SI) type POFs large mode coupling has been experimentally observed [73], while it has been proved that the mode coupling effect on the bandwidth in GIPOFs is smaller than in SIPOF [74].

The main effects for generating mode coupling are Rayleigh and Mie scattering which differ in the size of the scattering centers [75]. Rayleigh scattering arises through the molecular structure of matter which is why no material can have perfectly homogenous properties. Its optical density fluctuates around a mean value which represents the refractive index of the material. These fluctuations are very small and have typical sizes in the range of molecules (< μm). Rayleigh scattering depends on the wavelength and decreases with greater wavelengths as of the fourth power ($\sim \lambda^{-4}$). Mie scattering comes from the fluctuations of the refractive index which has greater typical lengths that mostly come about because of impurities in the material such as air bubbles or specks of dust which are large compared with the wavelength of light. The ensuing scattering has more of an effect on the direction of propagation of the light and is independent of the wavelength. A typical example for Mie scattering is the white color of emulsions such as milk which comes about because of the wavelength-independent scattering of the light. Regarding polymer optical fibres, investigations have shown that in standard step-index (SI) fibres Rayleigh scattering predominates in the core and Mie scattering at the core-cladding interface [76]. This shows that today's polymer fibres are drawn from very pure material. However, some problems still do arise at the interface. The latter occur in part because the core and cladding materials have different expansion coefficients which can result in tension. On the other hand, the drawing of the fibre can cause the cladding to acquire a rough surface. When thinking about these aspects mode coupling reveals itself as a

complex process which plays a great role in polymer fibres and has other effects than in conventional silica fibres [71, 72]. There are some approaches for the modeling of mode coupling which cannot be applied equally well in all propagation models [77-79]. Some descriptions present themselves rather in mode models [80, 81] while others are more limited to use in Ray Tracing models [68].

The coupling coefficients which describe the coupling between modes can either be described by analytical attempts which are based on observations of mode overlapping [82-85] or are defined in a more phenomenological manner. Examples of such phenomenological descriptions could be models for Mie and Rayleigh scattering or approximations based on measurements. The latter demonstrate that in real fibres, however, only very few modes effectively interact with each other so that a simpler description of the mode coupling suffices [86]. In addition to, investigations have shown that neighboring modes, i.e. those with similar propagation constants, primarily show strong mode coupling.

Going on from this, it is found that the strength of the mode coupling can be related to the difference of the propagation constant, $\Delta\beta(m,\lambda)$, between adjacent modes [87, 88]. Hereafter, dependencies of $\Delta\beta(m,\lambda)$ regarding the principal mode number m and wavelength λ are omitted for notational simplification within this section.

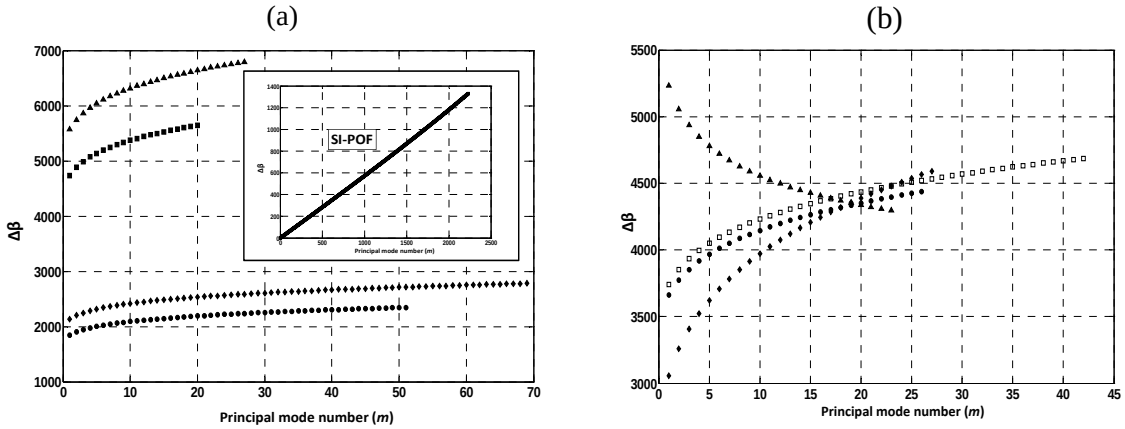

Fig. 3.6. (a) GIPOF dependence of the difference between propagation constants (Δβ) of adjacent modes at 1300nm and α=2.3. ■ 50 μm PF GIPOF ; ● 120 μm PF GIPOF ; ▲ 50 μm PMMA GIPOF ; ♦ 120 μm PMMA GIPOF. Inset: SI-POF case. (b) PF GIPOF dependence of the difference between propagation constants (Δβ) of adjacent modes. □ 62.5 μm@850nm, α=2.3 ; ● 62.5 μm@1300nm, α=2.3 ; ▲ 62.5μm@1300nm, α=2.7 ; ♦ 62.5μm@1300nm, α=1.7.

If the refractive index profile of a GIPOF can be approximated by the power-law equation then the propagation constant $\beta(m,\lambda)$ at a certain wavelength of a mode with a principal mode number m is a function of the core refractive index ($n_1(\lambda)$) and the relative refractive index difference $\Delta(\lambda)$. If two modes have the same propagation constant, namely $\Delta\beta = 0$, these modes are called degenerate modes. On the other hand, if the value of $\Delta\beta$ is large, the probability of energy transfer between these two modes decreases; thus little mode

coupling can be observed. Large $n_1(\lambda)$ and $\Delta(\lambda)$ values are expected to decrease the mode coupling in the GIPOF. The whole mathematical framework within this section will be presented in Section 3.6.

Different GIPOF fibre dependences of the $\Delta\beta$ values are calculated, and the results are shown in Fig. 3.6. Here, $\Delta\beta$ is defined as the propagation constant difference of *m*th- and (*m*+1)th-order modes. Each $\Delta\beta$ value is calculated from a refractive index profile near to the optimum and approximated by the three-term Sellmeier function. It can be seen from Fig. 3.6(a) that PMMA-based fibres show higher $\Delta\beta$ values with regards to their PF-based counterparts for the same conditions which means that less coupling strength is observed in those fibres, although same order values are obtained. Similarly, the $\Delta\beta$ values increase with decreasing the fibre core radius. This is expected as the number of modes propagating through the fibre is proportional to this parameter. On the other hand, from Fig. 3.6(b) it can be concluded that higher mode coupling at 1300nm than at 850nm is observed on PF GIPOFs although slight dependence is observed. This wavelength dependence is directly related to the different relative refractive index difference, $\Delta(\lambda)$ and, consequently, the different NAs for the fibres considered. The higher NA the lower mode coupling is observed. Finally, the SIPOF mode coupling strength is shown in inset of Fig. 3.6(a), which demonstrates the large mode coupling experimentally observed in SIPOF [73], as lower values of Δβ are achieved considering the same adjacent modes. This is due to the huge amount of modes propagating through the SIPOF fibre.

3.5 Differential Mode Attenuation in Polymer Optical Fibres

Differential mode attenuation (or namely mode-dependent attenuation) exists in multimode fibres and especially in polymer fibres with relatively high losses. Previous works such as [54, 89-93] have shown that the losses increase almost exponentially for the highest mode groups.

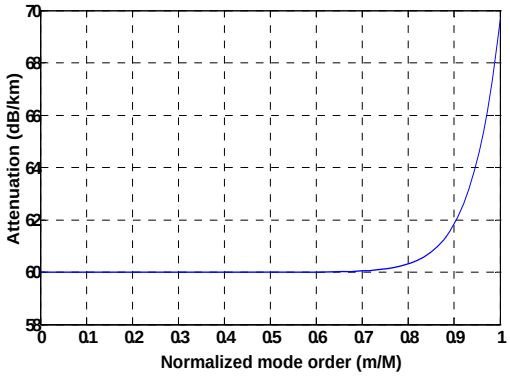

Figure 3.7.- Differential mode attenuation (DMA) as a function of the normalized mode order m/M for a=250μm, α=2 and λ=1300nm. The solid curve has been properly shifted in order to take a intrinsic attenuation of 60dB/km into account. Parameters ρ and η, described in Section 3.6, were set to 11 and 12.2, respectively.

The higher modes generally experience higher attenuation than the basic mode. There can be different reasons for this. In the mode description higher modes have more intensity in the vicinity of the core-cladding interface and even in the cladding itself which is why higher losses could be expected in non-ideal interfaces. It is worth noticing from Fig. 3.7 that the strength of the DMA in POFs, in general, follows mainly from the fact that the minimum attenuation (intrinsic to the fibre) is extremely large compared to silica optical fibres.

3.6 Graded-Index Polymer Optical Fibre Transfer Function

It has been previously stated that when the light is coupled into the multimode fibre, the total power is split up into the individual modes which then propagate at different speeds along the fibre, so that they arrive at the detector at the end of the fibre at different times. This fact leads to different signal parts reaching the end of the fibre at different times resulting in a distorted signal. It is possible to model this procedure by treating the output signal at the end of the fibre like a superposition of the input signal shifted in time by τ, including a weighting with the superposition of the signal parts resulting from the mode distribution. In a generic framework, it can be said:

$$P_O(t) = \sum_m \eta_m \cdot P_i(t - \tau_m) \tag{3.4}$$

Here $P_O(t)$ and $P_i(t)$ are the output and the input signal, respectively. Counting index *m* goes over all mode groups whereby η_m and τ_m are the share of the total power (i.e. the coupling efficiency in the respective mode) and the propagation time of the mode group, respectively.

Furthermore, the impulse response $h_{MMF}(t)$ results analogously by accepting a Dirac (unit) impulse as the input signal, as follows:

$$h_{MMF}(t) = \sum_m \eta_m \cdot \delta(t - \tau_m) \tag{3.5}$$

However, in this chapter a full dispersion model based on evaluating the frequency response of graded-index polymer optical fibres using the power flow equations instead of the direct calculation of the pulse broadening from the moments of the impulse response is presented, as described in [55]. The 3-dB bandwidth is analyzed through the study of the fibre transfer function which introduces the wavelength and modal effects as two separate filter functions. The formal derivation of the chromatic transfer function is analytical while the modal transfer function is obtained by numerically solving the power flow equation in the frequency domain. A friendly graphical interface as well as the numerical computations were performed using Matlab® software and are further documented into the Final Degree Project reported in [94].

To compute the GIPOF transfer function, it has been considered the refractive index profile of a graded-index optical fibre in the power-law form, commonly used for minimize dispersion effects, described by Eq. 3.6. Nevertheless, the approximation of the index profile by a ten-term polynomial function of the distance *r* from the center axis of the fibre could also be adopted [30, 74].

$$n(r,\lambda)=\begin{cases} n_1(\lambda)\left[1-2\Delta(\lambda)\left(\dfrac{r}{a}\right)^{\alpha}\right]^{1/2} & \text{for } 0\le r\le a \\ n_1(\lambda)\left[1-2\Delta(\lambda)\right]^{1/2} & \text{for } r\ge a \end{cases} \quad \text{with} \quad \Delta(\lambda)=\frac{n_1^{\,2}(\lambda)-n_2^{\,2}(\lambda)}{2n_1^{\,2}(\lambda)} \qquad (3.6)$$

where *r* is the offset distance from the core center, *a* is the fibre core radius (i.e. the radius at which the index $n(r,\lambda)$ reaches the cladding value $n_2(\lambda)=n_1(\lambda)[1-2\Delta(\lambda)]^{1/2}$), $n_1(\lambda)$ is the refractive index in the fibre core center, λ is the free space wavelength of the fibre excitation light, α is the refractive index exponent and $\Delta(\lambda)$ is the relative refractive index difference between the core and the cladding. It has also been assumed that the core and cladding refractive index materials of the GIPOF follow a three-term Sellmeier function of wavelength [18] given by:

$$n_i(\lambda)=\left(1+\sum_{k=1}^{3}\frac{A_{i,k}\lambda^2}{\lambda^2-\lambda_{i,k}^2}\right)^{1/2} \quad \text{with i=1 (core), 2 (cladding)} \qquad (3.7)$$

where $A_{i,k}$ and $\lambda_{i,k}$ are the oscillator strength and the oscillator wavelength, respectively (both parameters are often gathered under the term of Sellmeier constants).

Once the refractive index is known, the material dispersion $D(\lambda)$ and the corresponding dispersion slope in the core $S(\lambda)$ (where the light is guiding) can be obtained, respectively, from the definitions:

$$D(\lambda)=-\frac{\lambda}{c}\frac{d^2n_1(\lambda)}{d\lambda^2} \ \text{ps/(nm}\cdot\text{km)} \qquad (3.8)$$

$$S(\lambda)=-\frac{1}{c}\left(\frac{d^2n_1(\lambda)}{d\lambda^2}+\lambda\frac{d^3n_1(\lambda)}{d\lambda^3}\right) \ \text{ps/(nm}^2\cdot\text{km)} \qquad (3.9)$$

On the other hand, from the WKB analysis, the modal propagation constant can be approximately derived as following [55, 83], in which each guided mode has its own propagation constant and therefore propagates at its own particular velocity:

$$\beta(m,\lambda) = n_1(\lambda)k\left[1-2\Delta(\lambda)\left(\frac{m}{M(\alpha,\lambda)}\right)^{\frac{2\alpha}{\alpha+2}}\right]^{1/2} \tag{3.10}$$

where *m* stands for the principal mode number [16]. This so-called principal mode number (mode group number or mode number) can be defined as $m = 2\mu + \nu + 1$ in which the parameters μ and ν are referred to as radial and azimuthal mode number, respectively. Physically, μ and ν represent the maximum intensities that may appear in the radial and azimuthal direction in the field intensities of a given mode. For a deeper analysis works reported in [14, 83, 95]are recommended. On the other hand, $M(\alpha,\lambda)$ is the total number of mode groups that can be potentially guided in the fibre, given by [17]:

$$M(\alpha,\lambda) = 2\pi a\frac{n_1(\lambda)}{\lambda}\left[\frac{\alpha\cdot\Delta(\lambda)}{\alpha+2}\right]^{1/2} \tag{3.11}$$

As a consequence of Eq. 3.10, the delay time $\tau(m,\lambda)$ of a mode depends only on its principal mode number. The delay time of the guided modes (or modal delay per unit length) can be derived from (3.10) using the definition $\tau(m,\lambda) = -\frac{\lambda^2}{2\pi c}\frac{d\beta(m,\lambda)}{d\lambda}$ where *c* is the speed of light in vacuum, deriving in:

$$\tau(m,\lambda) = \frac{N_1(\lambda)}{c}\left[1-\frac{\Delta(\lambda)(4+\varepsilon(\lambda))}{\alpha+2}\left(\frac{m}{M}\right)^{\frac{2\alpha}{\alpha+2}}\right]\left[1-2\Delta(\lambda)\left(\frac{m}{M}\right)^{\frac{2\alpha}{\alpha+2}}\right]^{-1/2} \tag{3.12}$$

where $\varepsilon(\lambda)$ is the profile dispersion parameter given by [96]:

$$\varepsilon(\lambda) = -\frac{2n_1(\lambda)}{N_1(\lambda)}\frac{\lambda\frac{d\Delta(\lambda)}{d\lambda}}{\Delta(\lambda)} \tag{3.13}$$

and $N_1(\lambda)$ is the material group index defined by:

$$N_1(\lambda) = n_1(\lambda) - \lambda\frac{dn_1(\lambda)}{d\lambda} \tag{3.14}$$

It should be mentioned that are the differences in modal delay (i.e. differential mode delay, DMD) that determine the modal dispersion.

In a strict sense and coming back to the meaning of principal mode number *m*, this is a discrete integer parameter, which takes values ranging from unity to the total number of mode groups. However, it is possible to approximate the mode number *m* from a discrete

integer parameter to a continuous variable thus allowing the replacement of the discrete mode spectrum by a modal continuum [97]. As a result, the WKB method can be used and mode sums can be converted to integrals that are easier to handle with. In this analysis it is concluded that the large number of guided modes, generally believed to be the main condition, seems actually not required but even only two of them may constitute a continuum. The condition for the validity of the continuum approximation is defined by [97]:

$$W \geq \frac{\lambda^2}{\pi a N_1(\lambda)} \left[\frac{\alpha \Delta(\lambda)}{\alpha + 2} \right]^{1/2} \left(\frac{m}{M(\alpha, \lambda)} \right)^{\frac{\alpha-2}{\alpha+2}} \tag{3.15}$$

where W stands for the rms spectral linewidth of the optical source.

Some conditions are expected to be satisfied in practice such is the use of large enough linewidth sources, see Eq. 3.15, in which the signal bandwidth is smaller than the source bandwidth (fact that can be unsatisfied in very highly coherent systems). Assuming this latter fact and considering a graded-index multimode fibre characterized by the refractive index profile given by Eq. 3.6 as well as being linear in its input-output relationship [98], the ratio of the baseband spectra of the output and input light is signal-independent and is called the baseband power transfer function. Within multimode fibres, terms such as the light coupling efficiency into each mode as well as the fact that both loss and delay now depend on modes must be also introduced and the contribution of all propagated modes can be expressed as:

$$\begin{aligned} &H_{MMF}(\lambda_o, z, \Omega) = \\ &= \int_1^M \int_{-\infty}^{\infty} 2m \cdot P(\lambda, \lambda_o) \cdot C_{eff}(m, \lambda) \cdot G(m, \lambda, z, \Omega) \cdot L(m, \lambda, z) e^{-j\Omega\tau(m,\lambda)z} d\lambda dm \end{aligned} \tag{3.16}$$

where z is the length of the fibre, Ω is the angular baseband frequency, $P(\lambda_o, \lambda)$ is the time-independent optical source spectrum, $L(m, \lambda, z)$ is the modal loss that can be approximated by $L(m, \lambda, z) = e^{-\alpha_T(m,\lambda)z}$ in which $\alpha_T(m, \lambda)$ stands for the total mode attenuation, the function $G(m, \lambda, z, \Omega)$ reflects the account for the mode coupling (or so-called by other authors as mode mixing) effect, $\tau(m, \lambda)$ is the modal delay per unit length and $C_{eff}(m, \lambda)$ refers to the light coupling efficiency of each mode m. Finally, factor $2m$ denotes the degeneracy of level m.

Assuming that the dependence on wavelength of the launching efficiency, the mode coupling function and the differential mode attenuation is negligible in the transmission window of interest, it is possible to approximate the terms $C_{eff}(m, \lambda)$, $G(m, \lambda, z, \Omega)$ and $L(m, \lambda, z)$ by their respective values at the central wavelength λ_o.

On the other hand, the modal delay time $\tau(m, \lambda)$, which is given by Eq. 3.12, can be expressed as a Taylor series expansion, for the condition $W / 2\lambda_o \ll 1$, as:

$$\tau(m,\lambda) = \tau(m,\lambda_o) + D(m,\lambda_o)(\lambda-\lambda_o) + \frac{1}{2}S(m,\lambda_o)(\lambda-\lambda_o)^2 + \ldots \quad (3.17)$$

where

$$D(m,\lambda_o) = \left.\frac{d\tau(m,\lambda)}{d\lambda}\right|_{\lambda=\lambda_o} \quad (3.18)$$

and

$$S(m,\lambda_o) = \left.\frac{d^2\tau(m,\lambda)}{d\lambda^2}\right|_{\lambda=\lambda_o} \quad (3.19)$$

are the chromatic dispersion of mode *m* and the modal dispersion slope, respectively.

Under the assumption that $D(m,\lambda_o)$ and $S(m,\lambda_o)$ can be, respectively, replaced by averaged values $D_o(\lambda_o)$ and $S_o(\lambda_o)$, the transfer function of a generic multimode optical fibre can be modeled by a product of two filter function as follows[95]:

$$H_{MMF}(\lambda_o, z, \Omega) = H_{\text{chromatic}}(\lambda_o, z, \Omega) \cdot H_{\text{modal}}(\lambda_o, z, \Omega) \quad (3.20)$$

being

$$H_{\text{chromatic}}(\lambda_o, z, \Omega) = \int_{-\infty}^{\infty} P(\lambda,\lambda_o) \cdot e^{\left\{-j\Omega z[D_o(\lambda_o)(\lambda-\lambda_o)+\frac{1}{2}S_o(\lambda_o)(\lambda-\lambda_o)^2]\right\}} d\lambda \quad (3.21)$$

and

$$H_{\text{modal}}(\lambda_o, z, \Omega) = \int_{1}^{M} 2m \cdot C_{eff}(m,\lambda_o) \cdot G(m,\lambda_o,z,\Omega) \cdot L(m,\lambda_o,z) e^{-j\Omega\tau(m,\lambda_o)z} dm \quad (3.22)$$

where $H_{\text{chromatic}}(\lambda_o, z, \Omega)$ represents the chromatic dispersion effect and $H_{\text{modal}}(\lambda_o, z, \Omega)$ represents the modal dispersion effect, both with parameters, in argument, being the baseband angular frequency Ω and the transmission length *z*. Eq. 3.20 expresses the idea that chromatic and modal dispersions are independent effects that can be evaluated separately despite the mode coupling. The chromatic term results from the fact that the delay time of each propagated mode depends on wavelength whereas the modal term depends on less controlled variables such as the excitation conditions, the difference in delays among the modes, the DMA or the power coupling between modes.

Assuming that the power spectral density of the optical source has a Gausssian linewidth spectrum, as most of injection-lasers used in optical fibre communications have this lineshape [99], in which *W* is the rms spectral linewidth and λ_o is the central wavelength of the source spectrum, it yields:

$$P(\lambda,\lambda_o)=\frac{1}{W\sqrt{2\pi}}e^{-\frac{(\lambda-\lambda_o)^2}{2W^2}} \tag{3.23}$$

and the chromatic transfer function can be exactly calculated as [95, 100]:

$$H_{\text{chromatic}}(\lambda_o,z,\Omega)=\frac{1}{(1+j\Omega/w_2)^{1/2}}e^{-\frac{(\Omega/w_1)^2}{2(1+j\Omega/w_2)}} \tag{3.24}$$

in which w_1 and w_2 have been introduced as abbreviations for:

$$w_1=-\frac{1}{D_o(\lambda_o)Wz} \tag{3.25}$$

and

$$w_2=\frac{1}{\left[W^2\left(S_o(\lambda_o)+\frac{2D_o(\lambda_o)}{\lambda_o}\right)z\right]} \tag{3.26}$$

where $D_o(\lambda_o)$ is the modal velocity dispersion averaged over all guided modes and $S_o(\lambda_o)$ is the averaged dispersion slope, as previously stated. It is important to realize that for a system operated around a zero material disperion wavelength, the chromatic effect is not necessarily negligible because of the presence of the dispersion slope and, consequently, this term can not be ignored even in the zero dispersion region. It is also noteworthy that Eqs. 3.24, 3.25 and 3.26 are the same as those describing chromatic dispersion in singlemode fibres. The difference for multimode fibres (GIPOFs as well as silica-based fibres) is only that averaged values have to be used for the dispersion and the dispersion slope in order to include the contribution of all guided modes. Furthermore, the fact that averaged values are used for the dispersion and dispersion slope may cause the chromatic transfer function to slightly depend on all parameters that determine the propagation such as launching conditions, DMA or mode coupling effects. It should be also mentioned that when operating far from the zero dispersion region, the term w_2 is much larger than $|w_1|$ and Eq. 3.24 can be simplified into $\exp\left[-(\Omega/w_1)^2/2\right]$, which means that the contribution of the dispersion slope (i.e. $S_o(\lambda_o)$) is negligible in Eq. 3.21.

On the other hand, the modal transfer function described in Eq. 3.22 can also be written as:

$$H_{\text{modal}}(\lambda_o,z,\Omega)=\frac{\int_1^M 2\frac{m}{M(\lambda_o)}R(m,\lambda_o,z,\Omega)dm}{\int_1^M 2\frac{m}{M(\lambda_o)}R(m,\lambda_o,z,0)dm} \tag{3.27}$$

with

$$R(m,\lambda_o,z,\Omega) = C_{eff}(m,\lambda_o)\cdot G(m,\lambda_o,z,\Omega)\cdot L(m,\lambda_o,z)\cdot e^{-j\Omega\tau(m,\lambda_o)z} \qquad (3.28)$$

and where, again, *m* is the principal mode number, $M(\lambda_o)$ is the total number of mode groups that can be potentially guided in the fibre at $\lambda = \lambda_o$ and $R(m,\lambda_o,z,\Omega)$ is the modal power in Fourier domain being a solution of a partial differential equation (the power flow equation or diffusion equation), see Eq. 3.30, which incorporates not only the modal delay but also the DMA and mode coupling effects.

The denominator in the right hand side of Eq. 3.27 is a normalization factor representing the total power at position *z*, in such a way that:

$$\int_1^M 2\frac{m}{M(\lambda_o)} R(m,\lambda_o,z,0)\,dm = 1 \qquad (3.29)$$

Equation 3.28 is unusable as it stands because, although quantities such as the modal excitation efficiency $C_{eff}(m,\lambda)$, modal loss $L(m,\lambda,z)$ and modal delay $\tau(m,\lambda)$ can be estimated using WKB analysis, the mode coupling function $G(m,\lambda,\Omega,w)$ is so far from being exactly calculated. However, the power flow in propagated modes is best described by the following partial differential equation incorporating not only modal velocities but also DMA and mode-conversion effects [15, 16]. In a generic form:

$$\frac{\partial R(m,\lambda_o,z,\Omega)}{\partial z} = -\left[\, j\Omega\tau(m,\lambda_o) + \alpha_T(m,\lambda_o)\right] R(m,\lambda_o,z,\Omega) + \\ + \frac{1}{m}\frac{\partial}{\partial m}\left[m\cdot d(m,\lambda_o)\cdot\frac{\partial R(m,\lambda_o,z,\Omega)}{\partial z}\right] \qquad (3.30)$$

where $d(m,\lambda_o)$ is the mode coupling coefficient normalized to $M^2(\lambda_o)$ (which is an approximation to the total number of guided modes in the optical fibre), $\alpha_T(m,\lambda_o)$ is the differential mode attenuation (in absence of coupling effect) and $\tau(m,\lambda_o)$ is the modal delay per unit length.

This power flow equation can be solved exactly in certain simplified cases [16, 101]. In the more general situation, where all the parameters are mode-dependent, it has no analytical solutions available but can be solved only using a numerical procedure. A great variety of procedures are given in literature but the Crank-Nicholson procedure used to solve Eq. 3.30, which yields a stable solution that converges more rapidly than ordinary difference methods, has already been successfully applied to fibres [102-104]. Once the coefficients for $R(m,\lambda_o,z,\Omega)$ have been computed and determined, the modal transfer function can be derived by approximating Eq. 3.27 by any suitable numerical integration method. In the

simulations made within this chapter the Simpson's rule has been used in the frequency response simulations.

Regarding the differential mode attenuation (DMA), which causes the attenuation coefficient to vary from mode to mode in a different manner, it originates from conventional loss mechanisms that are present in usual optical fibres such as absorption [105], Rayleigh scattering [105, 106] or losses on reflection at the core-cladding interface [107]. The following functional expression or empirical formula for the DMA is proposed, in which the DMA increases when incresing the mode order [55]:

$$\alpha_T(m,\lambda) = \alpha_o(\lambda) + \alpha_o(\lambda) I_\rho \left[\eta \left(\frac{m-1}{M} \right)^{\frac{2\alpha}{\alpha+2}} \right] \tag{3.31}$$

where $\alpha_o(\lambda)$ is the attenuation of low-order modes (i.e intrinsic fibre attenuation), I_ρ is the ρ-th order modified Bessel function of the first kind and η is a weighting constant. This empirical formula is set up by noticing that most measured DMA data displayed in the literature for long wavelengths conform to the shape of modified Bessel functions [91, 93]. It is also worth mentioning that, during propagation, modes with fastest power loss may be stripped off or attenuated so strongly that they no longer significantly contribute to the dispersion. In other words, the DMA is a filtering effect, which may yield a certain bandwidth enhancement depending on the launching conditions and the transmission length. This fact will be proved in Section 3.8 regarding the experimental results.

As the contribution of the mode coupling phenomenon should be negligible over the lengths of GIPOF samples usually considered, the modal power can simply be calculated as:

$$R(m,\lambda,z,\Omega) = C_{rmeff}(m,\lambda) e^{-\alpha(m,\lambda)z} e^{-j\Omega\tau(m,\lambda)z} \tag{3.32}$$

where $C_{rmeff}(m,\lambda)$ is the mode excitation coefficient (or coupling/launching efficiency), $\alpha(m,\lambda)$ is the differential mode attenuation (or mode-dependent attenuation), see Eq. 3.31, and $\tau(m,\lambda)$ is the modal delay per unit length, see Eq. 3.12. The last term in Eq. 3.32 involves that modal dispersion is caused by the difference in the modal parameters.

The explanation of the assumption of negligible mode coupling is that the length-dependent mode coupling is a diffusion process resulting from small power exchanges on imperfections along the fibre and these exchanges can cause the modal delay times to be averaged [98]. Consequently, a bandwidth enhancement due to the mode coupling effect can be achieved if the transmission distance is long enough for each propagated mode to undergo a statistically large number of interactions before detection, a requirement that appears to be unsatisfied for usual GIPOF transmission lengths of a few hundred of meters. This is in relatively good agreement with the simulations and measurements presented and compared in Section 3.7 and 3.8, respectively.

On the other hand, the presence of the excitation coefficient $C_{rmeff}(m)$ permits the evaluation of the model under any launching condition. $C_{rmeff}(m)$ can be evaluated as the overlap integral of the electrical field of each fibre mode with the electrical field of the incident light. Considering a uniform launching condition, as in [17], the initial power distribution is, by assumption, the same for each mode, setting the coefficient $C_{rmeff}(m)$ to the unity, i.e. equal power is coupled into each mode at the input end of the fibre. This condition is realistic if a LED is used as a optical power source. But most of experiments so far carried out on the GIPOFs, in high-speed short- and middle-reach networks, employ light beams from semiconductor lasers or from VCSELs. Consequently, a power spectral density of the source with a Gausssian lineshape, see Eq. 3.23, is a more realistic assumption [99]. This leads to the employment of Restricted Launching Conditions (RML) into the GIPOF link, in which only a small subset of modes are excited and the Gaussian lineshape can be defined by the beam spot radius launched onto the GIPOF input end. Strictly speaking, this calculation should be carried out for the proper refractive index profile of the fibres in consideration. But, this is not an easy task since the modal fields can be determined analytically in terms of known functions only for $\alpha = 2$ and $\alpha = \infty$. However, as long as the refractive index remains nearly parabolic, as it is the case with modern GIPOFs, the distribution of the initial power is not expected to differ significantly from that of the perfectly parabolic profile. It is therefore appropiate to use the results of overlap integral calculation displayed in [108, 109].

In order to obtain the excitation coefficients when considering an optical power source with a Gaussian lineshape spectral density, it can be assumed that the fibre is excited centrally with a laser beam that forms a circularly symmetric spot on the the input surface, i.e. the fibre axis is well aligned with the beam axis as well as its end surface is well positioned in the focal plane. In such case the field of such a beam can be expressed in cartesian coordinates (taken the core center as the origin of axes) as:

$$E_{in}(x,y) = \frac{\sqrt{2}}{\sqrt{\pi}w} e^{-\frac{x^2}{w^2}} e^{-\frac{y^2}{w^2}} \tag{3.33}$$

where *w* stands for the beam spot radius.

Adopting the simplified approximation that the launching field given above excites solely the Hermite-Gauss fields of the fibre given by [110], then:

$$\psi_{\mu\nu}(x,y) = \frac{1}{w_o\sqrt{\pi 2^{\mu+\nu}\mu!\nu!}} H_\mu\left(\sqrt{2}\frac{x}{w_o}\right) H_\nu\left(\sqrt{2}\frac{y}{w_o}\right) e^{-\frac{x^2+y^2}{w_o^2}} \tag{3.34}$$

Where H_μ is the Hermite polynomial of degree μ and w_o is referred to as the beam radius of the fundamental modes given by:

$$w_o = \frac{1}{\left(2\Delta(\lambda)\right)^{1/4}}\left(\frac{a\lambda}{\pi n_1(\lambda)}\right)^{1/2} \tag{3.35}$$

The integral of Eq. 3.33 and 3.34 is calculated from the following definition, where the integration is taken over the input plane:

$$a_{\mu\nu} = \int_{(A)} E_{in}(x,y)\psi_{\mu\nu}(x,y)dxdy \tag{3.36}$$

Eq. 3.36 can be solved yielding [109]:

$$a_{\mu\nu} = \begin{cases} 0 & \text{for } \mu \text{ and } \nu \text{ odd} \\ \dfrac{\sqrt{2}}{\pi w_o w\sqrt{2^{\mu+\nu}u!\nu!}} I_\mu I_\nu & \text{for } \mu \text{ and } \nu \text{ even} \end{cases} \tag{3.37}$$

in which:

$$I_\mu = w_o(-1)^{\mu/2}2^{\mu-1}\cdot\frac{\Gamma(1/2)\Gamma[(\mu+1)/2]}{\sqrt{\pi z_o/2}}F(-\mu/2,1/2,1/2,1/z_o) \tag{3.38}$$

and

$$z_o = \frac{1}{2} + \frac{w_o^2}{2w^2} \tag{3.39}$$

where $\Gamma(x)$ is the gamma function and $F(x_1,x_2,x_3,x_4)$ is the hypergeometrical function.

Finally, the mean power excitation coefficient of modes in mode group number *m*, C_m, can be derived from Eq. 3.37 as:

$$C_m = \frac{1}{2m}\sum_{\mu=0}^{m-1}\left|a_{\mu,m-\mu-1}\right|^2 \tag{3.40}$$

3.7 Graded-Index Polymer Optical Fibre Transfer Function Simulations

As aforementioned, as an alternative to multimode silica optical fibres, polymer optical fibres (POFs), which are intrinsically multimode, are also being developed as important high-speed communication media for short- and middle-reach applications (100 ~ 500m). These fibres have a large core diameter and a large numerical aperture which allow easy conectorization of systems and efficient launching as well as being a low-cost physical

transmission medium compare to silica optical fibre (particularly to MMFs). Graded-Index Polymer Optical Fibres (GIPOFs) can combine these properties with a large capacity for transmission [6, 111]. Consequently, similar performances as those provided by silica-based MMFs but with lower cost can be obtained by means of GIPOFs. In order to get maximum performance in GIPOF links the availability of accurate models to give a full description of the dispersion, which incorporates all the parameters involved in the determination of the total bandwidth, is required. The baseband bandwidth performed in such type of fibres is indeed increased due to the strong differential mode attenuation (DMA). For the evaluation of the frequency response in a GIPOF link a closed-form has been developed and presented in the above section, based on the previous works reported in [55, 95, 112]. The numerical computations were performed using Matlab® software. Further details can be found in [94].

Different theoretical simulations have been studied with regards to several parameters affecting the frequency response of the GIPOF fibre link such as the link length, the graded index exponent of the fibre (α), the operating wavelength, the source linewidth or the launching conditions among others. To enable computer evaluations, it is assumed that the refractive indices of the core and cladding materials follow three-term Sellmeier functions of wavelength. The functional expression of the differential mode attenuation, see Eq. 3.31, has been considered for evaluating the DMA effects over the fibre bandwidth. By fitting Eq. 3.31 for $\eta = 12.2$ and $\rho = 11$ the results have been shown in Fig. 3.7, in which the DMA is shown as a function of the normalized mode order m/M. It can be seen that lower-order mode groups show similar attenuation (intrinsic fibre attenuation) whereas for higher-order mode groups (in this case $m/M > 0.8$) attenuation increases rapidly. Unfortunately, no measured DMA data for GIPOFs exist in literature yet. However, various measurements on silica optical fibres show that the DMA (with dB units), as a function of the principal mode group number *m*, depends on the wavelength and on the numerical aperture [90, 91, 93]. In other words, the fibre materials seem to have no significant effect on the DMA shape as long as the refractive index conforms to a circular-symmetric profile law in accordance with the definition given in Eq. 3.6. Therefore, it has been adopted a similar DMA profile given in Fig. 7(c) reported in [93] which is also in concordance with Fig. 3.7 within this document. The fitting process leaded to the aforementioned values of parameters ρ and η.

3.7.1 Optical power launching conditions

In order to achieve reproducible results with measurements for attenuation and dispersion, the modes should be in Equilibrium Mode Distribution (EMD). This can be achieved by using a launching fibre, although this is not very practical for polymer fibres since the required length of 30m to 60m would lead to high additional attenuation (6 dB to 12 dB for 200 dB/km attenuation). The dynamics of the measurement setup is reduced by this value. For comparison: for silica fibres, the length of the launching fibre is in the range of 1km to 2km producing an additional loss of 2 dB to 4 dB (for 2 dB/km of attenuation). Another possibility is coupling the light through a suitable optical arrangement with full core illumination and a numerical aperture corresponding to EMD. However, in this method it is

necessary to have the knowledge of the conditions for EMD, which are different from fibre to fibre. In practical applications, a mode scrambler (also called mode mixer) is frequently used thus the following effects occur: (a) due to the bends, higher order modes are radiated (radiation modes), (b) modes are converted into each other due to the bends (mode conversion), (c) due to faults at the interface between core and cladding, it is possible that several modes can be created from one mode (mode coupling). This latter process is dominant and depends on the respective type of fibre.

On the other hand, if the complete area and numerical aperture are uniformly illuminated (namely, full launching condition or overfilled launching condition OFL) all modes will carry initially the same power and a uniform excitation is achieved (also called UMD: Uniform Mode Distribution). This condition is achieved through a collimated light or light with an angle adapted to the fibre NA launched to into the POF. Nevertheless, it can be also achieved by using a SIPOF acting as a launching fibre [74], for instance. During the further passing of the light through the fibre, the rays propagating at a larger angle to the axis of the fibre experience greater attenuation than the rays with the lower angle since they have to travel a longer path and are reflected more often on the interface between the core and the cladding. For instance: in a fibre with NA = 0.5, n_1=1.497 of core refractive index and a core radius of 0.5 mm, the core ray, which is still just about reflected completely, runs at an angle of 19.5°, and over a length of 1 m the ray will be reflected approximately 350 times at the interface between the core and the cladding. Due to inhomogeneities at the core/cladding interface as well as in the core material, it is possible that power may propagate in two different directions (i.e. presence of mode coupling). In addition, mode conversion will cause power to be exchanged between the different propagation directions at bends within the optical fibre. These effects lead to a change in the mode distribution excited at the beginning of the fibre. After a certain distance, a steady state distribution is achieved and from thereon mode distribution remains constant achieving the EMD, provided no such faults occur that would again lead to mode coupling effects. If the excitation is with a small numerical aperture (namely, Restricted Mode Launching, RML, or under-filled launching condition), by means of a narrow optical source or if the light is launched through a SMF patch cord, there will be also EMD after a certain length due to the fact that higher order modes are created.

Two different polymer-based GIPOFs will be theoretically analyzed within this chapter, one manufactured from a non-fluorinated polymer such as polymethylmethacrylate (PMMA) whereas the second one comes from an amorphous perfluorinated polymer (PF), such is the polyperfluoro-butenylvinylether, leading to the so-called next generation PF GIPOF fibres.

3.7.2 PMMA Graded-Index Polymer Optical Fibre Sellmeier coefficients

In this section a polymethylmethacrylate (PMMA) GIPOF with 120/490μm of core/cladding diameter and an (arbitrary) intrinsic attenuation of 60dB/Km is considered for the evaluation of the theoretical model presented in this chapter. The refractive indices for the core and the cladding are calculated using a three-term Sellmeier function, given by

Eq. 3.7, with coefficients shown in Table 3.3 and reported in [18]. The numerical aperture at the core center is calculated as NA=0.238, from the core and cladding refractive indices obtained by Fig. 3.8(a) which are found to be $n_1 = n_{cc} = 1.501$ and $n_2 = n_{cl} = 1.482$, respectively, for a wavelength of 1300nm. The material dispersion and the corresponding dispersion slope at 1300nm are calculated (through Eq. 3.8 and 3.9) approximately to be -46.7ps/(nm.km) and -0.857ps/(nm^2.km), respectively. Furthermore, the refractive group index and the dispersion profile parameter, at 1300nm, take the value of $N_1 = 1.535$ and $\varepsilon = +0.361$ (through Eq. 3.13 and 3.14), respectively. Figure 3.8(b) plots the dependency of the material dispersion with the operating wavelength (i.e. $D(\lambda)$).

Core Sellmeier coefficients, $n_1 = n_1(\lambda)$		**Cladding Sellmeier coefficients,** $n_2 = n_2(\lambda)$	
$A_{1,1}$	0.4855	$A_{2,1}$	0.4963
$A_{1,2}$	0.7555	$A_{2,2}$	0.6965
$A_{1,3}$	0.4352	$A_{2,3}$	0.3223
$\lambda_{1,1}$	1.043e+02	$\lambda_{2,1}$	7.18e+01
$\lambda_{1,2}$	1.147e+02	$\lambda_{2,2}$	1.174e+02
$\lambda_{1,3}$	4.934e+04	$\lambda_{2,3}$	9.237e+03

Table 3.3. PMMA GIPOF Sellmeier coefficients of the core and cladding.

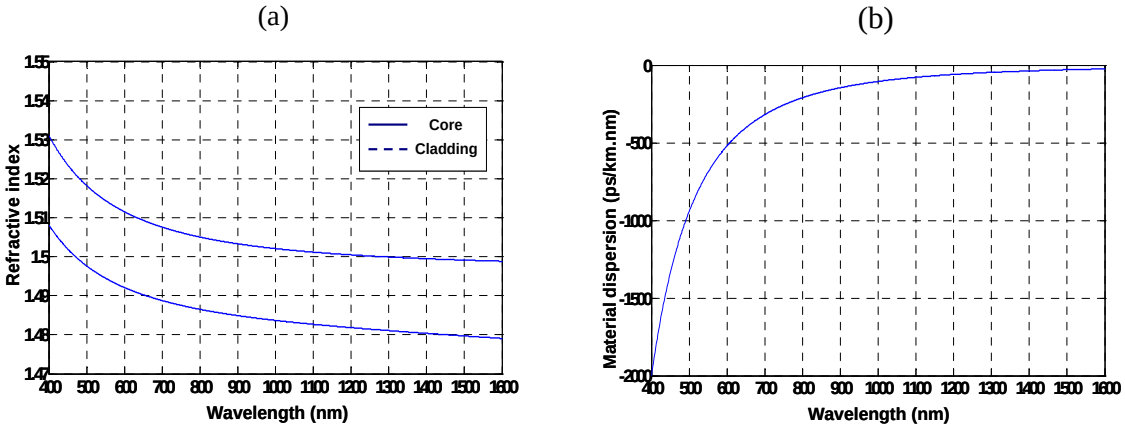

Figure 3.8.- (a) Refractive index of the fibre core and fibre cladding for the PMMA GIPOF. (b) Material dispersion of the central core region for the PMMA GIPOF as a function of the wavelength.

3.7.3 PF Graded-Index Polymer Optical Fibre Sellmeier coefficients

A perfluorinated (PF) GIPOF, which has been demonstrated to provide higher-bandwidth performance than PMMA-based counterparts, with 120/490μm of core/cladding diameter and an (arbitrary) intrinsic attenuation of 60dB/Km is used for the evaluation of the theoretical model presented in this chapter. The refractive indices for the core and the

cladding are calculated using a three-term Sellmeier function, given by Eq. 3.7 and shown in Fig. 3.9(a), with coefficients provided by the manufacturer shown in Table 3.4. The numerical aperture at the core center is calculated as NA=0.1866. The material dispersion, see Fig. 3.9(b), and the corresponding dispersion slope both at a wavelength of 1300nm are calculated approximately to be -14.5ps/(nm·km) and -0.165ps/(nm^2·km), respectively. These simulations results are in quite agreement with those reported in [113] where the fibre numerical aperture dependence of the material dispersion of PF polymer was analyzed. The refractive group index and the dispersion profile parameter, at such wavelength, are found to be $N_1 = 1.35422$ and $\varepsilon = +0.1854$ respectively.

Core Sellmeier coefficients, $n_1 = n_1(\lambda)$		**Cladding Sellmeier coefficients,** $n_2 = n_2(\lambda)$	
$A_{1,1}$	0.33845	$A_{2,1}$	0.33409
$A_{1,2}$	0.48089	$A_{2,2}$	0.4528
$A_{1,3}$	0.37437	$A_{2,3}$	0.53494
$\lambda_{1,1}$	8.45e+01	$\lambda_{2,1}$	8.12e+01
$\lambda_{1,2}$	8.25e+01	$\lambda_{2,2}$	7.74e+01
$\lambda_{1,3}$	1.22e+04	$\lambda_{2,3}$	1.23e+04

Table 3.4. PF GIPOF Sellmeier coefficients of the core and cladding (both provided by the manufacturer).

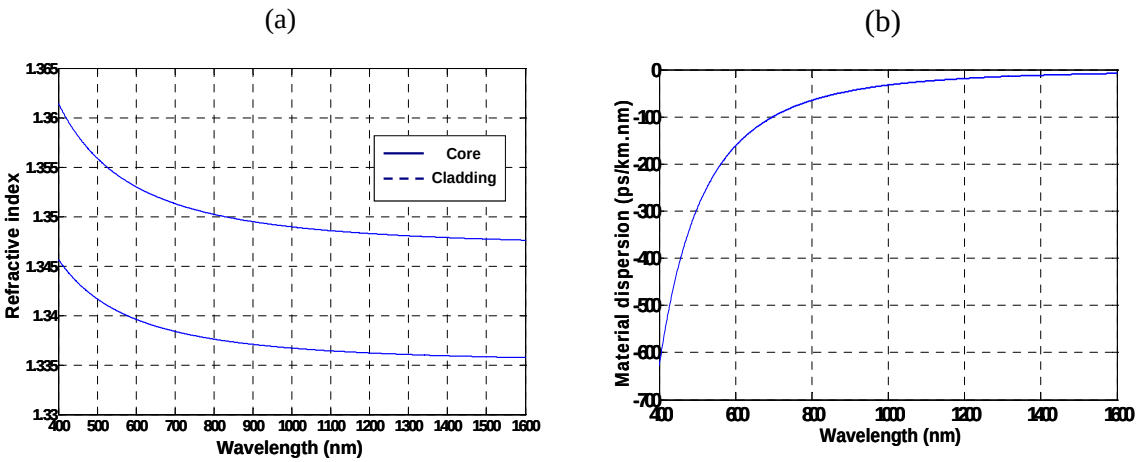

Figure 3.9.- (a) PF GIPOF refractive index of the fibre core and fibre cladding. (b) Material dispersion of the central core region as a function of the wavelength.

It is worth mentioning that with perfluorinated graded index profile polymer optical fibres (PF GIPOFs), a thermally determined alteration in the dopant material can come about, leading to changes in the refractive index, although new materials have just recently become available and behave with admirable stability in this issue [114].

3.7.4 Graded-Index Polymer Optical Fibre frequency response dependency with differential mode attenuation

In this subsection the influence of the differential mode attenuation (DMA) is evaluated. For the simulations it has been considered a 120/490μm GIPOF having a PMMA uniform cladding and a gradually varying concentration of benzyl benzoate dopant in the core. It is assumed that the exciting light source operates at 1300nm of wavelength with a rms linewidth of W=5nm. The graded index exponent has been set to $\alpha = 2$.

Figure 3.10(a) reports the transfer function, given by Eq. 3.20, of a 200m-long PMMA GIPOF when considering or not the effects of the DMA, for a Gaussian beam launching condition from the optical source. Furthermore, for comparison, Fig. 3.10(b) shows the frequency responses, independently one from the other, due to both the chromatic dispersion and modal dispersion for the same launching conditions as Fig. 3.10(a).

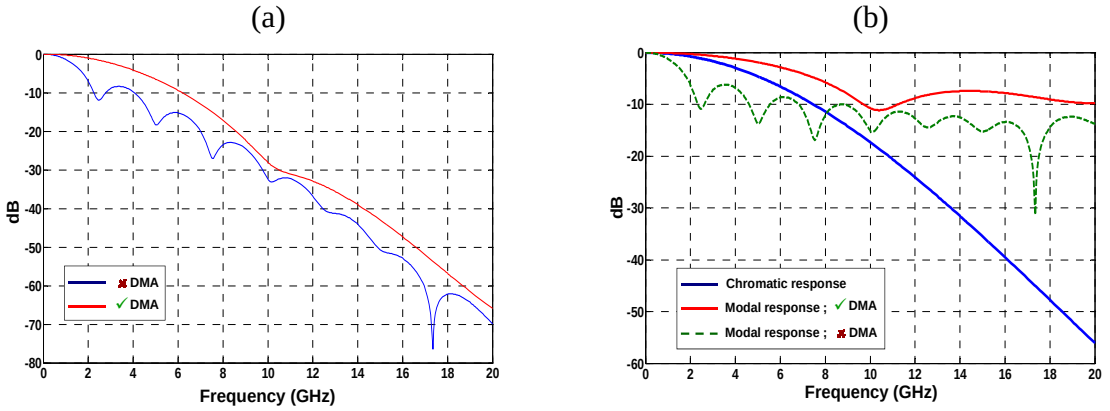

Figure 3.10.- (a) 200m-long PMMA GIPOF frequency response considering or not DMA effects. (b) Only chromatic and only modal frequency response considered separately.

Fig. 3.10(a) shows the effect of the differential mode attenuation. The results indicate that the presence of DMA is favorable for improving the frequency response of the GIPOF. It can be observed a dramatically large 3-dB bandwidth enhancement caused by the DMA, sweeping from 0.51GHz in case of no DMA effects to 3.1GHz when considering the DMA effects on the GIPOF transfer function. This result shows that the DMA is a determining factor for accurate assessment of the baseband in GIPOFs.

The same considerations can be made for perfluorinated (PF) GIPOFs. As expected, the 3-dB bandwidth is enhanced when considering DMA effects for such a fibre, sweeping from 1.65GHz to 5.01GHz. This fact can be seen in Fig. 3.11(a). On the other hand, Fig. 3.11(b) shows the frequency response due to both the chromatic dispersion and modal dispersion for the same launching conditions as Figs. 3.10(a) and 3.11(a).

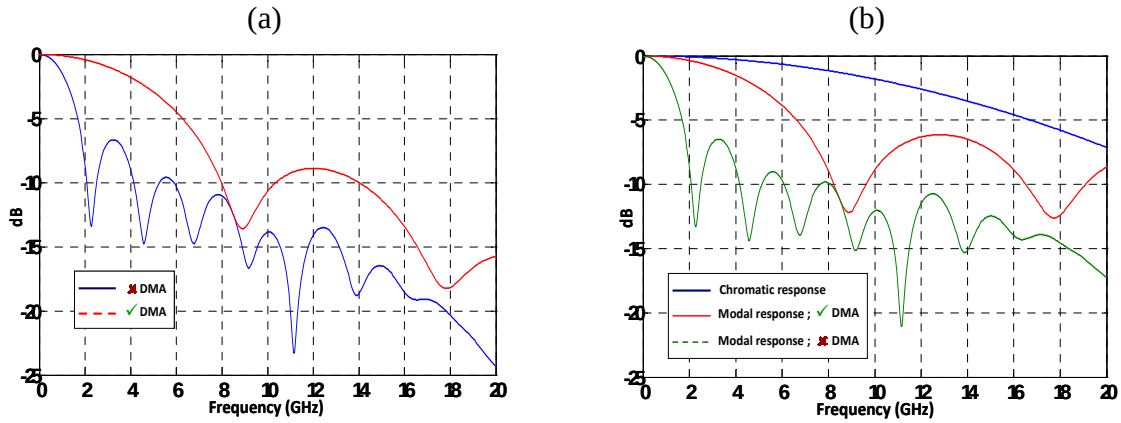

Figure 3.11.- (a) 200m-long PF GIPOF frequency response considering or not DMA effects. (b) Chromatic and modal frequency response considered separately.

3.7.5 Graded-Index Polymer Optical Fibre frequency response dependency with the graded index exponent of the fibre core

Under the assumption of a Gaussian excitation from the optical source and for the same parameter values as subsection before, in absence of DMA, the frequency response of a PMMA GIPOF when varying the graded index exponent (defined in Eq. 3.6) has been analyzed. Some of these results are displayed in Fig. 3.12 and Fig. 3.13 for a PMMA GIPOF link length of 200m and operating at a wavelength of 1300nm.

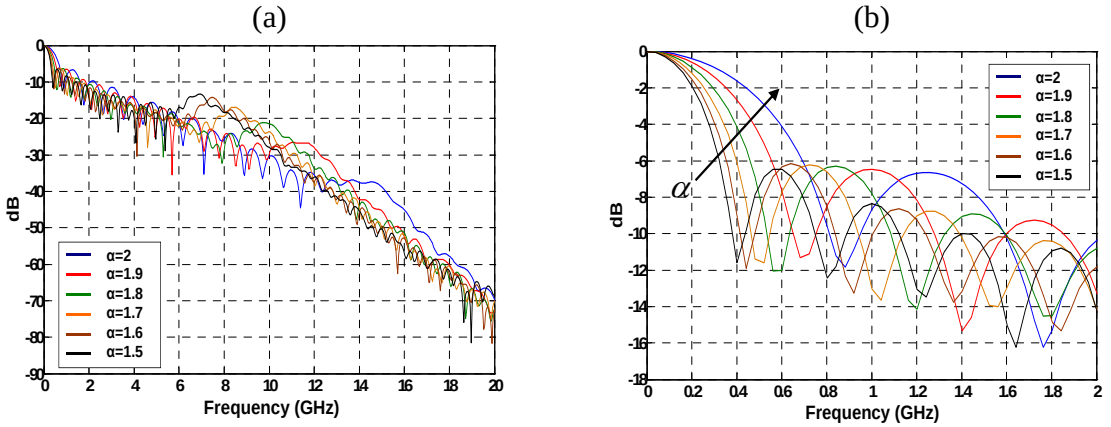

Figure 3.12.- (a) PMMA GIPOF frequency responses varying the index exponent from 2 to 1.5. (b) Zoom of Fig. 3.12(a) up to 2GHz.

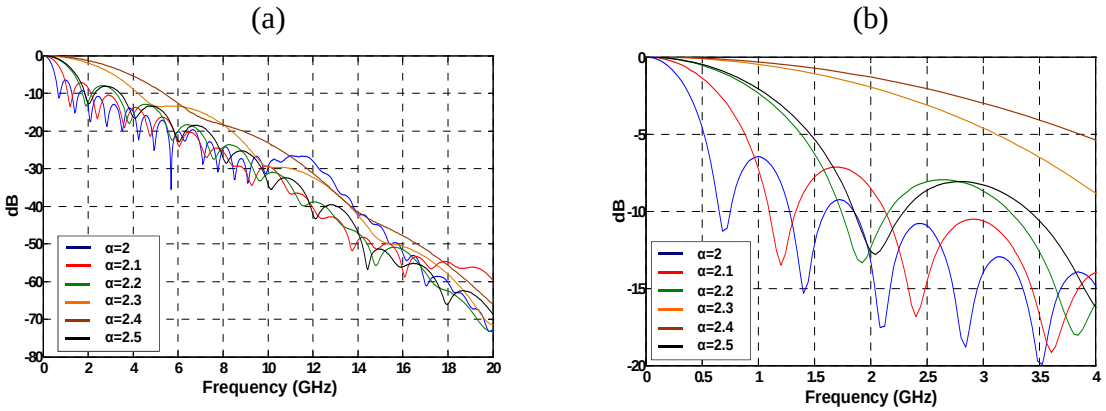

Figure 3.13.- (a) PMMA GIPOF frequency responses varying the index exponent from 2 to 2.5. (b) Zoom of Fig. 3.13(a) up to 4GHz.

The 3-dB baseband bandwidths corresponding to Figs. 3.12 and 3.13, when varying the graded index exponent α, are shown in Table 3.5. Optimum theoretical bandwidth stands at 3.52GHz for $\alpha = 2.36$. From this table it is deducted that it is possible to achieve a more than a tenfold enhancement in the baseband bandwidth with regards to the worst case of α considered. It is worth pointing out that the graded index exponent of the fibre core is given by the dopant concentration of the latter during the manufacturing process.

α	**PMMA GIPOF 3-dB bandwidth (GHz)**	α	**PMMA GIPOF 3-dB bandwidth (GHz)**
2.5	1.19	**1.9**	0.42
2.4	3.00	**1.8**	0.35
2.3	2.45	**1.7**	0.31
2.2	1.12	**1.6**	0.27
2.1	0.72	**1.5**	0.24
2	0.51		

Table 3.5.- 200m-long PMMA GIPOF 3-dB bandwidth for the different graded index exponents of the fibre core evaluated in this section.

Accordingly, the frequency responses shown in Fig. 3.14 have been obtained considering a PF GIPOF when varying the graded index exponent α following the same procedure as above. Table 3.6 shows their theoretical 3-dB bandwidth values. In such a fibre the optimum theoretical bandwidth stands at approximately $\alpha = 2.2$, which is slightly different from the PMMA one. From this table it is deducted that it is possible to achieve approximately a more than a thirty-time enhancement in the baseband bandwidth with regards to the worst case of α analyzed.

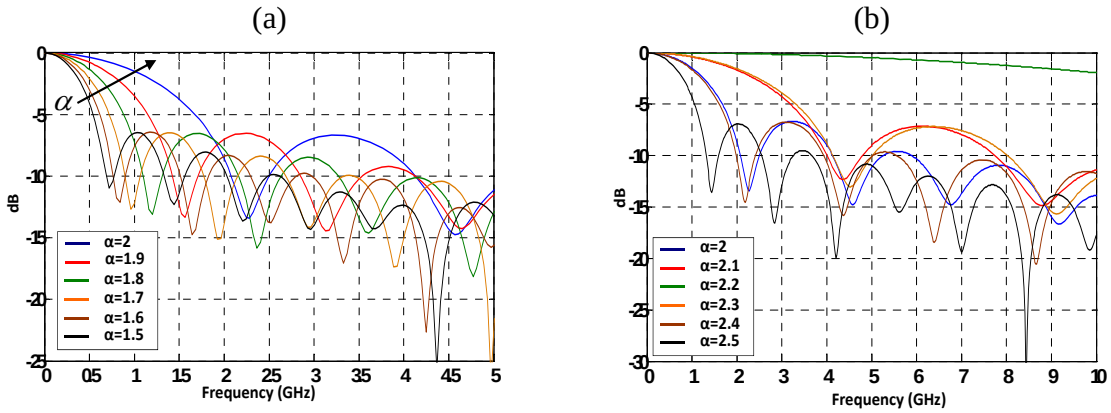

Figure 3.14.- (a) PF GIPOF frequency response up to 5GHz depending on the index exponent from 1.5 to 2. (b) PF GIPOF frequency response up to 5GHz depending on the index exponent from 2 to 2.5.

α	PF GIPOF 3-dB bandwidth (GHz)	α	PF GIPOF 3-dB bandwidth (GHz)
2.5	0.86	**1.9**	0.93
2.4	1.30	**1.8**	0.71
2.3	2.64	**1.7**	0.59
2.2	12.50	**1.6**	0.50
2.1	2.59	**1.5**	0.44
2	1.36		

Table 3.6.- 200m-long PF GIPOF 3-dB bandwidth for the different graded index exponents of the fibre core evaluated in this section.

On the other hand, it is well known that the bandwidth can be maximized by optimizing the shape of the graded index profile (i.e. its distribution) of the fibre core. When this profile distribution is expressed by a power law on the form defined in Eq. 3.6, the bandwidth is maximized when α becomes α_{opt}, given by:

$$\alpha_{opt} = 2 + \varepsilon - \Delta \frac{(4+\varepsilon)\cdot(3+\varepsilon)}{5+2\varepsilon} \tag{3.41}$$

where ε is the profile dispersion parameter. Therefore, without material dispersion (i.e. only modal dispersion is considered in a WKB analysis), it becomes simply:

$$\alpha_{opt} = 2 - \frac{12}{5}\Delta \tag{3.42}$$

To evaluate the correctness of the simulations and values obtained in this section a simple analysis, following described, can be made. In case of PMMA GIPOF, experimental values of the refractive indices of the core and cladding are provided by Fig. 3.8(a) thus obtaining $n_{cc} = 1.501$ and $n_{cl} = 1.482$, respectively, at 1300nm. These values lead to $\Delta = 0.01257$ and to a profile dispersion parameter of $\varepsilon = +0.361$. Evaluating Eq. 3.41 at this condition, an

optimum graded index profile of $\alpha_{opt} = 2.3288$ is obtained. This result is quite similar with that obtained for the simulations, as can be seen in Table 3.5.

Similarly, in case of PF GIPOF, experimental values of the refractive indices of the core and cladding are provided by Fig. 3.9(a) thus obtaining $n_{cc} = 1.3485$ and $n_{cl} = 1.3355$, respectively. These values lead to $\Delta = 0.00964$ and to a profile dispersion parameter of $\varepsilon = +0.1854$. Evaluating Eq. 3.41 at this condition, an optimum graded index profile of $\alpha_{opt} = 2.1614$ is obtained. This result is also in good agreement with that of obtained for the simulations, see Table 3.6.

From the theoretical data shown in this section, the relation between the refractive index profile and the bandwidth of the GIPOF is different depending if a PF-based or a PMMA-based is considered. Let parameter *s* be the relation between increments in the bandwidth related to variations in the graded index exponent α. In that case, *s* can be defined as $s = \Delta BW / \Delta\alpha$ with units of $GHz / \delta\alpha$ and corresponds to the slope of the relation defined previously. Different sensitivities are obtained in both fibres for the same variations on the graded index exponent α, when considering α-values near to the optimum one, typically $\alpha_{opt} \pm 0.15$. For giving an example, considering a +0.01 exponent deviation from the optimum value, it is obtained $s_{\text{PF-GIPOF}} = 0.986\text{GHz}$ and $s_{\text{PMMA-GIPOF}} = 0.165\text{GHz}$, respectively, which gives an estimation of the significant PF GIPOF bandwidth sensitivity with regards to α. This gives an idea of the importance of controlling such parameter during the manufacturing process. Differing from this, almost identical slopes in both fibre types are obtained for graded index exponents far from the range defined.

3.7.6 Graded-Index Polymer Optical Fibre frequency response dependency with the fibre core radius

Considering the influence of the fibre core diameter, Fig. 3.15 shows the PMMA GIPOF frequency response for four different core diameters, representing typical values of commercial graded-index polymer optical fibres. The index exponent is set to $\alpha = 2$ and the rest of parameters take the same value as the above theoretical simulations. However, special care must be taken on the launching conditions as varying the core radius could lead to a restricted-mode launching or, on the contrary, to an overfilled launching. The aforementioned Figures 3.15(a) and 3.15(b) deploy the PMMA-based GIPOF frequency response for a Gaussian beam excitation with a spot radius of $w = 250\mu\text{m}$, which means an overfilled launching condition. From the figures, similar 3-dB baseband bandwidths are obtained, independently from the core radius considered, although higher excursions in the intermediate notches can be observed as the core radius decreases. Again, considering DMA effects lead to an increase of the bandwidth value in any case.

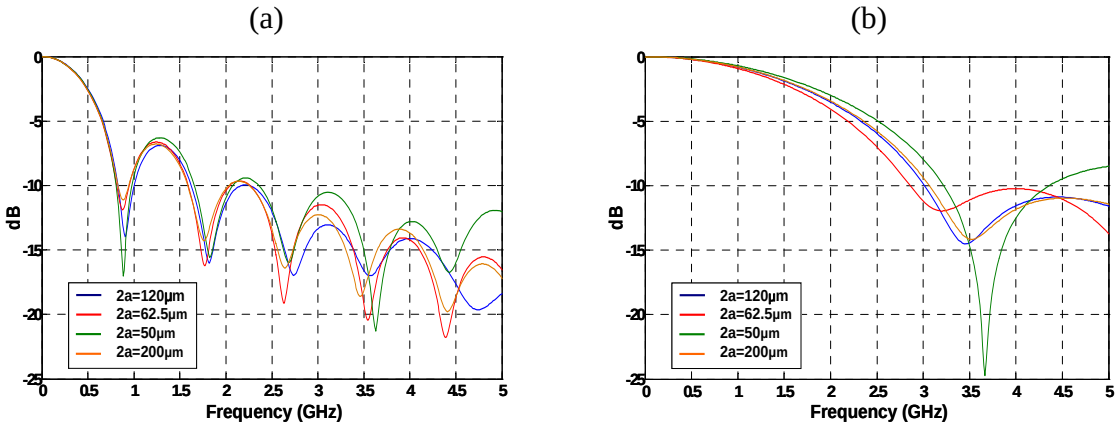

Figure 3.15.- (a) Influence of the core diameter on the frequency response at λ=1300nm for a 200m-long PMMA GIPOF, (a) neglecting DMA effects, (b) considering DMA effects.

On the other hand, the frequency responses of PF GIPOFs with different core radius are shown in Fig. 3.16. A restricted–mode launching (RML) condition, in any case, is imposed by setting the spot radius of the Gaussian excitation beam to $w = 5\mu m$. Contrary to the above figures, the lower fibre core radius produces a baseband bandwidth enhancement from 6GHz to 9GHz (see Fig. 3.16(a)), i.e. there is bandwidth dependence with the fibre core radius. This maximum 3-dB bandwidth occurs for a core radius a=25μm (i.e. the minimum core radius considered in the simulations) no matter the type (PMMA- or PF-based) of GIPOF considered. This result is quite in agreement with the fact that the bandwidth reduction is to be connected with the larger number of excited modes, which is directly proportional to the core radius, as defined in Eq. 3.11. Nevertheless, this dependence is strongly reduced when increasing the beam spot radius considered, as nearer OFL condition is reached.

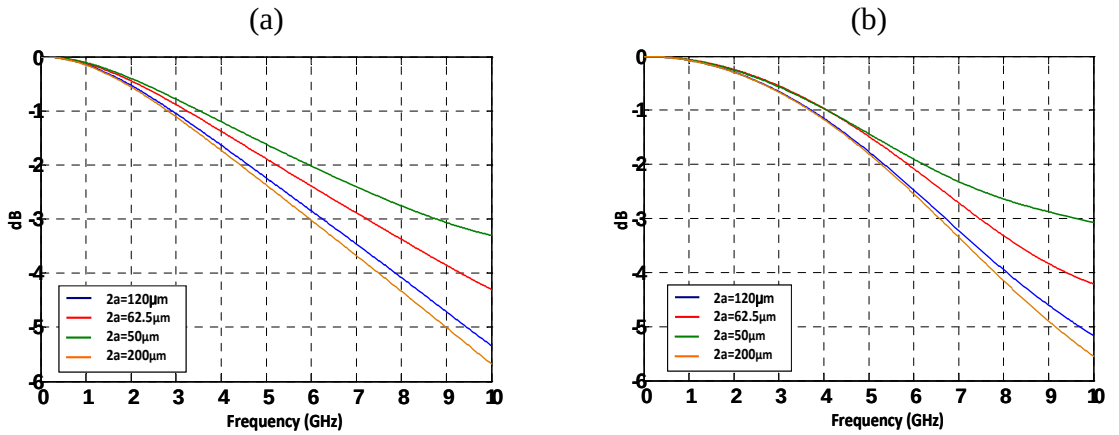

Figure 3.16.- (a) Influence of the core diameter on the frequency response at λ=1300nm for a 200m-long PF GIPOF, (a) neglecting DMA effects, (b) considering DMA effects.

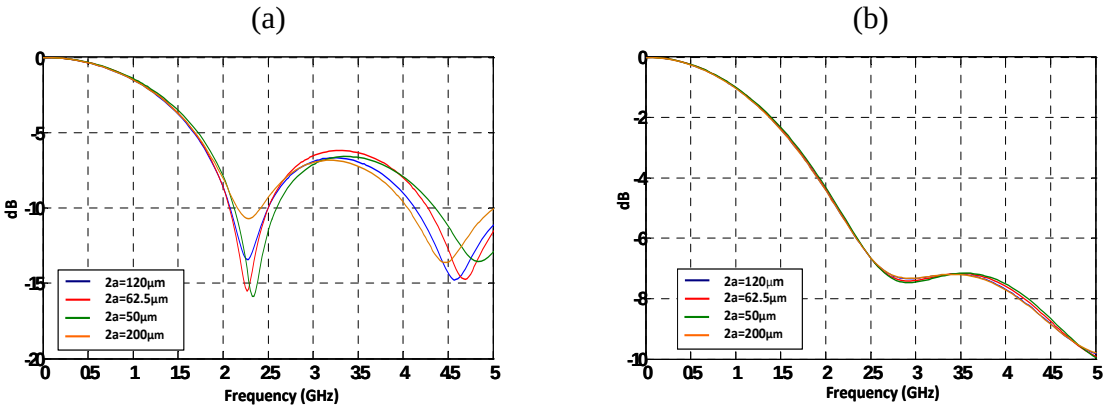

Figure 3.17.- (a) Influence of the core diameter on the frequency response at λ=1300nm for a 200m-long PF GIPOF, (a) w=250μm, i.e. OFL launching, (b) Uniform excitation.

Fig. 3.17(a) shows the PF GIPOF frequency response for an overfilled launching condition considering a Gaussian beam of the excitation source. As expected, the 3-dB bandwidth of the link remains constant, independently from the core radius of the fibre considered. The same results can be expected from a uniform excitation, by employing, for instance, a 1m-long SIPOF as a launching fibre. This launching condition dependence is shown in Fig. 3.17(b). In this latter case, lower excursions of the intermediate notches are observed, being practically eliminated.

3.7.7 Graded-Index Polymer Optical Fibre frequency response dependency with the light injection distribution of the optical source

The influence of the excitation coefficients $C_{rmeff}(m)$, which permits the evaluation of the model under any launching condition, is analyzed in this section considering a uniform launching condition in which the excitation coefficients are set to the unity or, on the other hand, considering a power spectral density of the source with a Gaussian lineshape, given by Eq. 3.23, which is a more realistic assumption, and depending on the excitation beam spot radius. The rest of parameters are set to the same values as the above figures.

PMMA-based and PF-based GIPOF frequency response simulations are displayed in Fig. 3.18(a) and Fig. 3.19(a), respectively, where the effects of the launching condition and that of the DMA are shown. The results indicate that both the uniform excitation and the presence of DMA are favorable for improving the frequency response in both cases compared to the case of a Gaussian beam excitation with spot radius $w = 60\mu m$, which illuminates the whole core of the GIPOF fibre (a 120μm core diameter fibre has been considered). This phenomenon can be explained by the mode coupling effects that are present in the GIPOF when the equilibrium mode distribution has not been reached, opposite from the uniform launching. On the other hand, uniform excitation is contingent with the use of a mode scrambler which produces the mode coupling phenomenon, with the

use of a 1-m SIPOF launching fibre patch cord or with the use of larger link lengths than the estimated coupling-length for graded-index polymer optical fibres.

On the other hand, it can be observed from both Fig. 3.18(b) and Fig. 3.19(b), where only the modal frequency response is simulated, that the bandwidth enhancement is mainly caused by the DMA, as expected.

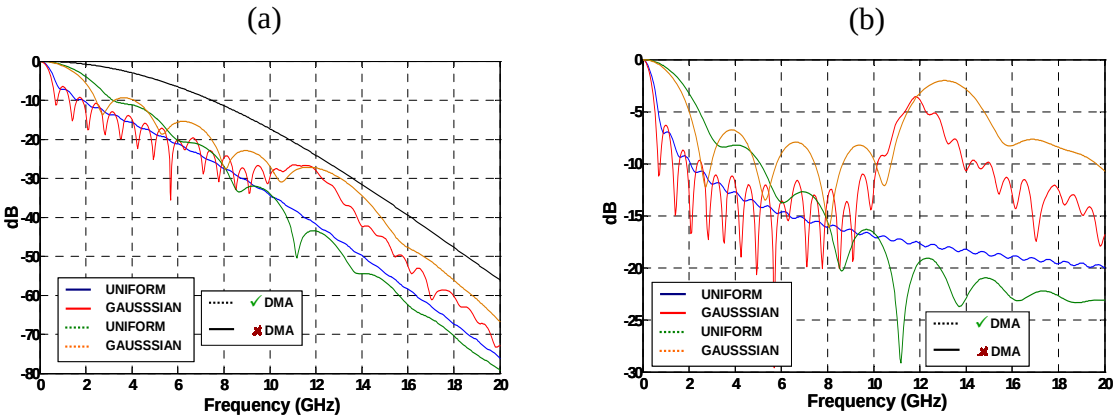

Figure 3.18.- (a) PMMA GIPOF frequency responses for a uniform excitation and for a Gaussian beam excitation with and without DMA effects. Black dotted curve represents the chromatic frequency response given for comparison. (b) Only modal frequency response for the same conditions as in (a).

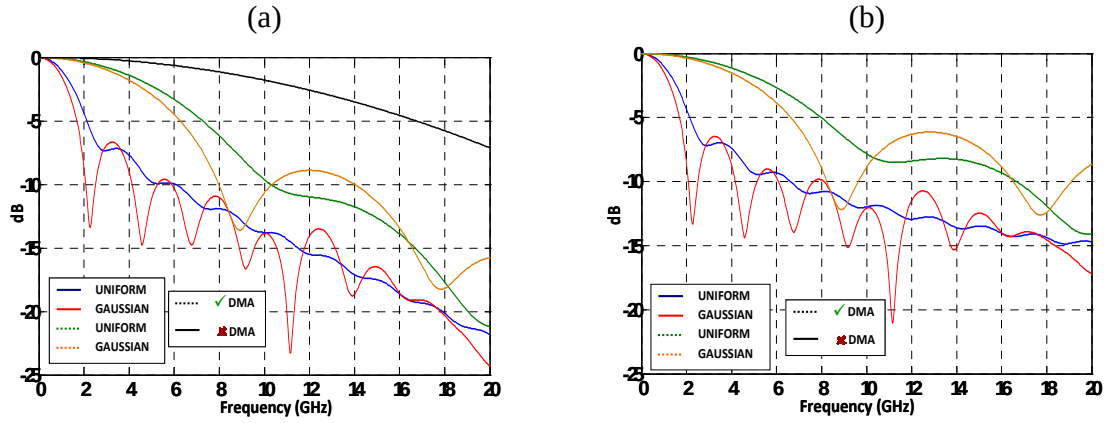

Figure 3.19.- (a) PF GIPOF frequency responses for a uniform excitation and for a Gaussian beam excitation with and without DMA effects. Black dotted curve represents the chromatic frequency response given for comparison. (b) Only modal frequency response for the same conditions as in (a).

It is worth mentioning that the frequency response dependence with the spot radius of the Gaussian beam excitation will be further discussed in a following section. This spot radius will determine the mode launching condition as well as the number of excited modes which propagate through the multimode fibre, leading to a mode-restricted launching (RML) or to a near condition of an overfilled launching (OFL).

3.7.8 Graded-Index Polymer Optical Fibre frequency response dependency with the operating wavelength

In this section the bandwidth dependence with the optical source operating wavelength, at three standard wavelengths, is analyzed. Rest of simulation parameters are set to the same values as above sections.

The dispersion of the fibre core material is reported in Fig. 3.8 and Fig. 3.9 for the cases of PMMA-based and PF-based GIPOFs. The results show that around 650nm the chromatic dispersion effect is clearly significant (compared to the other wavelengths) and the bandwidth will be affected not only by modal dispersion but also by chromatic dispersion, more strongly than in the case of $\lambda = 1300\text{nm}$ or $\lambda = 1550\text{nm}$. For these last two cases, the material dispersion takes the value of -46.7ps/nm·km and -26.5ps/nm·km for a PMMA GIPOF, and -14.5ps/nm·km and -8.54ps/nm·km for a PF GIPOF, respectively. On the other hand, in case of $\lambda = 650\text{nm}$, the material dispersion is seen to be as high as -400ps/nm·km (PMMA-based) and -125.5ps/nm·km (PF-based). In contrast, if a zero crossing material dispersion versus wavelength would be reported, the chromatic dispersion effect should be not significant and the 3-dB bandwidth should be mostly affected by modal dispersion.

In this framework, for the simulations, it has been supposed that the intrinsic fibre attenuation is the same for all wavelengths considered, thus reinforcing the concept of being the frequency response only affected by the different chromatic dispersion at such wavelengths. The optical source spectral width was set to 5nm in all cases and the dispersion slope at each wavelength considered has been also taken into account.

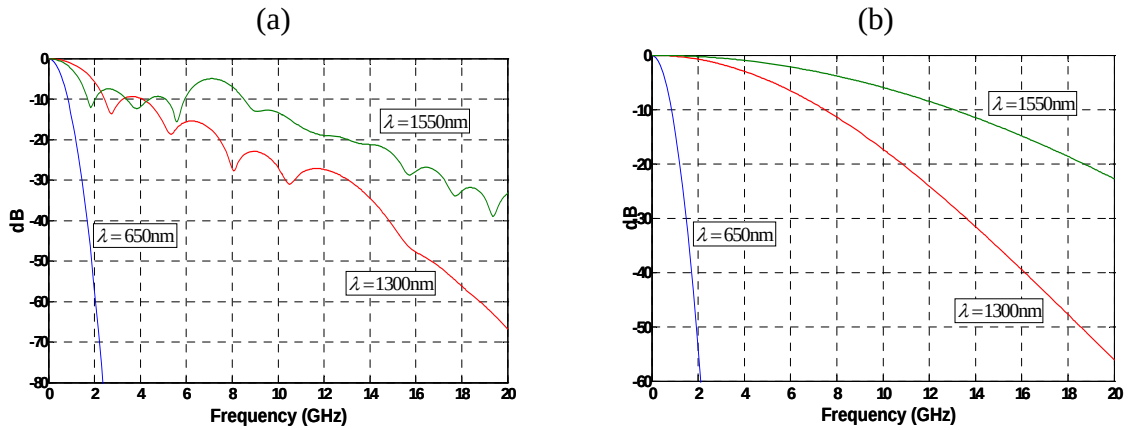

Figure 3.20.- (a) PMMA GIPOF frequency response depending on the wavelength. (b) Chromatic response at the same wavelengths.

The PMMA GIPOF frequency response at such standard wavelengths is shown in Fig. 3.20(a). DMA effects have been taken into account. As it can be seen, the 3-dB bandwidth at an operating wavelength of $\lambda = 1300\text{nm}$ becomes higher than the 3-dB bandwidth expected at $\lambda = 1550\text{nm}$ despite the lower material dispersion at this latter wavelength. This fact is supported by the bandwidth enhancement provided by considering DMA effects which are supposed to be stronger at 1300nm than that of at 1550nm. Opposite from this

fact, the PMMA GIPOF chromatic response, shown in Fig. 3.20(b), reports a higher chromatic bandwidth at $\lambda = 1550\text{nm}$ than $\lambda = 1300\text{nm}$, as expected from the lower material dispersion obtained by Fig. 3.8. This fact leads to think that the modal frequency response at $\lambda = 1550\text{nm}$ is severely limiting the total bandwidth for such a case. Fig. 3.21(a) and Fig. 3.21(b) lead to the same statements, for the case of perfluorinated (PF) GIPOFs.

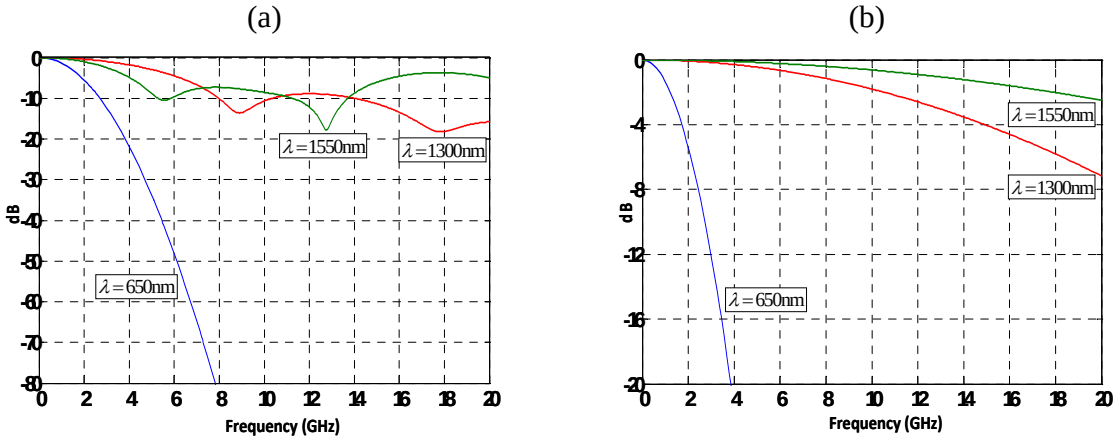

Figure 3.21.- (a) PF GIPOF frequency response depending on the wavelength. (b) Chromatic response at the same wavelengths.

3.7.9 Graded-Index Polymer Optical Fibre frequency response dependency with the source linewidth

In this section, the bandwidth dependence with the optical source linewidth is analyzed. Rest of simulation parameters are set to the same values as above sections. The operating wavelength has been set to $\lambda = 1300\text{nm}$ and DMA effects have been taken into consideration.

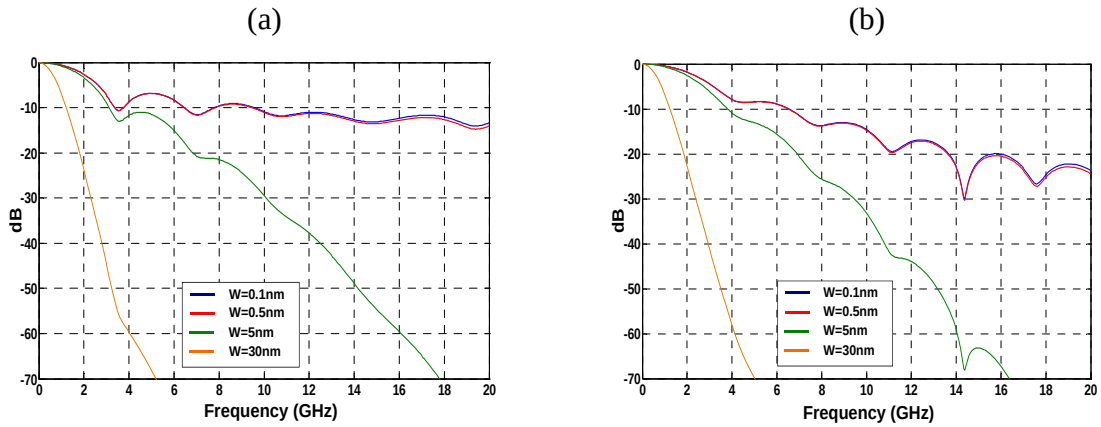

Figure 3.22- (a) PMMA GIPOF frequency response for different source linewidths for (a) Gaussian beam excitation and (b) Uniform excitation. Graded index exponent was set to $\alpha = 2.3$.

The effect caused by the source linewidth is reported in the following figures, Fig. 3.22(a) and Fig. 3.22(b), for a 200m-long PMMA GIPOF. A typical distributed feedback laser (DFB laser), Fabry-Perot laser (FP laser) and Light Emitting Diode (LED) have been considered in both figures, for a Gaussian beam excitation from the optical source or, alternatively, a uniform excitation. In both cases, the 3-dB baseband bandwidth of the PMMA GIPOF fibre is progressively penalised as the source linewidth is increased, being dramatically reduced in the case of a broadband LED source. Taking Fig. 3.22(a) as an example, in that case the 3-dB bandwidth is reduced from 1.85GHz (case W=0.1nm) to 0.7GHz (case W=30nm).

Consistent with the latter statement, similar results are achieved considering a PF GIPOF, as seen in Fig. 3.23. Again, higher 3-dB bandwidths of the GIPOF frequency response can be achieved at lower source linewidths, increasing from 2.1GHz (W=30nm) to 5.4GHz (W=0.1nm), taking Fig. 3.23(a) as an example. Furthermore, it is worth pointing out that, when considering a Gaussian excitation, it is possible to achieve a passband region at approximately 13GHz, directly related to the use of low linewidth sources, as will be also presented in the following section, but with 6dB of attenuation

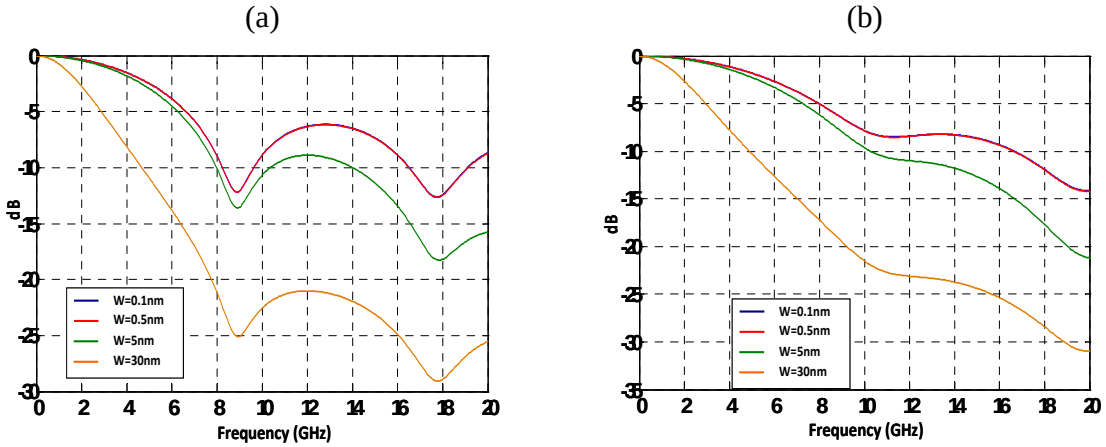

Figure 3.23.- (a) PF GIPOF frequency response for different source linewidths for (a) Gaussian beam excitation and (b) Uniform excitation. Graded index exponent was set to $\alpha = 2.1$.

To resume, spectral width dependence in the frequency response is clearly observed in the calculated curves when the index exponent closes to the optimum because the chromatic dispersion becomes dominant in such a fibre with nearly optimum profile. On the contrary, when the index exponent is large deviated from optimum, the bandwidth is dominated by the modal dispersion. This fact can also be seen in set of figures comprising Fig. 3.5.

3.7.10 Graded-Index Polymer Optical Fibre frequency response dependency with the link length

Different theoretical simulations have been studied regarding this parameter, which is considered to be one of the most important to evaluate, thus allowing multimode optical fibre links based on Graded-Index Polymer Optical Fibres for the cabling of Access Networks, Local Area Networks (LANs) [115] or in-building/home network solutions. Most significant of those are presented in the following figures. The graded index exponent of the fibre was set to $\alpha = 2$ with an operating source wavelength of $\lambda = 1300\text{nm}$ and 5nm of rms linewidth.

It is worth mentioning that are the introduction of the DMA in conjunction with possible mode coupling the causes for a bandwidth per length product to become length dependent. Consequently, a constant bandwidth-distance product is no longer meaningful. The differential delay (namely $\Delta\tau$) increases proportionally to a particular length, namely coupling length L_C; on the other hand, for longer lengths, this increase is sub-linear. So do the bandwidth values are expected. The following holds true:

$$\begin{aligned} &\Delta\tau \propto L \quad \text{for } L<L_C \\ &\Delta\tau \propto L^{\kappa} \quad \text{for } L>L_C \text{ with } \kappa<1 \end{aligned} \tag{3.43}$$

whereby the exponent κ must be determined for each fibre, and it is typically between 0.5 and 0.7. Fig. 3.24 depicts a schematically representation of the pulse broadening reflecting both effects.

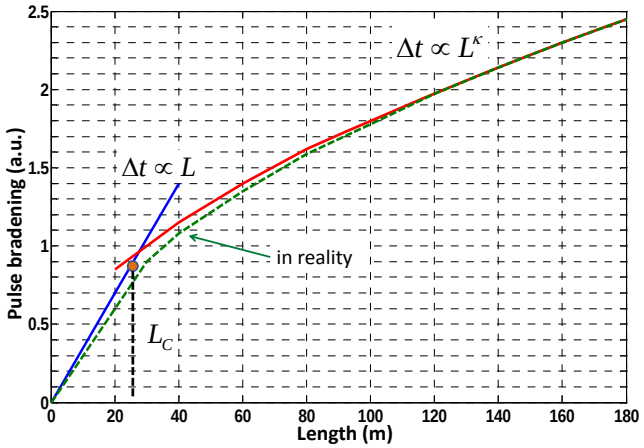

Figure 3.24.- Schematically representation of the pulse broadening when considering DMA and possible mode coupling effects [4]. An arbitrary L_c has been considered in the figure.

Nevertheless, the mode coupling effect on the bandwidth performance of the PMMA GIPOF (under the RML condition) has been confirmed to be negligible even after a 250m-long transmission.

Table 3.7 resumes the 3-dB bandwidths displayed in Fig. 3.25 when a RML Gaussian beam excitation from the optical source is applied. As expected higher 3-dB bandwidths can be achieved being inversely proportional with the PMMA GIPOF link length.

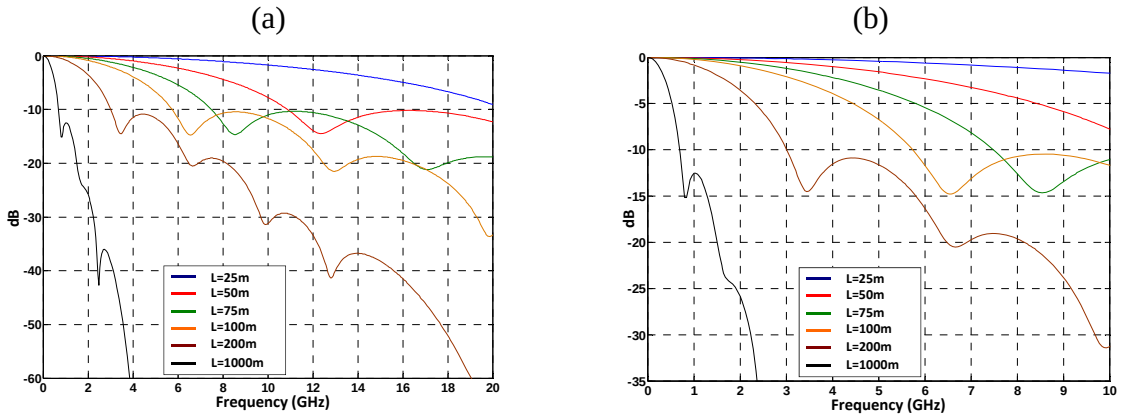

Figure 3.25.- (a) PMMA GIPOF frequency response for different link lengths. A RML Gaussian excitation of the source has been considered. (b) Zoom of figure Fig. 3.25(a).

L (m)	PMMA GIPOF 3-dB bandwidth Gaussian excitation (GHz)
25	14.75
50	7.71
75	5.30
100	4.05
200	2.11
1000	0.46

Table 3.7.- PMMA GIPOF 3-dB bandwidth for different link lengths regarding to Fig. 3.25.

On the other hand, Fig. 3.26(a) shows the PMMA GIPOF frequency response for different lengths when applying a uniform excitation from the source. Table 3.8 indicates the 3-dB bandwidths for such case. Furthermore, Fig. 3.26(b) plots the chromatic response in which the bandwidth per length product remains constant reinforcing the concept of the slight length dependency of this term also with the introduction of the differential mode attenuation.

Comparing both tables within this section, Table 3.7 and Table 3.8 respectively, higher 3-dB bandwidths can be achieved when a restricted mode launching excitation is considered, as it was previously stated.

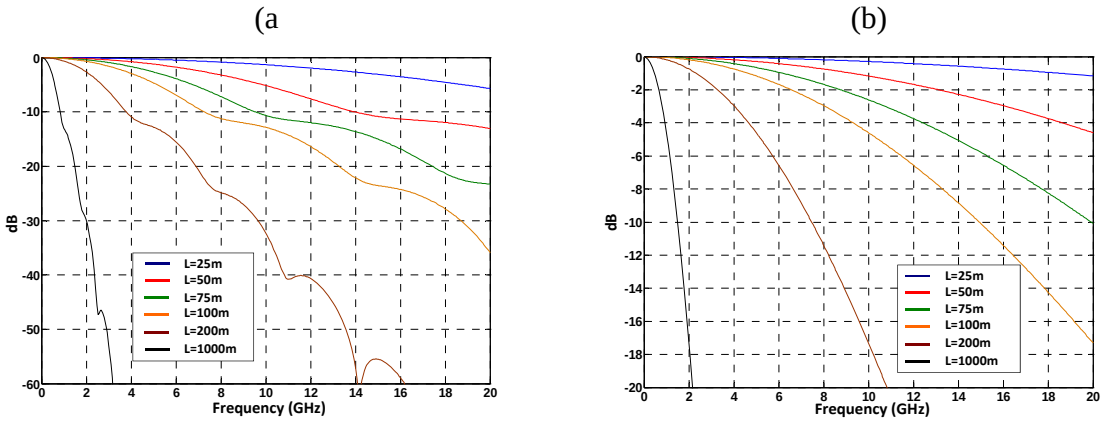

Figure 3.26.- (a) PMMA GIPOF frequency response for different link lengths. A uniform excitation of the source has been considered. (b) Chromatic response at different link lengths.

L (m)	PMMA GIPOF 3-dB bandwidth Uniform excitation (GHz)	PMMA GIPOF 3-dB bandwidth Chromatic response (GHz)
25	12.9	32.10
50	6.77	16.07
75	4.70	10.70
100	3.61	8.02
200	1.86	4.01
1000	0.42	0.81

Table 3.8.- PMMA GIPOF 3-dB bandwidth for different link lengths regarding to Fig. 3.26.

The same analysis can be made for PF GIPOF, in which Fig. 3.27 shows the frequency responses for different link lengths when applying a uniform excitation to the link. Source linewidth was set to 30nm.

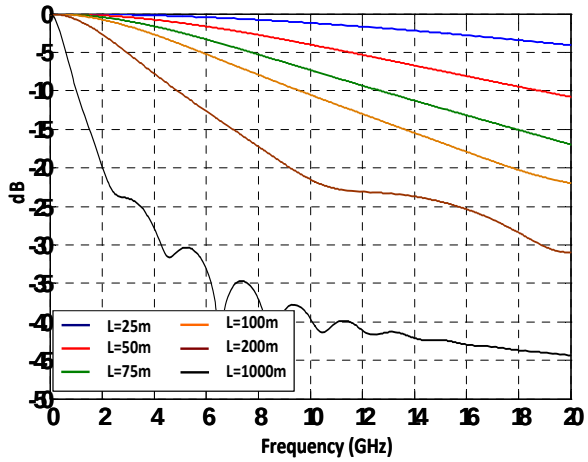

Figure 3.27.- PF GIPOF frequency response for different link lengths when uniform excitation and W=30nm.

3.7.11 Graded-Index Polymer Optical Fibre frequency response dependency with the input beam spot of a Gaussian-type excitation

As semiconductor lasers are commonly employed in telecommunications applications, including Radio-over-Fibre (RoF) transmissions, it is closest to the reality to adopt the assumption of a Gaussian-type shape for the input beam spot[99]. For the simulations it is additionally assumed that the fibre is excited centrally with a laser beam that forms a circularly symmetric spot on the input surface. It is equally considered that the fibre axis is well aligned with the beam axis, and that its end surface is well positioned in the focal plane.

The axial launching of the fibre by a Gaussian beam is schematically described in Fig. 3.28, where the highest order mode group is excited by the plane-wave component striking the fibre input surface at the maximal offset distance *w* from the core center and at the maximal numerical aperture $\sin\left(\theta_{i,w}\right)$.

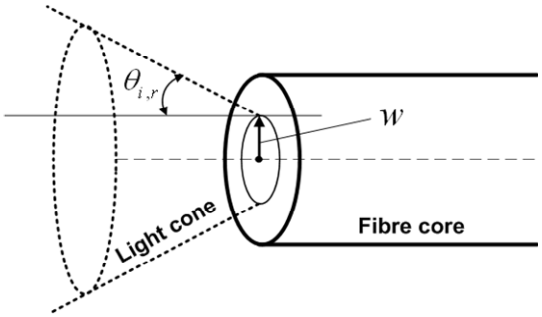

Figure 3.28.- Description of the launching with geometry of fibre excitation with an axial Gaussian beam.

The input light will excite all the modes supported by the fibre, imposed by waveoptics and expressed in Eq. 3.11, if the beam overfills the core region or it could form a small enough spot. Between the two situations, it is noteworthy that an optimum operation point exists for which a few modes as possible can be excited. Defining an optimal spot radius, considered to be the spot radius of the beam that excites only the fundamental modes, its expression is found to be [112]:

$$w_{opt} = \frac{1}{\left[\alpha \cdot \Delta(\lambda)\right]^{1/\alpha+2}} \cdot \left[\frac{\lambda \cdot a^{\alpha/2}}{\pi \cdot n_1(\lambda)}\right]^{\frac{2}{\alpha+2}} \tag{3.44}$$

From the GIPOF characteristics, and considering the particular case of parabolic index fibres ($\alpha = 2$), the optimal spot radius for the PMMA-based and PF-based fibres is found to be $w_{opt}\big|_{\text{PMMA}} = 10.21\mu m$ and $w_{opt}\big|_{\text{PF}} = 11.76\mu m$, respectively. From these results it can be concluded that projecting a small spot onto the center does not necessarily constitute a restricted launching, but a large number of modes, or even all the modes that can potentially propagate, could be excited. This is so because the numerical aperture is the

highest in the core center and corresponds to the nominal numerical aperture of the fibre. In other words, the positioning of a small beam spot against the center of the core should lead to the same bandwidth than the overfilling of the core region with a large spot. Furthermore, this fact has been addressed by some other authors, as reported in [54].

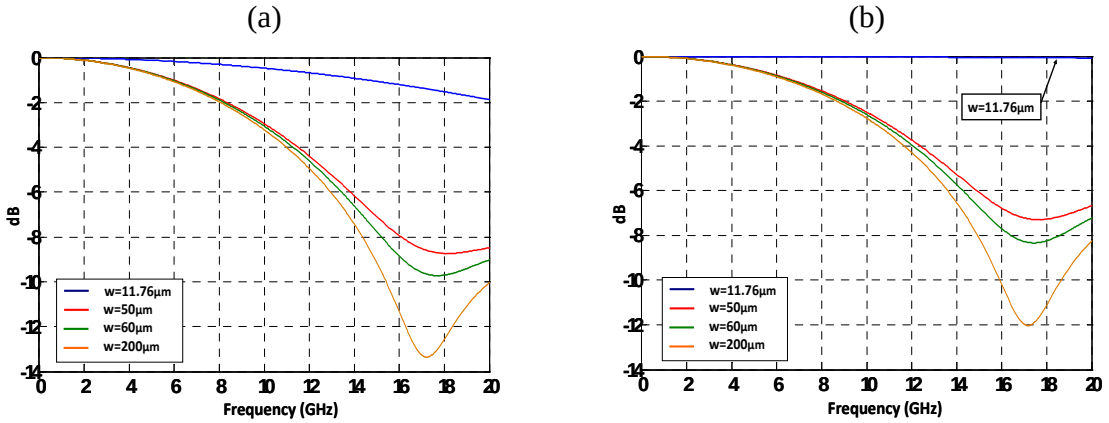

Figure 3.29.- (a) PF GIPOF frequency response at 1300nm as a function of the axial Gaussian beam spot radius. (b) Only PF GIPOF modal responses for different spot radius.

Fig. 3.29(a) deploys the theoretical frequency responses of a 120/490µm core/cladding diameter PF GIPOF fibre at transmission length of 100m at different spot radius, at 1300nm of wavelength. As aforementioned, the optimal spot radius for PF GIPOF was calculated to be 11.76µm and the frequency response of the fibre, in this case, is mainly limited by the chromatic dispersion. On the other hand, Fig. 3.29(b) shows the modal response of the PF GIPOF for different spot radius. It can be seen that selecting different spot radius far away from the optimal lead to a 3-dB bandwidth decrease in all cases whilst modal dispersion affecting the 3-dB bandwidth can be neglected in the case of a launching satisfying w_{opt} condition. This latter fact can be observed in the blue curve of Fig. 3.29(b).

Finally, Fig. 3.30 deploys the theoretical frequency responses at two different excitation conditions, in presence of DMA in all cases. A first sight that can be made from this figure is that the uniform excitation yields a much lower frequency response with respect to that of the Gaussian beam with optimum spot radius. This behavior remains true even in the presence of DMA, which was seen in section 3.7.4 to improve the 3-dB bandwidth of the frequency response. Regarding the Gaussian beam with optimal spot radius excitation, a 3-dB bandwidth of 26GHz can be achieved over the PF GIPOF 100m link length. These results clearly demonstrate that the input conditions play a much more significant role in providing a large bandwidth than the uniform excitation. Furthermore, these results indicate that the bandwidth (and also BER and power penalty-free state) performance of the link composed by the GIPOF shows optical transmitter dependence, because the launch conditions in the real optical link depend on the light source and other optical components.

It can be concluded that the GIPOF with the completely optimum profile in the whole core region is able to maintain its high-bandwidth performance not only under the uniform condition but also under misalignment in launching under the RML condition and under

static fibre bending, which causes mode coupling, as well. However, it is a great concern that the high-bandwidth performance under the RML condition can be degraded in the case of the GIPOF with an index profile that deviates from the optimum one due to such physical perturbations in the fibre. For instance, in the case of the GIPOF having an almost ideal index profile (in the PF case, $\alpha \simeq 2.2$), little launch condition dependence on the bandwidth is expected. This latter fact can be seen in Fig. 3.30(b) which depicts the frequency response of a 100m-long PF GIPOF link, with optimum index profile, for two launching conditions: RML with $w = 11.76\mu m$ (optimum spot radius of the excitation Gaussian beam) and OFL with $w = 60\mu m$. In both cases the frequency response turns to be the same.

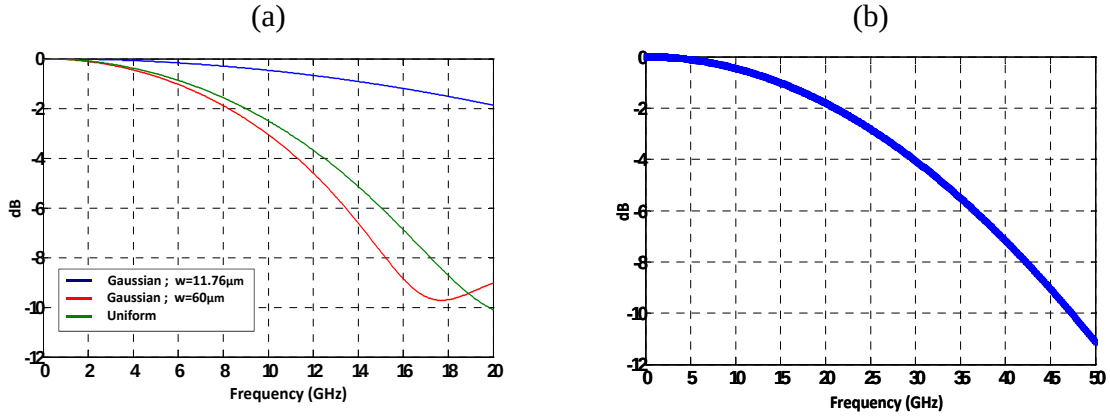

Figure 3.30.- (a) Theoretical frequency responses under three excitation conditions: (—) Gaussian beam excitation with optimum spot radius (w=11.76µm) → RML ; (---) Gaussian beam excitation with spot radius w=60µm → OFL ; (–·–) Uniform excitation. (b) 100m-long PF GIPOF link frequency response at two different launching conditions: RML and OFL. PF GIPOF was matched to its optimum index profile $\alpha = 2.2$.

To conclude this discussion, the main worry about the restricted-mode launching concerns the modal noise immunity of such selective systems [116, 117] and eventually their higher sensitivity to mechanical agitation compared to those using the classical overfilled launching. This modal noise has been tested not to degrade the bit error rate when using large core GIPOFs (300-1000µm) even when 200µm misalignment is occurred [43, 118]. This is because the large number of modes that are transmitted in the large core GIPOF. However, further research is needed for the case of recent GIPOFs with lower core diameters.

3.7.12 Conclusions on Graded-Index Polymer Optical Fibre simulations

The diverse measurements of fibre bandwidth values reported in literature have shown that the same principles are essentially valid for multimode silica and polymer optical fibres. Important effects are:

- The bandwidth drops with the square of the numerical aperture (NA) by increasing the differences in propagation time among the individual modes.

- The diameter of the fibre does not play a significant role with regards to the bandwidth.
- Strong differential mode attenuation increases the bandwidth of fibres, but it also leads to a rise in transmission losses.
- Multicore fibres and fibre bundles permit smaller NAs with the same bending radius and thus greater bandwidths.
- The bandwidth of fibres greatly depends on the launch and detection conditions. The difference can be more than tenfold for short fibre lengths. When stating the bandwidth in datasheets, measurements should always be made with uniform mode distribution (UMD) or equilibrium mode distribution (EMD).
- Graded index profiles increase the bandwidth up to two orders of magnitude. However, the index profile must be as ideal as possible. It should be parabolic when the chromatic dispersion is disregarded.
- In the case of a non-ideal GI profile a large bandwidth can still be attained through a selective launch.
- It is technically easier to produce a multi-stepped index profile, with which the bandwidth can clearly be increased, than a strict GI profile.

On the other hand, as mentioned before in previous sections, special care must be taken to the fact of that the GIPOF bandwidth increases with strong DMA. This is because, during the propagation of light through the fibre, high-order modes have the fastest attenuation gradually energy lost. Consequently, a small fraction of the number of guided modes supported by the fibre has significant power to be detected. In other words, the bandwidth enhancement follows from the filtering effect of the DMA. This, in fact, reflects the classical trade-off relation between dispersion and loss in multimode optical fibres in general. It is also interesting to mention that, because the GIPOF bandwidth is essentially limited by material dispersion (with graded index profiles near optimum), as a consequence of the DMA effect, its operation under a restricted mode excitation may not result in a significant bandwidth improvement. Nevertheless, a selective mode launching scheme could be implemented in the view of benefitting from the minimum loss advantage. In that case, indeed, low-order modes are involved that propagate near fibre axis with the slowest attenuation, which should cause a dramatic reduction of the inline power penalty thereby allowing for a less sensitive and certainly less expensive receiver to be employed. In summary, the DMA becomes a determining factor which should not be bypassed if appropriate GIPOF-based optical networks are to be deployed.

The model presented in this chapter incorporates most of the parameters involved in the determination of the baseband bandwidth. It provides a prediction tool for the achievements that can be made in this research field in order to previously evaluate, for instance, data rate transmissions in deployed (or not yet) GIPOF links. The mathematical development is based on analytically evaluating the frequency response of the fibre instead of the direct calculation of the pulse broadening from the moments of the impulse response. It is also developed under the assumption that mode coupling effects in GIPOFs are negligible considering the limited, to a few hundred meters, transmission lengths in GIPOFs. In this framework, PMMA-based and PF-based GIPOF transfer functions have been theoretically evaluated.

Furthermore, from the theoretical simulations in this section, the performance of the GIPOF transfer function model showed the following results:

- The results indicate that the presence of DMA is favourable for improving the frequency response of the GIPOF, showing that the evaluation of DMA effects is a determining factor for accurate assessment of the baseband in GIPOFs. Furthermore, it also increases the filtering effect of the frequency response.
- It is possible to achieve a baseband bandwidth enhancement depending on the graded index exponent of the fibre core, which is given by the dopant concentration of the core during the manufacturing process. Since the higher order modes carry higher optical power in their evanescent field than the lower order modes, the group delay of the high-order modes is considered to be strongly influenced by the index profile at the core-cladding boundary. For the PMMA-based GIPOF considered for the simulations, it is possible to obtain more than sixfold bandwidth enhancement depending on such parameter, with an optimum profile of $\alpha = 2.32$. In the case of PF-based GIPOFs bandwidth values of one order of magnitude higher can be achieved by properly manufacturing an index profile of $\alpha = 2.16$.
- Although different fibre core radius lead to similar 3-dB baseband bandwidths, lower excursions of the intermediate notches can be obtained by enlarging the core radius, i.e. by a possible strengthening of the mode coupling effect.
- The results indicate that both the Gaussian beam excitation from the optical source with RML and the presence of DMA are favourable for improving the frequency response of the GIPOF in contrast to consider a uniform excitation (i.e. OFL case).
- From the simulations, the 3-dB baseband bandwidth of the GIPOF fibre is progressively penalised as the source linewidth is increased, being dramatically reduced in the case of a broadband LED source. Consequently, the possibility of transmitting broadband signals at higher frequencies using a GIPOF link is contingent on the use of low linewidth sources.
- The introduction of the differential mode attenuation causes the bandwidth per length product to become slightly length dependent and, consequently, a constant bandwidth-distance product is no longer meaningful.
- It is emerged that the input conditions (i.e. mode launching) can lead to minimize the modal dispersion and, consequently, increasing the possible 3-dB transmission bandwidth. Furthermore, this parameter may play a much more significant role in minimizing the modal dispersion than the DMA or even, the mode coupling.

Finally, the following picture results from the simulations for data transmission in perfluorinated GIPOFs:

- PF GIPOF works in a range primarily determined by the DMA.
- Bandwidth and pulse broadening are, for the most part, independent of the launching conditions as of a certain length (namely coupling length).
- Typical mode coupling lengths for PF GIPOFs provide no standard values of that, but lie between 10 m and 100 m.

- In the latter case, the bandwidth drops a bit with the root of the length, as Fig. 3.24 deploys.
- The low material dispersion and low attenuation provided by PF GIPOFs, at near infrared region, can achieve higher bandwidths than the conventional silica-based multimode fibres from visible to 1.3μm wavelengths.

3.8 Graded-Index Polymer Optical Fibre Transfer Function model validation. Experimental results

In order to verify the theoretical results extensive series of measurements were performed over different PF-based graded-index polymer optical fibres from Chromis Fibreoptics. They are considered the most promising candidates for the short-reach networks (such as Gigabit Ethernet LANs) and access networks (including home networks). Measurements were principally taken at an operating wavelength of $\lambda = 1300\text{nm}$. This operating wavelength provides a local minimum attenuation of the PF GIPOF (see Fig. 3.1) and is included within the zero dispersion wavelength range, see Fig. 3.9(b), defined by the manufacturer.

Two standard excitations were applied to study the frequency response of the GIPOF link. Firstly, it is noteworthy that for practical use in a high-speed optical link, a laser diode (LD) is used. This laser diode generally excites only small mode groups, because of its small radiation angle and radiating area and, consequently, only a small spot and narrow divergence angle is supposed to be focused on the core center of the GIPOF. This launching condition is commonly called as restricted-mode launching (RML) or under-filled launching condition (UFL). Thus, the bandwidth performance has been investigated under this launching condition. The latter has been achieved by directly coupling the optical source to the GIPOF via 1m-long SMF patch cord (with estimated < 2dB loss). With this method, only subsets of mode groups are excited, which increases the bandwidth considerably as it will be seen in the following results.

On the other hand, generally in bandwidth measurements of multimode optical fibres, it has been preferred a steady state mode power distribution to be achieved, where all the modes are fully and uniformly excited. Therefore, in order to achieve the steady state mode power distribution, two mechanisms can be applied. On the one hand, a short SI POF (with FC connectors), with characteristics 1-m length, 980μm core diameter and NA=0.47, was used as the mode exciter to establish a uniform launching condition of all modes. This is because of the strong scattering effects that occur in step-index POF fibres, where a uniform mode power distribution takes place even at short distances. In this case, the optical signal from the optical source (a laser diode, generally) is injected into the SI POF patch cord and coupled to the GIPOF by directly butting their ends on a V-groove mount, for instance. Since the power distribution at the output end of the 1-m SIPOF is uniform in its core region (980μm) [74] and the NA of the SI POF (typ. 0.47) is sufficiently higher compare to the GIPOF (approx. to be 0.19 and with core diameter much smaller, 200μm, than that of the SI POF), the 1m-long SI POF is considered as an ideal mode exciter for a uniform

launch. Alternatively, a mode scrambler can be previously used before launching the optical power to also establish a uniform launching condition of all the modes.

The set-up scheme for the experimental measurements is shown in Fig. 3.31.

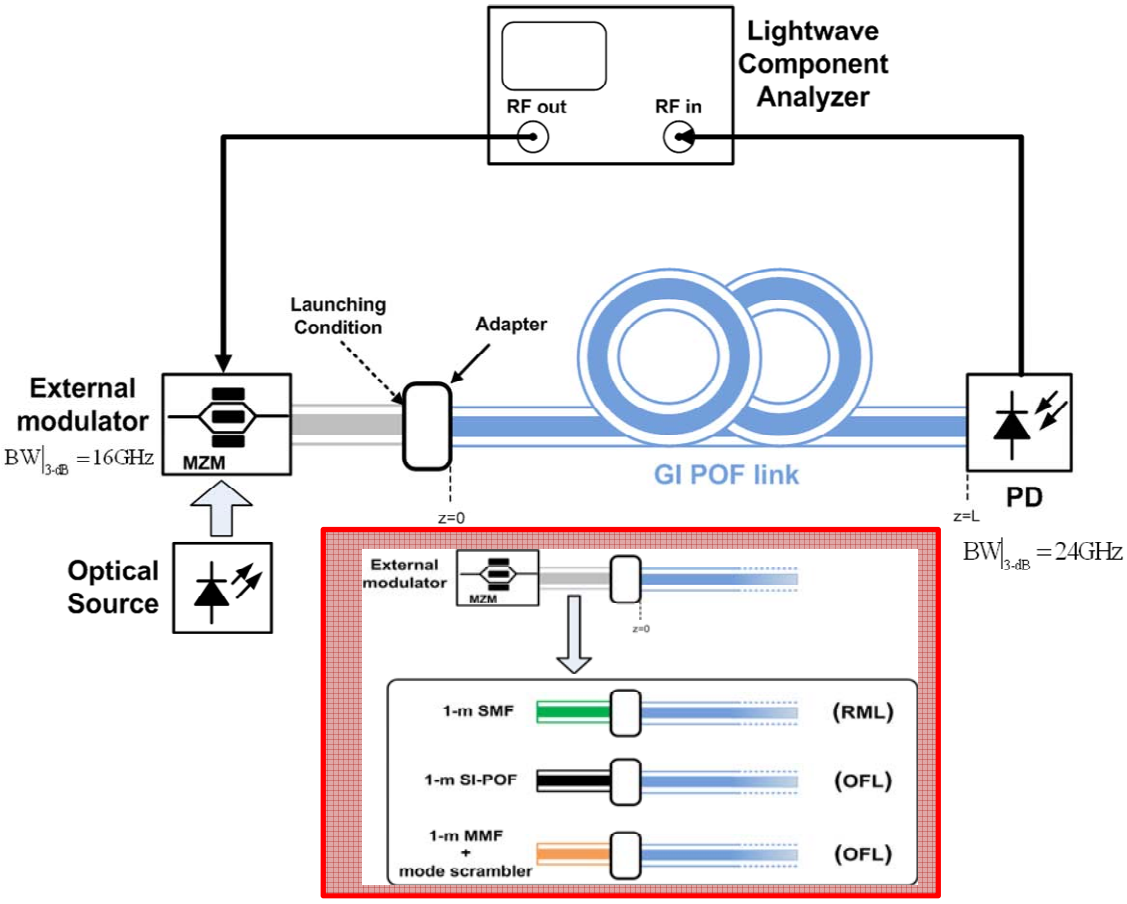

Figure 3.31.- Block diagram of the experimental set-up for the GIPOF link frequency response measurement up to 20GHz. Inset: diagram of the different launching conditions applied. Measured bandwidths of the devices are also indicated.

Extensive PF GIPOF frequency response sets of measurements have been done, for the above launching conditions described, and compared with the theoretical model proposed within this chapter. Different GIPOF link lengths, ranging from L=25m to L=200m, have been experimentally measured up to 20GHz. The GIPOF link consisted of PF-based GIPOF spools connected by using FC-type adapters. In all cases the laser was externally AM modulated with an RF sinusoidal signal up to 20GHz@1300nm of modulation bandwidth, by means of an electro-optic (E/O) Mach-Zehnder modulator (JDSU AM-130). The optical output of the E/O modulator was passed through an optical fibre patch cord (see inset of Fig. 3.31) before being launched, by means of FC/PC connectors, to the graded-index polymer optical fibre (GIPOF) link. At the receiver, the frequency response is detected by using a 24GHz-bandwidth high-speed PIN photodiode, model DSC30S, from Discovery Semiconductors. This device is specially designed for multimode fibre purposes. The frequency responses are finally measured using a Lightwave Component Analyzer (LCA,

Agilent 8703B, 50MHz – 20GHz). The frequency responses depicted in this section result from a 4-factor measurement averaging and were carried out by using this latter device.
Previous to the analysis of the frequency response, the electrical responses of both the electro-optical modulator and the photodetector were measured. These latter responses are illustrated in Fig. 3.32(a), where the electrical response of the photodiode shows a SNR of approximately 40dB, and Fig. 3.32(b), where the electrical response of the E/O modulator is displayed, respectively. The experimental results of the GIPOF link are calibrated with respect to both electrical responses.

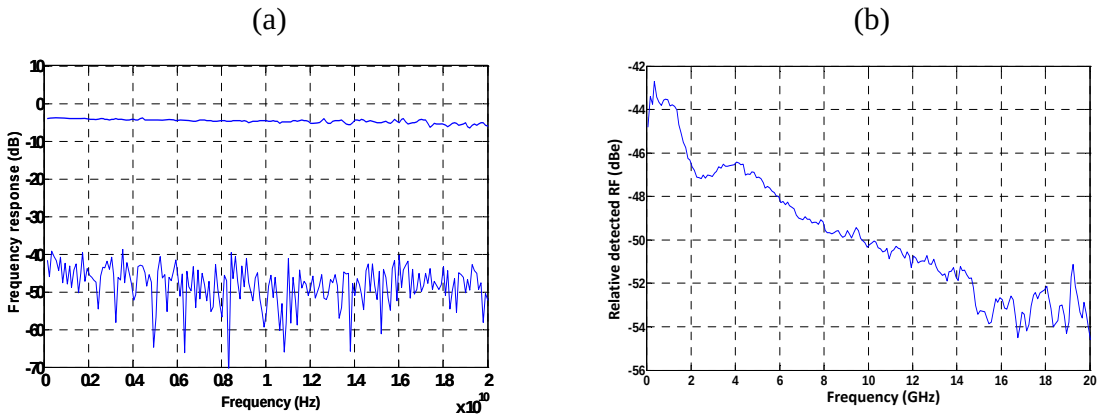

Figure 3.32.- (a) Measured electrical response of the DCS30S up to 20GHz. (b) Typical electrical response of the E/O modulator from JDSU AM-130.

Fig. 3.33 illustrates the normalized frequency responses of a 62.5µm core diameter GIPOF measured using the Lightwave Component Analyzer (LCA) 8703B from Agilent (ranging 50MHz – 20GHz) after calibrating the results with respect to both the modulator and detector electrical responses. The optical power launch was made via 1m-long SMF thus achieving a RML launching condition and all the theoretical curves were obtained by selecting a beam spot radius of $w = 20 \pm 3\mu m$. This deviation range of $\leq 3\mu m$ complies the practical alignment tolerance in the actual assembling process; and agrees with the tolerance specified for center and offset launch given by IEEE Standard 802.3aq [13].

In order to obtain the best fitted theoretical simulation (dashed lines in following figures) with regards to the experimental measurement, parameters such as the graded index exponent, the attenuation (manufacturer only assures <60dB/km@1300nm), parameters ρ and η defined in Eq. 3.31 relative to the functional expression of the DMA or the input beam spot radius were precisely adjusted. The fitting process is following described: once an arbitrary variable was adjusted to a logical value, the rest of the variables were swept to obtain a theoretical frequency response. Next, the same process is repeated but choosing another involved parameter, and so on to complete the high number of variables involved. The best-performance least squares fitting curve for each process is chosen. Finally, the frequency response of the whole set of parameters is compared with all the measurements involving such a GIPOF fibre (e.g. another launching condition) thus providing a feedback of the agreement. This is an iterative process to finally decide the suitable parameters that characterize the GIPOF fibre in its whole set of measurements concerning that fibre. The same process is done for each fibre whose frequency response has been measured.

For the experimental results, a Fabry-Perot (F-P) laser (Agilent 81655A) was used as the optical source to test the frequency responses, with 1300.98nm of central wavelength and a rms linewidth of 1.8nm (this value fulfils the condition given by Eq. 3.15 for the continuum approximation). It can be seen that the normalized frequency responses for the different PF GIPOF lengths are quite in agreement with the theoretical model presented within this chapter. Although 3-dB PF GIPOF bandwidth values for all cases were in the same order of magnitude there were slight variations in the results compared to those theoretically predicted.

Set of figures in Fig. 3.33 illustrate the frequency response of a 62.5µm core diameter PF GIPOF for different lengths and for a RML condition. The 3-dB measured bandwidth values and those theoretically expected, after the fitting process, are resumed in the Table 3.9.

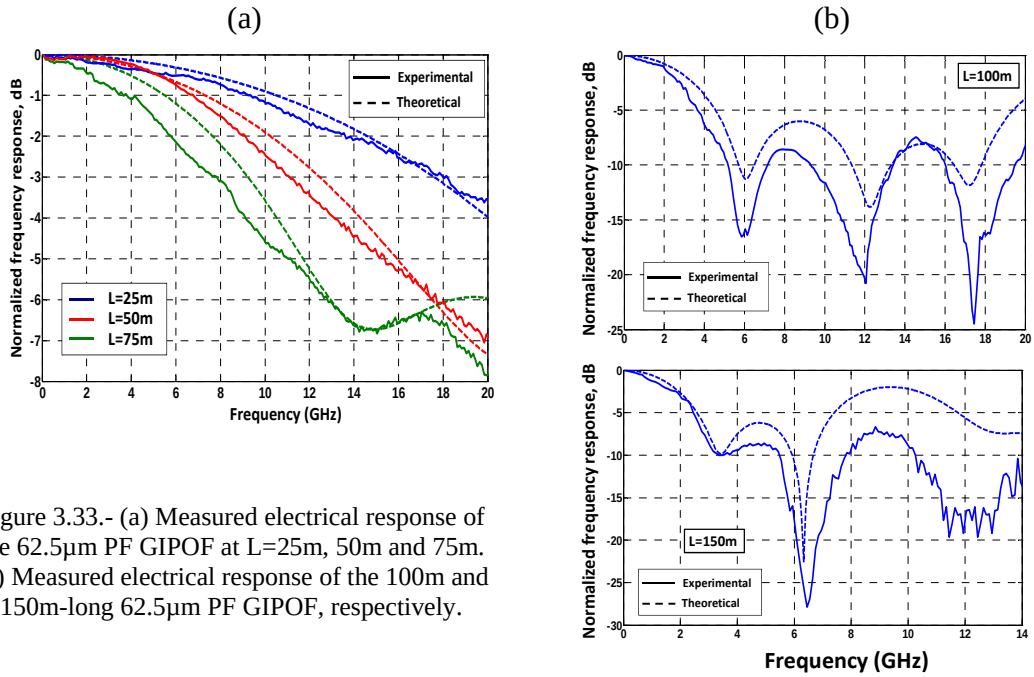

Figure 3.33.- (a) Measured electrical response of the 62.5µm PF GIPOF at L=25m, 50m and 75m. (b) Measured electrical response of the 100m and 150m-long 62.5µm PF GIPOF, respectively.

	62.5µm PF GIPOF 3-dBo bandwidth (GHz)	
	Theory	**Experimental**
L=25m	17.9	17.5
L=50m	12.5	11
L=75m	9.2	7.8
L=100m	3.7	2.9
L=125m	2	1.7
L=150m	1.8	1.8
L=200m	1.6	1.1

Table 3.9.- 62.5µm core diameter PF GIPOF 3-dBo bandwidth values for different lengths regarding to Fig. 3.33, under RML condition.

It can be seen that there is a quite good agreement between the frequency responses predicted by the model and the experimental results measured with the LCA.

The same procedure was applied in order to obtain the following pictures, shown in Fig. 3.34 and Fig. 3.35. Both illustrate the frequency response of a 120µm and 50µm core diameter PF GIPOF at different lengths for a RML condition, respectively. Again, a good agreement between the experimental results and the theoretical model is noticed. However, high deviations are observed with regards to the theory concerning de 120µm core diameter GIPOF. This fact can be attributed to the receiver effective area, which is designed for a 62.5µm core diameter input optical fibre, leading to a filtering effect of the higher-order modes received as well as an optical power loss and, consequently, to a higher optical power loss received. The latter could be the main reason for the noisy-like measurement results obtained with the 120µm core diameter fibre type. The bandwidth values are summarized in Table 3.10 and Table 3.11, respectively. It should be noted that the ripples observed at frequencies greater than 13GHz are caused by reflections in the optical system and are not features of the fibre response.

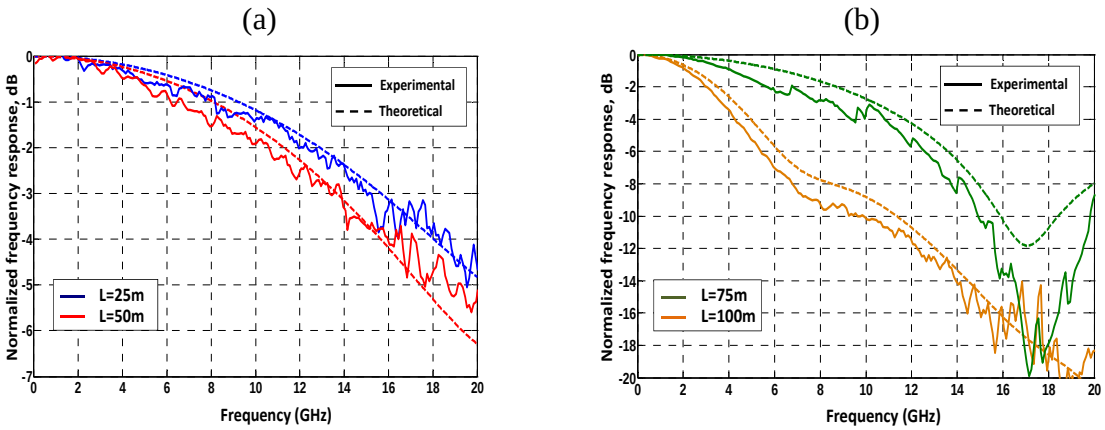

Figure 3.34.- (a) Measured electrical response of the 120µm PF GIPOF for L=25m and L=50m. (b) Measured electrical response of the 75m and 100m-long 120µm PF GIPOF.

	120µm PF GIPOF 3-dBo bandwidth (GHz)	
	Theory	**Experimental**
L=25m	15.9	15
L=50m	13.9	13.4
L=75m	10.4	7.9
L=100m	4.2	3.6
L=125m	1.7	2
L=150m	1.6	1.8
L=200m	1.5	0.8

Table 3.10.- 120µm core diameter PF GIPOF 3-dBo bandwidth values for different lengths regarding to Fig. 3.34, under RML condition.

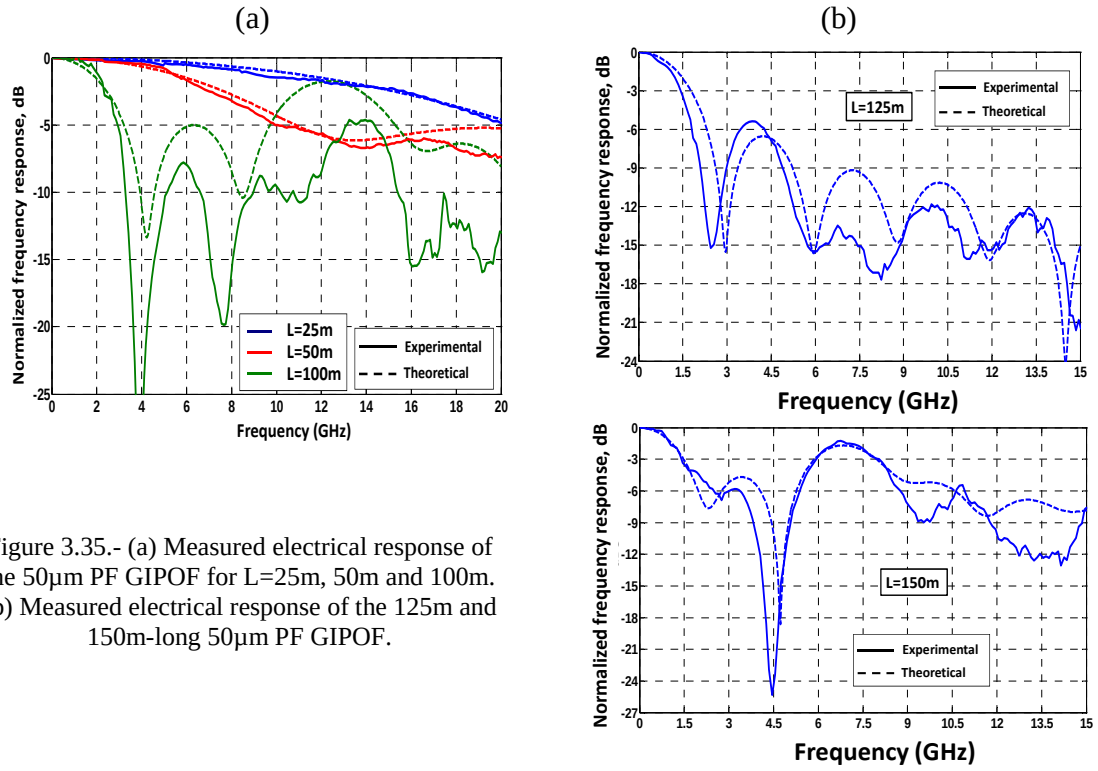

Figure 3.35.- (a) Measured electrical response of the 50µm PF GIPOF for L=25m, 50m and 100m. (b) Measured electrical response of the 125m and 150m-long 50µm PF GIPOF.

	50µm PF GIPOF 3-dBo bandwidth (GHz)	
	Theory	**Experimental**
L=25m	16.7	16.7
L=50m	9.0	7.9
L=75m	5.1	5.2
L=100m	2.8	2.5
L=125m	1.7	1.4
L=150m	1.5	1.4
L=200m	1.2	0.9

Table 3.11.- 50µm core diameter PF GIPOF 3-dBo bandwidth values for different lengths regarding to Fig. 5.35, under RML condition.

The experimental results of the PF GIPOF frequency response suggest that signals with carrier frequencies well beyond the 3-dB bandwidth can be transmitted. This fact can clearly be observed in Fig. 3.33(b) and Fig. 3.35(b), for instance. Moreover, it has been shown in these measurements as well as in several research works of other groups [119-121] that at high frequency regions the response stays relatively flat and has a rather high value. However, these latter have been mainly reported for silica-based multimode fibres rather than GIPOF counterparts.

Concurrent with the above results, measurements of the PF GIPOF frequency response at overfilled launching condition (uniform excitation of all the modes) were also made. The optical power was launched via 1m-long SIPOF, which is considered as an ideal exciter of

all the modes, and butt-joined to the PF GIPOF. Consistent with the RML condition, in order to obtain the best fitted theoretical simulation (dashed lines) with regards to the experimental measurement, parameters such as the graded index exponent, the GIPOF attenuation (dB/km), parameters ρ and η in Eq. 3.31 relative to the functional expression of the DMA were precisely evaluated. Fig. 3.36 illustrates the 62.5µm core diameter PF GIPOF frequency response under OFL condition, at link lengths 50m, 75m and 100m. The corresponding 3-dB bandwidth values are shown in Table 3.12.

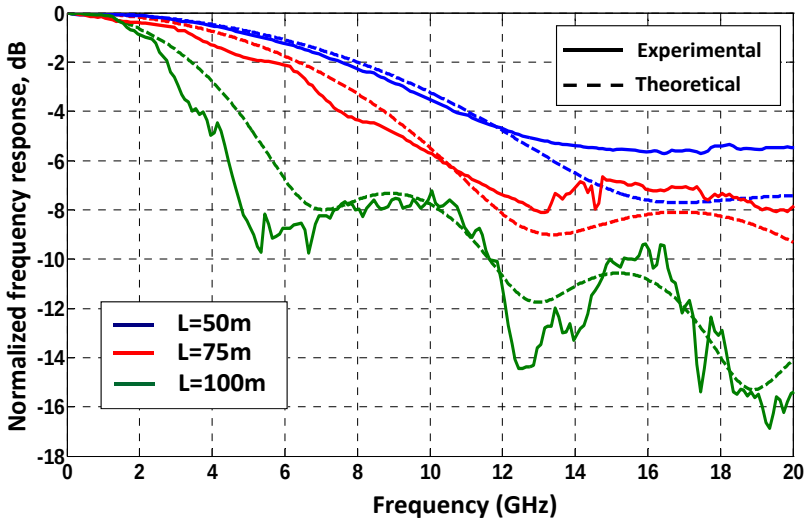

Figure 3.36.- Measured electrical response of the 62.5µm PF GIPOF for L=50, 75 and 100m under OFL excitation, via 1m-long SIPOF.

The same response performance was evaluated for a PF GIPOF fibre of 50µm core diameter. Experimental results are shown in Fig. 3.37 and measured 3-dB bandwidths are also presented in Table 3.12.

(a) (b)

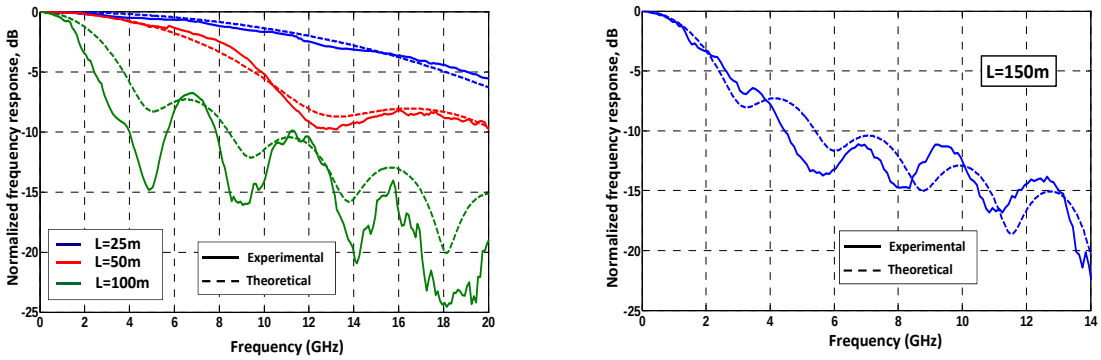

Figure 3.37.- (a) Measured electrical response of the 50µm PF GIPOF for L=25, 50 and 100m under OFL excitation. (b) Measured electrical response of a 150m-long 50µm PF GIPOF under OFL excitation, up to 14GHz.

	62.5µm PF GIPOF 3-dBo bandwidth (GHz)		50µm PF GIPOF 3-dBo bandwidth (GHz)	
	Theory	**Experimental**	**Theory**	**Experimental**
L=25m	16.7	18.4	15.1	13
L=50m	9.0	9.2	8.8	8.7
L=75m	5.1	6.7	5.2	3.2
L=100m	2.8	3.2	3	1.9
L=125m	1.7	1.7	2	1.4
L=150m	1.5	1.2	1.6	1.4
L=200m	1.2	0.9	1.2	0.8

Table 3.12.- 62.5µm and 50µm core diameter measured PF GIPOF 3-dBo bandwidth values for different lengths under OFL condition.

Fig. 3.38 plots the fibre bandwidth values reported in Table 3.12 as a function of the transmission length, showing a comparison of the model when including or not the effect of DMA. Both graded index exponents considered in this figure come from the fact that the measurements taken have led us to think that, as these lengths are provided by different fibre spools, they do not come from the same bulk or preform or even they were manufactured in a different process. The values of α=2.1 and α=2.3 have found to be the best approaches from the measurements. It is worth noting that this issue has been taken into account during the theoretical fitting, showed in all the above figures.

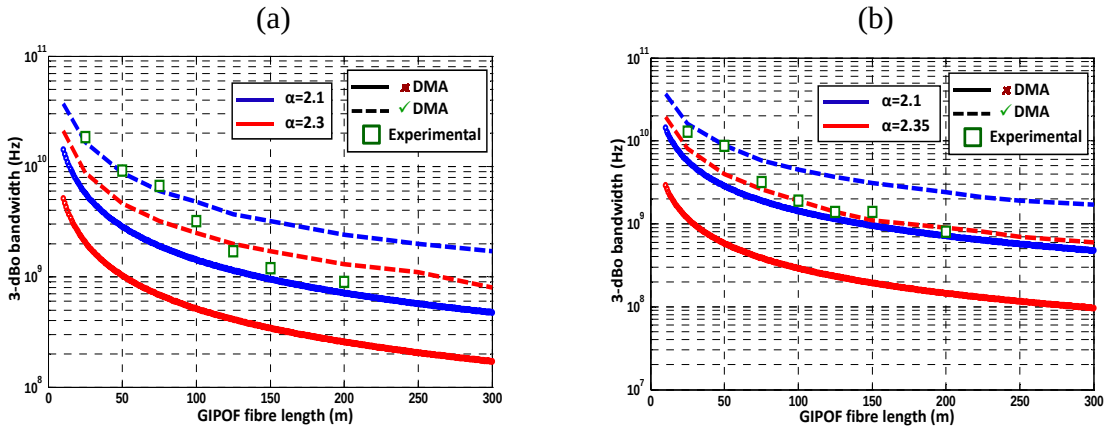

Figure 3.38.- (a) Total 3-dBo bandwidth of the 62.5µm PF GIPOF as a function of transmission length for an index exponent α=2.1 (blue line) and α=2.3 (red line) at a wavelength of 1300nm under OFL excitation. (b) Total 3-dBo bandwidth of the 50µm PF GIPOF as a function of transmission length for an index exponent α=2.1 (blue line) and α=2.3 (red line) and a wavelength of 1300nm under OFL excitation. (□) Experimental values, (---) including DMA effects, (—) without considering DMA effects.

Taking into consideration Fig. 3.38(a), i.e. the 62.5µm core diameter case, bandwidth values at transmission lengths of 25m, 50m and 75m can accurately be determined by an index exponent of α=2.1 considering DMA effects (blue dashed line), which is concordant with the index exponent fixed for the theoretical curves at OFL condition (see Fig. 3.36). On the contrary, for the frequency response fitting above 100m, an index exponent in the order of α=2.3 was found to be the best approach. A similar analysis can be made for the case of 50µm core diameter, depicted in Fig. 3.38(b), but only for 25m-long and 50m-long

cases. On the other hand, from the figure, it is theoretically clear again that the DMA enhances the total bandwidth to a considerable extent. Indeed, it can be seen from the figure that at least a fourfold bandwidth enhancement may be gained. Quantitatively very high approximation of the bandwidth values are observed for both core diameter measurements.

The series of length-dependent bandwidth value measurements is resumed in Fig. 3.39(a), considering the RML excitation. Slight dependence on the core radius is observed, although the behaviour indicates that the lower the core radius the lower bandwidth value. This fact has been previously predicted by [112] although the reasons are not thoroughly understood yet and should mainly result from the fact that the difference in propagation constant between next-neighbouring mode groups is inversely proportional to the core diameter [19] and therefore reduces as the core is enlarged. This fact have also been addressed by the work reported in [54]. It is also worth noting that the lower the spot radius is the higher the core radius dependence with the transmission length would be observed. Therefore, it can be concluded that by launching optical power with w around 20µm (and higher so) there is little influence of the core radius in the 3-dB bandwidth for different transmission lengths.

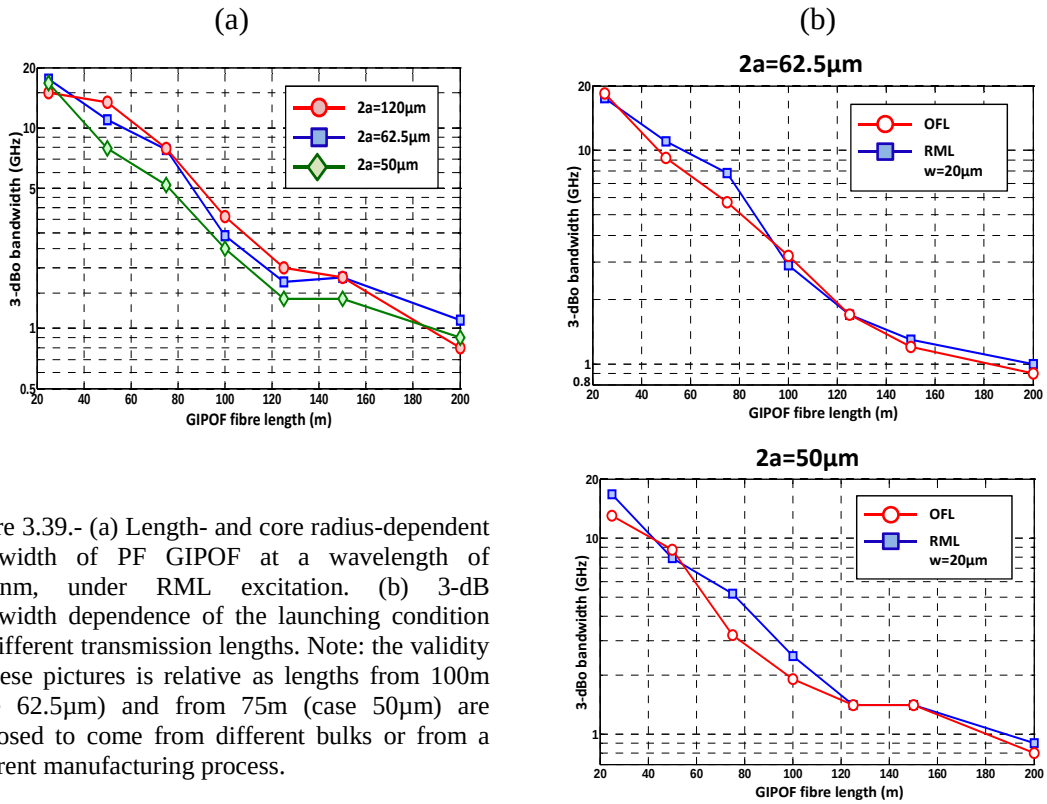

Figure 3.39.- (a) Length- and core radius-dependent bandwidth of PF GIPOF at a wavelength of 1300nm, under RML excitation. (b) 3-dB bandwidth dependence of the launching condition for different transmission lengths. Note: the validity of these pictures is relative as lengths from 100m (case 62.5µm) and from 75m (case 50µm) are supposed to come from different bulks or from a different manufacturing process.

From the above results depicted in Fig. 3.39(b), uniform mode distribution (OFL) yields lower bandwidth than RML condition. After a certain length, the so-called coupling length, both 3-dB bandwidth values at different launching conditions reach an equilibrium mode distribution (EMD). This results in now theoretically length independent values both for bandwidth and attenuation. This coupling length differs from fibre type to fibre type and even within one fibre type, depending on the manufacturer. Even if lower order modes were

launched under RML condition, the optical power gradually spreads to the high order modes due to the mode coupling after a certain propagation distance. Thus, the bandwidth performance would degrade and become close to that observed under the OFL condition. This fact can be seen on this figure, where the 3-dB bandwidth values become quite closer at both launching conditions for GIPOF lengths over 100m in case the 62.5µm core diameter and nearly 125m in case of the 50µm core diameter PF GIPOF. In this case it can be supposed that the equilibrium length of the fibre is nearly above 100m, leading to a rather stable performance, where the optical bandwidth stays around 1GHz for 200m, whatever fibre the launching condition is. These results regarding the coupling length are in the same range of values than those presented in [54], for instance.

It is interesting to mention that results of bandwidth values, in the same order than that of the above reported, have been also achieved for the OFL condition by using a 62.5µm silica multimode fibre in conjunction with a mode scrambler (see inset of Fig. 3.3.1). This trend leaded to higher losses in the optical power detected with regards to the 1m-long SIPOF butt coupling technique. This fact limited the transmission length to test, above the noise level of the LCA 8703B, no more than 75m, being impossible to measure higher link lengths than that value. Fig. 3.40 shows the measured (solid line) and theoretical (dashed line) frequency responses of the 120 µm core diameter PF GIPOF. The graded-index exponent of the fibre was set to 2.1, identical to their counterparts plotted in Fig. 3.34. The mode scrambler was introduced in the set-up thus providing a uniform excitation launching into the fibre. Both figures are also displayed after calibrating the results with respect to both the modulator and the detector electrical responses. Although 3-dB PF GIPOF bandwidths for all cases are in the same magnitude order, there are slight variations in measurements, having obtained 13.5GHz, 11.8GHz and 3.2GHz for L=25m, 50m and 75m respectively. These values are resumed in the following table and can be compared with those indicated in Table 3.10, regarding the RML excitation. As expected, higher bandwidth values are obtained for the latter case, i.e. for a RML condition.

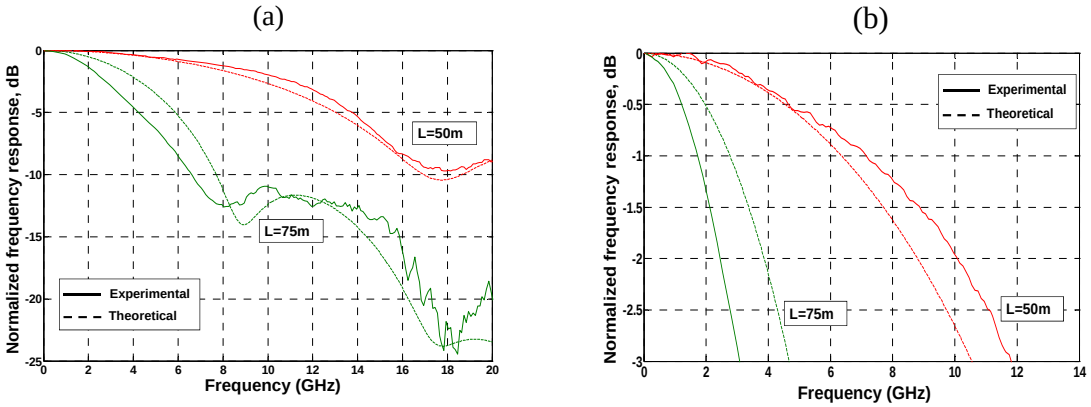

Figure 3.40.- (a) 120µm PF GIPOF frequency responses at 50m and 75m transmission lengths for a OFL condition achieved by using a 62.5µm silica MMF and a mode scrambler before the GIPOF link. (b) Theoretical and measured PF GIPOF 3-dB frequency responses from Fig. 3.40(a). Measurements are represented in solid lines. Dashed lines were obtained from theory.

	120µm PF GIPOF 3-dBo bandwidth (GHz)	
	Theory	Experimental
L=25m	12.2	12.5
L=50m	10.5	11.8
L=75m	4.4	3

Table 3.13.- 120µm core diameter measured PF GIPOF 3-dBo bandwidth values for different lengths under OFL condition using a silica MMF patch cord and a mode scrambler.

On the other hand, the RML condition can be also provided by a 62.5µm graded-index silica multimode fibre as a launch fibre onto the 120µm GIPOF. Basically in the RML launch condition, launched mode power distribution largely depends upon the optical source. In order to cover the variable mode power distribution created by the RML condition with a wide variety of transmitters, a 62.5µm silica-based MMF was also used to excite the lower to intermediate order modes. This fact is in contrast with the SMF-based RML excitation, which launch only limited number of low order modes. From the below experimental results shown in Fig. 3.41 it is found that a large bandwidth degradation is observed when the silica-based MMF was used as the mode exciter, compared with that of under SMF launch (see Table 3.10 for comparison).

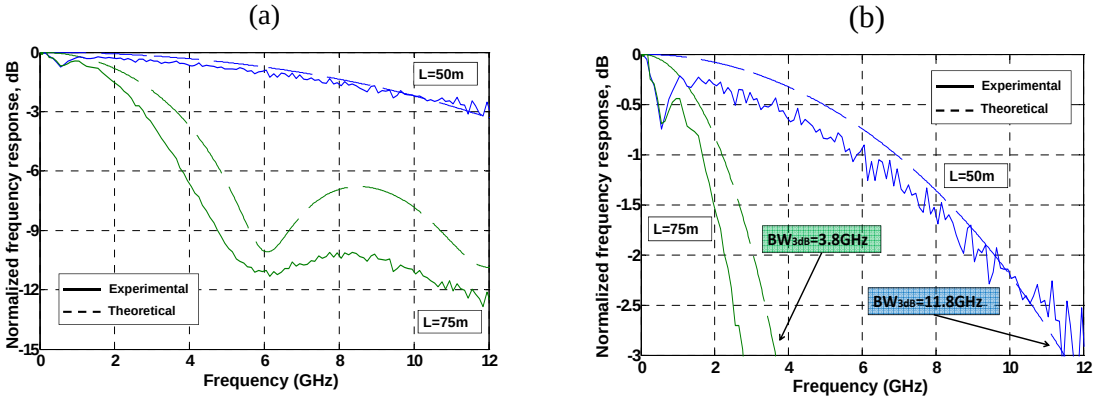

Figure 3.41.- (a) 120µm PF GIPOF frequency response at 50m and 75m transmission lengths for a RML condition achieved by using a 62.5µm silica MMF before the GIPOF link. (b) Theoretical and measured PF GIPOF frequency response, up to 3-dB of loss. Measurements are represented in solid lines. Dashed lines were obtained from theory. 3-dB bandwidth values are also indicated.

In the former section comprising the theoretical simulations, the frequency response and 3-dB bandwidth dependence on both the wavelength and source linewidth were addressed. Both parameters have also been evaluated under the RML condition, as light from the silica-based SMF patch cord was launched into the core of the PF GIPOF by means of a butt coupling. For the source linewidth dependence measurements a DFB optical source from Agilent (model 81989A), operating at 1550nm with $\Delta f < 5\text{MHz}$ of spectral width, as well as a LED@1300nm with 98nm of spectral width were used for launching the optical power to the PF GIPOF link. Furthermore, in the case of the measurements at an operating wavelength of 1550nm, the former external modulator was replaced from another model (JSDU AM-150) from the same vendor, which operates within the third optical

transmission window and with frequency response almost identical to that depicted in Fig. 3.32(b). Experimental results showed that there is little dependence on the 3-dB bandwidth with the fibre core diameter considered, as expected from theory. The following set of two figures within Fig. 3.42 resume the measurements done for evaluating both dependences. It is worth pointing out that, operating with a DFB source, theoretical curve concerning $\lambda = 1550\text{nm}$ in Fig. 3.42(b) must be treated with careful as the mode continuum approximation condition is quite close to its lowest limit.

Related to Fig. 3.42(a), despite of the lower chromatic dispersion in PF GIPOFs at 1550nm than at 1300nm, see Fig. 3.9(b), a higher 3-dB bandwidth can be achieved for a 1300nm operating wavelength. This fact is supported by the bandwidth enhancement provided by considering DMA effects, which are supposed to be stronger at 1300nm than that of 1550nm. This fact was also expected from the simulations depicted in section 3.7.8. On the other hand, a higher NA@1300nm (NA=0.1867) is obtained than that of NA@1550nm (NA=0.18165), which would mean that higher number of modes are propagating through the fibre and, consequently, the modal dispersion would increase thus leading a bandwidth decrease at 1300nm. However, as the PF GIPOF has an index profile near the optimum value, the bandwidth is not affected by the numerical aperture and becomes almost independent. This is because the modal dispersion is minimized. Being the same measured fibre patch cords, all the figures were set to the same graded index exponent $\alpha = 2.1$, which is quite near to the theoretical optimum. It is worth mentioning that the F-P source at 1550nm used for evaluating this wavelength dependence had a linewidth of $W = 1.6\text{nm}$, slightly lower than the F-P source at 1300nm case.

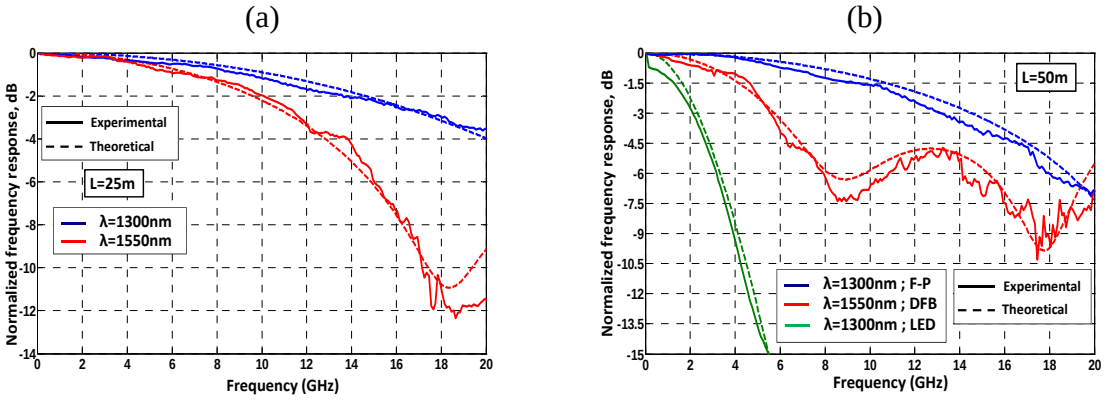

Figure 3.42.- (a) Measured wavelength-dependence of the electrical response of the 25m-long 62.5µm PF GIPOF. (b) Measured linewidth dependence of the electrical response of the 50m-long 62.5µm PF GIPOF. F-P: Fabry-Perot laser source, DFB: Distributed Feedback Laser, LED: Light Emitting Diode.

On the other hand, Fig. 3.42(b) depicts the source linewidth dependence of the PF GIPOF frequency response. Considering the 1300nm wavelength, it can be seen that the frequency response dramatically decreases when increasing the rms source linewidth. In this case, when a LED with $W = 98\text{nm}$ of spectral width is employed as the optical source, the 3-dB bandwidth decreases to 2GHz, opposite from the case when a F-P laser with $W = 1.8\text{nm}$ is employed, obtaining a 3-dB bandwidth of 13GHz for the same PF GIPOF length (and considering the same index profile as both measurements come from the same fibre spool).

Regarding the 1550nm wavelength, despite of employing a DFB source with $\Delta f < 5\text{MHz}$ of rms bandwidth, no higher bandwidth is achieved. This is caused, as in Fig. 3.42(a), by the lower material dispersion of the PF GIPOF at 1300nm. Furthermore, the material dispersion seriously affects the bandwidth performance of the PF GIPOF link when rms spectral width is much larger than the order of nanometers.

All the figures within this section prove that the measured normalized response obtained with the LCA is in agreement with the model presented for PF GIPOF-based systems in this chapter as well as in [55]. The results have been tested over an amorphous perfluorinated (PF) graded-index polymer optical fibre. In all cases, such fibre type fulfils the requirements of the IEC 60793-2-40 standard for the PF polymer-based POFs (types A4f, A4g and A4h) which fits a minimum bandwidth of 1500MHz@100m for A4f type and 1880Mhz@100m for A4g and A4h types, respectively. However, certain amount of disagreement between the theoretical and the experimental responses is observed from the figures. The differential mode attenuation (DMA), mode coupling, variance of the numerical aperture and the refractive index profile deviation along with the axial direction are considered to be the main factors of the disagreement. Other measurement error sources that can be clearly identified are the following, excluding those inherent to the equipment used in the experiments:

- It has been concerned that the modal noise degraded the 3-dB bandwidth (and consequently the bit error rate) in the case of a multimode fibre with laser diode in fibre-optic links. However, it is noteworthy that the large core GIPOFs (300-1000μm), which can transmit more than 30000 modes, causes no significant degradation of these parameters even if a laser diode with high coherency is used and when even 200μm of misalignment was occurred. Recent developed GIPOF fibres as well as those tested in this work have a core diameter comparable to those for conventional graded index multimode silica fibre. This fact as well as the intrinsic misalignment caused by the use of adapters/connectors possibly limits the performance of the GIPOF 3-dB bandwidth values measured and it is in concordance with the general behavior of the measured values.
- Additionally, losses resulting from the waveguide structure (that is, the optical fibre), especially arising from inhomogenities in the cladding region, should be taken into account, i.e. the effects of a non-ideal fibre.
- It has been proved in literature that the frequency response of multimode fibre links, including polymer optical fibres, depends, in general, on the launching conditions due to excitation-dependent modal group delays and on mode group coupling. Therefore, launching conditions, variable link lengths, installation bends, connector offsets and the introduction of any other error-source component along the multimode fibre link makes its frequency response unpredictable under arbitrary operating conditions. This fact imposes a great challenge for the extension of the bandwidth-dependent multimode fibre performance. All these factors, although having tried to minimize during experiments, are not free from undesirable deviations, thus affecting the frequency response of the transmission length.
- Back reflections from the fibre input surface into the laser source have not been avoided. Semiconductor lasers subjected to back-reflected waves in optical

communications systems may undergo different and complicated states of behaviors. Unless the reflected light is well monitored, optical feedback is often detrimental, because it enhances noise and introduces nonlinearity in the emission characteristics. Such impairment could be overcome by developing a coupling optics introducing antireflection lenses, for instance.

- It has been shown by previous works on silica-based multimode fibres, with 50 to 62.5μm core diameters, that the modal noise deteriorated the system performance. Although it has been also proved that in >120μm core diameter GIPOFs the modal noise is virtually eliminated because of the huge number of propagating modes, GIPOF fibres with core diameters in the same order as those for silica-based counterparts are expected to suffer the same effect. This modal noise is caused by using a multimode fibre with a coherent light source such as a laser or VCSELs. A speckle pattern in then formed by interference between the propagating modes on the output end of the fibre. Therefore, if an offset connection between two fibres (the launching fibre and the fibre link to test) is included in the multimode fibre link, the speckle power distribution is translated into intensity fluctuation, which is the modal noise. This fact can also contribute to the difference between the theory and the experimental data.

In addition to, all theoretical model assumptions that were clearly identified in Section 3.6 introduce disagreement sources, with meaning in differences between the measured results and the theoretical curves predicted by the model. Most relevant assumptions could be: (a) the empirical formula for the DMA, given by Eq. 3.31, (b) considering the mode coupling phenomenon as negligible and (c) having assumed that the fibre is excited centrally with a laser beam that forms a circularly symmetric spot on the input surface. These last three factors are probably the main causes of disagreement between theory and measurements.

3.9 Evaluation of the PF Graded-Index Polymer Optical Fibre link stability

POFs and polymer based optical components are referred as technical products, and are utilized for several optical applications under various environments. The environments can be mechanical, climatic, chemical, biological and radiometric. The optical transmission performance is a key issue for assessing the consistency or reliability of POF systems for desired long-term applications. The environmental factors certainly affect the optical transmission performance. As a result the lifetime of the POF system varies to a different extent. The optical transmission of a POF is determined mainly by its materials' physical and chemical properties. Therefore, during the practical operation of POFs, environmental factors bring both physical and chemical changes of materials and hence the optical transmission stability fluctuates. Additionally, polymers themselves undergo aging, which result in a variation of physical and chemical properties. However, the optical transmission durability of a POF depends on other factors such as the nature, the extent, and the frequency of the imposed environmental stresses. In this section the frequency response dependence of external agents of a PF GIPOF link is analyzed containing experimental measurements. Moreover, stability of the fibre frequency response is closely related to the

temporal coherence of the source. In general, a very coherent source (such as DFB lasers) will result in a considerable level of modal noise in a multimode optical fibre link, which is produced by variation of the coupling between low- and high-order modes together with spatial filtering at the fibre connectors. On the contrary, for the FP laser employed, the detected power is expected to present a non-variant response with time. So, modal noise effects affecting the GIPOF link frequency response can be considered negligible. Different sets of measurements give the idea of the stability of such a link, both in terms of the frequency response and the 3-dB bandwidth. Furthermore, the higher-frequency lobes, previously reported in the above section, are also supposed to be affected, even in a deeper extent. In order to measure the frequency response accurately, a calibration measurement was first carried out with the laser, the optical intensity modulator and the photodiode, as in section before.

Some PF GIPOF samples are studied to realize the effects of individual parameters and for forecasting long-term optical stability by short-term exposure tests. The optical source employed was a Fabry-Perot (FP) laser, model 81655A from Agilent operating at 1300nm. It is interesting to mention that vendor's specifications depict a long-term (24 hours) CW power stability of *typical±0.03dB* although no wavelength drift is mentioned within a period of time. The frequency response and 3-dB bandwidth values of a 25m-long commercially available jacketed 120µm core diameter PF GIPOF, under SMF-butt coupling launch condition, was evaluated. Continuous frequency response measurements were analyzed using the LCA during two days. Results are shown in Fig. 3.43(a) and Fig. 3.43(b), respectively. Varying launching conditions as well as environmental temperature deviations were tried to minimize as much as possible assuming practically negligible their influence on the measurements, without lose of information. Consequently, minor instabilities affecting the GIPOF link can be attributed to external conditions such as the different temperature air fluxes from the working devices near the set-up and the air conditioning. In such case the frequency response would be only affected by possible thermal drifts and thermal aging of the uncooled optical equipment used or due to the perfluorinated polymer (PF) degradation in time, which would lead to a dramatically different performance of the frequency response, for the same transmission length. Related to the latter fact, it has been reported the concern about the orientation of the polymer chains, which would relax during aging.

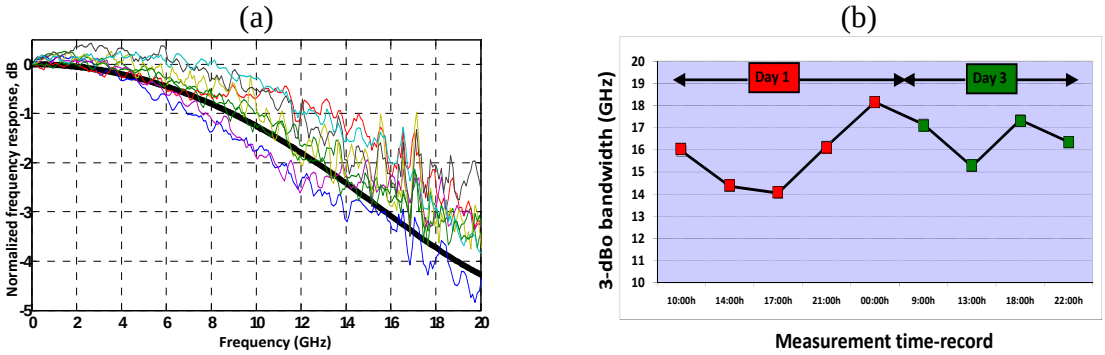

Figure 3.43.- (a) Frequency response of the 25m-long 120µm PF GIPOF link during two days of continuous measurements. Black solid line: theoretical curve. (b) 3-dBo bandwidth values during measurements (note: within Day 2 no measurements were taken).

During the experiments the environmental temperature was measured to be T=25±1ºC. From the above figures it can be seen that high deviations on the frequency response and the 3-dB bandwidth values are observed, mainly attributed to the optical devices performances during the measurement time in a short-term scenario. No averaged measurements were taken in this section. On the other hand, from the 3-dB bandwidth values recorded, an averaged value of 15.97GHz was obtained, quite closer to the theoretical one predicted by the model (15.7GHz). However, maximum fluctuations of even around the ±13% of the nominal value can also be observed, as shown in Fig. 3.43(b).

A similar set of measurements were made for a 62.5µm jacketed PF GIPOF, but increasing the measurement time up to 4 days. The results are shown in Fig. 3.44. Environmental temperature was measured to be T=25±1ºC, i.e. the same temperature condition as former figure. All possible external agents as well as launching conditions were minimized in their influence during the measurement time. Therefore, changes on the frequency response mainly could come up from the optical devices used for the experiments, with errors sources such as thermal drifts and short-term aging typically, as well as from the possible intrinsic degradation of the PF polymer. 3-dB bandwidth maximum deviation of about -21% from the expected theoretical value was observed.

From both figures it is worth mentioning that higher 3-dB bandwidth value deviations were observed for the PF GIPOF fibre with lower core diameter. This statement is true as both fibres share practically the same grade-index profile from the results shown in section 3.8 ($\alpha \simeq 2.1$) and, consequently, the deviations are mainly supposed to be caused by the difference in the core diameter of both fibres under study. The fact that fibres with larger core diameter tolerate higher launching condition misalignments, including different wavelength emission or different spectral linewidth, could be the reason for this behavior.

Although the short-term stability test are emerged as reasonable for approximating the relative optical transmission stability of polymer optical fibres, in general the absolute finding (in a short exposure period) of the optical transmission stability is very difficult since the optical transmission depends on several parameters, which could influence the optical transmission stability to a different extent during the test.

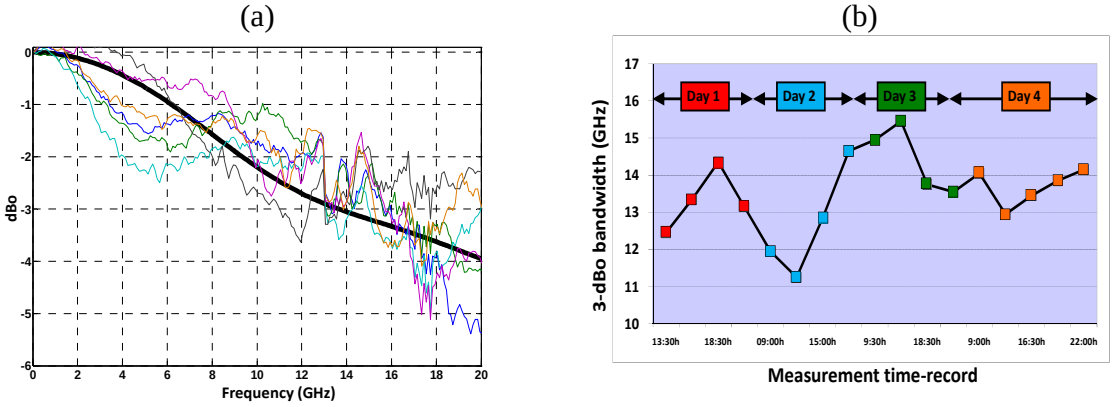

Figure 3.44.- (a) Frequency response of the 50m-long 62.5µm PF GIPOF during four days of continuous measurements. Black solid line: theoretical curve. (b) 3-dBo bandwidth values during measurements.

3.10 Thermal instabilities in PF Graded-Index Polymer Optical Fibre links

In order to realize the GIPOF link within the access network scenario, the thermal stability, the humidity stability and the long-term reliability become key issues. It has been confirmed that the dopant kind and concentration strongly influence the thermal stability of GIPOF. Thermal stability can become of significant importance, especially in the degradation of the refractive index profile of the GIPOF by the migration of dopant molecules [122] as well as the long-term attenuation of the fibre as a result of outdoor exposures. Furthermore, thermal stability producing deviations on the refractive index profile of the GIPOF directly affects the frequency response and bandwidth stability in GIPOF links, see Section 3.7.5. On the other hand, the hydrophilicity of the dopant is an important factor for the high humidity resistance of the GIPOF.

It has been stated that a greatly reduced dopant concentration allows the GIPOF to have the advantage of high-temperature stability [114]. However, the numerical aperture (NA) of the GIPOF is lowered by decreasing the feed concentration of the dopant, and thus bending loss increment is a concern. Consequently, there is a trade-off with regards to such fibre parameters [122]. Predictive accurate models of distortion in the frequency response of the fibres become necessary although other ways have been opened up such as adopting specified dopant added in the formation of the GIPOF. This is because the thermal stability of the latter strongly depends on the chemical structure of the dopant and the secondary interaction between dopant molecules and the polymer matrix in the fabrication process [123]. Several kinds of commercially available aromatic compounds have been adopted and studied, such as Diphenyl (DP), Benzyl Benzoate (BEN) or Diphenyl Sulfoxide (DPSO) among others. In case of the latter [122] no degradation of the index profile, and consequently on the bandwidth, was observed even after 10000h aging at 85ºC (this temperature value corresponds to the thermal stability standards of many cables including silica optical fibres). Furthermore, [114] reports the use of a methyl methacrylate (MMA)-2,2,2-trifluoroethyl methacrylate (3FMA) copolymer adopting in the cladding of the GIPOF, thus obtaining a high-temperature (5000 hours aging at 70ºC) and high-humidity (80% R.H.) stability in both attenuation and bandwidth.

Nevertheless all these studies have been principally applied to PMMA-based GIPOFs as well as PMMA-based SIPOFs [28], being the perfluorinated (PF)-based GIPOF thermal dependence not reported and not achieved at the level reached for its PMMA-based counterparts [124]. In contrast, fluorinated polymers have high humidity stability because the intermolecular energy is lower than that of nonfluorinated polymer [125] and, since the PF polymer is more stable than many other chemicals and is not flammable, much more stability can be expected. This suggests that outdoor use of the PF polymer based GIPOF will be possible (as well as for silica-based fibres). However, the restricted distribution of fundamental POF data by the manufacturers and the time consuming aging by climatic exposures restricts the results more or less to the samples investigated here.

In this section, the dependence of the frequency response with regards to short-term temperature deviations is analyzed. Measurements have been taken for temperatures from

T=21ºC (environmental) to T=60ºC. The heat-up and heat-down (natural cooling) rates were ~1ºC·min^{-1} and ~0.8ºC·min^{-1}, respectively, for a total test time of half an hour (40min heating cycle plus 50min cooling cycle). Four measurements were recorded at each temperature, displaying in the following figures the averaged frequency responses. The hysteresis cycle of the measurements was also evaluated. In order to only measure the temperature dependence, the frequency response has been calibrated with regards to the laser, the optical intensity modulator and the photodiode, as in section before, as well as to possible thermal drifts from the optical devices. The set-up follows a similar diagram as that depicted in Fig. 3.31. Test equipment was isolated from the heating source thus affecting the temperature deviation only to the PF GIPOF spool.

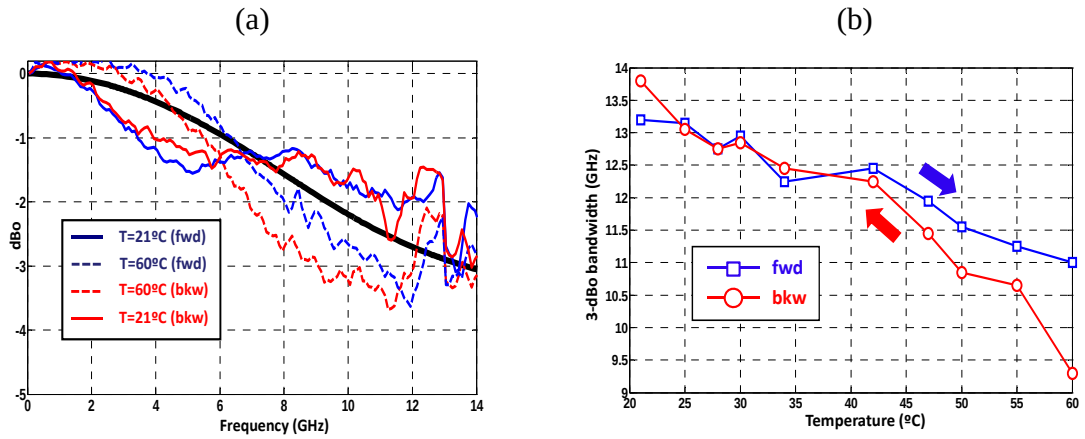

Figure 3.45.- (a) Experimental frequency response of the 50m-long 62.5µm PF GIPOF at T=21ºC and T=60ºC. Black solid line: theoretical curve. (b) 3-dBo bandwidth values during measurements. Fwd: forwards, Bkw: backwards

Fig. 3.45(a) shows the normalized frequency response of a 50m-long 62.5µm core diameter PF GIPOF link at T=21ºC and T=60ºC. Frequency responses at intermediate temperatures are not plotted for a better understanding of the picture. On the other hand, Fig. 3.45(b) plots the measured 3-dB bandwidth values at each intermediate temperature. In both figures, the term *'fwd'* refers to the temperature reached during the heating process whereas the term *'bkw'* refers to the case of the temperature reached during the cooling process. Consequently, the hysteresis of the 3-dB bandwidth temperature dependence is revealed. From the measurements taken, short-term temperature deviations can seriously affect the frequency response of any PF GIPOF link. In addition to, it can be concluded, as a general trend, that the higher temperature affecting the PF GIPOF length the lower 3-dB bandwidth performance. This fact can be explained by the change of some of the optical properties of the polymer optical fibres thus affecting key parameters such as the graded-index profile, the core/cladding diameters (by elongation/fibre deformation), their refractive indices (also meaning a different fibre NA) or introducing new irregularities and/or inhomogeneities in the core/cladding interface or even in the fibre core. Also it can be due to the fact that the difference in propagation constant between next-neighboring mode groups is inversely proportional to the core diameter [19] and therefore reduces as the core is enlarged.

A similar set of measurements has been applied to a 25m-long 120µm core diameter PF GIPOF link. Results are shown in Fig. 3.46(a) and Fig. 3.46(b), respectively. From the experimental results, again, a key issue is the decreasing performance of the 3-dB bandwidth with increasing the environmental temperature surrounding the PF GIPOF spool.

(a) (b)

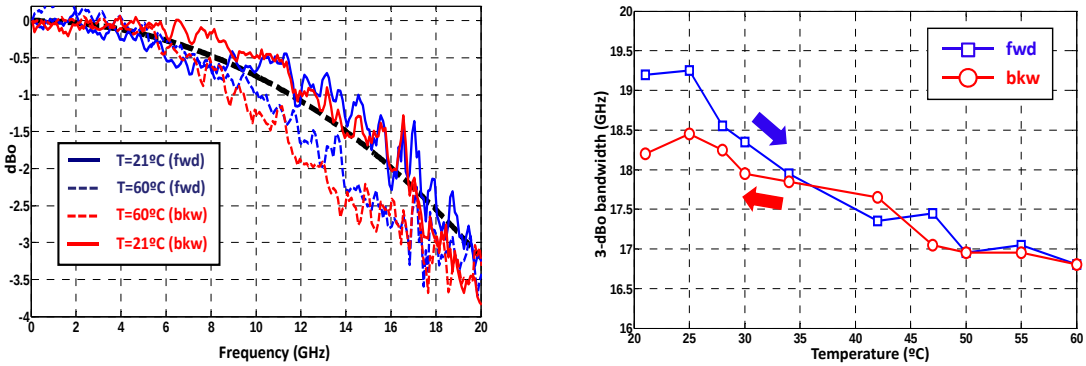

Figure 3.46.- (a) Experimental frequency response of the 25m-long 120µm PF GIPOF at T=21ºC and T=60ºC. Black solid line: theoretical curve. (b) 3-dBo bandwidth values during measurements. Fwd: forwards, Bkw: backwards

The results from the laboratory investigation of the temperature behaviour of the PF GIPOF show, by comparing pictures in Fig. 3.45 with those displayed in Fig. 3.46, that fibres with a larger diameter have a more stable performance in frequency response and 3-dB bandwidth against temperature deviations. Whereas in the 62.5µm-case a 3-dB bandwidth maximum deviation of approximately 5GHz is obtained which means a 30% full scale deviation from the nominal value, a 15% full scale deviation is obtained in the performance of the 120µm-case. As both fibres share practically the same grade-index profile from the results shown in section 3.8 ($\alpha \simeq 2.1$), the latter statement is supposed to mainly caused by the difference in the core diameter of both fibres under study. Therefore, larger core PF GIPOF fibres are more suitable for everyday use having better short-term temperature stability regarding lower core ones. However, it is also known that the long-term optical performance of POFs under different climatic aging conditions is unsatisfactory as compared to silica fibres. This fact will be studied in a following chapter.

3.11 Summary and Conclusions

The transmission characteristics of multimode (silica and polymer) optical fibre are usually assumed to follow a Gaussian low-pass frequency characteristic. However, in relatively short high-quality fibre links where mode coupling is practically negligible and chromatic dispersion is much smaller than modal dispersion, the impulse response of the link is a sequence of narrow impulses which correspond to te arrival times of the individual fibre guided modes. Therefore, next to its baseband transmission characteristics, a short, intrinsically multimode, GIPOF fibre link will show passband characteristics in higher frequency bands. However, the location and the shape of the passbands depend on the actual fibre characteristics, and may change due to environmental conditions and/or the

light launching conditions as well as the number of guided modes excited and the power distribution among them. Also the length of the fibre, the mode coupling processes, the source wavelength, the launching numerical aperture (i.e. the spot size of the input beam), the fibre core diameter or even offset of the launching beam with regards to the fibre axis influences the fibre frequency response. The influence of most of all these parameters has been addressed within this chapter by firstly developing the theoretical model concerning graded-index polymer optical fibres (GIPOFs), based on that of previously reported in [55] and [95], following by a huge set of theoretical simulations which study the influence of each parameter with regards to the frequency response as well as its 3-dB bandwidth value. A resume of the frequency response performance for each parameter can be read in Section 3.7.12. Most common graded-index fibre types have been theoretically addressed, that is, a perfluorinated (PF)-based one and its polymethylmethacrylate (PMMA)-based counterpart. At present, the former is considered to be the most promising candidate for the customer's premises network and short-reach telecom and computer interconnections.

Consequently, the frequency response and the 3-dB bandwidth values of different transmission lengths of commercially available perfluorinated (PF) graded-index poylmer optical fibre (GIPOF) with different core diameters have been measured, also at two different launching conditions. Firstly, using restricted-NA butt coupling launching from a singlemode fibre (SMF) as well as from a 62.5μm silica-based multimode fibre (MMF), thus achieving a restricted mode launching (RML) condition in which only small subsets of modes are excited and launched onto the GIPOF fibre. Secondly, via 1m-long SIPOF or using a silica-based MMF in conjunction with a mode scrambler, a uniform excitation of all the propagating modes (i.e. OFL condition) can be achieved. Two different optical sources operating at 1300nm and 1550nm central wavelengths have been employed. Furthermore, the internal modulator of the LCA device as well as an external Mach-Zehnder intensity modulator were also employed. The frequency responses depicted in the figures have been corrected for the frequency responses of the transmitter, of the external intensity modulator and of the receiver equipment.

Although no accurate agreement can be expected due to the many approximations made in the analysis presented in this chapter as well as the uncertainty of some of the fibre key parameters (such as the graded index exponent, the mode coupling effects, the exact DMA function approach or the beam spot radius launched onto the GIPOF link), the results reveal that the behaviour of frequency response expected by the theoretical model presented shows a good agreement with the experimental results that were carried out. To the author's knowledge this chapter shows for the first time experimental data that validate, with tolerable discrepancy, the model presented in section 3.6. Furthermore, the results reveal that the PF graded-index polymer optical fibre has some latent high-order passbands which, however suffer a higher attenuation than estimated. Nevertheless, this fact can open up the extend of the tranmission capabilities through these secondary lobes. Figures such as those plotted in Fig. 3.33(b) or 3.35(a) show this latter fact. Anyway, this higher attenuation could significantly be improved with lower fibre attenuation values.

It is worth noting that the experimental frequency response measurements have been adjusted to the theoretical model by sweeping parameters as those above indicated, i.e. the graded index exponent, the beam spot radius or the parameters that illustrate the DMA

effects (namely ρ and η). In all cases, these parameters were set to a logical and consistent values for all the adjusted simulations, although they may vary due to the use of different PF GIPOF spools even if they come from the same manufacturer. The rest of parameters, such as the operating wavelength, the source linewidth, material dispersion, dispersion slope or the type of excitation are imposed by the implemented set-up in each case or provided by the manufacturer, and introduced in the numerical computations.

From the experimental measurements reported in Section 3.8, the following conclusions can be made:

- As aforementioned, the theoretical model proposed is in quite agreement with the measured frequency response. Nevertheless, error sources such as those addressed in Section 3.8 are considered to be the main factors of disagreement.
- The results reveal that the PF graded-index polymer fibre has some latent high-order passbands which, however, suffer a higher attenuation. Through these passbands, high-frequency carrier transmission should be possible at the passbands central frequencies albeit a small power penalty. This fact would increase the GIPOF transmission capabilities as well as introduce the posibility of multiplexing techniques by using the higher transmission lobes.
- It has been also shown that the fibre 3-dB bandwidth values that are achievable using restricted mode launching (RML) are higher than those obtained using an over-filled (OFL) or uniform launching. However, obtaining a new data transmission record over PF GIPOF was not the main goal of this chapter. If so collimating and/or focusing lenses needed to be used to achieve a more mode-selective RML condition (plus including offset launching techniques), thus improving the bandwidth values reported within this chapter.
- A slight dependence of the 3-dB bandwidth with regards to the fibre core radius has been observed, although the behaviour indicates that the lower the core radius is the lower bandwidth value can be obtained. In other words, the large-core PF GIPOF fibre has more bandwidth potential. The physical reasons behind this trend are not throughly understood yet. Nevertheless, it can be due to the fact that the difference in propagation constant between next-neighboring mode groups is inversely proportional to the core diameter and therefore reduces as the core is enlarged. This dependence can be enhanced if lower beam spot radius is applied as a launching condition.
- Although it could not be experimentally tested due to the use of PF GIPOF spools with different graded index exponents, it is intuitively seen from Fig. 3.39 that PF GIPOFs used in the experiments show a coupling length which is in the range of 100m-150m, quite in agreement with the length value proposed by some authors elsewhere. In such a case, an equilibrium mode distribution is reached and quasi-length independent values of the 3-dB bandwidth could be observed. However, this value strongly depends on the fibre quality.
- The wavelength- and source linewidth-dependence of the frequency response have also been addressed through experimental results validating what is was expected through the theoretical simulations previously analyzed in Section 3.7.

- Regarding the transmission capabilities measured in this section, it was experimentally demonstrated that the PF GIPOF enabled Gigabit transmission over 200m approximately (and 10-Gigabit transmission over 50m). Anyway, these values strongly depend on the set-up launching condition. It is sure that these values can be significantly improved by including a more controlled set-up with regards to the launching condition.
- An important element in any POF link is the coupling to the source and coupling to the detector. In laboratory trials, lenses are commonly used for this task. However, for deployment of practical links effective coupling devices and schemes should become available as well as the development of a confident predictive tool to model this effects.
- As previously commented elsewhere, the system presented a high instability. All the captures and measurements have been made after stabilizing the system, taking special care of placing the connectors, cables and equipment to a fixed position, being not moved (and even touched) during the measurements.

On the other hand, due to organic chemical nature of POFs, they are sensitive to the environment conditions, mainly to temperature. Therefore, optical fibre properties are supposed to be sensitive as well. Hence, the optical stability is a key issue for long-term applications of POFs. Different measurements of the frequency response have been reported for giving the idea of the stability of such a PF GIPOF link. The experiment consisted on measuring the frequency response of different GIPOFs during 2-4 days without any change in the launching condition. Results have shown that the stability of such links is seriously affected by the short-term aging and thermal drifts of the optical devices used (i.e. not desirable or uncontrolled different launching conditions), affecting much more than in the case of the polymer (PF) degradation in time. In all cases, typical fluctuations were in the order of ±10-20% from the nominal value, which give the idea of how the launching condition as well as the optical equipment must be properly controlled in order to avoid undesirable performances of the PF GIPOF transmission link. As a matter of fact, it can be said that the larger core diameter PF GIPOF offers more stability in terms of the frequency response and its corresponding 3-dB bandwidth, by comparing Figs. 3.43(b) and 3.44(b), respectively.

In addition to, the dependence of the frequency response with regards to short-term temperature deviations has been also analyzed, ranging from T=21ºC to T=60ºC. The results showed a general trend consisting in the higher environmental temperature affecting the PF GIPOF the lower 3-dB bandwidth performance. Consistent with the former paragraph, fibres with larger diameter also offer a more stable performance in both the frequency response and the 3-dB bandwidth against temperature deviations. These latter are in the order of 15-30% full scale from the nominal value.

Finally, it is worth noting that the whole research described above has to be regarded as a starting point for further investigations.

3.12 References

[1] Y. Koike and T. Ishigure, "High-bandwidth Plastic Optical Fiber for Fiber to the Display," *J. Lightwave Technol.*, vol. 24, pp. 4541-4553, 2006.

[2] T. Ishigure, Y. Aruga, and Y. Koike, "High-bandwidth PVDF-clad GI POF with ultra-low bending loss," *J. Lightwave Technol.*, vol. 25, pp. 335-345, 2007.

[3] J. Meier, W. Lieber, W. Heinlein and W. Groh "Time-domain bandwidth measurement of step-index plastic fibres," *Electronics Letters*, vol. 22, pp. 1208-1209, 1987.

[4] Olaf Ziemann, J. Krauser, Peter E. Zamzow and Werner Daum, *POF Handbook: Optical Short Range Transmission Systems* 2nd Edition, Springer Berlin Heidelberg, 2008.

[5] T. Ishigure, E. Nihei, S. Yamazaki, K. Kobayashi and Y. Koike, "2.5Gbit/s 100mdata transmission using graded-index polymer optical fiber and high-speed laser diode at 650 nm wavelength,," *Electronics Letters*, vol. 31, pp. 467-468, 1995.

[6] Y. Koike, T. Ishigure, E. Nihei, "High-bandwidth graded-index polymer optical fiber (Invited Paper)," *J. Lightwave Technol.*, vol. 13, pp. 1475-1489, 1995.

[7] W. Li, G. Khoe, H.v.d. Boom, G. Yabre, H. de Waardt, Y. Koike, S. Yamazaki, K. Nakamura and Y. Kawaharada, "2.5 Gbit/s transmission experiment over 200mPMMAgraded index polymer optical fiber using 645 nm narrow spectrum laser and a silicon APD," *Microwave Optic. Technol. Lett.*, vol. 20, pp. 163-166, 1999.

[8] T. Ishigure, H. Endo, K. Ohdoko, and Y. Koike, "High-bandwidth plastic optical fiber with W-refractive index profile," *IEEE Photon. Tech. Lett.*, vol. 16, pp. 2081-2083, 2004.

[9] T. Ishigure, H. Endo, K. Ohdoko, K. Takahashi, and Y. Koike, "Modal bandwidth enhancement in a plastic optical fiber by W-refractive index profile," *J. Lightwave Technol.*, vol. 23, pp. 1754-1762, 2005.

[10] G. Giaretta, W. White, M. Wegmueller, R. V. Yelamarty, and T. Onishi, "11 Gb/s data transmission through 100 m of perfluorinated graded-index polymer optical fiber," *Proc. OFC/IOOC'99, Feb. 1999*, pp. PD14-1-PD14-3, 1999.

[11] I. Tafur Monroy, H. P. A. van den Boom, A. M. J. Koonen, G. D. Khoe, Y. Watanabe, Y. Koike, and T. Ishigure, "Data transmission over polymer optical fibers," *Optical Fiber Technology*, vol. 9, pp. 159-171, 2003.

[12] S. C. J. Lee, F. Breyer, S. Randel, B. Spinnler, I. L. L. Polo, D. Van Den Borne, J. Zeng, E. De Man, H. P. A. Van Den Boom, and A. M. J. Koonen, "10.7 Gbit/s transmission over 220 m polymer optical fiber using maximum likelihood sequence estimation," in *Optical Fiber Communication and the National Fiber Optic Engineers Conference OFC/NFOEC 2007*, 2007.

[13] IEEE Institute of Electrical and Electronics Engineers, http://www.ieee802.org/3/aq, (2006).

[14] D. Marcuse, *Theory of Dielectric Optical Waveguides*, 2nd Edition, Academic Press, 1991.

[15] D. Gloge, "Optical power flow in multimode fibers," *Bell Syst. Tech. J.*, vol. 51, pp. 1767-1783, 1972.

[16] R. Olshansky, "Mode coupling effects in graded-index core fibers," *Appl. Opt.*, vol. 14, pp. 935-945, 1975.

[17] R. Olshansky, D.B. Keck,, "Pulse broadening in graded-index optical fibers," *Appl. Opt.*, vol. 15, pp. 483-491, 1976.

[18] T. Ishigure, E. Nihei, Y. Koike, "Optimum refractive-index profile of the graded-index polymer optical fiber, toward gigabit data links,," *Appl. Opt.*, vol. 35, pp. 2048-2053, 1996.

[19] A. F. Garito, J. Wang, R. Gao, "Effects of random perturbations in plastic optical fibers," *Science*, vol. 281, pp. 962-967, 1998.

[20] S. Louvros and A. C. Iossifides, "Impulse response analysis of graded index polymer optical fiber," *Optical Fiber Technology*, vol. 12, pp. 262-264, 2006.

[21] J. Mateo, M. A. Losada, and J. Zubia, "Frequency response in step index plastic optical fibers obtained from the generalized power flow equation," *Opt. Express*, vol. 17, pp. 2850-2860, 2009.

[22] W. Daum, J. Krauser, P. Zamzow and O. Ziemann, *POF - Polymer Optical Fibers for Data Communication*. Germany: Springer, 2002.

[23] W. Groh, "Overtone absorption in macromolecules for polymer optical fibers," *Makromol. Chem.*, vol. 189, pp. 2861-2874, 1988.

[24] T. Ishigure, E. Nihei, and Y. Koike, "Graded-index polymer optical fiber for high-speed data communication," *Appl. Opt.*, vol. 33, pp. 4261-4266, 1994.

[25] H.P.A. van den Boom, W. Li, P. van Bennekom, I. T. Monroy and G. D. Khoe, "High capacity transmission over polymer optical fiber," *IEEE J. Sel. Top. Quant.* , vol. 7, pp. 461-470, 2001.

[26] E. Nihei, T. Ishigure, N. Tanio, and Y. Koikei, "Present prospect of graded-lndex plastic optical fiber in telecommunication," *IEICE Transactions on Electronics*, vol. E80-C, pp. 117-121, 1997.

[27] N. Tanio and Y. Koike, "What is the most transparent polymer?," *Polym. J.*, vol. 32, pp. 119-125, 2000.

[28] A. Appajaiah, "Climatic Stability of Polymer Optical Fibers (POF)," in *Mathematisch-Naturwissenschaftlichen Fakultät der Universität Potsdam* Potsdam, 16 August 2004.

[29] C.L. Chen, *Elements of optoelectronics and fiber optics*, Irwin, 1996.

[30] T. Ishigure, S. Tanaka, E. Kobayashi, and Y. Koike, "Accurate refractive index profiling in a graded-index plastic optical fiber exceeding gigabit transmission rates," *J. Lightwave Technol.*, vol. 20, pp. 1449-1456, 2002.

[31] T. Ishigure, Y. Koike, J.W. Fleming, "Optimum index profile of the perfluorinated polymer-based GI polymer optical fiber and its dispersion properties," *J. Lightwave Technol.*, vol. 18, pp. 178-184, 2000.

[32] Y. Koike, "High-bandwidth graded index polymer optical fiber," *J. Lightwave Technol.*, vol. 13, pp. 475-489, 1995.

[33] Y. Koike, "High-bandwidth graded-index polymer optical fibre," *Polymer*, vol. 32, pp. 1737-1745, 1991.

[34] T. Ishigure, A. Horibe, E. Nihei, and Y. Koike, "High-bandwidth, high-numerical aperture graded-index polymer optical fiber," *J. Lightwave Technol.*, vol. 13, pp. 1686-1691, 1995.

[35] N. Yoshiyuki, "Performance of Perfluorinated POF," in *International Conference on Plastic Optical Fibers (POF'1997)*, Kauai, pp. 27-28, 1997.

[36] H. Imai, "Applications of Perfluorinated Polymer Optical Fibers to Optical Transmission," in *International Conference on Plastic Optical Fibers (POF'1997)*, Kauai, pp. 29-30, 1997.

[37] H. Takahashi, T. Kanazawa, E. Ito, "Fabrication techniques of GI-POF toward mass production," in *International Conference on Plastic Optical Fibers (POF'1998)*, Berlin, Germany, pp. 50-54, 1998.

[38] W. Li, G.D. Khoe, H. P. A. v. d. Boom, G. Yabre, H. de Waardt, Y. Koike, M. Naritomi, N. Yoshihara, "Record 2.5 Gbit/s 550 m GI POF transmission experiments at 840 and 1310 nm wavelength," in *International Conference on Plastic optical Fibers (POF'1999)*, Chiba, pp. 60-63, 1999.

[39] G. Giaretta, W. White, M. Wegmuller, and T. Onishi, "High-speed (11 Gbit/s) data transmission using perfluorinated graded-index polymer optical fibers for short interconnects (<100 m)," *IEEE Photon. Technol. Lett.*, vol. 12, pp. 347-349, 2000.

[40] K. Kogenazawa, T. Onishi, "Progress in Perfluorinated GI-POF LUCINA™," in *International Conference on Plastic Optical Fibers (POF'2000)*, Boston, USA, pp. 19-21, 2000.

[41] H. P. A. van den Boom, T. Onishi, T. Tsukamoto, P. K. van Bennekom, L. J. P. Niessen, G. D. Khoe, A. M. J. Koonen, "Gigabit Ethernet Transmission over nearly 1 km GIPOF using an 840 nm VCSEL and a Silicon APD," in *International Conference on Plastic Optical Fibers (POF'2001)*, Amsterdam, Netherlands, pp. 207-212, 2001.

[42] B.G. Shin, J.H. Park, J.J. Kim, "Graded-Index Plastic Optical Fiber Fabrication by the Centrifugal Deposition Method " in *International Conference on Plastic Optical Fibers (POF'2002)*, Tokyo, Japan, 2002, pp. 57-59, 2002.

[43] T. Ishigure, K. Makino, S. Tanaka, and Y. Koike, "High-Bandwidth Graded-Index Polymer Optical Fiber Enabling Power Penalty-Free Gigabit Data Transmission," *J. Lightwave Technol.*, vol. 21, pp. 2923-2930, 2003.

[44] J. Goudeau, G. Widawski, M. Rossbach, B. Bareel, R. Helvenstein, L. Huff, "GI POF for Gb Ethernet links (Invited paper)," in *International Conference on Plastic Optical Fibers (POF'2004)*, Nuremberg, Germany, 2004, pp. 76-81, 2004.

[45] W. R. White, L. L. Blyler, Jr., R. Ratnagiri, and M. Park, "Manufacture of perfluorinated plastic optical fibers," in *Optical Fiber Communication Conference, 2004 OFC 2004*, p. 3 pp. vol.2, 2004.

[46] H. E. T. Ishigure, K. Takahashi, Y. Koike, "Total dispersion compenzation design of POF (Invited paper)," in *International Conference on Plastic Optical Fibers (POF'2004)*, Nuremberg, Germany, pp. 179-186, 2004.

[47] D. DuToit, "Perfluorinated Graded-Index POF," in *Optical Fiber Communication Conference OFC2007*, Anaheim, 2007.

[48] A. Polley, R. J. Gandhi, and S. E. Ralph, "40Gbps links using plastic optical fiber," in *Optical Fiber Communication and the National Fiber Optic Engineers Conference, 2007, OFC/NFOEC 2007. Conference on*, pp. 1-3, 2007.

[49] A. Polley, "High Performance Multimode Fiber Systems: A Comprehensive Approach." vol. Thesis: Georgia Institute of Technology, December 2008.

[50] K. Koike, T. Kado, Z. Satoh, Y. Okamoto, and Y. Koike, "Optical and thermal properties of methyl methacrylate and pentafluorophenyl methacrylate copolymer: Design of copolymers for low-loss optical fibers for gigabit in-home communications," *Polymer*, vol. 51, pp. 1377-1385, 2010.

[51] D. Visani, C. M. Okonkwo, S. Loquai, H. Yang, Y. Shi, H. P. A. van den Boom, A. M. H. Ditewig, G. Tartarini, B. Schmauss, S. Randel, A. M. J. Koonen, and E. Tangdiongga, "Record 5.3 Gbit/s transmission over 50m 1mm core diameter graded-index plastic optical fiber," in *Conference on Optical Fiber Communication (OFC), collocated National Fiber Optic Engineers Conference (OFC/NFOEC)*, pp. 1-3, 2010.

[52] H. Yang, S. C. J. Lee, E. Tangdiongga, C. Okonkwo, H. P. A. van den Boom, F. Breyer, S. Randel, and A. M. J. Koonen, "47.4 Gb/s Transmission Over 100 m Graded-Index Plastic Optical Fiber Based on Rate-Adaptive Discrete Multitone Modulation," *J. Lightwave Technol.*, vol. 28, pp. 352-359.

[53] C. Lethien, C. Loyez, J. P. Vilcot, and A. Goffin, "Differential mode delay measurements of fluorinated graded index polymer optical fiber," *IEEE Photon. Techn. Lett.*, vol. 20, pp. 1584-1586, 2008.

[54] S. E. Golowich, W. White, W. A. Reed, and E. Knudsen, "Quantitative estimates of mode coupling and differential modal attenuation in perfluorinated graded-index plastic optical fiber," *J. Lightwave Technol.*, vol. 21, pp. 111-121, 2003.

[55] G. Yabre, "Theoretical investigation on the dispersion of graded-index polymer optical fibers," *J. Lightwave Technol.*, vol. 18, pp. 869-877, 2000.

[56] M. C. J. Large, M. A. van Eijkelenborg, A. Argyros, J. Zagari, S. Manos, N. A. Issa, I. Bassett, and S. Fleming, "Single-mode microstructured polymer optical fibre," in *Optical Fiber Communication Conference and Exhibit, 2002 OFC 2002*, pp. 527-528, 2002.

[57] W. R. White, M. Dueser, W. A. Reed, and T. Onishi, "Intermodal dispersion and mode coupling in perfluorinated graded-index plastic optical fiber," *IEEE Photon. Tech. Lett.*, vol. 11, pp. 997-999, 1999.

[58] R. F. Shi, C. Koeppen, G. Jiang, J. Wang, and A. F. Garito, "Origin of high bandwidth performance of graded-index plastic optical fibers," *Applied Physics Letters*, vol. 71, pp. 3625-3627, 1997.

[59] D. Gloge, "Dispersion in Weakly Guiding Fibers," *Appl. Opt.*, vol. 10, pp. 2442-2445, 1971.

[60] A. Bhatti, H.S. Al-Raweshidy, G. Murtaza, "Finite element analysis of an optical fibre electric field sensor using piezoelectric polymer coating," *Journal of Modern Optics*, vol. 47, pp. 621-632, 2000.

[61] Y. E. Liu, B.M.A. Rahman, Y. N. Ning, K. T. V. Grattan, "Accurate Mode Characterization of Graded-Index Multimode Fibers for the Application of Mode-Noise Analysis," *Appl. Opt.*, vol. 34, pp. 1540-1543, 1995.

[62] J.B. Xiao, X.H. Sun, "A Modified full-vectorial finite-difference beam propagation method based on H-fields for optical waveguides with step-index profiles," *Optics Communications*, vol. 266, pp. 505-511, 2006.

[63] W. P. Huang, C.L. Xu, "Simulation of 3-Dimensional Optical Wave-Guides by a Full-Vector Beam-Propagation Method," *IEEE J. Quantum Electron.*, vol. 29, pp. 2639-2649, 1993.

[64] K. Ohdoko, T. Ishigure, and Y. Koike, "Propagating mode analysis and design of waveguide parameters of GI POF for very short-reach network use," *IEEE Photon. Tech. Lett.*, vol. 17, pp. 79-81, 2005.

[65] D. Gloge, "Impulse response of Clad Optical Multimode Fiber," *Bell Syst. Tech. J.*, vol. 52, pp. 801-815, 1973.

[66] E. A. J. Marcatili, "Modal Dispersion in Optical Fibers with Arbitrary Numerical Aperture and Profile Dispersion," *Bell Syst. Tech. J.*, vol. 6, pp. 49-63, 1977.

[67] W. Tschekalinskij, E. Pokrovskaya, N. Weber, S. Junger, "Field-theoretical approach for modeling frequency response of polymer step-index fiber," in *13th International Conference on Plastic Optical Fibers*, Nürnberg, Germany, pp. 203-209, 2004.

[68] J. Zubia, H. Poisel, C.A. Bunge, G. Aldabaldetreku, J. Arrue, "POF Modelling," in *International Conference on Plastic Optical Fiber POF2002*, Tokyo, Japan, pp. 221-224, 2002.

[69] G. Durana, G. Aldabaldetreku, J. Arrue, F. Jiménez, H. Poisel, J. Zubia, "Measurement and simulation of Coupling Losses in Multi-Step Optical Fibres " in *13th International Conference on Plastic Optical Fibers*, Nürnberg, Germany, pp. 217-224, 2004.

[70] M. Borecki, "Light behaviour in polymer optical fibre bend - a new analysis method," *Optica Applicata*, vol. 33, pp. 191-204, 2003.

[71] S. Savovic and A. Djordjevich, "Mode coupling in strained and unstrained step-index plastic optical fibers," *Appl. Opt.*, vol. 45, pp. 6775-6780, 2006.

[72] V. Ruddy and G. Shaw, "Mode coupling in large-diameter polymer-clad silica fibers," *Appl. Opt.*, vol. 34, pp. 1003-1006, 1995.

[73] S. Takahashi, "Experimental studies on launching conditions in evaluating transmission characteristics of POFs," in *Proc. Plastic Optical Fiber (POF)*, The Hague, The Netherlands, pp. 83-85, 1993.

[74] T. Ishigure, M. Kano, and Y. Koike, "Which is a more serious factor to the bandwidth of GI POF: Differential mode attenuation or mode coupling?," *J. Lightwave Technol.*, vol. 18, pp. 959-965, 2000.

[75] B. Çamak, "Modeling of Rayleigh Scattering in Optical Waveguides." vol. Master Thesis Ankara, Türkei: Middle East Technical University, 2003.

[76] C.A. Bunge, G. Kramer, H. Poisel, "Measurement of refractive-index profile by lateral illumination," in *International Conference on Plastic Optical Fibres POF'2004*, Nuremberg, Germany, pp. 513-520, 2004.

[77] M. Calzavara, R. Caponi, F. Cisternino, G. Coppa, "A New Approach to Investigating Mode-Coupling Phenomena in Graded-Index Optical Fibers," *Optical and Quantum Electronics*, vol. 17, pp. 157-167, 1985.

[78] G. Cancellieri, "Mode-Coupling in Graded-Index Optical Fibers Due to Perturbation of the Index Profile," *Applied Physics*, vol. 23, pp. 99-105, 1980.

[79] G. Cancellieri, "Mode-Coupling in Graded-Index Optical Fibers Due to Micro-Bending," *Applied Physics and Materials Science & Processing*, vol. 26, pp. 51-57, 1981.

[80] L. Su, K. S. Chiang, and C. Lu, "Microbend-induced mode coupling in a graded-index multimode fiber," *Appl. Opt.*, vol. 44, pp. 7394-7402, 2005.

[81] A. Hardy, "Exact Derivation of the Coupling Coefficient in Corrugated Wave-Guides with Arbitrary Cross-Section - Application to Optical Fibers," *IEEE J. Quantum Electron.*, vol. 31, pp. 505-511, 1995.

[82] A. Djordjevich and S. Savovic, "Investigation of mode coupling in step index plastic optical fibers using the power flow equation," *IEEE Photon. Tech. Lett.*, vol. 12, pp. 1489-1491, 2000.

[83] A. Djordjevich and S. Savovic, "Numerical solution of the power flow equation in step-index plastic optical fibers," *J. Opt. Soc. Am. B-Optical Physics*, vol. 21, pp. 1437-1442, 2004.

[84] M. S. Kovacevic, D. Nikezic, and A. Djordjevich, "Modeling of the loss and mode coupling due to an irregular core-cladding interface in step-index plastic optical fibers," *Appl. Opt.*, vol. 44, pp. 3898-3903, 2005.

[85] M. Ohashi, K. Kitayama, S. Seikai, "Mode-Coupling Effects in a Graded-Index Fiber Cable," *Appl. Opt.*, vol. 20, pp. 2433-2438, 1981.

[86] K. Kitayama, S. Sikai, N. Uchida, "Impulse-Response Prediction Based on Experimental Mode-Coupling Coefficient in a 10-Km Long Graded-Index Fiber," *IEEE J. Quantum Electron.*, vol. 16, pp. 356-362, 1980.

[87] T. Ishigure, K. Ohdoko, Y. Ishiyama, and Y. Koike, "Mode-coupling control and new index profile of GI POF for restricted-launch condition in very-short-reach networks," *J. Lightwave Technol.*, vol. 23, pp. 4155-4168, 2005.

[88] D. Donlagic, "Opportunities to enhance multimode fiber links by application of overfilled launch," *J. Lightwave Technol.*, vol. 23, pp. 3526-3540, 2005.

[89] R. Olshansky and S. M. Oaks, "Differential mode attenuation measurements in graded-index fibers," *Appl. Opt.*, vol. 17, pp. 1830-1835, 1978.

[90] R. Olshansky and D. A. Nolan, "Mode dependent attenuation in parabolic optical fibers," *Appl. Opt.*, vol. 16, pp. 1639-1641, 1977.

[91] R. Olshansky and D.A. Nolan, "Mode-dependent attenuation of optical fibers: Excess Loss," *Appl. Opt.*, vol. 15, pp. 1045-1047, 1976.

[92] S. Louvros, A. C. Iossifides, G. Economou, G. K. Karagiannidis, S. A. Kotsopoulos, and D. Zevgolis, "Time Domain Modeling and Characterization of Polymer Optical Fibers," *IEEE Photon. Tech. Lett.*, vol. 16, pp. 455-457, 2004.

[93] A. R. Mickelson, M. Eriksrud, "Mode-dependent attenuation in optical fibers," *J. Opt. Soc. Am.*, vol. 73, pp. 1282-1290, 1983.

[94] I. L. Fraile, "Análisis de enlaces de fibra óptica multimodo con tecnología radio sobre fibra para aplicaciones en el hogar," in *Dpto. de Tecnología Electrónica, Universidad Carlos III de Madrid*. vol. Final Degree Project, Junio de 2008.

[95] G. Yabre, "Comprehensive Theory of Dispersion in Graded-Index Optical Fibers," *J. Lightwave Technol.*, vol. 18, pp. 166-177, 2000.

[96] H. M. Presby and I.P. Kaminow, "Binary silica optical fibers: refractive index and profile dispersion measurements," *Appl. Opt.*, vol. 15, pp. 469-470, 1976.

[97] A. R. Mickelson and M. Eriksrud, "Mode-continuum approximation in optical fibers," *Opt. Lett.*, vol. 7, pp. 573-574, 1982.

[98] S. D. Personick, "Baseband linearity and equalization in fiber optic digital communication systems," *Bell Syst. Tech. J.*, vol. 52, pp. 1175-1195, 1973.

[99] T.P. Lee, C.A. Burrus, D. Marcuse, A.G. Dentai and R.J. Nelson, "Measurement of beam parameters of index-guided and gain-guided single-frequency InGaAsP injection lasers," *Electronics Letters*, vol. 1, pp. 902-904, 1982.

[100] E. G. Neumann, *Single-Mode Fibers*. Berlin, Heidelberg, Germany: Springer-verlag, 1988.

[101] D. Gloge, "Impulse response of Clad Optical Multimode Fibers," *Bell Syst. Tech. J.*, vol. 52, pp. 801-815, 1973.

[102] M. Rousseau and L. Jeunhomme, "Numerical solution of the coupledpower equation in step-index optical fibers," *IEEE Trans. Microwave Theory Tech.*, vol. MTT-25, pp. 577-585, 1977.

[103] T. P. Tanaka and S. Yamada, "Numerical solution of power flow in multimode W-type optical fibers," *Appl. Opt.*, vol. 19, pp. 1647-1652, 1980.

[104] M. Rousseau and L. Jeunhomme, "Optimum index profile in multimode optical fiber with respect to mode coupling " *Opt. Commun.*, vol. 23, pp. 275-278, 1977.

[105] R. Olshansky and D. A. Nolan, "Mode-dependent attenuation of optical fibers: Excess loss," *Appl. Opt.*, vol. 15, pp. 1045-1047, 1976.

[106] M. J. Yadlowsky and A. R. Mickelson, "Distributed loss and their effects on time-dependent propagation in multimode fibers," *Appl. Opt.*, vol. 32, pp. 6664-6678, 1993.

[107] D. Gloge, "Weakly guiding fibers," *Appl. Opt.*, vol. 10, pp. 2252-2258, 1971.

[108] J. Saijonmaa, A.B. Sharma, and S. J. Halme, "Selective excitation of parabolic-index optical fibers by Gaussian beams," *Appl. Opt.*, vol. 19, pp. 2442-2433, 1980.

[109] J. Saijonmaa and S. J. Halme, "Reduction of modal noise by using reduced spot excitation," *Appl. Opt.*, vol. 20, pp. 4302-4306, 1981.

[110] D. Marcuse, *Light Transmission Optics*. New York: Van Nostrand Reinhold, 1972.

[111] T. Ishigure and Y. Koike, "POF is overcoming silica in bit rate," in *Optical Fiber Communication Conference and Exhibit, OFC2001*, 2001, p. paper ThC7.

[112] G. Yabre, "Influence of core diameter on the 3-dB bandwidth of graded-index optical fibers," J. *Lightwave Technol.*, vol. 18, pp. 668-676, 2000.

[113] Y. Koike and T. Ishigure, "Status and challenges of GI POF in data-com. area," in *27th European Conference on Optical Communication, 2001. ECOC '01*, pp. 72-73 vol.1, 2001.

[114] T. Ishigure, M. Sato, A. Kondo, and Y. Koike, "High-bandwidth graded-index polymer optical fiber with high-temperature stability," *J. Lightwave Technol.*, vol. 20, pp. 1443-1448, 2002.

[115] F.W. Scholl, M.H. Coden, S.J. Anderson and B.V. Dutt, "Applications of Plastic Optical Fiber to LANs," in *Proc. Soc. Photo-Opt. Instrum. Eng.*, 1988, p. 190.

[116] G. C. Papen and G. M. Murphy, "Modal noise in multimode fibers under restricted launch conditions," *J. Lightwave Technol.*, vol. 17, pp. 817-822, 1999.

[117] T. Kanada, "Evaluation of modal noise in multimode fiber-optic systems," *J. Lightwave Technol.*, vol. 2, pp. 11-18, 1984.

[118] T. Ishigure, E. Nihei, and Y. Koike, "High-bandwidth, low-loss graded-index polymer optical fiber for near infrared use," in *European Conference on Optical Communication, ECOC*, 1998, pp. 231-232.

[119] L. Raddatz and I. H. White, "Overcoming the modal bandwidth limitation of multimode fiber by using passband modulation," *IEEE Photon. Tech. Lett.*, vol. 11, pp. 266-268, 1999.

[120] E. J. Tyler, M. Webster, R. V. Penty, I. H. White, S. Yu, and J. Rorison, "Subcarrier modulated transmission of 2.5 Gb/s over 300 m of 62.5µm-core diameter multimode fiber," *IEEE Photon. Tech. Lett.*, vol. 14, pp. 1743-1745, 2002.

[121] I. Gasulla and J. Capmany, "Transmission of high-frequency radio over fibre signals through short and middle reach Multimode Fibre links using a low-linewidth laser," in *IEEE International Topical Meeting on Microwave Photonics, 2007*, pp. 116-119, 2007.

[122] M. Sato, T. Ishigure, and Y. Koike, "Thermally stable high-bandwidth graded-index polymer optical fiber," *J. Lightwave Technol.*, vol. 18, pp. 952-958, 2000.

[123] M. Sato, M. Hirai, T. Ishigure, and Y. Koike, "High temperature resistant graded-index polymer optical fiber," *J. Lightwave Technol.*, vol. 18, pp. 2139-2145, 2000.

[124] T. Ishigure, M. Sato, A. Kondo, Y. Tsukimori, and Y. Koike, "Graded-index polymer optical fiber with high temperature and high humidity stability," *J. Lightwave Technol.*, vol. 20, pp. 1818-1825, 2002.

[125] L. Asahi Glass Co., "CYTOP Technical Bulletin," 1990.

Chapter 4

SILICA-BASED MULTIMODE OPTICAL FIBRE TRANSFER FUNCTION.

4.1 Introduction

The growing demand in data transmission, raised in particular by the Internet, will require the use of optical fibres as transmission media instead of coaxial cables, even at short distances. Coaxial cables are extremely lossy, susceptible to electromagnetic interference (EMI) and show a dramatic limitation in their capacity for digital transmission. On the other hand, optical fibres show a very low attenuation, a great potential for high-speed transmission and a complete immunity to EMI. This is true for singlemode fibres but also for the multimode versions, so either type of fibres can be employed in replacement of the metallic cables. However, more attention is being given to multimode fibres (MMFs) rather than singlemode fibres (SMFs) for use in local area networks (LANs). Multimode fibres are easier to fabricate, to connect and to manipulate because their large dimensions impose less stringent requirements on cabling, connecting, splicing and handling compared to the singlemode version. Moreover, the large core region of multimode fibres added to their large numerical aperture allows for efficient light coupling from semiconductor lasers, which offers large mechanical tolerances in transceivers development. It is clear that in the short-and middle-reach applications where many junctions and connections between adjacent sections are often necessary, the multimode version is the most appropriated in consideration of the whole system cost. In addition to this, it is worth mentioning that the majority of the installed fibre cable, five out of six, corresponds to multimode fibre as recommended by the ISO/IEC 802.11 standard, as Fig. 4.1 depicts [1]. Furthermore, in short- and middle-reach scenarios this ratio increases up to approximately between an 85% and a 90%. So there is recently an important drive to utilize this existing infrastructure to support the ever increasing capacity demand on high-speed services.

Despite the above advantages, the use of multimode fibres has been resisted for some years by fibre-optic link designers in favour of their singlemode counterparts since Epworth discovered the potentially catastrophic problem of modal noise [2]. Modal noise in laser-based MMF links has been recently more completely addressed and theoretical as well as experimental proofs have shown that long-wavelength operation of MMFs is robust to modal noise [3]. This explains the spectacular regain of interest for MMFs as the best solution for the cabling of LANs. The question that needs answer now in view of increasing the usefulness of multimode fibres concerns the improvement of their dispersion characteristics, which is related to their reduced bandwidth. Because MMFs propagate a large number of modes having different velocities, they produce a signal response inferior to that of singlemode fibres. For standard 62.5/125μm MMFs, the minimum bandwidths are

only specified to be 200MHz·km and 500MHz·km (up to 800MHz·km) in the 850nm and 1300nm transmission windows, respectively, under OverFilled Launch (OFL) condition, see ISO/IEC (International Standards Organization/International Electrotechnical Commission) 11801-"Generic cabling for customer premises". Even though these specifications do satisfy the information rate of many classical short-range links, it is clear that a 2km-long campus backbone cannot be realized for operation at the speed of Gigabit Ethernet. The restricted bandwidth of the silica-based multimode fibre has been one of the main causes that makes the specification and designing of the physical media dependent portions very difficult. In order to cover the conventional multimode fibre having a restricted bandwidth in the physical media dependent of Gigabit Ethernet standard the control of the launching condition, for instance, has been proposed as a bandwidth improvement method [4, 5]. Until novel multiplexing techniques become available and inexpensive, the potential MMF capacity for digital communication needs a greater exploitation to meet user requirements for higher data rates and to support emerging multimedia applications. To enable the design and utilization of MMFs with such enhanced speeds, the development of an accurate frequency response model is of prime importance. Through the dispersion modelling more likely performance limits can be established, thereby preventing eventual overdesign of systems and the resulting additional cost.

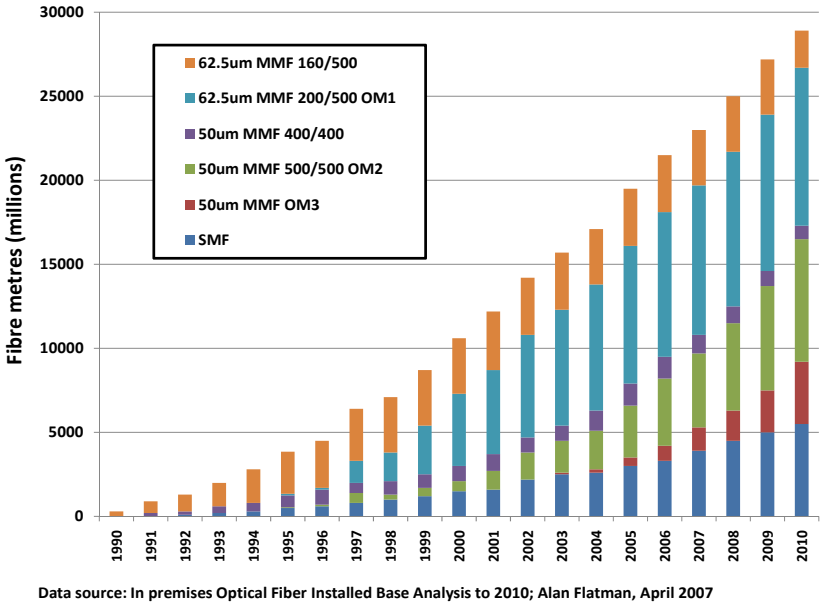

Figure 4.1.- Existing fibre infrastructure [1].

Traditionally, multimode fibres were made from silica. However, more recently Polymer Optical Fibres (POFs) have also emerged on the scene, promising increased ease of handling and reduced installation costs owing to the more ductile material and larger core size [6-8]. Anyway, both silica- and/or polymer-based multimode optical fibres offer the physical infrastructure to create a fusion and convergence to the access network for next-generation access services. This fact has been previously addressed in Chapter 2 of this document. However, in the case of POF, the higher-than-silica attenuation (> 10 dB/km) also inhibits their use in long link applications [7]. The potentials of MMFs to support broadband RF, microwave and millimetre wave transmission over short, intermediate and

long distances are yet to be fully known. This in turn is contingent on the availability of accurate models to describe the signal propagation through multimode fibres.

Since the mid-1970's, much work has been directed to the investigation of MMFs and their ability for high speed transmission. So far, different factors have clearly been identified to influence the information-carrying capacity, namely the material dispersion (in combination with the spectrum of the exciting source) [9-11], the launching conditions [12, 13] as well as the mode-dependent characteristics (i.e. delay [9], attenuation [14] and coupling coefficient [14-16]). Unfortunately, the achievements, so far accomplished, are not quite complete to enable precise frequency response and bandwidth prediction if an arbitrary operating condition is to be considered.

As previously pointed out, the interest in MMFs has revitalised due to several reasons. On one hand, MMF fibres can be employed to support high speed digital connections such as those required by GbE applications, if these links are complemented with low cost electronic equalizing circuits [17, 18]. Secondly, it has been recently found that the MMF bandwidth capability over short-reach distances can be expanded by means of different techniques (a description of some of the following, most commonly reported, was further addressed in Chapter 2), such as mode group diversity multiplexing [19-23], optical frequency multiplication [20], orthogonal frequency division multiplexing (OFDM) [24], subcarrier multiplexing (SCM) [19, 25, 26], wavelength division multiplexing (WDM) [27], and even a combination of SCM and WDM [28]. In addition, it should be noted that some of these techniques provide the possibility of short-reach transmission in Radio-over-Fibre (RoF) applications, such as in-building/house transmission of millimetre signals [29], and wireless access systems [30]. Lately as well, a particular way of exploiting the capacity of MMFs by the application of MIMO (Multiple Input Multiple Output) techniques has garnered significant research interest [31].

The most popular technique reported so far for the analysis of signal propagation through MMF fibres is that based on the coupled power-flow equations developed by Gloge [32] in the early 70's and later improved by Olshansky [16] and Marcuse [33], to account for the propagation and time spreading of digital pulses through MMFs. Most of the published models and subsequent work on the modelling of MMFs, [14, 15, 34-43], are based on this method in which the MMF power transfer function is solved by means of a numerical procedure like the Crank-Nicholson method [34, 37, 40], for instance. However, other methods rely on solving the system of coupled equations adopting the matrix formalism [44].

The power-flow equations are adequate for the description of digital pulse propagation through MMFs but present several limitations either when considering the propagation of analogue signals or when a detailed knowledge of the baseband and RF transfer function is required since in these situations the effect of the signal phase is important. To overcome these limitations it is necessary to employ a method relying on the propagation of electric field signals rather than optical power signals. Unfortunately, there are very few of such descriptions available in the literature with the exception of that developed by Saleh and Abdula for digital pulse propagation [45] and by Gasulla and Capmany in [46].

Previously to present a closed-form analytic expression to compute the baseband and RF transfer function of a MMF link based on the electric field propagation method, the impact of parameters appearing in silica MMFs such as fibre dispersion, mode coupling, differential mode attenuation (DMA) or modal noise are briefly studied.

4.2 Transmission in silica-based Multimode Optical Fibres

State-of-the art of MMF has specified bandwidths (measured under OFL conditions) of about 800 MHz·km for silica GI-MMFs. This bandwidth relates to the 3-dB (or baseband) bandwidth, and clearly, it is insufficient to meet the increasing demand for high-speed LAN applications, including Gigabit Ethernet for reasonable distances. For this reason, there is a lot of research looking into ways and means of increasing the capacity of MMFs [47-49]. Novel techniques to expand the MMF capabilities are continuously reported as those above mentioned, such as mode group diversity multiplexing, OFM, OFDM, SCM, WDM or SCM/WDM.

Nevertheless, it has been stated that the frequency response of MMF does not diminish monotonically to zero after the 3-dB bandwidth (the baseband bandwidth), but tends to have repeated passbands beyond that [46, 50]. In recent times, these high order passbands have been used in research to transmit independent streams of data (digital or analogue) in addition to the baseband bandwidth [12, 50, 51]. Therefore, in this way, the aggregated transmission capacity of MMF may exceed its baseband bandwidth. A similar conclusion was reported in Chapter 3, regarding PF graded-index polymer optical fibres.

Moreover, it is a current trend that the OFL condition is not necessarily a suitable launch condition for an MMF when an application to short-reach, high-speed network is considered [52]. Thus, another way to increase the capacity of MMFs is to use the Restricted Mode Launching, RML, (or so-called Under-Filled Launch, UFL) condition. It consists in reducing the number of modes propagated through the fibre by means of practical mode-filtering implementations at the transmitter and/or receiver [13, 53, 54]. The transmitter side mode-filtering is performed by exciting a limited number of lower modes in the MMFs and thus coupling only a small portion of the total power into the rest of the transmitted modes. This can be implemented for example, as seen in Chapter 3, by directly butt-coupling a singlemode fibre patch cord with the MMF. This fact concentrates most of the energy in the axial core region and reduces the amount of energy in the higher order modes. Since the propagating modes are fewer under RML launch conditions, the difference in propagating times between the fastest and slowest modes is smaller. Thus, modal dispersion is reduced, and the bandwidth increased. On the other hand, the mode-filtering at the receiver side consists in recovering the lower order propagated modes which implies some signal energy loss. The problem with both approaches is that the fibre performance may be unstable as it is strongly linked to the actual launch conditions [47]. Furthermore, fibre performance is also affected by environmental and mechanical factors, and by other factors including mode coupling, modal noise, and differential mode attenuation (DMA) [55-58].

The following table, Table 4.1, shows some data rate achievements concerning MMFs reported in literature. In the remarks is included some extra information of the referred experiments such as the use of equalizing techniques at reception, or whichever applied technique to expand the tranmission capability of the MMF link.

Year	Data rate	Distance (km)	Technique	λ (nm)	Remarks[1]	Ref.
1998	4x2.5Gbps	0.1	CWDM	820-865	VCSEL	[59]
1999	10Gbps	1.6	--	850	VCSEL	[60]
2000	4x10Gbps	0.31	CWDM	815-835	4 VCSEL channels	[61]
2001	15.6Gbps	1	--	850	VCSEL	[62]
2002	0.6Tbps	1	WDM	C-band	DWDM, QPSK	[63]
2006	40Gbps	3.4	WDM	1551.72	50μm core diameter MMF	[64]
2007	10Gps	0.3	--	1300	SCM	[65]
2007	24Gbps	0.73	--	850	VCSEL, Discrete Multi-tone modulation	[66]
2007	10x10Gbps	2.2	WDM	1300	DWDM, adaptative optics	[67]
2007	2.5Gbps	2.2	--	1500	VCSEL, hybrid SMF-MMF	[68]
2007	1.25Gbps	4.4	SCM	1310	M-QAM modulation	[69]
2007	40Gbps	3.7	--	1300	Mode-field matched center launching and mode-filtering at receiver	[54]
2008	10x20Gbps	5	WDM	C-band	DWDM, highest overall MMF data rate of 1Tbps·km	[70]
2009	16x10Gbps	12.2	WDM	C-band	Mode-field matched center launching DWDM, highest overall MMF data rate of 1.95Tbps·km	[71]

Table 4.1.- A review of published data of silica MMFs.

From the experiments shown in Table 4.1, for achieving the high bit rate transmission even by the legacy MMFs, a restricted launch condition is proposed and mainly utilized [72, 73]. Actually, the under-filled launch (UFL) o restricted-mode launching (RML) condition enables the silica-based MMF to transmit at tens of Gbps data rate for units of kilometres of distance.

[1] DWDM: Dense Wavelength Division Multiplexing; CWDM: Coarse Wavelength Division Multiplexing; QPSK: Quadrature Phase-Shift Keying; C-band:1530-1565nm; SCM: Subcarrier Multiplexing; VCSEL: Vertical-Cavity Surface-Emitting Laser; QAM: Quadrature Amplitude Modulation;

4.3 Dispersion in silica-based Multimode Optical Fibres

Silica-based multimode fibres (MMFs) follow the same dispersion mechanisms, as stated in Fig. 3.4 of Chapter 3 referring GIPOFs, regarding the impact of the fibre dispersion on the frequency response and the 3-dB baseband bandwidth.

On the one hand, chromatic dispersion refers to the wavelength-dependent pulse spreading that occurs as the optical signal propagates along the fibre. The end result is that different spectral components arrive at slightly different times, leading to wavelength-dependent pulse spreading (that means dispersion). There are two contributing factors to chromatic dispersion. The first one is the dependence of the fibre material's refractive index on the wavelength; referred to as material dispersion. The second factor is the waveguide dispersion, which is caused by the fact that light waves penetrate into the fibre cladding to various depths, depending on the wavelength of the light wave. Thus, the different speeds of the core and cladding parts result in pulse broadening. Since only a small portion of the light wave in higher modes of large diameter fibres spreads into the cladding, this effect is only considered for singlemode fibres. The pulse spreading due to chromatic dispersion is given, as in POFs, by Eq. 3.1. As a matter of fact, the broader the spectral width of the optical source is the greater the chromatic dispersion.

Similarly as the case of GIPOFs and considering a typical graded index silica-based multimode optical fibre with a SiO_2 core doped with 6.3 mol-% GeO_2 and a SiO_2 cladding, the refractive indices for the core and cladding can be calculated using a three-term Sellmeier function, given by Eq. 3.7. Sellmeier coefficients were provided by the manufacturer. So, the material dispersion as a function of the operating wavelength can be calculated. Fig. 4.2 depicts the material dispersion of a silica-based MMF with the above material characteristics. Also in the figure, the material dispersion of the commercial PF GIPOF used in Chapter 3 is plotted, for comparison. It is clearly seen the better performance in terms of material dispersion of the PF GIPOF compared to the silica-based counterpart, as expected.

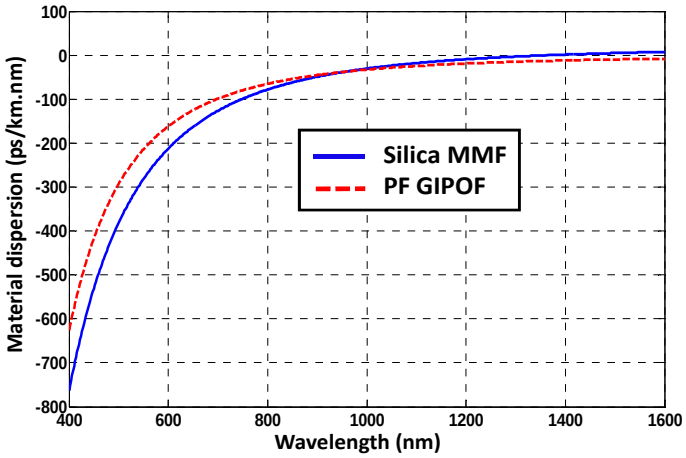

Figure 4.2. Material dispersion of the central core region for the silica-based MMF, as a function of the operating wavelength (blue solid line). Red dashed line represents the PF GIPOF material dispersion calculated from Chapter 3.

Furthermore, for silica fibres the material dispersion, $D(\lambda)$, may usually be approximated by the Sellmeier equation [74], being the standard info given by vendors:

$$D(\lambda) = \frac{S_O}{4}\left[\lambda - \frac{\lambda_o^4}{\lambda^3}\right] \tag{4.1}$$

where S_O is the zero dispersion slope, and λ_o is the zero-dispersion wavelength, which occurs around 1300nm. Typical $D(\lambda)$ values of silica fibres, calculated by this last method, are around -3 ps/nm·km and +17 ps/nm·km at 1310nm and 1550nm respectively [74]. In the case plotted in Fig. 4.2 results show $D(1300\text{nm}) = -2.8\text{ps/nm}\cdot\text{km}$ and $D(1550\text{nm}) = +7\text{ps/nm}\cdot\text{km}$, respectively, which are also in the same range.

It has been stated that chromatic dispersion is caused by the wavelength-dependent propagation times of the different spectral components which mean that the group delay time is different versus optical frequency. Relative to signal transmission, this fact causes that the upper and lower sidebands of a tone are phase-shifted one with regards to the other as the optical signal travels along a dispersive waveguide (i.e. optical fibre). When the value of this relative phase shift is 180 degrees, a fading of the tone takes place. This RF-fading [75], at a certain frequency and lengths of the optical fibre, corresponds to the Carrier Suppression Effect (CSE), widely known in singlemode fibre analogue links. The frequency of these nulls in transmission is given by:

$$\Omega_k = \sqrt{(2k+1)\pi \Big/ \beta_o^2 z} \tag{4.2}$$

being β_o^2 the second derivative of the propagation constant.

In order to illustrate the RF-fading effect of an AM tone, the baseband magnitude response of a MMF link with a length of 10km and 50km has been obtained using the software VPItransmissionMaker^{TM} v.8.0, see Fig. 4.3(a). On the contrary, Fig. 4.3(b) depicts the case when no chromatic dispersion is considered in the simulations. In both cases a laser at 230.7THz (λ=1300nm) with 1mW of average power is modulated in amplitude by an electric impulse with amplitude of 0.1 arbitrary units (a.u.) and a bias level of 0.5 a.u. Then the light is launched into a MMF fibre link. Ideal components have been used in the simulations, except for the fibre attenuation (0.55dB/km) as well as the fibre dispersion. The VPI schematic of the simulated transmission link is depicted in Fig. A.3 within Appendix A. In the frequency response depicted, it can be seen how notches appear at certain frequencies when considering chromatic dispersion, in opposition to the contrary case. This is due to the carrier fading or carrier suppression effect (CSE) that is also present in the transfer function of multimode RF analogue links caused by the chromatic dispersion and due to the phase offset between the upper and lower modulation sidebands

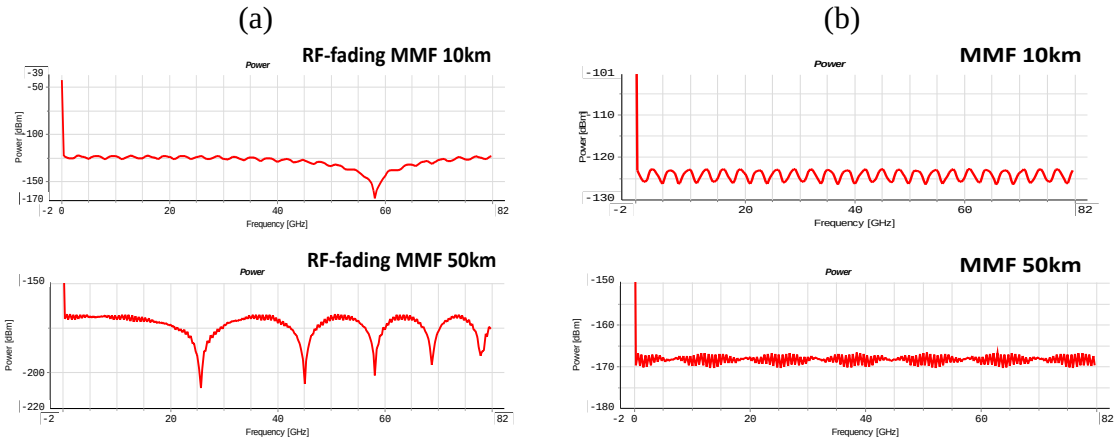

Figure 4.3. (a) Magnitude response of a MMF fibre optic link with lengths 10km and 50km and ideal components except for fibre dispersion (D=-2.8 ps/nm·km) and attenuation (A=0.55dB/km) at 1300nm (230.7THz). (b) Same magnitude response as before but not considering chromatic dispersion.

In Fig. 4.3(a) five nulls are encountered in the 50 km fibre length for a frequency range from baseband to 82GHz. The first null occurs at just 26GHz. Other nulls occur around 45GHz, 58GHz, 68GHz, and finally around 78GHz. However, in Fig. 4.3(b) no nulls are present if considering negligible the impact of the chromatic dispersion.

The second dispersion mechanism affecting the silica-based multimode fibre is the modal (or so-called intermodal) dispersion. The modal dispersion is the primary bandwidth-limiting mechanism in multimode fibres. At the wavelength of interest, graded-index MMF supports hundreds of propagating waveguide modes with different transverse electric field profiles, propagation constants, and group velocities. The launched optical power is distributed among different modes and arrives at the fibre end with different delays. This modal dispersion causes pulse broadening and inter-symbol interference (ISI) in any modulation-based optical communication link via MMF. As stated before, dispersion mechanisms described in Chapter 3 of this document for multimode polymer optical fibres also rules for silica-based counterparts.

For high bandwidth applications, Graded Index (GI) core profiles have been developed in order to reduce the limitations in bandwidth due to modal dispersion, in which the refractive index gradually decreases when moving from the centre to the core of the fibre. The fibre core is made up of a high refractive index material surrounded by a cladding consisting of a low refractive index material. The objective of the GI profile is to equalise the propagation times of the various propagating modes. The properties of wave guiding through a fibre are governed largely by the profile of the refractive index of the core and the cladding. In fibres with a graded index profile those rays propagating in the center travel a shorter distance, but because of the higher refractive index there, they travel at a lower speed. Furthermore, the smaller refractive index near the cladding causes the rays travelling there to have a higher velocity, but they also have a longer distance to travel. By choosing a suitable profile exponent it is possible to compensate for these differences in transit time. For negligible chromatic dispersion the ideal profile exponent is around 2. One then speaks of a parabolic index profile.

The graded refractive index profile can be approximated by the power law equation given by:

$$n(r,\lambda)=\begin{cases} n_1(\lambda)\left[1-2\Delta(\lambda)\left(\frac{r}{a}\right)^{\alpha}\right]^{1/2} & \text{for } 0\le r\le a \\ n_1(\lambda)\left[1-2\Delta(\lambda)\right]^{1/2}=n_2(\lambda) & \text{for } r\ge a \end{cases} \tag{4.3}$$

where α is the graded index exponent, r corresponds to the cylindrical radial coordinate (offset distance from the core center), $n_1(\lambda)$ and $n_2(\lambda)$ are the refractive indexes of the core centre and cladding, respectively, a is the core radius, and $\Delta(\lambda)$ is the relative refractive index difference given by:

$$\Delta(\lambda)=\frac{n_1^2(\lambda)-n_2^2(\lambda)}{2n_1^2(\lambda)} \tag{4.4}$$

The refractive index profile is determined by the index exponent, α. If $\alpha=1$, a linear profile is obtained. If $\alpha=2$, a parabolic index profile is obtained whereas the condition $\alpha\to\infty$ corresponds to a step index profile.

Modal dispersion characteristics of multimode fibres can be studied through either ray optics (i.e. ray tracing method, where the propagating light through an optical system can be seen as the propagation of individual light rays and all the individual light rays follow a slightly different path; these paths can be calculated using standard geometrical optics), or modal analysis using Maxwell's wave equations based on the Wentzel-Kramers-Brillouin (WKB) approximation of weakly guided fibres, assuming $\Delta\ll 1$. Both methods are applicable in highly multimode fibres; that is when the normalised frequency (or waveguide parameter) $V\ge 10$, and $V>>1$ for the ray optics and the WKB analyses respectively [76]. The total number of guided modes propagating in the multimode fibre is approximated given by:

$$N(\lambda)\approx\frac{1}{2}\frac{\alpha}{(\alpha+2)}\cdot V^2 \tag{4.5}$$

where α is the index exponent, and V is the normalised frequency (or normalised waveguide parameter) in which, for a certain wavelength, the fibre is singlemode if $V\le 2.405$. On the other hand, the fibre is multimode (and thus geometric ray-tracing model can be used) if $V >> 2.405$. The normalised frequency V is given by:

$$V=\frac{2\pi a}{\lambda_o}\sqrt{n_1^2(r,\lambda)-n_2^2(\lambda)}=\frac{2\pi a}{\lambda_o}NA(r,\lambda) \tag{4.6}$$

being $NA(r,\lambda)$ the (local) numerical aperture, function of parameters r and λ, previously defined.

Therefore, the number of guided modes in GI (with α=2) and SI ($\alpha\to\infty$) fibres can be approximated by Equations 4.7 and 4.8 respectively. From these two equations it is clear

that SI fibres support twice as many guided modes as GI fibres of similar physical properties do.

$$N_{GI} \approx \frac{V^2}{4} \tag{4.7}$$

$$N_{SI} \approx \frac{V^2}{2} \tag{4.8}$$

On the other hand, the numerical aperture of a fibre is related to the capture of the meridional rays by $\phi_{air,\max}(r,\lambda) = \arcsin NA(r,\lambda)$, where $\phi_{air,\max}(r,\lambda)$ is the maximum incident angle in air for which the fibre guides the incident light ray. This maximum angle is called the acceptance angle. Twice the acceptance angle is referred to the aperture angle. In GI fibres the radial refractive index is not constant across the core. The numerical aperture is a function of the refractive index and therefore it is not constant over the core. The local numerical aperture $NA(r,\lambda)$ is given by [77]:

$$NA(r,\lambda) = \sqrt{n_1^2(r,\lambda) - n_2^2(\lambda)} = \sqrt{n_1^2(0,\lambda)\left[1 - 2\Delta(\lambda)\left(\frac{r}{a}\right)^{\alpha}\right] - n_2^2(\lambda)} = NA(0,\lambda)\sqrt{1 - \left(\frac{r}{a}\right)^{\alpha}} \tag{4.9}$$

and the local acceptance angle, at a certain wavelength, is given by:

$$\phi_{air,\max}(r) = \arcsin NA(r) \tag{4.10}$$

From this, we can conclude that, for a parabolic index fibre, the acceptance angle decreases quadratically over the fibre core. Fibres with a large *NA* can capture light very easily. Because of the large *NA* in multimode fibres, coupling can be done very efficiently. But some attention must be paid to the varying *NA*. The largest numerical apertures exist only around the centre of the fibre core and that means that for light with a certain incident angle only a specific area of the fibre core can be used.

Finally, the total number of guided modes depends on the index profile, the core size, the operating wavelength λ_o and the numerical aperture *NA*, and it can be finally expressed as:

$$N(\lambda) \approx \frac{1}{2}\frac{\alpha}{\alpha+2}V^2 = \frac{\alpha}{\alpha+2}\cdot\left(\frac{\pi a}{\lambda}\right)^2 \cdot NA^2(0,\lambda) \tag{4.11}$$

4.4 Modal noise in silica-based Multimode Optical Fibres

Modal noise is an additive and signal-dependent amplitude noise that is specific to multimode fibre links [78], i.e. it appears as random fluctuations of the received light intensity. When a highly coherent light propagates through a MMF via a number of modes, interference between these modes yields a speckle pattern at the fibre end-face. This

speckle pattern is extremely sensitive to the phase difference among the modes, which can vary with time from a combination of the following conditions: a) a sufficiently narrow laser spectrum in conjunction with mode-selective losses in the multimode fibre optic link (such as microbending), b) changes in the source transmission wavelength (frequency) or c) time-varying fibre disturbances resulting from external forces or temperature changes. Moreover, the effect of modal noise can be increased if some form of spatial filtering is present at the end of the MMF, such as that caused by misaligned fibre joints and connectors.

Modal noise has been extensively explored and modeled in the early years of investigation on MMF links. It was first reported by Epworth in 1978 [2], and since then it has been intensively widely investigated [57, 79-82]. Modal noise can also result in a power penalty and, more importantly, can potentially result in an asymptotic bit-error-rate (BER) floor [58].

As the performance of a MMF transmission link can be dramatically degraded by modal noise, a wide number of studies on its statistics have been developed. For instance, properties of the first order statistics have been investigated in [83, 84], while the second order statistics, especially the temporal and spatial frequency correlation functions of modal noise at the output fibre end, have been reported in [79, 85].

It is worth pointing out that one of the most useful parameters for the evaluation of the impact of the modal noise in the performance of a data link is the speckle contrast [57]. It is defined as the normalized variance of the intensity distribution at the end of the multimode fibre link. The speckle contrast has previously been analyzed for different types of exciting sources, composed of one or various monochromatic or non-monochromatic optical sources, an reported elsewhere [78, 81]. Moreover, in [78] the statistical fluctuations of the detected intensity have also been examined for the case where the signal passes through one or various connectors. To resume, all the contributions in literature made in this field have been stated that the speckle contrast does not change significantly in Radio-over Multimode Fibre (RoMMF) links with the frequency of the modulating signal, i.e. the Signal-to Noise Ratio, SNR, due to modal noise presents no degradation with the electrical frequency [86]. Moreover, the latter work also shows that the speckle contrast is independent from the launching conditions and becomes almost negligible for distances above 3km, in a 62.5/125μm graded-index silica-based MMF optical link

4.5 Mode coupling in silica-based Multimode Optical Fibres

The term modal coupling refers to the process in which energy from one direction of propagation is transferred to several others. Mode coupling (or mode mixing) is rather a statistical process in which modes exchange power with each other. This effect generally occurs through irregularities in the fibre, whether they are roughness of the core-cladding interface or impurities in the core material or even elliptical core deformations. These irregularities are microscopic and lead to light scattering. This effect can therefore only be described with statistical means. A deeper analysis of mode coupling effects in multimode fibres, in general, is presented in Chapter 3, section 3.4. Nevertheless, to resume, many

experimental results clearly indicate that mode coupling occurs predominantly at the core/cladding interface. This can be explained by the fact that it is not possible to create an ideal surface in the sub-nanometer range when very large molecules are involved.

Mode coupling alters the bandwidth of a fibre. When collimated light is launched, energy is gradually transferred to the higher angle ranges so that mode dispersion increases and bandwidth decreases. If light is introduced in all angle ranges, so that maximum differential delays occur, energy is exchanged between the angles so that the initially slower rays become "faster" and vice versa. According to the laws of statistics, the differential delay (or more precisely, the standard deviation) does not increase in a linear relationship to the length but approximately only proportional to the square root of the length. Furthermore, when bending fibres the mode conversion that occurs due to this process, strictly speaking, can be described as a special case of mode coupling in which the number of modes of the propagation directions is not increased.

On the other hand, the length of a fibre in which a state of equilibrium arises through mode conversion and/or coupling is described as coupling length. The best known approach for approximately determining the coupling length of the fibre is the description with the aid of a length-dependent bandwidth, in the way $BW \propto L^{\gamma}$. Here the coupling length is the point in which the linear decrease ($\gamma \approx -1$) in the bandwidth turns to a root dependency ($\gamma \approx -0.5$) under strong mode coupling, as previously stated. Typical values of coupling lengths in silica-based GI MMFs are reported elsewhere [87] and are in the order of units of kilometers.

Efforts have been made to quantize the mode coupling efficiency. One of the widely used methods employs changing the launching condition to control the selective excitation of lower-order modes to higher-order modes. This can be performed by exciting the fibre with plane waves at different angles with the fibre end-face [88]. The larger angle excites the higher-order modes, whereas the normal incidence excites primarily the lower-order modes. Another method is to launch with a SMF at different offsets from the MMF core-center [89]. Increasing the offset from the core excites increasingly the higher-order modes, following the relation expressed in Eq. 4.12, where *r* is the distance from the core center to the position where the SMF is butted.

$$m/M = \left(r/a\right)^{\left(\frac{\alpha+2}{2}\right)} \tag{4.12}$$

The mode coupling among guided modes in MMFs may result from internal as well as external causes. Internal sources of mode coupling include imperfections such as core noncircularity [90] and refractive index fluctuations [91] caused by preform fabrication and fibre drawing process. In principle, mode coupling from core diameter variations should be negligible because perturbations due to the fibre fabrication process extend over many centimetres so that the phase matching condition is unsatisfied for power transfer between modes belonging to different mode groups. On the other hand, it is also possible to neglect the effect of refractive index variations and consider only external perturbations to be the most dominant source of coupling attending modern silica fibres made on using high-

performance PCVD (Plasma activated Chemical Vapour Deposition) method [92]. This is the case whenever fibres are used in such a way that they are subjected to external forces. This may occur whether from coating, cabling, packaging, storage drums, etc. Fibre winding on drum, for example, forces the fibre to partially conform to the crokkedness of the drum surface, which give rise to small deformations (microbends) that cause the coupling. An interesting and valuable study of this subject was previously presented by Olshansky [16, 93]. As indicated above, the fluctuations of the refractive index can be regarded as an extra mode coupling source [91]. As a matter of fact, there is for instance no practical way of separating the index fluctuations from the microbending effects.

Regarding to the dependence of the mode coupling effect with the index profile of the fibre, there is a significant difference in the mode conversion coefficient between step-index fibres and parabolic or nearly parabolic-index fibres (i.e. graded index fibres). Generally the mode coupling coefficient increases linearly with mode order, while it reduces at lower order modes. This means that in nearly parabolic-index fibres, higher-order modes have greater sensitivity to microbending than lower-order ones, but the situation is reversed in step-index fibres. This is the reason why these generally show stronger mode coupling effect than the graded-index type because, owing the fast attenuation of high-order modes, they are stripped off during propagation, or are not excited at all as in selective-mode launching schemes or low-numerical-aperture launch systems. It should be mentioned that this different behaviour between SI and GI fibres with regards to microbending was previously confirmed by [89]. But, because the refractive index is never perfectly parabolic in GI fibres, the measured coupling coefficient versus mode group number slightly departs from a linear characteristic.

Regarding fibre design, indeed, the mode coupling coefficient is seen to depend strongly on the fibre core radius and the relative refractive index difference. These parameters thus suggest three possible ways of designing fibres with high or low susceptibility to mode coupling from microbends. An increase of the core diameter and a reduction in the numerical aperture will increase the strength of the coupling. The influence of the core diameter [94] and that of the numerical aperture [95] have been qualitatively verified. Furthermore, considering different fibres drawn from the same preform in such a way that the ratio between the core and cladding diameters remains constant the thin one will be more sensitive to microbends and will exhibit higher bandwidth. However, one must be careful when acting on fibre geometry to gain more bandwidth by mode coupling. Indeed, the presence of coupling means not only power flow among guided modes during propagation, but also power transfer from guided to unguided modes causing extra loss. On the other hand, reducing the relative index difference will increase the difficulty of obtaining low-loss interconnection of cable segments and also will reduce the fibre's ability of gathering light, in particular if the light source is incoherent. These coupling loss penalties which are expected to increase with the strength of coupling must be weighted with the benefit of enhanced bandwidth. Finally, it is agreed that silica MMFs exhibit far less mode coupling compared to POF fibres. This is attributed to the difference in the material properties, [48, 96].

4.6 Differential Mode Attenuation in silica-based Multimode Optical Fibres

Differential mode attenuation in silica-based MMFs follows the same mechanisms as those described in Section 3.5 within Chapter 3 concerning GIPOFs. To resume, higher-order fibre modes have a higher loss than the lower-order fibre modes. The number of modes travelling in the fibre depends strongly on the launching conditions. If a fundamental mode from a laser is injected into the multimode fibre the fundamental mode instantly excites higher-order modes and due to mode coupling while travelling through the fibre, more modes will be excited. The fibre is sensitive to mechanical forces induced by e.g. bending, vibrations, strains and temperature changes. Because of these environmental changes, the path of the light guided through the fibre is changed, which corresponds to a change in the distribution of excited fibre modes. The fibre modes have a different loss, and if this distribution changes the output power will fluctuate, even if no spatial filtering occurs. This is called differential mode attenuation, DMA (or path dependent loss or mode-dependent loss).

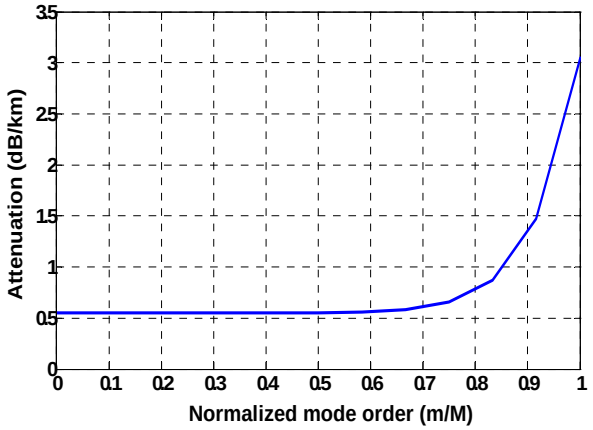

Figure 4.4.- Differential mode attenuation (DMA) as a function of the normalized mode order m/M for a=62.5μm, α=2 and λ=1300nm silica-based MMF. Parameters ρ and η, described in Section 3.5 Chapter 3, were set to 9 and 7.35, respectively.

4.7 Multimode Optical Fibre Transfer Function

In this section a closed-form analytic expression to compute the baseband and RF transfer function of a MMF link based on the electric field propagation method described in [41] is presented. By obtaining an accurate model it is possible to evaluate the conditions upon which broadband transmission is possible in RF regions far from baseband. From the transfer function developed in this section, MMFs offer the potential for broadband RoF transmission in the microwave and millimetre wave regions in short (2-5 km) and middle (10 km) reach distances. The model described in this section has been recently developed and reported in [97].

Figure 4.5 shows a generic optical transmission system scheme which employs a multimode optical fibre as a transmission medium. $E(t,\bar{r},z)$ represents the electric field at a point located at a distance z from the fibre origin and at a point $\bar{r}$ of its cross section. $E(t,\bar{r},0)$ represents the electric field at the fibre origin and at a point $\bar{r}$ of its cross section and $S(t)$ is the modulation signal composed of a RF tone with modulation index m_o.

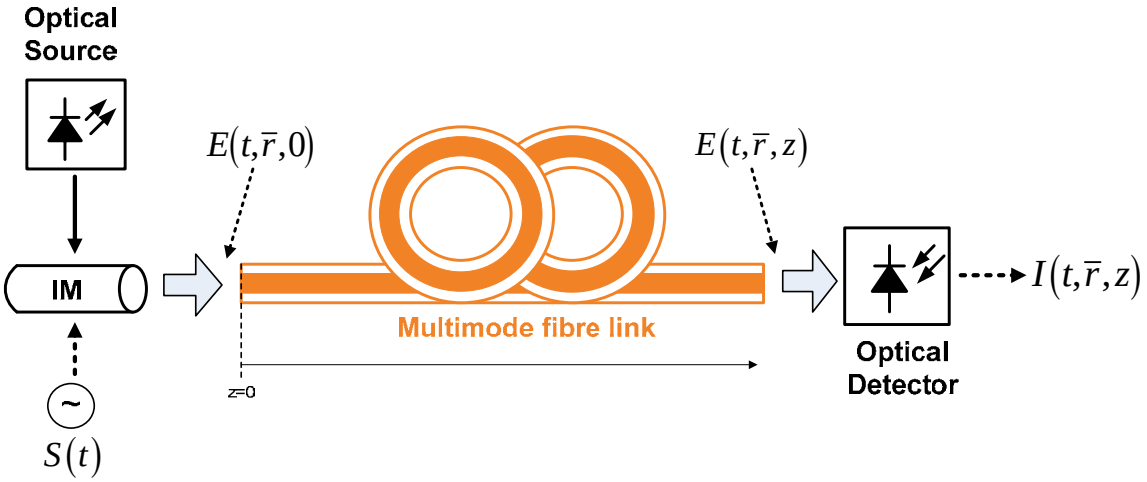

Figure 4.5.- Scheme of a generic Multimode Optical Fibre link. IM: intensity optical modulator.

Thus the optical intensity at a point z, $I(t,\bar{r},z)$, depends directly on the electric field $E(t,\bar{r},z)$ at a point located at a distance z from the fibre origin and at a point $\bar{r}$ of its cross section. Both the electric field and the optical intensity can be expressed, using the electric field propagation model and referred to the system described in Fig. 4.5, as:

$$E(t,\bar{r},z)=\sum_{\nu=1}^{N}\sum_{\mu=1}^{N}[h_{\mu\nu}(t)*E_{\nu}(t,0)]e_{\nu}(\bar{r}) \tag{4.13}$$

$$I(t,\bar{r},z)\propto\left\langle\left|E(t,\bar{r},z\right|^2\right\rangle=\sum_{\mu=1}^{N}\sum_{\nu=1}^{N}\sum_{\mu'=1}^{N}\sum_{\nu'=1}^{N}e_{\nu}^{*}(\bar{r})e_{\nu'}(\bar{r})\cdot \cdot\int_{-\infty}^{\infty}\int_{-\infty}^{\infty}\left\langle h_{\mu\nu}^{*}(t-t')h_{\mu'\nu'}(t-t'')\right\rangle\left\langle E_{\mu}^{*}(t',0)E_{\mu'}(t'',0)\right\rangle dt'dt'' \tag{4.14}$$

where N is the number of guided modes, $h_{\mu\nu}(t)$ is the impulse response at z caused by mode ν at the fibre origin over mode μ at z and $e_{\nu}(r)$ is the modal spatial profile of mode ν. It has been assumed that non linear effects are negligible.

Let $S(t)$ be the modulation signal composed of a RF tone with modulation index m_o assuming a linear modulation scheme (valid for direct and external modulation). The correlation function of the field at the source output can be expressed as:

$$\left\langle E_{\mu}^{*}(t',\bar{r}_1,0)E_{\mu'}(t'',\bar{r}_2,0)\right\rangle = \sqrt{S^{*}(t')}\sqrt{S(t'')}R(t',t'')\,R_S\left(\bar{r}_1,\bar{r}_2\right) \tag{4.15}$$

where it has been assumed that the source spatial and temporal coherence and the modulation characteristics are separable [98] and where $R(t',t'')$ is the source temporal coherence and $R_S\left(\bar{r}_1,\bar{r}_2\right)$ is the source spatial coherence, both given by autocorrelation. The mode correlation at the fibre input can be expressed as:

$$\left\langle E_{\mu}^{*}(t',0)E_{\mu'}(t'',0)\right\rangle = \sqrt{S^{*}(t')S\left(t''\right)}R(t',t'')C_{\nu\mu} \tag{4.16}$$

with

$$C_{\nu\mu} = \iint_{A_f} R_S(\bar{r}_1,\,\bar{r}_2)\cdot e_{\nu}^{*}\left(\bar{r}_1\right)\cdot e_{\mu}\left(\bar{r}_2\right)d\bar{r}_1 d\bar{r}_2 \tag{4.17}$$

On the one hand, Eq. 4.17 could be expressed as $C_{\nu\mu} = C_{\mu\mu}\delta_{\nu\mu}$ if a spatial incoherent source is supposed, that means $R_S\left(\bar{r}_1,\bar{r}_2\right) = \sqrt{I_S(\bar{r}_1)}\sqrt{I_S(\bar{r}_2)}\delta(\bar{r}_1-\bar{r}_2)$, and assuming a constant distribution of the optical intensity over the whole cross section, i.e. $I_S\left(\bar{r}\right) = I$. On the other hand, if a spatial coherent source is supposed, that means $R_S\left(\bar{r}_1,\bar{r}_2\right) = f_1^{*}(\bar{r}_1)\cdot f_2(\bar{r}_2)$ yielding a coefficient $C_{\nu\mu}$ in the form:

$$C_{\nu\mu} = \left(\int_{A_f} f_1^{*}\left(\bar{r}_1\right)\cdot e_{\nu}^{*}\left(\bar{r}_1\right)d\bar{r}_1\right)\cdot\left(\int_{A_f} f_2\left(\bar{r}_2\right)\cdot e_{\mu}^{*}\left(\bar{r}_2\right)d\bar{r}_2\right) \tag{4.18}$$

where A_f is the cross-section area of the multimode fibre.

Assuming a stationary temporal coherence of the source, which means $R(t',t'') = R\left(t'-t''\right)$, and assuming that the detector collects the light impinging on the detector area A_r, it produces an electrical current proportional to the optical power:

$$P(t) = \int_{A_r} I\left(t,\bar{r},z\right)d\bar{r} = \int_{-\infty}^{\infty}\int_{-\infty}^{\infty}\sqrt{S^{*}(t')S(t'')}\cdot Q(t-t',t-t'')dt'dt'' \tag{4.19}$$

being

$$Q(t',t'') = R(t',t'')Q_O(t',t'') \text{ and } Q_O(t',t'') = \sum_{\mu=1}^{N}\sum_{\nu=1}^{N}\sum_{\mu'=1}^{N}\sum_{\nu'=1}^{N}C_{\mu\mu'}\chi_{\nu\nu'}\left\langle h_{\mu\nu}^{*}(t')h_{\mu'\nu'}(t'')\right\rangle \tag{4.20}$$

From the above equations:

- The term $Q(t',t'')$ is referred to the influence of the source/fibre/detector system.
- The term $Q_O(t',t'')$ depends on the fibre and the power coupling from to the source

to the fibre and from the fibre to the detector.

- The spatial coherence of the source related to the fibre modes is provided by $C_{\mu\mu'}$.
- $\chi_{\nu\nu'}$ is defined as $\chi_{\nu\nu'} = \int_{A_r} e_{\nu}^{*}(\bar{r}) e_{\nu'}(\bar{r}) d\bar{r}$. In the special case where the detector collects all the incident light $\chi_{\nu\nu'} = \delta_{\nu\nu'}$.
- The term $\left\langle h_{\mu\nu}^{*}(t-t') h_{\mu'\nu'}(t-t'') \right\rangle$ is referred to the fibre dispersion and to the mode coupling.

This last term, relative to the propagation along the fibre, is composed of two parts, one describing the independent propagation of modes ($h_{\mu\nu}^{*}(t-t')$) and a second one describing the power coupling between modes $h_{\mu'\nu'}(t-t'')$. For analysing this term, it is required to consider the coupled mode propagation equations (field amplitudes) in the frequency domain, being $\tilde{E}_{\mu}(w,z)$ the frequency domain electrical field defined as $\tilde{E}_{\mu}(w,z) = \int_{-\infty}^{\infty} E_{\mu}(t,z) e^{-jwt} dt$. Consequently:

$$\frac{d\tilde{E}_{\mu}(w,z)}{dz} = -\Gamma_{\mu}(w)\tilde{E}_{\mu}(w,z) + \sum_{\substack{\nu=1 \\ \nu\neq\mu}}^{N} K_{\mu\nu} f(z) \tilde{E}_{\nu}(w,z) \tag{4.21}$$

where $\hat{K}_{\mu\nu} = K_{\mu\nu} f(z)$ is the coupling factor between modes μ and ν with units of [m^{-1}], describing $f(z)$ the actual geometric shape of the core boundary (see [32]), with units of [m] and $\Gamma_{\mu}(w) = \alpha_{\mu}(w) + j\beta_{\mu}(w)$, where $\alpha_{\mu}(w)$ and $\beta_{\mu}(w)$ are the field attenuation and the propagation constant of mode μ, respectively.

Assuming that *N* modes are propagated along the fibre, the coupled mode equation is transformed then to a vectorial equation:

$$\frac{d\tilde{E}(w,z)}{dz} = A(w,z)\tilde{E}(w,z) \tag{4.22}$$

where $\tilde{E}(w,z) = [\tilde{E}_1(w,z), \tilde{E}_2(w,z), ..., \tilde{E}_N(w,z)]$ and $A(w,z)$ is a matrix operator defined as:

$$A_{ij} = \begin{cases} -\Gamma_i(w) & \text{i=j} \\ K_{ij} f(z) & \text{i} \neq \text{j} \end{cases} \tag{4.23}$$

Solving Eq. 4.22 it is possible to define the fibre electric field transfer function $H(w)$:

$$\tilde{E}(w,z) = H(w)\tilde{E}(w,0) \tag{4.24}$$

$$H(w)=\exp\left[\int_0^z A'(z')dz'\right]=\sum_{l=0}^{\infty}\frac{\left[\int_0^z A'(z')dz'\right]^l}{l!} \tag{4.25}$$

Taking into account that the magnitude of Γ_μ is larger than the magnitude of $K_{\mu\nu}$:

$$H_{\mu\mu}(w)=\exp\left[-\Gamma_\mu(w)z\right] \quad \text{with} \quad h_{\mu\mu}(t)=\frac{1}{2\pi}\int_{-\infty}^{\infty}H_{\mu\mu}(w)e^{jwt}dw \tag{4.26}$$

and

$$H_{\mu\nu}(w)=K_{\mu\nu}\left[\int_0^z f(z')dz'\right]\Phi_{\mu\nu}(w), \quad \mu\neq\nu \quad \text{with} \quad h_{\mu\nu}(t)=\frac{1}{2\pi}\int_{-\infty}^{\infty}H_{\mu\nu}(w)e^{jwt}dw \tag{4.27}$$

where

$$\Phi_{\mu\nu}(w)=\frac{H_{\mu\mu}(w)-H_{\nu\nu}(w)}{\left[\Gamma_\nu(w)-\Gamma_\mu(w)\right]\cdot z} \tag{4.28}$$

Although Eq. 4.19 reveals a nonlinear relationship between the output and the input electrical signals being not possible to define a transfer function, under several conditions linearization is possible yielding to a linear system with impulse response $Q(t)$. This linear response is given [45, 99] by:

$$P(t)=\int_{-\infty}^{\infty}S(t')Q(t-t',t-t')dt' \tag{4.29}$$

The impulse response terms of the fibre can then be found by inverse Fourier transforming the above matrix elements. Upon substitution in Eq. 4.29 it is found that $P(t)$ is composed of two terms $P(t)=P^U(t)+P^C(t)$ being $P^U(t)$ the optical power in absence of mode coupling (that means $\mu=\nu$ and $\mu'=\nu'$) and $P^C(t)$ the contribution of modal coupling.

The uncoupled part of the received power is given by, see Eqs. 4.19 and 4.20:

$$P^U(t)=\int_{-\infty}^{\infty}\int_{-\infty}^{\infty}\sqrt{S^*(t')S(t'')}\cdot R(t',t'')\cdot Q_o^U(t-t',t-t'')dt'dt'' \tag{4.30}$$

with

$$Q_o^U(t',t'')=\sum_{\nu=1}^{N}\sum_{\nu'=1}^{N}C_{\nu\nu'}\chi_{\nu\nu'}\left\langle h_{\nu\nu}^*(t')h_{\nu'\nu'}(t'')\right\rangle \tag{4.31}$$

On the other hand, the coupled contribution to the total power is given by:

$$P^C(t) = g^2 \int_{-\infty}^{\infty}\int_{-\infty}^{\infty} \sqrt{S^*(t')S(t'')}\cdot R(t',t'')\cdot Q_o^C(t-t',t-t'')dt'dt'' \tag{4.32}$$

with, see Eq. 4.27,

$$\begin{aligned} Q_o^C(t',t'') &= \sum_{\mu=1}^{N}\sum_{\substack{\nu=1\\ \nu\neq\mu}}^{N}\sum_{\mu'=1}^{N}\sum_{\substack{\nu'=1\\ \nu'\neq\mu'}}^{N} C_{\mu\mu'}\chi_{\nu\nu'}\left\langle h^*_{\mu\nu}(t')h_{\mu'\nu'}(t'')\right\rangle = \\ &= \sum_{\mu=1}^{N}\sum_{\substack{\nu=1\\ \nu\neq\mu}}^{N}\sum_{\mu'=1}^{N}\sum_{\substack{\nu'=1\\ \nu'\neq\mu'}}^{N} C_{\mu\mu'}\chi_{\nu\nu'}K^*_{\mu\nu}K_{\mu'\nu'}\Phi^*_{\mu\nu}(t')\Phi_{\mu'\nu'}(t'') \end{aligned} \tag{4.33}$$

and

$$g^2 = \int_0^z\int_0^z \left\langle f^*(z_1)\,f(z_2)\right\rangle dz_1dz_2 = \int_0^z\int_0^z R_f(z_1-z_2)dz_1dz_2 \tag{4.34}$$

where $R_f(z_1-z_2)$ is the autocorrelation of the coupling function $f(z)$. Different autocorrelation functions can be attributed to the core boundary deformation of the multimode fibre. These functions are needed to compute the value of the coefficient g^2 given by Eq. 4.34. Such function could be:

- Uncorrelated fluctuations, [41]:

$$R_f(z_1-z_2) = \sigma^2\delta(z_1-z_2) \Rightarrow g^2 = \sigma^2 z \tag{4.35}$$

- Exponential function, [33]:

$$R_f(z_1-z_2) = \sigma^2 e^{-\frac{|z_1-z_2|}{\varsigma}} \Rightarrow g^2 = 2\varsigma\sigma^2\left[z+\varsigma\cdot\left(e^{-z/\varsigma}-1\right)\right] \tag{4.36}$$

- Gaussian function, [33, 36]:

$$R_f(z_1-z_2) = \sigma^2 e^{-\left(\frac{z_1-z_2}{\varsigma}\right)^2} \Rightarrow g^2 = \varsigma\sigma^2\left[z\sqrt{\pi}+\varsigma\cdot\left(e^{-(z/\varsigma)^2}-1\right)\right] \text{ if } z\gg\varsigma \tag{4.37}$$

where ς is the autocorrelation (or coupling) distance at which $R_f(z)$ has decreased to a fraction 1/e of its maximum value and σ^2 is the variance of $f(z)$.

The terms $h_{\mu\nu}(t)$ and $\Phi_{\mu\nu}(t)$ can be solved from both equations 4.27 and 4.28, respectively, but requires the knowledge of the dependence of $\Gamma_\mu(w)$ on w. Assuming, as

in [45], that $\alpha_\mu(w)$ is independent of w and $\beta_\mu(w)$ can be expanded in a Taylor's series around the central angular frequency w_o [100, 101] with a second order dispersion profile:

$$\alpha_\mu(w) \approx \alpha_\mu(w_o) = \alpha_\mu^o \tag{4.38}$$

and

$$\begin{aligned}\beta_\mu(w) &= \beta_\mu(w_o) + \left.\frac{d\beta_\mu(w)}{dw}\right|_{w=w_o}(w-w_o) + \frac{1}{2}\left.\frac{d\beta_\mu^2(w)}{dw^2}\right|_{w=w_o}(w-w_o)^2 + \ldots \\ &= \beta_\mu^o + \beta_\mu^1(w-w_o) + \frac{1}{2}\beta_\mu^2(w-w_o)^2 + \ldots\end{aligned} \tag{4.39}$$

Therefore, for the uncoupled part of the received power:

$$h_{\mu\mu}(t) = \frac{1}{2\pi}\int_{-\infty}^{\infty} e^{-\Gamma_\mu(w)z}e^{jwt}dw = e^{-(\alpha_\mu^0 + j\beta_\mu^0)z}\frac{1}{\sqrt{j2\pi\beta_\mu^2 z}}e^{-\left\{\frac{(t-\beta_\mu^1 z)^2}{2j\beta_\mu^2 z}\right\}} \tag{4.40}$$

where $H_{\mu\mu}(w) = e^{-\Gamma_\mu(w)z} = e^{-\alpha_\mu^0 z}\cdot e^{-j\left[\beta_\mu^0 + \beta_\mu^1(w-w_o) + \frac{1}{2}\beta_\mu^2(w-w_o)^2\right]z}$

and regarding the coupled part of the received power:

$$\begin{aligned}\Phi_{\mu\nu}(t) &= \frac{1}{2\pi}\int_{-\infty}^{\infty}\Phi_{\mu\nu}(w)e^{jwt}dw = \frac{h_{\mu\mu}(t) - h_{\nu\nu}(t)}{z\cdot\left[(\alpha_\nu^0 - \alpha_\mu^0) + j\left(\beta_\nu^0 - \beta_\mu^0\right)\right]} \\ \text{where}\quad \Phi_{\mu\nu}(w) &= \frac{e^{-\Gamma_\mu(w)z} - e^{-\Gamma_\nu(w)z}}{z\cdot\left[\Gamma_\nu(w) - \Gamma_\mu(w)\right]} = \frac{e^{-\Gamma_\mu(w)z} - e^{-\Gamma_\nu(w)z}}{z\cdot\left[(\alpha_\nu^0 - \alpha_\mu^0) + j\left(\beta_\nu^0 - \beta_\mu^0\right)\right]}\end{aligned} \tag{4.41}$$

where $\beta_\mu^2 \approx \beta_o^2 \ \forall\mu$, i.e. the second derivative of the propagation constant, has been considered to have the same value for all the propagating modes. The term $\left[\left(\beta_\nu^1 - \beta_\mu^1\right)(w-w_o)\right]$ has been considered negligible from the imaginary part of $\left[\Gamma_\nu(w) - \Gamma_\mu(w)\right]$. For a further analysis of the development of Eq. 4.40 and Eq. 4.41, the work reported in [46] is recommended.

Coming back to Eq. 4.21, this equation determines the *N* coupled mode propagation equations (field amplitudes) in the frequency domain which refer to an *N*-mode fibre. Each physical mode can be specified by a pair of numbers (*q*,*l*) which, respectively, count the number of radial and azimutal modal surfaces in the field intensities of that mode. However in literature, see [33], different physical modes can be grouped in sets where the modes in each group have a similar propagation constant. Mode groups are counted using the parameter *m* (namely principal mode number) where the propagation constant of each mode

β_μ depends only on this index which is given by *m=2q+l+1*. Taking into account this fact, the m[th] group consists of, approximately, 2·(m+1) degenerate modes for each state of polarization where:

$$l = m, m-2, ..., -(m-2), -m \tag{4.42}$$

The total number of mode groups *M* is then found by setting the total number of modes equal to *N*.

$$\sum_{m=1}^{M} 2(m+1) \approx M^2 = N \tag{4.43}$$

with a propagation constant, β_m, of the m[th] group of modes which can be approximated, following the WKB (Wentzel-Kramers-Brillouin) Method, by [16, 34, 40]:

$$\beta_m = \beta(m,\lambda) = n_1(\lambda) k \left[1 - 2\Delta(\lambda) \left(\frac{m}{M(\alpha)} \right)^{\frac{2\alpha}{\alpha+2}} \right]^{1/2} \tag{4.44}$$

with

$$M(\alpha,\lambda) = 2\pi a \frac{n_1(\lambda)}{\lambda} \left[\frac{\alpha \cdot \Delta(\lambda)}{\alpha+2} \right]^{1/2} \tag{4.45}$$

where *a* is the fibre core radius, $n_1(\lambda)$ is the refractive index in the fibre core center, λ is the free space wavelength of the fibre excitation light, α is the refractive index exponent and $\Delta(\lambda)$ is the relative refractive index difference (or refractive index contrast) between the core and the cladding and $k = 2\pi/\lambda$ is the free space wavenumber.

As a consequence of Eq. 4.44, the delay time τ_m of a generic mode μ depends only on its principal mode number *m*. The delay time of the guided modes per unit length can be derived from Eq.4.44 using the definition given by [34] and [102], in which $\tau_m(\lambda) = -\lambda^2 \frac{\beta_m^1(\lambda)}{2\pi c}$ is defined, yielding:

$$\tau_m = \tau(m,\lambda) = \frac{N_1(\lambda)}{c} \left[1 - \frac{\Delta(\lambda)(4+\varepsilon(\lambda))}{\alpha+2} \left(\frac{m}{M} \right)^{\frac{2\alpha}{\alpha+2}} \right] \left[1 - 2\Delta(\lambda) \left(\frac{m}{M} \right)^{\frac{2\alpha}{\alpha+2}} \right]^{-1/2} \tag{4.46}$$

where $\varepsilon(\lambda)$ is the profile dispersion parameter given by:

$$\varepsilon(\lambda) = -\frac{2n_1(\lambda)}{N_1(\lambda)} \frac{\lambda \dfrac{d\Delta(\lambda)}{d\lambda}}{\Delta(\lambda)} \tag{4.47}$$

being $N_1(\lambda)$ the material group index defined by:

$$N_1(\lambda) = n_1(\lambda) - \lambda \frac{dn_1(\lambda)}{d\lambda} \tag{4.48}$$

On the other hand, the attenuation α_μ of a generic mode μ and the coupling coefficient $K_{\mu\nu}$ between two modes (μ and ν) generally depend on the principal mode number *m*, see [16]. In [32], the power is distributed among all modes of each mode group for transitions between modes governed by $\Delta m = \pm 1$. Consequently, for each mode group, it is possible to define a quantity α_m which represents an average value of the attenuation of the mth group and a quantity $\left|K_{m,m\pm1}\right|^2$ which corresponds to an average value of the coupling between a mode of group *m+1* and a mode of group *m*.

Differential mode attenuation (DMA) effects have also been taken into account. It originates from conventional mechanisms that are present in usual fibres, that is, absorption, Rayleigh scattering and loss on reflection at the core-cladding interface. These different loss mechanisms act on each mode in a different manner, which causes the attenuation coefficient to vary from mode to mode. This differential mode attenuation (DMA) can be expressed by (empirically obtained in [34, 102]:

$$\alpha_m = \alpha_m(m,\lambda) = \alpha_o(\lambda) + \alpha_o(\lambda) \cdot I_\rho \left[\eta \left(\frac{m-1}{M} \right)^{\frac{2\alpha}{\alpha+2}} \right] \tag{4.49}$$

where $\alpha_o = \alpha_o(\lambda)$ is the power attenuation of low-order modes (i.e. intrinsic fibre attenuation), I_ρ is the ρth-order modified Bessel function of the first kind and η is a weighting constant.

On the other hand, the coupling losses from random bends in the optical fibre can be obtained from the coupled power equations [33]:

$$\frac{dP_\mu(z)}{dz} = -2\alpha_\mu P_\mu(z) + \sum_{\nu=1}^{N} d_{\mu\nu}\left[P_\nu(z) - P_\mu(z)\right] \tag{4.50}$$

being $d_{\mu\nu}$ the power coupling coefficient which is related to the coefficient $\hat{K}_{\mu\nu}$ according to the following expression:

$$d_{\mu\nu} = \left|K_{\mu\nu}\right|^2 \cdot \left\langle \left|F\left(\beta_\mu - \beta_\nu\right)\right|^2 \right\rangle \tag{4.51}$$

where $F\left(\beta_\mu - \beta_\nu\right)$ is the Fourier transform of the coupling function $f(z)$, that means $\left\langle \left|F\left(\beta_\mu - \beta_\nu\right)\right|^2 \right\rangle = \frac{1}{\sqrt{L}} \int_0^L f(z) \cdot e^{-j\left(\beta_\mu - \beta_\nu\right)z} dz$.

For a graded-index core with power transitions only between mode groups *m* and *m+1* the power coupling coefficient is given by, see [16]:

$$d(\alpha, m) = \frac{1}{8}\left(n_1 ka\right)^2 \cdot \left(\frac{m}{M(\alpha)}\right)^{\frac{4}{\alpha+2}} \cdot \left\langle \left|F\left(\beta_m - \beta_{m+1}\right)\right|^2 \right\rangle \cdot \left(\beta_m - \beta_{m+1}\right)^4 \tag{4.52}$$

Solving Eq. 4.50 it can be found that:

$$\left|K_{m,m+1}\right|^2 = \frac{1}{8}\left(n_1 ka\right)^2 \cdot \left(\frac{m}{M(\alpha)}\right)^{\frac{4}{\alpha+2}} \cdot \left(\beta_m^0 - \beta_{m+1}^0\right)^4 \tag{4.53}$$

where it has been assumed that $\beta_m(w) - \beta_{m+1}(w) \approx \beta_m^0 - \beta_{m+1}^0$.

For calculating the expression of the transfer function of a multimode fibre, the total power from the average power per mode of each level $\bar{P}_m(t)$ can be obtained, taking into account the *2m*-fold degeneracy of each group of modes, as:

$$P(t) = \sum_{m=1}^{M} P_m(t) = \sum_{m=1}^{M} 2m\bar{P}_m(t) \tag{4.54}$$

where $P_m(t)$ is the total power distribution of a mode group *m*.

As the propagation constant and the rest of the mode-dependent parameters (i.e. modal delay, DMA and coupling losses from random bends) have been defined as a function of the mode group number, equations 4.20, 4.31 and 4.33 refer actually to the sum of the average power per mode of each group considering the factor *2m*.

For the determination of the transfer function it has been assumed an electric modulating signal composed of a RF tone (with modulation index m_o), $S(t) = S_o\left[1 + m_o \cos\left(\Omega t\right)\right]$ with $m_o \ll 1$, which incorporates the source chirp α_C, and approximated by three terms of its Fourier series, following:

$$\sqrt{S(t)} = \sqrt{S_o}\left\{1 + \frac{m_o}{8}(1 + j\alpha_C)e^{j\Omega t} + \frac{m_o}{8}(1 + j\alpha_C)e^{-j\Omega t}\right\} \tag{4.55}$$

where S_o is proportional to the average optical power and Ω represents the frequency of the RF modulating signal. Note that $\sqrt{S(t)}$ is periodic with a period of $2\pi/\Omega$. It has also been assumed an optical source which has a finite linewidth spectrum (temporal coherence) with a Gaussian time domain autocorrelation function given by:

$$R(t'-t'') = e^{-\frac{(t'-t'')^2}{2\sigma_c^2}} \tag{4.56}$$

where $\sigma_c \approx 1/\sqrt{2}W$ is the source RMS (Root Mean Square) coherence time and W is the source RMS linewidth in absence of modulation.

Taking advantage of the theory involving the mode groups described elsewhere, generic Eq. 4.31 and Eq. 4.33 can be rewritten with regards to mode groups theory, without loss of meaning, by replacing subscripts from μ,ν,μ',ν' to m,n,m',n', respectively.

The uncoupled part can be divided into a linear $P^{UL}(t)$ and a non-linear $P^{UN}(t)$ term, respectively. In that case it yields $P^U(t) = P^{UL}(t) + P^{UN}(t)$. Note that in the former equations ν represented the mode number whereas from this point the mode group number will be noted as m taking into account the degeneracy factor $2m$, as previously stated.

$$P^U(t) = \sum_{m=1}^{M}\sum_{n=1}^{M} 2mC_{mn}\chi_{mn}\int_{-\infty}^{\infty}\int_{-\infty}^{\infty}\sqrt{S^*(t')}\sqrt{S(t'')}\cdot R(t',t'')\cdot h_{mm}^*(t-t')h_{nn}(t-t'')dt'dt'' \tag{4.57}$$

If only the term relative to $e^{-j\Omega t}$ from the product $\sqrt{S^*(t')}\sqrt{S(t'')}$ is considered then:

$$P^U(t) = S_o\frac{m_o}{8}\sum_{m=1}^{M}2m\sum_{n=1}^{M}C_{mn}\chi_{mn}\int_{-\infty}^{\infty}\int_{-\infty}^{\infty}\left[(1-j\alpha_C)e^{-j\Omega t'} + (1+j\alpha_C)e^{-j\Omega t''}\right]\cdot e^{-\frac{1}{2}\left(\frac{t'-t''}{\sigma_c}\right)^2}\cdot h_{mm}^*(t-t')h_{nn}(t-t'')dt'dt'' \tag{4.58}$$

Forcing $m=n$ in Eq. 4.30 and Eq. 4.31 it is possible to only evaluate the linear part leading to the following result:

$$\begin{aligned} P^{UL}(t) = {} & \sum_{m=1}^{M}2m\cdot C_{mm}\chi_{mm}\int_{-\infty}^{\infty}\int_{-\infty}^{\infty}\left\{1+\frac{m_o}{8}(1-j\alpha_C)e^{j\Omega t'} + \frac{m_o}{8}(1-j\alpha_C)e^{-j\Omega t'}\right\}\cdot \\ & \cdot\left\{1+\frac{m_o}{8}(1+j\alpha_C)e^{j\Omega t''} + \frac{m_o}{8}(1+j\alpha_C)e^{-j\Omega t''}\right\}\cdot e^{-\frac{1}{2}\left(\frac{t-t'}{\sigma_c}\right)^2}e^{-2\alpha_m z}\cdot\frac{1}{2\pi\beta_m^2 z}e^{\frac{(t-t'-\tau_m)^2}{2j\beta_m^2 z}}e^{-\frac{(t-t''-\tau_m)^2}{2j\beta_m^2 z}}\cdot dt'dt'' \end{aligned} \tag{4.59}$$

Finally solving the double integration in Eq. 4.59 and only evaluating the linear part, it can be obtained:

$$P^{UL}(t)=S_o\frac{m_o\pi}{4}\sqrt{1+\alpha_C^2}\left[\sum_{m=1}^{M}2m\cdot C_{mm}\chi_{mm}\cdot e^{-2\alpha_m z}e^{-\frac{1}{2}\left(\frac{\beta_m^2\Omega z}{\sigma_c}\right)^2}\cdot\cos\left(\frac{\beta_m^2\Omega^2 z}{2}+\arctan(\alpha_C)\right)e^{-j\Omega\tau_m z}\right]e^{-j\Omega t} \quad (4.60)$$

Following the same reasoning, the coupled power is also composed of a linear part $P^{CL}(t)$ from $P^C(t)=P^{CL}(t)+P^{CN}(t)$ which will be the one of interest in the evaluation of the transfer function and a non-linear part, which will contribute to the harmonic distorsion and intermodulation [100, 103].

$$\begin{aligned}P^C(t)=g^2\int_{-\infty}^{\infty}\int_{-\infty}^{\infty}\sqrt{S^*(t')}\sqrt{S(t'')}\cdot R(t',t'')\cdot\\ \cdot\sum_{m=1}^{M}\sum_{\substack{n=1\\ n\neq m}}^{M}\sum_{m'=1}^{M}\sum_{\substack{n'=1\\ n'\neq m'}}^{M}2mC_{mm'}\chi_{nn'}K_{mn}^*K_{m'n'}\cdot\Phi_{mn}^*(t-t')\Phi_{m'n'}(t-t'')dt'dt''\end{aligned} \quad (4.61)$$

being $\Phi_{mn}(t)$ defined by Eq. 4.41.

Following the same procedure as for the uncoupled part, consequently, the linear term of the coupled part is obtained forcing $m=m'$ and $n=n'$ in Eq. 4.61. This linear term can be expressed as follows:

$$P^{CL}(t)=S_o\frac{m_o\pi}{4}\sqrt{1+\alpha_C^2}\left[\sum_{m=1}^{M}2m\cdot G_{mm}e^{-2\alpha_m z}\cdot e^{-\frac{1}{2}\left(\frac{\beta_m^2\Omega z}{\sigma_c}\right)^2}\cdot\cos\left(\frac{\beta_m^2\Omega^2 z}{2}+\arctan(\alpha_C)\right)e^{-j\Omega\tau_m z}\right]e^{-j\Omega t} \quad (4.62)$$

with

$$G_{mn}=g^2\sum_{m'=1}^{M}\sum_{\substack{n'=1\\ n'\neq m'}}^{M}\left[\psi_{mn}(m',n')-\psi_{m'n}(m,n')-\psi_{mn'}(m',n)+\psi_{m'n'}(m,n)\right] \quad (4.63)$$

for the linear and non linear contributions and where

$$\psi_{mn}(r,s)=\begin{cases}\dfrac{C_{mn}\chi_{rs}K_{mr}^*K_{ns}}{f_{mr}^*f_{ns}} & \text{m}\neq\text{r \& n}\neq\text{s}\\ 0 & \text{otherwise}\end{cases} \quad (4.64)$$

and

$$f_{mr}=\left[\alpha_{m}-\alpha_r+j\left(\beta_m^0-\beta_r^0\right)\right]z \quad (4.65)$$

Grouping the linear contributions of the uncoupled, Eq. 4.60, and the coupled, Eq. 4.62, parts and comparing the power of the lineal part of the total power received (sum of

contributions from the coupled and uncoupled parts) with the power of one of the sidebands of the electric modulating signal $S(\Omega) = S_o \frac{m_o}{4}$:

$$H(\Omega) = \frac{P^{UL}(\Omega) + P^{CL}(\Omega)}{S(\Omega)} = \frac{P^{L}(\Omega)}{S(\Omega)} \tag{4.66}$$

It is possible to obtain the final overall RF transfer function, yielding:

$$H(\Omega) = \sqrt{1+\alpha_C^2} \sum_{m=1}^{M} 2m(C_{mm}\chi_{mm} + G_{mm}) e^{-2\alpha_m z} e^{-\frac{1}{2}\left(\frac{\beta_m^2 \Omega z}{\sigma_c}\right)^2} \cdot \cos\left(\frac{\beta_m^2 \Omega^2 z}{2} + \arctan(\alpha_C)\right) e^{-j\Omega\tau_m z} \tag{4.67}$$

If the second derivative of the propagation constant can be considered to have the same value for all the mode groups, then

$$\beta_m^2 = \beta_o^2, \quad \forall m \tag{4.68}$$

and the transfer function can be expressed as:

$$H(\Omega) = \sqrt{1+\alpha_C^2} \cdot e^{-\frac{1}{2}\left(\frac{\beta_o^2 \Omega z}{\sigma_c}\right)^2} \cdot \cos\left(\frac{\beta_o^2 \Omega^2 z}{2} + \arctan(\alpha_C)\right) \cdot \sum_{m=1}^{M} 2m(C_{mm}\chi_{mm} + G_{mm}) e^{-2\alpha_m z} e^{-j\Omega\tau_m z} \tag{4.69}$$

Assuming a photodetector capable of collecting the entire incident light and a source with a uniform current distribution (note that this assumption would additionally gives the non linear contribution of the uncoupled part equals to zero, i.e. $P^{UN}(t) = 0$):

$$\chi_{rs} = \delta_{rs} \tag{4.70}$$

$$C_{rs} = C_{rr}\delta_{rs} \tag{4.71}$$

that leads to simplify the coefficient G_{mm} for the linear contribution of the coupled part , $P^{CL}(t)$, into:

$$G_{mm} = g^2 \sum_{\substack{m'=1 \\ m' \neq m}}^{M} \left[\psi_{mm}(m', m') + \psi_{m'm'}(m, m)\right] \tag{4.72}$$

Moreover, adopting the same selection rules between neighbouring mode groups as in [16] and [32] it is possible to rewrite the coefficient G_{mm} as:

$$G_{mm} = 2g^2 \left[\psi_{mm}(m+1, m+1) + \psi_{m-1m-1}(m, m)\right] \tag{4.73}$$

where the coefficient g^2 is given by Eq. 4.34.

The expression of Eq. 4.69 provides a description of the main factors affecting the RF frequency response of a multimode fibre link and can be divided as the product of three terms of factors. From the left to the right, the first term is a low-pass frequency response which depends on the first order chromatic dispersion parameter β_o^2 which is assumed to be equal for all the modes guided by the fibre, see Eq. 4.68, and the parameter σ_c which is the source coherence time directly related to the source linewidth. The second term is related to the carrier suppression effect due to the phase offset between the upper and lower modulation sidebands. Finally, the third term represents a microwave photonic transversal filtering effect [104], in which each sample corresponds to a different mode group ν carried by the fibre. This last term involves that the periodic frequency response of transversal filters could permit broadband RF transmissions far from baseband and results showed that MMFs offer the potencial for broadband RoF transmission in the microwave and millimetre wave regions in short (2-5 km) and middle (10 km) reach distances.

4.8 Silica-based Multimode Optical Fibre Transfer Function Simulations

The MMF transfer function presented in Eq. 4.69 provides a description of the main factors affecting the RF frequency response of a multimode fibre link, including the temporal and spatial source coherence, the source chirp, chromatic and modal dispersion, mode coupling (MC), signal coupling to modes at the input of the fibre, coupling between the output signal from the fibre and the detector area, and the differential mode attenuation (DMA).

In this section, theoretical simulations are studied with regards to several parameters such as the link length, the graded-index exponent of the fibre, the core radius of the fibre, the source linewidth and the source chirp, in order to determine the optimal conditions for a higher transmission bandwidth in baseband and to investigate the potencials for broadband Radio-over-Fibre (RoF) systems in regions far from baseband using multimode fibre, as it behaves as a transversal filter whose coefficients depend on the injection coefficient C_{mm} and on the modal-coupling coefficient G_{mm}. Since transversal filters are periodic in frequency it should be, in principle, possible to consider the use of the high-order resonances placed far from baseband to transport RF signals. In this subsection the 3-dB bandwidth and the central wavelength of the high resonances will be also analyzed making silica-based MMFs useful to transport RF signals, leading for example to a cost-effective solution for the base stations in wireless access networks, as seen in Chapter 2.

For the simulation results in this section it has been considered a graded-index multimode fibre with a typically SiO_2 core doped with 6.3 mol-% GeO_2 and a SiO_2 cladding, and intrinsic attenuation of 0.55dB/km. This typical doping value has been provided by the manufacturer. The refractive indices were calculated using a three-term Sellmeier function for 1300nm and 1550nm wavelengths. The parameters relative to the differential mode

attenuation were fitted to $\rho = 9$ and $\eta = 7.35$. The fitting process of similar DMA profiles reported in literature leaded to the aforementioned values of parameters ρ and η. Chromatic dispersion was fitted at D=-3.5ps/(nm·km) at 1300nm, which leads to β_o^2=-3.824 (psec)^2/km (typical of the 1300nm region). Coefficient G_{mm} was obtained assuming a random coupling process defined by a Gaussian autocorrelation function [33], see Eq. 4.37. Overfilled launching condition (OFL) was also assumed so that the light injection coefficient was set to $C_{mm} = 1/M$, being M the total number of mode groups. A friendly graphical interface as well as numerical computations were performed using Matlab® software and are further documented into the Final Degree Project reported in [105], where it was firstly developed.

4.8.1 Silica-based Multimode Optical Fibre Sellmeier coefficients

Considering a graded index silica-based multimode optical fibre with a SiO_2 core doped with 6.3 mol-% GeO_2 and a SiO_2 cladding, the refractive indices for the core and cladding are calculated using a three-term Sellmeier function, given by Eq. 3.7, with coefficients shown in Table 4.2, which were provided by the manufacturer.

The numerical aperture at the core center is calculated as $NA(0,\lambda) = 0.158$ from the core and cladding refractive indices obtained by Fig. 4.6(a) which are $n_1 = n_{cc1} = 1.4558$ and $n_2 = n_{cl} = 1.4472$, respectively, for a wavelength of 1300nm. This figure also depicts for comparison the core refractive index for a different doped core consisting of 7.5 mol-% GeO_2. The material dispersion at 1300nm, in case of a doped fibre with 6.3 mol-% GeO_2, is plotted in Fig. 4.6(b) versus the operating wavelength. It is calculated approximately to be -2.8ps/(nm·km), similar to the expected value of around ~-3ps/(nm·km) previously addressed. The refractive group index and the dispersion profile parameter, also at 1300nm, are found to be $N_1 = 1.4703$ and $\varepsilon = -0.0482$, respectively.

Core Sellmeier coefficients, $n_1 = n_1(\lambda)$		**Cladding Sellmeier coefficients,** $n_2 = n_2(\lambda)$	
$A_{1,1}$	0.7083952	$A_{2,1}$	0.6965325
$A_{1,2}$	0.4203993	$A_{2,2}$	0.4083099
$A_{1,3}$	0.8663412	$A_{2,3}$	0.8968766
$\lambda_{1,1}$	0.0853842	$\lambda_{2,1}$	0.0660932
$\lambda_{1,2}$	0.1024838	$\lambda_{2,2}$	0.11811007
$\lambda_{1,3}$	9.896175	$\lambda_{2,3}$	9.8961604

Table 4.2. MMF Sellmeier coefficients of the core and cladding, for a GI silica-based fibre with SiO_2 core doped with 6.3mol-% GeO_2 and a SiO_2 cladding.

(a) (b)

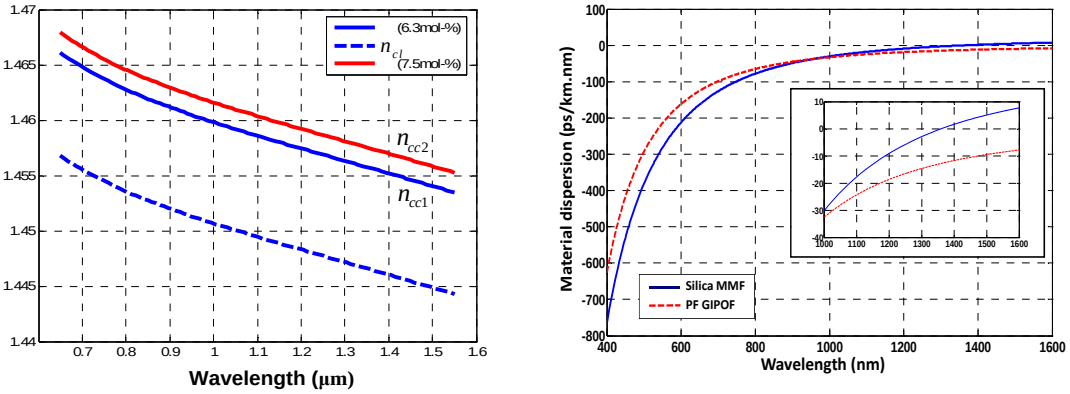

Figure 4.6.- (a) Core n_{cc-i} and cladding n_{cl} refractive indices considered for this section. (b) Material dispersion of the central core region for the silica-based MMF as a function of the operating wavelength (blue solid line). Red dashed line represents the PF GIPOF material dispersion calculated from Chapter 3. Inset: zoom ranging from 1000nm to 1600nm.

4.8.2 Silica-based Multimode Optical Fibre frequency response dependency with mode coupling and differential mode attenuation

In this subsection the influence of mode coupling (MC) in absence and presence of differential mode attenuation (DMA) is evaluated and vice versa. It has been considered for the simulations a 62.5/125μm graded-index multimode fibre with SiO_2 core doped with a 6.3mol-% of germanium (GeO_2) which is gradually decreased in the lateral direction to form the desired gradient and with a pure silica cladding. The refractive indices were approximated using a three-term Sellmeier function for a wavelength of 1300nm. The coefficient G_{mm} was defined by a Gaussian autocorrelation function with an rms deviation of $\sigma = 0.0009$ and a correlation length of $\varsigma = 115 \cdot a$, see Eq. 4.37, being a is the core radius. The rms linewidth of the source was set to 10MHz and its chirp parameter to zero. The frequency responses simulated over a fibre length L=3km and a graded-index exponent $\alpha = 2$ are displayed in the following figures.

From Fig. 4.7(a) it can be seen that the filtering effect caused by the DMA is decreased when considering the presence of the mode coupling phenomenon (i.e. lower excursions in the passband filter are achieved). Moreover, from Fig. 4.7(b) it is also appreciated that the RF baseband bandwidth is increased by mode coupling while the differential mode attenuation has little effect on the bandwidth itself. While in the first case the 3-dB bandwidth in baseband is approximately 0.7GHz, the second case (no MC is considered) obtains a 3-dB bandwidth in baseband of 0.55GHz, which is a 21% lower than if mode coupling effects are considered.

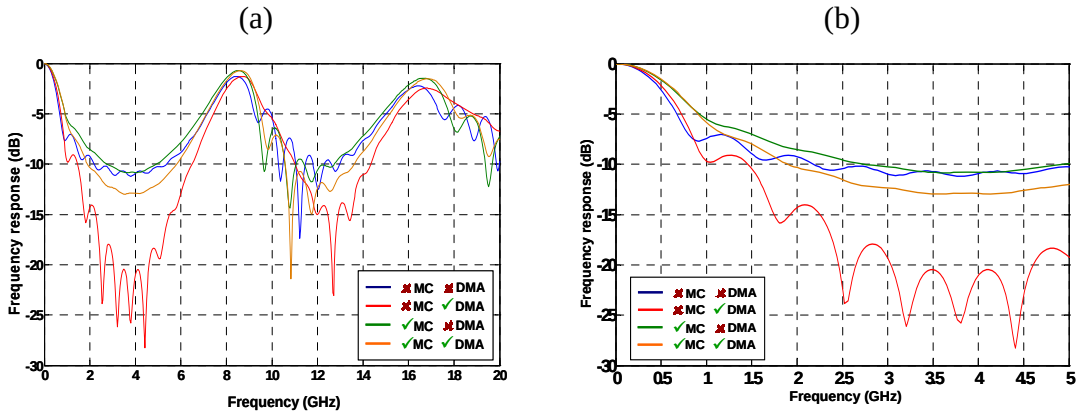

Figure 4.7.- (a) Frequency responses up to 20GHz for a 62.5/125μm multimode fibre showing the effect of mode coupling (MC) and the differential mode attenuation (DMA). L=3km and α=2. (b) Zoom of Fig. 4.3(a) up to 5GHz.

Anyway, not considering mode coupling effects, Fig. 4.7 illustrates the classical conflict relationship between dispersion and loss in MMFs in general. As a matter of fact, the large DMA of high-order modes necessarily causes a large power penalty during light propagation, but at the same time it yields a bandwidth enhancement as a result of the mode stripping effect.

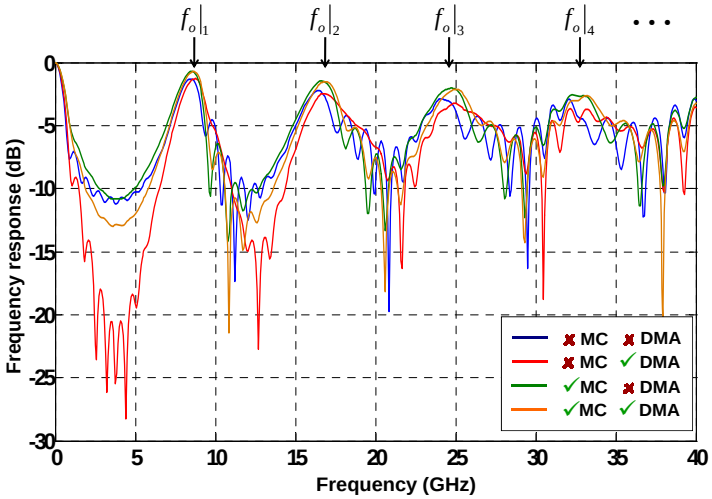

Figure 4.8.- Frequency responses up to 40GHz for a 62.5/125μm multimode fibre showing the effect of mode-coupling (MC) and the differential mode attenuation (DMA). L=3km and α=2.

From Fig. 4.8 it can be seen that higher order resonances far from baseband are slightly displaced over the frequency spectrum with changes in attenuation when considering or not both MC and DMA effects. If MC effects are present, there is no deviation on the resonances central frequency no matter the fibre DMA whilst DMA has a significant effect when no MC is considered. For this latter case, in the first resonance there is a deviation of $\Delta f_o|_1 = +0.3\text{GHz}$ for the case of DMA, being $f_o|_n$ the central frequency of the n^{th}-resonance (or n^{th}-bandpass) whereas in the third resonance a deviation of $\Delta f_o|_3 = +0.9\text{GHz}$ can be appreciated.

On the one hand, it has been previously stated that the autocorrelation coupling function follows a Gaussian function as described in Eq. 4.37. Consequently, the influence of the correlation length ς of the Gaussian coupling autocorrelation function in the MMF frequency response is studied. The rest of parameters take the same value as above. The simulations were performed for the case of no differential mode attenuation and for $\varsigma = 1 \cdot a,\ 30 \cdot a,\ 70 \cdot a$ and $140 \cdot a$ respectively.

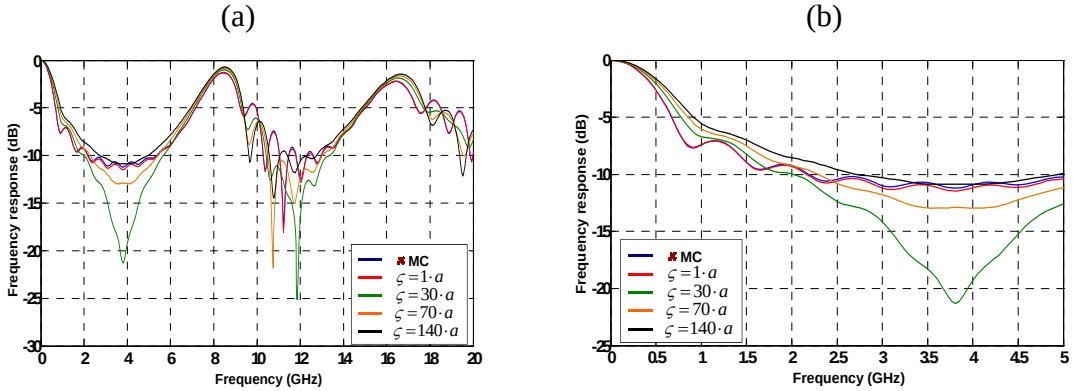

Figure 4.9.- Influence of the correlation length ς on the transfer function for a 62.5/125µm MMF silica fibre link of 3km and a rms deviation of $\sigma = 0.0009$ for frequencies up to (a) 20GHz and (b) 5GHz.

As it can be observed, increasing the correlation length (i.e. increasing mode coupling effects) results in a significant reduction of the filter notches plus broadening the 3-dB bandwidth of the transfer function baseband and the resonances. Again, the central frequencies of the same order resonance, for each case, are displaced over the frequency spectrum depending on the correlation length considered.

On the second hand, the influence of the rms deviation (σ) of the autocorrelation function, given by Eq. 4.37, on the transfer function is evaluated by fixing $\varsigma = 115 \cdot a$ and increasing the rms deviation from $\sigma = 0.0001$ to $\sigma = 0.003$. Same effects as those obtained for the correlation length ς where observed when varying σ.

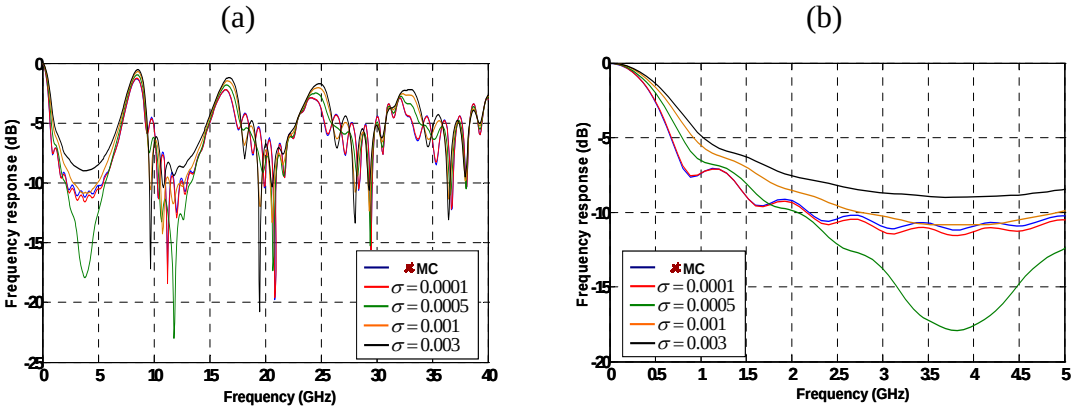

Figure 4.10.- Influence of the rms deviation of the correlation function on the transfer function for a 62.5/125µm MMF silica fibre link of 3km and for frequencies up to (a) 40GHz and (b) 5GHz.

4.8.3 Silica-based Multimode Optical Fibre frequency response dependency with the fibre parameters

In this subsection the influence of the optical fibre properties over the silica-based MMF frequency response is evaluated. Parameters defining its characteristics such as the core radius, the graded-index exponent, its length and the core refractive index are analyzed.

Firstly, the influence of the fibre core radius in the transfer function is studied. The cladding diameter was fixed at b=125μm and the graded index exponent was set to $\alpha = 2$. The rest of parameters for the simulation take the same value of previous sections. The simulations were performed for typical graded-index multimode silica optical fibre radii, such as a=25μm, 31.25μm, 40μm and 50μm. No differential mode attenuation effects have been considered. From Fig. 4.11(a) it can be seen that higher order resonances far from baseband are significantly displaced over the frequency spectrum providing slight changes in the 3-dB bandwidth of such regions but at different central frequencies. Central frequency of first resonance ($f_o|_1$) for a=25μm, 31.25μm, 40μm and 50μm occurs at $f_o|_1$=7.1GHz, 8.5GHz, 10.5GHz and 13.2GHz, respectively. Consequently, it is important to exactly determine the fibre core radius in order to determine the regions in which is possible to transport, for instance, RF carriers far from baseband. On the other hand, Fig. 4.11(b) shows the influence of the fibre core radius in the transfer function and the 3-dB baseband bandwidth for frequencies up to 5GHz. It can be seen that same baseband bandwidths are obtained although slightly higher excursions of the intermediate notches can be gained by enlarging the core radius.

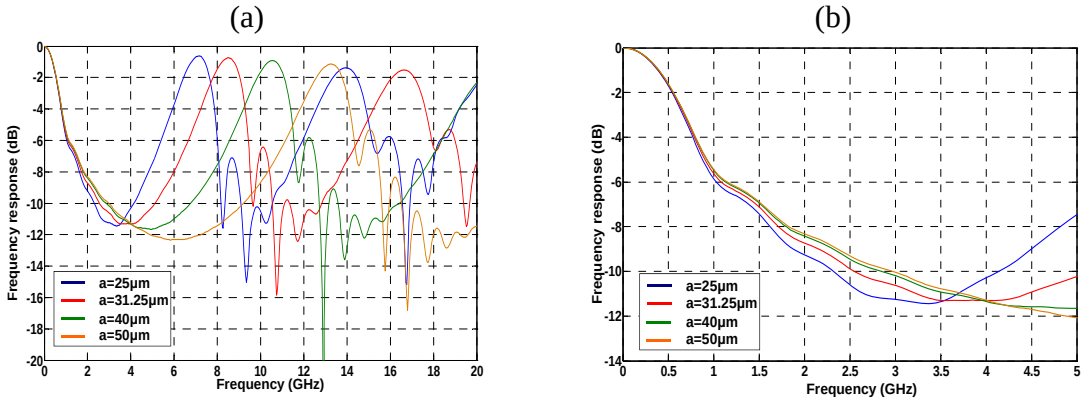

Figure 4.11.- Influence of the fibre core radius on the transfer function for a silica-based multimode optical fibre link of 3km for frequencies up to (a) 20GHz and (b) 5GHz. No DMA effects have been considered in the results.

One of the most important parameters that define the behaviour and performance of a graded-index optical fibre type is its graded index exponent α. It should be outlined that the index exponent α may slightly vary with wavelength, always due to the eventually nonlinear Sellmeier coefficients. As a consequence of this, a profile conceived to be optimal (in terms of bandwidth, for example) at a given wavelength may will be far from optimal at another wavelength. This fact was also addressed in Chapter 3 regarding the GIPOF wavelength-dependence of the index exponent. The α-dispersion is imposed by the

dopant and its concentration, so this impairment is not easy to overcome. A possible solution would consist on implementing the so-called multiple-α index profiles as proposed in [106] but the fibre fabrication will become huge complicated. Frequency responses are displayed in the following figures showing the influence of the graded index exponent of the fibre, defined in Eq. 4.3, on the RF transfer function in absence of differential mode attenuation and mode coupling effects. The rest of parameters for the simulations take the same value of previous sections.

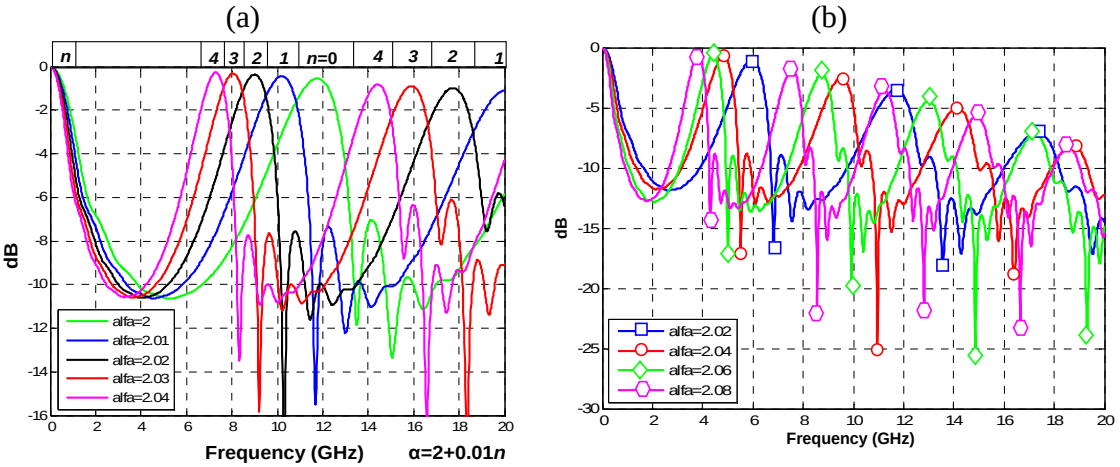

Figure 4.12.- (a) Frequency response of the MMF fibre link for different graded index exponents, α, when L=2km. (b) Frequency response of the MMF fibre link for different graded index exponents, α, when L=3km.

Fig. 4.12(a) and Fig. 4.12(b) show the frequency response of a silica-based MMF link for L=2km and L=3km, respectively, depending on the graded index exponent, α, of the fibre. Significant displacements of the higher order resonances over the frequency spectrum can be achieved with regards to this parameter. For example, from Fig. 4.12(a), an increase of α'=α+0.02 produces a change of the first-order resonance central frequency up to 2.8GHz. From both figures it can be seen that higher order resonances placed far from baseband also change the 3-dB bandwidth depending on such parameter.

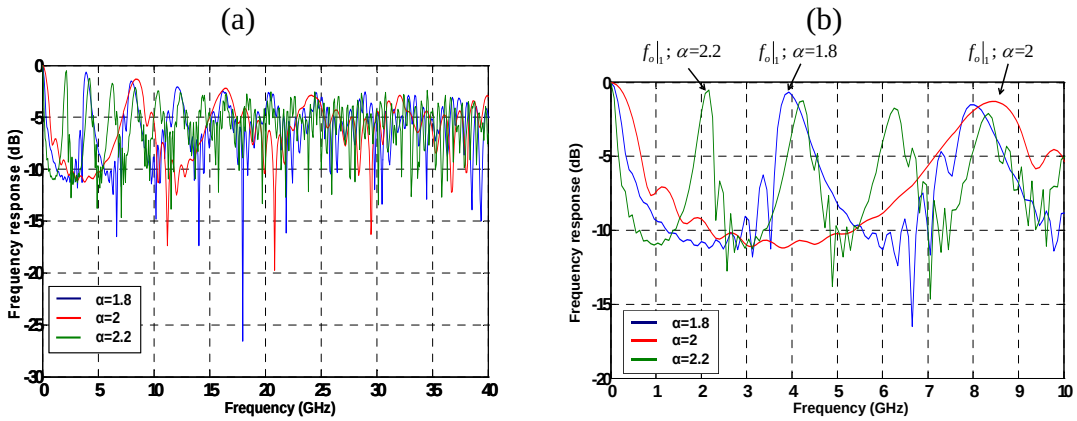

Figure 4.13.- (a) Frequency response of the silica-based MMF fibre link for different graded index exponents, α, when L=3km for frequencies up to 40GHz. (b) Zoom of Fig. 4.13(a).

From Fig. 4.13(a) and 4.13(b), as the graded index exponent of the fibre deviates from $\alpha = 2$, the FSR (Free Spectral Range) of the frequency response and the 3-dB bandwidth of the high-order resonances take lower values (see Table 4.3). This fact is coherent with the statement that there is an optimum index profile providing minimum dispersion effects. As $\alpha = 1.8$ and $\alpha = 2.2$ are quite far for the condition given by Eq. 4.74, the FSR and the 3-dB bandwidth of the high-order resonances take lower values, due to the increment of propagation time difference between the fastest mode ($\delta = 0$) and the slowest mode ($\delta = \Delta$), compare to the case in which $\alpha = 2$.

$$\alpha_{opt} = 2 + \varepsilon - \Delta \frac{(4+\varepsilon)\cdot(3+\varepsilon)}{5+2\varepsilon} \tag{4.74}$$

where ε is the profile dispersion parameter and Δ is the relative refractive index difference, at a specific wavelength, given by Eq. 4.47 and Eq. 4.4, respectively.

	FSR (GHz)	**n**	$\Delta f\|_{-3\text{dB}}$ **Baseband (GHz)**	$\Delta f_o\|_1\|_{-3\text{dB}}$ **(1st resonance) (GHz)**	$f_o\|_1$ **(1st resonance) (GHz)**
$\alpha = 1.8$	4	2	0.28	0.8	3.9
$\alpha = 2$	8.5	1	0.57	1.9	8.5
$\alpha = 2.2$	2.1	4	0.14	0.4	2.1

Table 4.3.- Simulation values concerning figure 4.13(b). Parameter n refers to the number of resonances within the 10GHz frequency SPAN depicted in the figure.

The results confirm that the FSR and the 3-dB resonance bandwidth are smaller in the cases of $\alpha = 1.8$ and $\alpha = 2.2$ than for a parabolic grading. This reduction is a consequence, as explained above, of the increased value of the difference between the modal group delays $\tau(m, \lambda)$ defined by Eq. 4.46.

The following figure, Fig. 4.14(a), shows the frequency response of a 3km silica-based MMF link considering a graded-index exponent of the fibre $\alpha < 2$. It can be seen that lower values of α provide a higher 3-dB resonance bandwidth and higher central frequencies of the resonances than cases $\alpha = 2$ and $\alpha > 2$, but with an attenuation penalty in the bandpass which is increased with the index difference with regards to the case of $\alpha = 2$. In conclusion it is possible to affirm that the optimum index profile exponent regarding the 3-dB resonance bandwidth (in order to transmit RF signals far from baseband through a silica-based multimode optical fibre) corresponds to those indexes in which $\alpha < 2$, as they provide the maximum bandwidths for each of the transversal filter resonances. Moreover, taking advantage of the expression which gives the optimum index profile in terms of 3-dB baseband bandwidth defined by Eq. 4.74, it yields $\alpha_{opt} = 1.938$ at 1300nm for the values $n_{core} = 1.4558$, $n_{cladding} = 1.4472$, $\Delta = 0.00589$ and $\varepsilon = -0.0482$. This optimized value is congruent with the simulation depicted in Fig. 4.14(b) in which the 3-dB baseband bandwidth takes its maximum value for the range $1.93 < \alpha < 1.94$.

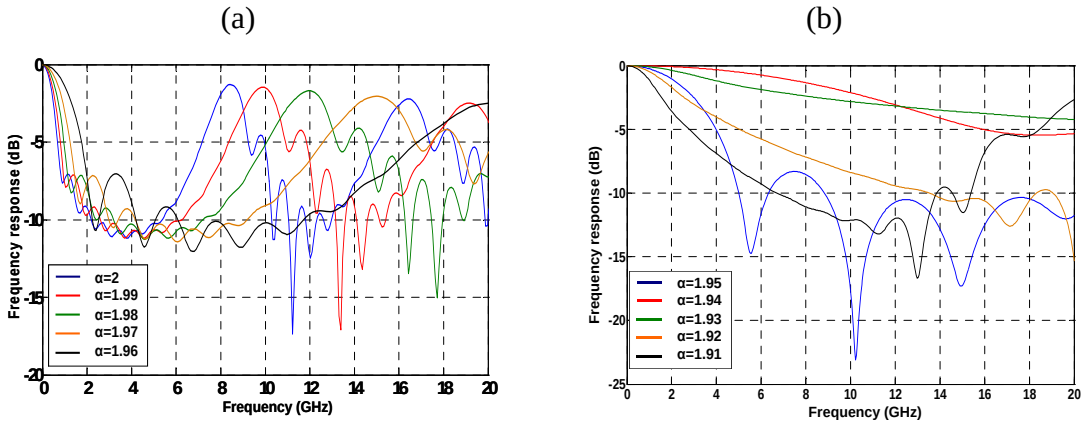

Figure 4.14.- (a) Frequency response of the silica-based MMF fibre link for different graded index exponents ranging $1.96 < \alpha < 2$ when L=3km. (b) Frequency response of the MMF fibre link for different graded index exponents ranging $1.91 < \alpha < 1.95$ when L=3km, in which the optimum index profile is observed.

The MMF frequency response dependence on the link length has also been studied. Most significant theoretical simulations results are presented in Fig. 4.15, considering a parabolic core grading ($\alpha = 2$) and a chirp free source. The rest of parameters are kept fixed at the same values of previous section.

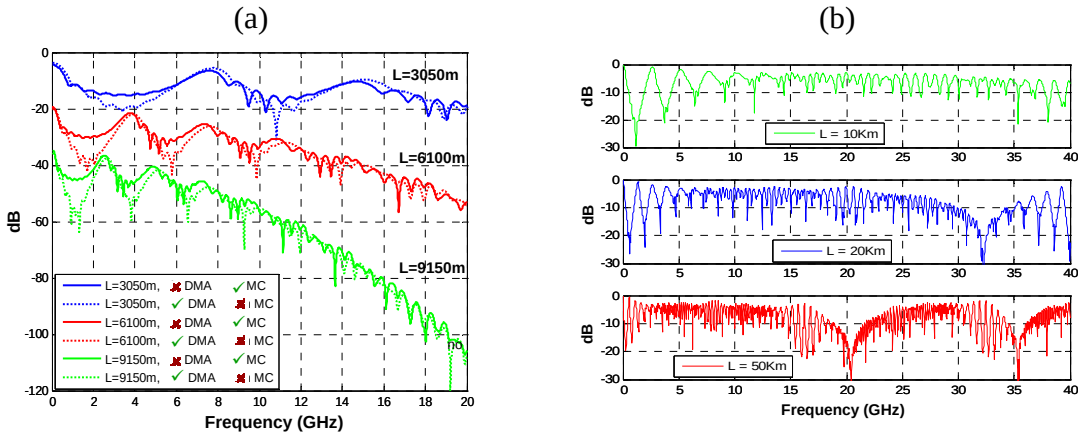

Figure 4.15.- (a) Frequency response of the MMF fibre link when considering or not the mode coupling (MC) and the differential mode attenuation (DMA) effects, with α=2 and for different fibre lengths. (b) Theoretical simulation of the transfer function for MMF link lengths with α=2 and L=10km, 20km and 50km, respectively.

On the one hand, Figure 4.15(a) shows the theoretical simulation of a MMF link frequency response for different lengths L=3050m, L= 6100m and L=9150m when considering or not the effects of the mode coupling (MC) and the differential mode attenuation (DMA). These lengths of fibre have been chosen for being exactly the same as those from the fibre spools being at the laboratory. It can be seen that higher order resonances far from baseband are slightly displaced over the frequency spectrum with changes in attenuation depending on the case. On the other hand, Figure 4.15(b) shows the theoretical simulation of a MMF link frequency response for different link lengths (L=10km, 20km and 50km). In this last figure the transmission regions can be easily identified as well as the effect of the carrier

suppression due to the presence of intermediate notches, see Fig. 4.15(b). This effect can not be overlooked but could be avoided using single sideband modulation. Nevertheless, both figures show how the ratio between different fibre lengths is inversely proportional to the ratio of resonance periodicities for those fibre lengths.

Finally, variations on the MMF core refractive index have also been analyzed. For example, this parameter strongly depends on the dopant concentration during the manufacturing process. A graded index multimode fibre with a SiO_2 core doped with GeO_2 and SiO_2 cladding and intrinsic attenuation of 0.55dB/km has been considered. Different core refractive indices (n_{cc1} and n_{cc2}) are calculated considering a 6.3mol-% and a 7.5mol-% GeO_2 doped core which imply different Sellmeier coefficients. A SiO_2 cladding is considered in both cases so they are assumed to have the same cladding refractive index (n_{cl}). Also for both cases a link length of L=2km is considered and the rest of parameters are kept fixed at the same values of previous sections. These doping concentrations and cladding correspond to identical core refractive indices and cladding index as those illustrated in Fig. 4.6(a). From this figure, it is estimated a core refractive index increment of approximately $\Delta n_{cc} = 1.783\times10^{-3}$ at an operating wavelength of 1300nm, which implies a numerical aperture deviation of $\Delta(\mathrm{NA}) = 0.015$, being a typical tolerance value provided by manufacturers.

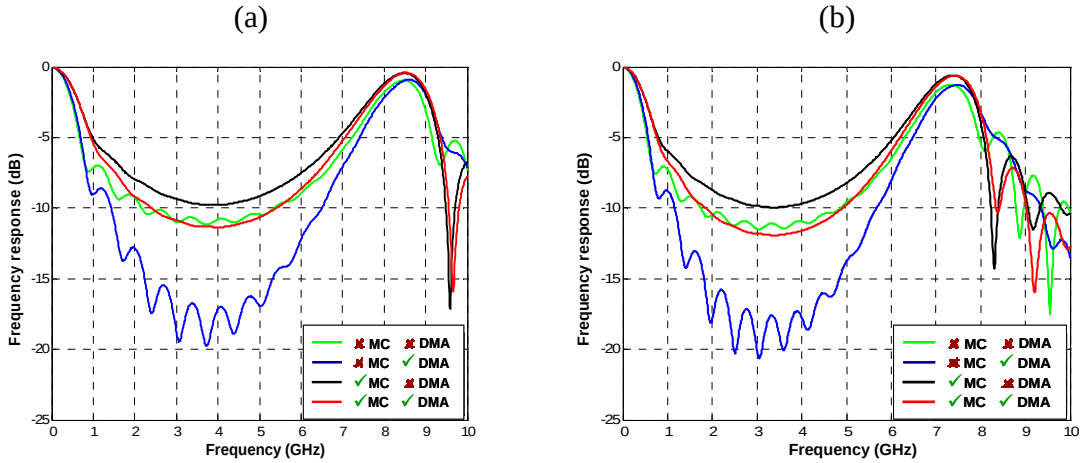

Figure 4.16.- (a) Frequency response for a 6.3mol-% GeO_2 doped SiO_2 core. (b) Frequency response for a 7.5mol-% GeO_2 doped SiO_2 core.

The frequency responses for both cases considered are shown in Fig. 4.16(a) and 4.16(b), respectively. It can be seen that different GeO_2 concentrations in the doped core provide different resonance frequencies, changing from 8.5GHz in case of (a) to 7.5GHz in case of (b), although the 3-dB resonance bandwidth in each case stands approximately at 1.7GHz. Consequently, it is also essential to determine the dependence of the core refractive index with the wavelength, i.e. $n = n(\lambda)$.

4.8.4 Silica-based Multimode Optical Fibre frequency response dependency with the source parameters.

In this subsection the influence of the optical source characteristics over the MMF frequency response is evaluated. Parameters defining its characteristics such as the linewidth, the chirp and the wavelength emission are analyzed.

At first, the effect caused by the source linewidth is reported in the following figures for a fibre length of 3km and 6km and a source chirp set to zero. It has been assumed a parabolic graded index exponent, i.e. $\alpha = 2$. The rest of parameters take the same value as those indicated in above sections. The frequency response is displayed for a typical Distributed Feedback laser (DFB laser) with a rms linewidth of 10MHz, a multimode Fabry-Perot laser (FP laser) with *W*=5.5nm and a Light Emitting Diode (LED) with *W*=30nm.

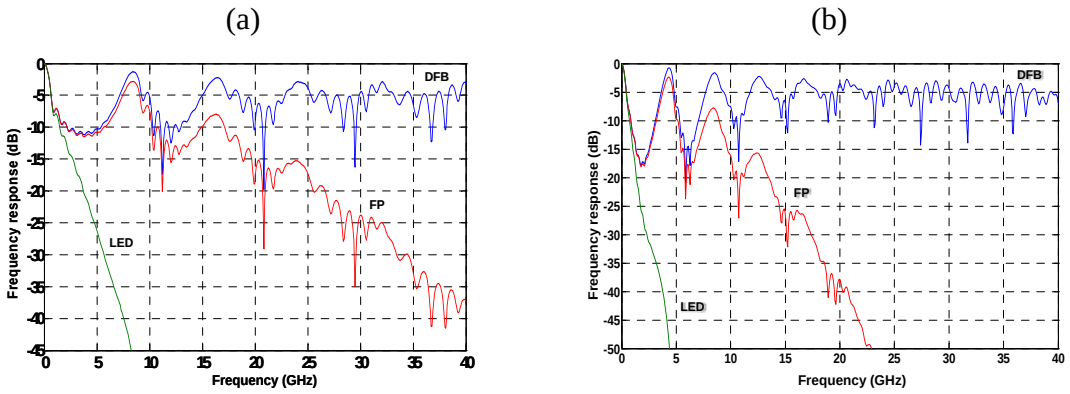

Figure 4.17.- (a) Influence of the optical source temporal coherence on the frequency response for a fibre link of L=3km. (b) Influence of the optical source temporal coherence on the frequency response for a fibre link of L=6km.

As it can be observed from Fig. 4.17(a), for the case of L=3km, a first resonance featuring a 3-dB bandwidth of around 2GHz in the case of the DFB laser and around 1.9GHz in the case of the FP laser is obtained, both at around a central frequency ($f_o|_1$) of 8.5GHz, due to the transversal filtering effect. On the other hand, no resonance is present when a broadband LED (broadband optical) source is applied. This is due to the fact that, in this later case, the low pass term in Eq. 4.69 dominates over the other two. Furthermore, for a DFB laser source the attenuation in the higher-than-first resonances remains under similar values whereas for a FP laser source the second and following resonances are rapidly decreased in optical power. Therefore, exploiting the possibility of transmitting broadband signals at high frequencies using a MMF link is contingent on the use of low linewidth sources, as it has been also stated in the work reported in [25]. A similar conclusion can be derived for the case of L=6km depicted in Fig. 4.17(b), in which the resonance decrease is even more noticeable for the FP source case.

Secondly, the influence of the source chirp over the silica-based MMF frequency response has been studied. For the simulations a source with a linewidth of 10MHz has been considered with a parabolic index profile optical fibre for a L=6km link length. Three values of the source chirp (0, -2 and -3) are illustrated in the following figure, namely Fig.

4.18. The chirp parameter is commonly used for describing sources which employ sinusoidal waveform modulations whose instantaneous frequency increases or decreases linearly over time. That is, $f(t) = f_S + \kappa \cdot t$, where f_S is the starting frequency and κ is the rate at which frequency increases/decreases, namely chirp rate or simply chirp. From an optical point of view, direct modulation of an optical source causes abrupt changes in the emission wavelength of the laser and therefore limits the signal reach via fibre. The rms deviation of the coupling autocorrelation function was adjusted to $\sigma = 0.0021$. The rest of the simulation parameters take the same value as aforementioned.

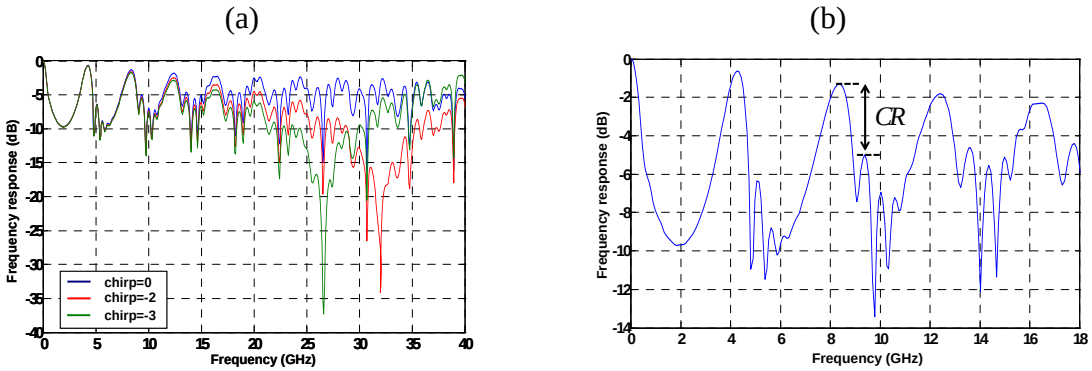

Figure 4.18.- (a) Frequency responses and Carrier Suppression Effect for different values of the source chirp for a fibre link of L=6km. (b) Zoom of the frequency response considering the condition chirp=0.

Considering the case of a chirp free source it can be observed that the contrast ratio, *CR* (or roll-off of the passband), between the transversal filter resonances and the secondary side-lobes is dramatically reduced as the RF frequency increases. This is due to the fact that the difference on the propagation delays between adjacent mode groups is not a constant value, i.e. the MMF link behaves as an imperfect transversal filter [104]. Consequently, it is possible to provide broadband transmissions at higher frequencies than baseband through a multimode optical fibre. This fact can be seen, particularly, in Fig. 4.18(a); chirp=0 featuring a region with small losses identified at frequencies above 20GHz. Below this region, RF transmission can also be performed but at determined bands corresponding to the filter resonances. From Fig. 4.18(b), which is a zoom of curve with chirp=0 depicted in Fig. 4.18(a), bands centered at $f_o\big|_n$=4.3GHz, 8.4GHz, 12.4GHz and 16.4GHz for $n = 1,2,3,4$ can be respectively obtained. And, furthermore, each band provides a minimum 3-dB bandwidth of around 1GHz. Cases selecting chirp=-2 and chirp=-3 illustrate the influence of the carrier suppression effect which can not be neglected. The first notch of the frequency response relative to a chirp=-2 is situated at approximately 32GHz while it appears at 26GHz for the condition of source chirp=-3.

Finally, the silica-based MMF frequency response is also evaluated regarding the wavelength emission provided by the optical source. This parameter also links with the optical fibre properties, as parameters such as the core and cladding refractive indices, the material dispersion, the propagation constant, the intrinsic attenuation and the number of propagated modes strongly depends on the optical wavelength launched into the fibre. Fig. 4.19 depicts a 2km-long silica-based MMF frequency response for two different sources,

namely a Distributed Feedback (DFB) laser and a Fabry-Perot (FP) laser, both for 650, 1300 and 1550nm operating wavelengths, respectively. The intrinsic attenuation was considered to be 3dB@650nm, 0.7dB@1300nm and 0.5dB@1550nm, respectively, which are typical attenuation values provided by manufacturers. Source linewidths were simulated with values of 10MHz and *W*=5nm for the DFB and FP optical sources, respectively. From both figures, it is worth pointing out that the high-order resonance central frequencies are located at different points and, what is more important, the 1300nm operating wavelength provides the highest 3-dB high-order resonance bandwidth comparing with that of the cases of 650nm and 1550nm. Moreover, in Fig. 4.19(b) it is clearly seen the influence of the material dispersion at 650nm for sources with low temporal coherence (i.e. high linewidth values). These facts are related with the dispersion values in silica-based MMFs, shown in Fig. 4.2, which are typically around -200 ps/(nm·km), -3 ps/(nm·km) and +17 ps/(nm·km) at 650nm, 1310nm and 1550nm, respectively.

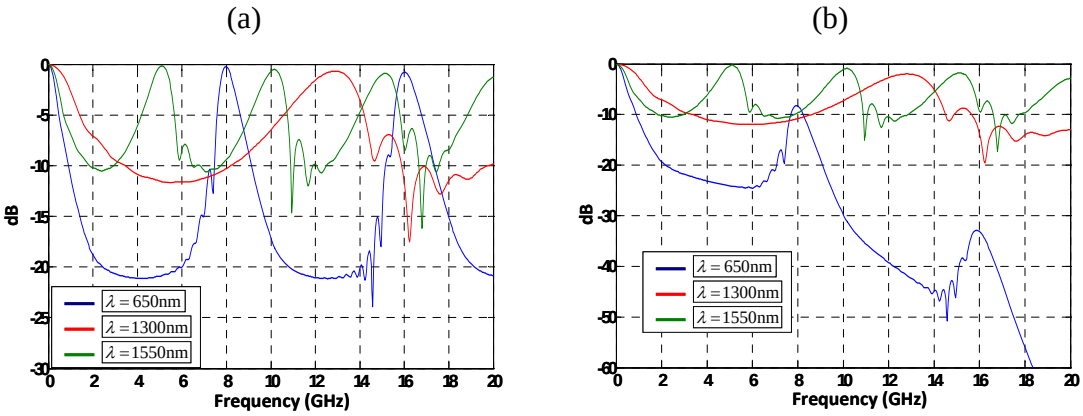

Figure 4.19.- (a) 2km-long MMF frequency response at different DFB (10MHz linewidth) source wavelengths. (b) 2km-long MMF frequency response at different FP (*W*=5nm) source wavelengths.

4.8.5 Conclusions on silica-based Multimode Optical Fibres simulations

In the previous section of this chapter, the RF transfer function of a MMF link based on the electric field propagation method is described and analyzed, based on the model previously reported in [97], in order to evaluate the conditions upon which broadband transmission is possible in RF regions far from baseband. From such a model it can be concluded that MMFs offer the potential for broadband RoF transmission in the microwave and millimeter wave regions in short- (2-5km) and middle- (~10km) reach distances. Much of this potential is related to the fact that the MMF link behaves like an imperfect microwave photonic transversal filter [99], featuring a non-constant delay between adjacent samples (i.e. mode groups). However, the potential for transmission over longer distances requires further research.

On the other hand, in the silica-based MMF transfer function model presented in this chapter most of the launching conditions (or guidance parameters) over the fibre as well as

the optical fibre properties have been considered. However, the passband regions provided by the photonic transversal filter behavior, in which it is possible broadband transmission far from baseband, have the disadvantage of being strongly dependent on the operating conditions, as seen in this chapter, so it is necessary to accurately define all the parameters included by the model. This fact seems to also be the main drawback.

With the aim to determine the end to end linear transfer function of the system, the most general conditions and multitude of practical sources of impairment have been taken into account, such as:

- Temporal and spatial source coherence.
- The source chirp.
- Chromatic and modal dispersions.
- Mode coupling.
- Input signal coupling to modes at the input of the fibre.
- Coupling between the output signal from the fibre to the detector area.
- Differential mode attenuation.

From the theoretical simulations provided in this chapter, the performance of the silica-based MMF transfer function model showed the following results:

- Considering mode coupling effects on the transfer function, the RF baseband bandwidth is increased while the differential mode attenuation has little effect on the bandwidth itself. Furthermore, slight deviations on the high order resonances central frequencies are observed when considering or not both effects. On the other hand, the filtering effect (i.e. excursions of the MMF frequency response resonances) is mainly driven by the differential mode attenuation, being decreased when considering mode coupling effects.
- Increasing the correlation length ς of the Gaussian coupling autocorrelation function results in a reduction of the filtering effect plus broadening the 3-dB bandwidth of both the baseband and resonances. Similar effects can be deducted by increasing the rms deviation of the autocorrelation function (σ).
- Although different fibre core radius lead to similar 3-dB baseband bandwidths, a variation of this parameter implies a displacement of the higher order resonances of the transfer function over the frequency spectrum as well as a slight broadening of the 3-dB bandwidth of the resonances.
- Small deviations from a parabolic index of the fibre, $\alpha = 2$, lead to significant displacements of the central frequency of the higher order resonances (higher/lower central frequencies are obtained when $\alpha < 2$ and $\alpha > 2$, respectively). Furthermore, these variations also imply a broadening of the 3-dB baseband and resonances bandwidth when $\alpha < 2$ or a constriction of the 3-dB baseband and resonances bandwidth when $\alpha > 2$.
- Exploiting the possibility of transmitting broadband signals at high frequencies within MMF links is contingent on the use of low linewidth sources (such as Distributed Feedback Lasers, DFB lasers) providing small attenuations in the second-order and following resonances, as the theoretical model predicts.

- Depending on the source chirp, notches on the frequency response must be taken into account due to the carrier suppression effect as they make impossible the transmission of RF signals at such frequencies.
- The ratio between different fibre lengths is inversely proportional to the ratio of the resonance periodicities for those fibre lengths, i.e. for the same guidance parameters and optical properties of the fibre there is a univocal relation between the MMF link length and central frequencies of the resonances.
- Although different fibre core radius refractive indices lead to similar 3-dB baseband bandwidths, this fact also implies different resonance frequencies of the transfer function over the frequency spectrum. This core refractive index is strongly dependent on the dopant concentration (mol-%) added in the fabrication process.

4.9 Silica-based Multimode Optical Fibre Transfer Function model validation. Experimental Results

In order to validate the transfer function model proposed in Section 4.8 some measurements have been carried out. A 62.5/125μm silica-based graded-index multimode optical fibre with 0.26dB/km of attenuation at 1300nm and numerical aperture at the core center NA=0.185 has been used. This silica-based multimode fibre complies class OM1 defined by ISO/IEC[2] 11801-"Generic cabling for customer premises" [107]. Such standard also assures <1dB/km for a wavelength range of $1300\text{nm} < \lambda \leq 1380\text{nm}$, with a bandwidth per length product of 500MHz·km defined at OFL condition. Consequently, for instance, 1GbE specifications for next generation access services described in Chapter 2 could be only fulfilled up to 550m approximately, being far from middle-reach deployments.

On the other hand, three different lengths have been evaluated: 3050m, 6100m and 9150m covering middle-reach distances. These distance values are representative of currently deployed moderate-length fibre links. Two typical wavelengths in optical communication systems such as 1300nm and 1550nm have been evaluated. An Agilent 8703B Lightwave Component Analyzer (LCA) has been used to measure the frequency response also allowing the possibility of modulate the optical power source. As an alternative, an electro-optical (E/O) intensity external modulator up to 16GHz from JDSU (JDSU AM-150S for 1550nm and AM-130S for 1300nm, respectively) has been employed. Alternatively to the photodetector provided by the 8703B device, an ultrafast photodiode from Discovery Semiconductor Inc. (DSC30S) with a 3-dB bandwidth of 24GHz has also been employed for the measurements taken in this section. In order to confirm the theoretical results shown in the above section, the silica-based MMF frequency response has been also measured for different optical sources:

- a tunable Distributed Feedback Laser (DFB, Agilent 81989A), characterized by a low linewidth, typically <5MHz, with a tuning wavelength range from 1465m to 1575nm,

[2] ISO/IEC: International Standards Organization / International Electrotechnical Commission

- a low-cost Fabry-Perot (FP, Agilent 81655A) laser with rms spectral linewidth of $\Delta\lambda = 1.8$nm and operating wavelength of 1300.98nm (hereafter it will be considered 1300nm), and
- a Broadband Light Source (BLS), model SLD09CS from Yokogawa, ranging from 1250nm to 1650nm.

It has been previously stated that an important approach to force less modal dispersion consists in reducing the number of modes propagated through the fibre, i.e. achieving Restricted-Mode Launching (RML), by means of practical mode-filtering implementations at the transmitter and/or receiver side. For the measurements, a transmitter-side mode-filtering is simply performed by central launching the light from a singlemode fibre (SMF) patch cord. On the other hand, Overfilled Launching condition (OFL), in which all the modes are fully excited, is obtained by means of a 2m-long 62.5µm core diameter silica-based MMF patch cord plus a mode scrambler before launching the optical power into the MMF link.

The schematic of the set-up for the experimental measurements is shown in Fig. 4.20. Figure inset also illustrates the set-up for the launching conditions considered in this section.

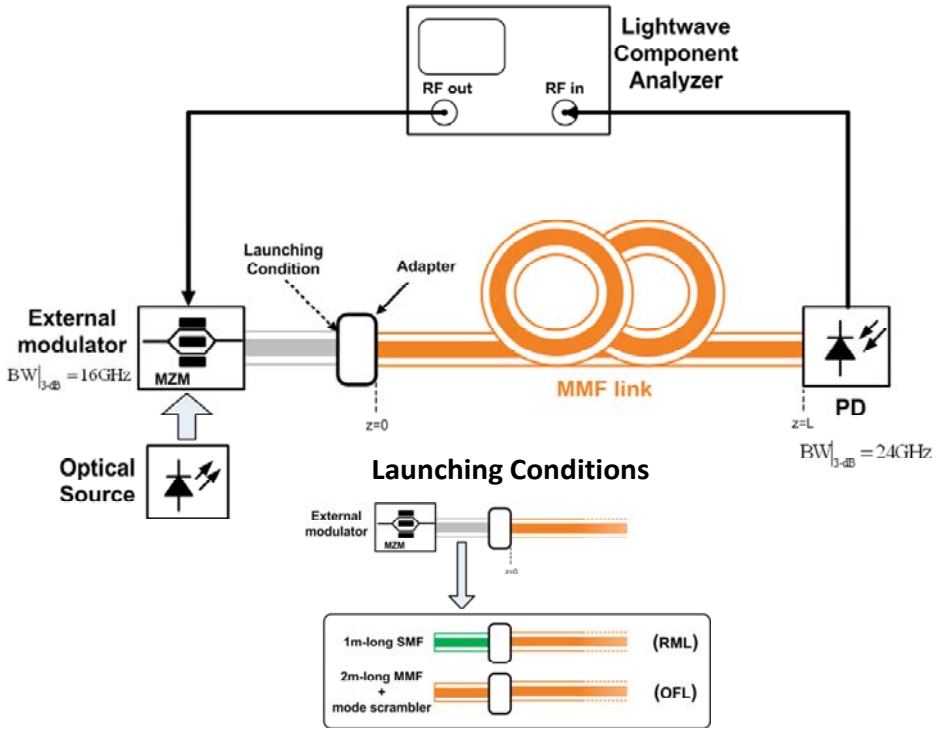

Figure 4.20.- Block diagram of the experimental set-up for the silica-based MMF link frequency response measurement up to 20GHz. Inset: diagram of the different launching conditions applied. Measured bandwidths of the devices are also indicated.

The electrical responses of both the electro-optical intensity modulator and the photodetector have been measured. It is illustrated in Fig. 4.21(a) the electrical response of the photodetector, showing a Signal-to-Noise Ratio (SNR) of around 40dB. Fig. 4.21(b)

shows the electrical response of the E/O modulator. The experimental results of the silica-based MMF link shown in this section will be calibrated with regards to both electrical responses, being therefore solely attributed to the MMF.

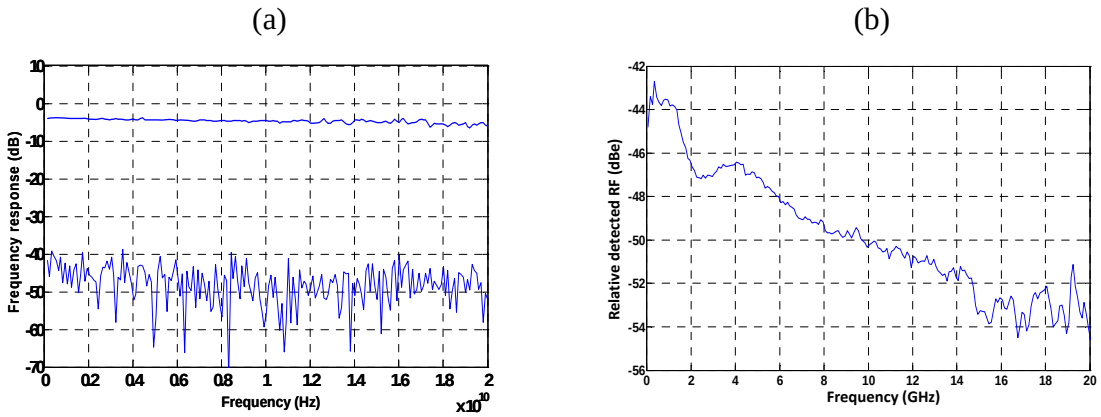

Figure 4.21.- (a) Measured electrical response of the DCS30S up to 20GHz. (b) Measured electrical response of the E/O modulator from JDSU AM-130.

Previous to a detailed analysis for further distances, the frequency response of the silica-based MMF, considering the model presented in this chapter developed by Gasulla *et al.* [46] as well as that presented in Chapter 3 developed by Yabre [34], have been evaluated for lengths of 10m and 20m with experimental measurements, at a first approach. The results are shown in Fig. 4.22(a) and Fig. 4.22(b), respectively. An OFL condition has been implemented by means of a 2m-long silica-based MMF patch cord plus a mode scrambler before launching the optical power into the link, thus achieving a steady state mode power distribution in which all the modes are fully excited.

The predicted frequency response shows a good agreement between both models considered. It can be noticed that, at a first sight, operating at 1300nm implies less attenuation and less material dispersion so higher bandwidths than at 1550nm can be expected. However, the higher source linewidth employed for the measurements at 1300nm compared to that employed at 1550nm can lead to think on the opposite behavior. The reason for the measurements obtained is that the link dependence with the source linewidth is negligible due to the extremely short distances employed at this approach. This dependence will increase for longer distances or with the employment of even a higher linewidth, as Broadband Light Sources (e.g. Light Emitting Diode, LED), as it will be seen in following figures. This latter case can be seen in Fig. 4.23, where the experimental results shown in Fig. 4.22 are compared with those obtained, for the same conditions, but employing a BLS as the optical source.

It is worth mentioning that the ripples observed in the frequency responses of Fig. 4.22 and Fig. 4.23 are caused by reflections in the optical set-up and are not features of the fibre response. This latter fact will be also appreciated in the following figures within this section.

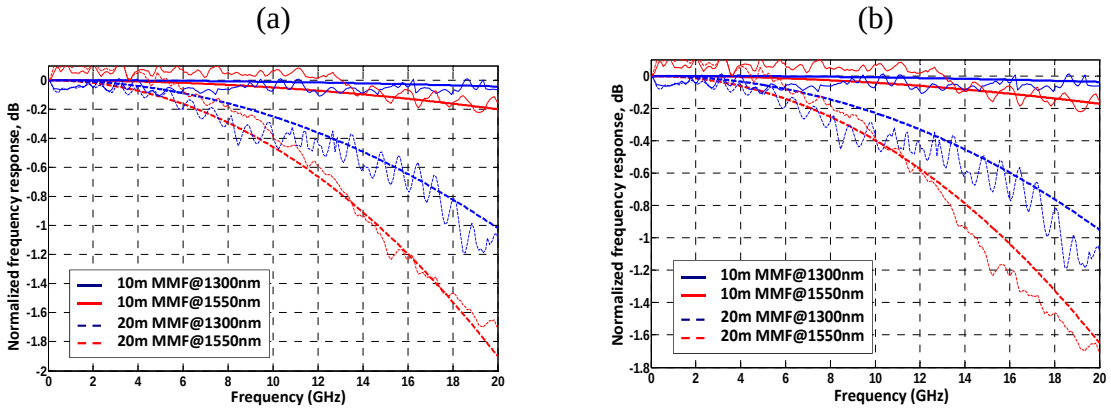

Figure 4.22.- (a) Silica-based MMF theoretical and measured frequency response considering the model presented in this chapter and developed in [46]. (b) Silica-based MMF theoretical and measured electrical response considering the model presented in Chapter 3 and developed in [34].

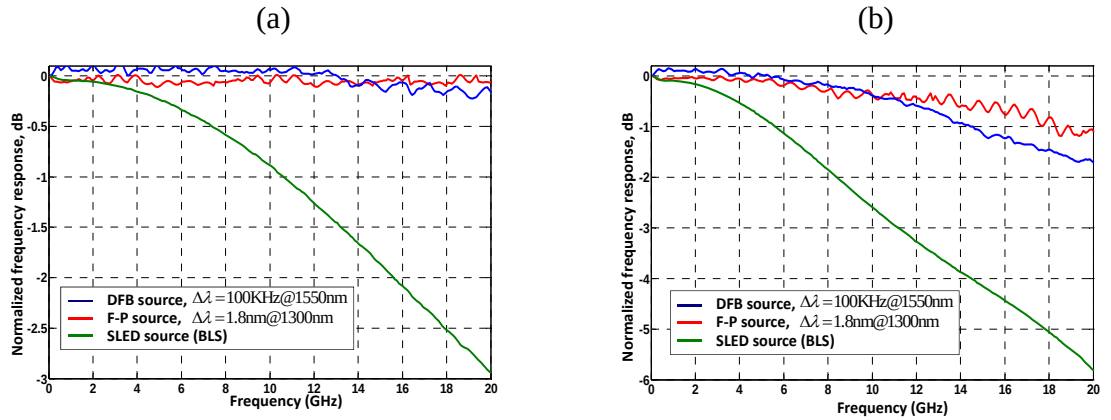

Figure 4.23.- (a) Measured frequency response of 10m-long silica-based MMF link for different optical source linewidths. (b) Measured electrical response of 20m-long silica-based MMF link for different optical source linewidths.

On the other hand, it should be noted that, hereafter, all depicted results within this section have been averaged with an average factor of Avg=8. The below set of figures, corresponding to Fig. 4.24, illustrate three normalized frequency responses measured using the 8703B Lightwave Component Analyzer after calibrating the results with regards to both the modulator and detector electrical responses for 3050m, 6100m and 9150m link lengths. In such figure the influence of the temporal coherence of the source is evaluated. After the modulator, the light has been directly launched to the 62.5µm core diameter GI-MMF by means of an FC/PC connector via a 2m-long MMF patch cord including a mode scrambler thus performing an OFL condition.

Fig. 4.24(a) shows the measured frequency response for a 3050m silica-based MMF link. As it was expected from the theory, while the response for the DFB laser (@1550nm) behaves relatively flat at high frequencies, with maximum variations of approximately ± 0.8 dB with regards to a mean level of approximately 0.7dB below the low frequency regime, the response relative to the FP laser (@1310nm) suffers from a low pass effect characterized by a 15dB fall at 20GHz. In the case of the Broadband Light Source (BLS),

the response falls dramatically after a few GHz. Therefore, we can conclude that exploiting the possibility of transmitting broadband RF signals at high frequencies is contingent on the use of narrow-linewidth sources. This latter performance stands regardless the operating wavelength from the optical source. It is worth mentioning that for the narrow-linewidth source, the detected power presents low variations with time (i.e. it presents a negligible level of modal noise), while the use of wider-linewidth sources resulted in a non-variant response. For comparison, the normalized frequency response of a 6100m and 9150m MMF link is depicted.

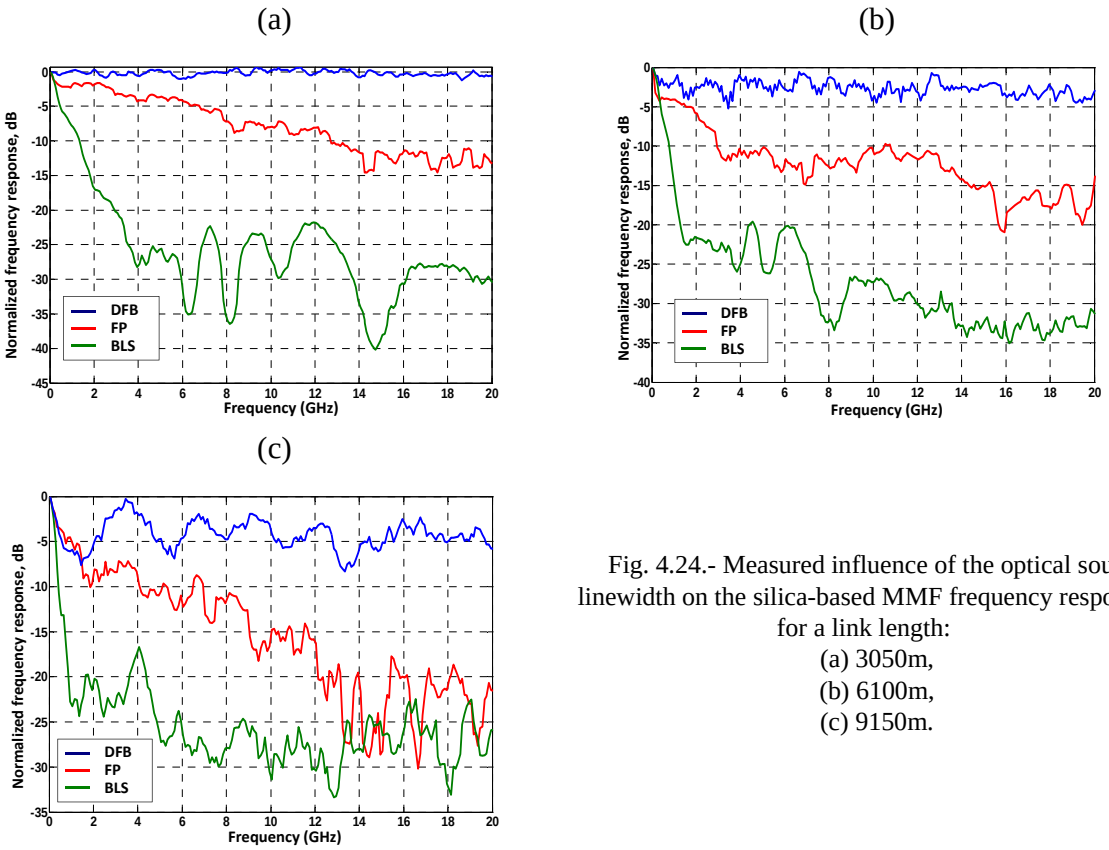

Fig. 4.24.- Measured influence of the optical source linewidth on the silica-based MMF frequency response for a link length:
(a) 3050m,
(b) 6100m,
(c) 9150m.

The silica-based MMF frequency response dependence on the link length is shown in the following figure for the case of a FP optical source operating at 1300nm, see Fig. 4.25(a), and for the case of a DFB optical source at 1550nm, see Fig. 4.25(b). Links of length 3050m, 6100m and 9150m have been evaluated, showing their normalized frequency response up to 20GHz. Comparing both figures, it is observed that, again, exploiting the data transmission in the high-order resonances is contingent with the use of low-linewidth sources, as expected. These resonances are clearly seen for the case of the DFB optical source and lower excursions and higher attenuation are achieved for the FP case.

In addition to, three effects can be noticed from both figures. However, we will focus on the figure on the right-hand, namely Fig.4.25(b). Firstly, the higher the MMF link length is, the higher number of side-lobes is present in a certain frequency range, i.e. the Free Spectral Range (FSR) of the resonances is reduced. Secondly, the contrast ratio between the

high-order resonances and the secondary side-lobes is dramatically reduced as lower link lengths are considered. Finally, higher 3-dB high-order resonance bandwidths are achievable when lower link lengths are considered. All these performances are due to the fact that the MMF link behaves as an imperfect transversal filter, i.e. the difference in the propagation delays between adjacent mode groups is not a constant value.

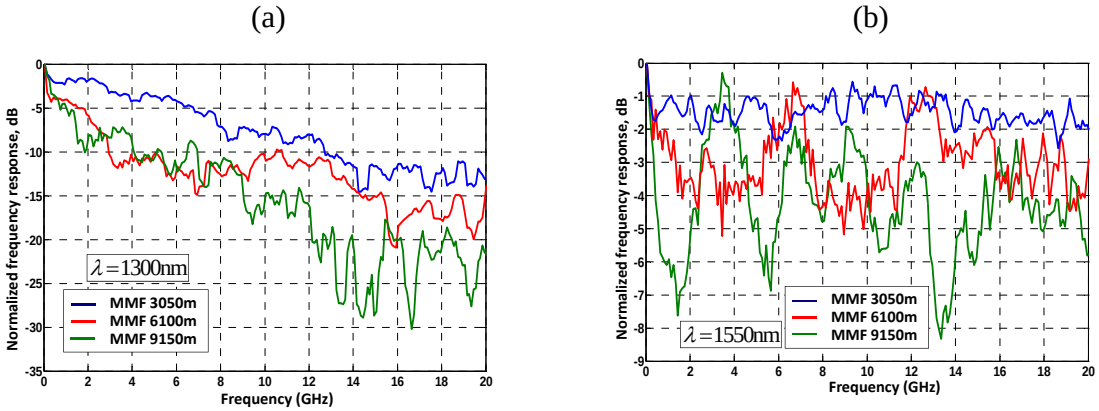

Figure 4.25.- (a) Measured frequency response of the silica-based MMF link at 1300nm for different lengths. A FP source was applied. (b) Measured frequency response of the silica-based MMF link at 1550nm for different lengths. A DFB source was applied.

With the aim of comparatively study the dependence on the launching condition over the MMF link, Fig. 4.26 shows the normalized measured frequency response for 6100m and 9150m lengths, respectively. Results have been carried out using the DFB laser source operating at 1550nm. RML launching has been achieved by directly launching the optical power from the source to the 62.5μm core diameter GI-MMF by means of an FC/PC connector via a 1m-long SMF patch cord thus achieving a selective central-launching (although errors from connector offsets should be considered). On the other hand, OFL excitation has been performed by launching the optical power to the GI-MMF link via a 2m-long MMF patch cord in combination with a mode scrambler.

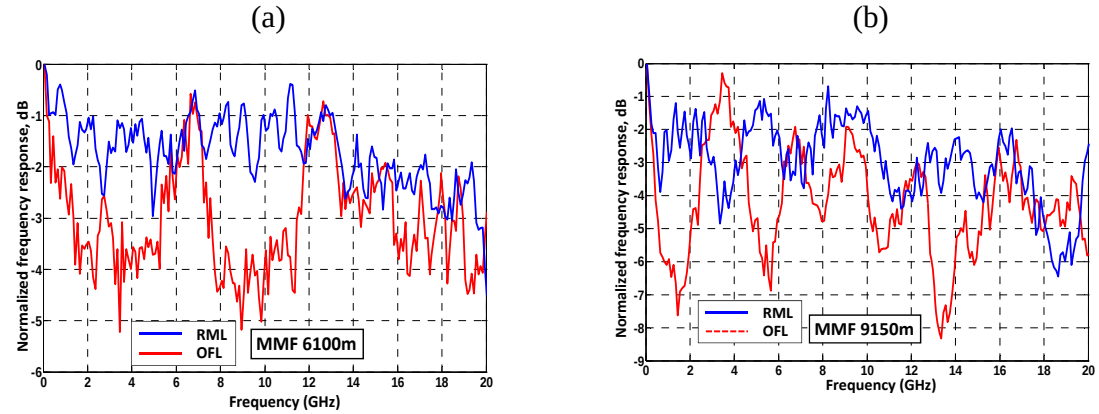

Figure 4.26.- (a) Measured frequency response of the 6100m-long silica-based MMF link at 1550nm for different launching conditions. (b) Measured frequency response of the 9150m-long silica-based MMF link at 1550nm for different launching conditions.

From the above figures it can be appreciated that for the RML condition, in which a limited number of modes is excited, the typical transversal filtering effect of the MMF is significantly reduced, thus achieving an increased flat response over the spectrum. Consequently, broadband RF, microwave and millimetre wave transmission overcoming the typical silica-based MMF bandwidth per length product could be possible, through a selective central–launching scheme or through different schemes but with the same goal of limiting the number of excited modes at launching. In addition to, MMF links with such launching configuration are also suitable for transmission in passband channels over a broad region of frequencies. These results follow the same selective-mode launch concept of previously reported works as well as those referenced in Chapter 3. Considering silica-based MMFs, for instance, in [13] the scheme investigated doubled the MMF bandwidth per length product by the selective launching of lower order modes into the fibre at the transmitting end and on filtering out, at the receiver, the fraction of the energy that was coupled into the higher order modes throughout the propagation in the multimode fibre. A later work [54] proposed a mode-field matched center launching (i.e. directly splicing a SMF with a MMF) achieving data rates of 40Gbps over 3.7km of a multimode fibre link.

It is noteworthy that the performance of the silica-based MMF fibre under test in both figures shows a bandwidth per length (BW·L) product, at OFL condition (dashed line), which is quite above to the worst-case BW·L specified, for the 62.5μm core diameter MMF, by various standards.

Finally, a brief validation, through some measurements, of the theoretical model developed in [46] is presented. Fig. 4.27 illustrates the theoretical and measured normalized frequency responses of a 62.5μm core diameter silica-based MMF. Sellmeier coefficients shown in Table 4.2 have been used to characterize the optical fibre. The optical power launch has been made via 2m-long silica-based MMF including a mode scrambler, thus achieving the OFL condition. All the theoretical curves have been obtained considering a graded index exponent $\alpha = 1.921$ and considering an attenuation coefficient of $\alpha_o(1300\text{nm}) = 0.26\text{dB/km}$ and $\alpha_o(1550\text{nm}) = 0.5\text{dB/km}$, respectively. These attenuation values have been measured by using Optical Time-Domain Reflectometer (OTDR) techniques and are further reported in Appendix D of this document. Source linewidths have been set to $\Delta f = 100\text{KHz}$ for the DFB source case and $\Delta f = 0.32\text{THz}$ (i.e. $\Delta\lambda = 1.8\text{nm}$) for the FP case. DMA and mode coupling effects have been also taken into account in the simulations, setting $\rho = 9$ and $\eta = 7.35$ as suggested in [34] for DMA (see Eq. 4.49). For the mode coupling effect model, given by Eq. 4.37, parameters $\varsigma = 0.0036\text{m}$ and $\sigma = 0.0012,\ 0.0017$ and 0.0022, for lengths 3050m, 6100m and 9150m respectively, have been selected. The fitting process is as follows: once an arbitrary variable was adjusted to a logical value, the rest of the variables were swept to obtain a theoretical frequency response. Next, the same process is repeated but choosing another parameter, and so on, to complete the high number of variables involved. The best-performance least squares fitting curve for each process is chosen. Finally, the frequency response of the whole set of parameters is compared with all the measurements involving such a MMF fibre (e.g. another launching condition) thus providing a feedback of the agreement. This is an iterative process to finally decide the suitable parameters that characterize the silica-

based MMF fibre in its whole set of measurements concerning that fibre. The same process is done for each fibre whose frequency response has been measured.

From Fig. 4.27 it can be seen that measured frequency responses at OFL condition for different silica-based MMF link lengths, as well as different wavelengths, show relative good agreement with their corresponding curves predicted by theory. Especially, it is interesting to observe the concordance in the central frequencies ($f_o|_n$) of the high-order resonances depending on the link length as well as on the source linewidth employed. In addition to, results also show that the 3-dB resonance bandwidths are higher in the cases of shorter link lengths. This latter fact can be examined by comparing Fig. 4.27(a) and Fig. 4.27(b), respectively. However, a significant discrepancy can be observed in the side-lobes excursions, being the measured ones not so pronounced compare to what the model predicts, i.e. the measured filtering effect is decreased compare to what it is expected. Many reasons can be attributed for this behaviour but, from the author`s view, mainly due to both the DMA and mode coupling modelling approaches. On the other hand, Fig. 4.27(c) addresses the high-order resonances suppression effect as the source linewidth increases. This is due to the fact that in this latter case the low pass term in Eq. 4.69 begins to dominate over the other two.

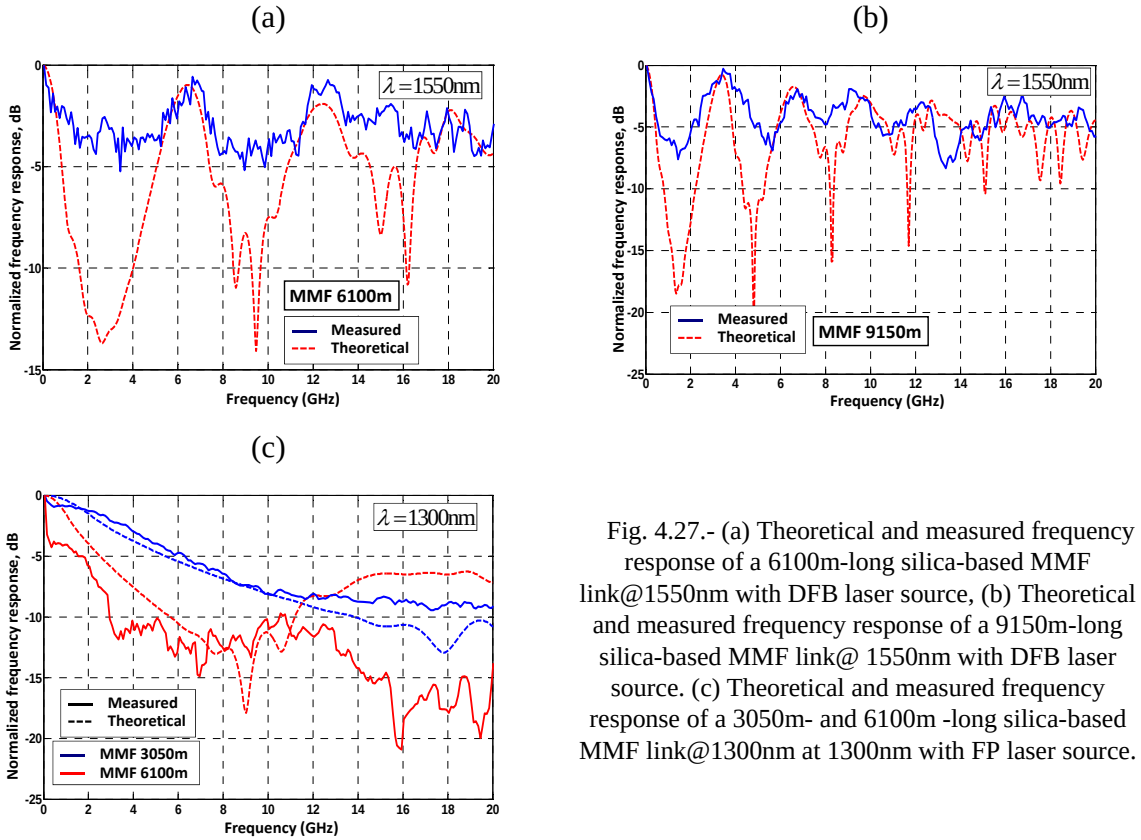

Fig. 4.27.- (a) Theoretical and measured frequency response of a 6100m-long silica-based MMF link@1550nm with DFB laser source, (b) Theoretical and measured frequency response of a 9150m-long silica-based MMF link@ 1550nm with DFB laser source. (c) Theoretical and measured frequency response of a 3050m- and 6100m -long silica-based MMF link@1300nm at 1300nm with FP laser source.

Coming back to the analysis of Figs. 4.27(a) and 4.27(b), the discrepancy of the silica-based MMF frequency response regarding the side-lobe excursions compared to the theoretical model could be also attributed to the high coherent (i.e. narrow-linewidth)

optical source used in the experiment and related to these figures. The following figure, namely Fig. 4.28, depicts the non-averaged (i.e. instantaneous) measurements of Fig. 4.27(b) for the case of a 9150m-long MMF link. From that figure, the type of fluctuation in which the high-order resonance attenuation varied over time but without central frequency change indicate that the powers of the mode group propagating in the fibre varied in time. The explanation of variable mode coupling during fibre propagation does not hold, as contemporary graded-index silica-based fibres have very low mode group coupling [108], being often assumed this approach. Moreover, it has been theoretically addressed that mode coupling causes a different frequency response behavior, namely it extends the baseband range, but tends to smooth over the high-order resonances and causes monothonic decrease of the response with frequency beyond baseband. It seems not to be the case for the measurements depicted in Fig. 4.27(b). Furthermore, the same performance can be observed in Fig. 4.27(a).

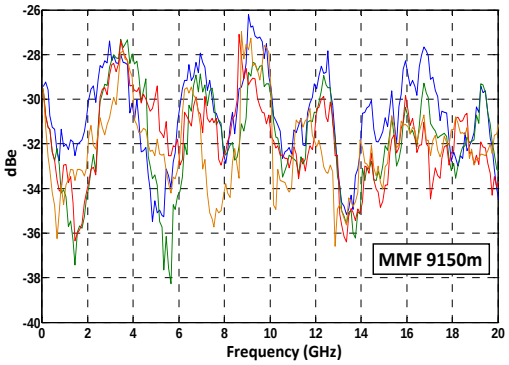

Fig. 4.28. Time variations of the optical frequency response of 9150m-long silica-based MMF link, related to Fig. 4.27(b).

It is interesting to mention that, unfortunately, two optical sources with the same linewidth but operating at the second and third transmission window, respectively, were not available at the laboratory. Such an experiment would have also been of great interest. Nevertheless, the measurement results can be anticipated. Working in the third transmission window results in a lower number of propagating modes through the fibre (as Eq. 4.45 reveals) compared to those obtained working at the second transmission window, thus leading to a decrease of the transversal filtering effect. Consequently, the fact of performing a second-transmission-window MMF link would lead to an increase of the FSR of the high-order resonances as well as to an increase of the 3-dB high-order resonances bandwith. This fact is also supported by the theory, as shown in Fig. 4.19.

Finally, although the 3-dB bandwidth of the baseband frequency response has not been paid much attention in this analysis, it is commonly agreed that the measurement uncertainty in characterizing this parameter is quite large and a standard deviation on the order of 10%-20% or more is not uncommon. This performance depends on the care of a particular lab in setting up the launch conditions and acquiring the data. This was verified in 1997 with an informal industry wide round robin [109]. Furthermore, it was, in fact, because of this that the industry standardized the overfilled launch (OFL) condition during the late 1990s [110].

4.10 Silica-based Multimode Optical Fibre impairment mitigation in RoF systems

In addition to the bandwidth limitation by the modal dispersion in MMFs, the frequency response of MMF links depends on the launching conditions due to excitation-dependent modal group delays and on mode group coupling or differential mode attenuation effects, making the MMF frequency response unpredictable under arbitrary operating conditions. Variations in temperature have also been demonstrated to change some of the optical properties of silica-based MMF such as the graded index exponent [111, 112]. This fact also imposes a great challenge for the extension of this bandwidth dependent MMF performance and, consequently, it is necessary to estimate its effect over the broadband transmission bands, for instance in an hypothetical RoMMF system.

Here, the temperature dependence of the bandwidth in a 3050m-long silica-based MMF fibre link, when the environmental temperature changes, is experimentally investigated. Measurements have been taken from T=28ºC (environment) to T=67ºC. The hysteresis cycle of the measurements has also been evaluated at the environmental temperature. A Fabry-Perot (FP) optical source at 1317nm (model SOF-131-C from Accelink) with $\Delta\lambda = 2.7\text{nm}$ of linewidth, modulated up to 20GHz by an external E/O intensity modulator (model JDSU AM130S) has been used to launch optical power into the fibre via a 2m-long silica-based MMF patch cord with mode scrambler thus providing an OFL launching condition. The optical power at the end of the fibre has been collected by the wide bandwidth InGaAs PIN photodiode (model DCS30S), and the frequency response has been analyzed by the LCA. Silica-based MMF specifications follow the same considerations as previously stated in former sections. Results depicted in Fig. 4.29 have been averaged with an average factor of Avg=16 for each temperature test measurement. Test equipment was isolated from the heating source, so that only temperature changes affecting the silica-based MMF fibre spool were measured. Theoretical frequency responses of the silica-based MMF link with L=3050m and L=10km, respectively, both provided by Eq. 4.69 and evaluated for different temperatures in which no variations on the high-order resonance frequencies are observed, are reported in [113].

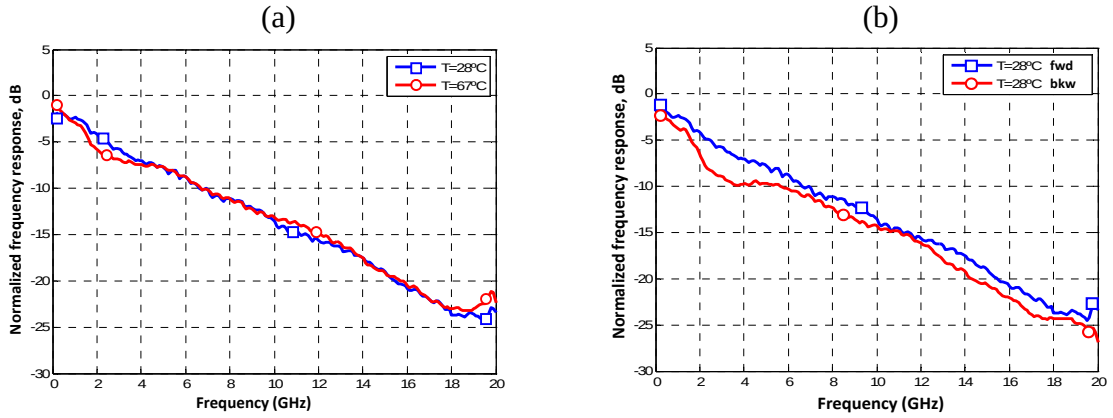

Figure 4.29.- (a) Averaged measured frequency response of the 3050m-long silica-based MMF link at T=28ºC and T=67ºC. Test has been performed at OFL condition with λ=1317nm and Δλ=2.7nm source linewidth. (b) Averaged hysteresis of the 3050m-long of former MMF link at the environmental temperature. Fwd: forwards; bkw: backwards.

Fig. 4.29(a) shows the normalized and averaged experimental measurement of the frequency response, at *T*=28ºC and *T*=67ºC, respectively. The frequency response, in this case, shows slight variations over the spectrum but with power offset at specific points of up to 3dB. It is worth mentioning that maximum deviations of 7dB for this frequency response without averaging factor have been monitored. On the other hand, Fig. 4.29(b) shows the averaged hysteresis cycle of the 3050m-long silica-based MMF link at *T*=28ºC (environmental temperature) when heating (forwards) up to 67ºC and, then, cooling (backwards) to T=28ºC again. It can be noticed a maximum averaged hysteresis deviation value of 4dB at 3GHz.

Considering the above results, it is expected that temperature changes seriously affect the location of the high-order resonances as well as their corresponding 3-dB bandwidths. Consequently, it would be interesting to evaluate the variation on the performance of the frequency response of an arbitrary single secondary side-lobe with regards to temperature. For this case, similar tests of frequency response temperature dependence and hysteresis as above have been performed but employing a DFB laser source (Agilent 81989A) operating at 1550nm. Temperature variations ranged from T=22ºC (environment) to T=80ºC. The following set of pictures in Fig. 4.30 are referred to the first-order resonance, which appears in the frequency response of a 9150m-long silica-based MMF link centered around $f_o\big|_1$ = 3.5GHz with a 3-dB bandwidth of 2GHz approximately, see Fig. 4.27(b). From Fig. 4.30(a) it can be observed that the central frequency of the first-order resonance shows almost no dependence with temperature whereas the 3-dB bandwidth of the resonance at different temperatures suffers from slight deviations. The results showed a nominal 3-dB first-resonance bandwidth of 2.4±0.2GHz, i.e. a deviation from the nominal value of ±8.3% in percentage. Conversely, results concerning hysteresis show that high-dependence on temperature cycles of heating (forwards) and cooling (backwards) are noticed. Fig. 4.30(b) shows some examples of this fact, where the optical power detected also suffer deviations of even 8dB depending on the case.

So, it is concluded that by controlling how the temperature affects the silica-based MMF fibre link it is possible to avoid the influence of this parameter over the high-order resonances and, consequently, to increase the bandwidth capability of these RoF broadband transmissions by means of an accurate addressing of the high-order secondary lobes in the MMF frequency response. However, in real situations where an optical link is deployed this has no sense, so predictive accurate models also considering the environmental temperature changes are required for fault link prevention and have to be developed.

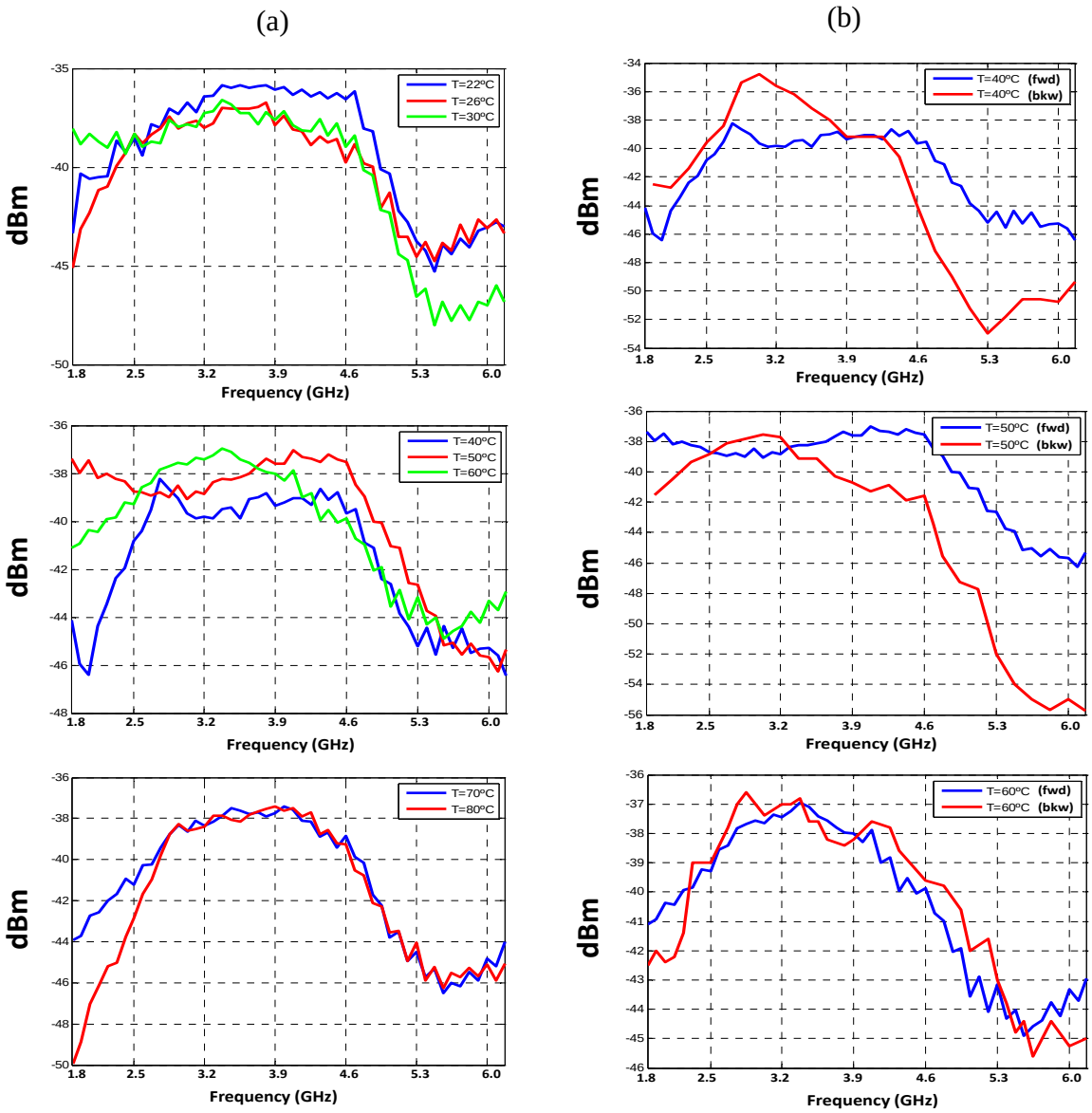

Figure 4.30.- (a) Averaged measured frequency response of the 9150m-long silica-based MMF link from T=22ºC to T=80ºC. Test has been performed at OFL condition with λ=1550nm and Δ*f*=100kHz source linewidth. (b) Averaged hysteresis of the 9150m-long of former MMF link at environmental temperature. Fwd: forwards; bkw: backwards.

4.11 Summary and Conclusions

Silica-based multimode fibres have been often used as a transmission media for short and medium distances in networks, such as LANs. The primary problem, when applying such a fibre, is its limited bandwidth (restricted to 800MHz·km typically), which makes it difficult to obtain high informational throughput and upgrade existing systems to higher bit rates, such as those required in 10-Gigabit Ethernet standard for instance. Many techniques have been reported to overcome this limitation and to expand link length capabilities. The latter

solution is based on the fact that the frequency response of silica-based MMFs does not decrease monotonically outside the baseband. On the contrary, beyond the baseband, there are observed relatively flat frequency ranges suitable for broadband transmission at both microwave and millimeter-wave regions as well as passband characteristics in higher frequencies than baseband. Consequently, high-frequency carrier transmission should be possible at these frequencies albeit a small power penalty enabling the extension of broadband transmissions.

However, the potentials of silica-based MMF to support broadband RF, microwave and millimetre-wave transmission over short, intermediate and long distances are yet to be fully known, as its frequency response seems to be unpredictable under arbitrary operating conditions as well as fibre characteristics. This in turn is contingent on the availability of accurate models to describe the signal propagation through multimode fibres. The influence of most the parameters involved has been addressed within this chapter by firstly developing a theoretical model concerning silica-based multimode optical fibres that employ a method relying on the propagation of electric field signals rather than optical power signals. This model better describes the propagation of analogue signals or when a detailed knowledge of the baseband and RF transfer function is required, and is based on that previously reported in [46]. A huge set of theoretical simulations, which study the influence of each parameter with regards to the frequency response and the high-order resonance characteristics, has been made. A resume of the silica-based MMF frequency response performance for each parameter considered has been reported in Section 4.8.5.

Concerning experimental measurements, the frequency response for different transmission lengths of a 62.5/125μm core/cladding diameter commercially available graded-index silica-based multimode fibre (GI-MMF) has been evaluated for different optical sources, operating at second (1300nm) and third (1550nm) transmission windows as well as with different linewidths. Moreover, two different launching conditions, namely RML and OFL, have been applied to test the silica-based MMF frequency response. An external Mach-Zehnder electro-optical intensity modulator and a wide bandwidth InGaAs PIN photodiode have also been used for the measurements. The measured frequency responses depicted in the figures have been corrected for the frequency responses of the transmitter, of the external intensity modulator and of the receiver equipment.

Although no accurate agreement can be expected due to the many approximations made in the theoretical analysis as well the amount of parameters involved in the frequency response in combination with the uncertainty of some key parameters such as the DMA or mode coupling effects, the results reveal a good agreement in the behaviour of the silica-based MMF frequency response high-order resonances. This fact is supported by set of figures in Fig. 4.27. To the author's knowledge, this chapter shows for the first time experimental data that validate, with tolerable discrepancy, the model presented in Section 4.7.

From the experimental data reported in Section 4.9, the following conclusions can be made:

- The use of narrow-linewidth optical sources, such as DFB lasers, results in a relatively flat silica-based MMF frequency response (up to the maximum measured

frequency of 20GHz). In contrast, higher source linewidths such as FP lasers or LEDs make more significant the low pass effect in the frequency response. Consequently, in those cases the silica-based MMF frequency response falls dramatically after a few GHz. Therefore, it can be concluded that exploiting the possibility of transmitting broadband RF signals at high frequencies is contingent with the use of narrow-linewidth optical sources.

- It has been experimentally verified that: (a) the Free Spectral Range (FSR) of the high-order resonances is reduced proportionally with the increase of the link length; (b) the contrast ratio between high-order resonances and the secondary side-lobes is reduced for lower link lengths; and (c) 3-dB high-order resonance bandwidths decrease at higher link lengths. All these performances are due to the fact that the silica-based MMF link behaves as an imperfect transversal filter.
- It has also been experimentally tested that the transversal filtering effect of the silica-based MMF link is significantly reduced when applying a RML condition.
- The combination of selective mode-launching schemes combined with the use of narrow-linewidth optical sources has been demonstrated to enable broadband RF, microwave and millimetre-wave transmission overcoming the typical silica-based GI-MMF bandwidth per length product. Consequently, standards such as Gigabit Ethernet and 10-Gigabit Ethernet can be easily fulfilled within short- and middle-reach fibre links employing silica-based MMF optical fibres. Furthermore, fixed services such as Gigabit Ethernet and broadband wireless services can be integrated on the same fibre infrastructure, thereby reducing system costs.
- As aforementioned, the theoretical model proposed is in good agreement with the measured silica-based MMF frequency response. Nevertheless, error sources such as those discussed in Section 4.9 are considered to be the main factors of disagreement.

On the other hand, thermal effects on the transmission through silica-based MMFs have been studied, so providing means to mitigate temperature-based performance degradations. An experimental analysis of the temperature dependence of the frequency response in silica-based multimode optical fibres with broadband transmission applications far from baseband is reported. The silica-based MMF link has been evaluated showing that temperature must be taken into account when selecting a transmission band far from baseband for high-speed data rates applications. Central frequencies of the high-order resonances as well as their respectively 3-dB bandwidths have been experimentally verified to show little dependence with environmental temperature. However, results concerning hysteresis show that high-dependence on temperature cycles of heating (forwards) and cooling (backwards) are noticed. Nevertheless, further research in temperature dependence is needed in order to evaluate the capability of these broadband transmissions.

4.12 References

[1] A. Flatman, "In-premises optical fiber installed base analysis to 2010," Presentation to the IEEE 802.3 10 Higher Speed Study Group, Ed., April, 2007.

[2] R. E. Epworth, "The phenomenon of modal noise in analog and digital optical fiber systems," in *Proc. 4th European Conference on Optical Communication, ECOC*, Genova, Italy, 1978.

[3] R.J.S. Bates, D.M. Kutcha, K.P. Jackson, "Improved multimode fibre link BER calculations due to modal noise and non-self-pulsating laser diodes," *Opt. and Quantum Electron.*, vol. 27, pp. 203-224, 1995.

[4] M.C. Nowell, D.G. Cunningham, "Evaluation of Gbp/s laser based fiber LAN links: Review of the Gigabit ethernet model," *Opt. Quantum Electron.*, vol. 32, pp. 169-192, 2000.

[5] L. Raddatz, I.H. White, D.G. Cunningham, M.C. Nowell, "An experimental and theoretical study of the offset launch technique for the enhancement of the bandwidth of multimode fiber links," *J. Lightwave Technol.*, vol. 16, pp. 324-331, 1998.

[6] Y. Koike, "POF Technology for the 21st Century," *Proc. of the Plastic Optical Fibres (POF) Conference*, pp. 5-8, 2001.

[7] Y. Watanabe, "Current Status of Perfluorinated GI-POF and 2.5 Gbps Data Transmission over it," in *Proc. of Optical Fiber Communication, OFC*, USA, 2003, pp. 12-13.

[8] T. Ishigure, A. Horibe, E. Nihei and Y. Koike, "High bandwidth and high numerical aperture graded-index polymer optical fibre," *J. Lightwave Technol.*, vol. 13, pp. 1686-1691, 1995.

[9] R. Olshansky, D.B. Keck, "Pulse broadening in graded-index optical fibers," *Appl. Opt.*, vol. 15, pp. 483-491, 1976.

[10] M.K. Soudagar, A.A. Wali, "Pulse broadening in graded-index optical fibers: errata," *Appl. Opt.*, vol. 32, pp. 6678-6678, 1993.

[11] M.J. Adams, D.N. Payne, F.M.E. Sladen, A.H. Hartog, "Optimum operating wavelength for chromatic equalisation in multimode optical fibers " *Electron. Lett.*, vol. 14, pp. 64-66, 1978.

[12] L. Raddatz, D. Hardacre, I. H. White, R. V. Penty, D. G. Cunningham, M. R. T. Tan, and S. Y. Wang, "High bandwidth data transmission in multimode fibre links using subcarrier multiplexing with VCSELs," *Electronics Letters*, vol. 34, pp. 686-688, 1998.

[13] Z. Haas and M. A. Santoro, "A Mode-Filtering Scheme for Improvement of the Bandwidth-Distance Product in Multimode Fiber Systems," *J. Lightwave Technol.*, vol. 11, pp. 1125-1131, 1993.

[14] M. J. Yadlowsky and A. R. Mickelson, "Distributed loss and mode coupling and their effect on time dependent propagation in multimode fibers," *Appl. Opt.*, vol. 32, pp. 6664-6677, 1993.

[15] D. Gloge, "Impulse response of Clad Optical Multimode Fibers," *Bell Syst. Tech. J.*, vol. 52, pp. 801-815, 1973.

[16] R. Olshansky, "Mode coupling effects in graded-index core fibers," *Appl. Opt.*, vol. 14, pp. 935-945, 1975.

[17] G. P. Agrawal, *Fiber-optic communication systems*, 3rd Edition ed.: John Wiley, 2002.

[18] P. Pepeljugoski, J. Schaub, J. Tierno ,B. Wilson, J. Kash, S. Gowda, H. Wu and A. Hajimiri, "Improved Performance of 10 Gb/s Multimode Fiber Optic Links Using Equalization," in *Proc. Optical Fiber Conference*, 2003, pp. 472-474.

[19] A. M. J. Koonen, "Novel signal multiplexing methods for integration of services in in-building broadband multimode fibre networks," in *Proceedings of ISSLS*, Edinburgh, Scotland, 2004.

[20] A. M .J. Koonen, A. Ng'Oma, H. P. A. van den Boom, I. Tafur Monroy and G. D. Khoe, "New techniques for extending the capabilities of multimode fibre networks," in *Proceedings of NOC*, 2003, pp. 204-211.

[21] A. M. J. Koonen, H. P. A. van den Boom, F. Willems, J. W. M. Bergmans and G. D. Khoe, "Broadband multiservice in-house networks using mode group diversity multiplexing," in *Proceedings of POF Conference*, 2002, pp. 87-90.

[22] M. Boer, C.P. Tsekrekos, A. Martinez, H. Kurniawan, J. W. Bergmans, A. M. J. Koonen, H. P. A. van den Boom, F. M. J. Willems, "A First Demonstrator For A Mode Group Diversity Multiplexing Communication System," in *Proceedings of IEEE Seminar on Optical Fibre Communication. and Electrical. Signal Processing*, London, England, 2005, pp. 16/1-16/5.

[23] H. R. Stuart, "Dispersive multiplexing in multimode fiber," *Science*, vol. 289, pp. 305-307, 2000.

[24] B. J. Dixon, R. D. Pollard, and S. Iezekiel, "Orthogonal frequency-division multiplexing in wireless communication systems with multimode fiber feeds," *IEEE Transactions on Microwave Theory and Techniques*, vol. 49, pp. 1404-1409, 2001.

[25] L. Raddatz and I. H. White, "Overcoming the Modal Bandwidth Limitation of Multimode Fiber by Using Passband Modulation," *IEEE Photon. Tech. Lett.*, vol. 11, pp. 266-268, 1999.

[26] S. Kanprachar a. I. Jacobs, "Diversity of coding for subcarrier multiplexing on multimode fibers," *IEEE Trans. Commun.*, vol. 51, pp. 1546-1553, 2003.

[27] X. J. Gu, W. Mohammed and P.W. Smith, "Demonstration of all-fiber WDM for multimode fiber local area networks," *IEEE Photon. Tech. Lett.*, vol. 18, pp. 244-246, 2006.

[28] E. J. Tyler, P. Kourtessis, M. Webster, E. Rochart, T. Quinlan, S. E. M. Dudley, S. D. Walker, R. V. Penty and I. H. White, "Toward Terabit-per-second capacities over multimode fiber links using SCM/WDM techniques," *J. Lightwave Technol.*, vol. 21, pp. 3237-3243, 2003.

[29] P. Pepeljugosky, "Next generation High-Speed Multimode Fiber Links and their specifications," in *Proceedings of Optical Fiber Communication OFC*, Anaheim, CA, USA, 2005, p. OWH1.

[30] R. Yuen, X.N. Fernando, K. Sridhar, "Radio Over Multimode Fiber for Wireless Access," in *Proceedings of. Canadian Conference on Electrical and Computer Engineering*, Ontario, Canada, 2004, pp. 1715-1718.

[31] A. R. Shah, R.C.J. Hsu, A. Tarighat, A. H. Sayed and B. Jalali, "Coherent optical MIMO (COMIMO)," *J. Lightwave Technol.*, vol. 23, pp. 2410-2419, 2005.

[32] D. Gloge, "Optical power flow in multimode fibers," *Bell Syst. Tech. J.*, vol. 51, pp. 1767-1783, 1972.

[33] D. Marcuse, *Theory of Dielectric Optical Waveguides*, 2nd Edition ed.: Academic Press, 1991.

[34] G. Yabre, "Comprehensive Theory of Dispersion in Graded-Index Optical Fibers," *J. Lightwave Technol.*, vol. 18, pp. 166-177, 2000.

[35] R. Steinberg, "Pulse propagation in Multimode Fibers with Frequency-Dependent Coupling," *IEEE Trans. Microwave Theory Tech.*, vol. 23, pp. 121-122, 1975.

[36] K. Tatekura, K. Itoh, T. Matsumoto, "Techniques and formulations for Mode Coupling of Multimode Optical Fibers," *IEEE Trans. Microwave Theory Tech.*, vol. 26, pp. 487-493, 1978.

[37] T. P. Toshiki a. S. Yamada, "Numerical solution of power flow in multimode W-type optical fibers," *Appl. Opt.*, vol. 19, pp. 1647-1652, 1985.

[38] A. Djordjevich and S. Savovic, "Investigation of Mode Coupling in Step Index Plastic Optical Fibers using the Power Flow Equation," *IEEE Photon. Tech. Lett.*, vol. 12, pp. 1489-1491, 2000.

[39] D. Yevick and B. Stoltz, "Effect of mode coupling on the total pulse response of perturbed optical fibers," *Appl. Opt.*, vol. 22, pp. 1010-1015, 1983.

[40] A. Djordjevich and S. Savovic, "Numerical solution of the power flow equation in step-index plastic optical fibers," *J. Opt. Soc. Am.*, vol. 21, pp. 1437-1442, 2004.

[41] G. Aldabaldetreku, G. Durana, J. Zubia and J. Arrue, "Analytical expression for measurement of Intrinsic Coupling Loss in Multistep Index Optical Fibers," *J. Lightwave Technol.*, vol. 24, pp. 1364-1375, 2006.

[42] M. A. Losada, I. Garcés, J. Mateo, I. Salinas, J. Lou and J. Zubia, "Mode coupling contribution to radiation losses in curvatures for high and low numerical aperture plastic optical fibers," *J. Lightwave Technol.*, vol. 20, pp. 1160-1164, 2002.

[43] J. Zubia, G. Durana, G. Aldabaldetreku, J. Arrue, M. A. Losada and M. Lopez-Higuera, "New method to calculate mode conversion coefficients in SI multimode optical fibers," *J. Lightwave Technol.*, vol. 21, pp. 776-781, 2003.

[44] G. Stepniak, J. Siuzdak, "An efficient method for calculation of the MM fiber frequency response in the presence of mode coupling," *Optical and Quantum Electronics*, vol. 38, pp. 1195-1201, 2006.

[45] B. E. A. Saleh and R. M. Abdula, "Optical Interference and Pulse Propagation in Multimode Fibers," *Fiber Integr. Opt.*, vol. 5, pp. 161-201, 1985.

[46] I. Gasulla and J. Capmany, "Transfer function of multimode fiber links using an electric field propagation model: Application to Radio over Fibre Systems," *Opt. Express*, vol. 14, pp. 9051-9070, 2006.

[47] S. E. Golowich, W.A. Reed, A.J. Ritger, "A New Modal Power Distribution Measurement for High-Speed Short-Reach Optical Systems," *J. Lightwave Technol.*, vol. 22, pp. 457-468, 2004.

[48] K. Ohdoko and T. Ishigure, "Propagating Mode Analysis and Design of Waveguide Parameters of GI POF for Very Short-Reach Network Use," *IEEE Photon. Tech. Lett.*, vol. 17, pp. 79-81, 2005.

[49] T. Ishigure, T. Kano, Y. Koike, "Which is a More Serious Factor to the Bandwidth of GIPOF: Differential Mode Attenuation or Mode Coupling?," *J. Lightwave Technol.*, vol. 18, pp. 959-965, 2000.

[50] J. D. Ingham, M. Webster, D. Wake, A. J. Seeds, R. V. Penty, and I. H. White, "Bidirectional Transmission of 32-QAM Radio Over a Single Multimode Fibre Using 850-nm Vertical-Cavity Half-Duplex Transceivers," in *28th European Conference on Optical Communication, ECOC 2002*, 2002, pp. 1-2.

[51] I. Gasulla and J. Capmany, "Simultaneous baseband and radio over fiber signal transmission over a 5 km MMF link," in *International Topics Meeting on Microwave Photonics, 2008. Jointly held with the 2008 Asia-Pacific Microwave Photonics Conference. MWP/APMP 2008*, 2008, pp. 209-212.

[52] D.G. Cunningham, W.G. Lane and B. Lane, *Gigabit Ethernet Networking*. Indianapolis, IN: Macmillan, 1999.

[53] S. S. H. Yam and F. Achten, "High-speed data transmission over 1 km broad wavelength window multimode fibre," *Opt. Lett.*, vol. 31, pp. 1954-1956, 2006.

[54] D. H. Sim, Y. Takushima, Y.C. Chung, "Transmission of 10-Gb/s and 40-Gb/s signals over 3.7 km of multimode fiber using mode-field matched center launching technique," in *Optical Fiber Conference OFC2007, OTuL3*, Anaheim, USA, 2007.

[55] S. E. Golowich, W. White, W. A. Reed, and E. Knudsen, "Quantitative estimates of mode coupling and differential modal attenuation in perfluorinated graded-index plastic optical fiber," *J. Lightwave Technol.*, vol. 21, pp. 111-121, 2003.

[56] P. Pepeljugoski, S. E. Golowich, A. J. Ritger, P. Kolesar, and A. Risteski, "Modeling and simulation of next-generation multimode fiber links," *J. Lightwave Technol.*, vol. 21, pp. 1242-1255, 2003.

[57] R. Dandliker, A. Bertholds, F. Maystre, "How Modal Noise in Multimode Fibers Depends on Source Spectrum and Fiber Dispersion," *J. Lightwave Technol.*, vol. 3, pp. 7-12, 1985.

[58] A. M. J. Koonen, "Bit-Error-Rate Degradation in a Multimode Fiber Optic Transmission Link Due to Modal Noise," *IEEE J. Select. Areas Commun.*, vol. SAC-4, 1986.

[59] L.B. Aronson, B.E. Lemoff, L.A. Buckman, and D.W. Dolfi, "Low-cost multimode WDM for local area networks up to 10 Gb/s," *IEEE Photon. Technol. Lett.*, vol. 10, pp. 1489-1491, 1998.

[60] R. Michalzik, G. Giaretta, A. J. Ritger, and Q. L. Williams, "10 gb/s vcsel based data transmission over 1.6km of new generation 850nm multimode fiber," in *Proceedings of LEOS*, 1999.

[61] R. Michalzik, G. Giaretta, K. Goossen, K. Walker, and M. Nuss, "40 gb/s coarse wdm data transmission with 825 nm wavelength vcsels over 310m multimode fiber," in *Proceedings of European Conference on Optical Communication, ECOC2000*, Munich, Germany, 2000.

[62] P. Pepeljugoski, D. Kuchta, Y. Kwark, P. Pleunis, and G. Kuyt, "15.6-Gb/s transmission over 1 km of next generation multimode fiber," *IEEE Photon. Tech. Lett.*, vol. 14, pp. 717-719, 2002.

[63] P. Kourtessis, T. Quinlan, E. Rochat, S. D. Walker, M. Webster, I. H. White, R. V. Penty, and M. C. Parker, "0.6 Tbit/s/km multimode fibre feasibility experiment using 40 channel DWDM over quadrature-subcarrier transmission," *Electronics Letters*, vol. 38, pp. 813-815, 2002.

[64] S. S. H. Yam and F. Achten, "Single wavelength 40 Gbit/s transmission over 3.4 km broad wavelength window multimode fibre," *Electronics Letters*, vol. 42, pp. 592-594, 2006.

[65] M. E. A. Diab, J.D. Ingham, R. V. Penty and I. H. White, "10-Gb/s Transmission on Single-Wavelength Multichannel SCM-Based FDDI-Grade MMF Links at Length Over 300 m: A Statistical Investigation," *J. Lightwave Technol.*, vol. 25, pp. 2976-2983, 2007.

[66] S.C.J. Lee, F. Breyer, S. Randel, M. Shcuster, J. Zeng, F. Huijskens, H.P.A van den Boom, A.M.J. Koonen, M. Hanik, "24-Gb/s Transmission over 730m of Multimode Fiber by direct Modulation of an 850-nm VCSEL using Discrete Multi-tone Modulation," in *Optical Fiber Communication Conference, OFC2007*, Anaheim, CA, USA, 2007, p. Paper PDP6.

[67] R. A. Panicker, J.P. Wilde, J. M. Khan, D. F. Welch and I. Lyubomirsky, "10x10 Gb/s DWDM transmission through 2.2-km multimode fiber using adaptive optics," *IEEE Photon. Technol. Lett.*, vol. 19, pp. 1154-1156, 2007.

[68] K. Jin Joo, K. Kyong Hon, L. Min-Hee, L. Hyun Sik, L. El-Hang, O. K. Kwon, R. Jay, and Y. Byueng-Su, "2.5-Gb/s Hybrid Single-Mode and Multimode Fiber Transmission of 1.5-μm Wavelength VCSEL," *IEEE Photon. Tech. Lett.*, vol. 19, pp. 297-299, 2007.

[69] J. Zeng, S. C. J. Lee, F. Breyer, S. Randel, Y. Yang, H.P.A van den Boom, A.M.J. Koonen, "Transmission of 1.25 Gb/s per Channel over 4.4. km silica Multimode Fibre Using QAM Subcarrier Multiplexing," in *European Conf. Opt. Commu., ECOC2007*, Berlin, Germany, 2007, Paper 7.4.3.

[70] I. Gasulla and J. Capmany, "1 Tb/s·km Multimode fiber link combining WDM transmission and low-linewidth lasers," *Opt. Express,* vol. 16, pp. 8033-8038, 2008.
[71] D. H. Sim, Y. Takushima, and Y. C. Chung, "High-Speed Multimode Fiber Transmission by Using Mode-Field Matched Center-Launching Technique," *J. Lightwave Technol.,* vol. 27, pp. 1018-1026, 2009.
[72] P. Pepeljugoski, M. J. Hackert, J. S. Abbott, S. E. Swanson, S. E. Golowich, A. J. Ritger, P. Kolesar, Y. C. Chen, and P. Pleunis, "Development of system specification for laser-optimized 50-µm multimode fiber for multigigabit short-wavelength LANs," *J. Lightwave Technol.,* vol. 21, pp. 1256-1275, 2003.
[73] J.B. Schlager, M.J. Hackert, P. Pepeljugoski, J. Gwinn, "Measurements for enhanced bandwidth eprformance over 62.5-um multimode fiber in short-wavelength local area networks," *J. Lightwave Technol.,* vol. 21, pp. 1276-1285, 2003.
[74] D. K. Mynbaev, L.L. Scheiner, *Fiber Optic Communications Technology*. New Jersey: Prentice Hall, 2001.
[75] F. Devaux, Y. Sorel and J. Kerdiles, "Simple measurement of fiber dispersion and of chirp parameter of intensity modulated light emitter," *J. Lightwave Technol.,* vol. 11, pp. 702-723, 1993.
[76] K. T. A. Ghatak, *Introduction to Fiber Optics*: Cambridge University Press, 1998.
[77] G. Keiser, *Optical Fiber Communications*: McGraw-Hill Companies Inc., 2000.
[78] P. Pepeljugoski, D. Kuchta, and A. Risteski, "Modal noise BER calculations in 10-Gb/s multimode fiber LAN links," *IEEE Photon. Tech. Lett.,* vol. 17, pp. 2586-2588, 2005.
[79] E.G. Rawson, J.W. Goodman, R.E. Norton, "Frequency dependence of modal noise in multimode fiber," *J. Opt. Soc. Am.,* vol. 70, pp. 968-976, 1980.
[80] B. Moslehi, J.W. Goodman, E.G. Rawson "Bandwidth estimation for multimode optical fibers using the frequency correlation function of speckle patterns," *Applied Optics,* vol. 22, pp. 995-999, 1983.
[81] T. Kanada, "Evaluation of Modal Noise in Multimode Fiber-optic Systems," *J. Lightwave Technol.,* vol. 5, pp. 11-18, 1984.
[82] G. Papen and G. Murphy, "Modal noise in multimode fibers under restricted launch conditions," *J. Lightwave Technol.,* vol. 17, pp. 817-822, 1999.
[83] E.G. Rawson, J.W. Goodman, R.E. Norton, "Analysis and measurement of the modal-noise probability distribution for a step-index optical fiber," *Opt. Lett.,* vol. 5, pp. 357-358, 1980.
[84] B. Daino, G. de Marchis, S. Piazzolla, "Analysis and measurement of modal noise in an optical fibre," *Electronics Letters*, vol. 15, pp. 755-756, 1979.
[85] J. Weierholt, E.G. Rawson, J.W. Goodman, "Frequency-correlation properties of optical waveguide intensity patterns," *J. Opt. Soc. Am. A,* vol. 1, pp. 201-205, 1984.
[86] I. Gasulla and J. Capmany, "Modal noise impact in Radio over Fiber multimode fiber links," *Opt. Express*, vol. 16, pp. 121-126, 2008.
[87] A. Polley, "High Performance Multimode Fiber Systems: A Comprehensive Approach." vol. Thesis: Georgia Institute of Technology, December 2008.
[88] W. A. Gambling, D. N. Payne, and H. Matsumura, "Mode conversion coefficients in optical fibers," *Appl. Opt.,* vol. 14, pp. 1538-1542, 1975.
[89] K. Nagano and S. Kawakami, "Measurements of mode conversion coefficients in graded-index fibers," *Appl. Opt.,* vol. 19, pp. 2426-2434, 1980.
[90] D. Marcuse, "Coupled mode theory of round optical fibers," *Bell Syst. Tech. J.*, vol. 52, pp. 817-843, 1973.
[91] J.N. Kutz, J.A. Cox, D. Smith, "Mode Mixing and Power Diffusion in Multimode Optical Fibers," *J. Lightwave Technol.,* vol. 16, pp. 1195-1202, 1998.
[92] H. Lydtin, "PCVD: A technique suitable for large-scale fabrication of optical fibers," *J. Lightwave Technol.,* vol. 4, pp. 1034-1038, 1986.
[93] R. Olshansky, "Distorsion losses in cabled optical fibers," *Appl. Opt.,* vol. 14, pp. 20-21, 1975.
[94] D. Gloge, "Weakly guiding fibers," *Appl. Opt.,* vol. 10, pp. 2252-2258, 1971.
[95] W. B. Gardner, "Microbending loss in optical fibers," *Bell Syst. Tech. J.*, vol. 54, pp. 457-465, 1975.
[96] S. Shaklan, "Measurement of Intermodal Coupling in Weakly guided Multimode Fibre Optics," *Electronics Letters,* vol. 26, pp. 2022-2024, 1990.
[97] I. Gasulla and J. Capmany, "Transmission of high-frequency radio over fibre signals through short and middle reach Multimode Fibre links using a low-linewidth laser," in *IEEE International Topical Meeting on Microwave Photonics*, 2007, pp. 116-119.
[98] J. Goodman, *Statistical Optics*. New York: John Wiley & Sons, 1985.

[99] B. Saleh and M. Irshid, "Coherence and intersymbol interference in digital fiber optic communication systems," *IEEE Journal of Quantum Electronics*, vol. 18, pp. 944-951, 1982.

[100] M. Miyagi and S. Nishida, "Pulse spreading in a single-mode fiber due to third-order dispersion," *Appl. Opt.*, vol. 18, pp. 678-682, 1979.

[101] M. Miyagi and S. Nishida, "Pulse spreading in a single-mode optical fiber due to third-order dispersion: effect of optical source bandwidth," *Appl. Opt.*, vol. 18, pp. 2237-2240, 1979.

[102] G. Yabre, "Influence of Core Diameter on the 3-dB Bandwidth of Graded-Index Optical Fibers " *J. Lightwave Technol.*, vol. 18, pp. 668-676, 2000.

[103] I. Gasulla and J. Capmany, "Analysis of the harmonic and intermodulation distortion in a multimode fiber optic link," *Opt. Express*, vol. 15, pp. 9366-9371, 2007.

[104] J. Capmany, B. Ortega, D. Pastor, S. Sales, "Discrete-Time Optical Signal Processing of Microwave Signals," *J. Lightwave Technol.*, vol. 23, pp. 703-723, 2005.

[105] I. L. Fraile, "Análisis de enlaces de fibra óptica multimodo con tecnología radio sobre fibra para aplicaciones en el hogar," in *Dpto. de Tecnología Electrónica, Universidad Carlos III de Madrid*. vol. Final Degree Project, Junio de 2008.

[106] R. Olshansky, "Multiple-alpha index profiles," *Appl. Opt.*, vol. 18, pp. 683-689, 1979.

[107] "ISO/IEC 11801 Information technology - Generic cabling for customer premise Standard".

[108] A. M. E. A. Diab, J. D. Ingham, R. V. Penty, and I. H. White, "Statistical analysis of subcarrier-modulated transmission over 300 m of 62.5-μm core-diameter multimode fiber," *J. Lightwave Technol.*, vol. 23, pp. 2380-2398, 2005.

[109] M. J. Hackert, "Characterizing multimode fiber bandwidth for Gigabit Ethernet applications," in *Proc. Symp. Optical Fiber Measurements*, Sept. 1998, pp. 113-118.

[110] EIA/TIA-455-54A (FOTP-54), "Mode Scrambler Requirements for overfilled Launching Conditions to Multi-Mode Fibers," Dec. 2001.

[111] A.A. Hamza, T.Z.N. Sokkar, K.A. El-Farahaty, H.M. El-Dessouky, "Influence of temperature on the optical and structural properties along the diameter of optical fibres," *Opt. and Lasers Eng.* , vol. 41, pp. 261-275, 2004.

[112] F. Tarrach, A. Ch'hayder, S. Guermazi, "Influence of thermal aging on optical fiber properties," *Opt. Eng.*, vol. 47, pp. 065006 (1-4), 2008.

[113] D. S. Montero, I. Gasulla, I. Mollers, D. Jager, J. Capmany, and C. Vazquez, "Experimental analysis of temperature dependence in multimode optical fiber links for radio-over-fiber applications," in *11th International Conference on Transparent Optical Networks, 2009, ICTON '09*, pp. 1-4.

Chapter 5

FREQUENCY-BASED SELF-REFERENCING TECHNIQUES FOR OPTICAL INTENSITY SENSORS

5.1 Introduction

Within this section, some interesting examples of self-referencing approaches, recently published, for fibre-optic intensity sensors are briefly described, engaging with the self-referencing techniques described in Chapter 2. It is worth mentioning that this chapter also addressed the possibility of including such fibre-optic intensity sensors in the building/home-field to achieve a full optical access network to provide future broadband services.

Most of the widely published self-referencing techniques for intensity-modulated optical sensors correspond to one of the following schemes: time-division normalization [1-3], wavelength normalization [4], fibre bypassing, which corresponds to the spatial separation technique aforementioned, and frequency-based referencing methods [5-7]; this latter scheme will be described in further detail in following sections. More recently, a method using counterpropagating signals has also been developed [8] as well as using Michelson [9] and Ring Resonators (RR) [10] topologies. Furthermore, the use of resonant structures as basis of a self-referencing intensity type sensor has been widely identified in literature [11-13], in an approach that is known as amplitude-phase conversion technique. In it, the optical power injected into the system is sine-wave-modulated. In the sensing head, a fraction of that power is not affected by the measurand, constituting a reference signal. The other fraction is intensity-modulated by the measured and constitutes the sensing signal. When both fractions are combined at the reception stage, it gives a resulting optical-power intensity sine wave. The phase of this signal, relative to the phase of the electrical signal that modulates the optical power emitted by the optical source, depends only on the optical loss induced in the sensor head by the measurand, including a constant factor determined by the length of the lead/return fibre). The same latter concept can be applied to the ratio between the amplitudes of the reference and the sensing signals, respectively. The evaluation of this ratio of amplitudes and/or the phase allows information to be obtained about the measurand status; independently of the optical power fluctuations that can occur outside the sensor head.

A time-division self-referencing mechanism is reported in [3] using as measurement parameter the ratio between the intensity of two optical pulses with a relative delay time. The technique consists on incorporating an intensity transducer in the feedback loop of a MMF ring resonator, thus modulating and delaying in time the intensity with regards to the

reference intensity pulse. In a similar way, in [1] is reported a fibre-optic displacement sensor with temporally separated signal and reference channels. The sensing technique is based on determining the relative amplitude of the signal and reference pulses that together formed a double pulse. The relative amplitude of the pulses in the double pulse is a function of the displacement measured by the sensor head consisting on a movable reflecting surface (generally, formed by a reflective and semitransparent mirror) which included a fibre-optic loop of 1m-long MMF in order to create the temporally separated channels. This time division mechanism has also been used to multiplex the measurement with a reference channel, as in [14] in a fibre loop topology.

A wavelength normalization strategy is described in [4] for self-referencing in microbend intensity fibre-optic sensors. In this work, a Broadband Light Source (BLS) is divided into two wavelengths at the sensing point, one reaching the sensor and one used as reference. These two wavelengths are then recombined and separated again at the receiver where the signals are processed to eliminate light level changes in the fibre link caused by cable bends or connector losses, that result in proportional signal modulation in both channels. The compensation of the light source intensity fluctuations can be performed using a reference light intensity signal provided by the transmitter resulting measurements proportional only to measurand-induced changes in the microbends.

A fibre bypassing strategy for self-referencing optical intensity sensors in a ladder topology is reported in [8]. In this work, the optical power is splitted by an 1x2 optical coupler and launched into the two fibre leads connected to the remote sensing point. The two counterpropagating signals reach the sensing point and the reference signal bypasses the sensor through an optical circulator. The main drawback of this configuration is the large number of components to build the complete remote link and the high insertion losses due to the use of two 2x1 optical couplers to perform the ladder as well as the need for polarization-insensitive fibre devices due to the lower efficiency of the system for cancelling mechanically induced noise. Considering a *N* fibre-optic intensity-based remote sensor network, this strategy would additionally deploy *2N* optical circulators (alternatively, a cost-effective solution would be *2N* optical couplers plus *2N* optical isolators). Nevertheless, the technique takes advantage of a compact configuration in the sensing point and a simple transmission and demodulation stages, because no frequency modulation is needed. Other sensing scheme using such strategy is reported in [15] where a fibre-optic refractometer for liquid refractive index measurements is developed. In this latter case, the light reaching the receiver is a function of the refractive index of the liquid surrounding but, since this parameter is strongly dependent on temperature and also, to a lesser degree, on wavelength, these effects need to be corrected as well as those coming from light source fluctuations and photodetector temperature-dependence sensitivities. The proposed solution is the use of a fibre bypassing combined with the measurement of the refractive index for a standard liquid and to compute both ratios into a final referencing parameter.

The content of this chapter comprises a brief state-of-the-art of frequency-based resonant topologies for self-referencing fibre-optic intensity sensors. All-optical and electro-optical approaches of reflective configurations, which include Fiber Bragg Gratings, are also described. Finally, a novel self-referencing parameter for the electro-optical topology

operating in reflective configuration for remote fibre-optic sensors is analyzed with theoretical and experimental results.

5.2 Frequency-based self-referencing techniques for Optical Intensity Sensors

In this section, the frequency-based self-referencing technique for fibre-optic intensity sensors is further described, as it is one of the most popular strategies for self-referencing schemes in the last decade. More recently, self-referencing has been achieved in a wavelength multiplexing configurations using SMFs instead of MMFs allowing long remote operation distances.

Frequency-based self-referencing methods have been reported using radio-frequency (RF) modulated Fabry-Perot (FP) [16, 17], Mach-Zehnder [5, 12], Michelson [5, 9, 13], Sagnac [18-21] and Ring Resonators (RR) [7, 22] incoherent configurations in fibre technology. In these works, the utilization of a resonant structure as the basis of a self-referencing intensity type sensor is widely deployed. And the basic idea is to encode the sensor intensity modulation in the radio-frequency magnitude and phase response of an incoherent configuration, and to deploy a normalization of the measurement parameter at the reception stage to achive the self-reference property. The frequency response of a fibre optic topology that allows two or more different paths from the input to the output produces an interference of the different propagating beams. Furthermore, this interference shows that some frequencies ensure a maximum output power (resonance frequencies) and others a decreased power level (off-resonance frequencies). Consequently, the intensity modulation at different frequencies of the light injected into a resonant fibre topology provides different output powers and phases via the fibre structure transfer function. If this closed structure is localized, i.e. if the paths are distinct only in a well defined region (sensing region) then the ratio (normalization) beween the optical power exiting the system at an off-resonance frequency and that obtained for a resonace frequency depends on the light modulation loss induced in the closed fibre structure. This ratio, also considered the quality factor of the resonator, is free from light source fluctuations and variable transmission losses induced ouside of it. Therefore, this factor ensures a self-referencing scheme that compensates for possible unwanted light modulation along the fibre system. Clearly, this concept is general to any closed (resonant) fibre topology, as those aforementioned. In the following, the basic general equations describing the radio-frequency self-referencing technique principle of operation are reported.

The Free Spectral Range (FSR) of the frequency response in such resonant configurations can be expressed as:

$$FSR = \frac{c}{n_g \cdot L} \tag{5.1}$$

where c is the speed of light in vacuum, n_g is the refractive index of the fibre and L is the path difference between the two arms of the resonant structure (i.e. generally the fibre coil

length inserted in such topology, although reflective Michelson topologies provide, for example, doubled effective path difference between the two arms that must be taken into account in the FSR calculation).

In the generic case, the off-resonance and resonance frequencies of the system can be determined by:

$$f_{resonance} = m \cdot FSR; \quad \text{m=0,1,2,...} \tag{5.2}$$

$$f_{off-resonance} = \left(\frac{2m-1}{2} \right) \cdot FSR; \quad \text{m=1,2,...} \tag{5.3}$$

On the other hand:

$$R = \frac{\left| H_{\text{off-resonance}} \right|}{\left| H_{\text{resonance}} \right|} \tag{5.4}$$

where R is the normalization parameter which provides the self-referencing property and $\left| H_{\text{off-resonance}} \right|$ and $\left| H_{\text{resonance}} \right|$ are the transfer function modules for the off-resonance and resonace frequencies of the fibre topology, respectively [23]. In the same way, the relative electrical phase response of the detected RF signal (relative to the phase of the electrical signal that modulates the optical power emitted by the optical source) provides a self-referenced measurement parameter.

It is also worth to point out that frequency-based strategies is particularly favorable in what concerns the minimization of the system noise. This happens because what it is monitored is the amplitude/phase of two sinewaves, i.e. the detection bandwidth can be made as narrow as practically feasible, with the consequent decrease of the system noise level.

5.2.1 Fabry-Perot filter-based self-referencing technique

In this approach, the separation between the fibre lead and the transducer losses is solved by placing the transducer within a radio-frequency (RF) fibre Fabry-Perot filter, performing a passive amplitude-phase conversion on the signal delivered by an amplitude-modulated source at a frequency *f*. An application of this scheme was reported in [16] in the case of a proximity sensor obtaining best sensitivities of 15º/μm (corresponding to approximately 300º/dB) and distance measurement range of more than 200μm. In this work, an optical cavity with 3.5 meters of MMF was realized with a fibre connector and a proximity sensor based on the power back-coupling on the fibre end, where the light was re-injected using a moving mirror.

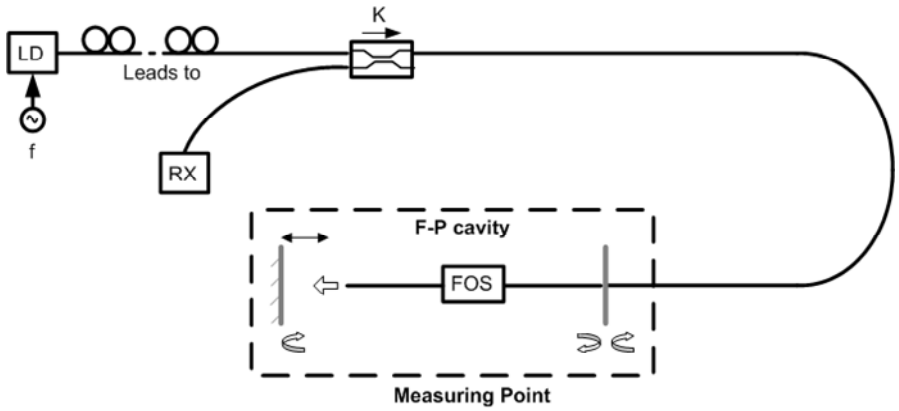

Figure 5.1.- Intensity-modulated sensor referencing with transducer within a Fabry-Perot cavity.

In addition to the separation between the fibre lead and the transducer damping, the design shown in Fig. 5.1 allows narrow band detection and, therefore, a high Signal-to-Noise Ratio (SNR) in the phase measurement of the radio-frequency signal. This Fabry-Perot (FP) configuration is also employed in [24] for self-referencing intensity sensors, employing simultaneous coherent and incoherent regimes of operation in order to combine the advantages of fibre interferometry and intensity-based devices into a single sensor system. In this latter case, a pressure and temperature sensor with resolutions as high as 0.02% of full scale are achieved by splitting the broadband light returned by the FP cavity into two channels in such a way that one channel (sensing) has a coherence length much longer than the cavity, generating effective transducing (and yielding information about the measurand), while the coherence length in the other channel (reference) was so short thus providing information about the source power, fibre attenuation and other optical loss factors in the optical path. Alternatively, a microbend sensor acting as a tranducer of the applied force is located in a RF passive self-referencing scheme using a FP configuration [17], thus providing self-referenced measurements. The phase of the RF output signal (f=2MHz) is evaluated achieving sensitivities of 0.6N/º.

In contrast with the latter case, it is worth to point out an example which takes advantage of F-P interferometric sensors performance regarding the coherence properties of the optical source and the F-P cavity length or the optical path length of the link, although these schemes are not frequency-based. Following this case, a liquid-level fibre-optic intensity sensor is reported in [25] where the linear cavity length changed induced by the liquid-level changes, being proportional to the optical intensity reflected back into the fibre lead. To overcome the limitation of thermally induced shifts in the optical source as well as short-term fluctuations in the received optical power, an hybrid self-compensated strategy is employed combining driving current and temperature control circuits plus ratiometric signal-processing methods applied for both the sensing and reference channels, to compensate the undesirable optical drifts in the link.

5.2.2 Mach-Zehnder resonant self-referencing topology

The Mach-Zehnder resonant topology for self-referencing fibre-optic intensity-based sensors is a versatile structure for the monitoring of static and dynamic physical parameters. It requires a small number of optical components and simple signal processing, in adittion to providing a self-referencing characteristic which naturally solve the problem of referentiation of optical power fluctuations along the system.

A generic self-referencing resonant intensity sensor based on a Mach-Zehnder topology is shown in Fig. 5.2 and Fig. 5.3, respectively, considering the transmissive and reflective configurations. The reflective elements are generally mirrors fabricated by silver deposition on the fibre ends.

Notice that the off-resonance and resonace frequencies are referred in both figures as f_{OR} and f_R, respectively.

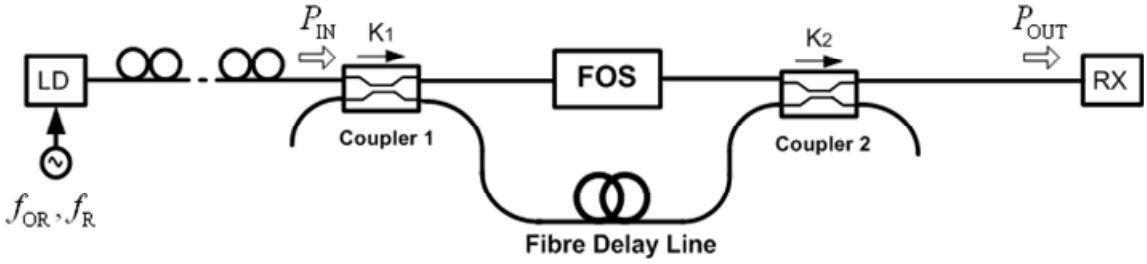

Figure 5.2.- Referencing scheme for an intensity sensor based on a Mach-Zehnder topology in transmissive configuration. FOS: fibre-optic intensity sensor.

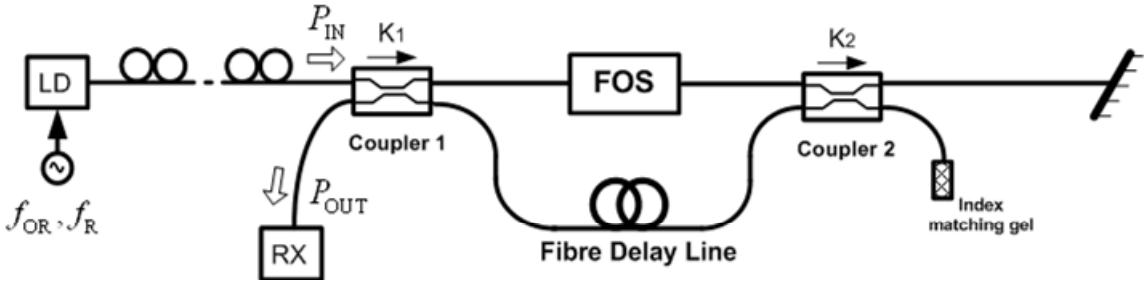

Figure 5.3.- Referencing scheme for an intensity sensor based on a Mach-Zehnder topology in reflective configuration. FOS: fibre-optic intensity sensor.

Both configurations are investigated in [12] concluding that overall the transmissive configuration exhibits a more favorable performance in terms of sensitivity and dynamic range compare to the reflective topology. However, the main disadvantages of both topologies are their effectiveness only assuming $K_1 = K_2$ (in transmissive configuration this condition rises up $K_1 = K_2 = 0.5$), which is difficult to achieve in commercial coupler devices as well as the use of a fibre coil as fibre delay line, which makes both topologies non-compact strategies in essence.

A micro-displacement sensor using a Long Period Fiber Grating (LPG) in the sensing head integrated in a self-referencing Mach-Zehnder topology is reported in [26]. It is based on the central wavelength shift of the grating when bending the LPG; obtaining a resolution below 10μm. A Mach-Zehnder configuration self-referenced LPG-based angular rotation sensor is also analyzed in [27] in which the attenuation peaks changed as a function of their angular rotation; obtaining an intrinsic resolution below 15º.

5.2.3 Michelson resonant self-referencing topology

The Michelson resonant topology for self-referencig fibre-optic intensity-based sensors has also been identified in literature; providing a similar feature of the self-referencing property with regards to the Mach-Zehnder topology showed before.

A generic self-referenced resonant intensity sensor based on the Michelson topology is shown in Fig. 5.4 and Fig. 5.5, respectively, considering both transmissive and reflective configuration. Observing the proposed schemes, it is interesting to point out the advantage that both Michelson configurations allow the sensing part to be located remotely and apart from the signal processing, therefore, not being necessary to draw another fibre lead from the sensing part to the signal processing, as it would be for the Mach-Zehnder topology (see Fig. 5.2) in the transmissive configuration.

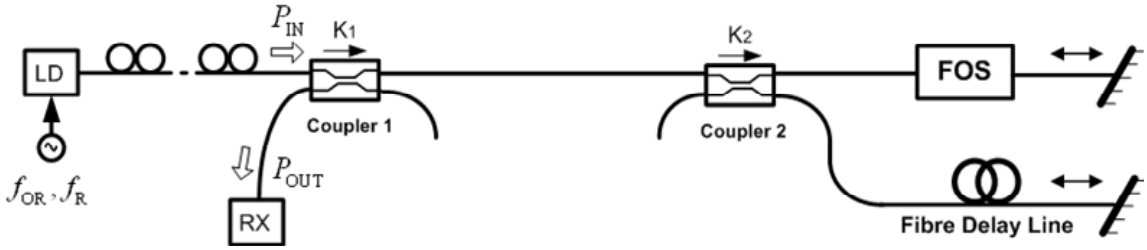

Figure 5.4.- Referencing scheme for an intensity sensor based on a Michelson topology in transmissive configuration. FOS: fibre-optic intensity sensor.

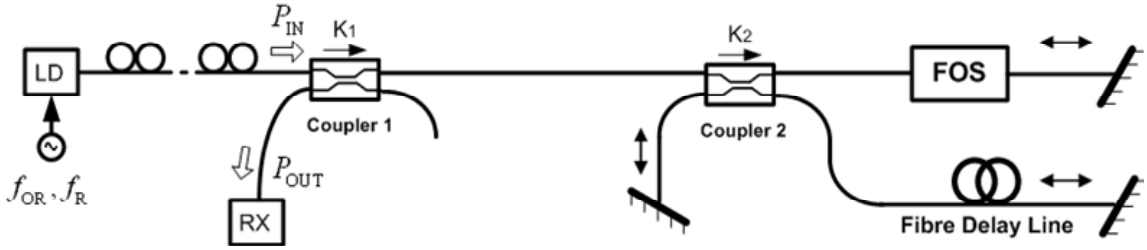

Figure 5.5.- Referencing scheme for an intensity sensor based on a Michelson topology in reflective configuration. FOS: fibre-optic intensity sensor.

Both configurations shown before are investigated in [9] concluding that the Michelson in reflective configuration exhibited overall a better result since it had a higher dynamic range and, consequently, could address a wider range of the normalization parameter.

Furthermore, this topology also showed a better performance in terms of sensitivity whereas the Michelson configuration in tranmisssion presented a slightly better result in respect to linearity. However, the main disadvantage of both topologies is the use of a fibre coil as fibre delay line, which makes both topologies non-compact strategies in essence.

On the other hand, Mach-Zehnder and Michelson topologies features are compared in [23] concluding that Michelson topologies show better results in terms of linearity and sensitivity. Furthermore, as the light in Michelson topology travels twice along the same path it accumulates a delay time plus an optical path length that doubles the one connected with the Mach-Zehnder topology resulting in operation frequencies half than Mach-Zehnder ones for the same configuration performance, see Eq. 5.2 and Eq. 5.3, leading to more simple and cost-effective demodulation strategies at the reception stage. All these features make the Michelson configuration more attractive in practice although higher dynamic ranges can be obtained considering Mach-Zehnder configurations.

Some examples reported in literature taking advantage of the Michelson topology are the following ones. A refractive index (in oils) measurement sensor integrated in a reflective self-referencing Michelson topology, consisting of a short length of MMF (5cm) to which the cladding was removed, is reported in [28]. It is based on the attenuation of the guided modes that propagate in the fibre depending on the refractive index of the medium that surrounds the unclad portion of the MMF obtaining a linear correlation coefficient of r=0.95 and a resolution of ≈0.002dB/√Hz. Another self-referenced intensity sensor based on a reflective Michelson configuration is developed in [29]. It consists on a microbend optical fibre sensing head embedded in Carbon Fibre Reinforced Plastic (CFRP) acting as a load cell for structural monitoring in civile engineering comprising a structure of thin parallel capillary tubes of stainless steel and performing measurements up to 750kPa.

5.2.4 Sagnac resonant self-referencing topology

A generic self-referenced resonant intensity sensor based on the Sagnac topology with optical feedback (or multiple beam) is shown in Fig. 5.6. This frequency-based Sagnac configuration is sligthly different from the conventional Sagnac resonant structure [30, 31] used mainly to measure rotation [32, 33] and reported widely in literature. It allows the static electric phase difference to be different from zero, since light that left coupler 2 after travelling once through the fibre loop interfered with light that had travelled twice, three times or more through the fibre loop due to one or more reflections in the mirror, resulting in a multiple beam interference system. The existence of this phase difference between these recirculating beams is responsible for the variation of the transfer function of the system accordingly to the frequency value at which light is being modulated.

From Fig. 5.6 a useful characteristic of the present configuration relates to the fact that the emission and detection stage (plus signal processing electronics) can be virtually located in the same region, while the actual sensing fibre resonator can be located remotely (as in Michelson and in contrast with the Mach-Zehnder topology).

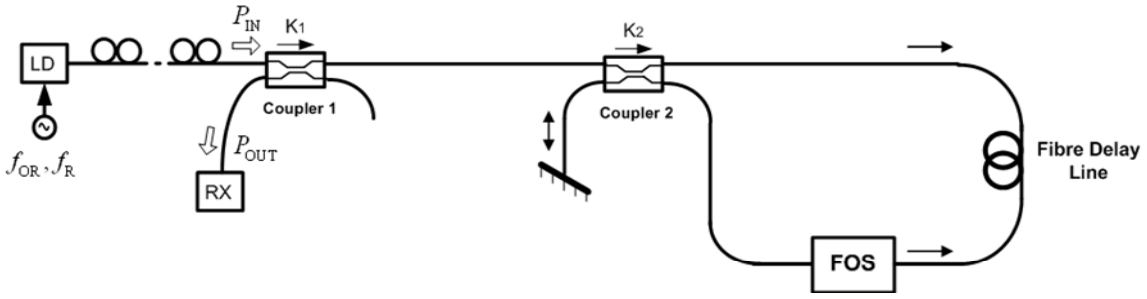

Figure 5.6.- Referencing scheme for an intensity sensor based on the multiple beam Sagnac topology. FOS: fibre-optic intensity sensor.

As an example, a strain and temperature sensing head based on a four-hole suspended-core fibre in a Sagnac interferometric topology is described in [19] obtaining a relative large strain sensitivity (≈1.94pm/με) but small temperature sensitivities (≈0.29pm/ºC) pointing to a temperature-independent strain sensor.

5.2.5 Ring Resonators (RR) self-referencing topology

Recirculating fibre-optic systems (i.e. ring resonators) have been demonstrated to offer promise for being used as delay lines in signal processing to implement transversal filters such as bandpass or notch configurations [34-40] for RF signals by using continuous single-mode fibre loops closed with one or more directional couplers in incoherent regime [41].

Frequency-based optical Infinite Impulse Response (IIR) RR configurations operating at incoherent regime for self-referencing fibre-optic intensity sensors, including SMF leads, are reported in [7, 10, 22, 42, 43]. In such reports, two self-referencing methods are described relying on the ratio between the amplitudes of the RF signals corresponding to the interference in an incoherent RR (as both numerator and denominator of the parameter are affected by the same random power fluctuations, the self-reference property of this measuring parameter is assured), namely *frequency normalization*, see Fig. 5.7 and *two-ports normalization*, see Fig. 5.8. While in the first case two frequency channels are used, a sensor channel at a frequency f_1 and a reference channel at a reference frequency f_2 , in the latter case the optical power is modulated by a single RF electrical signal at frequency f but deriving the sensor channel and the reference channel through using a directional coupler inside the RR loop and two returning fibre leads under identical external conditions. Alternatively, an optical attenuator and an amplifier can be located within the feedback loop to achieve a proper RR operating point. In order to assure incoherent regime, the feedback fibre loop length L must be greater than the coherence length of the light source l_C, so $l_C \ll L$ (being usually achieved by including a fibre patchcord). However, such schemes show, in certain cases, a phase-induced noise that can be much higher than the intensity noise induced by the optical source [44, 45] which is an undesirable characteristic and can be the main restriction for a practical implementation of this RR-based self-referencing configurations. In conclusion, the frequency-based self-referencing method

through frequency normalization is more suitable for remote operation of sensors than the two-ports normalization as there is only one downlead fibre from/to the sensor point. On the other hand, when simpler modulators and recepetion stages are preferred, the two-ports self-referencing method is the best option as it avoids the need for two modulating frequencies. This latter method is less cost-effective in case of remote operation as two downlead fibres are needed. Self-reference is only assured if both downleads are attached one to each other so that the environmental variations are exactly the same for both fibres (this is a premise for self-referencing schemes as seen in Chapter 2). Additionally, a second optical coupler is needed in the recirculating loop which can cause a large attenuation being an inconvenient with regards to the noise level of the measurements. Both cases analyzed, Fig. 5.7 and 5.8, are transmissive configurations although it is also possible to implement a reflective configuration [46], as shown in Fig. 5.9.

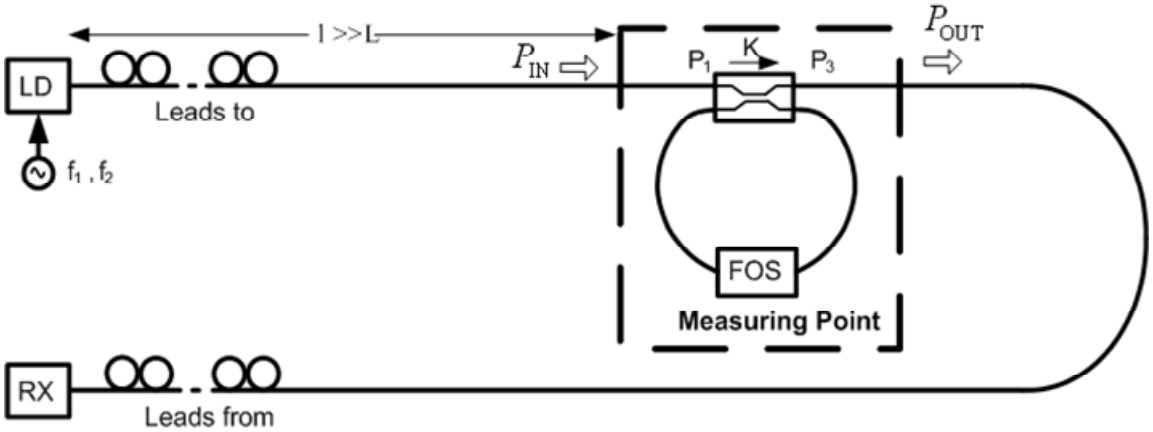

Figure 5.7.- General scheme for a RR for self-referencing FOS: frequency normalization method.

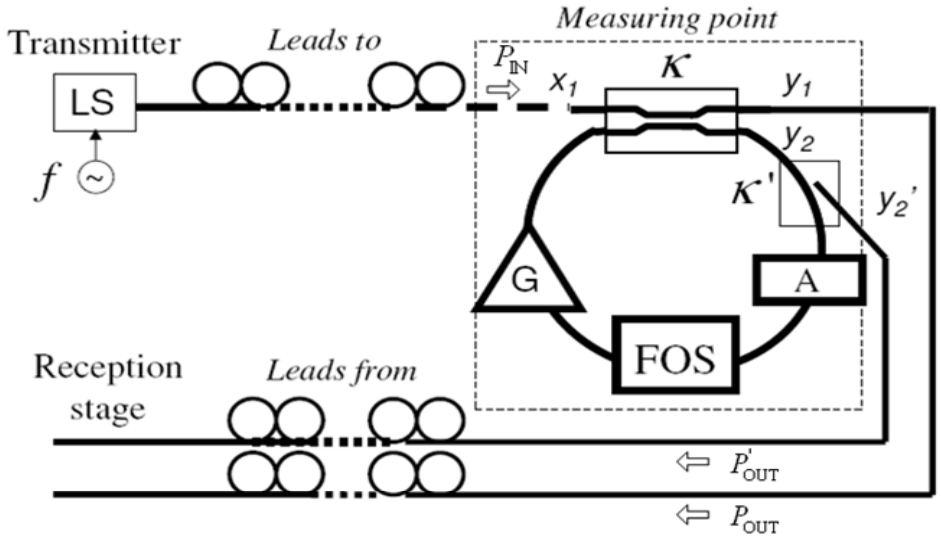

Figure 5.8.- General scheme for a RR for self-referencing FOS: two-ports normalization method. A: optical attenuator. G:amplifier.

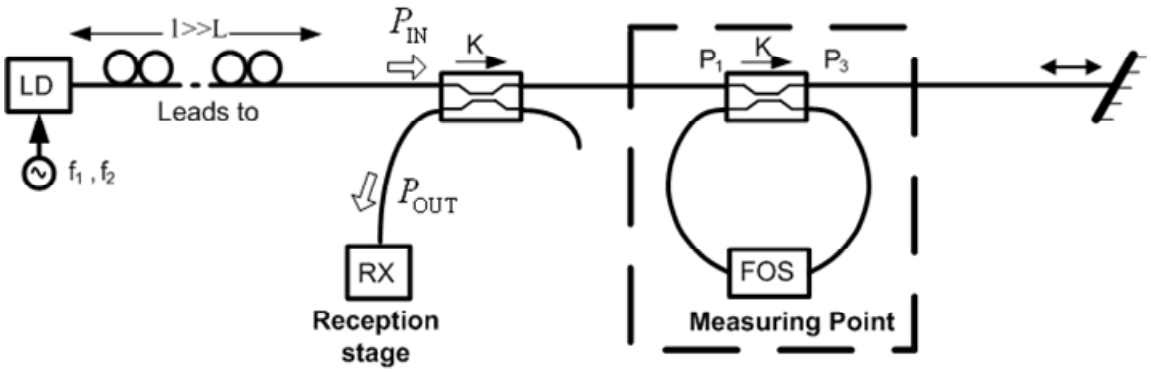

Figure 5.9.- Referencing scheme for an intensity sensor based on a ring resonator topology in reflective configuration. FOS: fibre-optic intensity sensor.

Both configurations, transmissive RR (corresponding to Fig. 5.7 or 5.8, alternatively) and reflective RR (corresponding to Fig. 5.9) are investigated in [46] concluding that the RR configuration in reflection exhibited overall a better result since it had a similar sensitivity to transducer losses and a higher dynamic range and, consequently, a wider range of the normalization parameter can be addresed. In addition to this fact, the reflective RR configuration operates at lower optical power levels as the sensing signal passes twice through the fibre-optic sensor. However, the main disadvantage of both topologies is the use of a fibre coil as fibre delay line, which makes both topologies non-compact strategies in essence, as the other frequency-based topologies presented in this chapter.

5.2.6 New approaches FBG-based in self-referencing topologies

Compared to the aforementioned transmisive self-referencing topologies, reflective self-referencing mirror-based fibre-optic intensity-based sensor topologies provide a sensitivity enhancement as the light of the sensing channel crosses twice the sensing head. However, novel optical devices, such as Fibre Bragg Gratings (FBGs) have been recently used in such topologies in order to assure a reflective operation of the sensing structure [47, 48] as well as opening up wavelength-division-multiplexing (WDM) capabilities. In these all-optical self-referencing technique schemes based on FBGs, a fibre coil of length *L* is inserted between the gratings to adjust the electrical phase difference between the reflected optical signals (reference and signal channels, respectively). For example, in [49] a reflective ladder topology using Fibre Bragg Gratings (FBGs) and a Michelson configuration at the remote sensing point is reported for wavelength multiplexing and self-referencing optical intensity sensors as an illustrative example of the capabilities provided by these FBG-based schemes.

In the following sections, such reflective FBG-based schemes plus a novel reflective self-referencing technique for optical intensity sensors, using FBGs with electronically reconfigurable delays instead of long fibre delay coil, is further described by defining two self-referencing parameters for the proposed topology.

5.3 Fibre Bragg Grating-based reflective configurations

Interrogation techniques based on Fibre Bragg Gratings (FBGs), a further description of such an optical device is presented in section 5.3.1, opposite from those mirror-based described in the previous section, are effective approaches for addressing optical intensity sensors, because they provide reflective configurations that permit the use of a single fibre lead in both propagating directions of the light as well as opening up wavelength-division-multiplexing (WDM) capabilities. In these configurations, the transmission and reception stages can be located in a single point, namely central office (CO). From this central office the light is leaded to the remote sensing point through a fibre link and the reflected light, which comprises the information of the sensor-induced intensity modulation returns to the central office through the same fibre link. A general scheme of a reflective topology can be seen in Fig. 5.10.

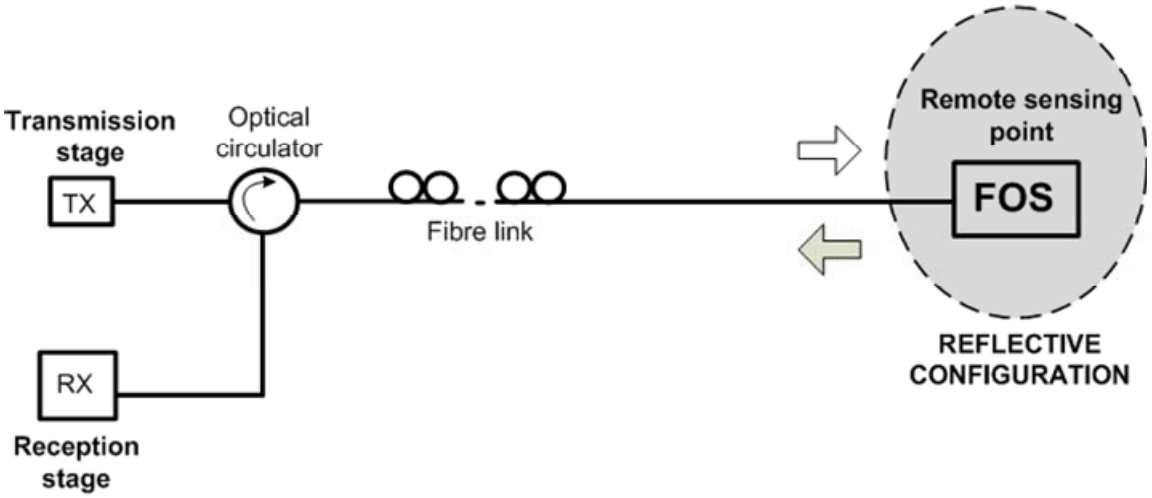

Figure 5.10.- General scheme of a bidirectional fibre link for remotely addressing fiber-optic intensity sensors (FOS) with a reflective configuration in the sensing point.

Not only the use of FBGs in sensor networks provide an effective and compact strategy for exploiting long-distance fibre links bidirectionally; actually the sensitivity of the transducer can be enhanced because it is possible to make the optical signal that travels through the intensity sensor twice, one for each propagating direction [47]. In this work, a ring resonator frequency-based self-referencing technique in a new reflection configuration for remote fibre-optic intensity sensors is demonstrated by adding a FBG at the RR output fibre. The main features of the novel configuration proposed are the doubled sensitivity in comparison with RR transmission configurations [10], uses a single fibre lead for interrogating the sensor and opens up wavelength-division-multiplexing (WDM) capabilities [50, 51]. A circulator is used to extract the reflected signal reducing the noise and simplifying the schematic. Furthermore, the configuration optimizes the second-order filter response in terms of symmetry because the decomposition of the topology leads to two rings which are physically identical being easier to adjust the operation point of the technique. This proposed configuration is shown in the following figure.

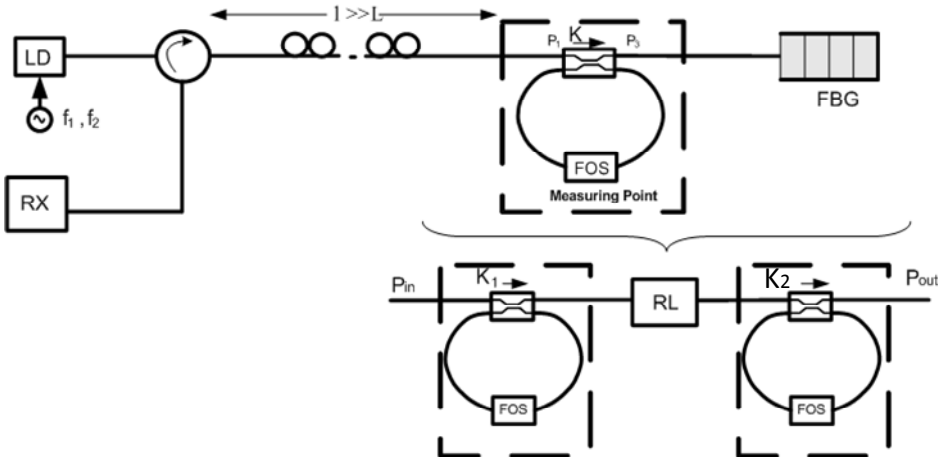

Figure 5.11.- RR FBG-based reflective self-referencing technique schematic for remote operation [47]. Inset: symmetric decomposition of the configuration in two RR in series, assuming bidirectional intensity sensor response, $K_1=K_2=K$..

All-optical FBG-based radio-frequency reflective self-referencing configurations including fibre delay coils have also been reported in literature, as in [52] in which the FBG is used to achieve a wavelength-based bypass self-referencing strategy. In this paper, the sensing head used two different-wavelength FBGs and a fibre delay coil of length *L* was inserted between the gratings to adjust the electrical phase difference between the reflected signals. This all-optical-based concept will be further discussed in section 5.3. Furthermore, similar to those described in section 5.1.3, a reflective RF FBG-based configuration employing a Michelson topology is reported in [49] based on a reflective ladder topology where the information of each sensor is carried by a specific wavelength associated to a dedicated FBG and discriminated by the use of appropriated WDM couplers, permitting at the reception the independent wavelength identification of each individual sensor.

All the strategies aforementioned rely also either on the magnitude response or the phase (relative phase) of the configuration versus modulation frequency to obtain the self-referencing parameter.

In this chapter, the configuration consisting of a fibre optic sensor and a fibre delay line coil located between two FBGs, as in [52, 53], is described as well as the self-referencing parameter based on the relative output phase difference of both channels (sensing and reference). Afterwards, a novel electro-optical configuration in which the fibre delay coil is replaced by electronically reconfigurable phase-shifts, based on [54] is presented and analyzed, through the Z-transform formalism. It is defined a new self-referencing parameter *R* as the ratio between voltage values at the reception stage for different electrical phase-shifts. Both measurement parameters are defined and a comparative study in terms of design parameters, linearity, sensitivity and resolution is reported on Chapter 6. By replacing the fibre delay coil by an electronic delay at the reception stage, a compact remote sensor head and a flexible demodulation scheme in the electronic domain can be achieved [55]. It is worth mentioning that a deeper analysis of the Z-transform formalism framework can be found in Appendix B of this document.

5.3.1 Fibre Bragg Gratings (FBGs)

Fibre Bragg gratings (FBGs) are passive components based on the properties of diffraction in periodical structures and the guiding properties in optical waveguides. Their operation consists on reflecting the optical power within a specific wideband with a characteristic central wavelength, namely λ_C, and letting the rest of the spectrum propagate in the transmission direction. The most important characteristic parameter of a FBG is the ratio between the reflected and the incident optical powers within the reflecting bandwidth, named reflectivity. Fig. 5.12 shows a typical spectrum of a FBG in transmission (a) and reflection (b) operation.

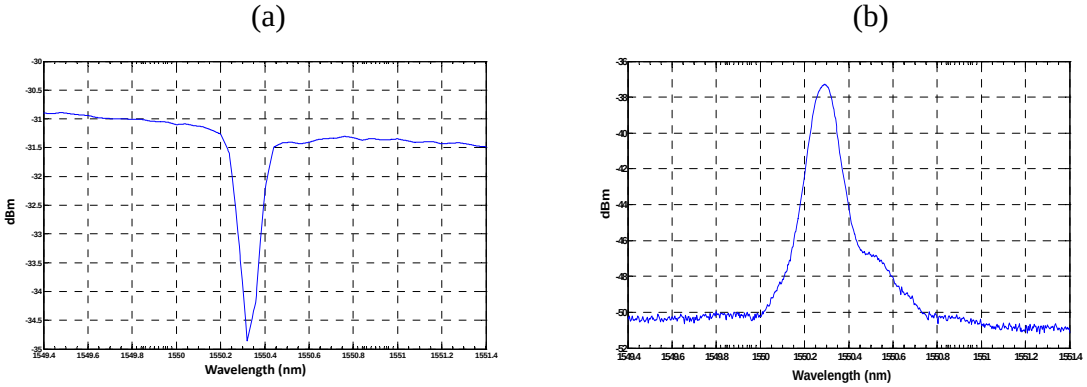

Figure 5.12.- FBG typical spectrum in transmission (a) and reflective (b) operation.

FBG devices are fabricated by "writing" a fibre grating onto the core of an optical fibre. This can be done in a number of ways. One method uses two short wavelength laser beams that are angled with respect to each other to form an interference pattern through the side of the optical fibre. The interference pattern consists of bright and dark bands that locally change the index of refraction of the core region of the fibre that is doped with germanium. Exposure time for these gratings varies from minutes to hours dependent upon dopant concentration in the fibre, the wavelengths used, the optical power level, and the imaging optics. Other methods that have been used include the use of phase masks and interference patterns induced by short high energy laser pulses. The short duration pulses have the potential to be used to write fibre gratings into the fibre as it is being drawn. Substantial efforts are being made by laboratories around the world to improve the manufacturability of these gratings as they have substantial potential to be used to support optical communication WDM-based as well as sensing technology.

The primary application of FBGs is in optical communications systems. They are specifically used as notch filters [56] but they are also used in optical multiplexers and demultiplexers with an optical circulator [57], or conforming Optical Add-Drop Multiplexers (OADM) [58, 59]. In this latter case, the FBG is set to reflect one of the channels back to a circulator where it is directed down and dropped out of the system. Since the channel has been dropped, another signal on that channel can be added at the same point in the network. Furthermore, FBG demultiplexers and OADMs can also be wavelength-tunable by strain or temperature [60] applied by a piezoelectric transducer.

Long haul interrogating sensor network methods have been reported for long-distance measurements in FBG-based sensor systems, as in [61], with potential to increase the measurement distance further to 150km. Such interrogating distances usually need the use of Raman optical amplification to extend the transmission length.

On the other hand, as well as being sensitive to strain, the Bragg wavelength is also sensitive to temperature. This means that fibre Bragg gratings can be used as sensing elements in optical fibre sensors. In a FBG sensor, the measurand causes a shift in the Bragg wavelength, $\Delta\lambda_C$. Such optical sensors have been widely reported in literature [62-66] providing one of the most powerful tools for infrastructure management, named structural health monitoring (SHM), which comprises the measurements of strain and temperature for civil infrastructures such as bridges, tunnels, railways or historical monuments [67-70].

In conclusion, FBGs are well-known, low-cost and an excellent technology to achieve WDM optical sensor networks, because they can be used as spectral filtering devices for broadband light sources and, consequently, can be used in self-referencing optical configurations for remotely addressing fibre-optic intensity sensors as well as opens up the possibilities of wavelength-division-multiplexing interrogation schemes for these fibre-optic intensity-based sensors.

5.4 All-optical FBG-based reflective configuration with fibre delay coil

The basic configuration, without frequency modulation, using two FBGs with different central wavelengths and an intensity sensor (FOS) located between them is shown in Fig. 5.13.

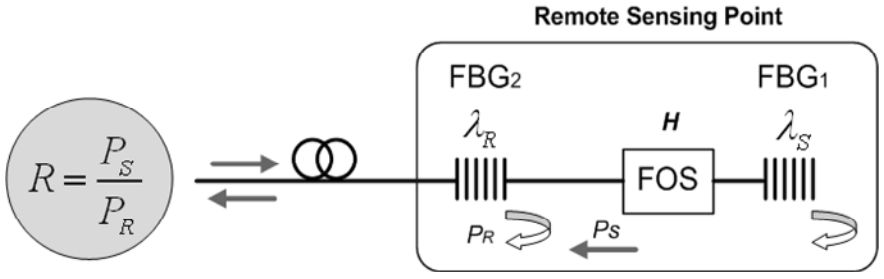

Figure 5.13.- FBG-based reflective configuration in the remote sensing point for self-referencing FOS.

Two continuous optical waves, at a reference wavelength λ_R and a sensor wavelength λ_S, reach the remote sensing point. In this basic configuration it is assumed that both reflected spectra at the two FBGs do not overlap in wavelength. The optical power reflected at the reference wavelength P_R is used as a reference channel, while the measurand induced attenuation H causes a power variation at the sensor wavelength, which can be read in signal P_S. The ratio between both reflected optical powers, $R = P_S / P_R$, can be used as self-

referenced measurement parameter because all the power fluctuations taking place out of the sensing point are identical at both the reference and sensor wavelengths, specially if both wavelengths are close one to each other. The sensor loss modulation *H*, which depends on the measurand, is squarely encoded in the self-referencing parameter *R* due to the reflective operation of the sensing structure as the light crosses twice the fibre-optic sensor (FOS).

Assuming that the reflectivities of the reference and sensor FBGs are $R(\lambda_R)$ and $R(\lambda_S)$, respectively, the self-referencing measurement parameter yields:

$$R = \frac{P_{os} \cdot R(\lambda_S)}{P_{or} \cdot R(\lambda_R)} \cdot T^2 \cdot H^2 \tag{5.5}$$

where P_{os} and P_{or} are the sensor-wavelength and reference-wavelength average powers, respectively, that reach the remote sensing point and *T* is the transmission coefficient, taking into account the loss induced at λ_S due to insertion losses in the reference FBG.

The main issues to consider regarding this configuration are the restrictions on the reflectivities of the FBGs and the measurand-induced intensity modulation range for a required signal-to-noise ratio (SNR) in the self-referencing measurement parameter.

On the other hand, a second topology in all-optical self-referencing technique schemes based on FBGs (Fiber Bragg Grating) can be achieved using a modulated light source at frequency f and emplacing a fibre coil of length *L* between the gratings to adjust the electrical phase difference between the reflected optical signals (λ_R and λ_S), see Fig. 5.14. It consists of an amplitude-to-phase conversion where the phase-shift, ϕ_{dif}, between the reflected light at a wavelength λ_R (reference) and λ_S (sensing) depends on the length (*L*) and on the modulation frequency (*f*) by the following equation[1]:

$$\phi_{dif} = \frac{2\pi}{c} \cdot n_g \cdot f \cdot 2L \tag{5.6}$$

where *c* is the speed of light in vacuum and n_g is the (single-mode) fibre effective group refractive index.

Eq. 5.6 determines the relative phase delay of the RF electrical signal at the sensing wavelength (from the sensing point) with regards to the electrical signal at the referencing wavelength.

[1] In Eq. 5.2 and Eq. 5.3 the term *2L*, in the denominator, refers to the fact that the light crosses twice through the fibre delay coil provided by the reflective topology.

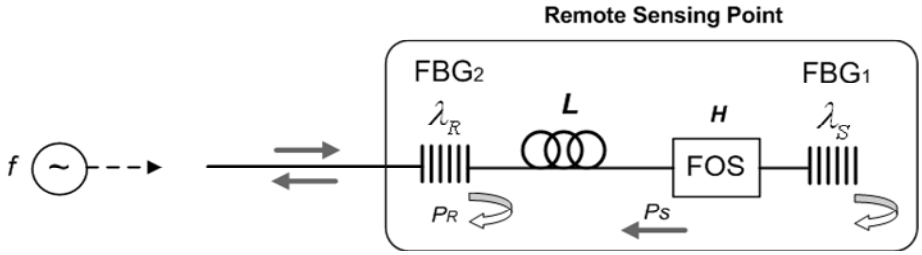

Figure 5.14.- Reflective configuration in the remote sensing point for self-referencing FOS using two FBGs and a fibre delay line.

The Free Spectral Range (FSR) of the configuration is given by:

$$FSR = \frac{c}{n_g \cdot 2 \cdot L} \tag{5.7}$$

From Eq. 5.6 it can be deduced that for a desired phase-shift value at the reception stage, the lower the frequency f the higher the (required) length of the optical fibre delay coil L. In the following table is shown the relationship between f and L for two arbitrary fixed phase-shift values, such as ϕ_{dif} =0.5π and ϕ_{dif} =0.67π.

$\phi_{dif} = 0.5\pi$		$\phi_{dif} = 0.67\pi$	
Modulation freq. (f)	***Delay fiber coil length (L)***	***Modulation freq. (f)***	***Delay fiber coil length (L)***
500Hz	51.7 km	500Hz	68.9 km
1kHz	25.8 km	1kHz	34.5 km
2kHz	13.9 km	2kHz	17.2 km
5kHz	5.2 km	5kHz	6.9 km
10kHz	2.6 km	10kHz	3.5 km
25kHz	1.04 km	25kHz	1.4 km
50kHz	500 m	50kHz	700 m
75kHz	340 m	75kHz	470 m
100kHz	250 m	100kHz	350 m
150kHz	170 m	150kHz	235 m

Table 5.1. Relationship between frequency modulation and delay fibre length for Ω=0.5π and Ω=0.67π. (c=2.99792458x10^8 m/s ; n_g=1.45)

In the optical configuration shown in Fig. 5.14, the power reflected at the first FBG (FBG_2, reference), P_R, is given in the time domain by:

$$P_R = P_{or}[1 + m_r \sin(2\pi ft + \phi_r)] \tag{5.8}$$

where P_{or}, m_r, f and ϕ_r are, respectively, the optical carrier power, the source modulation index at wavelength λ_R, the modulation frequency and the electrical phase of P_R. Identical expression to Eq. 5.8 for the power reflected from the second FBG (FBG_1, sensing), P_S, at a wavelength λ_S can be obtained with the equivalent parameters P_{os}, m_s, f and ϕ_s, see Eq. 5.9.

$$P_S = P_{os}[1 + m_s \sin(2\pi ft + \phi_s)] \tag{5.9}$$

The electrical phase difference between both reflected optical signals, $\phi_{dif} = \phi_s - \phi_r$, relative to λ_R and λ_S is given by Eq. 5.6 as a consequence of the group delay of the light in the fibre delay coil with length *L*.

The amplitudes of both signals P_R and P_S are related through a parameter dependent on the transducer losses, named β parameter, being defined as $P_{os} = \beta.P_{or}$ ($\beta \in [0,1]$). This β parameter, basically, depends on the modulation indexes at both wavelengths, the reflection coefficients of the two FBGs, the transducer response squared (optical signal λ_S passes through the transducer twice due to the reflective scheme as aforementioned) as well as the losses in the delay line and splices.

For this sensor scheme the optical power launched on the photodetector (which yields an electrical beating of signals at the detector) is given by:

$$P_O = P_R + P_S = P_{or} + P_{os} + P_o \sin(2\pi ft + \phi) \tag{5.10}$$

where

$$P_o = \left[(P_{or} m_r)^2 + (P_{os} m_s)^2 + 2P_{or} P_{os} m_r m_s \cos(\phi_{dif}) \right]^{1/2};\ \phi_{dif} = \phi_s - \phi_r \tag{5.11}$$

$$\phi = \arctan\left[\frac{(m_s / m_r)\beta + \cos(\phi_{dif})}{\sin(\phi_{dif})} \right] \tag{5.12}$$

From Eq. 5.12, the output phase parameter depends only on the optical signals phase difference, the modulation index ratio (m_s / m_r) and the β parameter being, consequently, insensitive to power fluctuations anywhere at the link. The phase difference will be a constant factor once the modulation frequency and the phase-shift between both signals are fixed. The dependence of ϕ on the absolute phase, ϕ_s, has been eliminated through the consideration of a reference-phase term.

If a photodetector with responsivities d_r and d_s at the reference and sensor wavelengths, respectively, is considered then the electric current signal obtained after the optical-to-electrical conversion in the photodetector can be described as follows :

$$I_O = d_r.P_R + d_s.P_S \tag{5.13}$$

After the current-to-voltage conversion of I_O in the reception electronics, a proportional voltage signal V_O is finally obtained:

$$V_O = k_o.I_O \tag{5.14}$$

where k_o is the global transimpedance constant related to the electronic receptor.

The sensor-induced power modulation *H* induces module (magnitude) and phase variations in this electrical signal V_O. Both the module ratio between two different arbitrary phase-shifts [11, 55] and the phase response [52, 54] can be used as a self-referencing measurement parameter.

The following figure shows the corresponding digital filter model of the all-optical configuration described in Fig. 5.14.

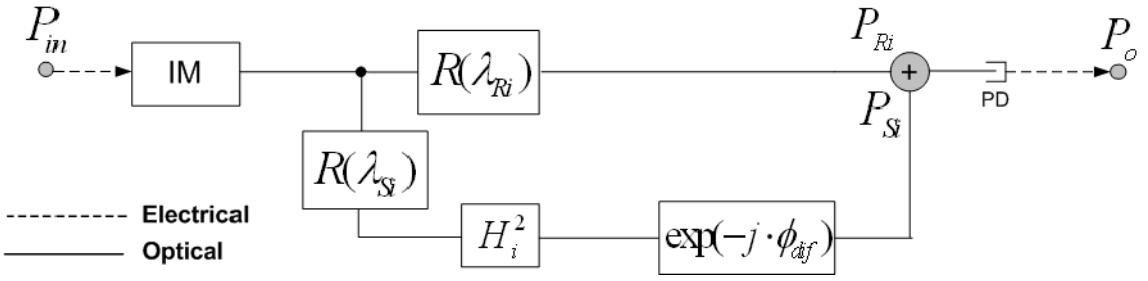

Figure 5.15.- Filter schematic for all-optical FBG-based self-referencing configuration of Fig. 5.14. IM: Intensity Modulator.

All-optical signal processors based on fibre-optic technology were reported in order to overcome the bandwidth constraints of microwave and RF signal filters. Incoherent regimes of operation can be assured when the time delays in the optical paths are much higher than the coherence time of the optical sources employed, given always positive coefficients for such filters [71].

On the other hand, when the time delays in the optical paths are comparable to the coherence time of the optical sources, the optical phase relations between the different ports are deterministic and coherent filters can be achieved [72]. The achievement of coherent optical interference is contingent with the development of integrated optics technology. Several photonic synthesis techniques based on transversal filters [73], delay line lattices [74] and ring resonators [40, 75] have been reported in literature providing greater design

flexibility plus higher processing bandwidths [76] achieving high-speed components for optical communication systems.

In the case of sensor networks, the amount of information to be addressed is usually very low and quasi-static being low-cost devices, efficient multiplexing topologies and self-referenced measurements the most important objectives to be achieved. In this situation, incoherent fibre-optic topologies including wavelength-division multiplexing (WDM) techniques and reflective operation are the most desirable approaches to reach.

In optical self-referencing configurations, as those described in this chapter, the optical power modulation of the sensor (at the sensing point) is related to the coefficients of the filter structure thus encoding the shape of the filter response either in magnitude or phase and performing self-referenced measurements. All-optical approaches require long fibre delay coils in which the propagation time of the light along the delay fibre is used to achieve a phase-shift Ω between the radio-frequency beating signals at the photodetector through Eq. 5.6, in case of a Michelson topology.

A novel electro-optical configuration which avoids the use of these long fibre delay coils for a required modulation frequency, see Table 5.1, is further discussed in the following section.

5.5 Electro-optical FBG-based reflective configuration without fibre delay coils

Different RF self-referencing configurations providing insensitivity to external power fluctuations, non-correlated to the sensor modulation, have been reported employing in the sensor heads interferometric schemes such as Michelson [23], ring resonators configurations [10] and non-compact all-optical fiber delay line filters [52, 53]. Recently, a novel electro-optical design which avoids the need for fiber delay coils has been reported thus achieving compact sensor heads [54]. By employing electrical filters at the reception stage it is possible to achieve:

- **Arbitrary modulation frequencies:** it is needed only one modulation frequency whose value can be chosen depending on the application. The self-referencing parameters defined for this electro-optical topology depend only on the phase-shifts selected at the reception stage.
- **Compact sensing point:** no fiber delay coils or complex schemes are needed in the sensing points being the performance of the all-optical configurations preserved. This is because the behavior of the self-referencing parameters versus power modulation at the sensing points depends only on the electrical phase-shifts configured at the reception stage.
- **Flexibility:** the behavior of the self-referencing technique can be modified in a single point and in an easy and flexible way just by changing the electrical phase-shifts (in the electrical domain) at the reception stage.

Furthermore, the optical power modulation of the sensor at the remote sensing point can be related to the coefficients of the filter structure thus encoding the filter response either in magnitude or in phase and performing self-referenced measurements.

In this section a self-referencing electro-optical FBG-based fiber-optic intensity sensor topology is analyzed. This configuration is based on a configuration previously reported in [54] but using two electrical phase-shifts and defining a new measurement parameter as the ratio between voltage values at the reception stage for different electrical phase-shifts. The transfer function of the remote sensing configuration using the digital filter theory and following the Z-transform formalism is analyzed; and the definition of both self-referencing measurement parameters is presented as well. In addition to this, measurements validating the theoretical model and the topology performance, in terms of self-reference property, for the two measurement parameters are reported. The performance of both parameters in terms of sensitivity, linearity and resolution will be discussed in the following chapter. Finally, the main conclusions of this topology are reported.

5.5.1 Theory

The response of the remote sensing configuration and the measurement technique realized for both self-referencing parameters are simultaneously considered for a generic remote sensing channel *i* containing both corresponding wavelengths λ_{Ri}, λ_{Si} and the electrical phase shifts Ω_1, Ω_2, leaving τ implied. The electro-optical topology with electronic delay lines proposed for a single generic remote optical sensor *i* is shown in Fig. 5.16(a). The digital filter schematic of the complete sensor topology is shown in Fig. 5.16(b) where the dashed lines correspond to the electrical domain and solid lines correspond to the optical domain.

A broadband light source (BLS), or alternatively two optical signals with optical power density around the two reference and sensing wavelengths, is modulated at a single frequency f by an intensity modulator (IM) and launched to the system through and optical circulator. In the remote sensing point, the optical signal is sliced in wavelength and reflected by two FBGs at the remote sensing point. The central wavelengths of the FBGs placed before and after the optical sensor (fibre-optic sensor) are named λ_R (reference) and λ_S (sensor), respectively. The sensor power modulation is defined as H_i. In the reception stage, two electrical phase-shifts (Ω_1 and Ω_2) are applied to the RF modulating signal at both wavelengths thus achieving a delay line filter deployed in the electrical domain but with a coefficient, β_i, which depends on the optical power modulation H_i in the sensing point. Those electrical phase-shifts $D(\lambda_{Ri}) = e^{-j\Omega_1}$ and $D(\lambda_{Si}) = e^{-j\Omega_2}$ are applied to the RF modulating signal and provide a flexible and easy-reconfigurable operation point of the remote intensity sensor.

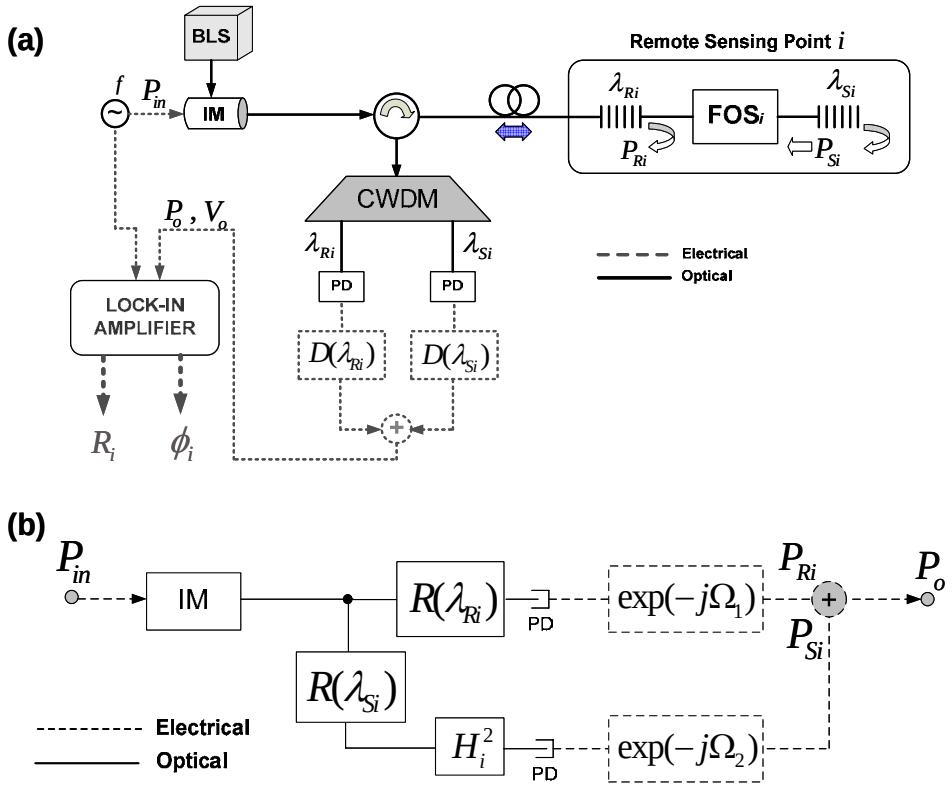

Figure 5.16.- (a) Point-to-point self-electro-optical configuration for a generic remote sensing point. (b) Filter model of the configuration for a remote sensing point with no fiber delay coil and electrical phase-shifts at the reception stage. BLS: broadband light source; IM: optical intensity modulator, PD: photodetector.

The system output in the time domain, see Fig. 5.16(b), can be expressed as follows:

$$p_0(t) = \alpha_i \cdot \left(p_{Ri}(t) + \beta_i \cdot p_{Si}(t) \right) \tag{5.15}$$

with

$$\alpha_i = m_{Ri}.R(\lambda_{Ri}).d_{Ri} \tag{5.16}$$

$$\beta_i = \frac{m_{Si}.R(\lambda_{Si}).d_{Si}}{m_{Ri}.R(\lambda_{Ri}).d_{Ri}} H_i^{\,2} \tag{5.17}$$

where m_{Ri}, $R(\lambda_{Ri})$ and d_{Ri} are the RF modulation index, the reflectivity of the FBG and the photodetector response at the reference wavelength λ_{Ri} for the generic remote sensing point *i*, respectively, and m_{Si}, $R(\lambda_{Si})$ and d_{Si} are the respective similar parameters for the sensor wavelength λ_{Si}.

The time domain signals of sensing channel *i* at modulation frequency *f*, $p_{Ri}(t) = \cos(2\pi \cdot f \cdot t - \Omega_1)$ (reference signal) and $p_{Si}(t) = \cos(2\pi \cdot f \cdot t - \Omega_2)$ (sensing

signal), can be studied under steady-state analysis using phasor transform of the corresponding sinusoidal signals:

$$\begin{aligned} P_{Ri} &= P_{in} \cdot \alpha_i \cdot \exp(-j \cdot \Omega_1) \\ P_{Si} &= P_{in} \cdot \alpha_i \cdot \beta_i \cdot \exp(-j \cdot \Omega_2) \end{aligned} \tag{5.18}$$

The output signal response as a phasor P_0 can be analyzed using the previous phasors and the resulting time-domain signal at frequency *f* (Hz) can be recovered by obtaining the real part of $P_0 \cdot \exp(-j \cdot 2\pi \cdot f \cdot t)$.

The expression of the normalized system output as a phasor is given by:

$$H_0 = \frac{P_0}{P_{in}} = \alpha_i^{'} \cdot \left[1 + \beta_i \cdot \exp\left[-j \cdot \left(\Omega_2 - \Omega_1\right)\right]\right] \tag{5.19}$$

being $\alpha_i^{'} = \alpha_i \cdot \exp(-j \cdot \Omega_1)$.

The expression of H_0 can be directly identified with the transfer function of a digital Finite Impulse Response (FIR) filter in the Z-Transform domain as follows:

$$H_0(z) = \alpha_i^{'} \cdot \left(1 + \beta_i \cdot z^{-1}\right) \tag{5.20}$$

where $z^{-1} = \exp(-j \cdot \Omega)$ with $\Omega = \Omega_2 - \Omega_1$. A further explanation of the theoretical framework involving the result given by Eq. 5.20 is reported in section C.1 of Appendix C within this document.

Using the transfer function $H_0(z)$ in the Z-Transform domain permits an easy study of the system frequency response in terms of generic design parameters, as reported in [54]. In this approach, the phase shift difference $\Omega = \Omega_2 - \Omega_1$ between the time domain reference and sensor signals represents, at the same time, the angular frequency of the digital filter $H_0(z)$.

The sensor loss modulation H_i, which depends on the measurand, is encoded in the transfer function of the self-referencing configuration by means of the parameter β_i. In Equation 5.17 it appears H_i^2 due to the reflective operation of the sensing structure (the light crosses the sensor twice).

Examining Eq. 5.20 it can be seen that β_i is a zero of the transfer function. So a zero transmission occurs when the following two conditions are fulfilled:

$$\beta_i = 1 \tag{5.21}$$

$$\Omega = \Omega_2 - \Omega_1 = \pi \cdot (2k - 1) \quad \text{for integer } k \tag{5.22}$$

The normalized magnitude response and the phase response versus the angular frequency Ω of the digital filter model of Fig. 5.16(b) are shown in Fig. 5.17 and Fig. 5.18, respectively, for different values of β_i. A symmetrical magnitude shape and an anti-symmetrical phase shape can be seen with regards to $\Omega = \pi$; and a zero transmission takes place at condition $\Omega = \pi$ for $\beta_i = 1$.

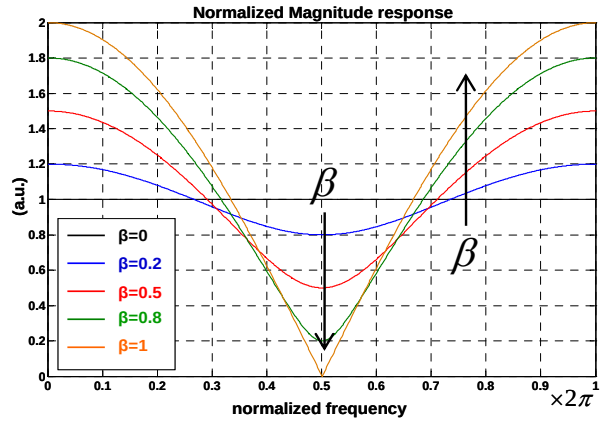

Figure 5.17.- Normalized magnitude response of the transfer function of the self-referencing configuration versus angular frequency for different values of β_i.

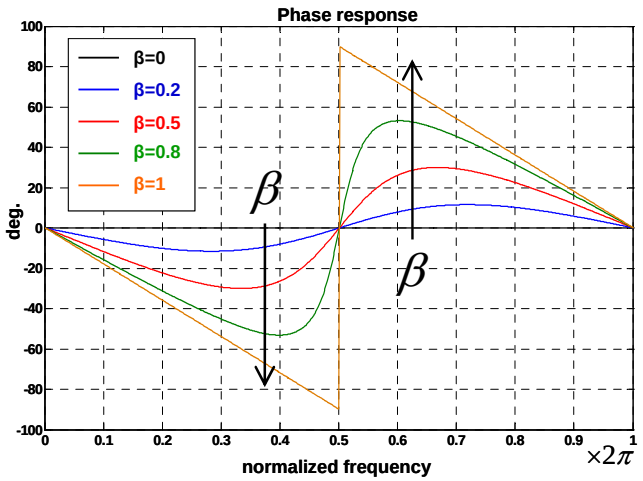

Figure 5.18.- Normalized phase response of the transfer function of the self-referencing configuration versus angular frequency for different values of β_i.

If $\beta_i < 1$, the phase response increases from zero to positive values as β_i takes greater values, being $\Omega > \pi$, and the maximum values (around 90 degrees) occur at angular frequencies tending to $\Omega = \pi^+$ (i.e. $\Omega = 180^{o+}$). For angular frequencies lower than $\Omega = \pi$

the phase response decreases from zero to negative values as β_i tends to one, and the peak value (around -90 degrees) takes place, once again, around angular frequencies tending to π^-, being $\Omega = \pi$ the frequency of the zero. This explanation is graphically illustrated in Fig. 5.18.

On the other hand, the Z-transform theory determines that a stable filter conditions is achieved when the modules of the poles are less than one, i.e. $|p_p| < 1$, as can be seen in Appendix B. The zero-pole diagram considering the unit circle of reference of the transfer function described by Eq. 5.20 is shown in the following figure:

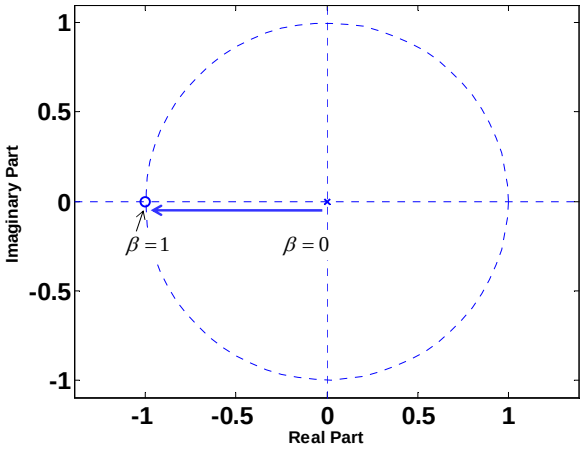

Figure 5.19.- Zero-pole diagram of the proposed self-referencing topology transfer function given by Eq. 5.20 consisting of a zero and no poles.

The transfer function defined by Eq. 5.20 shows no poles and only one zero which location depends on β_i values, $\beta_i \in [0,1]$ and, therefore, fulfilling the Nyquist stability criterion.

From now on, the parameter β_i will be considered the power modulation parameter of the self-referencing configuration; nevertheless, the relation of β_i to transducer intensity modulation is shown in Eq. 5.17.

At this point, two measurement parameters can be defined for the remote sensing point shown in Fig. 5.16(a). On the one hand the parameter R_i, which is defined as the ratio between voltage values at the reception stage for different electrical phase-shifts and on the other hand the output phase ϕ_i of the electrical signal for different electrical phase-shifts at the reception stage. The expression of both measurement parameters can be seen in Eq. 5.23 and Eq. 5.25, respectively.

Considering the aforementioned definition of R_i, this parameter can be expressed as (see the section C.2 in appendix C for further explanation):

$$R_i = \frac{V_O(f,\Omega_2)}{V_O(f,\Omega_1)} = \frac{M(f,\Omega_2)\big|_{\Omega_1=0}}{M(f,\Omega_1)\big|_{\Omega_2=0}} = \frac{[1+(\frac{2\beta_i}{1+\beta_i^2})\cos\Omega_2]^{1/2}}{[1+(\frac{2\beta_i}{1+\beta_i^2})\cos\Omega_1]^{1/2}} \tag{5.23}$$

where

$$M(f,\Omega_1,\Omega_2) = \alpha_i(1+2\beta_i\cos\Omega_i+\beta_i^2)^{1/2} \tag{5.24}$$

From 5.23, the expression of the magnitude corresponding to sensor *i* at angular frequencies Ω_1, Ω_2 can be written as a function of $\Omega_i = \Omega_2 - \Omega_1$.

The expression of the other parameter, the output phase ϕ_i for different electrical phase-shifts corresponding to sensor *i* can be written as:

$$\phi_i = \arctan\left[\frac{-(\sin\Omega_1+\beta_i\sin\Omega_2)}{(\cos\Omega_1+\beta_i\cos\Omega_2)}\right] \tag{5.25}$$

A further explanation of the theoretical framework involving both self-referencing parameters is reported in section C.1 of Appendix C within this document.

For a fixed value of the modulation frequency and the electrical shifts, both measurement parameters, R_i and ϕ_i, of the remote sensing point *i* depend only on β_i. Furthermore, Eq. 5.17 shows that β_i is insensitive to external power fluctuations that might take place in the optical link between the sensing point and the transmission stage, thus performing a self-reference parameter. Moreover, both self-referencing parameters can be determined for any pair of values of angular frequencies (Ω_1,Ω_2) providing flexibility to the measurement technique at the remote sensing network for any desired operation point. Fig. 5.20(a) and Fig. 5.20(b) show some theoretical curves for the R_i parameter and the output phase ϕ_i, respectively, for different phase-shift configurations.

An analysis of Fig. 5.20(a) shows that greater R_i values can be achieved by increasing the relative difference between both phase-shifts, Ω_1 and Ω_2, reaching its maximum value for $\Omega_1 - \Omega_2 = \pi$. R_i parameter shows a non-symmetrical behaviour with regards to the sign of the difference between Ω_1 and Ω_2 in contrast with the symmetrical behaviour of the output phase ϕ_i response, see Fig. 5.21(b). Higher R_i values can be obtained by selecting phase-shifts values in which the sign of the difference $\Omega_1 - \Omega_2$ is positive rather than negative ones.

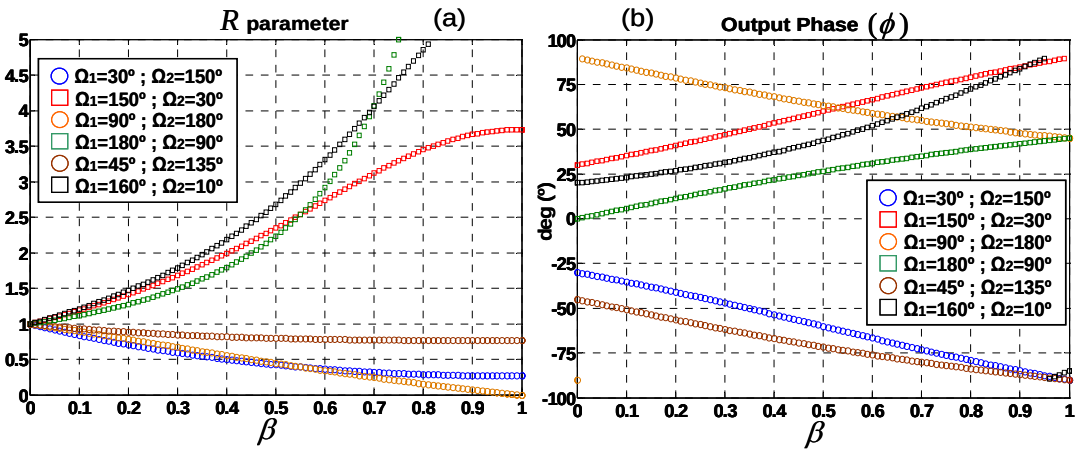

Figure 5.20.- Theoretical curves of the R_i parameter (a) and the output phase ϕ_i (b) versus β_i for different phase-shifts configurations at the reception stage.

Let $m(\phi_i)$ be the slope of the output phase response versus β_i. From the theoretical curves shown in Fig. 5.20 the performance of both parameters can be resumed as:

$$R_i > 1 \text{ and } m(\phi_i) > 0 \text{ when } \Omega_1 - \Omega_2 > 0.$$
$$R_i < 1 \text{ and } m(\phi_i) < 0 \text{ when } \Omega_1 - \Omega_2 < 0.$$

Other theoretical curves for both self-referencing parameters showing different performances are plotted in the following figures. Fig. 5.21(a) shows the R_i parameter versus phase-shift Ω_2 for different Ω_1 phase-shift values and for β_i=0.3, β_i=0.6 and β_i=1. As expected the R_i parameter shows a symmetrical behaviour with regards to $\Omega_2 = 180^o$ so it is possible to only consider the range of $\Omega_2 \in [0^o, 180^o]$ without losing any information about the performance of R_i. Nevertheless, from Fig. 5.21(a) it can be seen that for a fixed value of Ω_2 and β_i the greater value of Ω_1 the greater value of R_i but also depending on the β_i parameter value which provides greater values of R_i when β_i is around the unit. On the other hand, the output phase response shows a symmetrical behaviour with respect to the fixed arbitrary value of Ω_1 =90º and this response is also directly depending on the sign of the difference between Ω_1 and Ω_2, obtaining $\phi_i < 0$ when $\Omega_1 < \Omega_2$ (sensor signal is delayed with regards to the reference signal or, in the same way, the reference signal is advanced with regards to the sensor signal) and, on the contrary, $\phi_i > 0$ when $\Omega_1 > \Omega_2$. This fact is displayed in Fig. 5.21(b).

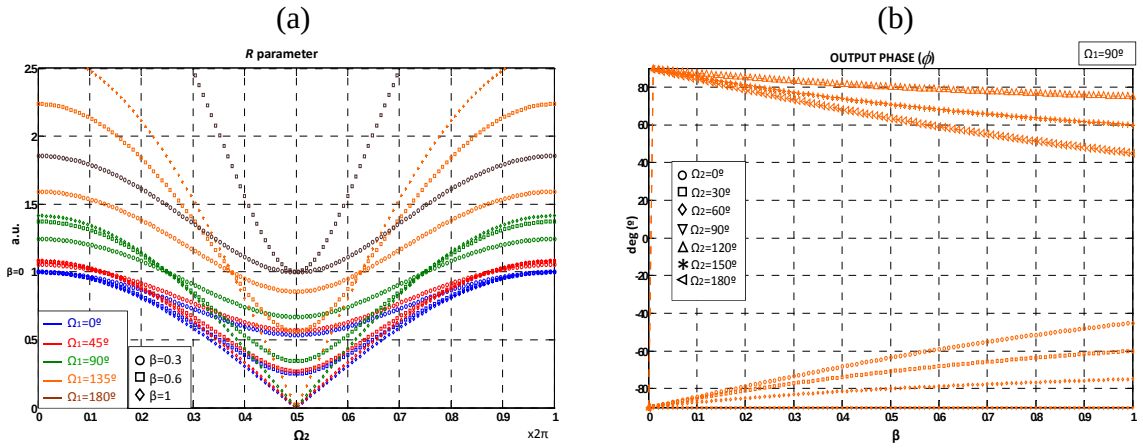

Figure 5.21.- (a) Theoretical curves of the R_i parameter versus Ω_2 for different values of Ω_1 and β. (b) Theoretical curves of the output phase ϕ_i versus β for different values of Ω_2 at the condition $\Omega_1 = 0.5\pi$ at the reception stage.

5.5.2 Measurements and experimental validation

A schematic of the experimental set-up is shown in Fig. 5.22, which has been implemented using single-mode fibre.

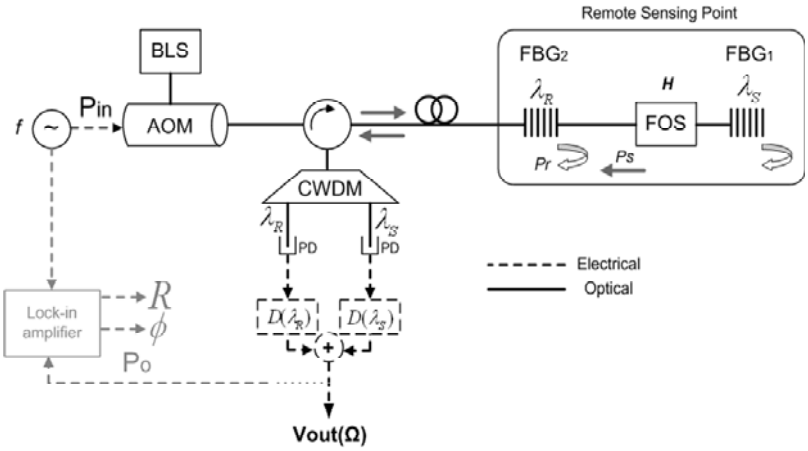

Figure 5.22.- Schematic of the experimental set-up for the calibration of the self-referencing parameters R_i and ϕ_i versus β. AOM: Acousto-Optic Modulator.

A Super-Luminiscent Broadband Light Source (Photonetics SLED Fiber Source-FiberWhite) modulated at a frequency $f = 10$kHz by an acousto-optic modulator (Brimrose Model BRI-AM-100-870-1550) has been employed to launch optical power within the C-band (1510-1560nm) into the configuration, see Fig. 5.23(a). Two FBGs with central wavelengths λ_R =1531.1nm and λ_S =1550.3nm, respectively, have been used in the remote sensing point plus a tapered single-mode fibre (fabricated at INESC-Porto), operating as a micro-displacement sensor using a micro-positioning stage on an optical table. The

reflected optical signals (λ_R and λ_S) have been passed through an optical circulator and demultiplexed by a CWDM (Coarse-Wavelength Division Demultiplexer) device. The magnitude response of the CWDM Demux used at the reception stage (Accelink Tech. Ltd.) is shown in the Figure 5.23(b) with a flat shape within the 1530nm and 1550nm bands. Both signals have been received into two different InGaAs detectors (Thorlabs PDA400C). An electronic delay line filter for each detected signal ($D(\lambda_R)$ and $D(\lambda_S)$) has been also implemented using commercial capacitors, variable resistors and operational amplifiers (LM471). Finally, the output P_O, measured directly from the electrical signal V_o detected at the reception stage, has been connected to a Lock-in Amplifier (Stanford Research Systems SR530) to obtain both the magnitude and the output phase. The following figures show the main features of the devices used in the experiment.

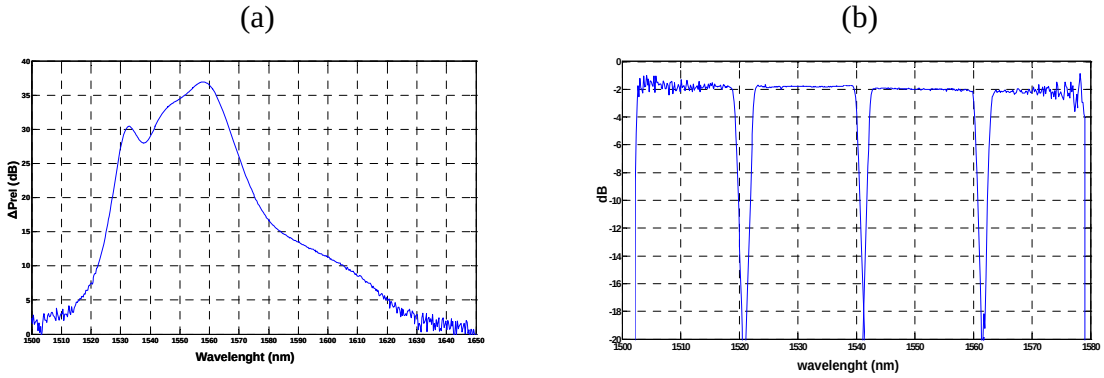

Figure 5.23.- (a) Optical Broadband Light Source (BLS) spectra (noise level scaled at 0dBm). (b) CWDM device magnitude response in demux operation.

Two Fibre Bragg Grating (FBG) operating at 1550nm and 1530nm windows were fabricated at INESC-Porto. Their tested central wavelengths were 1550.3nm and 1531.1nm, respectively. Both FBGs showed a 3dB bandwidth around 0.15nm each with reflectivities of 46% and 40% respectively. For their characterization, an Optical Spectrum Analyzer (OSA) model ANDO AQ-6315B was used. The following figures show the measurement results in reflective configuration:

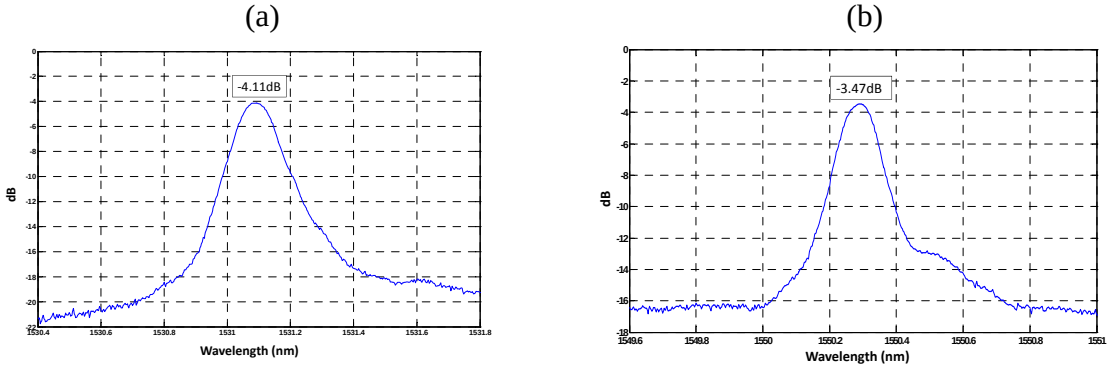

Figure 5.24.- (a) 1530nm and (b) 1550.3nm FBG (fabricated at INESC-Porto) behaviour for reflective configuration. Reflectivity measurement of 40% and 46% was obtained, respectively.

At both maximum peak values (3.47dB and 4.11dB) the measured set-up connector losses (~0.75dB) and circulator insertion losses (~0.7dB) were taken into account.

As aforementioned, the fibre-optic intensity-based sensor (FOS) was made of a self-made tapered single-mode fibre (in a Corning SMF-28 fiber by elongating the fiber during the arc discharge, which was provided by a splicing machine). It worked as a micro-displacement intensity sensor using a micro-positioning stage on an optical table, see Fig. 5.25(a). The intensity calibration curve of the taper response has been measured and represented in arbitrary units (a.u.), as seen in Fig. 5.25(b). In order to test the hysteresis of the sensor, two sets of measurements, marked as forward (*fwd*) and backward (*bkw*), have been taken for increasing and decreasing values of the displacement, respectively.

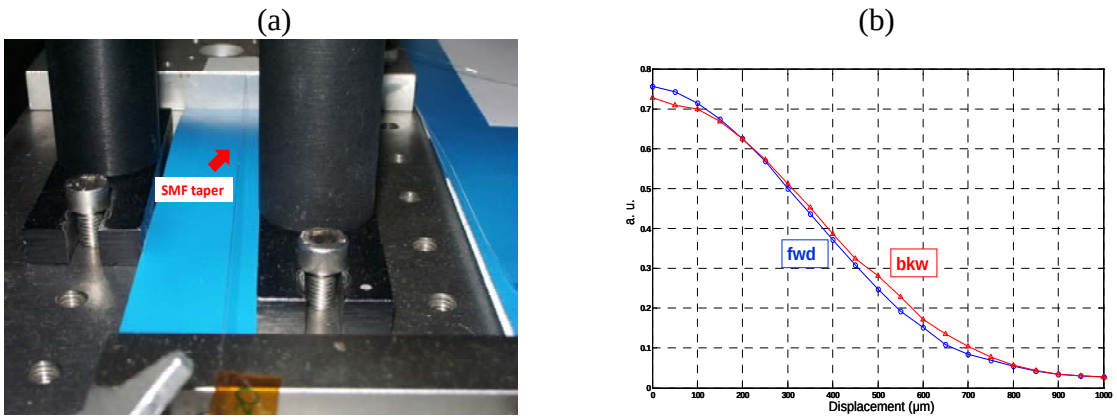

Figure 5.25.- (a) Photograph of the taper and the micro-positioning stage on the optical table. (b) Calibration curve and hysteresis of the transmission coefficient *H* @1550.3nm versus displacement. (fwd: forward; bkw: backward).

On the other hand, the broadband circulator receives the reflected optical upstream signal from the remote sensing point. This signal has been demultiplexed by a CWDM device and delivered to two InGaAs photodetectors.

The optical signals propagating along the optical path provided by the proposed topology, see Fig. 5.26, have been wavelength-characterized using an Optical Spectrum Analyzer (OSA). The Broadband Light Source has been employed with a total emitted power of 40mW (I=101.6mA). The results are shown in the following set of figures:

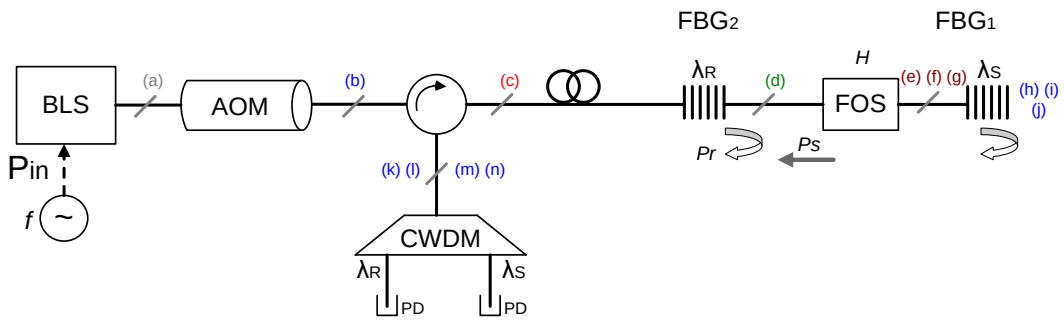

Figure 5.26.- Measuring points characterized with the Optical Spectrum Analyzer in the proposed topology.

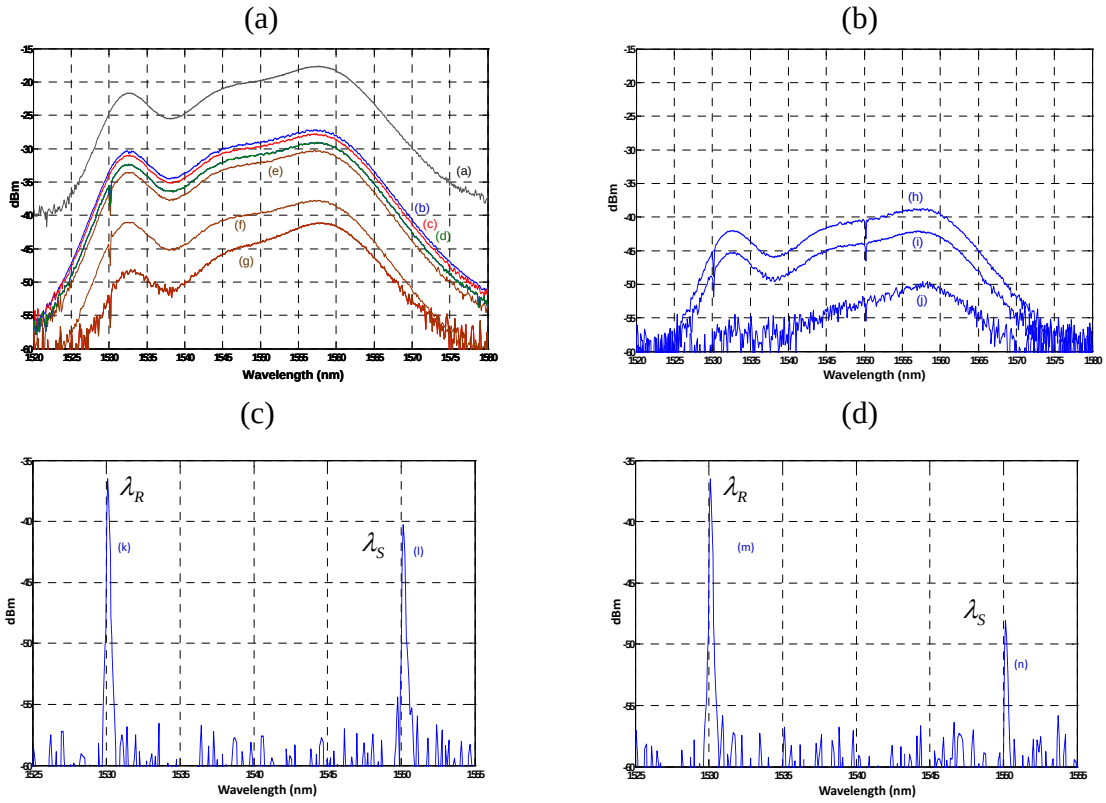

Figure 5.27.- Optical signals along the set-up optical path. Notes:
1) In Fig. 5.27(a) signals (e), (f) and (g) were taken at the same point but for different FOS losses.
2) In Fig. 5.27(b) signals (h), (i) and (j) were taken at the same point but for the same different FOS losses.
3) In Fig. 5.27(c) and 5.27(d) signals (l) and (n) refer to the sensing channel but for two different FOS losses.

From the latter figures it can be seen that acousto-optic modulator insertion losses were approximately 10dB while the optical circulator penalized only ~0.7dB as expected. Optical signals from (d) to (g) show the transmission spectra beyond FBG_2 (reference channel) and how λ_R is sliced and launched back to the reception stage through the same fibre lead. Signals (e), (f) and (g) are referred to the transmission spectra before reaching FBG_1 for different modulation losses provided by the FOS whereas Fig. 5.27(b) shows the transmission spectra after both FBGs where both reference and sensing channels are definitively sliced in wavelength. Finally, Fig. 5.27(c) and Fig. 5.27(d) show both channels at the reception stage sliced through the CWDM demultiplexer device into one standard CWDM channel each. Signals (l) and (n) show the received sensing channel for two different arbitrary modulation losses generated in the micro-displacement sensor.

In order to validate the theoretical model proposed in Section 5.5.1, different calibration curves of the system magnitude and both self-referencing parameters versus β were experimentally measured for different phase-shifting values. It is shown a good agreement

between theory and measurements[2]. The following figure, Fig. 5.28, resumes the magnitude data measured in this section compare to the theoretical curves provided by Eq. 5.24. Each symbol corresponds to the mean of three measurements at each phase-shift and β condition. Measurement deviations were negligible and are not represented within Fig. 5.28, although they increased as the selected phase-shift value was increased.

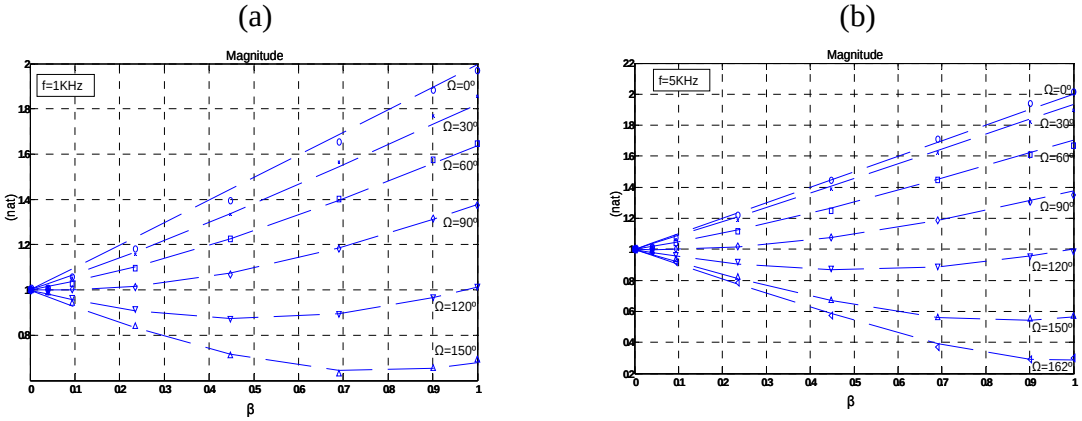

Figure 5.28.- Measurements of the transfer function magnitude versus β for different phase-shifts with $\Omega = \Omega_2 - \Omega_1$ at (a) f=1kHz and (b) f=5kHz. Theoretical curves are represented in dashed lines.

As expected, for a fixed phase-shift Ω, the magnitude is independent with regards to the frequency of modulation showing the same performance. This is one of the main advantages of the novel electro-optical configuration proposed.

On the other hand, different measurement calibration curves of the self-referencing R parameter, given by Eq. 5.23, versus β were obtained for different phase-shifting values. It can be shown good agreement between theory and measurements, Fig. 5.29 where it is reported the theoretical model validation regarding this measurement parameter.

From the below figures, it can be concluded that greater R values were achieved by increasing the relative difference between both phase-shifts, Ω_1 and Ω_2, reaching its maximum value for $\Omega_1 - \Omega_2 = +\pi$. Nevertheless, the R parameter showed a non-symmetrical behaviour with regards to the sign of the difference between Ω_1 and Ω_2, as expected. Furthermore, greater R values were obtained by selecting phase-shifts values in which the sign of the difference $\Omega_1 - \Omega_2$ was positive rather than negative. The flexibility of this configuration is also demonstrated by fixing an operation point with the electrical delay lines (Ω_1 and Ω_2) implemented at the reception stage. Multiple operation points can be chosen in the same way in order to improve sensitivity or another system property depending on specific requirements (this fact will be discussed in the following chapter of

[2] As the performance of a generic sensor channel, FOS_i, is exactly the same for both self-referencing parameters, from now on a generic parameter R or ϕ, no matter the remote sensing point is being considered, will be used.

this document). However, it is noteworthy that phase-shift values quite near $\Omega_1 - \Omega_2 = \pm\pi$ condition provide a highly-unstable measurement scenario. This fact can be clearly appreciated in the behavior of the green trace (with diamond symbol) within Fig. 5.29(c).

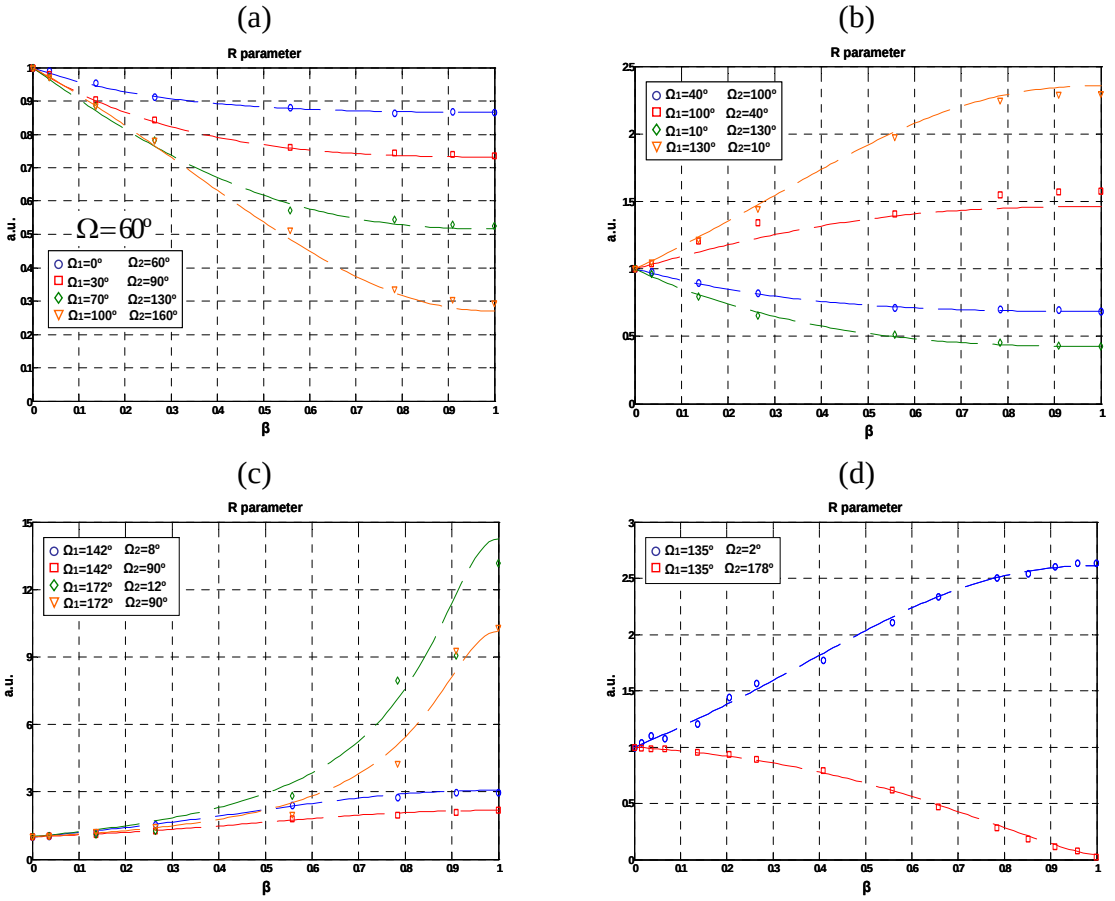

Figure 5.29.- Measurements and theoretical validation of the *R* parameter versus β for different selected phase-shift configurations at the reception stage.

The theoretical model proposed for the self-referencing ϕ output phase parameter, given by Eq. 5.25, versus β obtained for different phase-shifting values was also experimentally validated showing good agreement between theory and measurements. Fig. 5.30 resumes the calibration curves validating this measurement parameter concluding, as expected from theory, that the output phase response shows a symmetrical behaviour with respect to a fixed arbitrary value of $\Omega = 0.5\pi$ and this response is also directly dependent on the sign of the difference between Ω_1 and Ω_2, obtaining $\phi < 0$ for the condition $\Omega_1 < \Omega_2$ and $\phi > 0$ when $\Omega_1 > \Omega_2$. This latter fact is shown in Fig. 5.30(b). From this figure, it can also be seen the anti-symmetrical response of the output phase when ϕ reaches $\phi = +90^o$, switching to $\phi = -90^o$ at the condition $\beta \approx 0.87$ thus obtaining negative values from that condition. This ϕ parameter behavior becomes clear itself by the definition of ϕ given by Eq. 5.25.

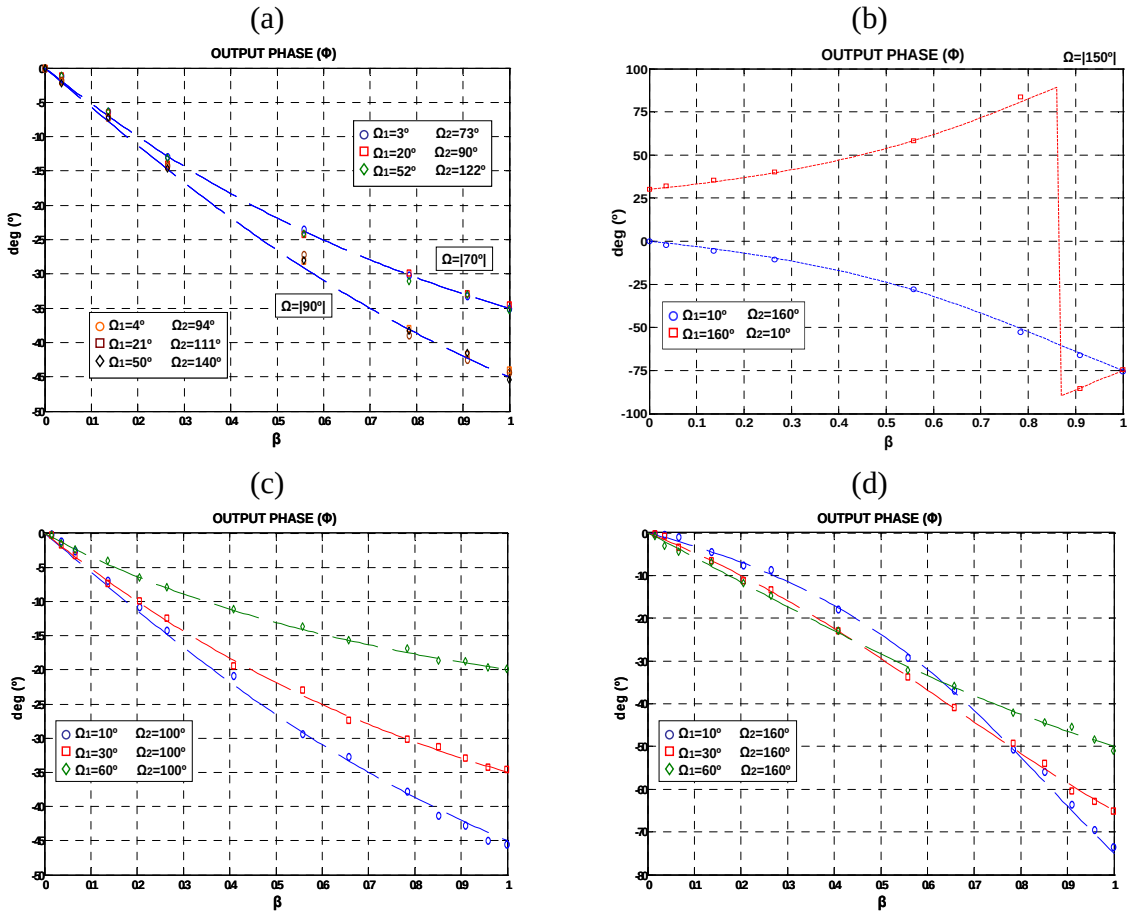

Figure 5.30.- Measurements and theoretical validation (dashed lines) of the output phase ϕ parameter versus β for different phase-shift configurations selected at the reception stage.

5.5.3 Self-reference test

In order to validate that both measurement parameters, R and ϕ, are insensitive to power fluctuations of the modulated optical source as well as to undesirable losses at any point in the optical fibre link, the self-reference property was tested using the same experimental set-up of previous section. Thus emulating unexpected power losses along the optical path linking the optical source with the remote sensing area. A tapered single-mode fibre, used as a variable optical attenuator (VOA), was located in two different points of the link (see Fig. 5.31):

a) At the transmission stage between the BLS (optical source) and the broadband circulator.
b) At the transmission stage between the broadband circulator and the reference FBG ($\lambda_R = 1531.1\,\text{nm}$)

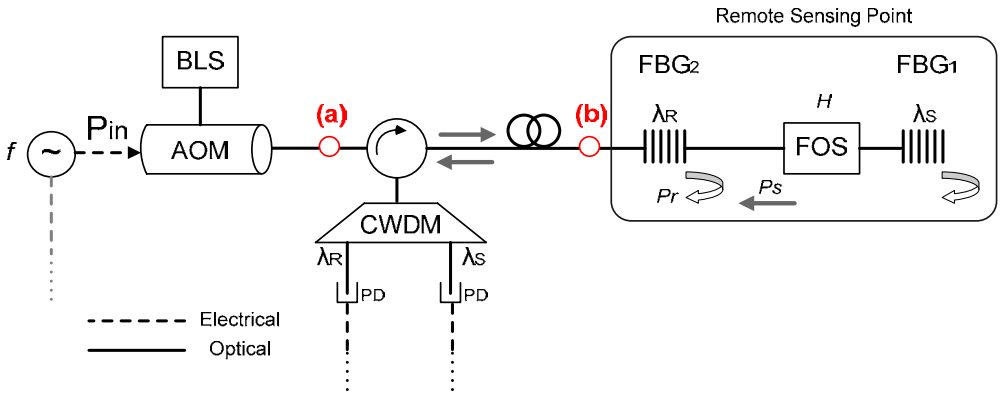

Figure 5.31.- Set-up scheme for the self-reference test. Points (a) and (b) show the location of the applied external attenuation.

The following figures show both measurement parameter values versus external attenuation. Losses up to 10dB are applied in point (a) for the set-up configuration described in Fig. 5.31 and for different values of the sensor loss modulation β. Measurements under those conditions are shown in Fig. 5.32.

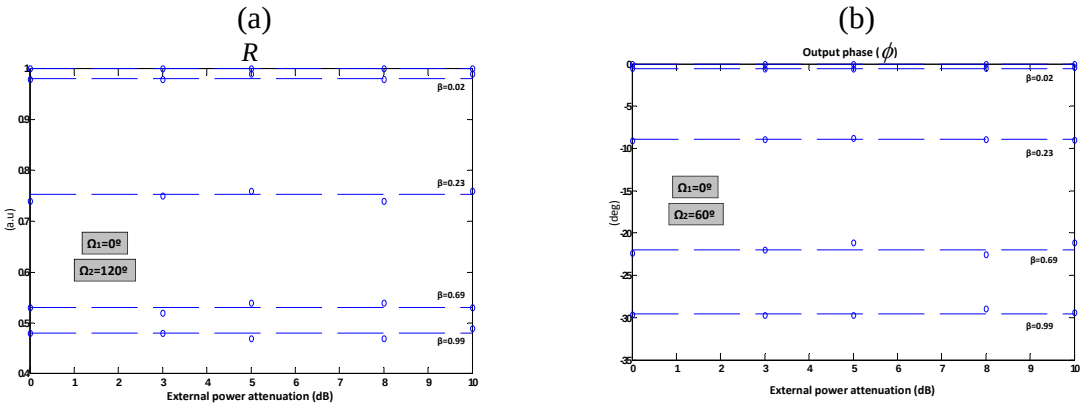

Figure 5.32.- (a) Self-reference test of R parameter versus induced external power attenuation up to 10dB for different values of β. (b) Self-reference test of the output phase ϕ versus induced external power attenuation up to 10dB for different values of β.

Both measurement parameter values versus external attenuation for losses up to 10dB applied in point (b), for different values of the sensor loss modulation β_i, are shown in Fig. 5.33. It is worth mentioning that, congruent with the scheme depicted in Fig 5.31, previously calibrated induced loss provided by the VOA doubles it effect due to both propagating directions of the light, when applied in point (b) within the reflective topology. This fact has been taken into account in order to plot both figures comprising Fig. 5.33.

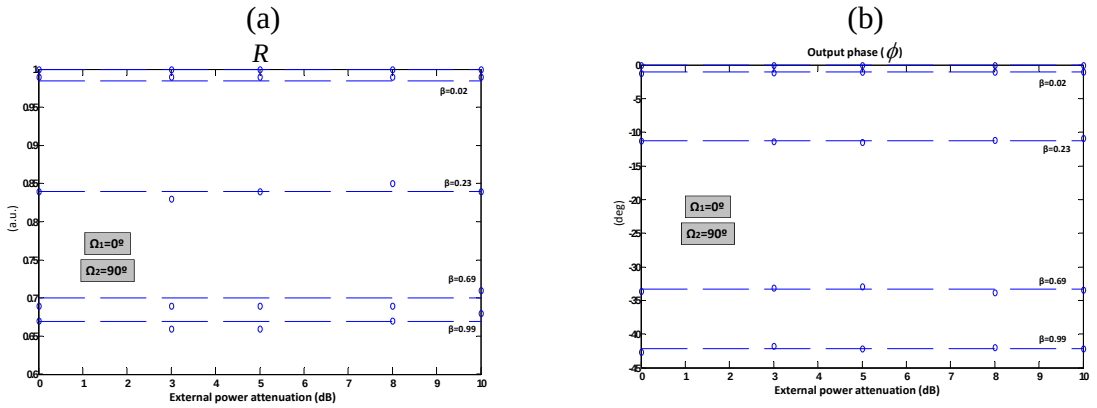

Figure 5.33.- (a) Self-reference test of *R* parameter versus induced external power attenuation up to 10dB for different values of β. (b) Self-reference test of the output phase ϕ versus induced external power attenuation up to 10dB for different values of β.

The above figures demonstrate that no correlation between the measurements on both self-referencing parameters, R and ϕ, and the external induced power attenuation (up to 10dB) is noticed as well as a good agreement between measurements and theory. In addition to that fact, it is also demonstrated that there is no influence of the phase-shift Ω with regards to the self-reference property.

A statistical analysis of the measurements taken in this section is shown in Table 5.2 and Table 5.3, respectively, for both configurations of the applied external attenuation, using the set-up displayed in Fig. 5.31. In both tables, five measurements per each value of β were taken, for any phase-shift configuration, thus obtaining the mean of the self-referencing parameters. Measurement deviations are given as standard deviation. Theoretical values predicted by the model, for both self-referencing parameters R and ϕ, as well as their measured mean values are also shown in both tables.

Considering the R parameter case in Table 5.2 and Table 5.3, errors were, in most cases, at least one order of magnitude below (third decimal) from the mean value. There were two cases in which the standard deviation rose up to 0.01 (second digit) not being considered representative in the whole measurement set. Despite this fact, it can be concluded that R assures a good performance to guarantee the self-referencing property. In concurrence with the latter fact, for the output phase ϕ errors were, in all cases, one order of magnitude below (first decimal) from the mean value. Likewise the above case, such standard deviations can be concluded as been quite acceptable in order to assure the self-reference property of the system.

		Theoretical		**Measurements**			
				Mean		**Standard Deviation**	
		R	ϕ	$\overline{R}$	$\overline{\phi}$	$\sigma_R(\pm)$	$\sigma_\phi(\pm)$
$\Omega_1 = 0^o$ $\Omega_2 = 60^o$	$\beta = 0.02$	0.990	-0.790	**0.992**	**-0.520**	**0.0045**	**0.0837**
	$\beta = 0.23$	0.919	-8.890	**0.924**	**-8.940**	**0.0089**	**0.1140**
	$\beta = 0.69$	0.846	-22.940	**0.840**	**-21.820**	**0.0071**	**0.6834**
	$\beta = 0.99$	0.819	-28.820	**0.816**	**-29.460**	**0.0055**	**0.3362**
$\Omega_1 = 0^o$ $\Omega_2 = 90^o$	$\beta = 0.02$	0.985	-1.026	**0.982**	**-1.420**	**0.0045**	**0.1095**
	$\beta = 0.23$	0.840	-11.240	**0.838**	**-11.340**	**0.0084**	**0.2510**
	$\beta = 0.69$	0.700	-33.350	**0.710**	**-32.340**	**0.0071**	**0.7765**
	$\beta = 0.99$	0.669	-42.170	**0.676**	**-42.700**	**0.0114**	**0.4690**
$\Omega_1 = 0^o$ $\Omega_2 = 120^o$	$\beta = 0.02$	0.980	-0.852	**0.984**	**-0.600**	**0.0055**	**0.0707**
	$\beta = 0.23$	0.756	-10.410	**0.750**	**-10.140**	**0.0100**	**0.4615**
	$\beta = 0.69$	0.530	-40.840	**0.532**	**-40.800**	**0.0084**	**0.8062**
	$\beta = 0.99$	0.493	-52.440	**0.478**	**-52.680**	**0.0084**	**0.5891**

Table 5.2.- Mean and standard deviation (σ) resume of the measurements shown in this section, using the set-up shown in Fig. 5.31 in which an external attenuation is applied at point (a).

		Theoretical		**Measurements**			
				Mean		**Standard Deviation**	
		R	ϕ	$\overline{R}$	$\overline{\phi}$	$\sigma_R(\pm)$	$\sigma_\phi(\pm)$
$\Omega_1 = 0^o$ $\Omega_2 = 60^o$	$\beta = 0.02$	0.990	-0.790	**0.992**	**-0.800**	**0.0045**	**0.0716**
	$\beta = 0.23$	0.919	-8.890	**0.910**	**-8.960**	**0.0071**	**0.1978**
	$\beta = 0.69$	0.846	-22.940	**0.846**	**-22.900**	**0.0055**	**0.1643**
	$\beta = 0.99$	0.819	-28.820	**0.818**	**-28.800**	**0.0084**	**0.2247**
$\Omega_1 = 0^o$ $\Omega_2 = 90^o$	$\beta = 0.02$	0.985	-1.026	**0.990**	**-1.060**	**0.0000**	**0.0972**
	$\beta = 0.23$	0.840	-11.240	**0.840**	**-11.260**	**0.0071**	**0.2313**
	$\beta = 0.69$	0.700	-33.350	**0.694**	**-33.360**	**0.0089**	**0.3649**
	$\beta = 0.99$	0.669	-42.170	**0.668**	**-42.180**	**0.0084**	**0.3349**
$\Omega_1 = 0^o$ $\Omega_2 = 120^o$	$\beta = 0.02$	0.980	-0.852	**0.978**	**-0.840**	**0.0045**	**0.0563**
	$\beta = 0.23$	0.756	-10.410	**0.754**	**-10.960**	**0.0055**	**0.6827**
	$\beta = 0.69$	0.530	-40.840	**0.532**	**-41.060**	**0.0084**	**0.4044**
	$\beta = 0.99$	0.493	-52.440	**0.498**	**-52.960**	**0.0084**	**0.7287**

Table 5.3.- Mean and standard deviation (σ) resume of the measurements shown in this section, using the set-up shown in Fig. 5.31 in which an external attenuation is applied at point (b).

On the other hand, the following table shows the averaged relative errors δ_R and δ_ϕ obtained when comparing the theoretical values of both self-referencing parameters and the measurements taken in this section. From this table, the R parameter shows relative errors around 1-2%, being the worst case a -3.04% when $[\Omega_1 = 0^o,\ \Omega_2 = 120^o;\ \beta = 0.99]$. Conversely, ϕ relative errors show higher values than R counterparts, which are around 3% with the exception on those cases in which $\beta \cong 0$, where the highest errors are obtained. Special cases are those highlighted in which it is supposed that the fibre-optic sensor calibration near $\beta = 0$ failed for any unknown reason. Nevertheless, results concerning VOA applied at point (b) for the same conditions seem to be reasonably expected, making us be confident about the experimental results.

		Theoretical		**Measurements**			
				Relative error[1]		**Relative error[2]**	
		R	ϕ	$\delta_R\|_{avg}$ (%)	$\delta_\phi\|_{avg}$ (%)	$\delta_R\|_{avg}$ (%)	$\delta_\phi\|_{avg}$ (%)
$\Omega_1 = 0^o$ $\Omega_2 = 60^o$	$\beta = 0.02$	0.990	-0.790	**+0.20**	**-34.17**	**+0.20**	**+1.26**
	$\beta = 0.23$	0.919	-8.890	**+0.54**	**+0.56**	**-0.98**	**+0.79**
	$\beta = 0.69$	0.846	-22.940	**-0.71**	**-4.88**	**+0.03**	**-0.17**
	$\beta = 0.99$	0.819	-28.820	**-0.36**	**+2.22**	**+0.12**	**-0.07**
$\Omega_1 = 0^o$ $\Omega_2 = 90^o$	$\beta = 0.02$	0.985	-1.026	**-0.31**	**+38.40.**	**+0.51**	**+3.31**
	$\beta = 0.23$	0.840	-11.240	**-0.24**	**+0.89**	**+0.02**	**-0.18**
	$\beta = 0.69$	0.700	-33.350	**+1.43**	**-3.03**	**-0.86**	**+0.03**
	$\beta = 0.99$	0.669	-42.170	**+1.05**	**+1.26**	**-0.15**	**+0.03**
$\Omega_1 = 0^o$ $\Omega_2 = 120^o$	$\beta = 0.02$	0.980	-0.852	**+0.41**	**-29.58**	**-0.20**	**-1.41**
	$\beta = 0.23$	0.756	-10.410	**-0.79**	**-2.59**	**-0.26**	**+5.28**
	$\beta = 0.69$	0.530	-40.840	**+0.38**	**-0.10**	**+0.38**	**+0.54**
	$\beta = 0.99$	0.493	-52.440	**-3.04**	**+0.46**	**+1.01**	**+0.99**

[1] Measurements when an external attenuation is applied at point (a) in Fig. 5.31
[2] Measurements when an external attenuation is applied at point (b) in Fig. 5.31

Table 5.4.- Measurement relative errors compared with the expected theoretical values.

To summarize, the validity of the measurements taken in this section has been proved with regards to fibre-optic intensity-based sensors using the self-referencing parameters given by Eq. 5.23 and 5.25.

5.6 Summary and Conclusions

Different compensation schemes for overcoming the undesirable optical signal losses that can appear in intensity-based fibre-optic point sensors have been reported in literature such

as time division normalization, wavelength normalization, fibre bypassing and frequency-based referencing methods. Recent approaches are widely based on the latter and different frequency-based self-referencing techniques for remotely addresing fibre-optic intensity sensors (FOS), which include the utilization of a resonant structure as the basis of the self-referencing property, are being developed.

In this chapter, the state-of-the-art of Fabry-Perot cavity, Mach-Zehnder, Michelson, Sagnac and Ring Resonator topologies for self-referencing fibre-optic intensity-based sensors have been briefly described. In most of the cases the method rely on the ratio between two signals (reference channel and sensing channel) in order to assure the property of self-reference which has been demonstrated to be a effective solution for self-referencing remote sensor networks.

Moreover, recent schemes concerning Fibre Bragg Grating (FBG)-based reflective configurations for self-referencing intensity-based optical sensors have been presented. It has also been addressed the trade-off when using long fibre coils in the remote sensing points in such topologies. The self-referencing technique is then performed by simultaneously modulating the input optical signal using two different frequencies.

On the other hand, a novel self-referencing parameter for electro-optical WDM networks in reflective configuration for remote fibre-optic intensity sensors is reported and experimentally tested. In this configuration electrical delay lines are deployed at the processing unit [54] instead of long delay fiber coils in each measuring point; providing a more compact sensor-head and an easy-reconfigurable operation point. The measurement parameter is defined as the ratio between voltage values at the reception stage for different electrical phase-shifts and it is analyzed following the Z-transform formalism. Furthermore, the same analysis has been made for the output phase self-referencing parameter reported in [53]. Any operation point for each remote sensor can be selected, by means of their associated electrical phase-shifts at the reception stage, in terms of improving linearity response, sensitivity or another system property depending on specific requirements. By including two delay lines (associated to Ω_1 and Ω_2) at the reception stage, implemented in the electrical domain, instead of using a single electrical delay line, arbitrary modulation frequencies can be set and phase shift reconfiguration can overcome tolerance errors allowing an easy-reconfigurable operation of the topology. Measurements validating the theoretical model are reported. In addition to this, self-referencing property of the proposed topology, for both measurement parameters, was validated by simulating undesirable link losses up to 10dB. Both self-referencing parameters will be further analyzed in the following chapter in terms of sensitivity, linear response and resolution.

It is worth pointing out that another advantage of the electro-optical configuration studied in this chapter is its compatibility with wavelength-division-multiplexed sensor networks, as it will be described and analyzed in the next chapter of this document.

5.7 References

[1] G. Adamovsky, "Fiber-optic displacement sensor with temporally separated signal and reference channels," *Appl. Opt.*, vol. 27, pp. 1313-1315, 1988.

[2] T. A. Lindsay *et al.*, "Standard interface for aerospace applications: time domain intensity normalization," in *Proc. of SPIE*, vol. 989, pp. 45-55, 1989.

[3] W. B. Spillman and J. R. Lord, "Self-Referencing Multiplexing Technique for Fiber-Optic Intensity Sensors," *J. Lightwave Technol.*, vol. LT-5, pp. 865-869, 1987.

[4] J. W. Berthold, "Historical Review of Microbend Fiber-Optic Sensors," *J. Lightwave Technol.*, vol. 13, pp. 1193-1199, 1995.

[5] J. M. Baptista, J.L. Santos and A. S. Lage, "Mach-Zehnder and Michelson topologies for self-referencing fiber optic intensity sensors," *Opt. Eng.*, vol. 39, pp. 1636-1644, 2000.

[6] G. Murtaza and J. M. Senior, "Methods for providing stable optical signals in dual wavelength referenced LED based sensors," *IEEE Photon. Tech. Lett.*, vol. 6, pp. 1020-1022, 1994.

[7] R. I. MacDonald and R. Nychka, "Differential Measurement Technique for Optical Fibre Sensors," *Electron. Lett.*, vol. 27, pp. 2194-2196, 1991.

[8] C. Sánchez, A. G. Valenzuela, G. E. Sandoval, J. Villatoro, and J. Hernández, "Technique for referencing of fiber-optic intensity-modulated sensors by use of counterpropagating signals," *Opt. Lett.*, vol. 13, pp. 1467-1469, 2004.

[9] J. M. Baptista, J. L. Santos, and A. S. Lage, "Fiber optic intensity sensors based on Michelson topologies," in *Microwave and Optoelectronics Conference, 1999. SBMO/IEEE MTT-S, APS and LEOS - IMOC '99. International*, 1999, pp. 420-424 vol. 2.

[10] C. Vázquez, J. Montalvo and P.C. Lallana, "Radio-frequency ring resonators for self-referencing fiber-optic intensity sensors," *Opt. Eng. Lett.*, vol. 44, pp. 1-2, 2005.

[11] J. M. Baptista, P. M. Cavaleiro and J. L. Santos, "Self-referencing intensity based Q-type fiber optic," *International Journal of Optoelectronics*, vol. 10, pp. 105-113, 1995.

[12] J. M. Baptista, P. M. Cavaleiro and J. L. Santos, "Self-referencing resonant fiber optic intensity sensor based on a Mach-Zehnder topology," *Review of Scientific Instruments*, vol. 67, pp. 3788-3794, 1996.

[13] D.E.N. Davies, J. Chaimowicz, G. Economou, J. Foley, "Displacement sensor using a compensated fiber link," in *Proc. 2nd International Conference on Optical Fiber Sensors*, Sttutgart, Germany, 1984, pp. 387-391.

[14] G. Adamovsky, "All-fibre sensing loop using pulse-modulated light-emitting diode," *Electronics Letters*, vol. 21, pp. 922-923, 1985.

[15] J. Turan, E. F. Carome, and L. Ovsenik, "Fiber optic refractometer for liquid index of refraction measurements," in *5th International Conference on Telecommunications in Modern Satellite, Cable and Broadcasting Service, 2001, TELSIKS 2001*, 2001, vol. 2, pp. 489-492, 2001.

[16] P. Sixt, G. Kotrotsios, L. Falco, and O. Parriaux, "Passive Fiber Fabry-Perot Filter for Intensity-Modulated Sensors Referencing," *J. Lightwave Technol.*, vol. LT-4, pp. 926-932, 1986.

[17] G. Kotrotsios, L. Falco, J.P. Jeanneret, O. Parriaux, "Radio frequency phas detection for intensity modulated fiber sensors," in *Proc. of SPIE Fiber Optics Sensors*, pp. 99-103, 1985.

[18] J. M. Baptista, J. L. Santos, and A. S. Lage, "Self-referenced fibre optic intensity sensor based on a multiple beam Sagnac topology," *Optics Communications*, vol. 181, pp. 287-294, 2000.

[19] O. Frazao, J. M. Baptista, J. L. Santos, J. Kobelke, and K. Schuster, "Strain and temperature characterisation of sensing head based on suspended-core fibre in Sagnac interferometer," *Electronics Letters*, vol. 44, pp. 1455-1456, 2008.

[20] J. M. Baptista, J. L. Santos, and A. S. Lage, "Sagnac topology for a self-referencing fiber optic sensor," in *IEEE Lasers and Electro-Optics Society 1999 12th Annual Meeting. LEOS '99*, vol. 1, pp. 251-252, 1999.

[21] X. Dong, H. Y. Tam, and P. Shum, "Temperature-insensitive strain sensor with polarization-maintaining photonic crystal fiber based Sagnac interferometer," *Applied Physics Letters*, vol. 90, pp. 151113-1 -- 151113-3, 2007.

[22] J. Montalvo and C. Vázquez, "Self-referencing intensity-encoded fibre optic sensors using radio-frequency ring resonators," in *Proc. SPIE 5840: Photonic Materials, Devices and Applications*, pp. 284-295, USA, July 2005..

[23] J. M. Baptista, J. L. Santos, and A. S. Lage, "Mach-Zehnder and Michelson topologies for self-referencing fiber optic intensity sensors," *Optical Engineering*, vol. 39, pp. 1636-1644, 2000.

[24] A. Wang, H. Xiao, J. Wang, Z. Wang, W. Zhao, and R. G. May, "Self-calibrated interferometric-intensity-based optical fiber sensors," *J. Lightwave Technol.*, vol. 19, pp. 1495-1501, 2001.

[25] T. Lü and S. Yang, "Extrinsic Fabry-Perot cavity optical fiber liquid-level sensor," *Appl. Opt.*, vol. 46, pp. 3682-3687, 2007.

[26] S. Cazacu, J. M. Martins, G. Rego, S. F. Santos, J. L. Santos, and J. M. Baptista, "Micro-displacement measurement using a long period fiber grating in a self-referenced fiber optic intensity sensor," in *The 17th Annual Meeting of the IEEE Lasers and Electro-Optics Society, 2004, LEOS 2004*, vol. 1, pp. 262-263, 2004.

[27] J. M. Baptista, S. F. Santos, G. Rego, O. Frazao, and J. L. Santos, "Measurement of angular rotation using a long period fiber grating in a self-referenced fiber optic intensity sensor," in *The 18th Annual Meeting of the IEEE Lasers and Electro-Optics Society, 2005, LEOS 2005*, pp. 806-807, 2005.

[28] J. M. Baptista, J. L. Santos, and A. S. Lage, "Measurement of refractive index in oils using a self-referenced fiber optic intensity sensor," in *The 14th Annual Meeting of the IEEE Lasers and Electro-Optics Society, 2001, LEOS 2001*, vol. 2, pp. 875-876, 2001.

[29] J. M. Baptista, O. J. Frazao, L. A. Ferreira, F. M. Araujo, J. L. Santos, and A. S. Lage, "Load cell for structural monitoring based on a microbend self-referenced fiber optic intensity sensor," in *The 16th Annual Meeting of the IEEE Lasers and Electro-Optics Society, LEOS 2003*, vol. 1, pp. 93-94, 2003 .

[30] H. J. Arditty and H. C. Leèfovre, "Sagnac effect in fiber gyroscopes," *Opt. Lett.*, vol. 6, pp. 401-403, 1981.

[31] E. J. Post, "Sagnac effect," *Rev. Mod. Phys.*, vol. 39, pp. 475-494, 1967.

[32] E. Udd, "Fiber optic smart structures," *Proceedings of the IEEE*, vol. 84, pp. 884-894, 1996.

[33] R. B. Smith, "Selected Papers on Fiber Optic Gyroscopes," in *SPIE Milestone Series*. vol. MS8 Bellingham, WA, 1989.

[34] K. Takiguchi, M. Itoh, and T. Shibata, "Optical-Signal-Processing Device Based on Waveguide-Type Variable Delay Lines and Optical Gates," *J. Lightwave Technol.*, vol. 24, p. 2593, 2006.

[35] C.T. Chang, J.A. Cassaboom and H.F. Taylor, "Fibre-optic delay-line devices for RF signal processing," *Electron. Lett.*, vol. 13, pp. 678-680, 1977.

[36] S. Newton, K. Jackson, J. Bowers, C. Cutler, and H. Shaw, "Fiber-optic delay line devices for GigaHertz signal processing," in *IEEE International Conference on Acoustics, Speech, and Signal Processing, ICASSP '83*, pp. 1204-1207, 1983.

[37] K. P. Jackson, S. A. Newton, B. Moslehi, M. Tur, C. C. Cutler, J. W. Goodman, and H. J. Shaw, "Optical Fiber Delay-Line Signal-Processing," *IEEE Transactions on Microwave Theory and Techniques*, vol. 33, pp. 193-210, 1985.

[38] X. Liu, M. J. Cobb, and X. Li, "Rapid scanning all-reflective optical delay line for real-time optical coherence tomography," *Opt. Lett.*, vol. 29, pp. 80-82, 2004.

[39] C. Caucheteur, A. Mussot, S. Bette, A. Kudlinski, M. Douay, E. Louvergneaux, P. Mégret, M. Taki, and M. Gonzalez-Herraez, "All-fiber tunable optical delay line," *Opt. Express*, vol. 18, pp. 3093-3100, 2010.

[40] M. C. Vazquez, B. Vizoso, M. Lopez-Amo, and M. A. Muriel, "Single and double amplified recirculating delay lines as fibre-optic filters," *Electronics Letters*, vol. 28, pp. 1017-1019, 1992.

[41] J. E. Bowers, S. A. Newton, W. V. Sorin, and H. J. Shaw, "Filter response of single-mode fibre recirculating delay lines," *Electronics Letters*, vol. 18, pp. 110-111, 1982.

[42] J. Montalvo, P.C. Lallana and C. Vázquez, "Self-referencing fibre-optic intensity strain sensors," in *Proc. SPIE 5855: 17th International Conference on Optical Fibre Sensors*, July 2005, pp. 767-770.

[43] C. Vázquez, J. Montalvo, D.S. Montero, and P.C. Lallana, "Self referencing techniques in photonics sensors and multiplexing," in *Proc. SPIE 6593: Photonic Materials, Devices and Applications II*, 2007.

[44] M. Tur and B. Moslehi, "Laser phase noise effects in fiber optic signal processors with recirculating loops," *Opt. Lett.*, vol. 4, pp. 229-231, 1983.

[45] M. Tur, B. Moslehi and J. W. Goodman, "Theory of Laser Phase Noise in Recirculating Fiber-Optic Delay Lines," *J. Lightwave Technol.*, vol. LT-3, pp. 20-31, 1985.

[46] J. M. Baptista, "Concepcao, Análise e Desenvolvimento de Sensores de Fibra Óptica de Intensidade Auto-Refereciados," in *Faculdade de Engenharia*. vol. Thesis, Porto: Universidade do Porto, 2002.

[47] C. Vazquez, J. Montalvo, D. S. Montero, and J. M. S. Pena, "Self-Referencing Fiber-Optic Intensity Sensors Using Ring Resonators and Fiber Bragg Gratings," IEEE *Photon. Tech. Lett.*, vol. 18, pp. 2374-2376, 2006.

[48] J. M. Baptista, S. Abad, G. Rego, L. A. Ferreira, F. M. Araujo, J. L. Santos, and A. S. Lage, "Multiplexing of self-referenced fibre optic intensity sensors using fibre Bragg gratings and wavelength division couplers," in *Optical Fiber Sensors Conference Technical Digest, OFS 2002*, vol. 1, pp. 243-246, 2002.

[49] J.M. Baptista, S. Abad, G.M. Rego, L.A. Ferreira, F.M. Araujo, J. L. Santos, and A.S. Lage, "Wavelength multiplexing of frequency-based self-referenced fiber optic intensity sensors," *Opt. Eng.*, vol. 43, pp. 702-707, 2004.

[50] J. Montalvo, C. Vázquez, and D. S. Montero, "CWDM self-referencing sensor network based on ring resonators in reflective configuration," *Opt. Express*, vol. 14, pp. 4601-4610, 2006.

[51] C. Vazquez, M. Julio, P. C. Lallana, and D. S. Montero, "Self-Referencing Technique in Reflection Mode for Fibre-Optic Intensity Sensors Using Ring Resonators," in *Optical Fiber Sensors*, 2006, p. ThE26.

[52] S. Abad, M. López-Amo, F. M. Araújo, L. A. Ferreira, and J. L. Santos, "Fiber Bragg grating-based self-referencing technique for wavelength-multiplexed intensity sensors," *Opt. Lett.*, vol. 27, pp. 222-224, 2002.

[53] J. Montalvo, O. Frazao, J. L. Santos, C. Vazquez, and J. M. Baptista, "Radio-Frequency Self-Referencing Technique With Enhanced Sensitivity for Coarse WDM Fiber Optic Intensity Sensors," J. *Lightwave Technol.*, vol. 27, pp. 475-482, 2009.

[54] J. Montalvo, F. M. Araujo, L. A. Ferreira, C. Vazquez, and J. M. Baptista, "Electrical FIR Filter With Optical Coefficients for Self-Referencing WDM Intensity Sensors," *IEEE Photon. Tech. Lett.*, vol. 20, pp. 45-47, 2008.

[55] D.S. Montero, C. Vazquez, J.M. Baptista, J.L. Santos, J. Montalvo, "Coarse WDM networking of self-referenced fiber-optic intensity sensors with reconfigurable characteristics," *Opt. Express*, vol. 18, pp. 4396-4410, 2010.

[56] D. Pastor, J. Capmany, and B. Ortega, "Broad-band tunable microwave transversal notch filter based on tunable uniform fiber Bragg gratings as slicing filters," *IEEE Photon. Tech. Lett.*, vol. 13, pp. 726-728, 2001.

[57] C. H. Henry, R. F. Kazarinov, Y. Shani, R. C. Kistler, V. Pol, and K. J. Orlowsky, "Four-channel wavelength division multiplexers and bandpass filters based on elliptical Bragg reflectors," *J. Lightwave Technol.*, vol. 8, pp. 748-755, 1990.

[58] I. Baumann, J. Seifert, W. Nowak, and M. Sauer, "Compact all-fiber add-drop-multiplexer using fiber Bragg gratings," *IEEE Photon. Tech. Lett.*, vol. 8, pp. 1331-1333, 1996.

[59] K. Takahashi, M. Tamura, T. Sano, K. Saito, and H. Suganuma, "Reconfigurable optical add/drop multiplexer using passive temperature-compensated wavelength tunable fiber Bragg grating," in *Optical Fiber Communication Conference and Exhibit, OFC 2001*, vol. 3, pp. WDD93-1--WDD93-3, 2001.

[60] K. O. Hill and G. Meltz, "Fiber Bragg grating technology fundamentals and overview," *J. Lightwave Technol.*, vol. 15, pp. 1263-1276, 1997.

[61] T. Saitoh, K. Nakamura, Y. Takahashi, H. Iida, Y. Iki, and K. Miyagi, "Ultra-Long-Distance Fiber Bragg Grating Sensor System," *IEEE Photon. Tech. Lett.*, vol. 19, pp. 1616-1618, 2007.

[62] G. P. Brady, K. Kalli, D. J. Webb, D. A. Jackson, L. Reekie, and J. L. Archambault, "Simultaneous measurement of strain and temperature using the first and second-order diffraction wavelengths of Bragg gratings," *IEEE Proceedings-Optoelectronics*, vol. 144, pp. 156-161, 1997.

[63] W. Tianshu, G. Yubin, Z. Xiaosu, Z. Ming, and W. Ke, "Simultaneous Measurements of Strain and Temperature with Dual Fiber Bragg Gratings for Pervasive Computing," in *1st International Symposium on Pervasive Computing and Applications*, pp. 786-790, 2006.

[64] G. S. Glaesemann, J. A. Smith, D. A. Clark, and R. Johnson, "Measuring thermal and mechanical stresses on optical fiber in a DC module using fiber Bragg gratings," *J. Lightwave Technol.*, vol. 23, pp. 3461-3468, 2005.

[65] S. Pal, S. Yonghang, J. Mandal, S. Tong, and K. T. V. Grattan, "Simultaneous measurement of strain (to 2000με) and temperature (to 600ºC) using a combined Sb-Er-Ge-codoped fiber-fluorescence and grating-based technique," *IEEE Sensors Journal*, vol. 5, pp. 1462-1468, 2005.

[66] M. S. Muller, L. Hoffmann, A. Sandmair, and A. W. Koch, "Full Strain Tensor Treatment of Fiber Bragg Grating Sensors," *IEEE Journal of Quantum Electronics*, vol. 45, pp. 547-553, 2009.

[67] H. F. Lima, R. da Silva Vicente, R. N. Nogueira, I. Abe, P. S. de Brito Andre, C. Fernandes, H. Rodrigues, H. Varum, H. J. Kalinowski, A. Costa, and J. de Lemos Pinto, "Structural Health Monitoring of the Church of Santa Casa da Misericórdia of Aveiro Using FBG Sensors," *IEEE Sensors Journal*, vol. 8, pp. 1236-1242, 2008.

[68] F. Elaldi, "An overview for structural health monitoring of composites in aerospace applications," in *Proceedings of 2nd International Conference on Recent Advances in Space Technologies, RAST 2005*, pp. 309-314, 2005.

[69] B.-l. Shang, B.F. Song, and F. Chang, "New sensor technologies in aircraft structural health monitoring," in *International Conference on Condition Monitoring and Diagnosis, CMD 2008*, pp. 701-704, 2008.

[70] Y. M. Gebremichael, W. Li, B. T. Meggitt, W. J. O. Boyle, K. T. V. Grattan, B. McKinley, L. F. Boswell, K. A. Aarnes, S. E. Aasen, B. Tynes, Y. Fonjallaz, and T. Triantafillou, "A field deployable, multiplexed Bragg grating sensor system used in an extensive highway bridge monitoring evaluation tests," *IEEE Sensors Journal*, vol. 5, pp. 510-519, 2005.

[71] K. P. Jackson, S. A. Newton, B. Moslehi, M. Tur, C. C. Cutler, J. W. Goodman, and H. J. Shaw, "Optical Fiber Delay-Line Signal Processing," *IEEE Transactions on, Microwave Theory and Techniques*, vol. 33, pp. 193-210, 1985.

[72] K. D. Merkel and W. R. Babbitt, "Coherent transient optical signal processing without brief pulses," *Appl. Opt.*, vol. 35, pp. 278-285, 1996.

[73] T. Mizuno, T. Saida, T. Kitoh, T. Shibata, and Y. Inoue, "Interleave Filter Based on Coherent Optical Transversal Filter," *J. Lightwave Technol.*, vol. 24, p. 2602, 2006.

[74] K. Jinguji and M. Kawachi, "Synthesis of coherent two-port lattice-form optical delay-line circuit," *J. Lightwave Technol.*, vol. 13, pp. 73-82, 1995.

[75] S. Vargas and C. Vazquez, "Synthesis of Optical Filters Using Sagnac Interferometer in Ring Resonator," *IEEE Photon. Tech. Lett.*, vol. 19, pp. 1877-1879, 2007.

[76] C.K. Madsen and J.H. Zhao, *Optical Filter Design and Analysis: A Signal processing Approach*. John Wiley and Sons Inc., USA, 1999.

Chapter 6

COARSE WDM PASSIVE OPTICAL NETWORKING OF SELF-REFERENCED FIBRE-OPTIC INTENSITY SENSORS WITH RECONFIGURABLE CHARACTERISTICS

6.1 Introduction

The application areas for fibre-optic sensors reported in literature include high-sensitivity military sensor systems, industrial process control sensors, building and home applications, chemical sensing, environmental monitoring and smart structural and material sensing, among others. In each of these areas, the ability to multiplex sensors in passive optical networks (PON) can be advantageous with regard to a number of system aspects, including reduced component costs, ease of E/O (electro-optical) interfacing and overall system immunity to electromagnetic interference (EMI) inherent to optical schemes. The development of efficient multiplexing techniques enhances the competitiveness of fibre sensors compared with conventional technologies in most application areas. Although these issues strongly affect the potential use of fibre sensors in smart materials and structures applications, the need for multiplexing is of even more fundamental importance to facilitate the efficient interrogation of tens or, perhaps, hundreds of sensors that may be required to be distributed over a complex smart structure. The handling of such large flows of sensor information is one of the key areas in the development of advanced structures. However, in the case of sensor networks, the amount of information to be addressed is usually very low and quasi-static, being low-cost devices, efficient multiplexing topologies and self-referenced measurements the most important objectives to be achieved. For example, 1000 sensors with a bandwidth requirement of 10kHz (as those described in Chapter 5 with the proposed topology) require a transmission bandwidth of only ~10MHz, relatively small compared to the bandwidths required for multi-gigabit data rate systems proposed and demonstrated in the optical fibre telecommunications field. In this way, multiplexing and the concomitant organizing of sensor outputs onto common fibre links can be viewed as the first stage of data manipulation and reduction, which is important for the management of large sensor arrays.

In general, a number of discrete sensors designed to operate as point sensors can be arranged in a network or array configuration. And they can be multiplexed using techniques common to RF/microwave systems, such as frequency-division multiplexing (FDM) or time-division multiplexing (TDM), or by using more specialized schemes developed for optical communications systems, such as wavelength-division multiplexing (WDM). Therefore, a state-of-the-art concerning multiplexing techniques for fibre-optic sensors is firstly presented focussing the wavelength-division-multiplexing (WDM) approach as being

one of the most promising topologies for the next generation optical communications FTTx access networks.

Related to this latter fact, this chapter deals with the performance of a radio-frequency FBG-based electro-optical CWDM fibre-optic intensity-based sensor network. It is experimentally analyzed the self-reference property, crosstalk, sensitivity, linearity and resolution features for both measurement parameters in a 2-sensor network with the proposed topology described in Chapter 5. It is also shown the flexibility of such configuration provided by the deployment of electronic delay lines at the reception stage. Finally, a new approach for individually monitoring optical power loss of drop fibres in access WDM-PON systems is presented, using the novel flexible and re-configurable RF self-referencing R parameter described in Chapter 5.

6.2 Passive Fibre Optic Sensor Networks

The ability to passively multiplex fibre optic sensors has been recognized since the inception of fibre optics sensor technology [1-3]. Passively multiplexing fibre optic sensors maintains the passive nature of the fibre optic sensor and permits totally passive networks of fibre optic sensors to be built. Over the years a wide variety of multiplexing schemes have been developed, each with their own set of attributes which makes them suitable for particular applications.

The motivation for multiplexing fibre optic sensors varies from application to application with the most fundamental reason being cost. Multiplexing allows the cost of the more expensive components to be amortized over an array of sensors, reducing the per sensor cost of the system, as long as the transducers themselves are inexpensive, which is typically the case in intensity-based fibre optic sensors. Reducing the number of optical fibres is another fundamental reason for multiplexing. Many sensing applications have a large number of sensors in the network and if each sensor required its own fibre then the fibre optic cable used to interrogate the network would become prohibitively large.

The choice of the multiplexing approach depends on the requirements of the sensor network. The relative importance of parameters such as cost, noise, bandwidth and flexibility form the basis for making a selection. These parameters have many components that vary in importance depending on the application. For example, in remote network applications, where there is a large separation between the processing unit and the sensor network, the cost of the cable connecting both aforementioned stages can be the cost driver. In this latter case, selecting a multiplexing scheme that reduces the number of fibres needed to interrogate the network could result in significant savings, even if the multiplexing approach increases the cost of other components in the network.

In general, multiplexing involves the concepts of network topology (i.e. network architecture), sensor addressing and sensor interrogation (i.e. demodulation) [4]. These concepts are frequently not independent, which means that the choice of one implies the selection of the other two. Other features are also relevant, conditioning the possible

configurations to solve a given problem. On the other hand, the sensor addressing can be in time, in frequency, in coherence, in wavelength and in polarization [5]. At a first approach, such multiplexing techniques for fibre-optic sensors can be efficiently classified by the following criteria: depending on the network topology (i.e. how the fibre-optic sensors are interconnected inside the sensor network). These basic topologies form the basis of the multiplexing. In addition to these physical fibre wiring diagrams, see Fig. 6.1, a method for encoding the sensor signals is required to allow different sensors to be addressed. These methods include time-, frequency-, code-, wavelength-, and polarization-division multiplexing (this fact is affected, at the same time, by the modulation mechanism provided by the measurand). The optical coherence properties of the optical source can also be used to encode the sensor signals.

All the above described topologies form the main core concerning passive optical networks (PON) in which there is no need for optical amplification. Generally, the physical topology of the optical networks, recently reported for multiple sensor interrogation, fits the communications PON architectures [6]. So hybrid networks can be considered as an interesting opportunity, sharing one optical fibre among multiple buildings/homes/subscribers/sensors. In addition to this, the communications mass-market has been promoting optical band-splitting devices and optical sources which offer a great potential for remote optical sensing.

In the following sections many of these passive network topologies as well as multiplexing concepts are generally described, emphasizing wavelength-division multiplexing as the most promising multiple-sensing network approach.

6.2.1 Fibre optic sensor multiplexing architectures

Fig. 6.1 shows the main topologies developed in literature [3, 5, 7] for implementing multiplexed fibre optic sensors or fibre sensor arrays. At a first approach, reflective configurations allow reducing the number of optical devices to be deployed, such as couplers or wavelength-division based multiplexers and demultiplexers. On the other hand, the noise level due to the light reinjection in the optical source in such reflective schemes could be the main problem if no optical isolators are also deployed, but increasing the cost of such networks.

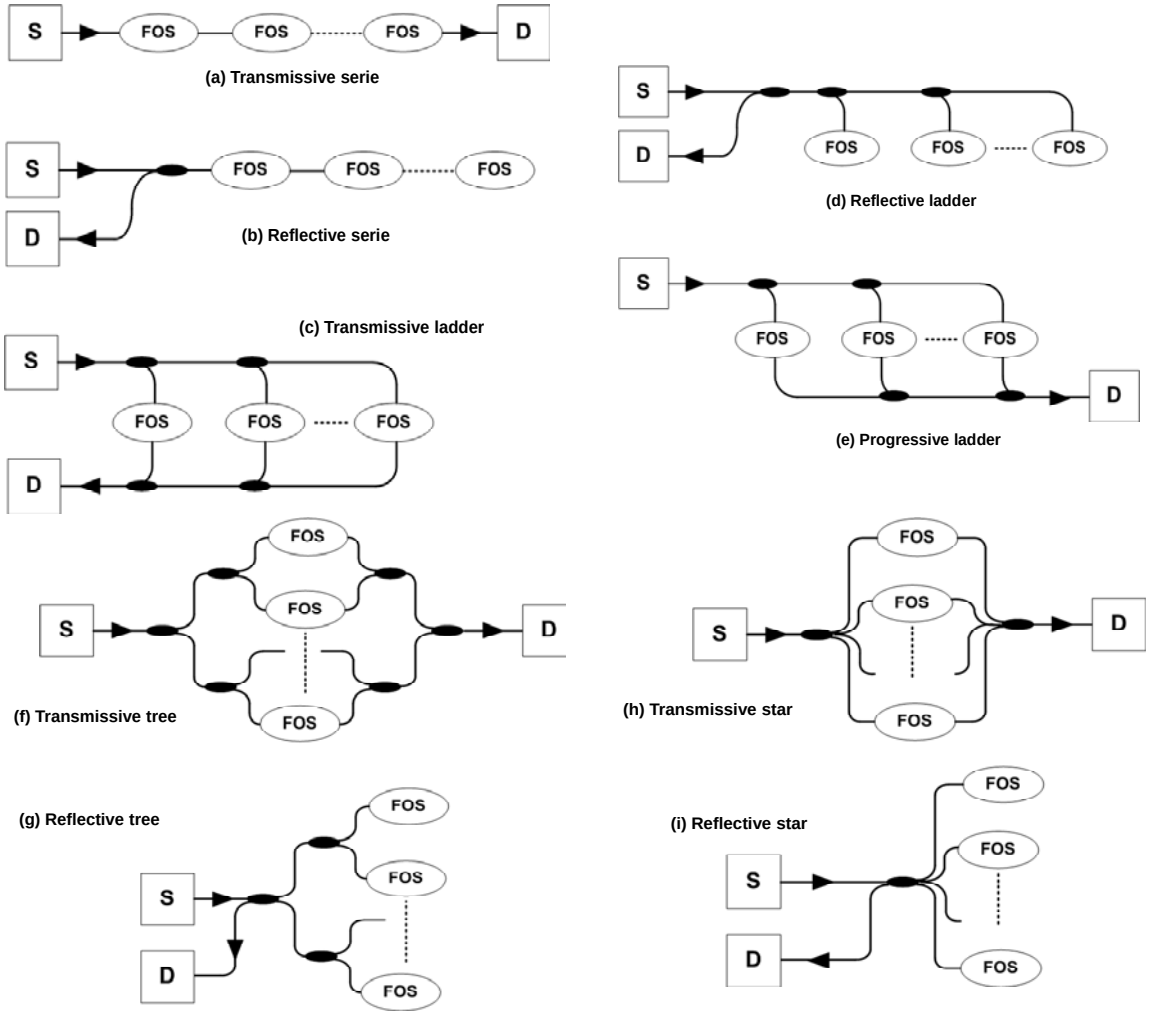

Figure 6.1.- Basic fibre optic sensor network architectures reported in literature. S: optical source; FOS: fibre-optic sensor; D: optical detector.

It is highly desirable that all the sensors in a given network return the same level of average optical power to the detection (reception) stage. For some topologies, this can be obtained without the need of imposing special constraints on the splitting devices which is obviously a significant advantage because it permits all these devices to be equal. In addition, it is desirable that in a network of *N* sensors, the number of optical devices is small and intrinsic crosstalk is not present (i.e. crosstalk related to the structure of the sensing array). It must be pointed out that the addressing scheme can introduce extra crosstalk between sensors.

Table 6.1 compares the topologies shown in Fig. 6.1 assuming a normalized average optical power injected into a network of *N* lossless sensors with unit transmissivity or reflectivity and using couplers as optical splitting devices. However, a multiplexing approach is reported in [8] which optimizes the power budget of the network by using *N*-Coarse WDM (CWDM) devices taking advantage of the low insertion losses of such devices provided by manufacturer.

Topology	Number of Couplers	Optical power per Sensor[1]	Intrinsic Crosstalk
Transmissive series	0	1	Yes
Reflective series	1	1/4	Yes
Transmissive ladder	2(N-1)	$1/N^2$	No
Reflective ladder	N	$1/4N^2$	No
Progressive ladder	2(N-1)	$1/2^{N+1}$	No
Transmissive tree	2(N-1)	$1/N^2$	No
Reflective tree	N-1	$1/N^2$	No
Transmissive star	$2^{(a)}$	$1/N^2$	No
Reflective star	$2^{(b)}$	$1/4N^2$	No

(a) 1xN coupler device

(b) One 2x2 coupler and the other 1xN

[1] Reaching the detector

Table 6.1.- Comparison of the network architectures shown in Fig. 6.1

Several other not commonly used sensing topologies have been considered in the literature, as the recursive series topology [9] and the tapped serial array [10]. However, in general, these configurations are, to some extent, constrained by the level of intrinsic crosstalk.

From Table 6.1 it can be seen that different topologies show different features. For example, a lower number of optical devices is needed in both series topologies [10] but with the disadvantage of introducing intrinsic crosstalk between sensors as the optical power injected into the network is not independently modulated in each sensor. Furthermore, the failure in the operation of one arbitrary sensor can lead to a global failure of the network, in contrast with the other topologies reported.

Considering the ladder topologies it is worth to point out that the transmissive ladder topology is probably the one that has been more utilized in sensing applications [11-13] although progressive ladders [14] and reflective ones have also been studied [15]. From Table 6.1, ladder topologies perform no intrinsic crosstalk between sensors being the reflective ladder topology the architecture which presents a more reduced number of components whereas is penalized in terms of optical power injected per sensor, which can lead to dynamic range and sensitivity network penalties.

On the other hand, tree-based topologies confirm that transmissive architectures double the number of components necessary to deploy such a network compare to the reflective option for the same performance in terms of crosstalk and average optical power per sensor. This latter performance is only improved by implementing both series-based topologies [16-18].

Finally star-based topologies, although performing a reduced number of optical components to be deployed and assuring a good returning optical power level per sensor, have the disadvantage of using 1xN and Nx1 optical couplers as such devices can increase the network costs as well as being not effective in terms of the optical power budget along the sensor network.

6.2.2 Addressing techniques for sensor multiplexing

A large number of multiplexing schemes have been developed, but generally they all fall into one of the following categories: fibre multiplexing, time-division multiplexing, code-division multiplexing, frequency-division multiplexing, coherence multiplexing, polarization-division multiplexing, wavelength-division multiplexing or hybrid approaches. This section will briefly introduce these categories and compare their performance. As well as the section described before, these different multiplexing schemes produce a landscape of tradeoffs that can be optimized for any given application. Table 6.2 at the end of this section will summarize the relative performance of the different multiplexing schemes. It is worth mentioning that interferometric sensor multiplexing is not under the scope of this work, so methods of remote demodulation suitable for use with multiplexed interferometric sensors are not described.

6.2.2.1 Fibre multiplexing

The simplest form of multiplexing fibre optic sensor networks is shown in Fig. 6.2, namely fibre multiplexing or Spatial Division Multiplexing (SDM) [19-21]. Instead of using a single optical source and a fibre per channel, fibre multiplexing uses a single optical source and divides the output among multiple sensors. This reduces the number of optical sources from *N* to one, amortizing the cost of the laser over the entire network. Consequently, the optical power available per sensor drops by a factor of *N*, as well, which ultimately limits the number of sensors that can be supported per optical source. In situations where the number of fibres is not an issue this is an excellent multiplexing approach which is very flexible in terms of sensor placement and sensor configuration. Furthermore, since there are individual fibres for each sensor, fibre multiplexed networks are immune to optical sensor-to-sensor crosstalk as well as having an intrinsically lower noise level between sensors due to the scheme.

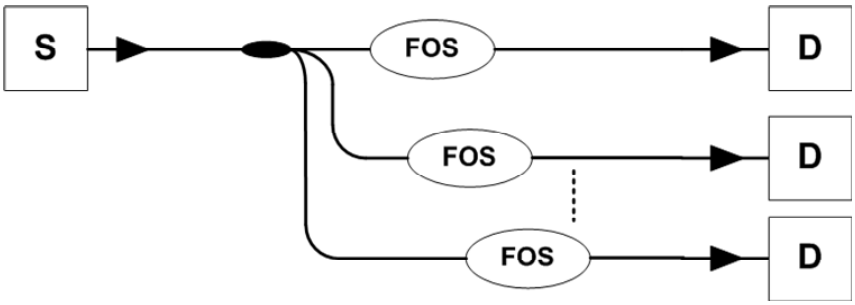

Figure 6.2.- Fibre-multiplexing sensor network, tree-based topology.

6.2.2.2 Time division multiplexing

Time division multiplexing (TDM) fibre optic networks have received a considerable amount of interest over years, in part due to the architectural flexibility of TDM [22-24]. Furthermore, recent advantages in optical amplifier technology have helped to overcome

the high loss of TDM architectures and have dramatically increased the multiplexing gain of time division multiplexed networks [25].

Time division multiplexing technique is based on the fact that sensor information is allocated to a particular time slot with a repetitive transmission period, i.e. time samples of the sensor outputs are interleaved in time sequence to produce a pulse train, as seen in Fig. 6.3. Either optical delay coils or simply the fibre itself between the sensors are used to control the time-of-flight (TOF) of the pulse as it passes through the network. Similar to fibre multiplexing, TDM uses a single optical source to interrogate many sensors. For example, a ladder-type network as the one reported in [26] and shown in Fig. 6.4. In this work, the sensors are spaced at different distances from the source and detector that a single pulse of appropriate duration input to the network produced in the output a series of distinct pulses. These pulses represent time samples of the sensors' outputs interleaved in time sequence. The required duration of the input pulse is determined by the effective optical delay of the fibre connecting the fibre-optic sensor elements and repetitive pulsing of the system allowing each sensor to be addressed by simple time-selective gating of the detector output. This fact forms the main issue of the TDM technique, independently of the network architecture proposed. As an example, a reflective tree-based topology for fibre-optic intensity-based sensors with Michelson topology at the sensing head, self-referenced in frequency, and applying TDM techniques for multiplexing is shown in Fig. 6.5.

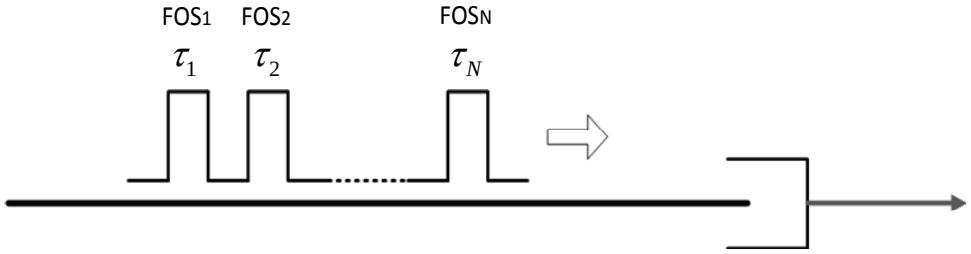

Figure 6.3.- TDM addressing technique for sensor multiplexing.

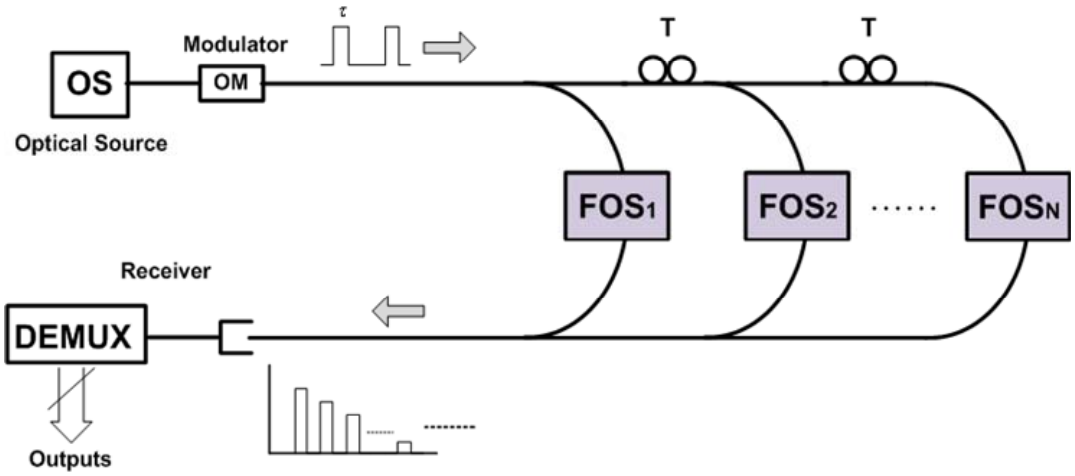

Figure 6.4.- Basic TDM approach for intensity-based fibre-optic sensors [26].

In general, from the basic scheme shown in Fig. 6.4, both fibre-multiplexing and wavelength-division multiplexing (this approach will be discussed later on in a further detail) approaches require a detector and demodulator per channel, while TDM uses a single detector and can significantly reduce the demodulation electronics. It is also worth to mention that in TDM networks the transducers are only illuminated a fraction of the time, which forms a sampled system that has inherent bandwidth limitations, depending on the optical delay T between adjacent sensor channels and the number of sensors in the network. Considering both terms, the maximum sample rate of a TDM network is given by:

$$f_m = \frac{1}{T \cdot N} \tag{6.1}$$

and from Nyquist's theorem the maximum signal bandwidth will be given by:

$$f_s = \frac{1}{2 \cdot T \cdot N} \tag{6.2}$$

i.e. one half of the sample rate. Nevertheless, depending on the interrogation approach used, some of the available bandwidth may be needed by the interrogation approach and the actual signal bandwidth could be considerably less.

On the other hand, the main drawback of such technique relies on the fact that if sensors with different spacing are desired, then the amount of fibre on the delay coil must be adjusted for each sensor to account for the different delays associated with the different spacing. This can be done within limits but it complicates significantly the network topology. However, the progressive ladder topology [14] improves this limitation since the optical pulse is coupled forward through the network and all the sensor returns see nominally the same number of components, number of splices, optical fibre loss, etc, thus the losses through the network are inherently balanced.

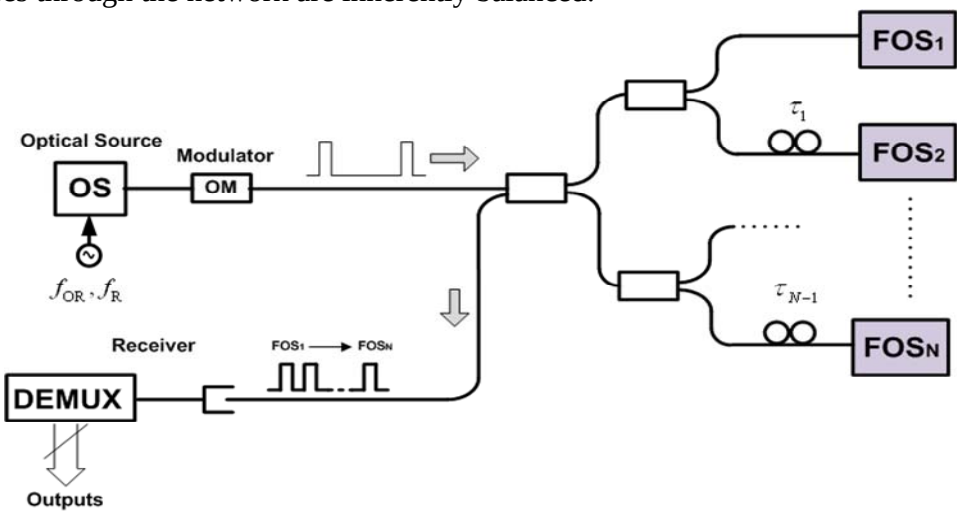

Figure 6.5.- Reflective tree-based topology for fibre-optic intensity-based sensors with Michelson topology, see Fig. 5.5, at the sensing head, self-referenced in frequency, and applying TDM techniques for multiplexing.

Finally, there are other interrogation approaches that are applicable to TDM networks, such as code division multiple access [27, 28], briefly described in the following section.

6.2.2.3 Code division multiplexing

Code division multiplexing (CDM) is based on the use of signal-encoding, typically binary, sequences which posses noise like properties. This property effectively spreads the sensor information over a bandwidth much larger than the sensor information alone. Codes with such properties, such as maximal-length (or *m*-sequence, which can be generated by a simple *m*-stage binary shift register with feedback) codes and Gold codes, have been examined extensively for use in communication systems and fibre-optic multiplexing schemes [29, 30]. In many aspects, the use of CDM to encode sensor outputs is closely related to frequency-division concepts. As in FDM systems, the sensor outputs are encoded at different subcarrier frequencies whereas in CDM systems, the noise like sequences encode the sensor outputs, see Fig. 6.6. Furthermore, in the FDM case, the sensor information is thus carried as sidebands of the subcarrier frequencies but in CDM the sensor signals are spread over the wide bandwidth of the code sequence. Anyway, the sensor signals can be recovered by synchronous detection (i.e. by mixing the received detector signal with a reference subcarrier or code), which returns the sensor signal to the baseband. This type of signal processing is mainly proposed and tested as a means for multiplexing interferometric sensors [31, 32]. The CDM technique relies on the modulation of the interrogating optical source using a pseudo-random bit sequence (PRBS), and correlation is used to provide synchronous detection to identify specific sensor positions. A delay equal to an integer multiple of the bit period separate the sensors. The received signals from the array are then encoded by delayed versions of the PRBS and correlation techniques can be used to extract the individual signals. The main advantage of this technique relies on the fact that very low crosstalk between adjacent sensors can be achieved provided that the code length is greater than the number of sensors in the array and taking advantage of the correlation electronics employed. Fig. 6.7 shows schematically the principle of operation of the CDM approach applied to an *N*-sensor array in a ladder topology.

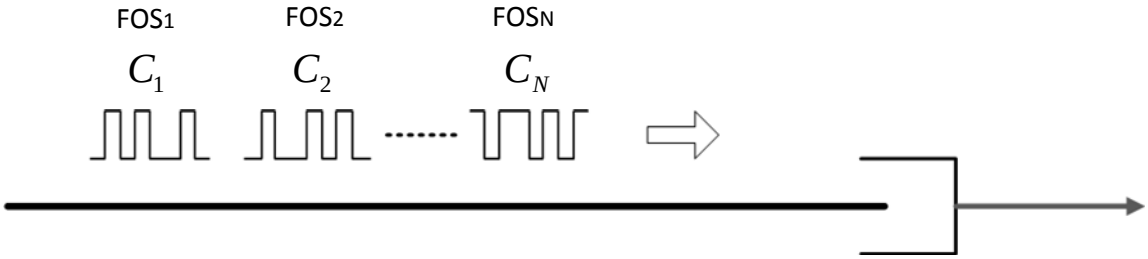

Figure 6.6.- CDM addressing technique for sensor multiplexing.

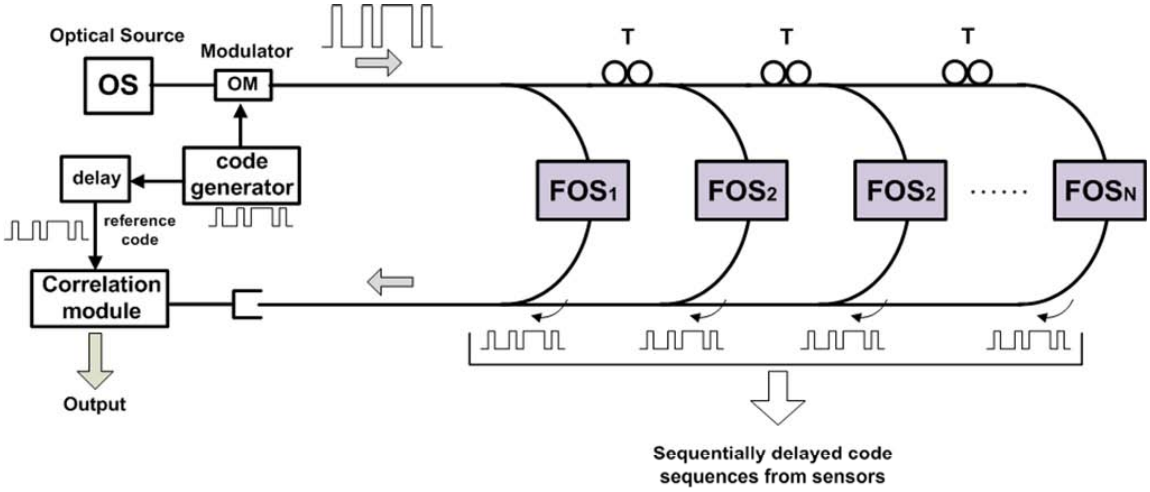

Figure 6.7.- Basic approach for code-division multiplexing.

Clearly, the CDM technique can also be considered a variant of conventional TDM. However, in general, the CDM method may provide advantages in terms of power budget over TDM systems, as stronger optical signals are produced at the output. This does not directly affect the signal-to-noise ratio (SNR) performance due to shot noise but can improve the limit due to the detector noise.

6.2.2.4 Frequency division multiplexing

In the frequency division multiplexing (FDM) approach, the sensor information is allocated to a particular frequency space, i.e. the sensor data is encoded on carriers, amplitude (AM), frequency (FM) or phase (PM) modulated, of different frequencies [33, 34]. This addressing technique is represented in Fig. 6.8. Such addressing scheme has been widely reported in literature concerning fibre-optic intensity-base sensors [35-37]. The FDM approach provides better performances with regards to the TDM approach concerning the average optical power injected per sensor which is intrinsically higher as well as simple electronic processing at the reception stage, as no fast recovery channel-circuitry is needed.

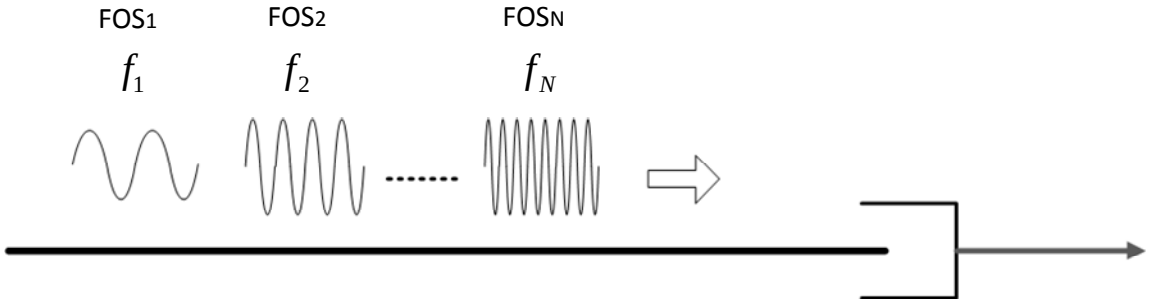

Figure 6.8.- FDM addressing technique for sensor multiplexing.

Fig. 6.9 shows a basic approach to frequency-division multiplexing of output optical signals from a network of fibre sensors that operate from a common source and from an

input fibre bus. It is the ladder topology reported in [38] in which it is developed a radar-based frequency-modulated continuous-wave (FMCW) technique to provide frequency-division-based discrimination between the sensor channels. A source modulated in intensity by a chirped radio-frequency (RF) signal is used to interrogate a number of intensity sensors arranged in a ladder topology, with delays incorporated between the various paths. Consequently, the detected signal comprises a series of RF-modulated signals from the sensors in the array. The detector output is electrically mixed with a reference chirp signal, which produces a beat frequency associated with each sensor element being the frequencies of the beat signals depending on the round-trip optical delays from the source to the detector for each sensor. The use of different delays for each sensor provides for the generation of different beat frequency components associated with each sensor thus allowing for frequency demultiplexing of the channels using band filtering.

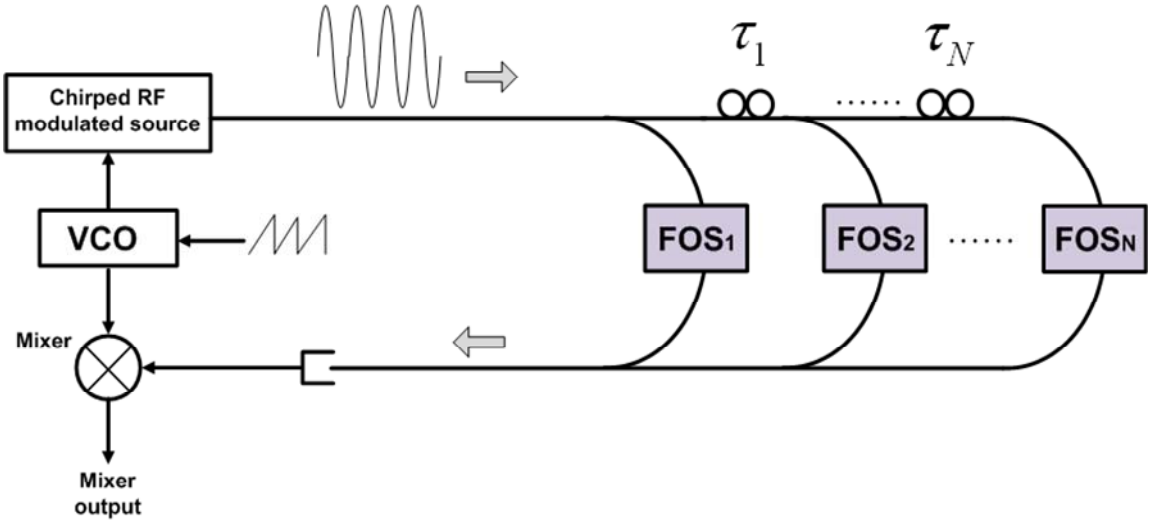

Figure 6.9.- Basic approach for frequency-division multiplexing (FMCW) [38].

Variations of such addressing method involve that the individual sensor is carried not by separate beat frequencies, but by the phase and amplitude of an RF subcarrier amplitude modulation of light source returned from the array sensor elements. Due to the differing delays between the source and detector for each sensor optical path, the resultant detector signal has a magnitude and phase which are (for a given set of sensor transmission factors) dependent on the source modulation frequency. Modulation of the source at a number of discrete (nonharmonic) frequencies provides enough information to allow the status of each sensor to be interpreted [35].

Another technique for the multiplexing of fibre sensors which is based on subcarrier signal processing utilizes a series of fibre transversal filters consisting of two fibres of unequal length connected in parallel. In response to an RF intensity-modulated source, the recombined light at the output of such a filter exhibits a series of minima when the differential delay in the two optical fibre paths corresponds to a half-integral number of cycles of the modulation frequency. This latter system has been used to multiplex three temperature sensors [39].

6.2.2.5 Coherence multiplexing

In coherence multiplexing (CM) approach, the sensor information is differentially encoded on components of the optical carrier which have different degrees of mutual coherence with respect to some reference carrier, see Fig. 6.10. Due to its characteristics, coherence multiplexing has been traditionally used for multiplexing interferometric sensors [40, 41] by using the coherence properties of the light from an optical source with short coherence length. By building the network such that only the optical path mismatch of the desired sensor is within the coherence length of the source, we can ensure that only that signal will coherently interfere.

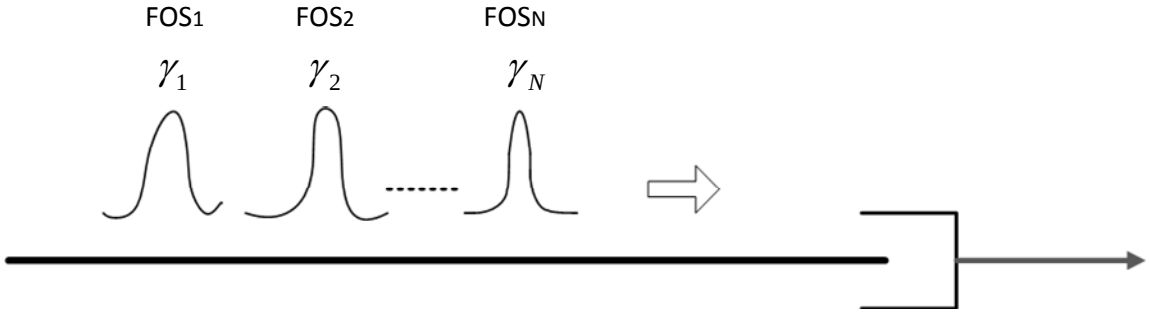

Figure 6.10.- Coherence multiplexing addressing technique for sensor multiplexing.

All other paths through the network are sufficiently longer than the coherence length of the source that there is no coherent interference other than the desired optical path. A receiving interferometer is used to match the path mismatch of a particular sensor and provide for coherent interference. The main drawback of such approach is the poor noise performance which is a problem and generally precludes the CM technique use in many practical applications. This noise behaves like incoherent leakage light in TDM networks and can be reduced by using the broadest source available (shortest coherence length) and spreading the noise over the greatest bandwidth. Of course, very short coherence lengths mean that the receiving interferometers must be perfectly matched with the sensors to maintain coherence and minimize the source-induced phase noise. As a result of the noise impact of multiple incoherent optical paths, the number of sensors that can be supported with CM is severely limited. Primarily, as a result of this noise performance, the CM approach has not seen much use in interferometric fibre-optic sensor networks.

Figures 6.11(a) and 6.11(b) show two most common configurations for coherence multiplexing of interferometric sensors based on optical path-matched differential interferometry (PMDI) using a serial and parallel topologies [42, 43]. Both works utilized Mach-Zehnder interferometer pairs at the receiver in conjunction with an optical source of coherence length much less than the imbalance between any two optical paths through the system. For each sensor-receiver interferometer pair, there are matched optical paths through the network which give rise to an interference output at each detector. Furthermore, the phase shift of the interference signal generated at a particular detector is dependent on the differential phase delay between the arms of the associated sensing and receiver interferometers. Due to the large number of unmatched optical paths, as the serial network shown in Fig. 6.11(a), the sensitivity of CM interferometric sensors is limited by excess

phase-induced intensity noise which arise due to delayed self-homodyne mixing of the laser at the output at each detector. Consequently, this fact gives rise to sizable excess noise, even when the sensor and receiver are accurately matched. On the other hand, it has theoretically been demonstrated that the only way to reduce the excess noise is contingent with the use of low coherence length optical sources (broadband light sources), such that the noise power is spread over a larger bandwidth at the detectors [41].

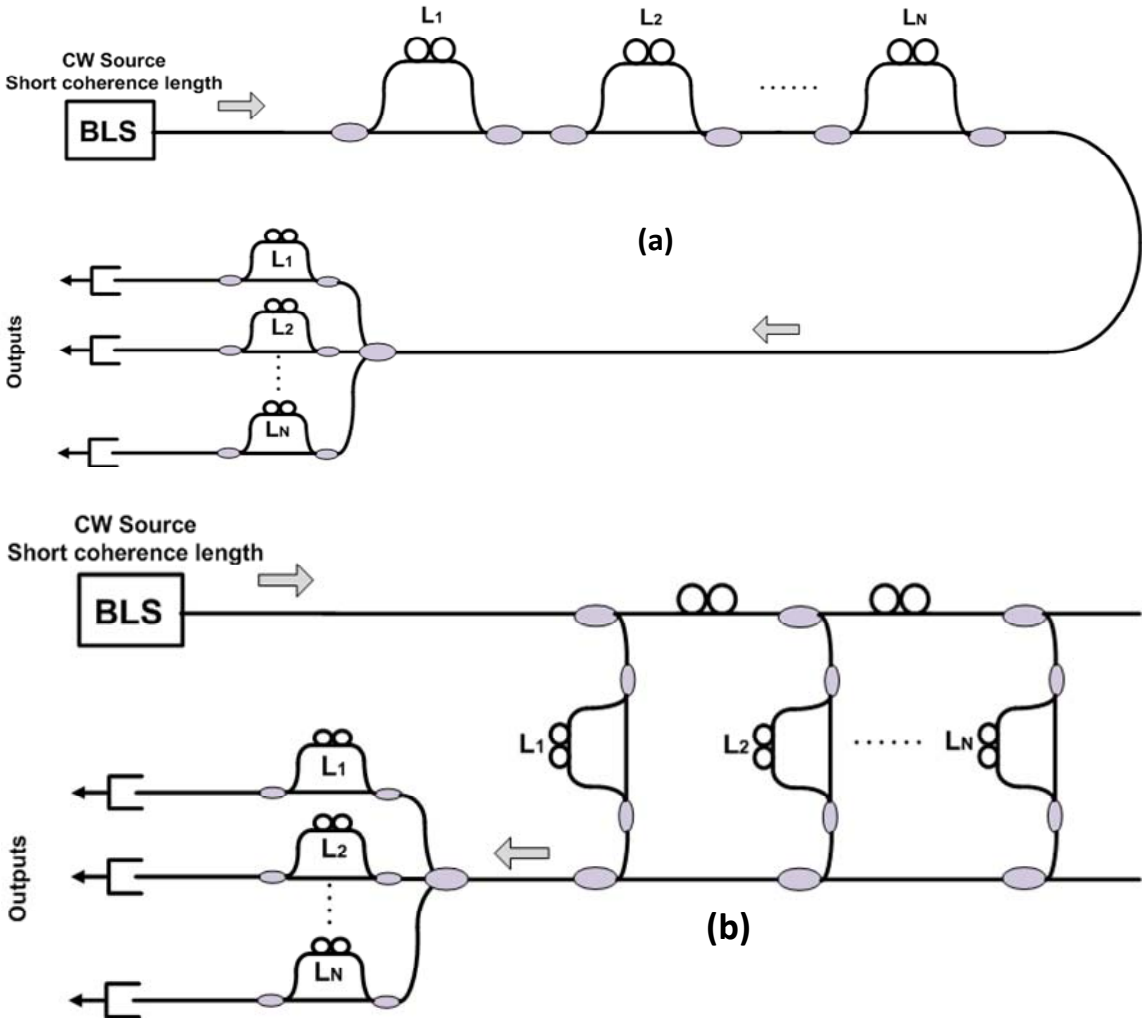

Figure 6.11.- Serial (a) and parallel (b) topologies for coherence multiplexing of interferometric sensors.

6.2.2.6 Polarization division multiplexing

A further parameter of an optical system that can be used to encode optical sensor signals is that of polarization; driving to the polarization-division multiplexing (PDM) approach. In this case, the sensor signals are encoded on orthogonal components of polarization of the input light source, as can be seen in Fig. 6.12. At the detector, the received light is resolved into the two component polarization states, which can be separately detected to demultiplex

the sensor outputs. The principal limitation of this approach is that only two channels of information (sensor signals) can be encoded onto a signal carrier [44]. Variations of this basic approach are, however, possible utilizing subcarrier modulation of the state of polarization. Such schemes are strictly hybrids of PDM and FDM processing [45, 46].

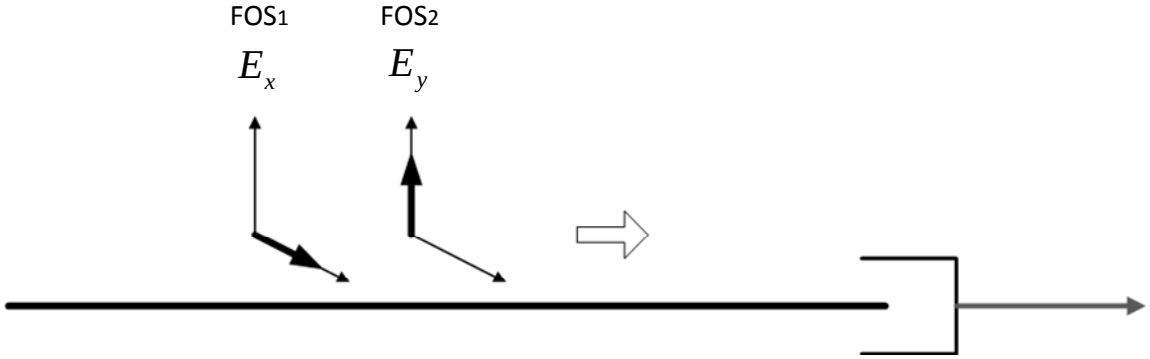

Figure 6.12.- PDM addressing technique for sensor multiplexing.

6.2.2.7 Wavelength division multiplexing

In the wavelength division multiplexing (WDM) approach, the sensor information is allocated to a particular optical wavelength, i.e. the sensor data are encoded on optical carrier at different wavelengths. A scheme of such addressing technique is represented in Fig. 6.13.

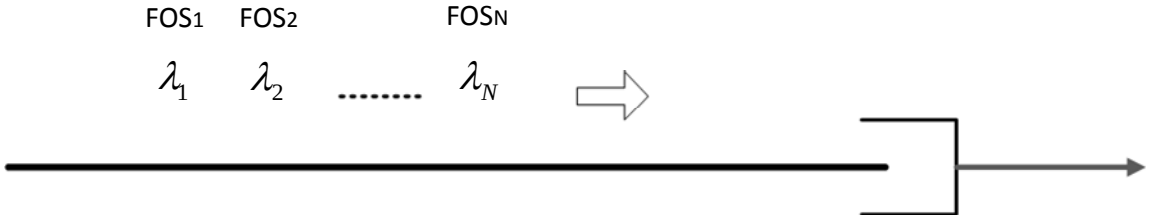

Figure 6.13.- WDM addressing technique for sensor multiplexing.

Wavelength division multiplexing has been evaluated experimentally for use in fibre communication systems for many years [47-49], being this deployment approach considered in the long-term the target architecture in FTTx access networks. The technique provides for greatly increased channel capacity in coherent and noncoherent-based communication systems.

Conceptually, the WDM approach, as said before, is the same as frequency-division multiplexing (FDM) with the consideration that in WDM, sensor channels must be properly spaced to avoid interchannel interference. The key system features are as follows, both for optical communication systems and multiplexing sensor networks:

- **Capacity upgrade:** each wavelength supports and independent network signal of perhaps a few gigabits per second, so WDM can increase the capacity of a fibre network dramatically.

- **Transparency:** an important aspect of WDM is that each optical channel can carry any transmission format (or addressing time-based technique). Thus, using different wavelengths, fast or slow asynchronous and synchronous digital data and analog information can be sent simultaneously, and independently, over the same fibre, without the need for a common signal structure.

- **Wavelength routing:** in addition to using multiple wavelengths to increase link capacity and flexibility, the use of wavelength-sensitive optical routing devices makes it possible to use wavelength as another dimension, in addition to time and space, in designing communication networks and switches. Wavelength-routed networks use the actual wavelength of a signal as the intermediate or final address.

- **Wavelength switching:** whereas wavelength-routed networks are based on a rigid fibre structure, wavelength-switched architectures allow reconfigurations of the optical layer.

The WDM approach for multiplexing fibre-optic sensors can take advantage of such aforementioned features and the usefulness of this technique in sensor applications has also been demonstrated [50, 51]. The use of this technique in sensor application has not, however, received as much practical attention. Fig. 6.14 shows an example of the type of possible topology using the WDM approach in a reflective star configuration, in which the reflected optical channels are received by means of an optical circulator.

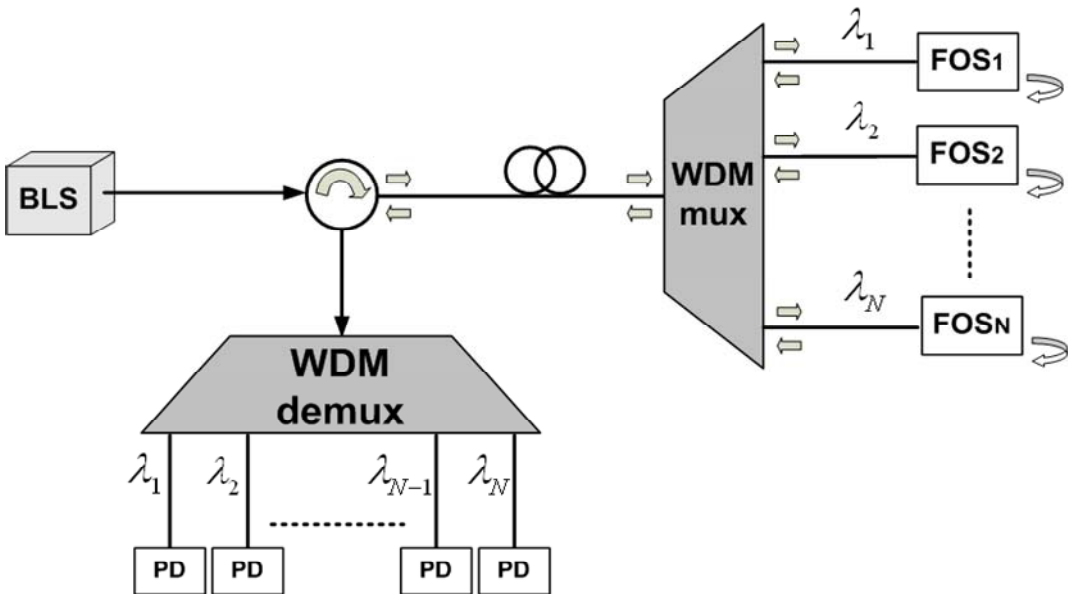

Figure 6.14.- WDM reflective star configuration for supporting *N*-self-referenced optical fibre intensity sensors.

In the WDM approach, the input light to the sensor array is divided into a number of wavelength bands that are selectively routed toward specific sensor elements, using wavelength-dependent splitters/recombiners/multiplexers. Such approach is theoretically the most efficient technique possible, as all the injected power from a source could be in principle directed to a particular sensor element and then onto a corresponding photodetector with minimal excess loss. The reason for the lack of practical demonstrations of WDM-based array sensors is due to the limited wavelength selectivity of these previous devices although scalability of such approach can be possible through cascaded CWDM and DWDM devices [52, 53]. However, obviously WDM techniques are mostly used in fiber Bragg grating systems for discrete intensity-based sensing. Different optical devices providing band-splitting are now commercially available, such as:

- **Coarse Wavelength Multiplexers (CWDM),** from 4 to 16 channles counts spaced 20nm , with typical insertion losses from 1.4dB to 4.3dB respectively.

- **Dense Wavelength Multiplexers (DWDM),** from 4 to 80 channels counts spaced from 200GHz to 50GHz , with typical insetion losses from 2dB to 5dB, respectively.

- **Arrayed Waveband Gratings (AWG),** available in the 1528-1622nm range (C+L communications band) fitting the ITU-T Spectral Grid with 50-100GHz channel separation with up to 80 channels counts and from 2.8dB to 4dB insertion loss per channel, respectively. These devices can also operate in the S-band and E-band**.**

- **Fiber Bragg Gratings (FBG),** combined with optical circulators provide also band-splitting performances with 50-100GHz channel spacing, although this approach is less compact and the insertion losses are higher.

Scalable multiplexing schemes to increase the number of sensors and to reduce the number of components are very desirable aspects for optical sensor networks. Optical configurations based on FBGs are effective approaches for efficiently addressing optical intensity sensors because they provide reflective configurations. Furthermore, they can be easily integrated in WDM networks due to its intrinsically band-splitting feature, and in combination with optical circulators, for spectral filtering devices and broadband light sources.

Wavelength-division-multiplexing intensity sensor networks have been reported in reflective star and ladder topologies using FBGs and fused biconical wavelength selective couplers [15] or CWDM devices [8]. Interrogation techniques for multipoint FBG sensors in series have been reported using modelocked wavelength-swept lasers [54] and Sagnac loop filters [55, 56].

Up to date, the most recent CWDM-PON based approach for self-referencing optical sensors proposes an all-optical reflective sensor network in a double star topology, using FBGs as self-referencing measurement technique, as seen in Fig. 6.15 [57]. This work performs enhanced sensitivity and optimizes the power budget in the network by means of

the CWDM devices thus increasing the number of multiplexed sensors or the distance between the light source and the remote measuring points.

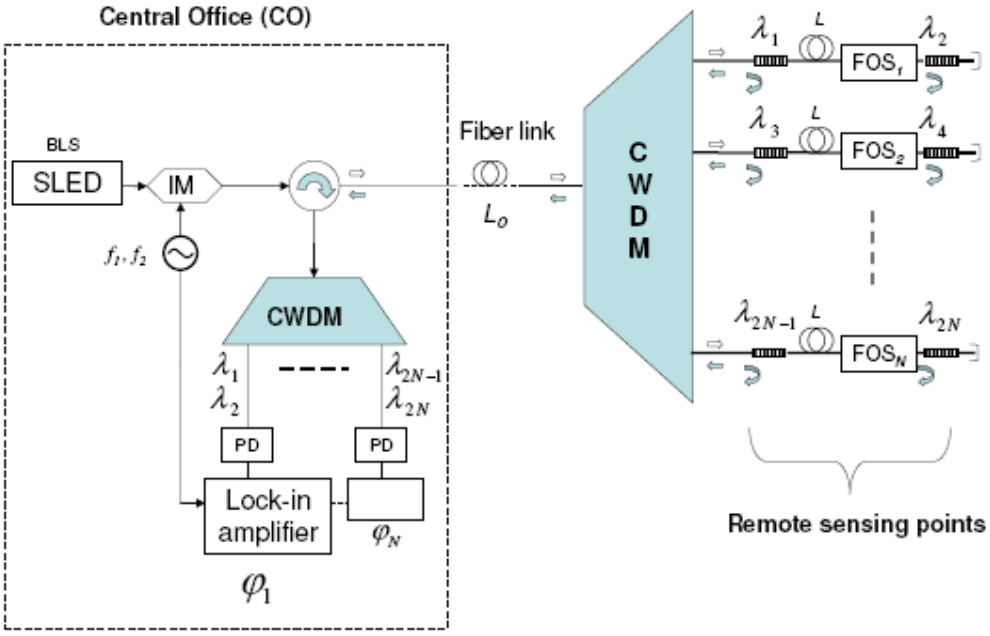

Figure 6.15.- Schematic of the porposed CWDM network for self-referencing N intensity fibre-optic sensors (FOS) using two FBGs and a fibre delay coil of length L, at each remote sensing point. SLED: Super-Luminiscent Erbium-Doped-Fiber Source; IM: Intensity Modulator, PD: Photodetector.

6.2.2.8 Hybrid approaches

The previous sections have detailed the characteristics of the basic addressing approaches for multiplexing fibre optic sensors. Each of these approaches have fairly distinct features (see Table 6.2 of this chapter) which, in general, have not much overlap with each other. Nevertheless, by blending two or more multiplexing approaches together the performance characteristics of the multiplexed network can be tailored to operational requirements. Multiplexing schemes that incorporate two or more approaches are generally referred to as hybrid approaches. Furthermore, FDM can be considered a hybrid approach combining fibre multiplexing and WDM. In FDM the frequency carrier is used to discriminate between the different wavelengths instead of using optical wavelength division multiplexers.

Combining TDM and WDM is the most commonly reported topology in literature, to form hybrid arrays of sensors, providing a very flexible approach multiplexing scheme. Fig. 6.16 shows a generic TDM/WDM network where different wavelengths are used to interrogate individual TDM arrays. This looks much like WDM networks where the individual sensors have been replaced with TDM arrays. Hybrid TDM/WDM networks combine the high multiplexing gains of TDM with the efficient use of the fibre bandwidth. Networks of several hundred sensors can be multiplexed over a single fibre lead in this manner.

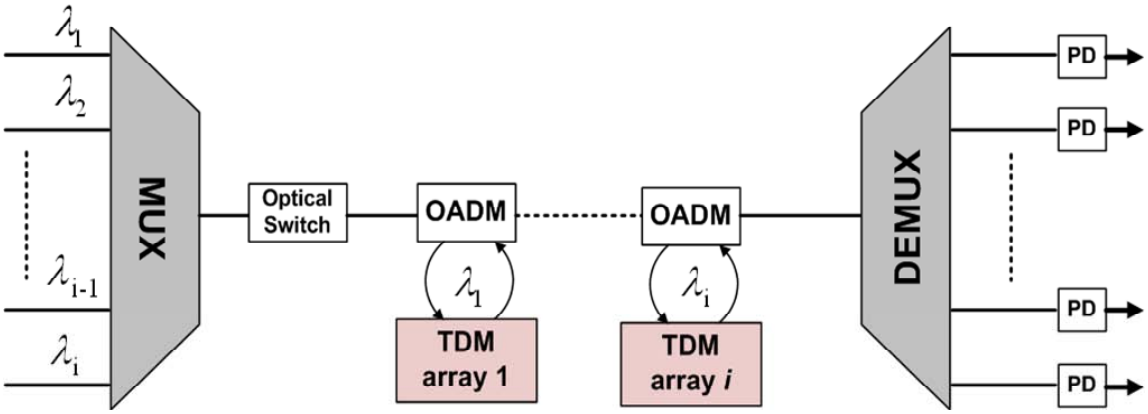

Figure 6.16.- Hybrid TDM/WDM network scheme. OADM: Optical Add/Drop Multiplexer; PD:photodetector.

6.2.2.9 Sensor multiplexing schemes discussion

To resume, multiplexing is the simulatenous transmission of two or more information channels along a common fibre optical path. Information from sensor elements in a network can be multiplexed by defining various multiplexing topologies or addressing schemes that can be used in optical sensor systems. In all cases, sensor networks are highly desirable in order to increase the number of sensing points and decrease the per sensor cost figure. Passive fibre optic sensor networks maintain the passive nature of the fibre.

A wide range of enabling techniques for implemented multiplexed fibre-optic sensor networks have been described. These techniques encompass a diverse range of addressing approaches and topologies which provide compatibility with practically all forms of fibre sensors developed to date. A large number of factors determine the suitability of a sensor networking scheme for a particular application. These include the format of the sensor information, i.e. analog or digital, the optical parameter onto which the sensor information is encoded, i.e. intensity, phase, wavelength, modulation (subcarrier) frequency, etc., and the application requirements in terms of topology and performances of the network, i.e. noise level, bandwidth, dynamic range, number of fibres, flexibility (placement and configuration of the remote optical sensors), complexity, cost, etc. The relative performance of the different multiplexing schemes, excepting PDM and CDM as being minimum-deployed approaches, is tabulated in Table 6.2 [5]. It can be concluded that no one multiplexing scheme is the answer for all applications, but there is enough flexibility in both, the basic schemes and hybrid combinations, that an optimum scheme can be developed for any application. Furthermore, passive wavelength multiplexing technology has matured very quickly and now low loss wavelength-selective components are readily available at practically any wavelength. As a result, the WDM approach in sensor networks is an area of considerable interest. From Table 6.2, it is worth mentioning the consideration of the optical power per sensor, for the WDM technique, to be $\sim 1/N$. It comes from the fact that of considering the WDM approach similar to the fibre-multiplexing counterpart.

The latter is relatively true as devices such as OADMs and/or multiplexers and demultiplexers provide an additional cumulative loss within the configuration of few dB of excess loss, which is close to the attenuation in the fibre-multiplexing technique.

Multiplexing Technique	**Cost**	**Performance**			**Flexibility**		
		Optical power per sensor	**Noise**	**BW**	**Config**	**Location**	**Complex**
None	H	1	Shot	H	H	H	L
Fibre	M	1/N	Shot	H	H	H	L
WDM	H	~1/N	Shot	H	H	H	M
TDM	L	$1/N^2$	Leakage Aliased Shot	L	L to H	L to H	M
FDM	M	1/N	Shot	H	H	H	H
Hybrid TDM/WDM	L	I^2/N^2	Leakage Aliased Shot	M	L to H	L to H	M

Table 6.2.- Different multiplexing schemes comparative [5]. H: High; M: Medium; L: Low; N: number of sensors in the network; I: number of WDM sources in the hybrid approach network.

6.3 Coarse WDM PON Electro-Optical Network for Self-Referencing Fibre-Optic Intensity Sensors

Currently, employing a similar topology than emerging communication access WDM-PONs is an attractive feature. So, a reflective star sensor network is proposed and demonstrated using an electro-optical remote self-referencing configuration thus providing an easy reconfiguration of the network performances. In this configuration, delay lines are electronically deployed at the reception stage through an electronic filter.

In this section, the self-referenced electro-optical FBG-based fibre-optic intensity sensor network with electronic delay lines at the reception stage, described in Chapter 5 of this document, is demonstrated in a CWDM optical intensity sensor network. This configuration consists on a reflective star network topology for multiplexing and interrogation of *N* quasi-distributed self-referencing remote sensing points. Moreover, the scalability of the topology could permit a higher amount of addressed sensor channels by employing devices such as arrayed-waveguide gratings (AWG) for dense WDM (DWDM) instead of CWDM devices if required. The two measurement parameters described, previously, in Chapter 5 are analyzed in terms of their self-reference property, crosstalk between sensors, sensitivity, linear response and resolution.

The proposed electro-optical fiber-optic topology for remotely addressing *N* intensity-based optical sensors placed within two Fiber Bragg Gratings (FBGs) is shown in Fig. 6.17 [51].

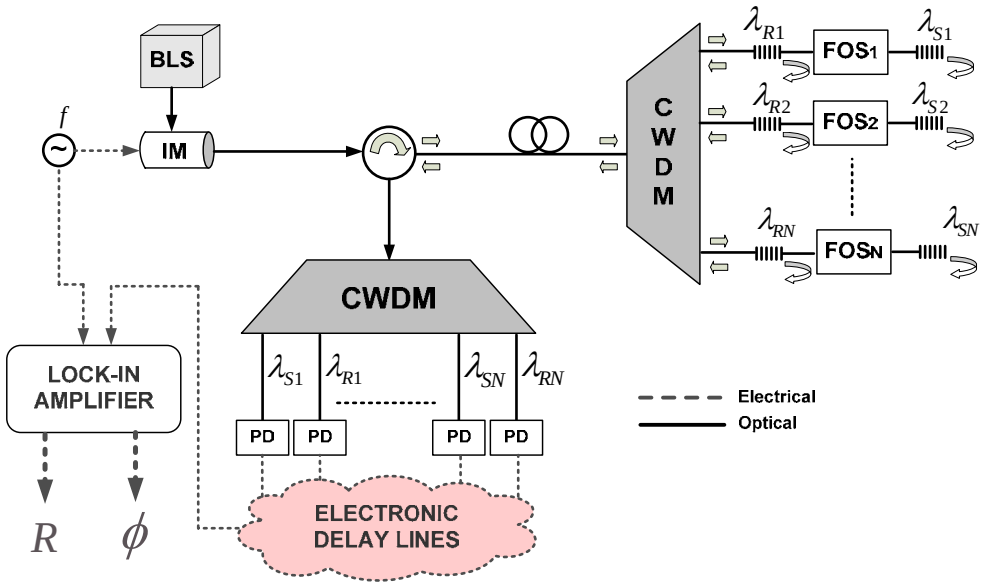

Fig. 6.17.- Schematic of the proposed electro-optical CWDM network for supporting *N* self-referenced optical fiber intensity sensors (FOS_i, i=1,…,*N*). BLS: Broadband Light Source, IM: Intensity Modulator, PD: Photodetector, FOS: Fiber Optic Sensor.

Taking advantage of the theoretical study of both self-referencing parameters demonstrated in Chapter 5, two measurement parameters can be defined for each remote sensing point shown in Fig. 6.17. The expression of both measurement parameters can be seen in Eq. (6.3) and Eq. (6.5), respectively.

$$R_i = \frac{V_O(f,\Omega_2)}{V_O(f,\Omega_1)} = \frac{M(f,\Omega_2)\big|_{\Omega_1=0}}{M(f,\Omega_1)\big|_{\Omega_2=0}} = \frac{[1+(\frac{2\beta_i}{1+\beta_i^2})\cos\Omega_2]^{1/2}}{[1+(\frac{2\beta_i}{1+\beta_i^2})\cos\Omega_1]^{1/2}} \tag{6.3}$$

where

$$M(f,\Omega_1,\Omega_2) = \alpha_i(1+2\beta_i\cos\Omega_i+\beta_i^2)^{1/2} \tag{6.4}$$

$$\phi_i = \arctan\left[\frac{-(\sin\Omega_1+\beta_i\sin\Omega_2)}{(\cos\Omega_1+\beta_i\cos\Omega_2)}\right] \tag{6.5}$$

Again, from Eq. 6.4, the expression of the magnitude corresponding to sensor *i* at angular frequencies Ω_1, Ω_2 can be written as a function of $\Omega_i = \Omega_2 - \Omega_1$. Consequently, for a fixed value of the modulation frequency and the electrical delays, both measurement parameters, R_i and ϕ_i, of the remote sensing point *i* depend only on β_i, beinginsensitive to external power fluctuations that might take place in the optical link between the sensing point and the transmission stage, thus performing a self-referencing parameter. Moreover,

both self-referencing parameters can be determined for any pair values of angular frequencies (Ω_1, Ω_2) providing flexibility to the measurement technique, at the remote sensing network, for any desired operation point.

The electro-optical network configuration shown in Fig. 6.17 has been implemented using single-mode fiber in order to experimentally validate both self-referencing parameters simultaneously, for two remote sensor channels. An erbium-doped broadband light source modulated at *f*=10kHz by an acousto-optic modulator is employed to launch optical power into the configuration through the broadband circulator. A pair of low-cost FBGs are used for each remote sensing point, including their complementary ones (same central wavelengths) at the reception stage. Their central wavelengths were $\lambda_{R1} = 1530.1nm$, $\lambda_{S1} = 1535nm$ for FOS_1 and $\lambda_{R2} = 1550.3nm, \lambda_{S2} = 1552.1nm$ for FOS_2, compatible with standard ITU G.694.2 for CWDM networks, see Fig. 6.18. Two single-mode tapers operating as micro-displacement sensors are placed between each pair of FBGs with sensor loss modulations H_1 and H_2, respectively. The tapers are obtained by elongation of single-mode fibre using a semi-automatic fabrication process. Once the tapers are fixed onto a micro-positioning system, the optical loss transmission coefficients of the tapers are sensitive to the displacement between the two fibre ends. Due to the tolerance of the elongation and positioning semi-automatic processes for obtaining the fiber sensors, there is a difference between sensors sensitivity to mechanical displacement. The reflected signals are demultiplexed by a CWDM demux, collected by InGaAs photodetectors and phase-shifted by the electronic delay filters at the reception stage. A lock-in amplifier is used in this stage in order to obtain both self-referencing parameters R_i and ϕ_i (i=1, 2).

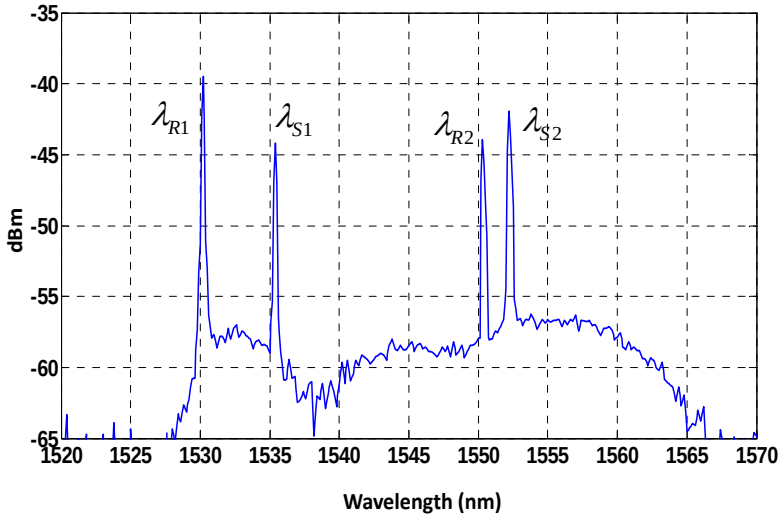

Fig. 6.18.- Optical reference and sensing channels along the CWDM 2-sensor network evaluated.

Fig. 6.19 shows the calibration curves of sensor loss modulation H_i (i=1,2) for both sensors versus displacement. In order to test the hysteresis of the sensors, two sets of measurements, marked as *fwd* (forward) and *bkw* (backward), are taken for increasing and decreasing values of the displacement, respectively.

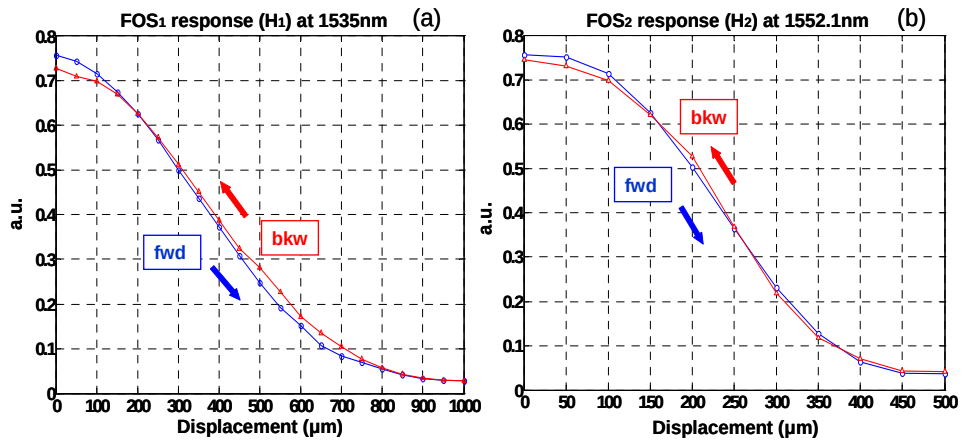

Fig. 6.19.- Calibration curves and hysteresis of the sensor loss modulations H_1 (a) and H_2 (b) for the taper-based displacement sensors.

6.3.1 Self-reference test

The self-reference property of both measurement parameters is tested with regards to power fluctuations of the optical source. A single-mode variable optical attenuator (VOA) is located before the optical circulator in the transmission stage thus emulating unexpected power losses along the optical link from the optical source to the remote sensing point, up to 12dB.

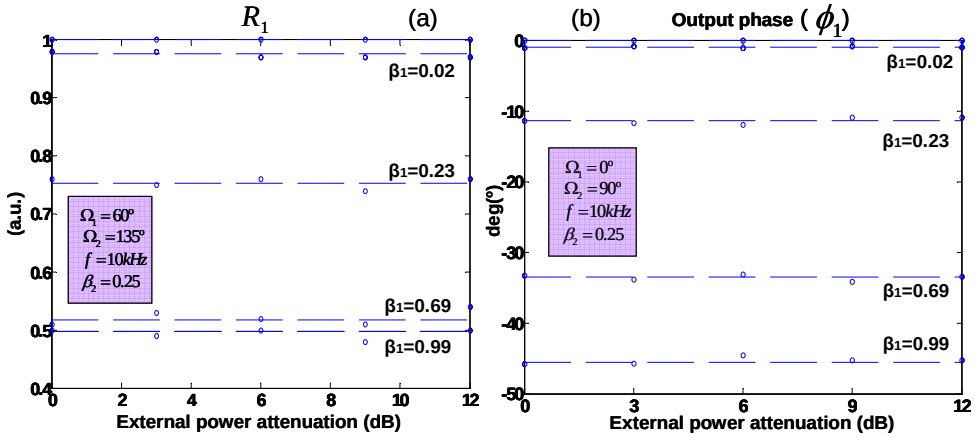

Fig. 6.20.- (a) Self-reference test of R_1 versus power fluctuations, up to 12dB, for different values of β_1 and $\beta_2 = 0.25$. (b) Self-reference test of ϕ_1 versus power fluctuations, up to 12dB, for different values of β_1 and $\beta_2 = 0.25$.

Fig. 6.20(a) and Fig. 6.20(b) show, respectively that there is no correlation between the measurements of both self-referencing parameters (R_1 and ϕ_1) and the induced power

attenuation with the VOA, thus providing the self-reference property to the remote sensor network.

6.3.2 Crosstalk analysis

In order to test the crosstalk between two sensors operating in adjacent CWDM channels, several measurements of the self-referencing parameters R_1 and ϕ_1 (FOS_1) have been taken for different values of the sensor losses modulation β_2 (FOS_2) and in different operation points in terms of Ω_i, as shown in Fig. 6.21(a) and Fig. 6.21(b).

Similar results are obtained when monitoring R_2 and ϕ_2 (FOS_2) when β_1 (FOS_1) is changed. In both cases, no crosstalk is induced due to changes in the sensor loss modulation of one sensor to the other. So, both sensors can be interrogated simultaneously without mutual interference as both self-referencing parameters associated to a sensor have the same performance, no matter the point of operation of other sensors in the network. It is a consequence of the spacing between the sensors' associated Bragg wavelengths and the isolation provided by the WDM mux/demux (≥ 30 dB).

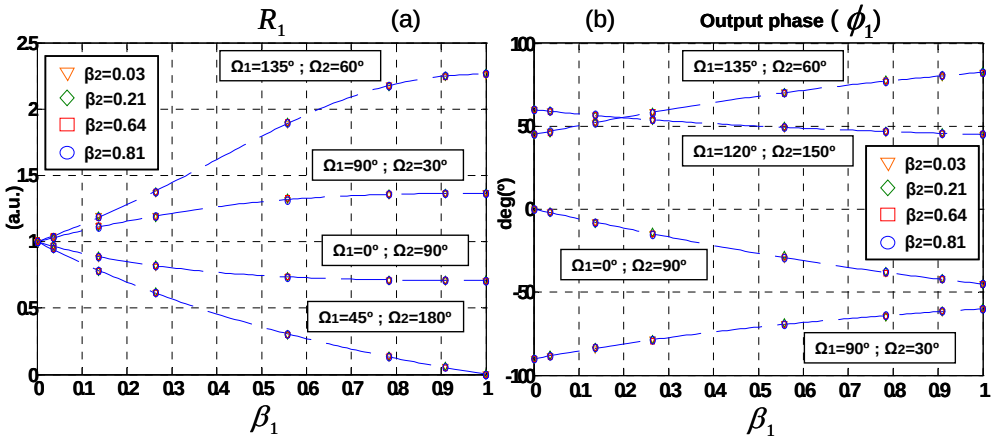

Fig. 6.21.- Measurements of the R_1 parameter (a) and the output phase ϕ_1 (b) versus β_1 (FOS_1) for different values of β_2 (FOS_2).

6.3.3 Sensitivity analysis

This subsection will be divided in two, concerning each self-referencing parameter. This is because the same analysis leads to different performances depending on the measurement parameter to be considered. It is worth pointing out that the main objective is to evaluate tendencies, in terms of sensitivity, that help to optimize both self-referencing parameters' performance.

As the performance of both sensor channels (those including FOS_1 and FOS_2) is exactly the same for both self-referencing parameters, from now on, it is used a generic parameter R or ϕ, no matter the remote sensing point is being considered.

As defined in Chapter 5, $\Omega = \Omega_2 - \Omega_1$ being the difference between both phase-shifts (related to the sensor which is being interrogated) selected at the reception stage.

6.3.3.1 R parameter

The sensitivity of the system S_R to sensor losses (by means of β), defined as the partial derivative of R with respect to β, $S_R = \frac{\partial R}{\partial \beta}$, is given by (see the section C.3 in Appendix C for further explanation):

$$S_R(\Omega_1, \Omega_2, \beta) = \frac{(\cos\Omega_2 - \cos\Omega_1)[1-\beta^2]}{(1+2\beta\cos\Omega_1+\beta^2)^{3/2}(1+2\beta\cos\Omega_2+\beta^2)^{1/2}} \qquad (6.6)$$

From Eq. 6.6, S_R depends on the phase-shifts (Ω_1, Ω_2) selected at the reception stage and not on the signal absolute phase or power, apart from β.

Fig. 6.22(a) shows both measurements and theoretical curves (dashed lines) of the sensitivity of the R parameter versus sensor losses, β, for different values of Ω_1 and Ω_2 when $\Omega > 0$. Notice that when $\Omega_1 = 90^o$ and $\Omega_2 = 180^o$ a performance of $|S_R| \approx 1$ can be obtained in the whole range of β. Different measurements concerning S_R versus β when $\Omega < 0$ have also been tested showing good agreement with theoretical predictions as can be seen in Fig. 6.22(b). From this figure it is also shown that higher sensitivities can be obtained with $\Omega < 0$ at the reception stage.

Different calibration curves of the sensitivity of the R parameter versus β have been obtained for different phase-shift configurations at the reception stage, as Fig. 6.23 shows. From the theory and measurements shown in this subsection the performance of R with regards to the sensitivity shows the following results:

a) The sensitivity of the transfer function for a generic remote sensing point depends not only on the absolute difference of the phase-shifts related to that sensor selected at the reception stage but also on the pair of values selected in any case (see Fig. 6.22(a) and Fig. 6.22(b)).
b) The sensitivity response depends on the sign of Ω and higher sensitivities are obtained at $\Omega < 0$ for higher absolute values of Ω (see Fig. 6.22(b)).
c) For a fixed phase-shift difference Ω, the highest sensitivity values are obtained when $\Omega_1 = 180^o$ providing big variations in the whole range of $\beta \in [0,1]$.

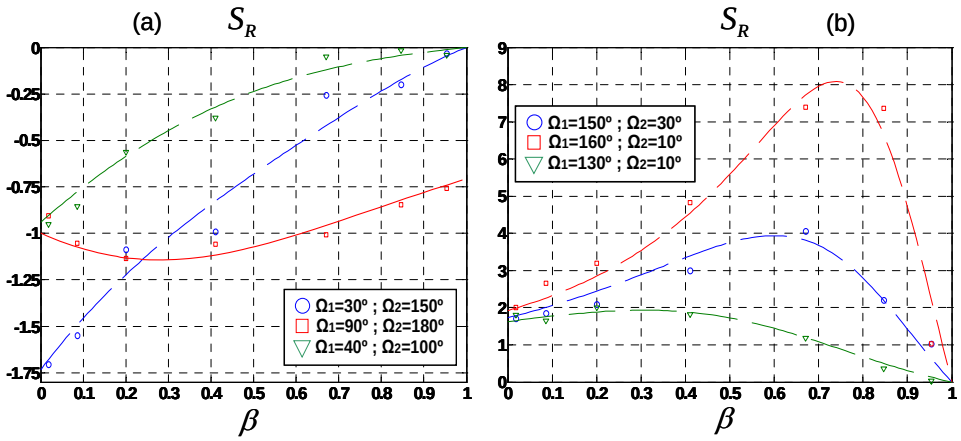

Fig. 6.22.- (a) S_R versus β for different values of the phase-shifts at the reception stage with $\Omega > 0$. (b) S_R versus β for different phase-shifts at the reception stage with $\Omega < 0$. In both cases dashed lines are obtained from the theory.

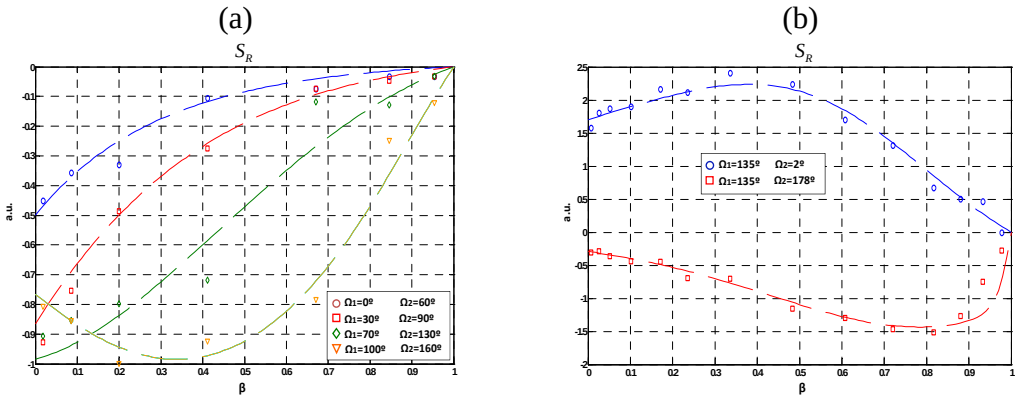

Fig. 6.23.- S_R versus β for different arbitrary values of the phase-shifts at the reception stage. In both cases dashed lines are obtained from the theory.

6.3.3.2 Output phase ϕ parameter

The sensitivity of the system S_ϕ to sensor losses (by means of β), defined as the partial derivative of ϕ with respect to β, $S_\phi = \dfrac{\partial \phi}{\partial \beta}$, can be expressed as follows (see the section C.3 in Appendix C for further explanation):

$$S_\phi(\Omega_1, \Omega_2, \beta) = \frac{\sin(\Omega_1 - \Omega_2)}{1 + 2\beta\cos(\Omega_1 - \Omega_2) + \beta^2} \qquad (6.7)$$

From Eq. 6.7, S_ϕ depends on the phase-shift difference between Ω_1 and Ω_2 selected at the reception stage and not on the signal absolute phase.

Fig. 6.24(a) shows the theoretical curves of the absolute values of S_ϕ versus sensor loss, β, for different phase-shift difference values. As the performance of S_ϕ is symmetrical with regards to $\Omega = 90^o$, all the possible pair combinations of (Ω_1, Ω_2) resulting with identical absolute value of Ω will lead to similar results in terms of $|S_\phi|$. Different measurements concerning S_ϕ versus β have been tested showing good agreement with theory predictions as can be seen in Fig. 6.24(b).

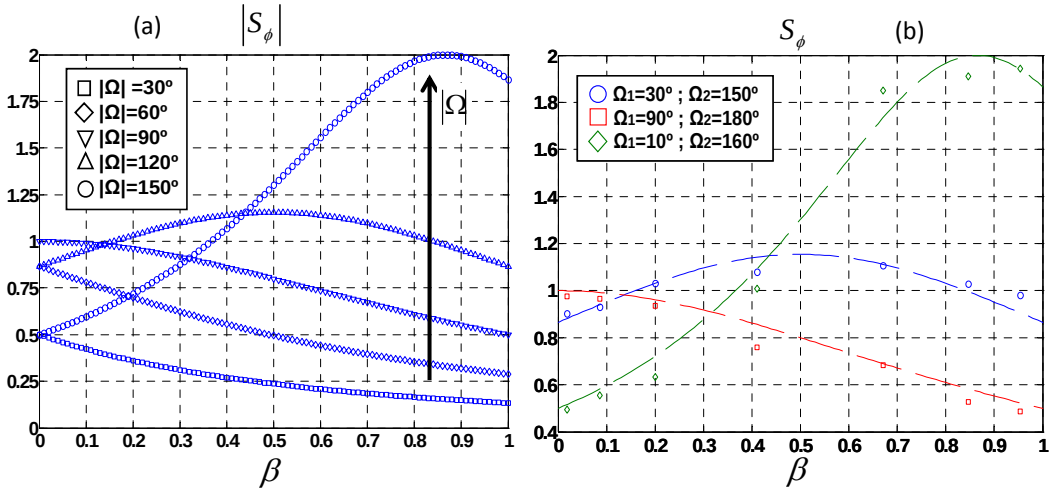

Fig. 6.24.- (a) Theoretical sensitivity (absolute value) of the output phase ϕ versus β for different values of Ω. (b) Measurements of the sensitivity S_ϕ of the output phase versus β for different phase-shift configurations at the reception stage (dashed lines give the values obtained from the theory).

More calibration curves of the sensitivity of the output phase, S_ϕ, versus β have been obtained for different phase-shift configurations at the reception stage, as shown in Fig. 6.25. From the theory and measurements shown in this subsection the performance of the output phase ϕ with regards to the sensitivity shows the following results:

a) The sensitivity of the transfer function for a generic remote sensing point depends only on the absolute value of the phase-shifts difference (Ω) related to that sensor, selected at the reception stage. The modulus is independent from the sign of that phase-shift difference (see Fig. 6.24(a)).
b) Highest sensitivity values can be obtained at $|\Omega| = 150^o$, providing great variations in the whole range of $\beta \in [0,1]$. This fact can be seen in the experimental measurements concerning ◊ symbol and its associated theoretical curve, -green dashed line-, of Fig. 6.24(b).

c) For obtaining high sensitivities with low slope variations, providing $|S_\phi| \approx 1$, in the whole range of the sensor response, $\Omega = |120^o|$ is the best option.

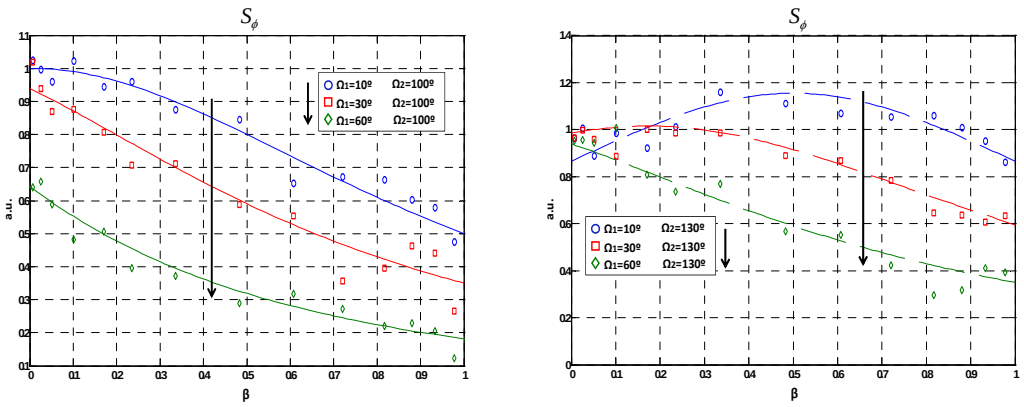

Fig. 6.25.- Measurements of the sensitivity S_ϕ of the output phase versus β for different phase-shift configurations at the reception stage (dashed lines give the values obtained from the theory).

6.3.4 Linear response

As the electro-optical topology proposed in this paper provides flexibility in terms of selecting specific operation points of the network for each remote sensing point; in this section the linear response, which can be a desirable property when considering sensor performances, of both measurement parameters will be studied. It will also be provided phase-shift values at the reception in order to obtain the best performance in terms of linearity.

As in previous section 6.3.3, the analysis of the linear response will be studied separately with regards to the self-referencing parameter considered, leading to different approaches.

6.3.4.1 R parameter

Different theoretical curves of the R parameter versus β have been obtained for different phase-shift configurations at the reception stage. The performance of this measurement parameter has been analyzed showing the following results:

a) The linear response of the R parameter tends to be better when higher values of Ω_2 at the reception stage are applied, independent of the values of Ω_1 selected.
b) $(\Omega_1, \Omega_2) = (104^o, 180^o)$ provides the best performance in terms of linearity with a linear regression coefficient of r=0.9997 in the whole β range.

Fig. 6.26 shows the measurements, theoretical curve and linear fit of the R parameter versus β when $(\Omega_1,\Omega_2)=(104^o,179^o)$ is applied at the reception stage. The coefficient of linear adjustment to the experimental points was found to be r=0.9992, close to the unit and to the theoretical value predicted by the model. Results comprising $(\Omega_1,\Omega_2)=(104^o,180^o)$ condition were not able to be carried out due to the high unstable data values obtained at such condition.

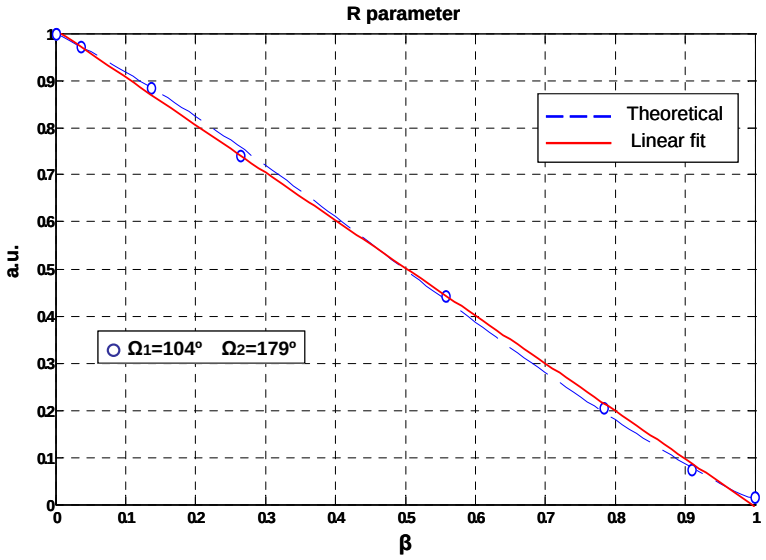

Fig. 6.26.- Measurement of R versus β when $(\Omega_1,\Omega_2)=(104^o,179^o)$ is applied at the reception stage (linear regression in solid line and theoretical curve in dashed line).

6.3.4.2 Output phase ϕ parameter

Taking into account the output phase ϕ versus β, the performance of this measurement parameter shows the following results:

a) The best response in terms of linearity is provided by those phase-shift configurations at the reception stage when $|\Omega|=120^o$ is applied, with a linear coefficient of r=0.9993 in the whole β range.

b) Consequently, the best linear response is obtained when $\phi|_{\beta=0}=\alpha$ and $\phi|_{\beta=1}=\alpha\pm 60^o$. This means that maximum linearity is obtained when the output phase response varies $\Delta\phi=|60^o|$ from $\beta=0$ to $\beta=1$.

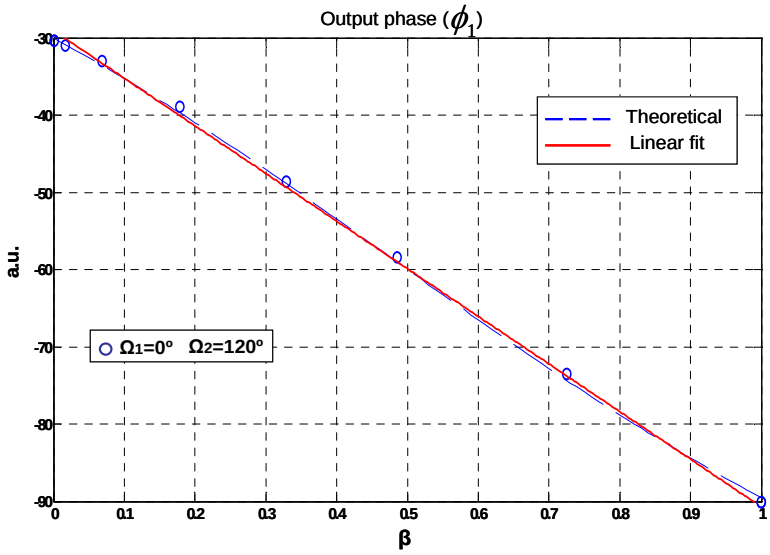

Fig. 6.27.- Measurement of ϕ versus β when $(\Omega_1, \Omega_2) = (0^o, 120^o)$ is applied at the reception stage (linear regression in solid line and theoretical curve in dashed line).

Fig. 6.27 shows the measurements, theoretical curve and linear fit of the output phase ϕ versus β when $(\Omega_1, \Omega_2) = (0^o, 120^o)$ is applied at the reception stage. The coefficient of linear adjustment of the experimental points is found to be *r*=0.9990, close to the unit and to the theoretical value predicted by the model.

6.3.5 Resolution

In this section an estimation of the resolution of both measurement parameters of the network is presented. No uncertainty factors (such as thermal dependency or frequency-dependent noise) have been taking into account for this analysis.

Considering a generic function $f(x)$ it is truth that $\Delta f(x) = f'(x) \cdot \Delta x$. Analogously, if both parameters are considered as $f(\beta) = R(\beta)$ and $f(\beta) = \phi(\beta)$, the following relations, for any phase-shift configuration, can be obtained:

$$\Delta\beta_{\min} = \frac{\Delta\phi_{\min}}{S_\phi} \tag{6.8}$$

and

$$\Delta\beta_{\min} = \frac{\Delta R_{\min}}{S_R} \tag{6.9}$$

where S_i refers to the sensitivity of the parameter response considered and $\Delta\beta_{\min}$, $\Delta\phi_{\min}$ and $\Delta R_{\min}$ are minimum deviations considered for the input β and the outputs R and ϕ, respectively.

Considering those minimum deviations as measurement uncertainties provided by the resolution of the Lock-in amplifier ($\Delta\phi_{\min} = 0.05^{\circ}$; $\Delta M_{\min} = 9\cdot10^{-5}\,\mathrm{V}$) but taking also into account the error propagation in the function $f(\beta) = R(\beta) = M_1 / M_2$ with respect of its two variables (considering separately the contribution due to both uncertainties), with $M_1 = M\left(f,\Omega_2\right)\big|_{\Omega_1=0}$ and $M_2 = M\left(f,\Omega_1\right)\big|_{\Omega_2=0}$, see Eq. 6.3.

It can be found that the parameter $\Delta R_{\min}$ is given by:

$$\Delta R_{\min} = \left(\frac{\Delta M_1}{M_1} + \frac{\Delta M_2}{M_2}\right)\cdot\frac{M_1}{M_2} = \Delta M\cdot\left(\frac{1}{M_1} + \frac{M_1}{M_2^2}\right) \approx \frac{\Delta M}{M}\cdot 2 \qquad (6.10)$$

with the approach $M_1 \simeq M_2$ and where the term ΔM corresponds to the Lock-in magnitude resolution ($9\text{x}10^{-5}$V) used in the measurements and M takes the value of 200mV (experimental value). That gives a value of $\Delta R_{\min} = 9\cdot10^{-4}\,\mathrm{V}$.

Consequently, for both outputs it is possible to obtain the minimal input, $\Delta\beta_{\min}$, required in the fibre-optic sensor from Eq. 6.8 and Eq. 6.9 to have a measurable output. The following table estimates both parameters separately and comparatively at the same phase-shift configurations (see Table 6.3 footnote) at the reception stage, for a β range from 0 to 0.5 with constant sensitivity. It must be noticed that the term $Slope_P$ refers to the sensitivity of the parameter of study, i.e. $Slope_P = S_P$.

	R		ϕ	
(Ω_1,Ω_2)	$Slope_R$	$\Delta\beta_{\min}$	$Slope_\phi$	$\Delta\beta_{\min}$
$(135^{\circ},60^{\circ})$[(a)]	1.75	$\sim5\cdot10^{-6}$	50	10^{-3}
$(30^{\circ},150^{\circ})$[(b)]	1.75	$\sim5\cdot10^{-6}$	60	$8\cdot10^{-4}$
$(160^{\circ},10^{\circ})$[(c)]	8	$\sim10^{-6}$	80	$6.3\cdot10^{-4}$
$(104^{\circ},180^{\circ})$[(d)]	1	$\sim9\cdot10^{-6}$	40	$1.3\cdot10^{-3}$

(a) arbitrary electrical phase-shifts

(b) best linearity condition for the output phase

(c) highest *R* sensitivity plotted in Fig. 6.22(b)

(d) best linearity condition for the *R* parameter

Table 6.3.- Comparative of R and ϕ parameters in terms of resolution.

In all cases, with the approach of the *R* parameter (with the equipment used in these measurements) better resolutions can be obtained and, therefore, smaller increments of the sensor loss (β) could be detected. From these data it can be also seen the influence of selecting each pair of electrical phase-shifts at the reception stage, on the final resolution. So two phase-shifts instead of using only one, provides flexibility to the self-referencing technique.

6.3.6 Scalability of the Network: DWDM upgrade

The experiment is carried out evaluating two fibre-optic intensity sensors (FOS) and employing Coarse Wavelength-division Multiplexing (CWDM) devices. Nevertheless, commercially available Dense WDM devices, promoted by the high-speed optical communications market, can be used to scale the sensor network reported in this work. A DWDM (1.6nm channel spacing, ITU-T G.694.1) upgrading of the 5 CWDM channels within the C+L bands (1528-1622nm) can be achieved by employing commercial bandsplitting based on commercial Arrayed Waveguide Gratings (AWG). These devices can achieve 50GHz channel separation and 40 channel counts within a single CWDM band (20nm channel spacing). On the other hand, FBGs provide central wavelength accuracy around 0.1nm at 3dB bandwidth, thus making possible to use such devices in a FBG-based electro-optical self-referencing technique in a DWDM upgrading scenario. By adding 40 channels within each of the 5 CWDM bands in the 1520-1610nm range, a maximum number over 200 multiplexed optical intensity sensors could be addressed with this upgrade approach. On the other hand, as the power density per sensor channel is reduced, remote amplification or different transmission stages might be also required [57].

6.4 Radio-Frequency Self-Referencing System for Monitoring Drop Fibres in WDM Passive Optical Networks

During last years, new multimedia services such as Internet Protocol Television (IPTV) or Video on Demand (VoD), as well as an increased data traffic driven by High-Definition TV (HDTV), Peer-to-Peer (P2P) applications and Content Distribution Networks (CDN) have been demanding an increase of the optical broadband access network capacity.

FTTH/N (Fiber to the Home/Node) deployments are being prepared or carried out worldwide by telecom operators as the more future proof solution, being the copper based x-Digital Subscriber Line (xDSL) infrastructure progressively replaced by a fibre-based outside plant with thousands of optical ports in Central Offices (CO) and optical fibre branches towards residential and business users.

Time-Division-Multiplexing (TDM) Passive Optical Networks, fully supported by Recommendations and Standards from the International Telecommunication Union (ITU-T) and the Institute of Electrical and Electronic Engineers (IEEE), such as Gigabit-PON

(ITU-T G.984) and Ethernet-PON (IEEE 802.3av), are ready for massive deployment worldwide. TDM-PON is the first-generation of optical access systems overcoming the physical reach, bandwidth limitations and scalability of xDSL technologies.

More recently, new PON systems are emerging that employ Wavelength Division Multiplexing (WDM) techniques in an exhaustive way. It is a more efficient way to deliver traffic to Customer Premises Equipment (CPE) devices, where the end-users are connected to the services, in an individual way with a dedicated capacity of up to 10 Gbps full-duplex for each single customer [58-60]. These systems, commonly referred to as WDM-PON, are still under standardization process and field trials but constituting the present and future next generation access network deployment.

In this scenario, Telecom operators have come across the challenge of supervising a new outside plant with Passive Optical Network (PON) architectures in point-to-multipoint topologies, in order to achieve a low operational cost of the network, a reduced risk of service disruption and a rapid recovery time in case of failure at the optical physical layer. Typical fibre problems that may take place in the distribution and drop stages of a PON outside fibre plant are dirty contacts between connectors, damaged connectors, macrobending and fibre breaks. While these problems can be easily detected in point-to-point optical fibre links using conventional Optical Time Domain Reflectometer (OTDR) techniques, the monitoring of FTTH/N systems with point-to-multipoint physical configurations is a new challenge to take into account, because the reflected signal detected in the OTDR consists of the sum of different Rayleigh backscattered light powers coming from different drop fibres, which cannot be distinguished in time in a trivial way. On the other hand, due to the limitation of the Optical Network Terminal (ONT) intelligence to reduce its cost, while the quality of the data signals exchanged between the central office equipment and the ONTs is known by the system, the real-time fibre link quality information is not available without a monitoring system.

To overcome the limited performance of conventional OTDR measurements in a TDM point-to-multipoint optical network, some authors have proposed different techniques in order to ensure that each individual branch contributes to the OTDR trace in a distinguishable way, such as using OTDR and FBG [61-63], Raman amplification [64], Optical Code Division Multiplexing (OCDM) [65], embedded low-cost OTDR inside ONTs [66] or drop-fibres with individually-assigned Brillouin frequency shifts [67]. A spectral analysis using an Optical Spectrum Analyzer (OSA) instead of OTDR equipment has also been reported with the same purpose [68].

In the case of WDM-PON systems, the problem of identifying OTDR traces from different drop fibres can be partially avoided, due to the spectral characteristics of the optical multiplexers and de-multiplexers which are used in the fibre plant instead of optical power splitters. Several authors have used tuneable OTDR and FBGs with different central wavelengths at the end of branch fibres in order to reduce the effect of unwanted reflections from the branches which are not under test in the WDM-PON [69, 70]. Taking advantage of the cyclic response of the optical filters, a monitoring technique which employs a continuous wave supercontinuum light source, simultaneously exciting a wavelength-

locked Fabry-Perot Laser Diode (FP-LD) with data and monitoring signals in L-band and U-band, respectively, has also been demonstrated [71].

Even though these approaches can be very useful in certain situations, still they may require expensive equipment (Tuneable OTDR, Brillouin OTDR, OSA), non scalable and inefficient fibre deployment (Brillouin frequency-shifted drop fibres) or do not avoid the need for end-user collaboration (OTDR at ONTs).

In this section, a low cost and flexible measuring system for preventive monitoring is proposed, allowing individual measurement of power attenuation taking place within drop fibres in WDM-PON systems, thus helping to identify physical layer problems at the last stage of the PON before the CPE is alarmed or the service provided to the customers of the network is interrupted. Furthermore, it is basically based on the self-referenced topology presented in this chapter.

Figure 6.28 shows a generic WDM-PON system with the proposed self-referencing system for monitoring the optical attenuation of *N* drop fibres, using coloured FBGs in the Remote Node (RN) and in the Demarcation Points located at the end of the drop fibres.

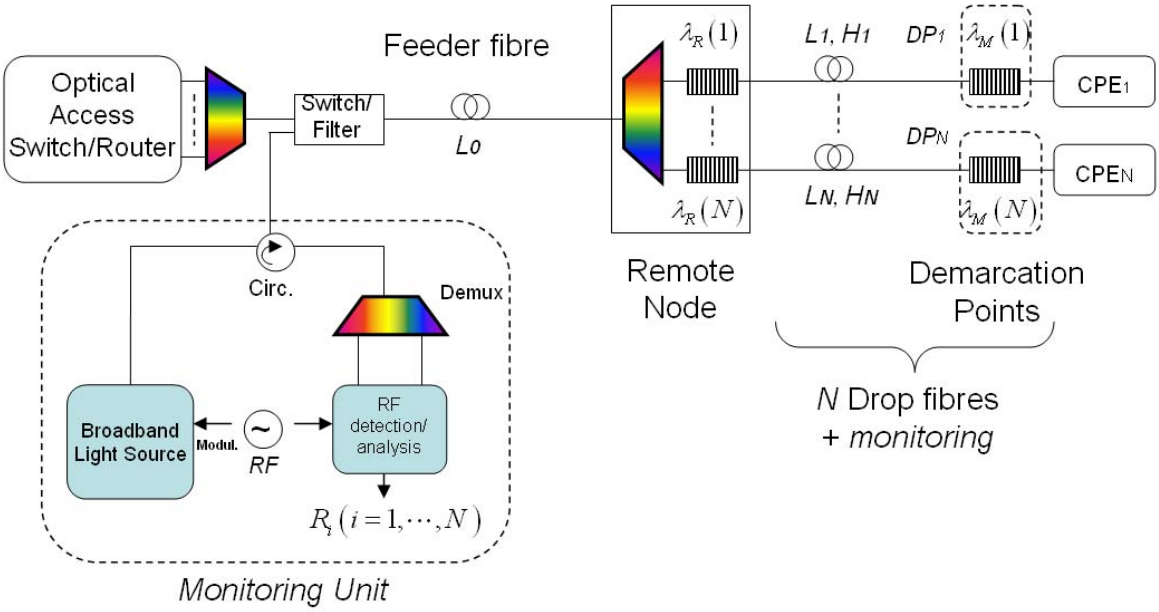

Fig. 6.28.- Proposed self-referencing monitoring system for drop fibres in WDM-PON; CPE: Customer Premises Equipment;. *DPi*: Demarcation Point of drop fibre *i*; *Li, Hi*: Length and attenuation of drop fibre i, respectively.(i=1,…,N).

In the proposed monitoring system, a Broadband Light Source (BLS) is intensity-modulated with a RF signal inside the monitoring unit and launched into the WDM-PON feeder fibre using a passive optical element (Switch/Filter), either an optical switch, a wavelength MUX-DEMUX or a passive splitter, depending on power budget. In each drop fibre behind the remote node (RN), a first FBG ($\lambda_R(i)$) is required in order to obtain a

reference signal in the Central Office. A second FBG ($\lambda_M(i)$) for measuring the optical attenuation (H_i) of the drop fibre number *i* is added inside the Demarcation Point (DP) before the Customer Premises Equipment (CPE). The central wavelength and bandwidth of both FBGs must be within the passband of each port of the passive device installed in the Remote Node and the Switch/Filter optical element in the Central Office. The reflections from the FBG are collected back at the monitoring unit where the signal processing of the FBG reflections is carried out by an analog filter and a lock-in amplifier. The self-referencing measurement parameter R_i is obtained for each drop fibre (i=1,…,N). This parameter provides the measurement of the optical loss of each drop fibre with the advantages of self-referencing and increased sensitivity [51] for monitoring access PON systems.

A detailed architecture of the monitoring system and the demultiplexers at the reception stage can be seen in Fig. 6.29(a) and Fig. 6.29(b).

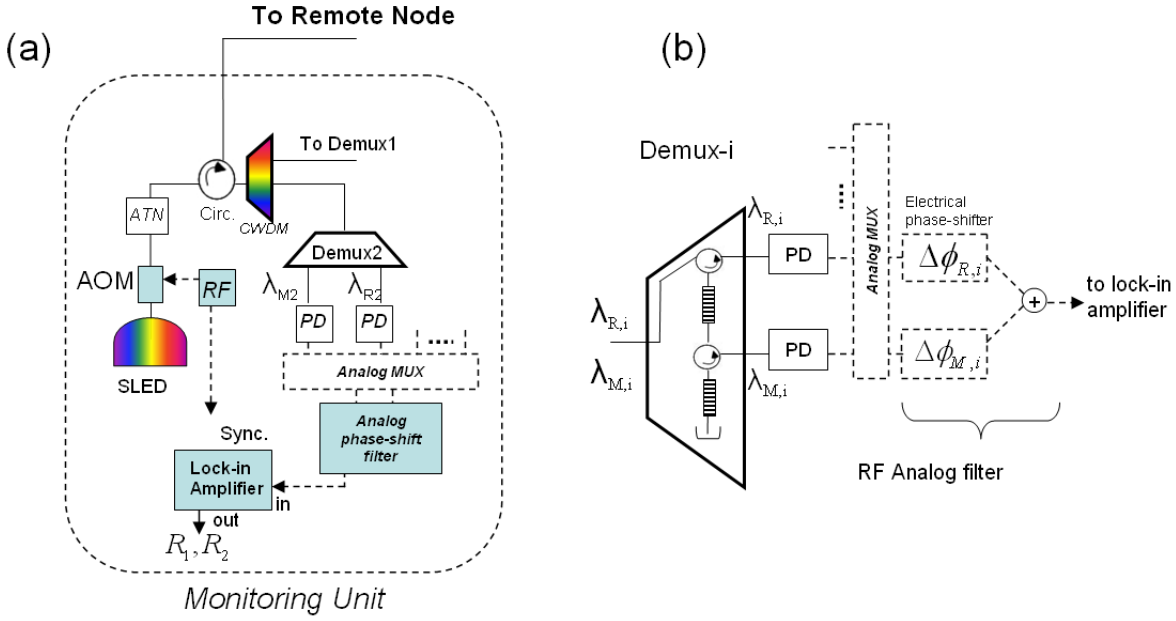

Fig. 6.29.- Implementation of the (a) monitoring unit and (b) diagram of a demultiplexer at the recepcion stage.

The digital signal representation of the RF analog filter of the proposed monitoring unit is identical to Fig. 5.16(b) and the self-referencing parameter for monitoring is given by Eq. 5.23. It must be noticed that the phase-shift of the monitoring wavelength is the sum of the electronic shift that can be adjusted in the monitoring unit by means of the analog filter and the fixed shift caused by the propagation time through the drop fibre *i* , given by Eq.5.6. In addition to this, the phase shift due to the propagation time in the feeder fibre is not considered in the model as it is the same for the reference and the monitoring wavelengths. Consequently, for a fixed value of the modulation frequency, the self-referencing parameter R_i for the drop fibre *i* depends only on the parameter β_i, which is insensitive to external

power fluctuations that might take place in the optical link between the Central Office and the Remote Node, thus performing as a robust self-referencing measurement parameter.

This parameter is very flexible and can be optimized in order to increase the sensitivity or linearity with regards to the optical attenuation of the drop fibre, *Hi*. The most sensitive behaviour is obtained as Ω_R tends to π and Ω_M tends to 0, see Fig. 6.30, but in this situation the parameter shows a non-linear performance. In Fig. 6.30(d) the sensitivity of the self-referencing parameter for $\Omega_M = 0$ is increased more than 200% with regards to the attenuation coefficient β. Other configurations can be chosen in the same way in order to improve another system property depending on specific requirements.

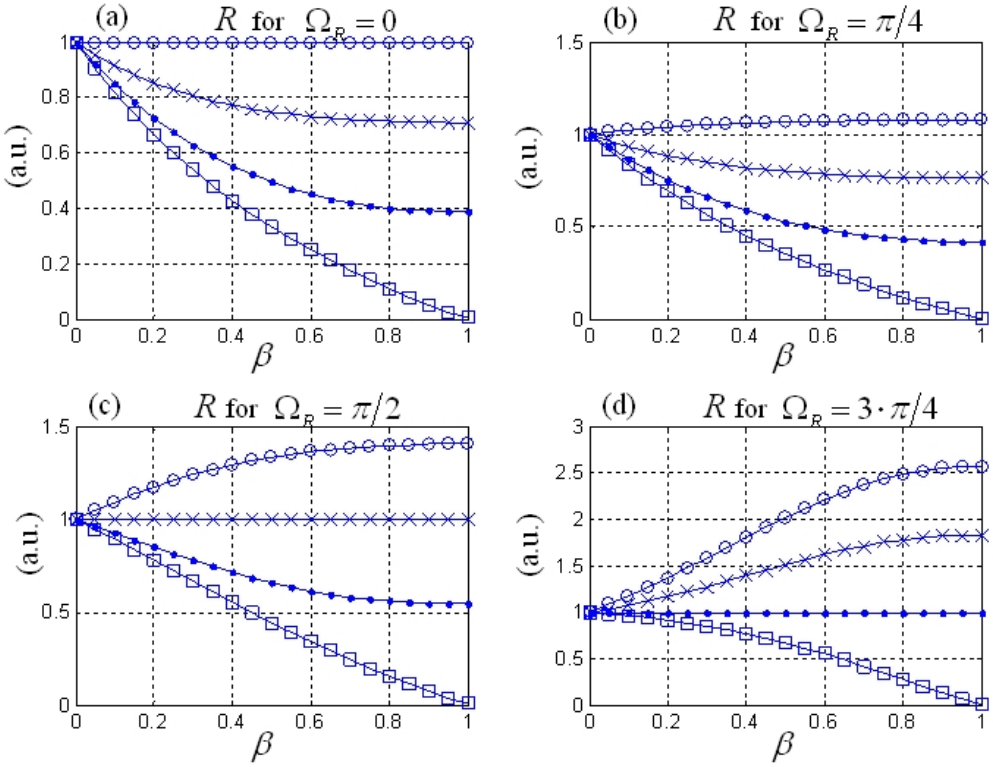

Fig. 6.30.- Theoretical curves for R parameter versus optical attenuation coefficient of the drop fibre β at different phase-shifts: (o) $\Omega_M = 0$, (x) $\Omega_M = \pi/4$, (•) $\Omega_M = 3\cdot\pi/4$, (□) $\Omega_M = \pi$.

When employing the proposed self-referencing technique, the reduction of the CWDM-PON power budget in the network is caused by the Optical Switch installed in the Central Office, and by the FBGs installed in the fibre outside plant.

The insertion loss of a typical MEMS 2x1 optical switch equals 0.7 dB. We measured negligible FBG transmission losses due to wavelength filtering, so the main attenuation of the data channels mainly consists of splicing losses, which equals 0.4 dB per drop fibre (considering 0.1 dB average splicing loss) being, consequently, 1.1dB the total attenuation of the components used in the proposed monitoring system for CWDM-PON.

Finally, a comparative analysis of the proposed RF-self-referencing and the most relevant monitoring techniques for WDM-PON systems is shown in Table 6.4, showing that the proposed technique can be considered a cost-effective approach with medium impact on the power budget of the network. Simple outside plant modifications are required, but this should not be considered a restriction, as even more complex modifications are also required in most of the previously reported techniques in literature.

	Proposed RF self-referencing+FBGs	U-band monitoring [13]	Brillouin OTDR+Brillouin shifted fibres [8]	Tunable OTDR+FBG[11]	ONT with Embedded OTDR [7]
Equipment cost and complexity	Very low	High	Very high	Very high	High
Number of elements	High	Low	High	High/Low	Very low
Outside plant modifications	Yes (simple)	No	Yes (very complex)	Yes (very simple)	Yes (complex)
Impact on power budget	Medium	Medium	Very low	Low	Very low

Table 6.4.- Comparative of the proposed RF self-referencing technique and other WDM-PON monitoring techniques [72].

The monitoring technique proposed in this section is suitable for in-service monitoring of Dense WDM-PON systems, while an optical switch is required in the Central Office for avoiding interference with data signals in active Coarse WDM-PON architectures. Furthermore, the proposed system can be applied to Dense WDM-PON systems cyclic with an AWG as Remote Node for in-service real time monitoring, taking advantage of the *N*-channel periodic response of the AWG filter in the O-band, E-band, S-band, C-band and L-band. As commercial WDM-PON systems use C-band for upstream transmission and E or L bands for downstream, the use of either O or S windows for transmission of the monitoring optical broadband signal can be proposed.

6.5 Summary and Conclusions

In this chapter, state-of-the-art of multiplexing techniques for passively addressing fibre-optic sensors has been developed. The main sensor network topologies for multiplexing have been described and compared between them in terms of optical power level per sensor, intrinsic crosstalk and number of components. On the other hand, different addressing techniques, focused on fibre-optic intensity-based sensor networks, have been presented showing their performance and limitations and, finally, emphasyzing wavelength division multiplexing (WDM) approaches. It can be concluded that these different multiplexing schemes produce a landscape of tradeoffs that can be optimized for any given application.

On the other hand, a radio-frequency electro-optical FBG-based CWDM sensor star network in reflective operation has been reported for self-referencing optical fibre intensity sensors. As previously seen in Chapter 5, by including two delay lines at the reception stage implemented in the electrical domain instead of using a single electrical delay line, arbitrary modulation frequencies can be set and phase shift reconfiguration can overcome tolerance errors permitting an easy-reconfigurable operation of the network. This means that any operation point for each remote sensor can be selected by means of their associated electrical phase-shifts at the reception stage, in terms of linearity response, sensitivity, resolution or another system property depending on specific requirements. In addition to this, the RF modulation permits also to avoid the effect of the flicker noise (1/f) at the reception stage.

Two self-referencing parameters, previously studied through the Z-transform formalism in Chapter 5, were experimentally tested. It was validated the self-reference property by simulating undesirable link losses up to 12dB. Also, it was demonstrated that no crosstalk is induced when two sensors operating in adjacent CWDM channels are simultaneously interrogated. The performance of the network in terms of sensitivity, linear response and resolution was studied showing that both parameters allow a linear response of the topology. Furthermore, in terms of sensitivity and resolution, the parameter R_i showed a better response than the output phase ϕ_i, that means, higher sensitivities can be achieved and resolutions around two orders of magnitude below can be obtained. However, whereas the output phase parameter provides multiple choices of the phase-shifts at the reception stage leading to the same network performance, the parameter R_i needs a more specific and controlled phase-shifts configuration at the reception stage in order to select an operation point for each remote sensing point. So depending on the specific characteristic of the sensor and the main target (as for example resolution or linearity in a greater range) one or another configuration will be selected.

The reported network follows the topology of WDM PON for broadband access in the optical communications market, so low-cost off-the-shelf devices are available for building and scaling the network. Furthermore, the development of this sensor network topology can enhance the automation and integration of sensor applications and systems within the next-generation broadband access network.

Finally, a new approach for individually monitoring optical power loss of drop fibres in access WDM-PON systems is presented, using the novel flexible and re-configurable RF self-referencing parameter described in Chapter %. The monitoring technique has been studied for Coarse WDM-PON architectures as a first approach to in-service monitoring of Dense WDM-PON systems.

6.6 References

[1] A.D. Kersey, A. Dandridge, A.B. Tveten, "Overview of Multiplexing Techniques for Interferometric Sensors," in *Proc. of SPIE: Fiber Optic and Laser Sensors*, 1987, pp. 184-193.

[2] E. Udd, *Fiber Optic Sensors: An Introduction for Engineers and Scientists*. New York: Wiley Interscience, 1991.

[3] E. Udd, *Fiber Optic Smart Structures*. New York: John Wiley&Sons Inc., 1995.

[4] B. Culshaw, J.P. Dakin, *Optical Fibre Sensors: Systems and Applications* vol. 2, pp. 511. London: Artech, 1989.

[5] J. M. López-Higuera, *Handbook of Optical Fibre Sensing Technology*. New York: John Wiley&Sons Inc., 2002.

[6] J. Prat, *Next-Generation FTTH Passive Optical Networks*. Barcelona: Springer, 2008.

[7] D. A. Jackson, A. B. L. Ribeiro, L. Reekie, and J. L. Archambault, "Simple multiplexing scheme for a fiber-optic grating sensor network," *Opt. Lett.*, vol. 18, pp. 1192-1194, 1993.

[8] J. Montalvo, C. Vázquez, and D. S. Montero, "CWDM self-referencing sensor network based on ring resonators in reflective configuration," *Opt. Express*, vol. 14, pp. 4601-4610, 2006.

[9] B. Moslehi, M. R. Layton, and H. J. Shaw, "Efficient fiber-optic structure with applications to sensor arrays," *J. Lightwave Technol.*, vol. 7, pp. 236-243, 1989.

[10] A. D. Kersey, A. Dandridge, and K. L. Dorsey, "Transmissive serial interferometric fiber sensor array," J. *Lightwave Technol.*, vol. 7, pp. 846-854, 1989.

[11] S. Abad, M. López-Amo, J. M. López-Higuera, D. Benito, A. Unanua, and E. Achaerandio, "Single and double distributed optical amplifier fiber bus networks with wavelength-division multiplexing for photonic sensors," *Opt. Lett.*, vol. 24, pp. 805-807, 1999.

[12] M. Lopez-Amo, L. T. Blair, and P. Urquhart, "Wavelength-division-multiplexed distributed optical fiber amplifier bus network for data and sensors," *Opt. Lett.*, vol. 18, pp. 1159-1161, 1993.

[13] R. Hernandez-Lorenzo, M. Lopez-Amo, and P. Urquhart, "Single and double distributed optical amplifier fiber bus networks with wavelength division multiplexing for photonic sensors," J. *Lightwave Technol.*, vol. 16, pp. 485-489, 1998.

[14] A. B. L. Ribeiro, R. F. Caleya, and J. L. Santos, "Progressive ladder network topology combining interferometric and intensity fiber-optic-based sensors," *Appl. Opt.*, vol. 34, pp. 6481-6488, 1995.

[15] S. Abad, F. M. Araujo, L. A. Ferreira, J. L. Santos, and M. Lopez-Amo, "Multiplexing of fibre optic intensity sensors using fused biconical wavelength selective couplers," *Electronics Letters*, vol. 37, pp. 490-491, 2001.

[16] A. B. L. Ribeiro, Y. J. Rao, L. Zhang, I. Bennion, and D. A. Jackson, "Time-and-spatial-multiplexing tree topology for fiber-optic Bragg-grating sensors with interferometric wavelength-shift detection," *Appl. Opt.*, vol. 35, pp. 2267-2273, 1996.

[17] C. McGarrity and D. A. Jackson, "Time-Division Multiplexed Topology for Michelson Interferometer Sensors to Measure Low-Frequency Measurands," *Optics Communications*, vol. 104, pp. 280-284, 1994.

[18] C. McGarrity and D. A. Jackson, "4-Sensor Time-Division Multiplexed Michelson Topology for Low-Frequency Measurands," *Distributed and Multiplexed Fiber Optic Sensors Ii*, vol. 1797, pp. 218-227, 1993.

[19] J. C. Walker, R. Holmes, and G. R. Jones, "Multiplexing optical sensors using spatial light modulator," *Electronics Letters*, vol. 27, pp. 2022-2023, 1991.

[20] Y. Hu and S. Chen, "Spatial-frequency-multiplexed optical fiber sensor array for structure monitoring," *Opt. Lett.*, vol. 20, pp. 2143-2145, 1995.

[21] Y. Hu and S. Chen, "Spatial frequency multiplexing of optical fiber sensor arrays," *Opt. Lett.*, vol. 20, pp. 1207-1209, 1995.

[22] A. D. Kersey, A. Dandridge, and A. B. Tveten, "Time-division multiplexing of interferometric fiber sensors using passive phase-generated carrier interrogation," *Opt. Lett.*, vol. 12, pp. 775-777, 1987.

[23] A. R. Nelson, D. H. McMahon, and H. van de Vaart, "Multiplexing system for fibre optic sensors using pulse compression techniques," *Electronics Letters*, vol. 17, pp. 263-264, 1981.

[24] L.A. Ferreira, P. Cavaleiro and J.L. Santos, "Demodulation of two time-multiplexed fibre Bragg sensors using spectral characteristics," *Pure and Applied Optics*, vol. 6, p. 717, 1997.

[25] S. Joar and B. Kjell, "Optical Amplifiers in Time Domain Multiplexed Sensor Systems," in *Optical Fiber Sensors*, 1997, p. OThD6.

[26] A. R. Nelson, D. H. McMahon, and R. L. Gravel, "Passive multiplexing system for fiber-optic sensors," *Appl. Opt.*, vol. 19, pp. 2917-2920, 1980.

[27] A. D. Kersey, A. Dandridge, and M. A. Davis, "Code-division Multiplexed Interferometric Array With Phase Noise Reduction And Low Crosstalk," in *Optical Fiber Sensors Conference, 1992. 8th*, 1992, pp. 266-269.

[28] A. D. Kersey, A. Dandridge, and M. A. Davis, "Low-crosstalk code-division multiplexed interferometric array," *Electronics Letters*, vol. 28, pp. 351-352, 1992.

[29] Y. H. Huang, L. Chao, P. Wai, and H. Y. Tam, "Large-scale FBG sensors utilizing code division multiplexing," in *Conference on Lasers and Electro-Optics and Conference on Quantum Electronics and Laser Science. CLEO/QELS 2008*, pp. 1-2, 2008.

[30] J. C. Walker, R. Holmes, and G. R. Jones, "Network of 12 optical sensors using code-division multiplexing," *Electronics Letters*, vol. 28, pp. 2074-2075, 1992.

[31] D. G. Uttamchandani and H. S. Al-Raweshidy, "Spread spectrum technique for passive multiplexing of interferometric optical fiber sensors," in *Fiber Optic Sensors: Engineering and Applications*, The Hague, Netherlands, 1991, pp. 212-219.

[32] F. Kullander, C. Laurent, S. Zyra, and H. Geis, "Crosstalk reduction in a code division multiplexed optical fiber sensor system," *Optical Engineering*, vol. 37, pp. 2104-2107, 1998.

[33] P. K. C. Chang, W. Jin, and M. S. Demokan, "Frequency division multiplexed operation of fiber Bragg grating sensors using sub carrierintensity modulation," in *Optical Fiber Sensors*, 1997, p. OThC15.

[34] D.-T. Jong and K. Hotate, "Frequency division multiplexing of optical fiber sensors using an optical delay loop with a frequency shifter," *Appl. Opt.*, vol. 28, pp. 1289-1297, 1989.

[35] J. Mlodzianowski, D. Uttamchandani, and B. Culshaw, "A simple frequency domain multiplexing system for optical point sensors," J. *Lightwave Technol.*, vol. 5, pp. 1002-1007, 1987.

[36] C. A. Wade, M. J. Marrone, A. D. Kersey, and A. Dandridge, "Multiplexing of sensors based on fibre-optic differential delay RF filters," *Electronics Letters*, vol. 24, pp. 1557-1559, 1988.

[37] J. R. Lord, P. L. Fuhr, J. W. B. Spillman, and B. R. Kline, "Self-referencing frequency division multiplexing technique for fiber optic sensors," *Optical Engineering*, vol. 29, pp. 148-153, 1990.

[38] K. I. Mallalieu, R. Youngquist, and D. E. N. Davies, "FMCW of optical source envelope modulation for passive multiplexing of frequency-based fibre-optic sensors," *Electronics Letters*, vol. 22, pp. 809-810, 1986.

[39] M.J. Marrone, A. D. Kersey, A. Dandridge, C.A. Wade, "Quasi-distributed fiber optic sensor system with subcarrier filtering," in *Optical Fibre Sensors OFS'89*, Berlin, 1989, p. 519.

[40] V. Gusmeroli, "High-performance serial array of coherence multiplexed interferometric fiber-optic sensors," J. *Lightwave Technol.*, vol. 11, pp. 1681-1686, 1993.

[41] A. D. Kersey and A. Dandridge, "Phase-noise reduction in coherence-multiplexed interferometric fibre sensors," *Electronics Letters*, vol. 22, pp. 616-618, 1986.

[42] J. L. Brooks, B. Y. Kim, H. J. Shaw, M. Tur, and R. C. Youngquist, "Coherence multiplexing of fiber-optic interferometer sensors," in *Optical Fiber Sensors*, 1985, p. ThBB4.

[43] J. Brooks, R. Wentworth, R. Youngquist, M. Tur, K. Byoung, and H. Shaw, "Coherence multiplexing of fiber-optic interferometric sensors," J. *Lightwave Technol.*, vol. 3, pp. 1062-1072, 1985.

[44] Z. Wang and C. Xie, "Automatic optical polarization demultiplexingfor polarization division multiplexed signals," *Opt. Express*, vol. 17, pp. 3183-3189, 2009.

[45] F. Yamashita, J. Abe, K. Kobayashi, and K. Ohata, "Polarization Tracking Free Ku Broadband Mobile Satellite Communications System- Variable Polarization Frequency Division Multiplexing (VPFDM)," in *4th Advanced Satellite Mobile Systems, ASMS 2008*, pp. 60-65, 2008.

[46] J. Abe, F. Yamashita, and K. Kobayashi, "Adaptive Multi-Carrier Demodulator for Variable Polarization Frequency Division Multiplexing," in *IEEE 70th Vehicular Technology Conference Fall (VTC 2009-Fall)*, pp. 1-5, 2009.

[47] G. Maier, M. Martinelli, A. Pattavina, and E. Salvadori, "Design and cost performance of the multistage WDM-PON access networks," J. *Lightwave Technol.*, vol. 18, pp. 125-143, 2000.

[48] M. P. McGarry, M. Reisslein, and M. Maier, "WDM Ethernet passive optical networks," *IEEE Communications Magazine*, vol. 44, pp. 15-22, 2006.

[49] C. Wang-Rong, L. Hui-Tang, H. Sheng-Jhe, and L. Chai-Lin, "A Novel WDM EPON Architecture with Wavelength Spatial Reuse in High-Speed Access Networks," in *15th IEEE International Conference on Networks, 2007. ICON 2007*, pp. 155-160, 2007.

[50] E. Achaerandio, S. Jarabo, S. Abad, and M. Lopez-Amo, "New WDM amplified network for optical sensor multiplexing," *IEEE Photon. Tech. Lett.*, vol. 11, pp. 1644-1646, 1999.

[51] D.S. Montero, C. Vazquez, J.M. Baptista, J.L. Santos, J. Montalvo, "Coarse WDM networking of self-referenced fiber-optic intensity sensors with reconfigurable characteristics," *Opt. Express*, vol. 18, pp. 4396-4410, 2010.

[52] K. P. Koo, A. B. Tveten, and S. T. Vohra, "DWDM of fiber Bragg grating sensors without sensor spectral dynamic range limitation using CDMA," in *Optical Fiber Communication Conference, 1999, and the International Conference on Integrated Optics and Optical Fiber Communication. OFC/IOOC '99. Technical Digest*, 1999, pp. 168-170 vol.4.

[53] G. A. Cranch and P. J. Nash, "Large-scale multiplexing of interferometric fiber-optic sensors using TDM and DWDM," *J. Lightwave Technol.*, vol. 19, pp. 687-699, 2001.

[54] X. Wan and H. F. Taylor, "Multiplexing of FBG sensors using modelocked wavelength-swept fibre laser," *Electronics Letters*, vol. 39, pp. 1512-1514, 2003.

[55] K. Chang-Seok, L. Tae Ho, J. Myung Yung, Y. Yun Sik, H. Young-Geun, and L. Sang Bae, "Multiple FBG Sensor Interrogation Using Cascaded Fiber Sagnac Loop Filters," in *Optical Fiber Sensors*, 2006, p. TuE14.

[56] C.S. Kim, T. H. Lee, Y. S. Yu, Y.G. Han, S. B. Lee, and M. Y. Jeong, "Multi-point interrogation of FBG sensors using cascaded flexible wavelength-division Sagnac loop filters," *Opt. Express*, vol. 14, pp. 8546-8551, 2006.

[57] J. Montalvo, O. Frazao, J. L. Santos, C. Vazquez, and J. M. Baptista, "Radio-Frequency Self-Referencing Technique With Enhanced Sensitivity for Coarse WDM Fiber Optic Intensity Sensors," *J. Lightwave Technol.*, vol. 27, pp. 475-482, 2009.

[58] C. Xiaofei, W. Yang Jing, X. Zhaowen, S. Xu, W. Yixin, and Y. Yong-kee, "10-Gb/s WDM-PON transmission using uncooled, directly modulated free-running 1.55-μm VCSELs," in *34th European Conference on Optical Communication, 2008. ECOC 2008*, 2008, pp. 1-2.

[59] X. Zhaowen, W. Yang Jing, C. Chang-Joon, W. Yixin, and L. Chao, "10 Gb/s WDM-PON upstream transmission using injection-locked Fabry-Perot laser diodes," in *Optical Fiber Communication Conference, 2006 and the 2006 National Fiber Optic Engineers Conference. OFC 2006*, pp. 3, 2006.

[60] Z. Xu, Y. J. Wen, W.-D. Zhong, T. H. Cheng, X. Cheng, Y. Wang, and Y.-K. Yeo, "10-Gb/s WDM-PON based on FP-LDs injection locked by downlink optical carrier," *Optics Communications*, vol. 281, pp. 5213-5217, 2008.

[61] N. Nakao, H. Izumita, T. Inoue, Y. Enomoto, N. Araki, and N. Tomita, "Maintenance method using 1650-nm wavelength band for optical fiber cable networks," J. *Lightwave Technol.*, vol. 19, pp. 1513-1520, 2001.

[62] K. Enbutsu, N. Araki, N. Honda, and Y. Azuma, "Individual fiber line testing technique for PON using wavelength assigned FBG termination and TLS-OTDR enhanced with reflected trace analysis method," in *Joint conference of the Opto-Electronics and Communications Conference, 2008 and the 2008 Australian Conference on Optical Fibre Technology. OECC/ACOFT 2008*, 2008, pp. 1-2.

[63] K. Enbutsu, N. Araki, N. Honda, and Y. Azuma, "Individual fiber line testing technique for PONs using TLS-OTDR enhanced with reflected backward light analysis method," in *Optical Fiber Communication - incudes post deadline papers, 2009. OFC 2009. Conference on*, 2009, pp. 1-3.

[64] K. Yuksel, S. Letheux, A. Grillet, M. Wuilpart, D. Giannone, J. Hancq, G. Ravet, and P. Megret, "Centralised Optical Monitoring of Tree-structured Passive Optical Networks using a Raman-assisted OTDR," in *9th International Conference on Transparent Optical Networks, 2007. ICTON '07*, 2007, pp. 175-178.

[65] H. Fathallah and L. A. Rusch, "Code-division multiplexing for in-service out-of-band monitoring of live FTTH-PONs," *J. Opt. Netw.*, vol. 6, pp. 819-829, 2007.

[66] W. Chen, B. de Mulder, J. Vandewege and X.Z. Qiu, "Embedded OTDR monitoring of the fiber plant behind the PON power splitter," in *Proc. Symp. IEEE/LEOS Benelux Chap.*, Eindhoven, Netherlands, 2006, pp. 13-16.

[67] N. Honda, D. Iida, H. Izumita, and F. Ito, "Bending and connection loss measurement of PON branching fibers with individually assigned Brillouin frequency shifts," in *Optical Fiber Communication Conference, 2006 and the 2006 National Fiber Optic Engineers Conference. OFC 2006*, 2006, p. 3 pp.

[68] L. Yao, W. Daoyi, and L. Jing, "FTTH remote fiber monitoring using optical wavelength domain reflectometry (OWDR) and wavelength coded tag (WCT)," in *Optical Fiber Communication Conference, 2006 and the 2006 National Fiber Optic Engineers Conference. OFC 2006*, 2006, p. 3 pp.

[69] M. Thollabandi, K. Tae-Young, H. Swook, and P. Chang-Soo, "Tunable OTDR Based on Direct Modulation of Self-Injection-Locked RSOA for In-Service Monitoring of WDM-PON," IEEE *Photon. Tech. Lett.*, vol. 20, pp. 1323-1325, 2008.

[70] J. Park, J. Baik, and C. Lee, "Fault-detection technique in a WDM-PON," *Opt. Express*, vol. 15, pp. 1461-1466, 2007.

[71] L. Ju Han, L. Kwanil, H. Young-Geun, L. Sang Bae, and K. Chul Han, "Single, Depolarized, CW Supercontinuum-Based Wavelength-Division-Multiplexed Passive Optical Network Architecture With C-Band OLT, L-Band ONU, and U-Band Monitoring," J. *Lightwave Technol.*, vol. 25, pp. 2891-2897, 2007.

[72] D. S. M. J. Montalvo, C. Vázquez, J.M. Baptista, J.L. Santos, "Radio-Frequency Self-Referencing System for Monitoring Drop Fibres in WDM Passive Optical Networks," *IET Optoelectronics*, vol.4(6), pp. 226-234,, 2010.

Chapter 7

CONCLUSIONS AND FUTURE WORK

7.1 Research Contributions

The residential user has a growing need for multiple groups of broadband services, such as (increasingly personalized) video services, fast internet, high-quality audio, etc, commonly grouped as next-generation access (NGA) services. Moreover, these new interactive services require a broadband communications access network, which should extend into the customer's premises, and even up to the terminals. In addition to the multimedia services described so far, sensing and control applications are gaining more and more interest in the in-building scenario. There is a widely-spread consensus that FTTx is the most powerful and future-proof access network architecture for providing broadband services to residential users. Furthermore, FTTx deployments with WDM-PON topologies are considered in the long-term the target architecture for the next-generation access networks. And singlemode optical fibre, by virtue of its tremendous bandwidth and huge transport capacity for many services, is used in the FTTx system concepts deployed up to now.

However, multimode optical fibres (MMF), both silica- and polymer-based, can also offer the physical infrastructure to create a fusion and convergence of the access network via FFTx for next-generation access (NGA) services. Furthermore, the increasing in-building networking feasibility can enhance the automation and integration of optical sensor applications and systems, and vice versa. Both fibres types may be used not only to transport fixed data services but also to transparently distribute in-building (and also for short- and medium-reach links) signals of present and future broadband services leading to a significant system-wide cost reduction. In addition to, in-building optical-based sensing and control applications are of utmost importance for the reliability requirements of these networks.

So, a full-optical convergent deployment scenario of such emerging NGA network technology is contingent with the research and evaluation of predictive models for the frequency response, both for silica-based multimode optical fibres and graded-index polymer optical fibres, respectively.

In this research field, some contributions on the development and validation of those models are reported. We summarize them as follows:

- The influence of most paremeters that modify the frequency response in such multimode fibres has been addressed by means of a set of theoretical simulations. Those simulations have been carried out for a standard silica-based multimode optical fibre as well as for a PMMA-based and PF-based GIPOF.

- The results reveal that the behavior of the PF GIPOF frequency response expected by the theoretical model presented shows a good agreement with the experimental measurements. To the author's knowledge the PF GIPOF frequency response experimental measurements show, for the first time, experimental data that validate, with tolerable discrepancy, the model. Furthermore, the results reveal that also the PF GIPOF has some latent high-order passbands which opens up the extend of the tranmission capabilities through these secondary lobes.

- It has been proved that PF GIPOF 3-dB bandwidth values that are achievable using restricted mode launching (RML) are higher than those obtained using an over-filled (OFL) or uniform launching. It has been experimentally demonstrated that PF GIPOF enables Gigabit transmission over 200m and 10-Gigabit transmission over 50m, although these values can be improved by including a more controlled launching condition set-up. In addition to, the fibre core radius, wavelength and source linewidth-dependence of the PF GIPOF frequency response have also been addressed through experimental results.

- The long-term stability and temperature dependence of PF GIPOF link has also been addressed showing that both effects must be considered and properly controlled because they affect significantly the frequency response performance. PF GIPOF 3-dB bandwidth deviations against temperature have been measured to be in the order of 15-30% full scale from the nominal value.

- The use of narrow-linewidth optical sources results in a relatively flat silica-based MMF frequency response (up to the maximum measured frequency of 20GHz). In contrast, higher source linewidths, such as Fabry-Perot lasers, Broadband Light Sources or LEDs, make more significant the low-pass effect in the silica-based MMF frequency response. In those cases, the MMF frequency response falls dramatically after a few GHz. It has also been experimentally tested that the transversal filtering effect of the MMF link is significantly reduced when applying a RML condition. Consequently, the combination of selective mode-launching schemes combined with the use of narrow-linewidth optical sources has been confirmed to enable broadband RF, microwave and millimetre-wave transmission in short- and middle-reach distances, overcoming the typical silica-based MMF bandwidth per length product, as other authors have been recently proposed in literature.

- It has been experimentally verified in silica-based MMFs that: (a) the Free Spectral Range (FSR) of the high-order resonances is reduced proportionally with the increase of the link length; (b) the contrast ratio between high-order resonances and the secondary side-lobes is reduced for lower link lengths; and

(c) 3-dB high-order resonance bandwidths decrease at higher link lengths. All these performances are due to the fact that the MMF link behaves as an imperfect transversal filter. These facts together have been confirmed by experimental measurements.

- In addition to, thermal effects on the silica-based MMF frequency response have been studied demonstrating their influence on the high-order resonances. It has been demonstrated that temperature must be taken into account when selecting a transmission band far from baseband for high-speed data rates applications. Secondary lobes central frequencies and 3-dB secondary lobe-bandwidths have been experimentally verified to show little dependence with environmental temperature. However, results concerning hysteresis show that high-dependence on temperature cycles of heating/cooling are noticed.

On the other hand, fibre-optic sensors exhibit a set of very attractive characteristics, including immunity to electromagnetic interference, resistance to hostile environments that may comprise hazardous chemicals or of any other kind, flexibility, geometric versatility, sensor multiplexing and distributed sensing over a single fibre. These are some reasons underlying the increasingly gaining interest of applications and systems based in fibre-optic technology, in the building/home scenario. This work focuses on those ones based on intensity modulation, in which the magnitude to be measured produces a detectable change in the intensity of light. This approach has been proved to provide simple (and potentially) low-cost devices because it is easier to measure the optical power than the phase or the state-of-polarisation. Accordingly, a state-of-the-art of the different self-referencing techniques for optical intensity sensors has been reported, paying special attention to frequency-based methods which include resonant structures operating in an incoherent regime. In addition to this interrogation technique, a special focus has been given to reflective Fibre Bragg Grating (FBG) based configurations because they have been demonstrated to be effective approaches for addressing optical intensity sensors that permit the use of a single fibre lead in both propagating directions of the light, as well as opening up wavelength-division-multiplexing (WDM) capabilities. Related to this latter fact, an efficient multiplexing and self-referencing scheme for optical fibre intensity sensors described in this work has also been demonstrated. Furthermore, a new approach for individually monitoring optical power loss of drop fibres in access WDM-PON systems has been reported, based on the self-referencing configuration and the measurement parameter proposed, as a first approach to their application in Dense Wavelength-Division-Multiplexing Passive Optical Networks (WDM-PON). These WDM-PON topologies are considered in the long-term the target architecture for the next-generation access networks in FTTx deployments. Finally, the Z-transform formalism, inside the discrete-time optical signal processing framework, has been applied to the mathematical analysis of the proposed configuration and multiplexing scheme for self-referencing fibre-optic intensity-based sensors.

Within this research field, some original contributions to the state-of-the-art of self-referencing techniques are reported. We summarize them as follows:

- The digital filter theory has been applied to the design and analysis of the proposed self-referencing technique. Closed-form formulas for the description of the transfer function versus sensor-induced power modulation have been reported.

- Two different self-referencing measurement parameters have been studied and experimentally verified partially using a previously proposed electro-optical configuration consisting of two Fibre Bragg Gratings with an optical intensity sensor located between them, avoiding the use of a long delay fibre coil. Such configuration provides arbitrary modulation frequencies, compact sensing heads and flexibility of operation because of the deployment of two electronic delays, instead of one, made of low cost commercial components, at the reception stage. One of the novel measurement parameters, namely R, is defined as the ratio between voltages (associated to the reference and sensing channel, respectively) at the reception stage and is reported for the first time in such a self-referencing configuration.

- A novel electro-optical self-referencing radio-frequency FBG-based CWDM fibre-optic intensity sensor network with a reflective star topology for multiplexing and interrogation of *N* remote sensing points has been proposed and analyzed. By including two delay lines at the reception stage implemented in the electrical domain instead of using a single electrical delay line, arbitrary modulation frequencies can be set and phase shift reconfiguration can overcome tolerance errors permitting an easy-reconfigurable operation of the network. This means that any operation point for each remote sensor can be selected by means of their associated electrical phase-shifts at the reception stage, in terms of linearity response, sensitivity, resolution or another system property depending on specific requirements. The proposed configuration has been studied for two defined measurement parameters (R, defined above, and the output phase ϕ) for a generic remote sensing point of the network. The self-reference property, by simulating undesirable link losses up to 12dB, has been validated. Also, it has been demonstrated that no crosstalk is induced when two sensors operating in adjacent CWDM channels are simultaneously interrogated. The performance of the network in terms of sensitivity, linear response and resolution was studied showing that both parameters allow a linear response of the topology. Furthermore, in terms of sensitivity and resolution, the parameter R showed a better response than the output phase ϕ that means, higher sensitivities can be achieved and resolutions around two orders of magnitude below can be obtained considering R as the self-referencing parameter of the network.

- The R self-referencing parameter using RF-modulation has been applied for individually monitoring optical power loss of drop fibres in access WDM-PON systems by deploying low-cost electrical delay line filters in the monitoring unit. The monitoring technique is suitable for in-service monitoring of Dense WDM-PON systems, while an optical switch is required in the Central Office for

avoiding interference with data signals in active Coarse WDM-PON architectures. All the components and devices of the monitoring system are low cost and available in the mass-market, thus providing a cost-effective approach for monitoring the outside plant of WDM-PON. The monitoring system has been experimentally validated in a Coarse WDM in star topology, with two simultaneous monitoring channels and a reach distance of 10 km. Improving the reflectivity of the FBGs we estimate a maximum reach of 25 km. By using a Broadband Light Source with a spectrum within the 1270 to 1610 nm band, we estimate that a low-cost monitoring system for a CWDM PON with up to 16 drop fibres could be demonstrated.

7.2 Future Research Directions

Finally, several issues related to the results reported in this work can be considered in a further detail as future research. Some of them are described below.

The theoretical models described within this work, and developed elsewhere; try to analyzed the influence of several factors that can have a large impact on the data rate transmission performance in multimode optical fibre links, thus allowing an estimation of the frequency response and the total bandwidth. However, effects such as the presence of peaks/dips at the core centre or other core profile imperfections, effects due to the polarization of the light propagating, connector misalignments that could lead to significant variations in the coupled power into the fibre modes or the mode power distribution along the link, and environmental temperature changes over the fibre link, for instance, have not been directly included. Also, other effects have not been fully addressed or have been assumed by means of statistical processes. As it has been addressed during this work, both types of multimode optical fibre link have big possibilities but require further research and evaluation of, even more, accurate predictive models for the frequency response. Other most specific topics to be covered are:

- A theoretically and experimentally comparative study of both models evaluated within this work would be an interesting topic. Although they try to solve the numerous factors affecting the frequency response of multimode optical fibres, the different assumptions made during the development of the mathematical framework needs to be carefully analyzed before making any comparison.

- In order to accurately evaluate selective mode-launching conditions, a XYZ-mounted stage to allow the positioning of the incident light relative to the multimode fibre, for both silica- and polymer-based counterparts, can be applied. Multiple measurements of parameters such as the offset launch, the axial launch, the launching angle or the incident beam spot diameter could be experimentally tested and included in the fibre frequency response theoretical models. Even novel twin-spot launch schemes, which can provide better performances in terms of bandwidth, could also be investigated. Currently, our research group is putting

much effort on this topic with a recently purchased motorized and automated micro positioning stage.

- Commercially available Dense WDM devices, promoted by the high-speed optical communications market, can be used to scale the sensor network reported in this work. A colorless DWDM (1.6nm channel spacing, ITU-T G.694.1) upgrading of the 5 CWDM channels within the C+L bands (1528-1622nm) can be achieved by employing commercial band splitting based on commercial Arrayed Waveguide Gratings (AWG). These devices can achieve 50GHz channel separation. By adding 40 channels within each of the 5 CWDM bands in the 1520-1610nm range, a maximum number over 200 multiplexed optical intensity sensors could be addressed with this upgrade approach. On the other hand, as the power density per sensor channel is reduced, remote amplification or different transmission stages might also be required.

- The proposed self-referencing configuration has been experimentally validated in a Coarse WDM star topology with two simultaneous monitoring channels and a reach distance of 10 km. Improving the reflectivity of the FBGs we estimate a maximum reach of 25 km. However, the concept of remote sensing is applied to fibre-optic sensor systems ranging from 2 m up to 230 km depending on the application. Most of the recently reported remote sensing systems consider 50 km as the reference length. In order to overcome the limitation due to power budget in this self-referencing configuration, optical amplification could be proposed and implemented. Still, the inclusion of active fibre within the network originates a new source of noise, namely, amplified spontaneous emission noise (ASE) which reduces the optical signal-to-noise ratio of the system and, therefore, limits the operation range and sensitivity of the multiplexed sensors. To achieve a remote distance enhancement, an Erbium-Doped Fiber Amplifier (EDFA) or Raman amplification could be included in the proposed technique for self-referencing remote interrogation of sensors.

- The monitoring system can be applied to colourless Dense WDM-PON systems with a cyclic AWG, as Remote Node for in-service real time monitoring, taking advantage of the *N*-channel periodic response of the AWG filter in the O-band, E-band, S-band, C-band and L-band. As communication applications tend to use mainly C-band and L-band, monitoring systems can take advantage of deployed WDM-PON AWG-based networks in the O-band, E-band or S-band in order to not interfere with data traffic thus providing an on-line network monitoring method.

- Linked with the latter proposal, measurements of data traffic and remote sensor networks integrated in the same WDM-PON topology would be of great interest where the relevance of the inter-channel effect must be taken into account as well as parameters such as the Bit Error Rate (BER) or dispersion compensation effects. As different wavelength-bands would be used, it is supposed that no interference between both measurements will be noticed. Furthermore,

simulations performed with the software from VPIphotonics, considering an optical WDM-PON communications link plus an associated monitoring system could be interesting to validate the idea, previously to undertake the experimental measurements. As VPIphotonics software is a powerful tool for designing and evaluating optical communication networks, efforts should be focused on efficiently describing the proposed electro-optical configuration in such a tool.

Capítulo 8

RESUMEN DEL TRABAJO REALIZADO

8.1 Introducción

La demanda e incursión en la sociedad de nuevos servicios multimedia, tales como televisión por Internet (IPTV, Internet Protocol Television) o video-bajo-demanda (VoD, Video on Demand) junto con el incremento del tráfico de datos requerido para nuevas aplicaciones como la televisión por alta definición (HDTV, High-Definition Television) y transferencias P2P (Peer-to-Peer) exigen un aumento de la capacidad de las redes de datos desplegadas hoy en día. Para hacer frente a este aumento de la demanda de capacidad de las redes de acceso, los proveedores de estos servicios multimedia están reemplazando las infraestructuras de las redes de acceso basadas en cable coaxial, tales como xDSL (x-Digital Subscriber Line), por otras nuevas de mayor capacidad desplegadas en fibra óptica, permitiendo la interconexión de los nodos de red con los múltiples hogares y negocios de los abonados, constituyendo el núcleo de lo que es conocido como “fibra hasta el hogar/nodo/edificio” o redes FTTx.

Tradicionalmente el despliegue de las redes ópticas se ha realizado mediante fibra óptica monomodo de sílice (SMF, Singlemode Fibre). Ello es debido a su gran ancho de banda que permite una gran capacidad de transporte de servicios y datos. Es por ello que en base a este tipo de fibra se ha realizado el despliegue de redes de distribución y metropolitanas y, de un tiempo a esta parte, incluso penetrando su instalación en las redes de acceso. Junto con lo anteriormente expuesto, existe una necesidad de convergencia de servicios e infraestructuras dentro de las redes de acceso. Actualmente, cables coaxiales, par trenzado de cobre e incluso señales inalámbricas se encuentran entremezcladas dentro del hogar proporcionando servicios diferentes con apenas cooperación entre ellos. Una infraestructura común dentro del hogar en el que una gran cantidad de servicios pudieran ser integrados y soportados por la misma sería un aspecto deseable. Y es más, frente a las desventajas de infraestructuras basadas en cable de cobre (cable coaxial y par trenzado) como son susceptibilidad a interferencias electromagnéticas, presencia de crosstalk y relativa baja capacidad de transporte de datos, las fibras ópticas (tanto en su versión monomodo como multimodo) presentan las ventajas de un menor volumen, mayor flexibilidad y menor peso junto con una capacidad mayor de transmisión de datos sobre distancias mayores. Es por esto que éstas últimas constituyen la base para las futuras redes de acceso en el hogar.

Por una parte, debido a su reducido tamaño de núcleo de fibra (unidades de micrómetros), para la fibra monomodo se requieren elementos mecánicos de alta precisión y personal altamente cualificado para su manipulación. Por una parte, este hecho no ha sido obstáculo para el despliegue de redes ópticas de largo alcance. Sin embargo a medida que la red

óptica penetra cada vez más cerca del usuario final, el coste asociado a su instalación y mantenimiento constituye un elemento clave, llegando a no ser económicamente viable el despliegue de las redes ópticas de acceso de nueva generación mediante fibra óptica monomodo. Por el contrario, la fibra óptica multimodo (tanto en su versión de plástico como de sílice) presenta una alternativa con ahorro de costes comparada con la SMF. Ello es debido a que aquélla presenta un núcleo de fibra de dimensiones mayores que la fibra monomodo siendo, por tanto, más fácil de instalar y manipular, más fácil acoplar luz desde una fuente óptica a la propia fibra, más fácil para empalmar (del término anglosajón 'splice') dos tramos de fibra multimodo con menores pérdidas o presentando una mayor tolerancia a desalineamientos entre fibras. Todo lo anterior redunda en que la fibra óptica multimodo presenta una conectorización más barata junto con unos equipos ópticos asociados también más baratos. Además se necesita un personal menos cualificado a la hora de su manipulación, resultando todo ello en un ahorro significativo de costes de instalación y mantenimiento. Por otra parte, dentro de las fibras ópticas multimodo, las fibras ópticas de plástico (POF, Polymer Optical Fibre) presentan un menor coste asociado debido a su mayor facilidad de manipulación, conectorización y flexibilidad respecto de las basadas en sílice. Por todo lo anteriormente expuesto la fibra óptica multimodo (en ambas versiones de sílice o plástico) es la candidata ideal para el despliegue de las futuras redes ópticas de acceso en el hogar. Sin embargo presenta el inconveniente de poseer un ancho de banda menor, y por tanto menor capacidad de transmisión de datos, comparado con las SMF, debido a la dispersión modal producida por la propagación de un número determinado de modos a lo largo de la fibra.

Numerosas técnicas han sido propuestas en la literatura científica para extender esta limitación en la capacidad de transmisión impuesta por las fibras ópticas multimodo y así cumplir con los requerimientos de ancho de banda debidos a la demanda de servicios multimedia por parte de los usuarios. Técnicas como la multiplexación por diversidad de grupos modales (MGDM, Mode Group Diversity Multiplexing), la multiplicación de frecuencias en el dominio óptico (OFM, Optical Frequency Multiplication), la multiplexación por subportadora (SCM, SubCarrier Multiplexing) o la multiplexación por división en longitud de onda (WDM, Wavelength Division Multiplexing) han sido propuestas. Además, algunas de estas técnicas permiten incluso del empleo de aplicaciones de Radio-sobre-Fibra (RoF, Radio-over-Fibre), como son la transmisión de señales de acceso inalámbricas.

Una manera de aumentar la capacidad de transmisión intrínseca de las fibras ópticas multimodo es mediante el estudio de su respuesta en frecuencia, abriendo la posibilidad de transmitir señales e información más allá de la banda base, bien en la región de microondas (unidades de GHz) o, incluso, en la región de ondas milimétricas (decenas de GHz). Varios autores han sugerido que la característica espectral de las fibras ópticas multimodo presenta componentes o lóbulos a altas frecuencias siendo posible, por ejemplo, la transmisión de información modulada mediante una portadora situada en la región central de uno de esos lóbulos o incluso en regiones donde la respuesta en frecuencia presenta una respuesta casi plana a frecuencias mucho más allá de las frecuencias de banda base.

Por otra parte, es necesario para el despliegue de estas fibras ópticas multimodo en las futuras redes de acceso en el hogar, para la provisión de servicios multimedia a los

usuarios, el desarrollo y evaluación de modelos matemáticos predictivos lo más exactos posibles de la respuesta en frecuencia de dichas fibras, tanto en su versión de sílice como en su versión de plástico. Dicho modelo puede ayudar a aumentar la capacidad de transporte de datos en dichas fibras, para atender los requerimientos de datos, información y servicios demandados por parte de los usuarios, mediante el empleo de estas bandas de paso más allá del ancho de banda en banda base. Este hecho permite cumplimentar los requisitos de estándares de transmisión de información tales como Gigabit Ethernet y 10-Gigabit Ethernet, cuyas tasas de información se adecuan a las actuales demandas de capacidad por parte de los proveedores de servicios así como por parte de los usuarios. Además, mediante el empleo de este tipo de fibras se podrían integrar todos los servicios actualmente presentes en el hogar mediante una misma única infraestructura de 'dominio óptico' con sus inherentes ventajas anteriormente expuestas.

La primera parte de este trabajo se centrará en el análisis y evaluación experimental de modelos teóricos propuestos tanto para fibra óptica multimodo de sílice como para fibra óptica de plástico perfluorinada de índice gradual (PF GIPOF). El hecho de estudiar ambos tipos de fibra es, por una parte, el hecho de que entre el 85-90% del cableado óptico de las redes de acceso es fundamentalmente fibra multimodo de sílice con lo cual existe un claro interés por aprovechar este tipo de infraestructura ya instalada. Por otra parte, la fibra óptica de plástico perfluorinada de índice gradual es considerada por muchos autores como la infraestructura más prometedora para las redes de acceso en el hogar, aunque su despliegue no se encuentra al nivel de la fibra de sílice, puesto que presenta anchos de banda comparables o incluso superiores a las fibras ópticas multimodo, junto con una mayor flexibilidad y facilidad de manipulación gracias a su núcleo de fibra de tamaño mayor. Para ambos modelos, se han desarrollado simulaciones teóricas evaluando cómo se ve afectada la respuesta en frecuencia, en ambos tipos de fibra, en función de multitud de parámetros tales como la atenuación diferencial modal o el acoplo modal (ambos específicos de fibras ópticas multimodo), parámetros propios de la fibra óptica (radio del núcleo, longitud de la fibra o índice de refracción del núcleo) o parámetros propios de la fuente óptica empleada (anchura espectral, chirp o longitud de onda de emisión). Junto con ello, medidas experimentales para ambos tipos de fibra han sido llevadas a cabo, validando las conclusiones obtenidas teóricamente a partir de los modelos propuestos, junto con un análisis de cómo afectan otros parámetros externos, no considerados por los modelos, tales como la temperatura ambiente a la que se encuentra sometida la fibra.

Por otra parte, el campo de investigación de tecnologías de sensores es una de las áreas de mayor crecimiento actualmente, como puede deducirse de la enorme cantidad de artículos publicados sobre este tema durante las tres últimas décadas. Entre la amplia variedad de esquemas que actúan como sensores, los sensores de fibra óptica están ganando una importancia considerable, siendo su principal estímulo el desarrollo y avance de las comunicaciones a través de fibra óptica. Es más, la necesidad de convergencia en una única infraestructura en el dominio óptico para las redes de acceso en el hogar junto con la creciente demanda de automatización, control y sensado planeados en infraestructuras tanto de edificios como en hogares particulares (denominados Hogar Digital o Edificio Inteligente) ha impulsado definitivamente este tipo de tecnología. En los sensores de tipo óptico la información acerca del parámetro a medir se obtiene a partir de un haz de luz, a través de diferentes mecanismos que modulan ese haz de forma variable cuando sobre él

actúa un estímulo externo (físico, químico o biológico). Este efecto de la modulación puede traducirse en cambios directamente medibles como son cambios de la intensidad, la fase o la polarización de la luz. Los sensores ópticos son muy adecuados debido a que proporcionan una alta sensibilidad y una respuesta prácticamente inmediata, son inmunes a interferencias electromagnéticas, robustos y versátiles y por estas razones han encontrado muchas aplicaciones prácticas en monitorización medioambiental, procesos industriales y de control y en el campo biomédico. Así se están empleando en ambientes con grandes campos electromagnéticos (ej. centrales generación eléctrica), o en el entorno donde la generación de señales eléctricas es peligroso. (ej. oleoductos, centrales de producción de biogas, aviones, tanques de combustible), o en aplicaciones donde se precisan sistemas de pequeño tamaño y compatibles con el objeto u organismo a medir (ej. sensores biomédicos) o bien en lugares donde la temperatura ambiente es tan elevada que los sensores tradicionales no funcionan adecuadamente debido a múltiples factores (ej. acerías, fundiciones, soldadura).

La avanzada tecnología de bajo coste disponible es crucial para el éxito de los sistemas de sensores ópticos, que pueden aprovecharse de la tecnología de fibra y los métodos de fabricación de dispositivos producidos para telecomunicaciones. El principal esfuerzo de los investigadores se ha realizado en producir un conjunto de técnicas basadas en fibra óptica que puedan usarse para una amplia variedad de propósitos, proporcionando una buena base para una tecnología de medida efectiva que pueda complementar los métodos convencionales. Esta es la clave del éxito de los sensores de fibra óptica: la toma de medidas en situaciones difíciles para ambientes específicos, donde el uso de los sensores convencionales no es posible.

La aplicación de fibras ópticas tanto para transportar la señal como para operar como elemento activo del sensor (transductor) presenta una serie de ventajas en comparación con los sensores basados en medidas eléctricas como son inmunidad a interferencias electromagnéticas (ya que no hay corrientes eléctricas fluyendo por el sensor), intrínsicamente seguros en entornos hostiles o con peligro de explosión, baja atenuación (permitiendo medidas remotas del orden de decenas de km), capacidad de realizar medidas puntuales o distribuidas en muchos km de fibra, obtención de sensores compactos, ligeros y de tamaño reducido (lo cual facilita su transporte, instalación y mantenimiento), alta resistencia a la corrosión, aislamiento eléctrico y pasividad química, posibilidad de multiplexación (además de mejorar la eficiencia con la posibilidad de compatibilizar en una misma red de fibra las aplicaciones de comunicaciones con las de metrología) y accesibilidad a espacios difíciles, entre otras.

Dentro de la gran diversidad de las técnicas de instrumentación de medidas ópticas, los sensores de intensidad óptica son unos de los más utilizados e investigados en la actualidad, en los que la magnitud física provoca variaciones en la intensidad óptica transmitida por la fibra. Este tipo de sensores es extremadamente competitivo desde el punto de vista tecnológico y económico, pues, además de su simplicidad, los componentes asociados a este tipo de sensores son dispositivos comerciales de bajo coste. Estos sensores de fibra óptica han sido ampliamente investigados para la medida de parámetros tales como temperatura, presión, humedad, desplazamiento o nivel de líquidos, entre muchas otras. Sin embargo, a pesar de sus inherentes ventajas, presentan una serie de limitaciones, impuestas

por las fluctuaciones indeseables de potencia en el sistema debidas a variaciones en las pérdidas por conectores, empalmes, curvaturas producidas en la fibra o las debidas a los propios equipos emisores y detectores de luz. Por tanto, es necesaria la inclusión de estrategias de auto-referencia para el sensado remoto de los sensores de intensidad óptica que permitan minimizar o evitar la influencia de las variaciones de potencia óptica debidas a los equipos emisores y receptores, bien por envejecimiento de los mismos o inestabilidades térmicas de las condiciones ambientales, así como las fluctuaciones de potencia indeseadas, debidas a accidentes que afecten al cableado de fibra, actualizaciones de la topología de red o manipulación de los conectores entre otros motivos, producidas en el enlace que conecta la oficina central, donde las medidas son procesadas, con las cabezas sensoras, para así obtener medidas estrechamente ligadas a la magnitud que se desea medir de una manera fiable e independiente de las variaciones aleatorias de intensidad óptica anteriormente mencionadas.

Por otra parte, la capacidad de multiplexar de manera pasiva un determinado número de sensores constituye un gran atractivo desde el punto de vista de la eficiencia y de la reducción de costes asociados a este tipo de tecnología. Numerosos esquemas y técnicas de multiplexación de sensores ópticos, análogos a los esquemas propuestos para las comunicaciones por fibra óptica, han sido propuestos y desarrollados, siendo la división por tiempo (TDM, Time Division Multiplexing), frecuencia (FDM, Frequency Division Multiplexing) o longitud de onda (WDM, Wavelength Division Multiplexing) los más utilizados en los sistemas de comunicaciones actuales, véase las redes SONET o FTTx, por ejemplo.

Este despliegue de redes FTTx incluye las denominadas redes ópticas pasivas (PON, Passive Optical Network), esquemas actualmente en uso y que proporcionan tasas de transferencia de Gigabit por segundo, habiéndose desarrollado estándares tales como Gigabit Ethernet perfectamente soportados por este tipo de redes. Actualmente, existe una tendencia a plantear una nueva migración de las redes de acceso aprovechando el desarrollo de equipos basados en tecnología WDM, tales como CWDM (Coarse WDM, Multiplexado Vasto en Longitud de Onda) o DWDM (Dense WDM, Multiplexado Denso en Longitud de Onda), que permiten esquemas más eficientes para la distribución de los servicios de tráfico de datos entre los diferentes nodos y/o abonados. Estas redes son conocidas como redes WDM-PON y actualmente se encuentran en proceso de investigación, estandarización y desarrollo y constituyen el núcleo de las redes de acceso de nueva generación como un paso más frente a las redes FTTx. Este tipo de redes presenta la ventaja de proporcionar mayores distancias entre el nodo y el usuario puesto que presenta un mejor balance de potencia respecto a los tradicionales divisores de potencia (splitters) utilizados para conectar a los diferentes usuarios con los nodos de acceso de los proveedores de servicios. En este punto, redes de sensores basadas en técnicas de división por longitud de onda (WDM) constituyen una solución eficiente y de bajo coste puesto que permiten la integración de ambos tipos de redes, de sensores y de datos, bajo una misma topología.

En este escenario, este trabajo se focaliza en el desarrollo de redes pasivas de sensores de intensidad óptica con auto-referencia para topologías de multiplexación WDM. La topología propuesta opera en reflexión, mediante redes de Bragg, con configuración electro-óptica en recepción siendo la potencia óptica del emisor modulada en

radiofrecuencia (RF). Mediante la inclusión de redes de retardo electrónicas en la etapa de recepción se elimina la necesidad de utilizar largos tramos de fibras ópticas en el sensor proporcionando un diseño más compacto y robusto para esta configuración, a la vez que permite una fácil reconfiguración del punto de operación de cada sensor remoto de la red. Dos parámetros de auto-referencia son estudiados teóricamente, experimentalmente analizados y comparados en términos de linealidad, sensibilidad y resolución. La topología propuesta es modelada mediante la transformada Z permitiendo un análisis eficiente de la respuesta en frecuencia del esquema propuesto, mostrando gran similitud las curvas teóricas con las medidas realizadas.

Por otra parte, se propone un sistema de monitorización, manteniendo la auto-referencia de las medidas, para evaluar las pérdidas producidas en las fibras que constituyen el enlace entre el nodo (o unidad central) y el usuario, aplicado a las redes de acceso WDM-PON de nueva generación. La técnica propuesta de auto-referencia consiste en la normalización en amplitud de la intensidad óptica recibida proveniente de dos canales, el de sensado y el de referencia, con modulación RF de la potencia óptica y aprovechando las ventajas inherentes de división espectral de longitud de onda de las redes de Bragg.

Este trabajo se ha desarrollado en el marco de las actividades de investigación realizadas en el Grupo de Displays y Aplicaciones Fotónicas (GDAF) de la Universidad Carlos III de Madrid.

8.2 Conclusiones y Trabajos Futuros

En el presente documento se ha presentado la actual necesidad de convergencia en una infraestructura de red de acceso de nueva generación que permita atender las actuales demandas de servicios multimedia por parte de los usuarios. Junto a ello, el incremento de la automatización, control y sensado dentro de los edificios y hogares hace, si cabe, más fuerte esta necesidad.

Las fibras ópticas multimodo, tanto de sílice como de plástico, son la solución ideal a esta necesidad de convergencia en las redes de acceso, tanto para el transporte de datos como la integración de sensores ópticos, con ventajas frente a otro tipo de tecnologías como puedan ser fibras ópticas monomodo o cableado basado en cobre (par trenzado y cable coaxial). Por el contrario, presentan limitaciones en cuanto al ancho de banda y, por tanto, en cuanto a capacidad de transportar información para atender a las actuales demandas. Sin embargo, es necesaria la investigación y desarrollo de modelos teóricos fiables y predictivos en cuanto a la capacidad proporcionada por este tipo de fibras.

En este escenario, se han descrito contribuciones originales en el desarrollo y validación de los modelos teóricos propuestos en este documento:

- La influencia de la mayoría de los parámetros que afectan a la respuesta en frecuencia de la fibra óptica multimodo de sílice y la fibra óptica de plástico

perfluorinada de índice gradual ha sido analizada mediante un amplio abanico de simulaciones teóricas.

- Los resultados demuestran que el modelo propuesto por otros autores, relativo a la respuesta en frecuencia de la fibra óptica de plástico perfluorinada de índice gradual, presenta gran similitud con las medidas experimentales realizadas. Además, dichas medidas demuestran que este tipo de fibra presenta bandas de paso 'latentes' en su función de transferencia abriendo la posibilidad de aumentar la capacidad de este tipo de enlaces mediante la transmisión de información a través de estas bandas de paso secundarias más allá del límite impuesto por la banda base.

- Se ha demostrado experimentalmente que mayores anchos de banda en banda base se pueden obtener aplicando condiciones de inyección selectivas en modos (RML, Restricted Mode Launching) frente a esquemas de inyección uniforme donde todos los modos son excitados y lanzados a la fibra (OFL, Overfilled Launching), tal y como otros autores han sugerido en la literatura. También se ha demostrado que la fibra óptica de plástico permite la transmisión de Gigabit Ethernet sobre 200m y 10-Gigabit Ethernet sobre 50m, aunque estos valores podrían mejorarse mejorando las condiciones de inyección de potencia óptica en la fibra. Adicionalmente, medidas experimentales han corroborado el comportamiento predicho por las simulaciones teóricas en cuanto a la dependencia de la respuesta en frecuencia con respecto al radio del núcleo de la fibra, a la longitud de onda de trabajo y la anchura espectral de la fuente óptica utilizada.

- La estabilidad a largo plazo y la dependencia con la temperatura ambiental de un enlace de fibra óptica de plástico perfluorinada de índice gradual se ha evaluado mostrando que ambos efectos deben tenerse en cuenta puesto que afectan al comportamiento de la respuesta en frecuencia de la fibra. Se han medido variaciones con la temperatura del ancho de banda a 3-dB de la respuesta en frecuencia del orden de 15-30% respecto del valor nominal.

- La dependencia de la respuesta en frecuencia de un enlace de fibra óptica multimodo de sílice con la anchura espectral de la fuente ha sido evaluada mediante medidas experimentales. Se concluye de dichas medidas, y de acuerdo con las simulaciones teóricas realizadas, que el uso de fuentes ópticas de muy poca anchura espectral resulta en zonas del espectro con respuestas relativamente planas más allá de la banda base. También se ha verificado que el efecto de filtrado transversal, característico de las fibras ópticas multimodo, se reduce al aplicar condiciones de inyección selectivas en modo (RML). Por tanto, la combinación de esquemas de inyección selectivos en modos junto con el uso de fuentes ópticas de achura espectral estrecha permite la transmisión de señales e información mucho más allá del producto ancho de banda por longitud típico de las fibras ópticas multimodo de sílice, tal y como otros autores han propuesto recientemente en la literatura.

- Por otra parte, se ha verificado experimentalmente para las fibras ópticas multimodo de sílice que: (a) el rango espectral libre (FSR, Free Spectral Range) de las bandas de paso se reduce proporcionalmente con la longitud del enlace de fibra y (b) el ancho de banda de 3-dB de una determinada banda de paso se reduce a medida que aumenta la longitud del enlace. Este comportamiento es debido a que la fibra óptica multimodo de sílice se comporta como un filtro transversal imperfecto.

- Adicionalmente, los efectos de cambios en la temperatura ambiental con respecto a la respuesta en frecuencia de la fibra óptica multimodo de sílice han sido evaluados experimentalmente, demostrándose que cambios en la temperatura afectan poco significativamente tanto a las frecuencias centrales como a los anchos de banda en las bandas de paso. Sin embargo, existe una gran dependencia de la histéresis con la temperatura, no recuperándose valores originales de anchos de banda para una misma banda de paso para una misma temperatura, tras un proceso de enfriado y calentado.

Por otra parte, los sensores ópticos de intensidad, en los que la magnitud a medir provoca una variación en la intensidad de la luz que se propaga por la fibra, gracias a su simplicidad y bajo coste están ganando terreno en aplicaciones tanto para la automatización, control y sensado tanto en edificios como en áreas residenciales. La integración de este tipo de sensores en edificios inteligentes o en el Hogar Digital, junto con la necesidad hacia una convergencia en el dominio óptico de la infraestructura de las redes de acceso de nueva generación, hacen que en este trabajo se planteen contribuciones originales en el campo de la auto-referencia de sensores ópticos de intensidad. Además, aprovechando este desarrollo, se propone el desarrollo de un sistema de monitorización de pérdidas en la fibra óptica, entre el nodo central y el cliente/abonado, en redes ópticas pasivas basadas en multiplexación en longitud de onda, puesto que éstas constituyen el futuro despliegue en las redes de acceso de nueva generación para la difusión de servicios multimedia.

En este trabajo se ha descrito una contribución original al estado del arte de las técnicas de auto-referencia basadas en radio frecuencia y con estructura resonante para la multiplexación de sensores ópticos de intensidad:

- Se ha desarrollado la teoría de filtros digitales para el diseño y el análisis de la técnica de auto-referencia propuesta. Empleando la transformada Z se ha analizado la función de transferencia frente a las pérdidas ópticas producidas en el sensor óptico de intensidad.

- Se han estudiado y verificado experimentalmente dos parámetros de medida remota (R y ϕ) con auto-referencia sobre sensores ópticos, definido uno de ellos por primera vez (parámetro R), para una topología electro-óptica que utiliza dos redes de Bragg situándose entre ellas el sensor de intensidad y en la que retardos electrónicos en recepción son aplicados en vez de emplear largas líneas de retardo en fibra. Mediante el empleo de la configuración electro-óptica es posible

emplear una frecuencia de modulación de valor bajo y arbitrario, manteniendo las prestaciones de otras configuraciones y reduciendo muy significativamente el tamaño de las cabezas sensoras remotas.

- Se ha propuesto y analizado una nueva topología en estrella operando en reflexión para la interrogación simultánea de sensores ópticos de intensidad en una red de sensores con auto-referencia con multiplexación vasta en longitud de onda (CWDM). Cada cabeza sensora consta de dos redes de Bragg, entre las cuales se incluye el sensor, y dos retardos electrónicos asociados en recepción. Mediante la inclusión de estos dos retardos por sensor se permite una fácil reconfiguración multipunto de la técnica de medida desde un solo punto de localización, pudiendo elegirse de una manera muy flexible el punto de operación de la red para cada sensor. Esta topología propuesta se ha analizado y comparado para los dos parámetros de medida definidos anteriormente. La propiedad de auto-referencia se ha verificado para pérdidas en la red de hasta 12dB. A su vez, también se ha demostrado que la presencia de crosstalk en la red es despreciable, por lo que dos sensores operando en canales adyacentes pueden ser interrogados simultáneamente. El comportamiento de ambos parámetros de medida en la red propuesta se ha analizado en términos de linealidad, sensibilidad y resolución mostrando que, aunque ambos permiten un punto de operación lineal, el nuevo parámetro R ofrece mayores sensibilidades y resoluciones de dos órdenes de magnitud menores.

- Se ha propuesto y evaluado, asimismo, un sistema de monitorización para la medida de atenuación de fibras en una red WDM-PON. El sistema de monitorización está basado en la configuración electro-óptica con auto-referencia propuesta anteriormente, siendo R el parámetro de medida propuesto, siendo posible evaluar pérdidas indeseables en tramos del enlace punto a multipunto tales como dobleces en la fibra, mala conectorización o roturas en la fibra. Este sistema se ha evaluado para una red CWDM de 10km de longitud siendo posible su escalado a sistemas DWDM.

Como comentario final, cabe destacar que el empleo de dispositivos CWDM para construir redes de sensores con la topología en estrella de las redes ópticas pasivas (PON) de comunicaciones para el acceso a banda ancha constituye una solución eficiente para medidas remotas de varios sensores ópticos, mejorando el balance de potencia respecto a las PON convencionales con divisores de potencia. Se ha demostrado experimentalmente que esta topología multiplexada es compatible con la técnica de auto-referencia propuesta en el presente trabajo. Ésta, además, está considerada como la futura topología a desplegar para las redes de acceso de nueva generación, constituyendo el corazón de los futuros despliegues FTTx.

Publications related to this Work

International Papers

- J. Montalvo, C. Vázquez and D.S. Montero, **CWDM self-referencing sensor network based on ring resonators in reflective configurations**, *Optics Express*, 14(11), pp. 4601-4610, 2006.
- C. Vázquez, J. Montalvo, D.S. Montero and J.M.S. Pena, **Self-referencing fiber-optic intensity sensors using Ring Resonators and Fiber Bragg Gratings**, *IEEE Photonics Technology Letters*, 18(22), pp. 2374-2376, 2006.
- D.S. Montero, C. Vázquez, I. Möllers, J. Arrue and D. Jäger, **Self-referencing Intensity Based Polymer Optical Fiber Sensor for Liquid Detection**, *Sensors*, 9(8), pp. 6446-6455, 2009.
- J. Montalvo, D.S. Montero, C. Vázquez, J.M. Baptista and J.L. Santos, **Radio-Frequency Self-Referencing System for Monitoring Drop Fibres in WDM Passive Optical Networks**, *IET Optoelectronics*, 4(6), pp. 226-234, 2010.
- M. Parker, S.D. Walker, R. Llorente, M. Morant, M. Beltrán, I. Möllers, D. Jäger, C. Vázquez, D.S. Montero, I. Librán, S. Mikroulis, S. Karabetsos and A. Bogris, **Radio-over fibre technologies arising from the Building the Future Optical Network in Europe (BONE) project**, *IET Optoelectronics*, 4(6), 247-261, 2010.
- D.S. Montero, C. Vázquez, J.M. Baptista, J.L. Santos and J. Montalvo, **Coarse WDM networking of self-referenced fiber-optic intensity sensors with reconfigurable characteristics**, *Optics Express*, 18(5), pp. 4396-4410, 2010.

International Conferences[1]

- C. Vázquez, J. Montalvo, P.C. Lallana and D.S. Montero, **Self-referencing Technique in Reflection Mode for Fibre-Optic Intensity Sensors using Ring Resonators**, *18th International Conference on Optical Fibre Sensors OFS-18*, 14(11), paper ThE26, Cancún (Mexico), 2006.
- C. Vázquez, J. Montalvo, D.S. Montero and P.C. Lallana, **Self-referencing Techniques in Photonics Sensors and Multiplexing**, (Invited Paper) *Proc. SPIE 6593: Photonics Materials, Devices and Applications II*, paper 65931X, Maspalomas (Spain), 2007.

[1] In proceedings after revision

- C. Vázquez, P.C. Lallana, D.S. Montero and J. Montalvo, **Self-reference intensity sensor techniques and and advance devices in WDM networks**, *(Invited Paper) VI Symposium on Enabling Optical Networks and Sensors SEON 2008*, pp. 3-6, Lisbon (Portugal), 2008.
- D.S. Montero, C. Vázquez, J.M. Baptista and J.L. Santos, **Self-referencing model for electro-optical WDM fiber-optic intensity-based sensor network**, *Proc. SPIE 7503, 20th International Conference on Optical Fibre Sensors (OFS-20)*, paper 75031R, Edinburg (Scotland), 2009.
- J. Montalvo, D.S. Montero, C. Vázquez, J.M. Baptista and J.L Santos, **Radio-Frequency Self-referencing Monitoring Techniques for Access Passive Optical Networks**, *(Invited Paper) VII Symposium on Enabling Optical Networks and Sensors SEON 2009*, Amadora (Portugal), 2009.
- D.S. Montero, I. Gasulla, I. Möllers, D. Jäger, J. Capmany and C. Vázquez, **Experimental analysis of temperature dependence in multimode optical fiber links for Radio-over-Fiber applications**, *11th International Conference on Transparent Optical Networks (ICTON2009)*, Azores Islands, paper Mo.C5.2, (Portugal), 2009.
- J. Montalvo, K. Yüksel, D.S. Montero, M. Wuilpart, P. Mégret and C. Vázquez, **New Radio-Frequency Techniques for Individual Drop Fibre Monitoring and Temperature Sensing in PONs**, *15th International Conference on Optical Network Design and Modeling ONDM 2011*, submitted.

National conferences

- C. Vázquez, J.M.S. Pena, S. Vargas, A.B. Gonzalo, J. Montalvo, P.C. Lallana, D.S. Montero, K.K. Afshar, A. Ferreiro and J.J. Romeral, **DISFOTON: Dispositivos Fotónicos para redes de Multiplexado Vasto en Longitud e Onda (TIC 2003-03783)**, *Jornadas de seguimiento de proyectos en Tecnología Electrónica*, Barcelona (Spain), Sept. 2005.
- D.S. Montero and C. Vázquez, **Sensor de fibra óptica de plástico para detección de presencia de líquido basado en acoplador autoreferenciado**, *5ª Reunión Nacional de Optoelectrónica OPTOEL2007*, pp. 573-578, Bilbao (Spain), Jul. 2007.
- D.S. Montero, C. Vázquez, P.C. Lallana and J.M. Baptista, **Nueva configuración electro-óptica para redes WDM de sensores de intensidad óptica con autoreferencia,** *6ª Reunión Nacional de Optoelectrónica OPTOEL2009*, pp. 329-334, Málaga (Spain), Jul. 2009.

Other related works

- P.C. Lallana, C. Vázquez, B. Vinouze, K. Heggarty and D.S. Montero, **Multiplexer and Variable Optical Attenuator Based on PDLC for Polymer Optical Fiber Networks**, *Molecular Crystals and Liquid Crystals*, vol. 502, pp. 130-142, 2009.
- C. Vázquez and D.S. Montero, *Spanish National Patent, nº. 2339205*, **Sistema de medición de nivel de combustible en ultraligeros**, submitted February 2008 and published on 23rd August 2010.
- M.A. Jurado Pontes, C. Vázquez, J.M.S. Pena D.S. Montero and P.C. Lallana, **Variable optical attenuator for perfluorinated gradual index polymer optical fiber using a polymer dispersed liquid crystal cell**, *Proc. SPIE 5947: Liquid Crystals: Optics and Applications*, pp. 59470H.1-59470H.12, Warsaw (Poland), 2005.
- C. Vázquez, J.L. Nombela, C. Sobrino, M. de Vega, J. Zubia and D.S. Montero, **Plastic fiber-optic probes for characterizing fluidized beds in bubbling regime**, *16th International Conference on Plastic Optical Fibers ICPOF2007*, paper SEN-II-2, Torino (Italy), 2007.
- D.S. Montero, C. Vázquez, and J. Arrue, **Plastic optical fibre sensor for fuel level measurements applied to paramotoring and powered paragliding**, *18th International Conference on Plastic Optical Fibers ICPOF2009*, paper SENS-11, Sydney (Australia), 2009.
- D.S. Montero, C. Vázquez, P.C. Lallana and J. Zubia, **Polymer optical fibre sensor for liquid detection applied to volumetric flasks**, *19th International Conference on Plastic Optical Fibers ICPOF2010*, paper P-28, Tokyo (Japan), 2010.

Appendix A

Simulation of Optical Fibre Transmission Links using VPIphotonics™

VPIphotonics™ is a powerful software tool for technical simulation developed in 1998. This Photonic Design Automation software comprises a number of products[1]. The main goal for the researchers is to resolve ordinary problems in electrical and optical systems but at the same time obtain high-quality and stable results in complex photonic networks. VPI has been widely used because it allows free modelling of the system design by the alteration of multiple parameters inside the components of the network. The availability of this type of software gives freedom to the industry since it is possible to simulate several networks allowing a reduction of the cost production for the development of prototypes. It also provides an easy-to-use GUI (Graphical User Interface) which permits to control a simulation engine with a large database of optical, electrical and logical components that can be easily interconnected. Figure A.1 shows the GUI (Graphical User Interface) of the standard VPIsystems®.

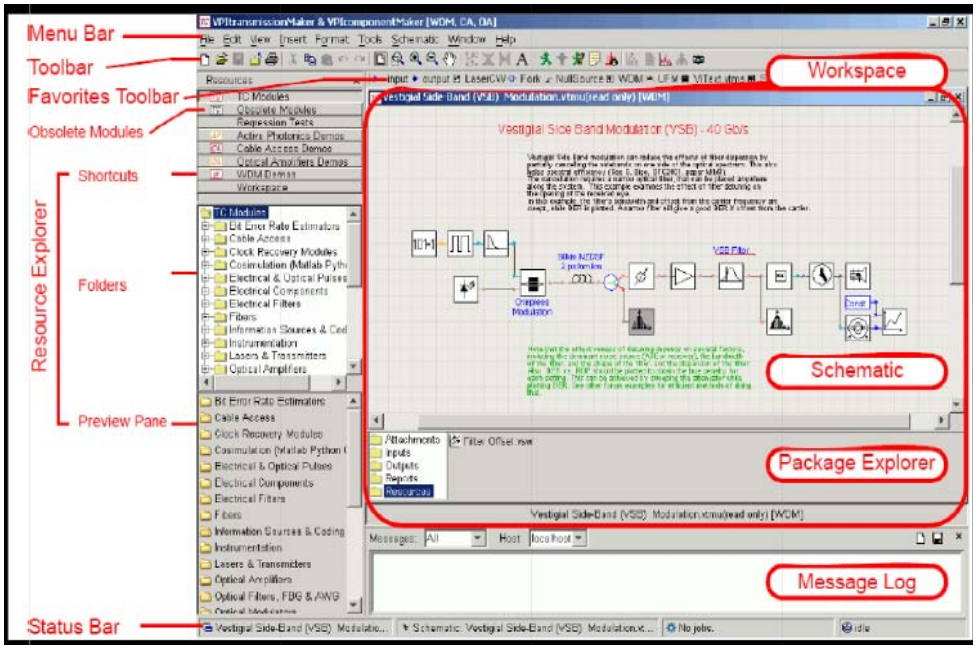

Fig, A.1.- GUI in an open schematic (VPI help).

[1] VPItransmissionMaker WDM, VPItransmissionMaker Cable Access, VPIcomponentMaker, VPIlinkConfigurator, VPIplayer, among others.

It is important to reference that VPIphotonics™ wins this high popularity due to the fact that the construction of the system is done in a graphical console by the interconnection of the block modules. VPI is also attractive for its large data base of electrical and optical components as well as visualizers, with the possibility of creating novel component for specific requirements. Further details of this powerful software can be found in [2]. The integration of all products and tools comprises the following logic scheme, Fig. A.2:

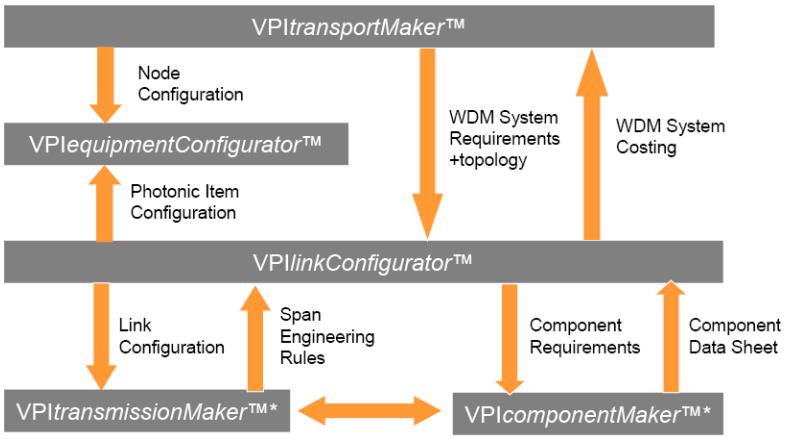

Fig, A.2.- Integration of design tools in VPI.

A.1 Optical Signal Mode and Representation

For a particular simulation, the first choice to make is whether the interaction between the modules is bidirectional or unidirectional. This choice can be made by setting the **OutputDataType** parameter at the source of the signal either to *Block Mode* (unidirectional interaction) or to *Sample Mode* (bidirectional interaction).

In *Sample Mode* simulations, the signals are passed bidirectionally between interconnected modules on a sample by sample basis, thus allowing very close coupling between components, for example lasers and external resonators, so that optical resonances can be modelled. This signal mode is suitable for individual component design, where recirculations and reflections of optical signals must be taken into account.

The other signal mode is *Block Mode*, and it is used to pass signals unidirectionally. Each block contains enough samples to fill a **TimeWindow**, which specifies, among other things, the length of Fourier transforms used in spectral analysis, hence the frequency resolution. This signal mode is suitable for the simulation of multi-wavelength optical systems including digital transmitters and error detection modules.

The second choice to make is what kind of data, optical or electrical, is passed between the different simulation modules during their interaction. *Optical Signals* are passed as sampled waveforms, and each sample contains optical field information with two polarizations

[2] *VPIcomponentMaker Active Photonics User's Manual*. VPIsystems Incorporated, 2005.

representing the phase and amplitude of the optical field during a slice of time. Samples are passed individually and sort between modules in Sample Mode, or collected into blocks and passed in one go in Block Mode. On the other hand, *Electrical Signals* are also passed as sampled waveforms, but they contain electrical voltage or current information during a slice of time. Again, individual samples can be collected together into blocks and passed in one go when the Block Mode is selected.

A.2 Bandwidth and Frequency Resolution of a Simulation

In Sample Mode simulations, the rate at which samples are passed is set by the global parameter **SampleModeBandwidth**, and represents the optical bandwidth over which the simulation operates, being the electrical bandwidth one half of it. In Block Mode simulations, the simulation bandwidth is set by the parameter **SampleRate**.

In Sample Mode, the signals represent the optical waveform by extracting a carrier frequency from it, set by the global variable **SampleModeCenterFrequency**. The remaining envelope is a complex waveform, which completely represents the optical channels and noise over a bandwidth centered around the **SampleModeCenterFrequency**. On the other hand, sources whose output is set to Block Mode usually produce a modelled optical bandwidth centered around their **EmissionFrequency**. The frequency resolution of the Fourier transforms used in spectral analysis is the inverse of the global parameter **TimeWindow**. The product SampleRate x TimeWindow is exactly the number of samples of the simulation and must always be equal to a power of two, i.e 2^n.

On the other hand, in simulations with digital transmitters involved, the parameter **BitRateDefault** sets the bit rate, namely B. The number of samples corresponding to each bit period, namely S, must be integer. At the same time, the number of bits over the **TimeWindow** must also be a power of two (2^p for integer p). These restrictions are expressed as follows:

$$\begin{aligned} TimeWindow &= 2^p \cdot B^{-1} \\ SampleRate &= S \cdot B \end{aligned} \qquad \text{(A.1)}$$

If S is equal to a power of two, i.e $S=2^q$ for integer q, then yields the product:

$$SampleRate \cdot TimeWindow = 2^n \quad \text{where } n = p + q \qquad \text{(A.2)}$$

A.3 Configuration of a MMF transmission link

To simulate the performance in terms of frequency response of a multimode optical fibre based transmission link Block Mode signals must be employed, because most of the required modules are not compatible with the Sample Mode signal representation. Global parameters have been set to:

- *TimeWindow* = 64/10e9 s
- *SampleModeBandwidth* = 160e9 Hz
- *SampleRateDefault* = 160e9 Hz
- *BitRateDefault* = 10e9 bit/s

Therefore, frequency resolution is set to 156.25MHz with 16 samples per bit period.

Fig. A.3 depicts the VPI schematic generated, considered for the simulations regarding Fig. 4.3 in page 132. The schematic simulates the frequency response of the system, using a low-amplitude electrical impulse (on a bias level) to drive the modulator. The output of the modulator is an optical carrier and sidebands at all frequency points. The bias level is neccesary, otherwise the optical carrier would not be present, and so, the spectrum would be flat, i.e. the system would be excited at all optical frequencies, equally. The system is ideal, apart from fibre chromatic dispersion. This chromatic dispersion causes the magnitude response to have nulls at baseband frequencies where the two dominant sidebands in the optical spectrum are, as well, rotated in relative phase by 180 degrees. The rotation is due to the dispersion of the optical fibre, which imposes a group delay on the optical wave proportional to the optical frequency of the sideband. The phase response then flips by 180-degrees at each null.

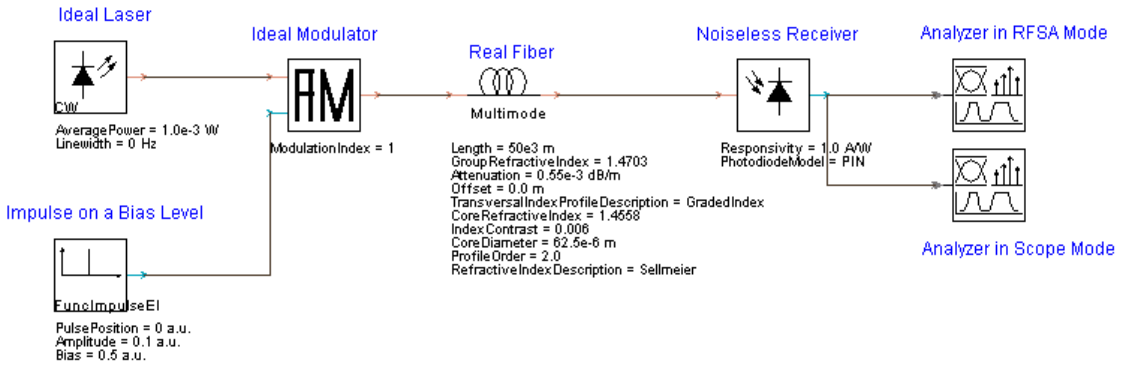

Fig, A.3.- Schematic of the VPI simulations to test the performance of a silica-based MMF transmission link using ideal components except for the fibre.

On the other hand, considering the 'Multimode Fiber' module, it simulates the propagation in multimode fibres with arbitrary transversal refractive index profiles. Some of its features are that this module permits a wavelength-dependent refractive index profile to be calculated using the Sellmeier formula and, moreover, the internal mode solver calculates the mode coupling coefficients using transversal modes and input field profiles. The main multimode optical fibre parameters have been set to the values depicted within Fig. A.3.

Applications of VPIphotonics™ involve topics such as link configuration and engineering, optical networking, modulation formats, high-speed/high-capacity systems, optical access technologies, fibre amplifiers and lasers or semiconductor lasers. Nevertheless, most of these applications are focused on singlemode fibres (SMFs) and little attention has been

paid to multimode fibres. Furthermore, the kernel of the physics theory of this simulation tool is unknown for the author which leads to think that simulation results concerning multimode fibres must be treated with caution.

Appendix B

Introduction to Discrete-Time Optical Signal Processing

This appendix deploys the mathematical notation that will be followed in the rest of the document. The Z-transform formalism is used for describing a theoretical framework with the most important concepts regarding linear systems and signal processing focussing on the theory of optical filter design and analysis [1].

The described mathematical analysis is applied to some of the most important optical configurations, such as the Mach-Zehnder, Michelson, Sagnac and Ring Resonators [2, 3], which are deeply employed in self-referencing topologies. In reference [4] a general theory of microwave optical discrete-time signal processing is presented in more detail. Furthermore, for an in depth treatment of digital signal processing and fibre-optic delay lines for digital filters, texts such as [5-7] are recommended.

B.1 Notations and Definitions

A discrete-time signal $x[n]$ is a finite or infinite sequence of numbers, generally complex that can be obtained from sampling a continuous-time signal $x(t)$ at instants $t = n \cdot \tau$, being τ the sampling period for integer *n*.

The impulse response of a multi-stage delay line optical filter, where every optical transit time is a multiple of a characteristic time delay τ, can be described using a sequence. In the analysis of this kind of filters, the delay time τ is identified with an equivalent sampling period or the unit delay associated with the discrete impulse response, as in the case of a digital filter. Recently, the demand for digital optical filters is increasing rapidly because of the deployment of commercial wavelength-division-multiplexed (WDM) optical communication systems, as they can provide a multiplexing, demultiplexing and add/drop technology for very closely spaced channels. They are also playing a major role in gain equalization and dispersion compensation with low loss optical fibres and broadband optical amplifiers. WDM systems have the potential to harness a huge bandwidth and to increase the capacity, and digital optical filters are essential for realizing this goal by decreasing the channel spacing and, therefore, using the bandwidth already covered more efficiently.

On the other hand, the impulse response of an optical filter, where each stage has a delay which is an integer multiple of the unit delay, is described by a discrete sequence. This allows employing very powerful and well established mathematical theories, as the

Discrete-Time Fourier Transform (DTFT) and its generalization, the Z-Transform, for the study of this kind of optical filters. In the following, there is an introduction to both transforms with the definitions and notations that will be used all along this document.

Optical filters are completely described by their frequency response, which specifies how the magnitude and phase of each frequency component of an incoming signal is modified by the filter. The fundamental relationships between optical waveguides and digital filters were developed by Moleshi et al. [8] in 1984. Both digital and optical filters consist of splitters, delays and combiners and many stages can be formed by concatenating single stages or combining stages in various architectures. In such filters, the optical path lengths are typically an integer multiple of the smallest path length difference. The characteristic transit time or unit delay is defined as $\tau = L_U \cdot n/c$ where L_U is the smallest path length and is called the unit delay length. Digital signal processing techniques are relevant to optical filters because they are linear, time-invariant systems that have discrete delays and, because the delays are discrete values of the unit delay. The frequency response is periodic, with period defined as the Free Spectral Range (FSR) as it will be seen later in this Appendix.

B.1.1 Discrete-time Fourier Transform (DTFT)

The DTFT of a sequence has the expression:

$$X(\Omega) = \sum_{n=-\infty}^{\infty} x[n] \cdot \left(e^{j\Omega}\right)^{-n}, \qquad \Omega \in \mathbb{R} \tag{B.1}$$

being X periodical with period 2π. The infinite sum exists for functions that are absolutely summable, i.e.:

$$\sum_{n=-\infty}^{\infty} |x[n]| < \infty \tag{B.2}$$

A system whose impulse response satisfies this criterion is stable since it can easily be shown that it has a bounded output for a bounded input [7]. The inverse DTFT is defined as follows:

$$x[n] = \frac{1}{2\pi} \int_{-\pi}^{\pi} X(\Omega) \cdot e^{j \cdot \Omega \cdot n} d\Omega \tag{B.3}$$

A discrete function in one domain is transformed to a periodic function in the other domain. Optical filters with characteristic transit times, i.e. discrete time delays, have always a periodical frequency response. This fact will be seen in Chapter 5 for the digital filter model of the proposed configuration.

Any discrete signal can be represented by a sum of products of different constants times the delayed delta function:

$$x[n]=\sum_{k=-\infty}^{\infty} x[k]\cdot\delta[n-k] \tag{B.4}$$

where $\delta[n]$ is the Kronecker delta function, which is defined as follows:

$$\delta[n]=\begin{cases}1, & n=0\\ 0, & n\neq 0\end{cases} \tag{B.5}$$

The response of a discrete-time system to the Kronecker delta function input defines its impulse response. The response of a linear, time-invariant system to a shifted input is given as follows, where $L\{\ \}$ denotes a linear system function and *h[n]* the impulse response of a discrete-time linear time-invariant system:

$$h[n-k]=L\{\delta[n-k]\} \tag{B.6}$$

Similar to the continuous-time case, the system output is the convolution of the input signal and the system impulse response:

$$y[n]=L\left\{\sum_{k=-\infty}^{\infty} x[k]\cdot\delta[n-k]\right\}=\sum_{k=-\infty}^{\infty} h[n-k]\cdot x[k] \tag{B.7}$$

The DTFT of this convolution operation simplifies to multiplication as follows:

$$\begin{aligned} Y(\Omega)&=\sum_{n=-\infty}^{\infty}\left[\sum_{k=-\infty}^{\infty} h[k]\cdot x[n-k]\right]\cdot\left(e^{j\Omega}\right)^{-n}=\\ &=\sum_{k=-\infty}^{\infty} h[k]\left[\sum_{n=-\infty}^{\infty} x[n-k]\cdot\left(e^{j\Omega}\right)^{-n}\right]=\\ &=X(\Omega)\cdot\sum_{k=-\infty}^{\infty} h[k]\left(e^{j\Omega}\right)^{-k}=X(\Omega)\cdot H(\Omega)\end{aligned} \tag{B.8}$$

In the framework of this work, Ω represents the angular frequency (rad) defined by:

$$\Omega=\frac{2\pi f}{FSR} \tag{B.9}$$

where f is the frequency (Hz) and the Free spectral Range (FSR) is defined as follows:

$$FSR=\frac{1}{\tau} \tag{B.10}$$

The normalized frequency is defined in the following way:

$$\nu = f \cdot \tau \tag{B.11}$$

For a given finite sequence $x[n]$ of N numbers, the N coefficients of the Fourier series representation of the infinite periodical signal, $X(k)$, which is constructed from repeating the finite sequence, can be calculated through the expression:

$$X(k) = \sum_{n=0}^{N-1} x[n] \cdot \left(e^{j\frac{2\pi}{N} \cdot k} \right)^{-n}, \qquad \mathrm{k} = 0,...,N-1 \tag{B.12}$$

In the former equation it can be noted that these coefficients correspond to the values of the DTFT of the original finite sequence, but evaluated in N points, this is:

$$X(k) = X(\Omega)\Big|_{\Omega=\frac{2\pi}{N} \cdot k}, \qquad \mathrm{k} = 0,...,N-1 \tag{B.13}$$

It is interesting to notice that the coefficients in the time and frequency domain are related by the Weiner-Klintchine theorem (or Parseval's identity):

$$\sum_{n=0}^{N-1} |x(n)|^2 = \frac{1}{N} \sum_{k=0}^{N-1} \left| X\left(\frac{2\pi}{N} \cdot k \right) \right|^2 \tag{B.14}$$

From Eq. B.14 both domains have the same number of coefficients and the total energy (i.e. power) is conserved.

B.1.2 Z-Transform of a Sequence

The Z-transform is an analytic extension of the DTFT for discrete signals, similar to the relationship between the Laplace transform and the Fourier transform for continuous signals. The Laplace transform is used to describe analog filters, while the Z-transform is used to describe digital filters. For a discrete-time linear time-invariant system with impulse response $h[n]$ the system response $y[n]$ to a complex exponential input z^n is:

$$y[n] = H(z) \cdot z^n \tag{B.15}$$

where

$$H(z) = \sum_{n=-\infty}^{+\infty} h[n] \cdot z^{-n} \tag{B.16}$$

Equation (B.16), namely analysis equation, defines de Z-transform of the system impulse response. This series does not necessarily converge in all the points of the complex plane, but only in the Region of Convergence (ROC).

The DTFT is a particularization of the Z-transform, evaluated in the points of the circle whose radius equals one. This fact can be seen comparing the expressions given by Eqs. B.1 and B.16.

The inverse Z-transform is found by applying the Cauchy integral theorem to Eq. B.16 to obtain:

$$h[n] = \frac{1}{2\pi j}\oint H(z)z^{n-1}dz \tag{B.17}$$

The convolution resulting from filtering in the time domain:

$$y[n] = x[n] * h[n] = \sum_{m=-\infty}^{\infty} x[m]\cdot h[n-m] \tag{B.18}$$

reduces to multiplication in the Z-domain:

$$Y(z) = H(z)\cdot X(z) \tag{B.19}$$

Equation B.19 shows that a filter's transfer function, *H(z)*, can be obtained by dividing the output by the input in the Z-domain:

$$H(z) = \frac{Y(z)}{X(z)} \tag{B.20}$$

A fundamental property of the Z-transform relates *h[n-1]* to *H(z)* as shown in Eq. B.21:

$$\sum_{n=-\infty}^{\infty} h[n-1]z^{-n} = z^{-1}\sum_{n=-\infty}^{\infty} h[n]z^{-n} = z^{-1}H(z) \tag{B.21}$$

The impulse response is assumed to be causal so that *h[n]=0* for *n<0*. The context of applications of this transform comprises the design and analysis of optical filters with characteristic transient times. This is caused, among other reasons, because of the fact that a delay time has a very simple representation on the Z-transform domain, because of the following property:

$$\sum_{n=-\infty}^{\infty} \delta[n-N]\cdot z^{-n} = z^{-N} \tag{B.22}$$

A delay of one unit results in multiplication by z^{-1} in the Z-domain, and a delay of N units results in multiplication by z^{-N}. This allows to obtain very easily the impulse response of delay line optical filters in the discrete-time domain from the system representation in the Z-transform domain. A detailed example of this procedure can be found in [3] for the optical ring resonator configuration.

The Z-transform allows:

- The representation of digital systems in terms of blocks of linear and time-invariant systems, described with rational complex functions.
- The analysis and characterization of the frequency response of digital filters in a comfortable way.
- The study of the stability and frequency response of feedback systems using simple techniques.

The techniques related to the Z-transform theory are mainly the zero-pole diagrams, the root-locus analysis and the Nyquist stability criterion. These techniques can be directly employed for the case of optical and electrical delay line filters, as it has been shown in Chapters 5 and 6.

B.2 Digital filters: Modelling Optical configurations as Linear Systems

Digital signal processing techniques are relevant to optical filters because they are linear, time-invariant systems that have discrete delays. A linear optical filter with time delays multiples of a characteristic transit time τ can be modelled as a digital filter through the following difference equation:

$$y(n) = \sum_{k=0}^{M} b_k \cdot x(n-k) - \sum_{p=1}^{N} a_p \cdot y(n-p) \qquad \text{(B.23)}$$

In Eq. B.23, x and y represent the input and output sequence to the filter, respectively. For feedback optical configurations N may tend to infinite.

For this kind of optical configurations, the characteristic transit time τ is physically related to the characteristic delay length L as follows:

$$L = \frac{c}{n_g \cdot \tau} \qquad \text{(B.24)}$$

where c is the speed of light in vacuum and n_g is the effective group refractive index of the optical paths of the filter configuration. Any optical path of the optical configuration (either

waveguides or optical fibres) have a length which can be an integer multiple of the characteristic delay length *L*.

The impulse response of the digital filter in the Z-transform domain is:

$$H(z)=\frac{\sum_{k=0}^{M} b_k \cdot z^{-k}}{1+\sum_{p=0}^{N} a_p \cdot z^{-p}}=\frac{B(z)}{A(z)} \qquad \text{(B.25)}$$

Note that in Eq. B.25, *B* and *A* are two polynomials with order *M* and *N*, respectively.

The numerator represents the finite impulse response part (i.e., nonrecursive or FIR) of the system function, whereas the denominator accounts for the infinite impulse part (i.e., recursive or IIR) of the system function. Furthermore, if $a_p = 0$ for all *p* in Eq. B.25 the filter is nonrecursive and is also known as transversal filter. Otherwise the filter is recursive an it is common to use the term recirculating delay line [9].

The model using characteristic polinomials in the Z-transform domain links the optical filters theory with the algebra of complex numbers, which is deeply developed from a mathematical point of view. The roots z_k of the polinomial *B* are the zeros of the system transfer function; on the other hand, the roots p_p of the polynomial *A* are the poles. These roots are, in general, complex numbers. The Z-transform theory determines that for a stable filter the modules of the poles must be less than one, i.e. $|p_p|<1$.

An alternative to the representation in Eq. B.25 where the poles and the zeros appear explicitly is [6]:

$$H(z)=\Gamma\cdot\frac{\prod_{k=1}^{M}(1-z_k\cdot z^{-1})}{\prod_{p=1}^{N}(1-p_p\cdot z^{-1})}=\Gamma\cdot\frac{z^{N-M}\prod_{k=1}^{M}(z-z_k)}{\prod_{p=1}^{N}(z-p_p)} \qquad \text{(B.26)}$$

The roots are complex numbers and are given different names depending on whether they are from the numerator or denominator polynomials. The zeros of the numerator, also called the zeros of *H(z)*, are represented by z_k. A zero that occurs on the unit circle, $|z_k|=1$, results in zero transmission at that frequency. The roots of the denominator polynomial, designated by p_p, are called poles. The gain is set by Γ. For passive filters, the transfer function can never be greater than 1, so Γ has a maximum value determined by $\max\left\{\left|H(z)\right|_{z=e^{jw}}\right\}=1$.

Digital filters are classified by the polynomials defined in Eq. B.26. A filter which has only zeros is also referred to as a Finite Impulse Response (FIR) filter and consists only of feed-

forward paths. On the other hand, filters which have at least one pole in their transfer function are referred to as Infinite Impulse Response (IIR) filters.

There are two conditions that must be met for practical filters: stability and causality. A filter is stable if it has a bounded output response given a bounded input [7]. An absolutely summable impulse response satisfies this requirement:

$$\left|y(n)\right| \le \sum_{k=-\infty}^{\infty} \left|h(k)\right|\left|x(n-k)\right| \le M_x \sum_{k=-\infty}^{\infty} \left|h(k)\right| \tag{B.27}$$

where M_x represents the bounded input. For the Z-transform, the region of convergence must include the unit circle.

On the other hand, for a realizable filter, there can be no output before an input is applied. That is, if $x(n) = 0$ for $n < 0$, then $y(n) = 0$ for $n < 0$. This property is known as causality.

When the module of a filter is evaluated in the unit circle of the complex plane, using the change of variable:

$$z = e^{j\cdot\Omega} \tag{B.28}$$

and Euler's identity:

$$e^{j\cdot\Omega} = \cos\Omega + j\cdot\sin\Omega \tag{B.29}$$

the system frequency response is obtained.

This model provides the physical interpretation of the optical configuration behaviour by using:

$$\Omega = \frac{2\pi}{\lambda}\cdot n_g \cdot L = 2\pi\cdot\frac{n_g \cdot L}{c}\cdot f \tag{B.30}$$

In Eq. B.30, λ and f are the operating optical wavelength and frequency, respectively. The latter equation reveals that Ω represents the optical phase shift or the optical wave at frequency f after propagation through the characteristic delay path.

Identifying B.9 and B.30, the physical meaning of the Free Spectral Range is also revealed:

$$FSR = \frac{c}{n_g \cdot L} \tag{B.31}$$

The system output magnitude tends to zero or to infinite in the frequencies corresponding to the roots whose module equals one, depending on whether they are zeros or poles,

respectively. The zeros with module greater than one are called maximum-phase zeros; the zeros with modules less than one are called minimum-phase zeros.

By using the Z-transform formalism, the frequency response of linear optical filters with a characteristic transit time can be analyzed in a very comfortable and efficient way. The mathematical framework can be useful not only for analysis, but also for the development of optical filters synthesis algorithms [1, 10-13]. Additionally, the theory can be easily interpreted from a physical point of view.

B.2.1 Magnitude Response

A filter's magnitude response is equal to the modulus of its transfer function, $|H(z)|$ evaluated at $z = e^{j\cdot\Omega}$. Based on the pole/zero representation of *H(z)*, the distance of the poles and zeros to the unit circle in the complex plane, in which one trip around the unit circle is equal to one FSR, is the only aspect determining the magnitude response of a transfer function.

It is common to use the expression of the filter magnitude squared, which is:

$$\left|H\left(\Omega\right)\right|^2 = \left(\left\{\Re H(z)\right\}^2 + \left\{\Im H(z)\right\}^2\right)\Big|_{z=e^{j\Omega}} = \left|\Gamma\right|^2 \cdot \frac{\prod_{k=1}^{M}\left(1-2\left|z_k\right|\cos\left(\Omega-\phi_{z_k}\right)+\left|z_k\right|^2\right)}{\prod_{p=1}^{N}\left(1-2\left|p_p\right|\cos\left(\Omega-\phi_{p_p}\right)+\left|p_p\right|^2\right)} \quad \text{(B.32)}$$

B.2.2 Phase Response

The group delay, normalized with respect to the characteristic transit time τ of a digital filter, defined as the negative derivative of the phase of the transfer function with respect to the angular frequency, has the following expression:

$$\tau_n = -\frac{d}{d\Omega}\left[\arctan\left(\frac{\Im H(z)}{\Re H(z)}\right)\right]_{z=e^{j\Omega}} \quad \text{(B.33)}$$

where τ_n is normalized to the characteristic transit time (i.e. unit delay) τ.

The absolute group delay is:

$$\tau_g = \tau \cdot \tau_n \quad \text{(B.34)}$$

The delay is the slope of the phase at the frequency where it is being evaluated, equivalent to the definitions in electromagnetic theory.

For a filter with *M* zeros and *N* poles, the general expression of the normalized group delay is [14]:

$$\tau_n = \sum_{i=1}^{N} \frac{|p_i| \cdot \left(\cos(\Omega - \phi_{p_i}) - |p_i|\right)}{1 - 2|p_i| \cdot \cos(\Omega - \phi_{p_i}) + |p_i|^2} - \sum_{i=1}^{M} \frac{|z_i| \cdot \left(\cos(\Omega - \phi_{z_i}) - |z_i|\right)}{1 - 2|z_i| \cdot \cos(\Omega - \phi_{z_i}) + |z_i|^2} \qquad \text{(B.35)}$$

Two zeros with inverse modules and the same phase provide a group delay which equals 1, thus achieving a filter with a linear phase response versus frequency, as they are located at reciprocal points about the unit circle and will cancel each other's frequency dependence, resulting in a constant group delay. The frequency response of such a filter can be described as follows:

$$H(\Omega) = A(\Omega) \cdot e^{-j \cdot (\Omega + \varphi)} \qquad \text{(B.36)}$$

where $A(\Omega)$ is real and φ is an arbitrary constant phase factor that does not change the linear-phase property. The group delay (or sum of the group delays if the filter has a higher order) is a constant in this case and no phase distortion is induced on the signal.

B.2.3 Regime of Operation of Optical Filters

When it is verified a deterministic relationship of the magnitude and the optical phase between the different ports of an optical network, where an optical carrier has been launched into, the optical fields interfere in each port and the regime of operation is called *coherent*. In this case, the optical power to electric current conversion operation at the photodetector generates an interference term[1]. This coherent regime of interference can be only achieved by employing optical sources with coherence time much longer than any transit time between the optical ports of the configuration or, conversely, when the longest delay time is much shorter than the coherence times of the source, namely τ_C. The coherence time is inversely proportional to the source spectral width, so the above condition is satisfied if $\tau_C \gg N \cdot \tau$ where *N* is the filter order and τ the characteristic transit time or unit delay. In this case, the transfer function of an optical filter has a spectral periodicity much greater than the spectral linewidth of the optical source. Under coherent regime of operation, the optical phase of the optical contributions plays a predominant role in the overall time and frequency response of the processor, and filters with negative and complex coefficients can be implemented. This kind of filters provides greater design flexibility and higher processing bandwidths, up to several terahertz. Given the desire to make compact circuits for higher levels of integration and the narrow source spectral widths required for transmitting high data rate signals over dispersive optical fibres, coherent interference of waves travelling along different paths is extremely important. In this case, the optical power losses correspond to the squared magnitude response of the

[1] The optical power at the photodetector input is proportional to the squared modulus of the overall electric field at the same point, which in turn is composed of the sum of the electric fields of the different samples (or optical contributions). Hence the optical power contains the contributions of the different beatings or cross terms of the electric field.

filter at the operating optical frequency. Such coherent systems can be difficult to implement in practice and are usually more complicated than incoherent systems because of the stringent requirements on the stability of the source and the optical delay paths. Coherent filters are used to achieve high-speed components for communication systems such as switches, modulators and tunable filters. On the other hand, since the filter operation relies on optical interference, any slight change in the propagation characteristics of any part of the optical processor (length of any delay line, refractive index changes due to the alteration of environmental conditions, etc.) drastically affects the filter response and its properties. While coherent operation provides the possibility of implementing any kind of desired transfer function, these structures are very sensitive to environmental conditions [15]. Yet coherent effects can appear even under incoherent operation [16]. This circumstance constitutes a very serious practical limitation for the implementation of these filters since a very stable platform and considerable electronic feedback loops must be provided for successful operation. These undesirable coherent effects may be overcome, for instance by the use of birrefringent fibre delay lines [17] or by implementing different techniques providing spatial and temporal averaging of the carrier, to insure that coherent interference of the optical carrier is minimal. In this latter case, when delay-line portions of a temporally coherent carrier impinge on a detector from different angles, a phase variation exists in the plane of the detector. Since this phase variation is quite large for small angular separations, the detector averages over the area of the wavefront intercepted by the detector. This yields an output proportional to the sum of the optical powers. Even if spatial averaging is not present, a carrier with a broad range of frequency components is used thus providing temporal averaging of the signal components. If signal outputs of a delay line are spatially coherent, but the carrier has a broad spectrum, then the frequency components of the carrier will beat against each other and be effectively averaged over time provided the detector integration time is sufficiently long. The necessary condition for obtaining temporal averaging is given by:

$$\tau_C \ll T_{\text{int}} \ll T_o \qquad \text{(B.37)}$$

where T_o is the time delay between delayed signals, T_{int} is the integration time of the detector and τ_C the coherence time of the carrier, which is roughly given by $\tau_C \sim 1/\Delta\upsilon$. Fortunately, semiconductor laser diodes can exhibit both a broadband spectrum and the ability to be directly modulated at speeds up to several gigahertz. They are therefore the sources of choice for most optical fibre delay-line applications.

Conversely, when the coherence time of the optical source launched into the optical filter is much less than the transit times between the ports (i.e. the shortest relative delay is longer than the coherence length), the optical phase at each one is completely random (i.e. is lost) and the system responds linearly to the signal intensity instead of the fields. The interference is lost and the optical power reaching the photodetector input is the sum of the optical powers of the filter samples or the optical powers that contribute to the filter implementation (i.e. there is no beating term involving the optical phase). In this case, the regime of operation is called *incoherent*. In this case, the filter structure is free from environmental effects and thus very stable and its performance is quite repeatable. The

main drawback of this approach is that filter coefficients can only be positive (since they are implemented by optical power signals which can only be positive or zero, i.e. there is no negative light) in principle. This leads to a serious limitation of the range of transfer functions that can be implemented, although very compact and robust filters can be achieved. Fortunately, there are solutions available for the implementation of incoherent filters with negative coefficients. This operation regime was reported in order to overcome the bandwidth constraints of microwave and radio-frequency (RF) signal filters [18] achieving positive coefficients of the filters. In this incoherent regime to obtain the total power attenuation of the light is not trivial. This is caused because the spectral periodicity, this is the FSR, is much smaller than the spectral width of the optical source. In this situation, the power density of the optical source is scaled by a different value at each optical frequency. For this case is very useful to model the modulated intensity on an optical carrier to an optical incoherent filter as a random complex signal, $I_{in}e^{j\Omega_m t}$, where Ω_m is the modulation angular frequency. These signals are usually described by a reduced number of statistical parameters rather than using their samples, which are unpredictable in each realization of the experiment. Nevertheless, it is possible to know the effect of an optical filter over the random signal, called stochastic process. On the other hand, assuming that the highest practical modulation frequencies, limited by electrical modulators, are on the order of 50GHz, it is interesting to note that incoherent processing operates on frequency ranges which are approximately 4 orders of magnitude smaller than for coherent processing, where the frequency of interest is on the order of 200THz (1550nm). For FSRs in the range of 10MHz to 50GHz, the unit delay length ranges from 21m to 4mm, given by Eq. B.31 assuming $n_g = 1.45$. Practically, the minimum FSR is limited by the wafer size and loss for planar waveguides. For small FSRs, optical fibre circuits, which can easily contain low-loss delay lengths, are more practical.

To summarize, optical fibre delay-line signal processing is set apart from other delay-line techniques by fundamental differences, that stem from the fact that most optically encoded signals are modulated onto a carrier whose frequency is thousands of times greater than that of the highest signal frequency component. This fact leads to that optical detectors are square-law devices that respond to the incident optical power and none is fast enough to respond to the carrier frequency.

Finally, in case of sensor networks, the amount of information to be addressed is usually very low and quasi-static being low-cost devices, efficient multiplexing topologies and self-referencing measurements relevant topics. In this environment, incoherent fibre-optic configurations are the most desirable approach.

B.3 References

[1] J. H. Zhao, C.K. Madsen, *Optical Filter Design and Analysis: A Signal processing Approach*. USA: John Wiley and Sons Inc., 1999.

[2] S. E. Vargas, "Contribución al Diseño de Filtros Ópticos para Redes con Multiplexación en longitud de Onda." vol. PhD Thesis: Universidad Carlos III de Madrid, 2003.

[3] C. Vázquez, "Contribución al desarrollo de Dispositivos y Estructuras Fotónicas con Amplificación para Procesado Óptico." vol. PhD Thesis: Universidad Politécnica de Madrid, 1995.
[4] J. Capmany, B. Ortega, D. Pastor, S. Sales, "Discrete-Time Optical Signal Processing of Microwave Signals," *J. of Lightwave Technol.*, vol. 23, pp. 703-723, 2005.
[5] L. Jackson, *Digital Filters and Signal Processing* Boston, MA: Kluwer Academic, 1996.
[6] A. Oppenheim and R. Schafer, *Digital Signal Processing*, 2nd Ed. ed. Englewood, N.J.: Prentice Hall Inc., 1975.
[7] J. Proakis and D. Manolakis, *Digital Signal Processing: Principles, Algorithms and Applications*, 3rd Ed. ed. Upper Saddle River, NJ: Prentice-Hall 1996.
[8] B. Moslehi, J. W. Goodman, M. Tur, and H. J. Shaw, "Fiber-optic lattice signal processing," *Proceedings of the IEEE*, vol. 72, pp. 909-930, 1984.
[9] M. C. Vazquez, B. Vizoso, M. Lopez-Amo, and M. A. Muriel, "Single and double amplified recirculating delay lines as fibre-optic filters," *Electronics Letters*, vol. 28, pp. 1017-1019, 1992.
[10] C. K. Madsen, "General IIR optical filter design for WDM applications using all-pass filters," *J. of Lightwave Technol.*, vol. 18, pp. 860-868, 2000.
[11] T. Mizuno, T. Saida, T. Kitoh, T. Shibata, and Y. Inoue, "Interleave filter based on coherent optical transversal filter," *J. of Lightwave Technol.*, vol. 24, pp. 2602-2617, 2006.
[12] J. Capmany, J. Cascon, J. L. Martin, S. Sales, D. Pastor, and J. Marti, "Synthesis of fiber-optic delay line filters," *J. of Lightwave Technol.*, vol. 13, pp. 2003-2012, 1995.
[13] S. Vargas and C. Vazquez, "Synthesis of Optical Filters Using Sagnac Interferometer in Ring Resonator," *IEEE Photon. Tech. Lett.*, vol. 19, pp. 1877-1879, 2007.
[14] A. Deczky, "Synthesis of Recursive Digital Filters Using the minimum p-Error Criterion," *IEEE Trans. Audio Electroacoustics*, vol. 20, pp. 257-263, 1972.
[15] C.T. Chang, J. A. Cassaboom , H.F. Taylor, "Fibre-optic delay-line devices for RF signal processing," *Electronics. Letters*, vol. 13, pp. 678-680, 1977.
[16] S. Sales, J. Capmany, J. Marti, and D. Pastor, "Novel and significant results on the non-recirculating delay line with a fiber loop," *IEEE Photon. Tech. Lett.*, vol. 7, pp. 1439-1440, 1995.
[17] W. Zhang, J. A. R. Williams, and I. Bennion, "Optical fibre delay line filter free of limitation imposed by optical coherence," *Electronics Letters*, vol. 35, pp. 2133-2134, 1999.
[18] K. P. Jackson, S. A. Newton, B. Moslehi, M. Tur, C. C. Cutler, J. W. Goodman, and H. J. Shaw, "Optical Fiber Delay-Line Signal Processing," *IEEE Transactions on Microwave Theory and Techniques*, vol. 33, pp. 193-210, 1985.

Appendix C

Development of the analytical expressions for the self-referencing parameters and their sensitivities

C.1 Transfer function of the digital FIR filter in the Z-domain

We recall from Fig. 5.16(b), on Chapter 5 page 205, the filter model of the configuration for a remote sensing point, shown in Fig. C.1:

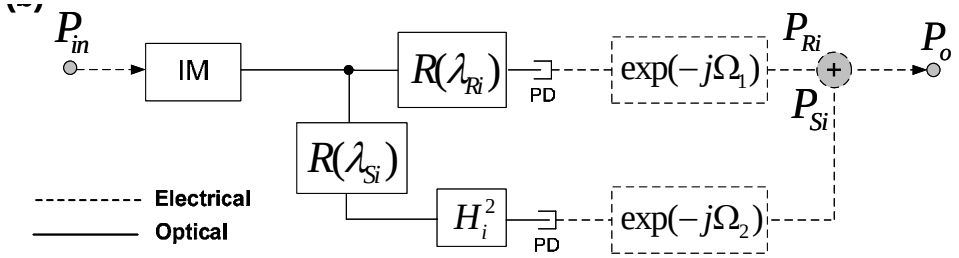

Figure C.1.- Filter model of the electro-optical configuration for a remote sensing point and two electrical phase-shifts at the reception stage.

The system output of Fig. C.1 in the time domain, $p_o(t)$, can be expressed as follows:

$$p_0(t) = \alpha_i \cdot \left(p_{Ri}(t) + \beta_i \cdot p_{Si}(t) \right) \tag{C.1}$$

with

$$\alpha_i = m_{Ri}.R(\lambda_{Ri}).d_{Ri} \tag{C.2}$$

$$\beta_i = \frac{m_{Si}.R(\lambda_{Si}).d_{Si}}{m_{Ri}.R(\lambda_{Ri}).d_{Ri}} H_i^{\,2} \tag{C.3}$$

where m_{Ri}, $R(\lambda_{Ri})$ and d_{Ri} are the RF modulation index, the reflectivity of the FBG and the photodetector response at the reference wavelength λ_{Ri} for the generic remote sensing point *i*, respectively, and m_{Si}, $R(\lambda_{Si})$ and d_{Si} are the respective similar parameters for the sensor wavelength λ_{Si}.

The time domain signals of the reference and sensing channel *i*, respectively, at modulation frequency *f* are defined by:

$$p_{Ri}(t) = \cos(2\pi \cdot f \cdot t - \Omega_1) \tag{C.4}$$

$$p_{Si}(t) = \cos(2\pi \cdot f \cdot t - \Omega_2) \tag{C.5}$$

yielding:

$$p_o(t) = \alpha_i \cdot \left[\cos(2\pi \cdot f \cdot t - \Omega_1) + \beta_i \cdot \cos(2\pi \cdot f \cdot t - \Omega_2)\right] \tag{C.6}$$

However, Eq. C.6 can be studied under steady-state analysis using phasor transform of the corresponding sinusoidal signals:

$$\begin{aligned} P_{Ri} &= P_{in} \cdot \alpha_i \cdot \exp(-j \cdot \Omega_1) \\ P_{Si} &= P_{in} \cdot \alpha_i \cdot \beta_i \cdot \exp(-j \cdot \Omega_2) \end{aligned} \tag{C.7}$$

The output signal response as a phasor P_O can be analyzed using the previous phasors and the resulting time-domain signal at frequency *f* (Hz) can be recovered by obtaining the real part of $P_0 \cdot \exp(-j \cdot 2\pi \cdot f \cdot t)$. Consequently:

$$\begin{aligned} P_O &= \alpha_i \cdot \left[P_{in} \cdot \exp(-j \cdot \Omega_1) + \beta_i \cdot P_{in} \cdot \exp(-j \cdot \Omega_2)\right] = \\ &= P_{in} \cdot \alpha_i \cdot \left[\exp(-j \cdot \Omega_1) + \beta_i \cdot \exp(-j \cdot \Omega_2)\right] = \\ &= P_{in} \cdot \alpha_i \cdot \exp(-j \cdot \Omega_1) \cdot \left[1 + \beta_i \cdot \exp(-j \cdot (\Omega_2 - \Omega_1))\right] \end{aligned} \tag{C.8}$$

Finally, the expression of the normalized system output as a phasor is given by:

$$H_0 = \frac{P_0}{P_{in}} = \alpha_i^{'} \cdot \left[1 + \beta_i \cdot \exp\left[-j \cdot (\Omega_2 - \Omega_1)\right]\right] \tag{C.9}$$

being $\alpha_i^{'} = \alpha_i \cdot \exp(-j \cdot \Omega_1)$.

The expression of H_0 can be directly identified with the transfer function of a digital Finite Impulse Response (FIR) filter in the Z-Transform domain as follows:

$$H_0(z) = \alpha_i^{'} \cdot \left(1 + \beta_i \cdot z^{-1}\right) \tag{C.10}$$

where $z^{-1} = \exp(-j \cdot \Omega)$ with $\Omega = \Omega_2 - \Omega_1$.

C.2 Self-referencing parameters

We recall from Eq. 5.20, on Chapter 5 page 206, the expression of the transfer function of a digital Finite Impulse Response (FIR) filter, shown in Fig. C.1, in the Z-transform domain with two electrical phase-shifts:

$$H_0(z) = \alpha_i^{'} \cdot \left(1 + \beta_i \cdot z^{-1}\right) \tag{C.11}$$

being $\alpha_i^{'} = \alpha_i \cdot \exp(-j \cdot \Omega_1)$.

Identifying a generic electrical phase-shift (Ω_i) with the characteristic transient time of an equivalent filter:

$$z^{-1} = e^{-j \cdot \Omega_i} \tag{C.12}$$

with $\Omega_i = \Omega_2 - \Omega_1$ and taking advantage of the Euler's identity:

$$e^{-j \cdot \Omega_i} = \cos\Omega_i - j \cdot \sin\Omega_i \tag{C.13}$$

then, Eq. C.11 can be rewritten as follows:

$$H(\Omega) = \left[\alpha_i \cdot (\cos\Omega_1 + \beta_i \cdot \cos\Omega_2)\right] - j \cdot \left[\alpha_i \cdot (\sin\Omega_1 + \beta_i \cdot \sin\Omega_2)\right] \tag{C.14}$$

Identifying the Real and Imaginary terms of the transfer function given in Eq. C.14 in the complex plane, it yields:

$$\begin{aligned} \left\{\Re H(\Omega)\right\} &= \alpha_i^{'} \cdot (1 + \beta_i \cdot \cos\Omega) = \left[\alpha_i \cdot (\cos\Omega_1 + \beta_i \cdot \cos\Omega_2)\right] \\ \left\{\Im H(\Omega)\right\} &= -\alpha_i^{'} \cdot \beta_i \cdot \sin\Omega = -\left[\alpha_i \cdot (\sin\Omega_1 + \beta_i \cdot \sin\Omega_2)\right] \end{aligned} \tag{C.15}$$

The magnitude response of the filter (or the modulus of its transfer function) is defined as:

$$M(\Omega) = \left|H(\Omega)\right| = \left(\left\{\Re H(\Omega)\right\}^2 + \left\{\Im H(\Omega)\right\}^2\right)^{1/2} \tag{C.16}$$

Eq. C.16 can be expressed in terms of the power modulation parameter of the self-referencing configuration, by means of the parameter β_i (see Eq. C.13). Taking advantage of the trigonometric identities defined by:

$$\begin{aligned} \sin^2(x) + \cos^2(x) &= 1 \\ \cos(\theta_x - \theta_y) &= \cos\theta_x \cos\theta_y + \sin\theta_x \sin\theta_y \end{aligned} \tag{C.17}$$

this leads to the following final expression of the magnitude response, as follows:

$$M(\Omega) = \alpha_i^{'}(1 + 2\beta_i \cos\Omega + \beta_i^{\,2})^{1/2} = \alpha_i^{'}\left[1 + (\frac{2\beta_i}{1+\beta_i^{\,2}})\cos\Omega\right]^{1/2} \qquad \text{(C.18)}$$

where $\Omega = \Omega_2 - \Omega_1$.

Defining the self-referencing parameter R_i as the ratio between voltages at the reception stage for different electrical phase-shifts, it yields:

$$R_i = \frac{V_O(f,\Omega_2)}{V_O(f,\Omega_1)} = \frac{M(f,\Omega_2)\big|_{\Omega_1=0}}{M(f,\Omega_1)\big|_{\Omega_2=0}} = \frac{[1+(\frac{2\beta_i}{1+\beta_i^{\,2}})\cos\Omega_2]^{1/2}}{[1+(\frac{2\beta_i}{1+\beta_i^{\,2}})\cos\Omega_1]^{1/2}} \qquad \text{(C.19)}$$

where f is the modulation frequency of the optical light source and Ω_1 and Ω_2 are the electrical phase-shifts applied to the RF modulating signal at the reference and sensing channel, respectively.

On the other hand, the output phase self-referencing parameter ϕ_i, through the phasor theory, can be given by:

$$\phi_i = \arctan\left(\frac{\Im H(z)}{\Re H(z)}\right) \qquad \text{(C.20)}$$

Taking advantage of Eq. C.15, ϕ_i finally yields:

$$\phi_i = \arctan\left[\frac{-(\sin\Omega_1 + \beta_i \sin\Omega_2)}{(\cos\Omega_1 + \beta_i \cos\Omega_2)}\right] \qquad \text{(C.21)}$$

C.3 Self-referencing parameters sensitivity

In order to have a more precise information, the detailed analysis of the mathematical expression of the sensitivity of both self-referencing parameters R and ϕ, versus the power modulation β, is considered in this section.

Let S_m be the sensitivity of the intensity sensor with regards to the variations of a measurand, *m*.

$$S_m = \frac{\partial F(m)}{\partial m} \qquad \text{(C.22)}$$

In order to highlight the performance of the self-referencing parameter R, by means of its sensitivity with regards to the power modulation β, Eq. C.22 can be applied yielding:

$$S_R = \frac{\partial R(\Omega_1, \Omega_2, \beta)}{\partial \beta} \tag{C.23}$$

Considering the expression of R in Eq. C.19 and using the derivative rule of a quotient given by:

$$\left(\frac{f}{g}\right)' = \frac{f' \cdot g - f \cdot g'}{g^2} \tag{C.24}$$

Operating in Eq. C.23, it can be obtained:

$$S_R = \frac{\partial R(\Omega_1, \Omega_2, \beta)}{d\beta} = -\frac{(1+2\beta\cos\Omega_2+\beta^2)^{1/2}(2\beta+2\cos\Omega_1)}{2(1+2\beta\cos\Omega_1+\beta^2)^{3/2}} + \\ + \frac{2\beta+2\cos\Omega_2}{2(1+2\beta\cos\Omega_2+\beta^2)^{1/2}(1+2\beta\cos\Omega_1+\beta^2)^{1/2}} \tag{C.25}$$

Simplifying the above expression, it yields to the one given by Eq. 6.6 on page 250:

$$S_R(\Omega_1, \Omega_2, \beta) = \frac{(\cos\Omega_2 - \cos\Omega_1)[1-\beta^2]}{(1+2\beta\cos\Omega_1+\beta^2)^{3/2}(1+2\beta\cos\Omega_2+\beta^2)^{1/2}} \tag{C.26}$$

On the other hand, in order to highlight the performance of the self-referencing parameter ϕ, by means of its sensitivity with regards to the power modulation β, Eq. C.22 can be applied yielding:

$$S_\phi = \frac{\partial \phi(\Omega_1, \Omega_2, \beta)}{\partial \beta} \tag{C.27}$$

Similarly, considering the expression of ϕ in Eq. C.21 and using the derivative rule of an inverse trigonometric function given by:

$$\frac{d\,arctag(x)}{dx} = \frac{x'}{1+x^2} \tag{C.28}$$

Operating in Eq. C.27 it can be obtained:

$$S_\phi = \frac{\partial \phi(\Omega_1, \Omega_2, \beta)}{d\beta} = -\frac{\sin\Omega_2}{\beta\cos\Omega_2+\cos\Omega_1} - \frac{\cos\Omega_2(-\beta\sin\Omega_2-\sin\Omega_1)}{(\beta\cos\Omega_2+\cos\Omega_1)^2} \tag{C.29}$$

Taking advantage of the trigonometric identities defined by:

$$\begin{aligned}\sin(\theta_x - \theta_y) &= \sin\theta_x \cos\theta_y - \cos\theta_x \sin\theta_y \\ \cos(\theta_x - \theta_y) &= \cos\theta_x \cos\theta_y + \sin\theta_x \sin\theta_y\end{aligned} \tag{C.30}$$

the above expression can be simplified, yielding to the one given by Eq. 6.7 on page 251:

$$S_\phi(\Omega_1, \Omega_2, \beta) = \frac{\sin(\Omega_1 - \Omega_2)}{1 + 2\beta\cos(\Omega_1 - \Omega_2) + \beta^2} \tag{C.31}$$

Appendix D

Specifications and characterization of the lab equipment

D.1 Optical sources

The optical sources used for the different experiments within all this work are the following ones (in order of appearance):

- Laser diode Model RS3a635-5 (Power Technology Inc., www.**powertechnology**.com) ; C2[1]

Specifications of this device can be seen in Table D.1.

Module specs.	RSa635-5
Wavelength (nm)	635
Maximum Output Power (mW)	5 (Class IIIa)
Operating Voltage (Vdc)	3.3 - 9
Max. Operating Current (mA)	65
Max. Laser Drive (mA)	60
Diode Compatibility	N-type

Table D.1.- Main features from the laser diode model RS3a635-5.

- Single F-P laser source Model 81655A (Agilent Technologies, www.**home.agilent**.com); C3 and C4

The Agilent 81655A Fabry-Perot laser source is a single-wavelength module. The 81655A Fabry-Perot laser module is insensitive to back reflections and is stabilized for short and long-term applications. Specifications apply to the end of a 2m-long fibre cable (as specified under fibre type) with Diamond® HMS-10/Agilent connectors attached. All specifications are valid for an attenuation setting of 0.0 dB. The module requires straight output connectors, in this case, FC/PC. Moreover, the output power of the source module can be attenuated from 0 dB to 6 dB in steps of 0.1 dB and it provides an internal coherence control for linewidth broadening. Table D.2 shows its main technical specifications.

[1] Hereafter, Ci refers to the Chapter number in which the optical source appears. For instance, C2 denotes that the optical source considered was used within the scope of Chapter 2.

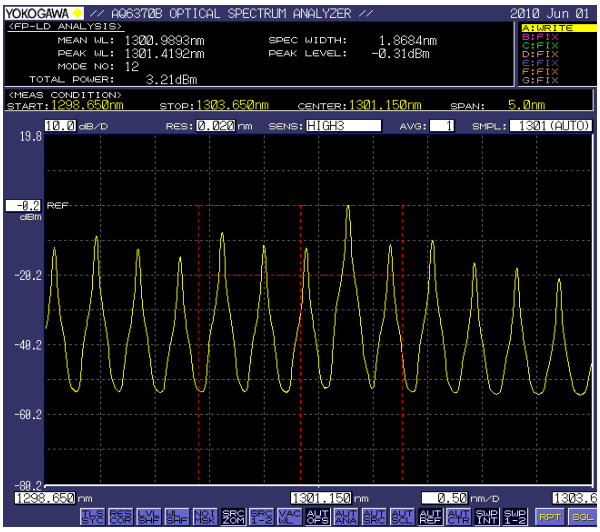

Fig. D.1.- Measured 81655A rms linewith by means of an Optical Spectrum Analyzer (model AQ6370 from Yokogawa).

	Agilent 81655A
Type	Fabry-Perot Laser
Center wavelength	1310nm±15nm
Spectral linewidth (rms)	<5.5nm
Output power	>+13dBm (20mW) Class 1M
CW power stability[1,2]	
Short term (15 minutes)	<±0.005dB Typical <±0.003dB with coherence control active
Long term (24 hours)	Typical ±0.03dB
To back reflection (RL≥14dB)	Typical ±0.003dB
Operating temperature	0ºC to 45ºC
Warm-up time	60 minutes

Table D.2.- Technical specifications for Fabry-Perot source module.
Note. 1) Warm-up time 20, min if previously stored at the same temperature.
2) Controlled environment (ΔT=±1ºC).

- Compact tunable DFB laser source Model 81989A (Agilent Technologies, www.**home.agilent**.com); C3 and C4

The Distributed Feedback (DFB) laser source type below specified is a tunable laser source for which the wavelength can be varied through a specified range. It also allows to set the output power and to choose between continuous wave (CW) or modulated wave. However, during the experiments the wavelength was set to 1550nm, with an output power of +6dBm in CW mode. The following table, Table D.3, resumes its main features. Fig. D.2 depicts the measured laser source measured linewidth. As the highest wavelength resolution provided by the OSA is ~0.02nm (identical to that measured for the source linewidth) we can conclude that there is no wavelength resolution to determine the effective optical source linewidth, being the latter, at least, <0.018nm (i.e. Δf<2.24THz, which yields within the specifications).

	Agilent 81989A
Type	Distributed Feedback (DFB) Laser
Laser Type	ECL[2]-Laser InGaAsP
Wavelength range	1465nm-1575nm
Max. CW output power (rms)	30mW
Beam waist diameter	9 µm
Numerical aperture	0.1
Laser class	1M
Wavelength resolution	5pm, 625MHz at 1550nm
Absolute wavelength accuracy	±100pm
Wavelength repeatability	±5pm
Wavelength stability (typ. over 24h)[1]	±5pm
Linewidth (typ.), coherence control off Effective linewidth (typ.), coherence control on[2]	100kHz >50MHz (1525nm-1575nm)
Maximum output power (continuous power during tuning)	≥+14.5dBm peak (typ.) ≥+13dBm (1525nm-1575nm) ≥+10dBm (1465nm-1575nm)
Power linearity	±0.1dB
Power stability[1]	±0.01dB over 1 hour typ. ±0.0075dB over 1 hour typ. ±0.03dB over 24 hours
Power flatness versus wavelength	±0.2dB, typ. ±0.1dB (1525nm-1575nm) ±0.3dB, typ. ±0.15dB (full range)
Side-mode suppression ratio (typ.)[2]	≥50dB
Signal to source spontaneous emission ratio[1]	≥25dB ≥30dB (1525nm-1575nm)
Relative intensity noise (RIN) (typ.)[1]	-145dB/Hz (0.1GHz-6GHz)

Table D.3.- Technical specifications for DFB laser source module.
Note. 1) At constant temperature ±0.5ºK.
2) At maximum output power as specified per wavelength range.

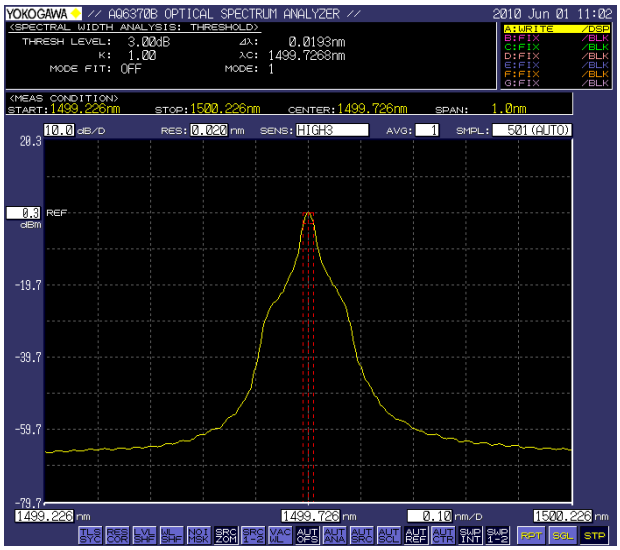

Fig. D.2.- Measured 81989A rms linewith by means of an Optical Spectrum Analyzer (model AQ6370 from Yokogawa).

[2] ECL: Electrogenerated Chemiluminiscent

- Light Emitting Diode (LED) Model AF-OS420 (Advanced Fiber Solutions, www.**afsi**.us); C3

The AF-OS420 is a rugged, low cost LED light source optimized for testing 50µm and 62.5µm multimode applications. The AF-OS420 has two LED outputs, a 850nm and a 1300nm fixed ST-connectorized active device mounts. The unit features a three position slide switch, 850nm-OFF-1300nm with a low battery indicator. Fig. D.3 depicts the measured *W*=98nm rms source linewidth.

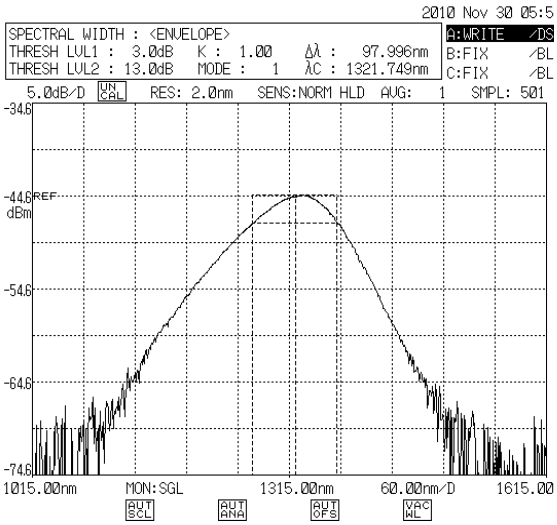

Fig. D.3.- Measured LED rms linewith by means of an Optical Spectrum Analyzer (model AQ-6315A from ANDO, lately Yokogawa).

Table D.4 resumes its main features:

	AF-OS420
Type	LED
Wavelength	850nm / 1300nm
Modulated frequencies	CW
Stability per hour	Less than 0.05dB
Power output	>-20dBm
Connector style	ST
Operation temperature	-10ºC to +50ºC (45% Hum, non condensing)

Table D.4.- Technical specifications for the LED optical source module.

- Broadband Light Source Fibolux Multi 9SLD-Source (Agilent Technologies, www.**home.agilent**.com); C4

The Fibolux light source provides a depolarized output which covers a wavelength range from 1250nm to 1650nm. Moreover, to eliminate back reflection and resulting interference the light source is equipped with isolators at both outputs. Due to this, source reflections do almost not result in any change of the output power or wavelength. Fig. D.4 depicts the measured optical spectrum.

Fig. D.4.- Measured LED rms linewith by means of an Optical Spectrum Analyzer (model AQ6370 from Yokogawa).

Table D.5 resumes its main features:

	9SLD
Type	SLED (Superluminiscent Diode)
Spectral range	1250nm - 1650nm
Spectral power density	Min. -30dBm/nm@spectral range Min. -25dBm/nm@360nm of spectral range
Total power	Typ. 40mW
Power stability	±20mdB@15min
Connector style	FC/PC
Environmental condition	non condensing 5ºC - 35ºC (operation) non condensing -20ºC - 60ºC (storage)

Table D.5.- Technical specifications for the LED optical source module.

- Broadband Light Source, Superluminiscent Erbium-Doped SLED Model 93/3627/EOG/01 (Photonetics FiberWhite, www.**home.agilent**.com); C5 and C6

The FiberWhite optical source is a high-power broadband erbium-doped fibre source emitting in the 1.55µm telecommunication window. This optical source was available at INESC-Porto facilities. This optical source provides a spectral density within the C-band (1510-1560nm) with an adjustable maximum total emitted power of 84mW.

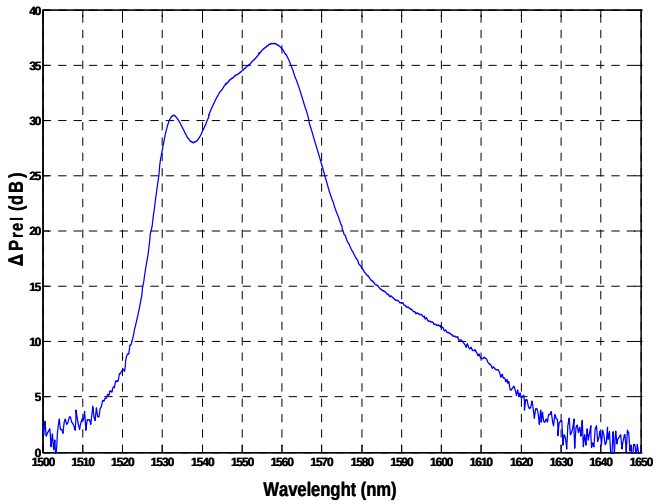

Fig. D.5.- Measured SLED spectrum by means of an Optical Spectrum Analyzer (model AQ-6315 from ANDO, lately Yokogawa).

D.2.- Optical detectors

The optical detectors used for the different experiments within all this work are the following ones (in order of appearance):

- High-speed PIN photodiode, Model DSC30S (Discovery Seminconductors Inc., www.**discoverysemi**.com); C3 and C4

This high-speed photodiode is hermetically sealed, with high reliability, low harmonic distortion with a minimum bandwidth of 18GHz and a 50Ω internal termination. Fig. D.6 depicts the measured optical spectrum, provided by the Lightwave Component Analyzer (LCA 8703B), latter described. It can be observed the flat response over a 20GHz frequency span.

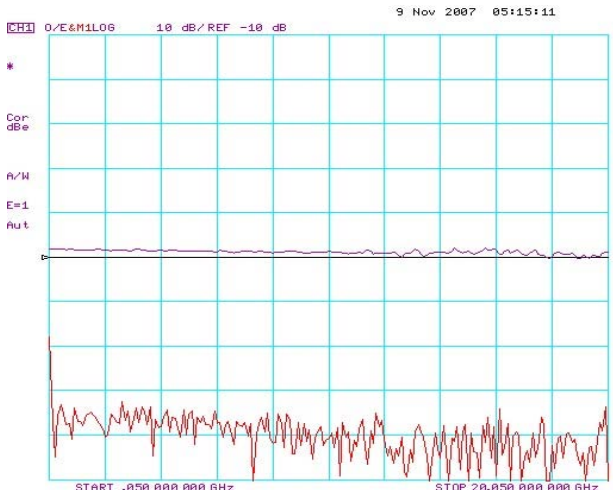

Fig. D.6.- Measured electrical response of the DSC30S provided by the LCA.

Table D.6 resumes its main features:

	DSC30S
Usable spectral wavelength	800nm – 1650nm
Responsitivity	0.8A/W@1550nm 0.8A/W@1310nm
Ripple[1]	±1dB
Group delay[2]	±7 ps
3-dB bandwidth	Min. 18GHz ; Typ. 22GHz
Dark current@25ºC, 5V	Typ. 10nA ; Max. 100nA
Optical return Loss	Min. 27dB ; Typ. 30dB
2nd Order Harmonic Distortion[3]	Min. -70dBc
3rd Order Harmonic Distortion[3]	Min. -75dBc
Polarization Dependent Loss (PDL)@1550nm	Typ. 0.05dB ; Max. 0.12dB
Operating temperature	0ºC to +70ºC
Optical Input Power Damage Threshold	+16dBm

Table D.6.- Technical specifications for the DSC30S photodiode.
Note. 1) Flatness – DC to 70% of the 3-dB bandwidth.
2) Group delay – DC to 70% of the 3-dB bandwidth.
3) At +4dBm Optical Power and 5.8 GHz fundamental.

- Switchable Gain, Amplified InGaAs photodetector, Model PDA400-EC (Thorlabs Inc., www.**thorlabs**.com); C5 and C6

The PDA400 is an amplified, switchable-gain, InGaAs detector designed for detection of light signals from DC to 10MHz. A five-position rotary allows the user to vary the gain in 10dB steps. A buffered output drives a 50ohm load impedance up to 5 volts. The PDA400 housing also includes a removable threaded coupler compatible with FC/APC connectors. This device was available at INESC-Porto facilities. Table D.7 resumes its main features:

	PDA400-EC
Detector	InGaAs
Active diameter	1mm
Wavelength Range	800nm – 1750nm
Peak response	0.95A/W@1550nm
Bandwidth	DC to 10MHz
NEP (Noise Equivalent Power)@1300nm	0dB Gain → $8.2 \cdot 10^{-12}$ W/√Hz 10dB Gain → $6 \cdot 10^{-12}$ W/√Hz 20dB Gain → $3.8 \cdot 10^{-12}$ W/√Hz 30dB Gain → $3.4 \cdot 10^{-12}$ W/√Hz 40dB Gain → $2.9 \cdot 10^{-12}$ W/√Hz
Transimpedance Gain	0dB Gain → $1.5 \cdot 10^{4}$ V/A 10dB Gain → $4.7 \cdot 10^{4}$ V/A 20dB Gain → $1.5 \cdot 10^{5}$ V/A 30dB Gain → $4.7 \cdot 10^{5}$ V/A 40dB Gain → $1.5 \cdot 10^{6}$ V/A
Output Voltage (50Ω)	0 to 5V
Output Impedance	50 ohms
Gain steps	0, 10, 20, 30, 40 dB
Output type	BNC
Operating temperature	-40ºC to +85ºC
Optical Input Power Damage Threshold	+16dBm

Table D.7.- Technical specifications for the PDA400-EC optical detector.

D.3.- Optical modulators

Three different optical intensity modulators have been used within the scope of this work. Whereas in the first part of this document, high-speed modulators (at both 1300nm and 1550nm) were needed, the second part of this work, related to the self-referencing sensor network scheme, requires also the use of an optical intensity modulator but with dramatically less operation frequency.

As the external modulator employed in the MMF link configuration at 1300nm and 1550nm come from the same manufacturer but operate at different wavelengths they will be grouped under the same subsection.

- Microwave analog intensity modulator, Models AM-130 & AM-150 (JDSU Uniphase Corp., www.**jdsu**.com); C3 and C4

Both analog intensity (amplitude) modulators are designed for use in microwave fibre-optic links that operate at frequencies up to 20GHz and beyond. Both provide an electro-optical (E/O) interface.

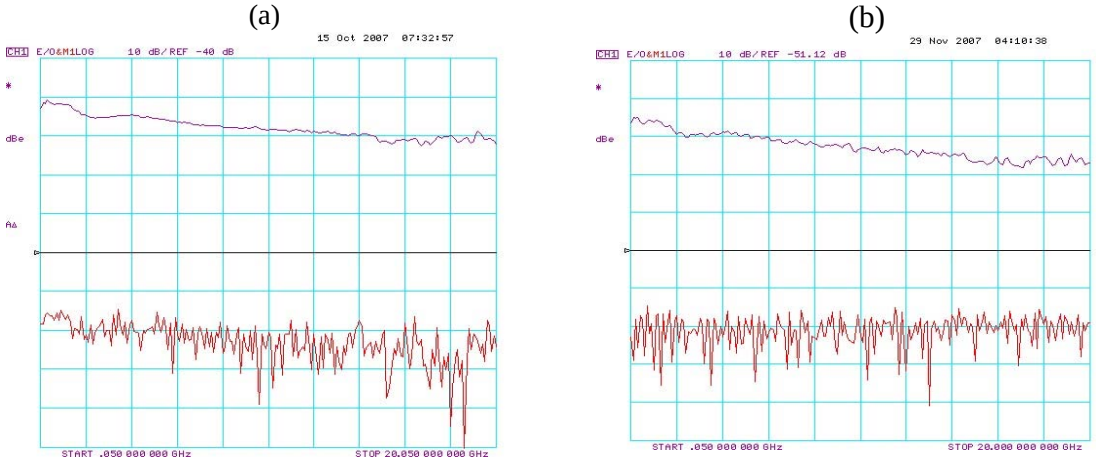

Fig. D.7.- (a) Measured electrical response of the E/O intensity modulator model JDSU AM-130 operating at 1300nm. (b) Measured electrical response of the E/O intensity modulator model JDSU AM-150 operating at 1550nm.

Table D.8 resumes their main features:

	AM-130	**AM-150**
Operating wavelength	1320±10nm	1550±10nm
Insertion loss	Max. 5dB	
On/off extinction ratio	Min. 20dB	
Optical return loss	Max. -45dB	
RF input power	Max. 27dBm	
RF port impedance	50Ω	
Input optical power	Max. 200mW	
Electrical connectors	SMA connectors	
Fibres 1320nm device, PM input 1320nm device, SM output 1550nm device, PM input 1550nm device, SM output	 Fujikura SM 13-P-7/125-UV/UV-100 SMF-28 Fujikura SM 15-P-8/125-UV/UV-100 SMF-28	
Operating temperature	0ºC to +70ºC	

Table D.8.- Technical specifications for the JDSU AM-130 and AM-150 analog modulators, respectively.

- Acousto-optic modulator, Model BRI-AM-100-870-1550 (Brimrose Corporation of America, www.**brimrose**.com); C5 and C6

The following figures refer to the device characterization:

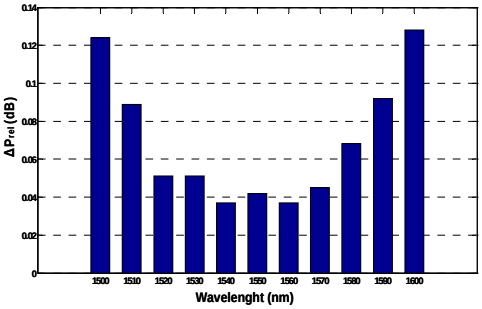

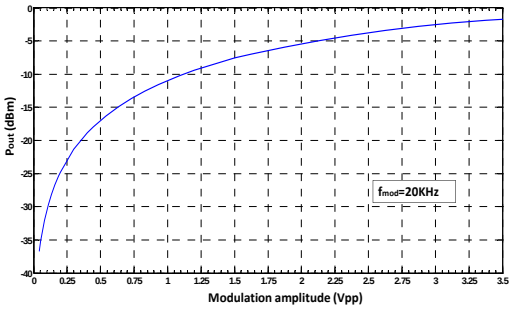

(b)

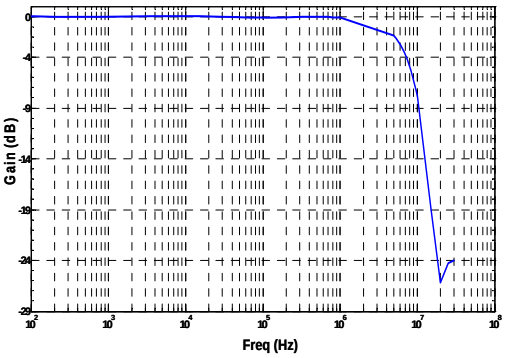

(c)

Fig. D.8.- (a) Modulator relative insertion losses versus wavelength. For a range of 1520-1570nm the modulator shows the maximum losses for a fixed input power value. Modulation amplitude and frequency modulation are fixed at 3Vpp and 20kHz, respectively. (b) Optical output power of the modulator versus applied modulation amplitude (clearly shows an exponential dependence) at 1550nm operating wavelength. Modulation frequency was set to 20kHz. (c) Bode diagram of the modulator for λ=1550nm. Cut-off frequency stands at 5Mhz approximately.

.

Acousto-optic modulators (AOM), also called Bragg cells, use the acousto-optic effect to diffract and shift the frequency of light using sound waves (usually at radio-frequency). A piezoelectric transducer is attached to a material such as glass. An oscillating electric signal drives the transducer to vibrate, which creates sound waves in the glass. These can be through of as moving periodic planes of expansion and compression that change the index of refraction. Incoming light scatters off the resulting periodic index modulation and interference occurs similar to in Bragg diffraction. Fig. D.9 shows a photograph of the device as well as its driver and Table D.9 resumes the main features of the model used in the experiments:

Figure D.9.- Photographs of the acousto-optic modulator (left) and its driver (right).

	AMM-100-8
Data performed@	1550nm
Optical power density	≤3W/mm^2
Center frequency	100MHz
Rise time	68ns
Digital Modulation Bandwidth	8MHz
Analog Video Bandwidth	5MHz
Optical Transmission	>95%
Bragg Angle	31mrad
Separation angle	62mrad
Maximum RF power	1W
Input impedance	50ohms

Table D.9.- Technical specifications for the Brimrose AM-100-8 acousto-optic modulator.

D.4.- Lightwave Component Analyzer

The Agilent 8703B Lightwave Component Analyzer (LCA), see Fig. D.10, is a general purpose instrument with calibrated 20 GHz capability for measuring optical, electrooptical and electrical components, assemblies and devices. In the following, the main specifications of the instrument and operation details for the calibrated measurements are reported.

The 8703B used in this work contains an internal lightwave source, an electro-optical modulator and a receiver for operation around 1555 nm (option 155). It also contains an internal microwave source and a receiver with operation bandwidth from 50 MHz to 20.05 GHz. This device it has been used to test the performance of silica-based MMF and PF GIPOF links within the scope of chapters 3 and 4.

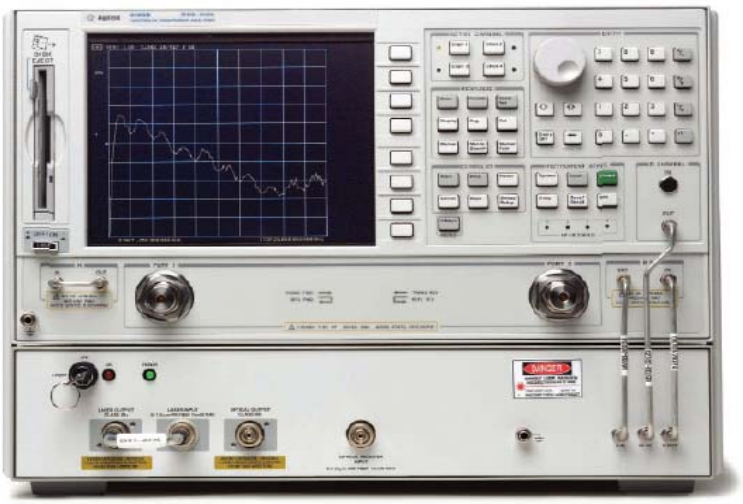

Figure D.10.- Front view of the Agilent 8703B LCA.

It is recommended that the operation temperature of the 8703B is in the range of +20ºC to +30ºC, after having a warm-up time of two hours in a stable ambient temperature. Its

internal lightwave source has an spectral width lower than 20 MHz and emits an average output power of +5 dBm. This laser can be modulated from 50 MHz to 20.05 GHz with an spectral accuracy of 1 Hz by an internal electro-optical modulator with an insertion loss of 9dB. The 8703B also accepts external light sources. On the other hand, the lightwave receiver can detect optical signals between 1000- 1600 nm. In the reception block of the 8703B an intermediate frequency (IF) filter with an electrical bandwidth from 10 to 6000 Hz is available. Averaging and smoothing of the captured signals is also possible, as it is typical in this kind of instruments.

One of the key benefits of the 8703B is its ability to perform calibrated measurements on optical components. Through the temperature-compensated optical components and error-correction algorithms, the 8703B removes the systematic errors from the measured data of a device under test (DUT).

A response calibration, which accounts for magnitude and phase errors due to the system modulation frequency, has been used for measuring the transmission characteristics of the multimode fibre links with the 8703B. Either the internal laser of the 8703B or an external lightwave source can be connected to the internal electro-optical modulator through a fiber jumper. Nevertheless, an external modulator can be also applied and calibrated. First, the response calibration is performed, measuring the transmission response of the transmitter-receiver pair, employing a 1 meter fiber jumper instead of the fibre link to evaluate. This fiber jumper performs as an optical calibration standard. Using this calibration data, the frequency and phase responses of the optical source, the electro-optical modulator and the photodetector are removed from the measurements.

D.5.- Optical fibres

Optical attenuation coefficients concerning the optical fibres employed for the measurements made in this work have been evaluated, by means of an OTDR. These coefficients have been evaluated for both silica- based MMF and PF GIPOF, respectively. In this section, some of the measured OTDR traces at the wavelengths 1310nm and 1550nm are presented.

The following pictures illustrate the OTDR traces from a 3050m-long 62.5/125µm core/cladding diameter silica-based MMF at 1310nm and 1550nm, a 100m-long 50/490µm core/cladding diameter PF GIPOF at 1310nm and 1500nm, a 50m-long 62.5/490µm core/cladding diameter PF GIPOF at 1310nm and a 100m-long 120/490µm core/cladding diameter PF GIPOF at 1310nm.

Table D.10 resumes the measured attenuation coefficients of the optical fibres shown in the following pictures. In all cases they fulfill with vendor’s specifications. The rest of fibres employed within this work take very similar attenuation values.

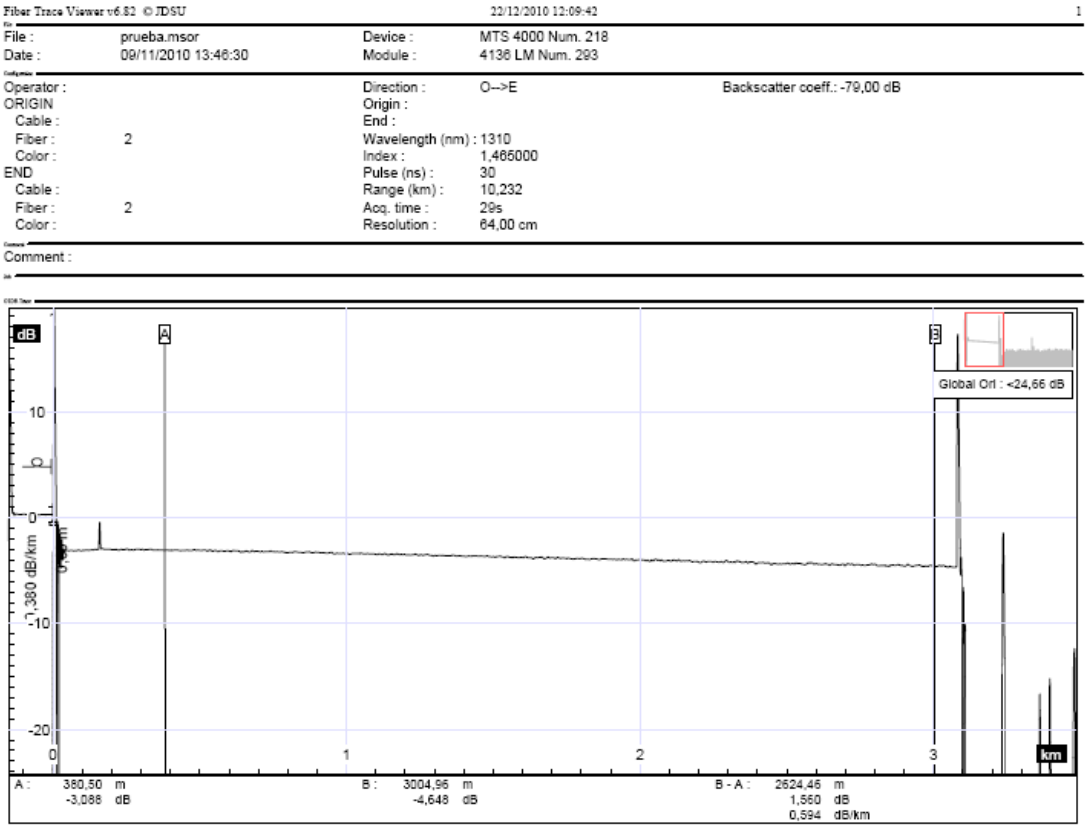

Figure D.11.- 3050m-long 62.5/125µm silica-based MMF OTDR trace @1310nm.

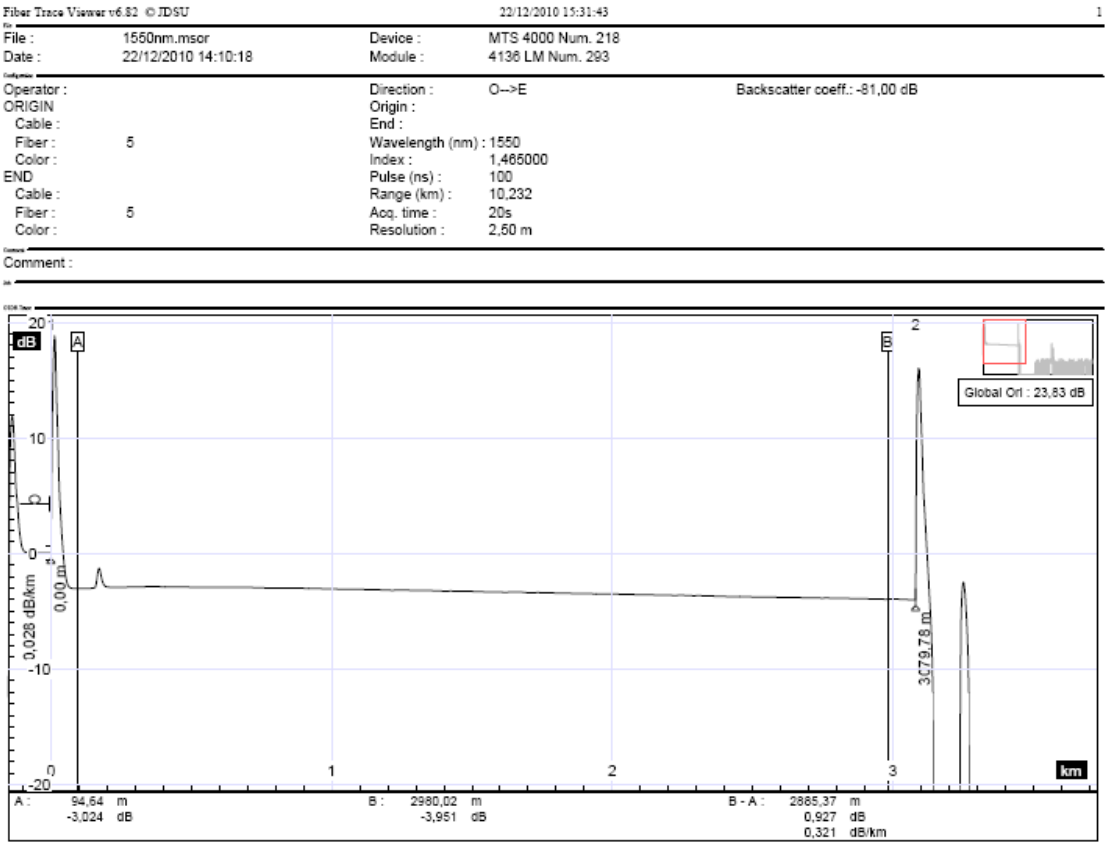

Figure D.12.- 3050m-long 62.5/125µm silica-based MMF OTDR trace @1550nm.

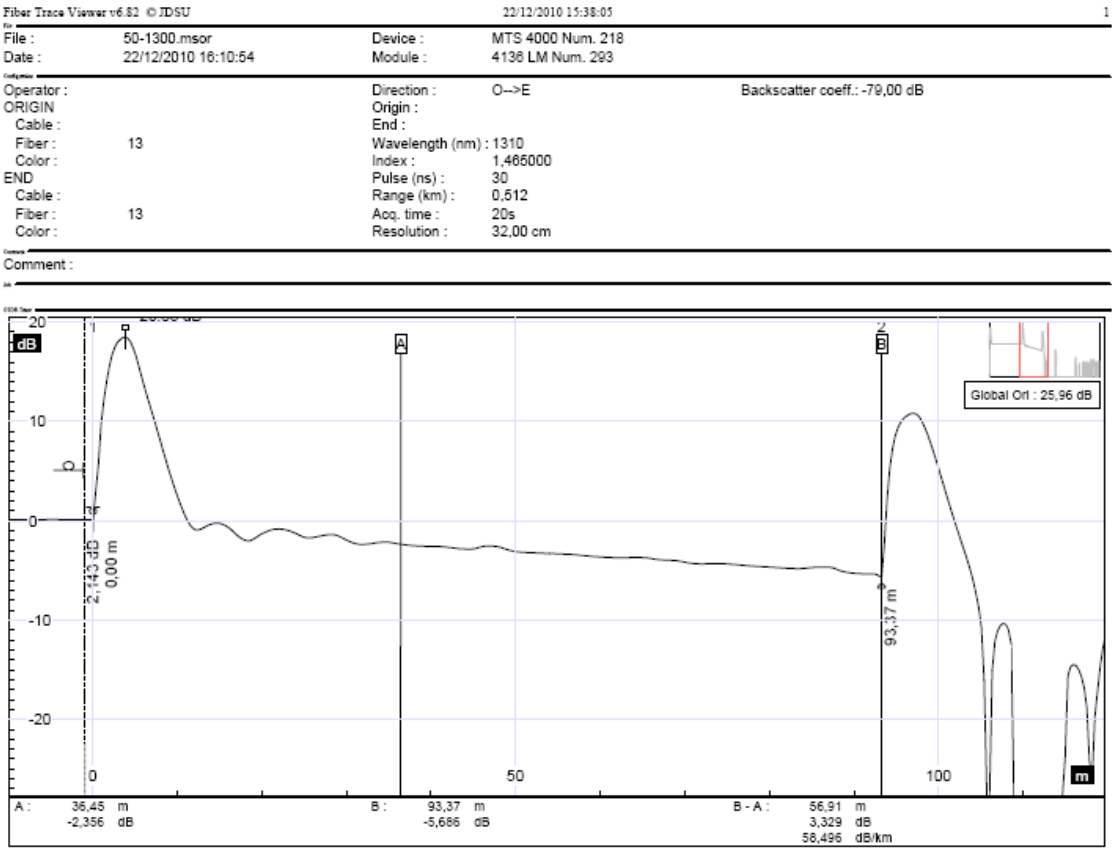

Figure D.13.- 100m-long 50/490µm PF GIPOF OTDR trace @1310nm.

Figure D.14.- 100m-long 50/490µm PF GIPOF OTDR trace @1550nm.

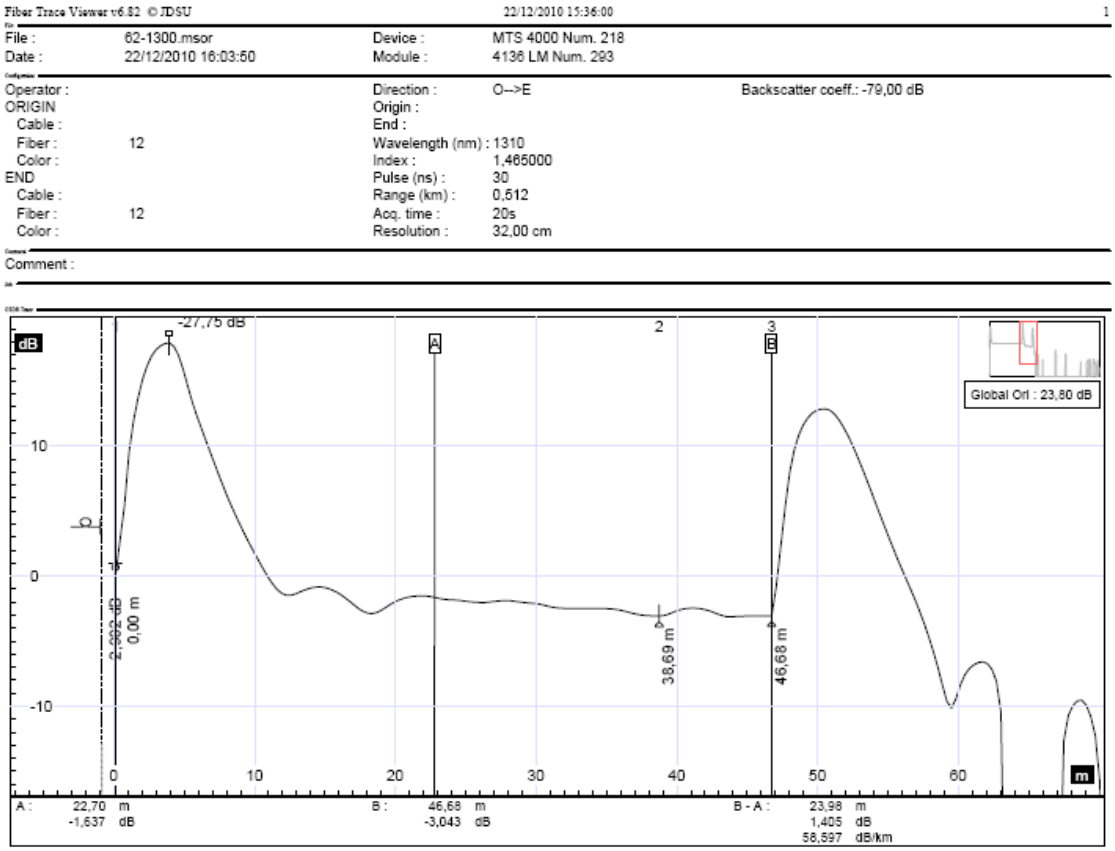

Figure D.15.- 50m-long 62.5/490µm PF GIPOF OTDR trace @1310nm.

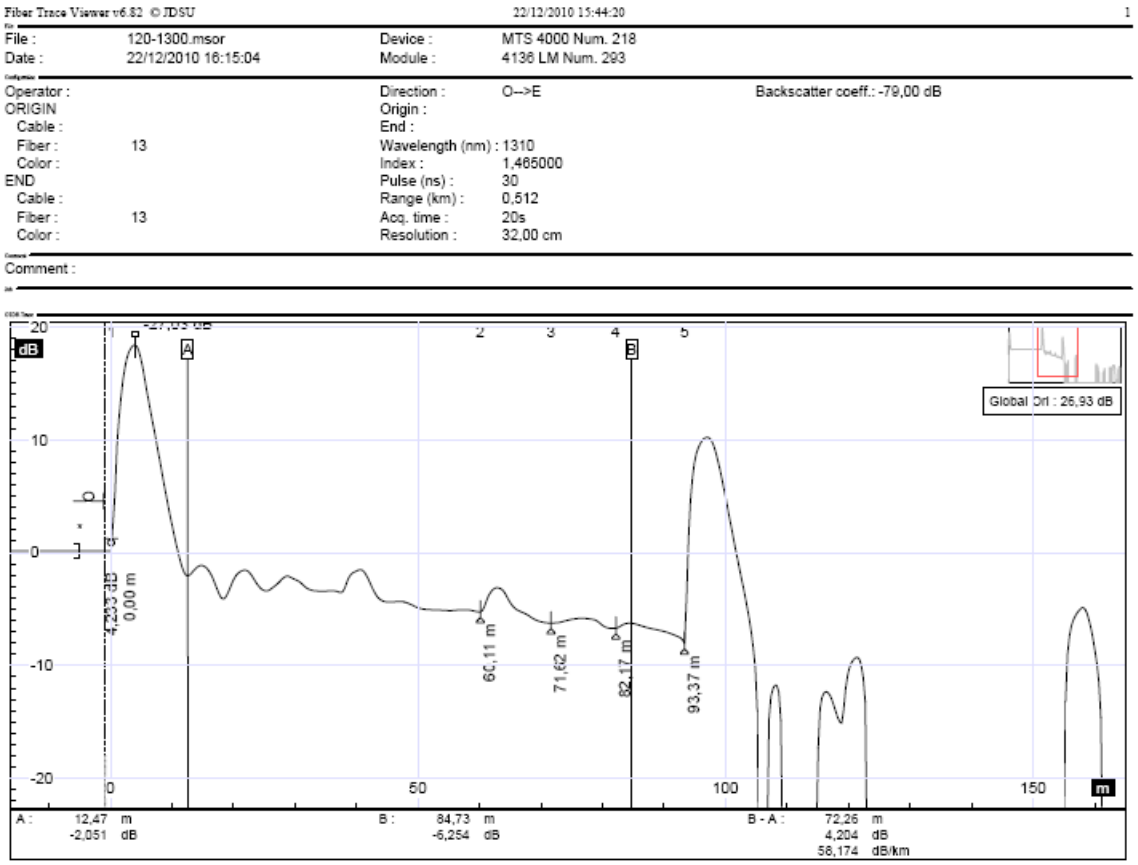

Figure D.16.- 100m-long 120/490µm PF GIPOF OTDR trace @1310nm.

Fibre Type	**Attenuation $\alpha_o(\lambda)$ (dB/km)**
3050m-long 62.5/125µm silica-based MMF @1310nm	0.594
3050m-long 62.5/125µm silica-based MMF @1550nm	0.321
100m-long 50/490µm PF GIPOF @1310nm	58.495
100m-long 50/490µm PF GIPOF @1550nm	57.794
50m-long 62.5/490µm PF GIPOF @1310nm	56.597
100m-long 120/490µm PF GIPOF @1310nm	58.174

Table D.10.- Optical attenuation coefficients of the optical fibres from the OTDR traces, from Fig. D.11 to Fig. D.16.

D.6.- Instrumentation

- Lock-In Amplifier, Model SR530 (Stanford Research Systems, www.**thinksrs**.com); C5 and C6

The SR530 is an analog lock-in amplifier which can measure AC signals as small as nanovolts in the presence of much larger noise levels. The dual phase SR530 has low-noise voltage and current inputs, high dynamic reserve, two stages of time constants, and an internal oscillator.

Table D.11 resumes its main features:

	SR530
Full scale sensitivity	Voltage: 100nV (10nV on expand) to 500mV Current: 100fA to 0.5µA
Maximum Inputs	Voltage: 100VDC, 10VAC damage threshold 2VAC peak-to-peak saturation Current: 10mA damage threshold 1µA ac peak-to-peak saturation
Noise	Voltage: 7nV/√Hz at 1kHz Current: 0.13pA/√Hz at 1kHz
Gain accuracy	1% (2Hz to 100kHz)
Gain stability	200ppm/ºC
Dynamic Reserve	20dB LOW (1µV to 500mV sensitivity) 40dB NORM (100nV to 50mV sensitivity) 60dB HIGH (100nV to 5mV sensitivity) Bandpass filter adds 20 dB to dynamic reserve Line notch filters increase dynamic reserve to 100dB
Reference channel	
Frequency	0.5Hz to 100kHz
Input Impedance	1MΩ, ac coupled
Trigger	SINE: 100mV minimum, 1Vrms nominal PULSE: ±1 Volt, 1µsec minimum width
Slew Rate	1 decade per 10 S at 1kHz
Phase control	90º shifts Fine shifts in 0.025º steps
Phase noise	0.01º rms at 1kHz, 100msec, 12dB TC
Phase error	Less than 1º above 10Hz

Table D.11.- Technical specifications for the SR530 Lock-In Amplifier from Stanford Research Systems.